

18  
SBIE

1 LEVEL

19  
AD-E440 018  
NOV 1978

14  
ARLCB-SP-74913

6

PROCEEDINGS OF THE

1

AD A062296

**US ARMY SYMPOSIUM ON GUN DYNAMICS (2nd)**

Held at THE INSTITUTE ON MAN AND SCIENCE,  
RENSSELAERVILLE, N.Y.

Official Rept.

19-22 SEPTEMBER 1978

7DC FILE COPY

11 Sep 78

10  
Thomas E. Simkins  
Julian S. Wu

12 369p.

DDC  
RECEIVED  
DEC 19 1978  
B

SPONSORED BY  
**US ARMY ARMAMENT RESEARCH AND DEVELOPMENT COMMAND**  
**LARGE CALIBER WEAPON SYSTEMS LABORATORY**  
BENET WEAPONS LABORATORY  
WATERVLIET, N.Y. 12189

DISTRIBUTION STATEMENT A  
Approved for public release  
Distribution Unlimited

449 224

78 11 15 034

REPORT DOCUMENTATION PAGE		READ INSTRUCTIONS BEFORE COMPLETING FORM
1. REPORT NUMBER ARLCB-SP-78013	2. GOVT ACCESSION NO.	3. RECIPIENT'S CATALOG NUMBER
4. TITLE (and Subtitle) Proceedings, Second U.S. Army Symposium on Gun Dynamics		5. TYPE OF REPORT & PERIOD COVERED  FINAL
		6. PERFORMING ORG. REPORT NUMBER
7. AUTHOR(s) EDITORS: T. E. Simkins J. J. Wu		8. CONTRACT OR GRANT NUMBER(s)
9. PERFORMING ORGANIZATION NAME AND ADDRESS US Army Armament Research & Development Command Watervliet Arsenal, Watervliet, NY 12189 ATTN: DRDAR-LCB-R		10. PROGRAM ELEMENT, PROJECT, TASK AREA & WORK UNIT NUMBERS
11. CONTROLLING OFFICE NAME AND ADDRESS		12. REPORT DATE September 1978
		13. NUMBER OF PAGES
14. MONITORING AGENCY NAME & ADDRESS (if different from Controlling Office)		15. SECURITY CLASS. (of this report)  UNCLASSIFIED
		15a. DECLASSIFICATION/DOWNGRADING SCHEDULE
16. DISTRIBUTION STATEMENT (of this Report)		
<div style="display: flex; justify-content: space-between; align-items: center;"> <div>NO RESTRICTION</div> <div style="border: 1px solid black; padding: 5px; text-align: center;"> <b>DISTRIBUTION STATEMENT A</b>            Approved for public release;            Distribution Unlimited         </div> </div>		
17. DISTRIBUTION STATEMENT (of the abstract entered in Block 20, if different from Report)		
18. SUPPLEMENTARY NOTES		
19. KEY WORDS (Continue on reverse side if necessary and identify by block number)  Ballistics, Precision, Target Acquisition, Dynamics, Barrel Vibration, Stabilization		
20. ABSTRACT (Continue on reverse side if necessary and identify by block number)  Twenty papers on various aspects of analysis, design and instrumentation of gun dynamics are presented by authors from five universities, five industrial research laboratories and various laboratories of the U.S. Army, Navy, and Air Force.		

D D C  
RECEIVED  
DEC 19 1978  
B

ARLCB-SP-78013

PROCEEDINGS OF THE  
**SECOND US ARMY SYMPOSIUM ON GUN DYNAMICS**

THE INSTITUTE ON MAN AND SCIENCE  
RENSSELAERVILLE, N.Y.

19 - 22 SEPTEMBER 1978

EDITORS:

THOMAS E. SIMKINS, BENÉT WEAPONS LABORATORY, LCWSL, ARRADCOM  
JULIAN J. WU, BENÉT WEAPONS LABORATORY, LCWSL, ARRADCOM

SPONSORED BY

**US ARMY ARMAMENT RESEARCH AND DEVELOPMENT COMMAND**  
**LARGE CALIBER WEAPON SYSTEMS LABORATORY**  
BENÉT WEAPONS LABORATORY  
WATERVLIET, N.Y. 12189

**DISTRIBUTION STATEMENT A**

**Approved for public release;  
Distribution Unlimited**

## FOREWORD

The precision of a gun system clearly involves the dynamics of the gun carrier, ground characteristics, interior and exterior ballistics. It is a problem of enormous complexity and is often divided into different phases for investigation purposes. While the division of the task is convenient and often necessary, one should always keep in mind that the different phases interact and the dynamic forces are usually coupled. This fact necessitates an interactive process or, better yet, a complete system approach, if at all possible, to the precision problem.

During recent years, one has witnessed great strides in various branches of continuum mechanics, kinematic designs, numerical-and-computer techniques for solving problems of great complexity as well as in the areas of experimental mechanics and instrumentation. It appears feasible now more than ever to gain understanding and to improve the design of gun systems for greater accuracy by exploiting the new technological advances. The present Symposium represents the continuing interest of the U.S. Army in this direction.

ACCESS		
NTIS	Section	<input checked="" type="checkbox"/>
DDC	Section	<input type="checkbox"/>
UNANNOUNCED		<input type="checkbox"/>
JUSTIFICATION		
BY		
DISTRIBUTION/AVAILABILITY CODES		
Dist. AVAIL and/or SPECIAL		
A		



These proceedings contain twenty papers presented at the Symposium held at Institute on Man and Science, Rensselaerville, N.Y. during 19-22 September 1978. The papers represent the current research efforts on gun dynamics and its effect on precision and design by industrial, university and Department of Defense laboratories.

## LIST OF SPEAKERS, SESSION CHAIRMEN AND AUTHORS

### SPEAKERS:

OPENING REMARKS: BG D. W. Einsel, Jr., ARRADCOM

BANQUET SPEAKER: Mr. R. E. Falconer, SUNYA

### SESSION CHAIRMEN:

SESSION I: Dr. D. A. Gyrog, ARRADCOM

SESSION II: Dr. F. W. Schmiedeshoff, ARO

SESSION III: Dr. T. E. Davidson, ARRADCOM

SESSION IV: Dr. J. T. Frasier, ARRADCOM

### AUTHORS:

G. A. Benedetti, Sandia Corporation  
R. M. Blakney, Falcon R&D, Inc.  
A. P. Boresi, University of Illinois  
K. Y. Chang, University of Iowa  
C. J. Chen, University of Iowa  
P. A. Cox, Southwest Research Institute  
W. Donnally, Telemetry Br., ARRADCOM  
P. E. Ehle, SCWSL, ARRADCOM  
K. S. Fansler, Ballistic Research Laboratory, ARRADCOM  
E. J. Haug, University of Iowa  
C. L. Henry, Ballistic Research Laboratory, ARRADCOM  
J. C. Hokanson, Southwest Research Institute  
G. Soo Hoo, Naval Surface Weapons Center  
R. C. Huang, University of Iowa  
T. D. Hutchings, ARRADCOM  
R. E. Kasten, Ware Simulation Centre, Rock Island Arsenal  
H. C. Langhaar, University of Illinois  
V. Levin, Innovative Technology, Inc.  
S. C. Lin, University of Iowa  
R. K. Loder, Ballistic Research Laboratory, ARRADCOM  
N. K. Loh, University of Iowa  
E. O. Macagno, University of Iowa  
A. N. Madiwale, Ware Simulation Division, Rock Island Arsenal  
R. E. Miller, University of Illinois  
R. M. Montoya, Naval Ordnance Station  
W. A. Nash, University of Massachusetts

J. O. Pilcher, Ballistic Research Laboratory, ARRADCOM  
E. M. Schmidt, Ballistic Research Laboratory, ARRADCOM  
C. N. Shen, Benet Weapons Laboratory, LCWSL, ARRADCOM  
T. E. Simkins, Benet Weapons Laboratory, ARRADCOM  
B. K. Stearns, General Electric Armament System Department  
F. D. Stockton, University of Massachusetts  
R. C. Walker, General Electric Armament Systems Department  
E. M. Wineholt, Ballistic Research Laboratory, ARRADCOM  
J. J. Wu, Benet Weapons Laboratory, LCWSL, ARRADCOM  
S. M. Wu, Ware Simulation Centre, Rock Island Arsenal

MEMBERS OF STEERING COMMITTEE

Dr. Thomas E. Simkins, General Chairman  
Benet Weapons Laboratory, LCWSL, ARRADCOM

Mr. Willard Benson  
Applied Science Division, LCWSL, ARRADCOM

Mr. Paul Ehle  
SCWSL, ARRADCOM

Dr. Edward J. Haug  
University of Iowa

Mr. Otto Heiney  
U.S. Air Force Armament Laboratory

Mr. Bruce Knutelsky  
Applied Science Division, LCWSL, ARRADCOM

Mr. James Pilcher  
Ballistic Research Laboratory, ARRADCOM

Dr. Ronald L. Racicot  
Benet Weapons Laboratory, LCWSL, ARRADCOM

Mr. Thomas Tscharin  
Naval Surface Weapons Laboratory

Dr. Julian J. Wu  
Benet Weapons Laboratory, LCWSL, ARRADCOM

## TABLE OF CONTENTS

	<u>Page</u>
SECTION I: GUN TUBE DYNAMICS DURING FIRING	
1. Measurement of Gun Barrel Motion with Optical Trackers B. K. Stearns and R. C. Walker, General Electric Armament Systems Dept	I-1
2. Measurement of Angular Muzzle Motion of a 105 mm Tank Gun During Firing R. M. Blakney, Falcon Research & Development Company	I-18
3. Muzzle Motions of the M68 105 mm Gun P. A. Cox and J. C. Hokanson, Southwest Research Institute	I-34
4. Excitation of a Gun Barrel Due to Firing H. L. Langhaar, R. E. Miller, and A. P. Boresi University of Illinois	I-58
5. Transverse Response of Gun Tubes to Curvature-Induced Load Functions T. E. Simkins, Benet Weapons Laboratory, LCWSL, ARRADCOM	I-66
SECTION II: MATHEMATICAL METHODS AND OPTIMIZATION PROCEDURES FOR PROBLEMS IN GUN SYSTEM DYNAMICS	
1. Dynamic Analysis and Design of Weapon Mechanisms with Intermittent Motion P. E. Ehle, ARRADCOM, R. C. Huang, and E. J. Haug, University of Iowa	II-1
2. Design Sensitivity Analysis of a Recoiling Gun on Elastic Supports E. J. Haug and R. C. Huang, University of Iowa	II-31
3. State Space Design for Helicopter Pointing and Tracking Systems N. K. Loh, University of Iowa, T. D. Hutchings, ARRADCOM, and R. Kasten, Ware Simulation Division, Rock Island Arsenal	II-52
4. Application of the Method of Characteristics to Gun Tube Problems W. A. Nash and F. D. Stockton, University of Massachusetts	II-69
5. Gun Dynamic Analysis by the Use of Unconstrained, Adjoint Variational Formulations J. J. Wu, Benet Weapons Laboratory, LCWSL, ARRADCOM	II-80

SECTION III: RECOIL RELATED PROBLEMS IN GUN DYNAMICS

1. A Study of Orifice Area and Orifice Discharge Coefficient in Recoil Mechanisms  
C. J. Chen, E. O. Macagno, K. Y. Chang, and S. C. Lin,  
Iowa Inst. of Hydraulic Research, University of Iowa III-1
2. Experimental Design for Evaluating the Dynamics of Soil/Mount Interaction  
L. B. Gardner, ARRADCOM III-17
3. Counter Recoil System Effects on Projectile Velocity in the Naval 5-Inch, 54-Caliber Gun  
R. M. Montoya, Naval Ordnance Station III-34
4. On the Sensitivity Coefficient of Exterior Ballistics and its Potential Matching to Interior Ballistics Sensitivity  
C. N. Shen, Benet Weapons Laboratory, LCWSL, ARRADCOM III-49
5. Closed Loop Control of Recoil Mechanisms  
R. E. Kasten, A. N. Madiwale, and S. M. Wu  
Ware Simulation Division, Rock Island Arsenal III-76

SECTION IV: PROJECTILE LAUNCH DISTURBANCES AND INSTRUMENTATION TECHNIQUES

1. A New In-Bore Data Acquisition Technique for Gun Tube/Projectile Dynamics  
W. Donnally, ARRADCOM IV-1
2. Muzzle Blast Induced Trajectory Perturbation of Nonconical and Conical Boattail Projectiles  
K. S. Fansler and E. M. Schmidt  
Ballistic Research Laboratory, ARRADCOM IV-12
3. Measurement of Balloting and Free Run Effects for a Projectile During Gun Launch  
G. A. Benedetti, Sandia Laboratories IV-28
4. Experimental Correlation of a Theoretical Model for Predicting Projectile Balloting  
G. Soo Hoo, Naval Surface Weapons Center IV-51
5. Accuracy Improvement of Flexible Gun Tubes - A Kalman Filter Approach  
V. Levin, Innovative Technology Inc. IV-67

**\*STEARNS and WALKER**

**TITLE: Measurement of Gun Barrel Motion with  
Optical Trackers**

**BURDETT K. STEARNS and R.C. WALKER  
General Electric Company  
Burlington, Vermont 05401**

**ABSTRACT:**

The measurement of gun barrel transverse and angular motion during firing is complicated by the relatively large recoil movement which occurs at the same time. Standard transducers are not designed to function under compound motion conditions and so other instrumentation techniques must be employed. The General Electric Company has been using optical trackers for such measurements for the last few years. This paper describes the procedures and equipment used and gives some typical test results for both linear and angular motion measurements. Two different schemes are used to measure angular motion. In one approach, two transverse linear displacement measurements are made at two closely spaced points. In the other scheme, a single tracker is used in conjunction with a small mirror mounted to the barrel. Muzzle flash and blast pressure from gun firing can cause distortion of optical measurements. Modifications of instrumentation procedures are suggested to minimize these effects.

**BIOGRAPHY:**

**PRESENT ASSIGNMENT: Development Engineer, Analytical Techniques,  
Armament Systems Department.**

**PAST EXPERIENCE: Structural Engineer, Boeing Airplane Company,  
Seattle, Washington, 1951-1954; Staff Member, Sandia Corp., Albuquerque,  
N.M., 1956-1961; Instructor, Structural Engineering Dept., Cornell  
Univ., Ithaca, N.Y., 1961-1965; Assistant Professor, Univ. of Vermont,  
Burlington, Vt., 1965-1968.**

**DEGREES HELD: Bachelor of Science, Univ. of Vermont, Burlington,  
Vt., 1950; Master of Science, Univ. of Illinois, Urbana, Ill., 1951;  
PhD. Cornell Univ., Ithaca, N.Y., 1965.**

\*STEARNS & WALKER

## MEASUREMENT OF GUN BARREL MOTION WITH OPTICAL TRACKERS

\*BURDETT K. STEARNS, PhD  
ROGER C. WALKER  
GENERAL ELECTRIC ARMAMENT SYSTEMS DEPARTMENT  
BURLINGTON, VERMONT 05401

### INTRODUCTION

The measurement of gun barrel transverse and angular motion during firing is complicated by the relatively large recoil movement which occurs at the same time. Standard measuring transducers are not designed to function under compound motion conditions and so other instrumentation techniques must be employed. However, there are a number of possible alternatives. One approach is to use high speed cine camera recording with subsequent data reduction to digital form. Another method is to use variable impedance transducers which operate on the eddy-current loss principle. A third method is to make use of the optical follower as a measuring device.

At General Electric, we have selected the latter approach and have been using optical trackers for gun barrel motion measurements for the last three years.<sup>(1)</sup> This paper describes the procedures and equipment used and gives some typical test results for both linear and angular motion measurements.

### OPTICAL TRACKERS

The trackers used for barrel motion measurement were manufactured by Optron, a Division of Universal Technology Incorporated of Woodbridge, Connecticut. The presentation in this section of the paper is, to a large extent, a synopsis of their instructional literature.

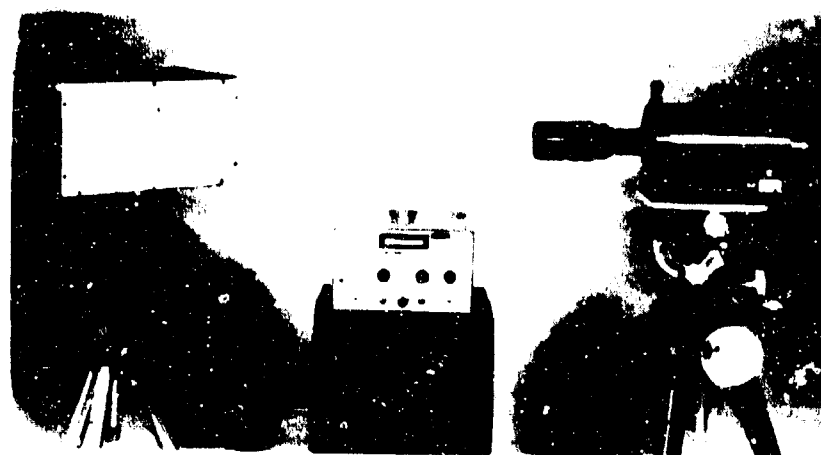
An optical tracker is an electro-optical displacement follower which is designed to track a target having a discontinuity in the intensity of light, reflected or emitted. In an Optron follower, the optics focus the target discontinuity onto a photo cathode of an image dissector tube. Electrons are emitted from the cathode as a function of the intensity of projected light. These electrons are accelerated



**\*STEARNS & WALKER**

and enter a small aperture where they are amplified to give a current output proportional to the number entering. A servo loop control positions the electron beam so that the target discontinuity is centered on the aperture. If the image moves, the control voltage changes so that the electron image is moved back to the original locked-on position by current in the tracker's deflection coils. The amount of current required to keep the electron image centered on the aperture is a measure of target displacement.

A complete tracking system consists of a control unit, a lens system, and an optical head. A photograph of the equipment is shown in Figure 1. The full scale measuring range of this system can be varied from .002 inches maximum to infinity by an appropriate selection of the lens system. Variable focus lenses and a variety of extension tubes are used to provide flexibility in adjusting field of view.



Light Source

Control Unit

Lens & Optical Head

Figure 1. Tracking System

The control unit provides an analog output suitable for recording on oscilloscopes, oscillographs, and tape recorders. The output is linearly proportional to displacement of the target and has a full scale value of 5 volts.

A target switch is located on the control unit which allows the system to track vertically or horizontally a dark target on a light background or a light target on a dark background. For the tracker to lock onto a target, the contrast in light intensities should be better than three to one.

\*STEARNS & WALKER

A viewing port is located on the optical head and is used for focusing and target alignment. A sketch of what is actually seen through the viewing port is shown in Figure 2. This is a typical set-up for measuring vertical motion with a single axis tracker. The rated linear displacement range of the system is indicated by the smaller square. The tracker should be located and adjusted so that the estimated maximum motion to be measured falls within this interior rectangular space. This will assure maximum accuracy. A 100 percent over-range allowance is provided in case the motion should exceed the rated displacement. However, linearity of the system is not guaranteed in this outer range.

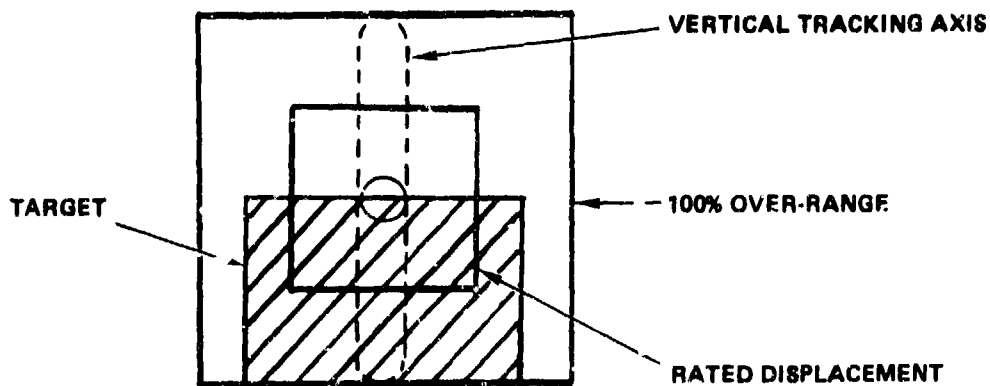


Figure 2. View Through Viewing Port

The closed dashed line in Figure 2 is not actually seen in the viewer but is included to indicate the region where the measurement is made. The target must be at least as wide as the tracking axis; however, much wider targets are easier to follow. Lock-on will be lost if the target moves entirely to one side of the vertical tracking axis.

Two different schemes are used for illuminating the target. If a discrete light to dark interface is used, such as a white surface partially covered with flat black paint, light is directed from the front. If an inherently dark target is used, light is directed from the back. This is done by placing a low power lamp and diffuser on the side of the target away from the tracker. The lamp is aimed directly into the lens, with the target interrupting the light. Usually, the back-lit target is easier to focus and track than other target configurations. A D.C. light source must be used because the tracker will detect any cyclical change in light intensity.

The optical tracking system resolution is less than 0.1 percent of the lens displacement. This is affected by low light levels, an improper lock-on, and an out-of-focus target.

### LINEAR AND ANGULAR MOTION MEASUREMENTS

A number of different exploratory tests were conducted on cylindrical rods to gain familiarity with optical tracker instrumentation. Initial displacement dynamic tests and vibration tests were used in establishing equipment set-up and procedural methods. Some of these tests are described in the following paragraphs for both linear and angular motion measurement.

An illustration of the typical set-up used for vertical motion measurement is shown in Figure 3. This was the arrangement used for an initial displacement dynamic test in which measurements were made of the motion of a solid cylindrical steel rod. The rod was 2.0 inches in diameter and was cantilevered from a test stand with an overhang of 60 inches. A concentrated weight was applied to the end of the rod to produce initial displacement. The load was then released suddenly and the rod tip vertical motion was measured.

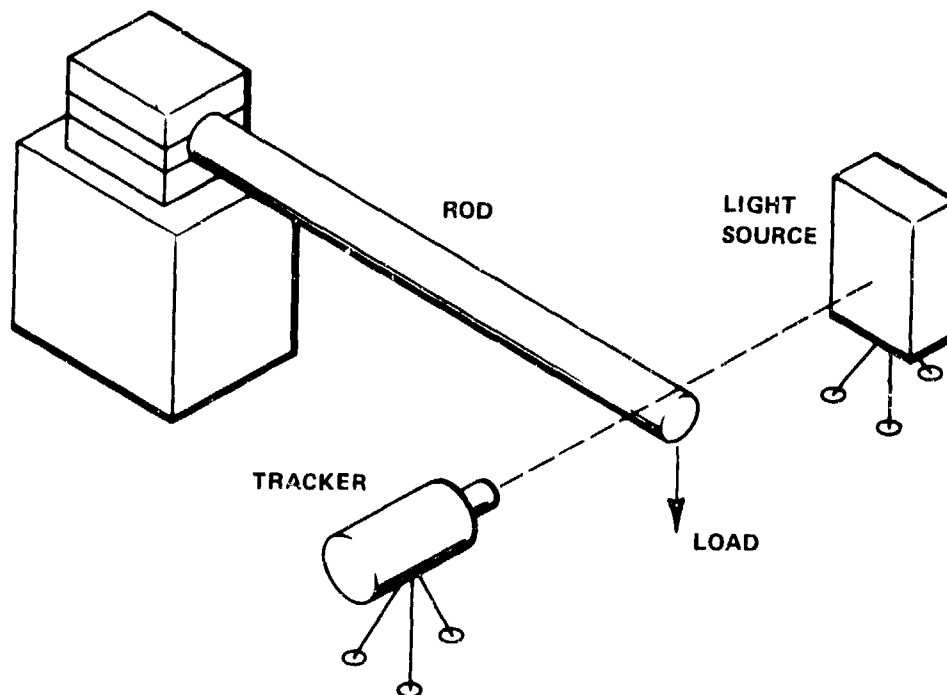


Figure 3. Initial Displacement Test Set-up

The tracker was tripod-mounted and elevated to the same height as the test rod. A D.C. light source was located on the opposite side of the barrel and pointed into the lens of the tracker. The dark surface of the rod served as the target. The tracker field of view was centered on the top of the rod, as shown in Figure 4, so that the entire lower half of the field was dark.

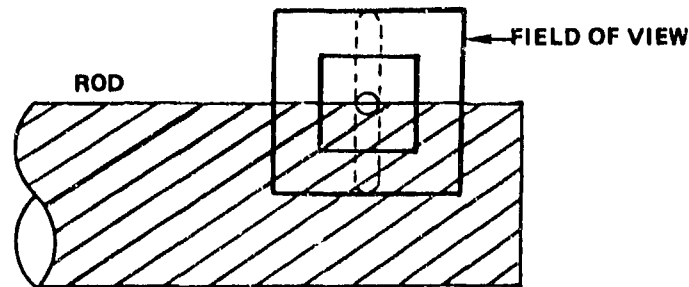


Figure 4. Field of View

To obtain high accuracy with the measuring system, the field of view was chosen to be only slightly larger than the initial displacement of the rod end. A 200 mm lens, with a 25 mm extension, was used with the tracker to target distance set at 40 inches. This combination of parameters was selected from available charts to give a  $\pm 0.26$  inch rated field of view.

Tracker calibration was carried out by placing gage blocks of various dimensions, in addition to a dial indicator, on top of the target and recording the tracker response on an oscillograph. The gage width versus response measurements are plotted in Figure 5. A 45-degree reference line is also shown. The response was quite linear for this particular set-up.

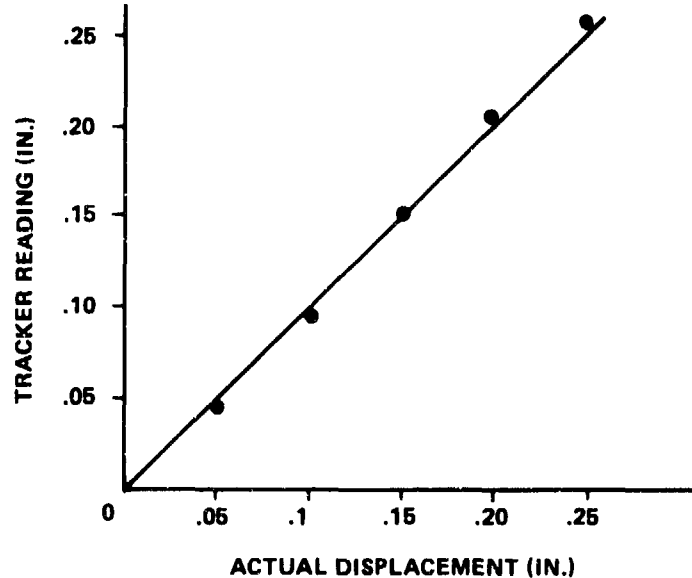


Figure 5. Linear Motion Calibration Curve

\*STEARNS & WALKER

A segment of the recorded vertical motion measurement is shown in Figure 6. Also included, for comparison purposes, is a plot of calculated motion from a 9-noded finite element analysis<sup>(2)</sup> which did not consider damping. The two curves correlate very well for this lightly damped structure, and reflect the effects of higher harmonics.

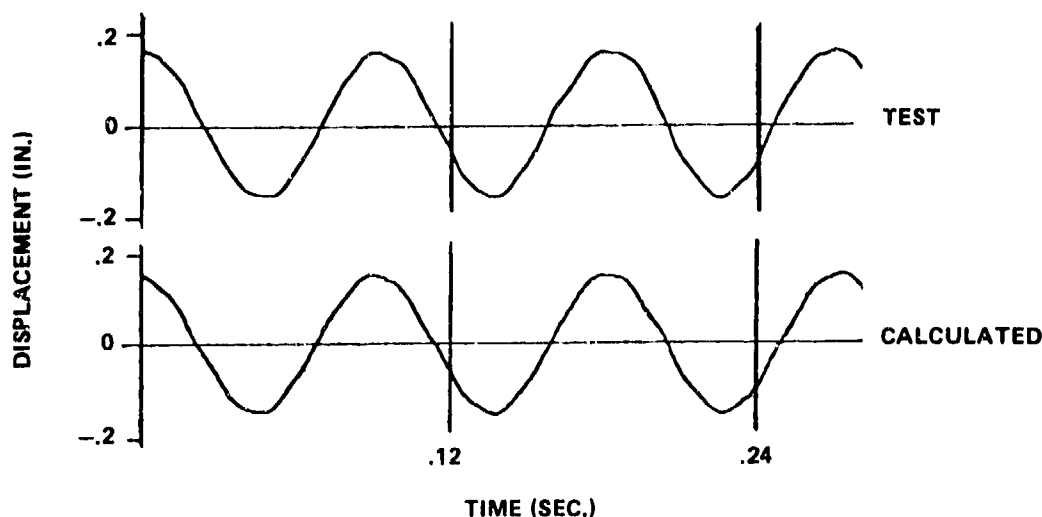


Figure 6. Vertical Motion

Two different schemes were used to measure angular motion. In one approach, two trackers are used to measure linear motion at two closely spaced points. An approximation of the angular motion is the algebraic sum of these two readings divided by the distance between the points. This procedure is automated electronically by combining the two signals in an analog circuit and applying a constant scale factor to include the division operation. The output to an oscillograph then gives the angular motion directly. Calibration is a logical extension of that used for displacement measurement. An example of this approach is shown in the next section.

\*STEARNS & WALKER

The second method of angular motion measurement is more difficult to set up but provides greater accuracy. A single tracker is used in conjunction with a small mirror mounted on the cylindrical rod. The mirror is attached to a small machined plate with epoxy cement and the plate in turn is clamped to the barrel at the specific location to be measured. See Figure 7.

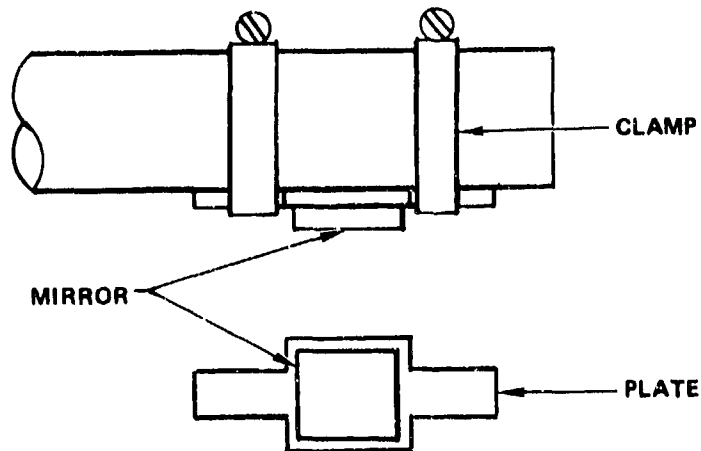


Figure 7. Mirror Mount

A typical tracker and target set-up for measuring pitching motion is sketched in Figure 8.

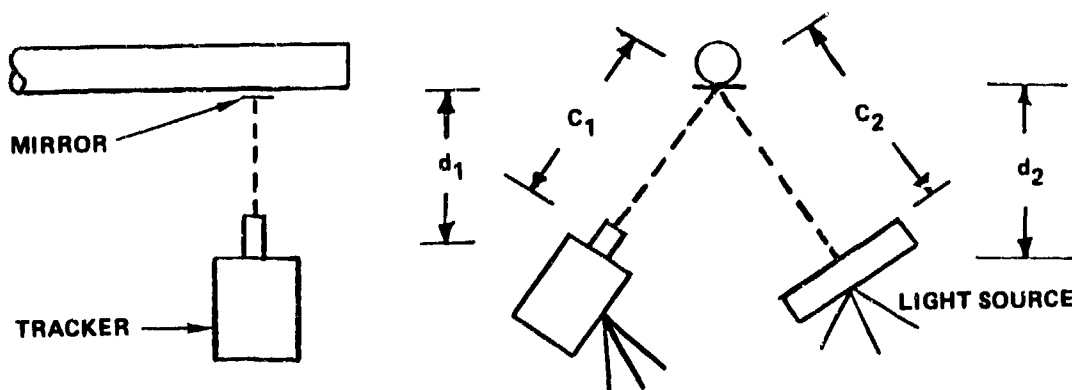


Figure 8. Angular Motion Set-up

\*STEARNS & WALKER

The tracker and light source are located in a plane perpendicular to the axis of the barrel. The tracker is focused on the mirror which reflects the image of the light source. A black tape or other covering is applied to the light source to form a straight black on white edge which is in the plane of the tracker axis. This is used as the target. The tracker is switched to measure horizontal motion, and in the initial set-up, the field of view is dark to the left and light to the right. The angular deflection of the barrel is then the apparent displacement of the target divided by the vertical distance from the tracker to the mirror. If the tracker and the light source are not located equidistant from the mirror, the angular deflection can be calculated using the equation in Figure 9. These calculations are reasonably accurate for small angular motion. The linear constants in the equation can be included as a single scale factor during calibration.

Calibration of angular measurement has been carried out by three methods. One approach is to move the complete rod through a specific measured angle. It is also possible to use a displacement measurement at the target and then apply a modification of the equations given in Figure 9. A third approach, which was used in the majority of tests, is to place a second mirror in front of the test mirror at a known angle.

Slope of Mirror,  $\alpha = \beta + \gamma$

Apparent Angle Seen  
by Tracker,  $\beta \approx \frac{z}{d_1}$

$$h = \frac{z(d_1 - d_2)}{d_1}$$

$$\gamma = \frac{h}{2d_2}$$

$$\alpha = \frac{z}{d_1} + \frac{z(d_1 - d_2)}{2d_1d_2}$$

$$\alpha = z(K)$$

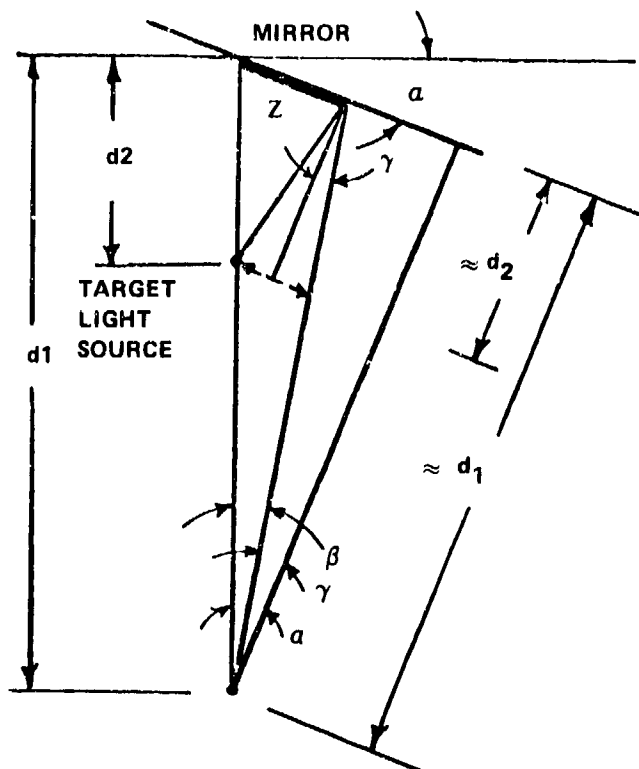


Figure 9. Angular Displacement Geometry

\*STEARNS & WALKER

One of the tests performed in the exploration of this second method of angular measurement was the vibration of a cylindrical rod cantilevered from a shaker table. The dimensions and overhang of the rod were similar to that described previously. A mirror was attached to the end of the rod and a sweep was performed with the shaker to determine the first few natural frequencies. The tracker was set up to measure pitching angle as shown in Figure 8.

The fundamental frequency was found to be 11.5 cps. The angular measurement for a sweep through this frequency is shown in Figure 10. The test was repeated with an accelerometer mounted at the end of the rod to confirm the frequency measurements. The results compared within less than one percent.

FREQUENCY = 11.5 CPS

MAGNITUDE  $\pm 0.005$  RAD.

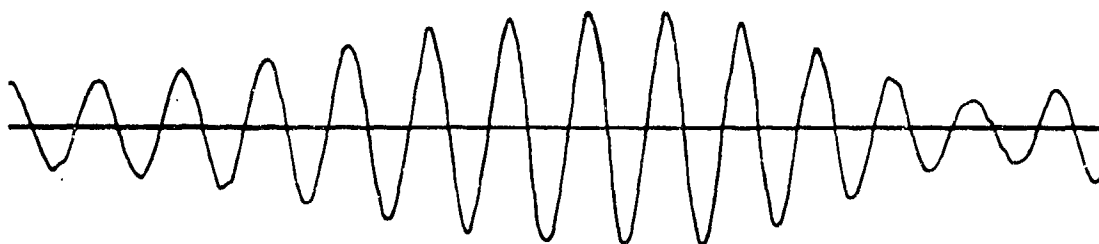


Figure 10. Vibration Test

Another test was performed using the single tracker angular measurement method. This was an initial displacement test of a cantilevered rod. The same test specimen and support arrangement was used as in the set-up shown in Figure 3. In this test, an attempt was made to explore the accuracy of the method. With the tracker and target each located 30 inches from the mirror, it was not difficult to set the maximum rated field of view at 3.7 milliradians. This was only slightly larger than the initially displaced angle of the mirror which was 3.6 milliradians. The results of this test are shown in Figure 11, along with calculated values from a finite element dynamic analysis.<sup>(2)</sup> The higher frequency motion is in especially good agreement.



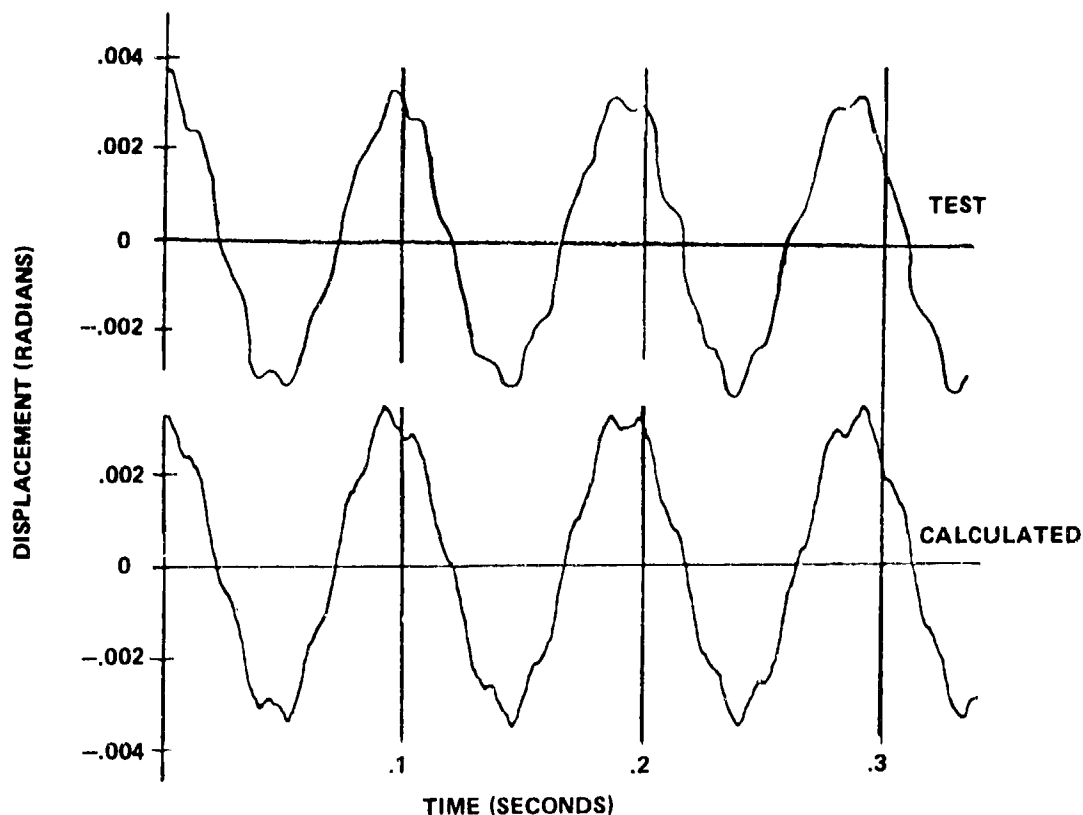


Figure 11. Angular Measurement

#### MEASUREMENTS DURING GUN FIRING

The procedures used for tracker measurements during gun firing are basically the same as described in the previous section, but with some modifications to compensate for the effects of the firing environment. These differences are pointed out in the fire test examples given in the following paragraphs.

An example of linear motion measurement during gun firing is shown in Figure 12. This is a measurement of recoil motion from a single shot firing of a 30 mm multi-barrel gatling gun. A plot of reduced movie film data, from a separate firing of this same weapon, is also shown in the figure, and is included for comparison purposes.

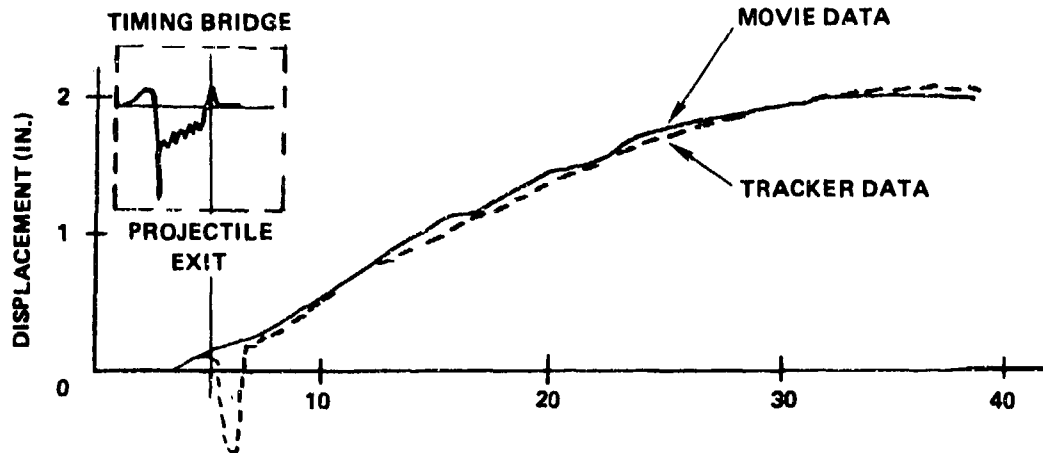


Figure 12. Recoil Motion

In this test, the tracker was located about 3 feet from the gun and was focused on a muzzle clamp a short distance from the end of the firing barrel. The maximum recoil motion was known to be about 2.0 inches and the equipment was adjusted to give a rated field of view of 2.4 inches to allow for possible overshoot. As in most of the firing tests, a 200 mm lens was used with an appropriate lens extension tube.

The movie and tracker results compare reasonably well considering that they were taken from two separate firings. The movie camera speed was 1000 frames per second, or one frame every millisecond. Since the duration to peak recoil motion was about 40 milliseconds, there was a sufficient number of data points for curve plotting. If the action of interest occurred in a much shorter time, or if the magnitude of displacement had been a great deal smaller, movie film would not provide satisfactory results. The mechanics of film motion within the camera limits the accuracy of such measurements.

\*STEARNS & WALKER

The insert shown in Figure 12 is the response from a muzzle mounted strain gage timing bridge. This indicates the time at which the projectile leaves the barrel. It can be seen that immediately following this, an unexpected, sudden pulse occurs in the tracker response. This is an erroneous reading caused by muzzle flash effects. The flash is produced by the burning gun gases as they leave the muzzle behind the fired projectile. At this time, the momentary high intensity light source may enter the cathode follower and cause it to temporarily lose tracking ability. However, as can be observed in Figure 12, as soon as the flash subsides, the follower again locks onto the target. If the light is too bright, it can do temporary damage to the tracker. The solution to this problem has been to focus on a point two or three inches aft of the muzzle tip, so that the flash does not fall directly in the field of view of the lens.

The next illustrative example is a fire test of a multi-barrel gun conducted to measure angular motion using the two tracker method. Of particular interest in this test was the angular displacement, or pitching angle, of the muzzle at the time of projectile exit, as this influences the initial heading and accuracy of each round.<sup>(3)</sup>

The two trackers were located 60 inches from the gun and were focused at points 3.0 and 9.0 inches, respectively, aft of the firing barrel muzzle. The signals from the trackers were combined and modified by a scale factor to give angular measurement. The results from three successive single shots are shown in Figure 13. It can be observed from these tests that the angular displacement at time of projectile exit, a value of 7.2 milliradians, is quite repeatable for single shot firing.

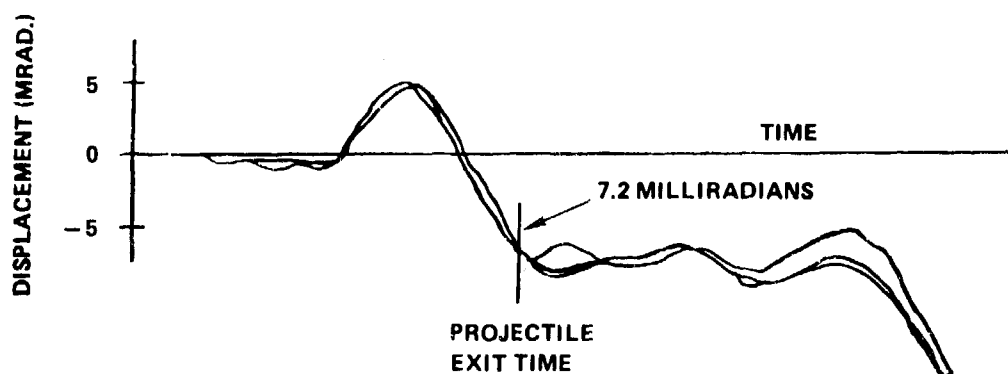


Figure 13. Two Tracker Angular Measurement

\*STEARNS & WALKER

It should be noted that if a tracker is locked-on to the tapered edge of a barrel, any pitching motion will not affect the transverse motion measurement. However, any substantial recoil motion, which occurs at the same time, can produce an erroneous reading. This linear effect can be compensated for provided the axial motion is known. The difficulty can be avoided completely by painting half of the barrel white, and using the centerline of the barrel as the target. This then requires front lighting.

The preceding tests were conducted in a test cell which was completely open to the outside environment on the downrange side. Daylight conditions presented no particular problems because the resultant lighting within the cell was fairly uniform. It has been found that optical trackers operate properly with a constant background lighting. They even operate well in outside weather conditions, under grey or clear sunny sky. However, patchy or puffy clouds on a sunny day produce sporadic results. Under these latter conditions, it is best to provide a cover to attenuate backlight variation effects, especially when using sky as a comparator.

In the third and final example, a fire test of a 30 mm single barrel fixture was carried out and the angular motion was measured with a single tracker and mirror arrangement. A photo of the test set-up is shown in Figure 14. Here it can be seen that both the tracker and the light source are quite well protected from the direct muzzle blast pressure by a substantial wall. Such protection is not usually the case and some consideration must be given to this dynamic pressure loading, for it can produce motion of the tracker. This will produce erroneous results. Often the tripods are weighted and rigidly clamped, or other stiff support mounts are constructed to avoid this occurrence. The need for such precautions depends on weapon size and round design. The influence of blast pressure on the instrumentation can be easily determined by fire testing with the tracker focused on a stationary target. Any response shown by the instrumentation will be the relative motion of the tracker due to blast effects.

In this type of angular measurement testing, some difficulty was encountered in keeping the mirror attached to the barrel during firing. Back surface glass mirrors were used and were attached with epoxy to the mounting plate. Each mirror held for an average of only 4 shots. Front surface plexiglas mirrors might be more suitable for this purpose.

The results of the angular measurement in this final test are shown in Figure 15. The angle at projectile exit was measured as 1.2 milliradians using a maximum rated field of view of 8.0 milliradians. The recording of this event on magnetic tape permits a more detailed study during slow speed playback.

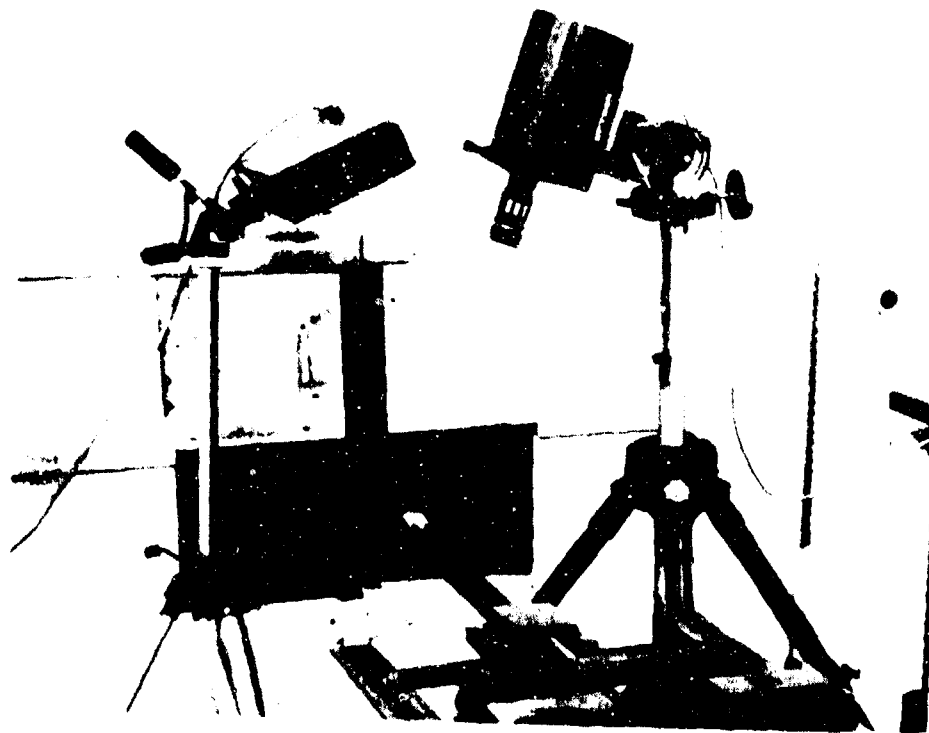


Figure 14. Angular Motion Test

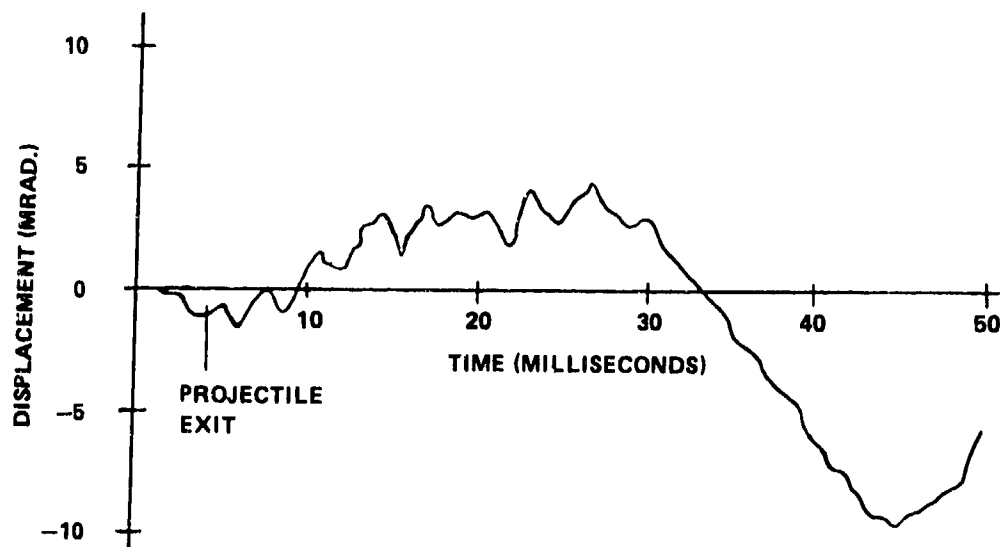


Figure 15. Angular Motion Using Mirror

Optical trackers during gun firing have proven to give extremely accurate measurements and provide a continuous record of direct measurement. The accuracy of this instrumentation is sufficient to describe the measurement of the angular muzzle displacement at time of projectile exit.

\*STEARNS & WALKER

#### ACKNOWLEDGEMENT

The writers gratefully acknowledge the contribution of the General Electric Engineering Development Laboratory in recent barrel motion testing and experimental work. We wish especially to thank Wayne Alexander for his instruction in tracker optics, and Francis Noel, Larry Brainard, and James Farnsworth for their efforts in instrumentation. The assistance of David Maher in performing finite element analyses is also greatly appreciated.

#### REFERENCES

1. B. K. Stearns, Effects of Eccentric Firing, Proc., First Conf. on: Dynamics of Precision Gun Weapons, Rock Island, Illinois, Jan. 26-27, 1977
2. J. S. Przemieniecki, Theory of Matrix Structural Analysis, McGraw-Hill, 1968.
3. H. P. Gay, An Interim Report on the Dynamics of Automatic Weapons. (U). Ballistic Research Labs Aberdeen Proving Ground, Md., Sept. 1974.

ABSTRACT

BLAKNEY

TITLE: Measurement of Angular Muzzle Motion of a 105 mm Tank Gun  
During Firing

ROBERT M. BLAKNEY

Falcon Research and Development Company

2350 Alamo Avenue, S.E.

Albuquerque, New Mexico 87106

ABSTRACT:

A system for measuring the angular motion of the muzzle of artillery weapons during firing is described. The system provides a continuous (analog) recording of the angular deflection of the muzzle referred to the breech of the gun with an angular resolution of 0.1 mrad and a frequency response in excess of 6 kHz. The technique of measurement involves reflecting a beam of light from a mirror on the muzzle to an analog, two-axis, position sensing detector; both light source and detector are mounted at the breech end of the tube. The displacement of the light beam at the detector is a direct measure of the angular deflection of the muzzle relative to the breech. A description is given of the design of the system and its calibration. Firing tests were conducted with the system on a statically mounted 105 mm tank gun at Aberdeen Proving Ground, MD. Data from nine firings were digitized and used to produce graphical representations of the muzzle motion prior to and after round exit. Some of these data are presented. A mechanism is proposed and developed which appears to account for the dominant features of the observed muzzle motion.

BIOGRAPHY:

PRESENT ASSIGNMENT: Senior Research Physicist, Falcon Research and Development Company

PAST EXPERIENCE: Chief Scientist, Albuquerque Division of EG&G, Inc., 1971-1978; General Manager and Director of Research of the Santa Monica Division of EG&G, Inc., 1965-1971; Associate Professor of Optics, Institute of Optics, University of Rochester, 1959-1965; Section Leader responsible for Xerographic plate research at Xerox, Inc., Rochester, NY, 1954-1959.

DEGREES HELD: Bachelor of Arts in Physics, Williams College, Williamstown, MA, 1946; PhD in Physics and Optics, University of Rochester, Rochester, NY, 1954.



BLAKNEY

MEASUREMENT OF ANGULAR MUZZLE MOTION ON A  
105 mm TANK GUN DURING FIRING

ROBERT M. BLAKNEY, DR.  
FALCON RESEARCH AND DEVELOPMENT COMPANY  
2350 ALAMO AVENUE, S.E.  
ALBUQUERQUE, NM 87106

Section 1--Muzzle Deflection Measurement

This paper describes the design and test of a prototype Muzzle Deflection Measurement System (MDMS) for measuring the angular deflection of the muzzle of a 105 mm tank gun during firing. The system provides a continuous (analog) recording of the angular deflection of the muzzle referred to the breech of the gun with a resolution of 0.1 mrad and a frequency response in excess of 6 kHz. The technique of measurement involves reflecting a beam of light from a mirror on the tube muzzle to an analog, two-axis position sensing detector; both the light source and detector are mounted at the breech end of the tube. A direct measure of the angular deflection of the muzzle relative to the breech is given by the displacement of the light beam at the detector.

The prototype MDMS was tested successfully at Aberdeen Proving Ground, MD, during the week of 5 December 1977 and nine firings were recorded during this period, on which data on muzzle motion were obtained. The test vehicle for this test was a statically mounted gun; modification to the mounting hardware for the MDMS would be required to mount the system on a tank-mounted weapon.

The purpose of this report is to describe the design of the MDMS, its calibration, and the results obtained in the field test. Section 1 describes the measurement technique and the objectives of the present study. The design features of the MDMS are discussed in Section 2, and in Section 3 the results of laboratory performance test and system calibration are presented. Results of the firing tests are given in Section 4 along with an analysis of the data.

The technique used for the measurement of angular muzzle motion is illustrated in Figure 1. A transmitter/receiver assembly is mounted at the breech end of the tube, and a mirror is rigidly attached to the muzzle. The transmitter is an optical projection system which projects a collimated beam of light to the muzzle mirror, where it is reflected back into the aperture of the receiver. The receiver is basically a camera which focuses the collimated beam onto a position-sensing detector (PSD) in the focal plane of the camera lens. As the gun tube bends, the vector defining the muzzle pointing direction changes, and the (vector) normal to the muzzle mirror undergoes the same change. This causes the reflected beam to be deflected by an amount equal to twice the angular deflection of the muzzle vector. Angular motion of the beam causes the focused spot on the PSD to translate linearly a distance proportional to the muzzle deflection angle. By measuring the vector displacement of the spot on the PSD as a function of time, a direct quantitative measure of muzzle motion is obtained.

An objective of the MDMS development was to produce a muzzle motion sensing system capable of measuring both the slow changes in the muzzle vector due to changing environmental conditions, as well as the rapid motions which occur during passage of the round down the tube. The design objective was a system sensitivity of 0.1 mrad over a dynamic range of  $\pm 5$  mrad and a frequency response of at least 5 kHz. Reliable operation was to be obtained in the shock and vibration environment of a 105 mm tank gun. The specifications on this environment were: At the muzzle, 500 g along the tube axis, and 1000 g at 5 kHz transverse to the axis. At the turret/gun interface, the specifications were 500 g at 5 kHz, and an overpressure of 3 psi.

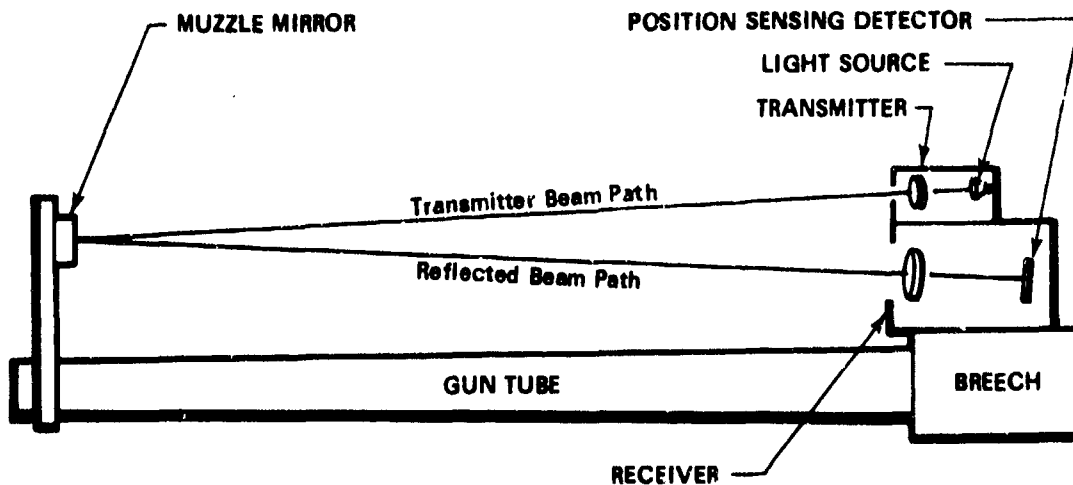


FIGURE 1. CONFIGURATION OF MUZZLE DEFLECTION MEASUREMENT SYSTEM

Section 2--MDMS Design Features

A block diagram of the MDMS is shown in Figure 2.

There are three major subsystems: (1) transmitter, (2) receiver, and (3) control unit. The configuration of the system as mounted on the test gun is shown in Figure 3, where the main components are identified by the numbers in the figure. The receiver and transmitter are shown at (2) and (4), respectively, and were mounted on a heavy steel bracket (1). This, in turn, was bolted to the yoke of the gun. The muzzle mirror assembly, shown at (3), was fastened to an existing sleeve on the muzzle at a distance of 380 cm from the plane containing the transmitter and receiver apertures.

The transmitter assembly consists of a laser diode source, the radiation from which is collimated by an aspheric lens and projected toward the receiver, via the muzzle mirror. Temperature control of the laser diode is provided by thermoelectric elements mounted in the transmitter housing. Adjustments are provided for collimation and alignment of the laser diode axis with the optical axis of the projection lens.

The receiver subsystem is composed of an  $f/1.4$ , 135 mm camera lens (NORITAR) with the PSD in its focal plane. It also contains the pre-amplifiers for the PSD outputs which buffer these signals for transmission to the position computer located off the gun in the Control Unit.

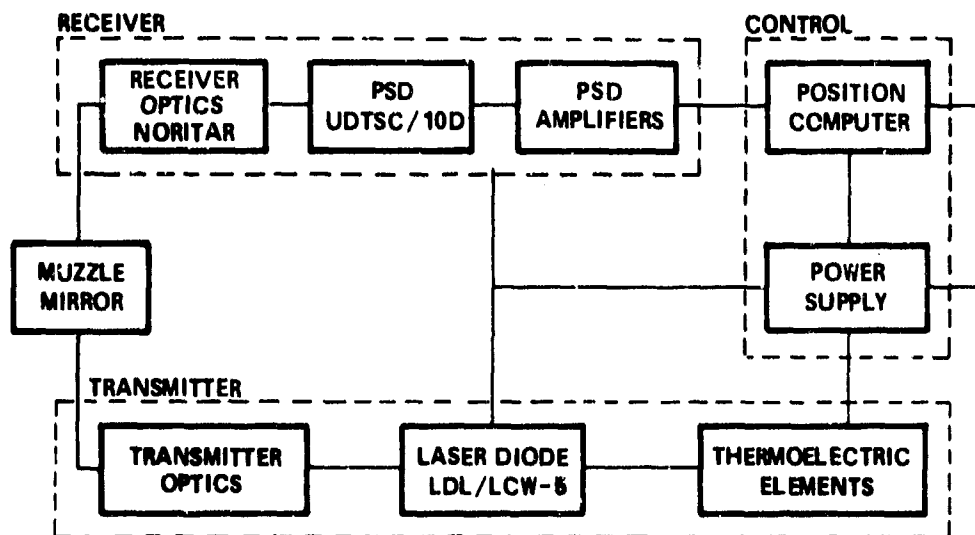


FIGURE 2. BLOCK DIAGRAM OF MUZZLE DEFLECTION MEASUREMENT SYSTEM

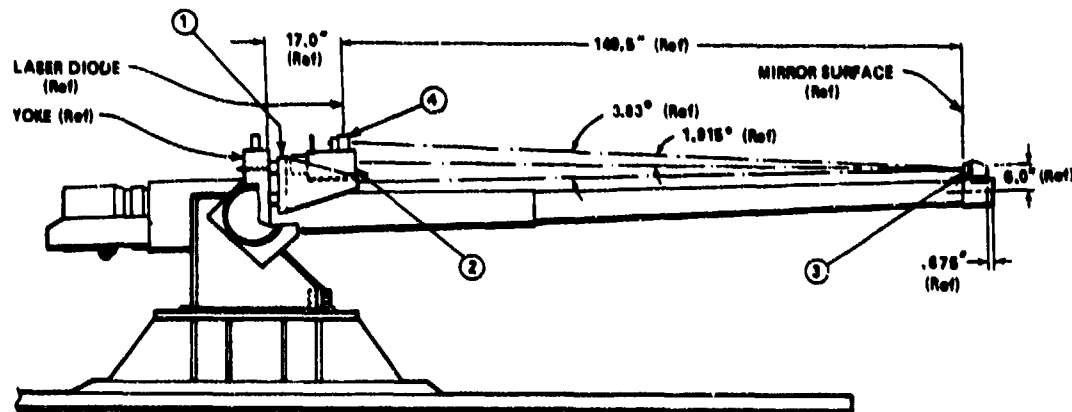


FIGURE 3. GUN MOUNTED CONFIGURATION OF MDMS

Adjustments are provided for positioning the electrical center of the PSD on the optical axis of the NORITAR and for aligning its axes in the horizontal and vertical planes.

The control subsystem contains the position computer, all power supplies and control elements (such as switches, potentiometers and indicator lights, etc.) for remote control of the MDMS. It was mounted off the gun and outside the blast enclosure.

Stringent requirements are placed on the receiver optics by the large separation between it and the muzzle mirror, and by the relatively small extent of the most linear region of the PSD. With an angular dynamic range of  $\pm 5$  mrad for muzzle motion, the transmitter beam reflected from the mirror will swing through a range of  $\pm 10$  mrad. The linear distance traversed by the beam at the receiver aperture (380 cm distant) is 7.6 cm, which is the lower bound for the diameter of the aperture. This must be increased by the diameter of the transmitter beam if vignetting is to be avoided. For the MDMS, the minimum beam diameter at the receiver was 1.6 cm; this required a receiver aperture of at least 9.2 cm.

The function of the lens is to focus the collimated beam to a small spot on the PSD, which measures the centroid of the light distribution in this spot. The PSD is a square silicon wafer with four electrodes defining orthogonal, rectangular (X-Y) axes, with the region of the greatest linearity (0.5%) contained in an area 0.25 cm in diameter at the origin. Thus, the focused spot should remain within this area. For an angular range of  $\pm 10$  mrad, this condition implies that the lens should have a focal length of 12.5 cm. Since the aperture diameter of the lens must be at least 9.2 cm, this implies an f/number of f/1.4. Furthermore, the lens must be well corrected if an angular resolution

of 0.1 mrad is to be achieved. Note that 0.1 mrad corresponds to a displacement of the centroid of about 12 microns; thus, the effect of aberrations must cause the centroid to move much less than this as the beam traverses the lens aperture. The lens chosen for the MDMS was the f/1.4, 135 mm NORITAR and closely meets those requirements.

The PSD chosen for the MDMS is a planar diffused PIN photodiode, with four contacts defining the X- and Y-axes (see Figure 4). Light absorbed at its surface causes a photocurrent to flow out through the four contacts. If  $i_1$  and  $i_2$  are the currents associated with one axis (i.e., X-axis), then it can be shown in a one-dimensional approximation that  $i_2 - i_1 = [\bar{X}/(L/2)]i_s$ . Here,  $L$  is the dimension of the PSD,  $\bar{X}$  is the displacement of the centroid of the light spot from its electrical center along the X-axis and  $i_s = i_1 + i_2$  is the total photocurrent. From these two relations one obtains

$$\bar{X} = (L/2) [(i_2 - i_1)/(i_2 + i_1)] \quad (1)$$

Thus, the position of the centroid of the light spot is proportional to the ratio of the difference and sum currents flowing out of the pairs of contacts defining the X- and Y-axes. Note that Eq. (1) is independent of the magnitude of the photocurrent, so that measurement of the centroid position is independent of the absorbed light power. This result has been verified with the MDMS and holds over a wide range of transmitter beam power.

Figure 4 is a block diagram of the position computer which performs the operations indicated by Eq. (1). The four currents from the

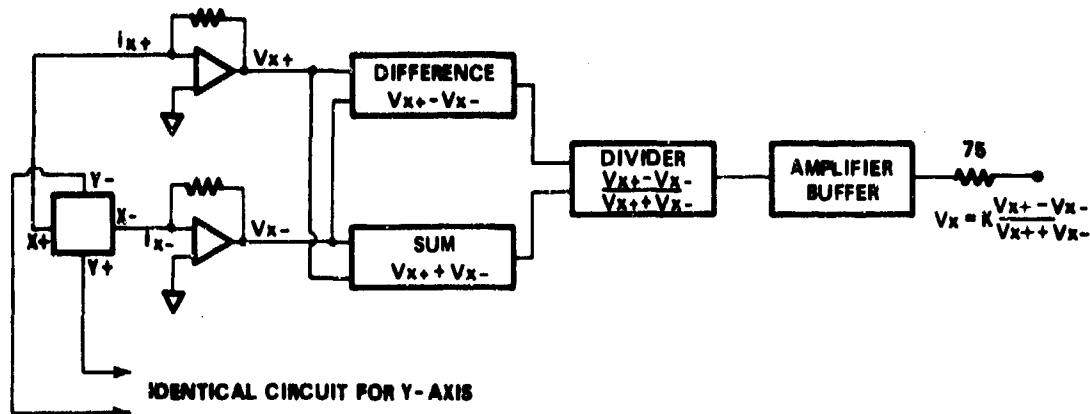


FIGURE 4. BLOCK DIAGRAM OF POSITION COMPUTER

PSD are first transformed to voltages which are then transmitted to the position computer (in the Control Unit, off the gun). For each electrode pair, the difference and sum of the voltages  $V_{X+}$  and  $V_{X-}$  are formed and the ratio taken in accordance with the prescription of Eq. (1). The output voltage from the computer is

$$V_X = K(V_{X+} - V_{X-}) / (V_{X+} + V_{X-}) \quad (2)$$

where K is a scale factor to be determined by calibration of the MDMS.

### Section 3--MDMS Calibration

For angular calibration, the MDMS was mounted on an I-beam in the configuration of Figure 3, with the transmitter/receiver and muzzle mirror separated by 380 cm, the planned separation on the gun. The muzzle mirror was contained in a two-axis mount which could be rotated by micrometer adjustment about the X- and Y-axes. Angular tilt of the muzzle mirror was measured with a Kollmorgan Model K222 Dual Axis Autocollimator. This instrument directly measures the tilt of the mirror and has a sensitivity and repeatability of 0.1 sec of arc.

The general procedure for calibration was to rotate the mirror through a small angle about one of its axes, measure the amount of rotation with the autocollimator and record the output from the position computer for each increment of tilt. It was first necessary to align the PSD axes with the axes defined by the mirror mount. When the MDMS was transferred to the gun, the PSD axes became the reference coordinate system for the gun measurements. Following this alignment, the focused light spot was moved to the electrical center of the PSD (zero output from X- and Y-channels). The mirror was then tilted in increments of one minute of arc (0.29 mrad) about the X-axis, for example, and then rotated about the Y-axis to sweep the transmitter beam horizontally across the receiver aperture. The output of the position computer was recorded on an X-Y recorder. This gave a line on the chart parallel to the X-axis with a measured angular displacement from it. By repeating this process for both axes, a grid was traced, with the grid lines spaced at measured one minute intervals. If the MDMS is linear, a rectangular grid is the result. With this presentation, it is easy to detect nonlinear effects and where they occur on the PSD. Figure 5 shows the results of a calibration scan.

A transfer function for the MDMS can be obtained by plotting the voltage output as a function of the mirror tilt. This is shown in Figure 6 in which the plotted points represent measured values of voltage and tilt angle along the X- and Y-axes. Points on the curve in the figure marked + represent measured points on the X-axis; points marked • are for the Y-axis. For the final system calibration, these data were represented by the function

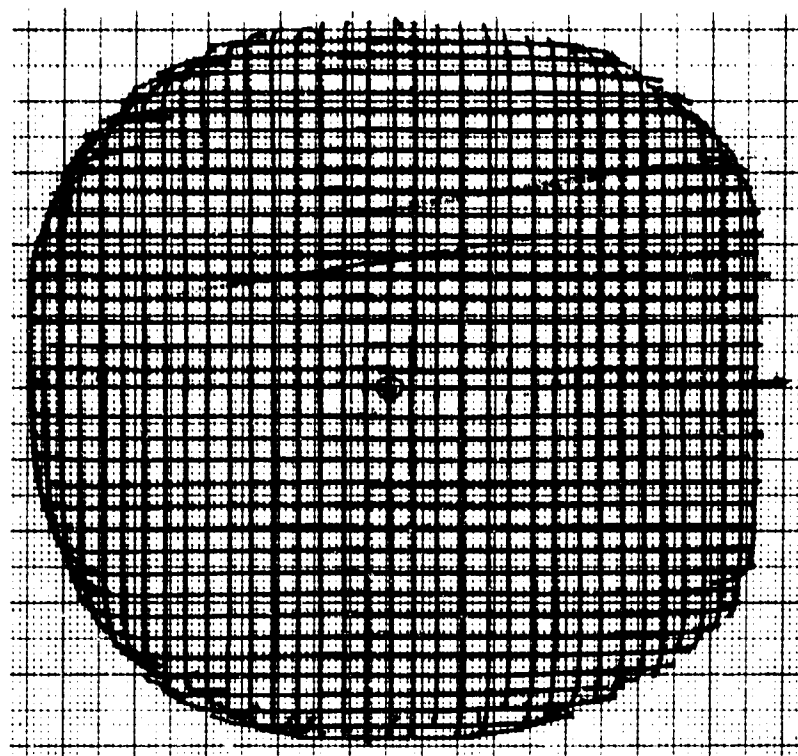


FIGURE 5. X-Y ANGULAR SCAN FOR MDMS PLOT SCALE, 2 V/cm;  
BEAM POWER 0.43 mw. GRID SPACING, 1 MINUTE  
OF ARC (0.29 mrad)

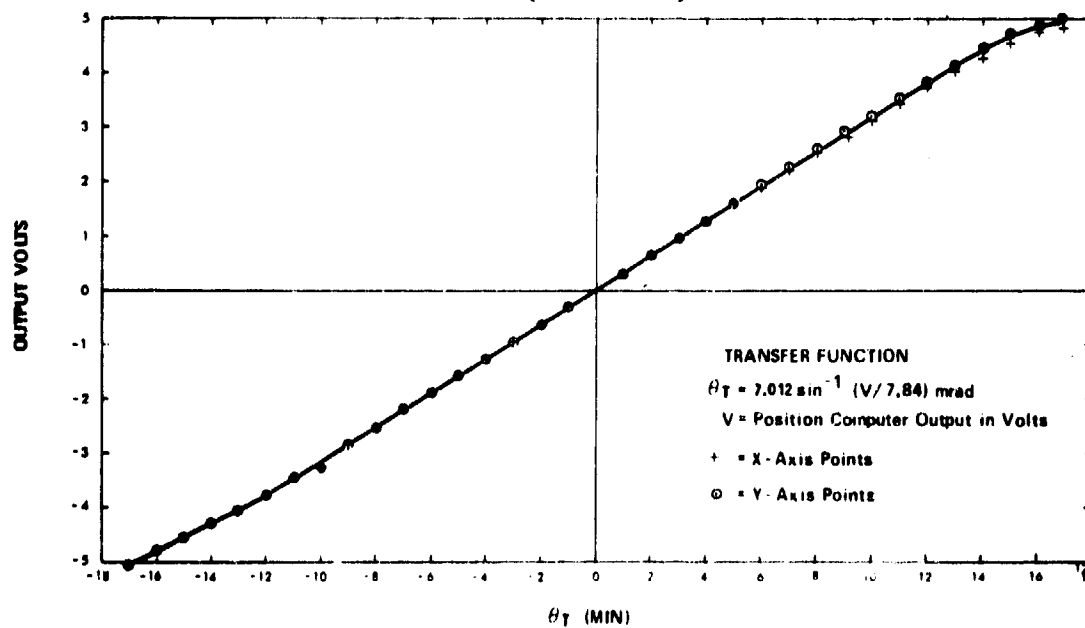


FIGURE 6. TRANSFER FUNCTION FOR MDMS PROTOTYPE

$$\theta_{TCY} = 7.012 \sin^{-1}(V_{MY}/7.844) \text{ mrad} \quad (3)$$

In this expression,  $\gamma = X$  or  $Y$ ,  $V_{MY}$  is the output of the position computer for the  $\gamma$  channel and  $\theta_{TCY}$  is the mirror tilt angle as computed by the position computer along the  $\gamma$ -axis.

The transfer function of Eq. (3) can be used to determine the composite tilt of the mirror in the X-Y plane. As a check on the accuracy of the transfer function, Eq. (3) was used to predict the mirror tilt at the intersections of the grid lines, where the angles are known from the autocollimator measurements. This was done for 48 off-axis points spanning the full  $\pm 5$  mrad range. In all cases, the difference between angles measured by the autocollimator and the position computer was less than 0.1 mrad. The conclusion is that the accuracy of the mirror tilt measurement made by the MDMS is at least 0.1 mrad.

The non-linearity exhibited by the transfer functions of Figure 6 is due primarily to vignetting of the laser beam at the edge of the receiver aperture. When part of the beam is vignetted, the centroid of the light distribution on the PSD shifts toward the center. Thus, the incremental change in centroid position with increasing mirror tilt becomes progressively less for large angles as more of the beam is vignetted.

Frequency response of the MDMS was measured by reflecting a He-Ne laser beam from a sinusoidally oscillating mirror into the receiver aperture. As the frequency of oscillation was changed, the amplitude was kept constant at approximately 3 mrad. MDMS response was found to be flat to 1 kHz and then to roll off with a single time constant, falling to 80% of its low frequency value at 6 kHz. This behavior is due solely to the frequency response of the position computer, which had a nominal bandwidth of 15 kHz (3 db point).

#### Section 4--Results of Firing Tests

Nine firing tests were performed with the MDMS on a statically mounted 105 mm gun at Aberdeen Proving Ground, MD. On five of the firings, standard M392 APDS rounds were used; proof slugs were used for the remainder. The gun was additionally instrumented to detect the events of round emergence and round exit, and to measure the distance of tube retraction in recoil as a function of time. The latter measurement showed that at the time of round exit, the tube had begun recoil and had moved approximately 3 cm.

The analog data from the X- and Y-channels of the position computer were digitized at 5  $\mu$ sec intervals. The data were then processed to convert the digitized counts to angular units in milliradians, according to the prescription of Eq. (3). A measure of the noise in the data



was obtained by computing the standard deviation of counts during a 2 ms interval prior to the beginning of round motion.

Figures 7 and 8 show the angular motion of the muzzle in the X- and Y-directions for one of the shots. The vertical line on the right side of each figure indicates the time of round exit, and the legends give the initial off-set and noise in milliradians. Time is referenced to an arbitrary origin and has the units of milliseconds.

The motion of the muzzle can also be displayed as a Lissajous plot from Figures 7 and 8. Figure 9 is such a plot for the same shot and spans a one millisecond interval centered on the time of round exit. The events of round emergence and round exit are indicated by the symbols X and O, respectively. A measure of the RMS uncertainty in this plot, due to system noise, is given by the separation of the two straight lines labeled  $\sigma$  at the right of the figure.

The angular behavior of the muzzle in the X-Y plane during firing is shown in Figure 10 for seven shots. These are smoothed traces from the computer plots. Each row represents one shot and shows the motion in successive one millisecond intervals, starting at the left. Round emergence and exit occurs in the fifth column of the figure, and these events are marked as previously described, if they were recorded. On five of the shots, data drop-outs were experienced near the time of round exit and were due to obscuration of the laser beam by the ejection

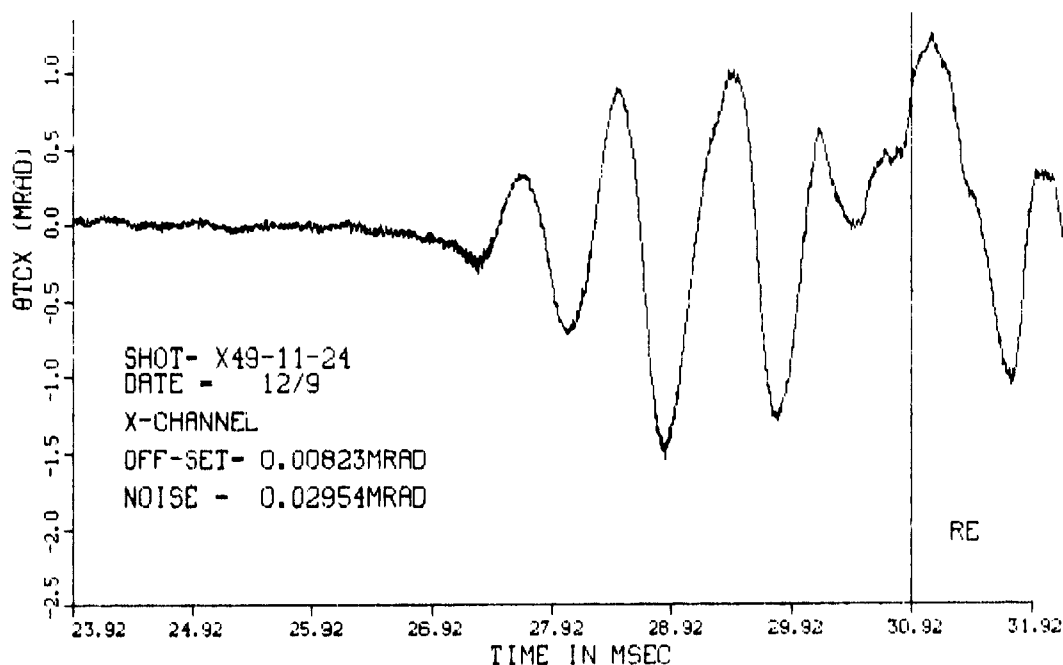


FIGURE 7. X-COMPONENT OF MUZZLE MOTION VS. TIME  
105 mm TANK GUN

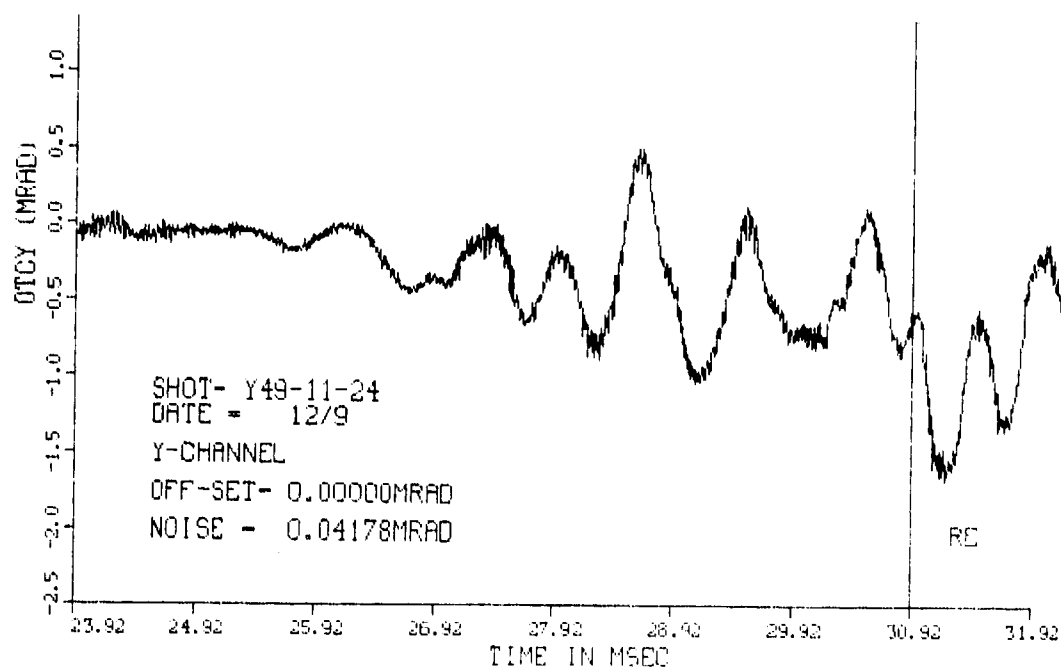


FIGURE 8. Y-COMPONENT OF MUZZLE MOTION VS. TIME  
105 mm TANK GUN

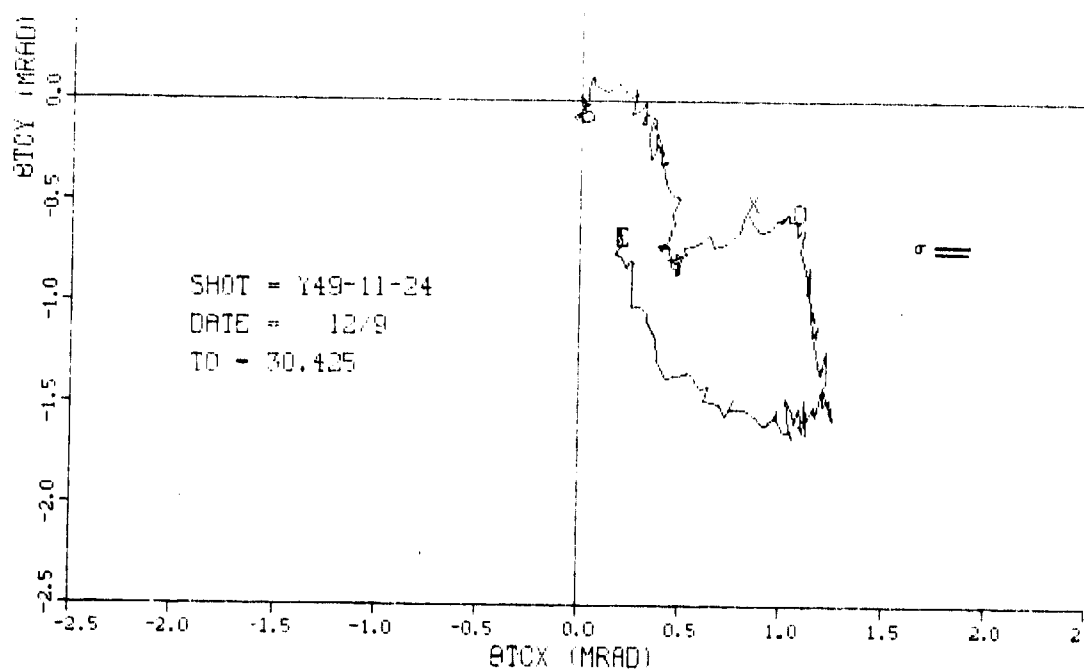


FIGURE 9. LISSAJOUS PLOT OF MUZZLE MOTION  
NEAR ROUND EXIT

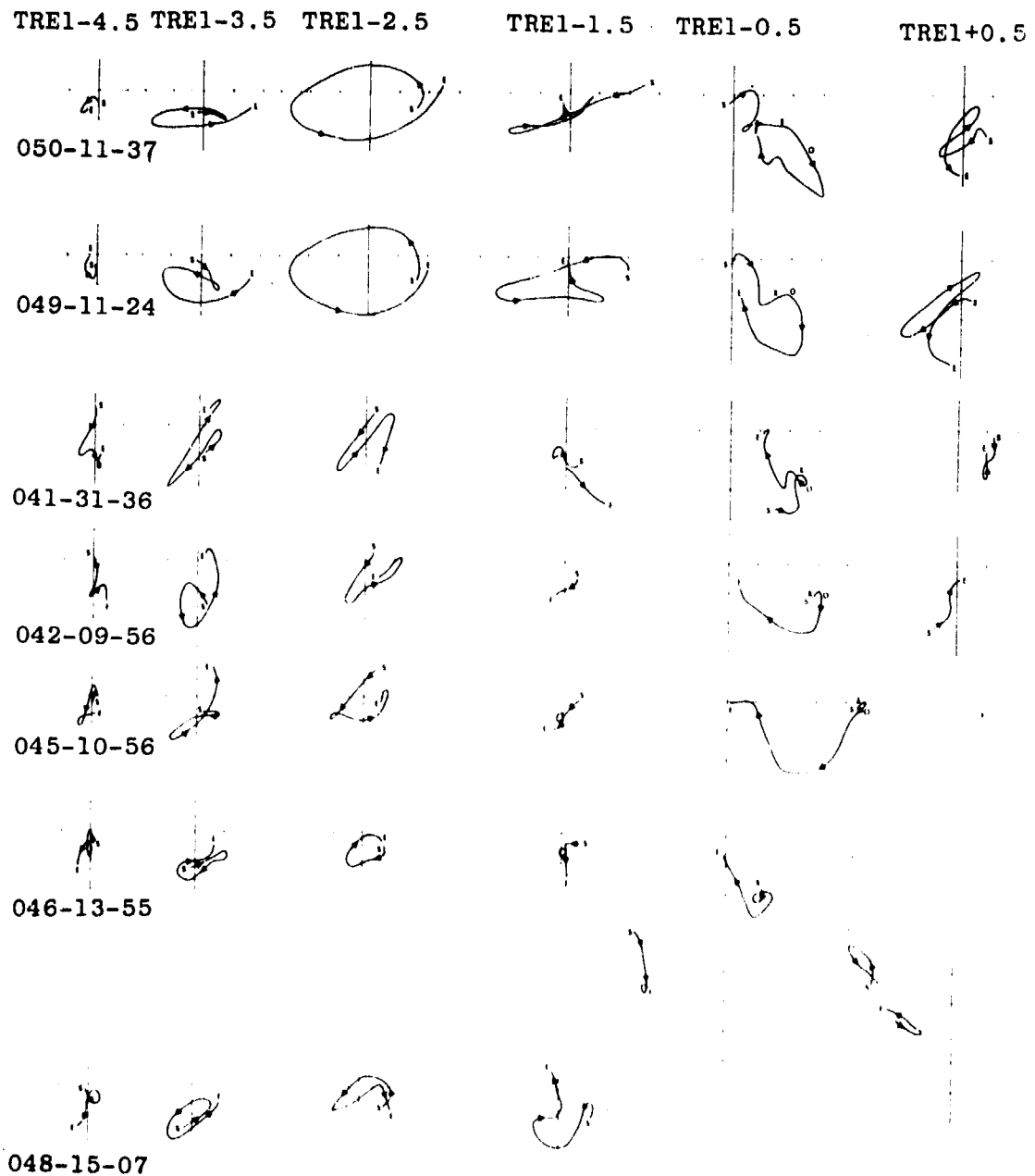


FIGURE 10. SUMMARY OF MUZZLE MOTION FOR SEVEN FIRINGS  
LISSAJOUS PLOTS AT 1 ms INTERVALS

of combustion products from an uncovered bore evacuator hole at the top of the tube. This accounts for the discontinuities in some of the traces. The problem was corrected prior to firing the two shots shown at the top of the figure.

For five of the shots, the event of round emergence was recorded and the angle of the muzzle at this event could be measured. On the remaining two shots, round emergence occurred during a drop-out; the muzzle angle could be closely estimated, however, from the X- and Y-plots against time. From this limited sample, the standard deviation of muzzle pointing angle at round emergence was estimated to be 1.8 mrad. This suggests that the contribution to the total dispersion due to this effect would be a circle 3.6 m in diameter at 1 km.

A prominent feature of muzzle motion shown clearly in Figures 7 and 8 is its oscillatory character, which is interpreted as tube bending. The period of oscillation in both the X- and Y-directions was the same for all firings and is in the range 0.8 ms to 1 ms, implying a dominant frequency on the order of 1 kHz to 1.3 kHz. This is well above the natural resonant frequency of bending of the gun tube and suggests the existence of a driving force at this frequency. A plausible mechanism for this force is suggesting by considering the forces acting on the tube in reaction to the accelerating shell, which is forced to rotate by the rifling grooves. Figure 11 illustrates the force components resolved along and perpendicular to the direction of a rifling groove.  $F_T$  is the net torquing force acting at right angles to the tube which causes it to twist in a counterclockwise direction, if shell rotation is clockwise.  $F_T$  also can produce a bending moment about the breech which would cause the muzzle to be deflected. Since  $F_T$  rotates with the shell, the time dependence of its components along the X- and Y-axes is of interest.

The forcing function for the X-component of tube motion is:

$$F_{TX} = F_T(t) \cos(\omega_s t) \quad (4)$$

where,  $\omega_s$  is the angular rotation rate of the shell and  $t$  is time. If  $v(t)$  is the shell velocity in the tube and  $R$  is the number of revolutions per unit length made by the shell, then:

$$\omega_s = 2\pi R v(t) \quad (5)$$

For a 105 mm tank gun, the rifling rotates the shell in a clockwise direction one revolution in 18 calibers. This gives  $R = 0.53$  rev/m. Measured data on shell velocity in the tube were obtained from the U. S. Army Ballistic Research Laboratory, Aberdeen, MD, are represented by the curve in Figure 12. This curve was differentiated to obtain the shell acceleration, which is proportional to  $F_T$ . For purposes of evaluating the postulated forcing function of Eq. (4), the shell velocity and acceleration were approximated by the following expressions:

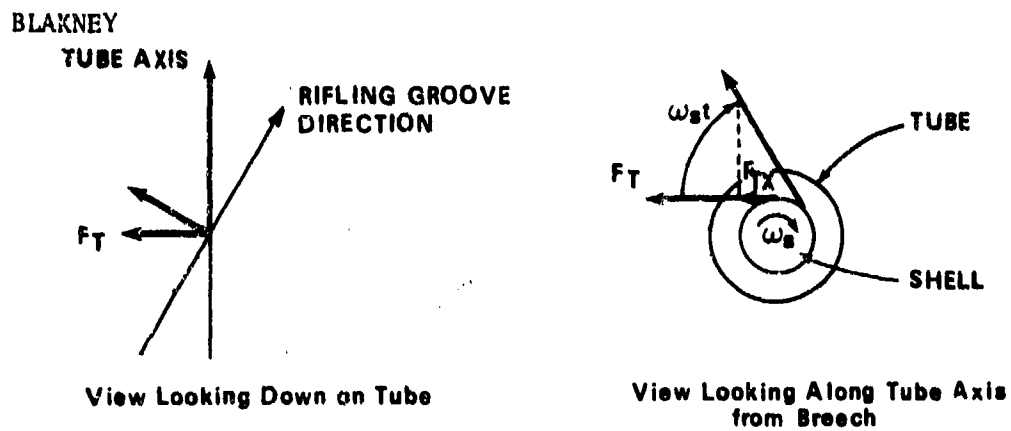


FIGURE 11. RESOLUTION OF FORCES ON TUBE DUE TO ACCELERATING AND ROTATING ROUND

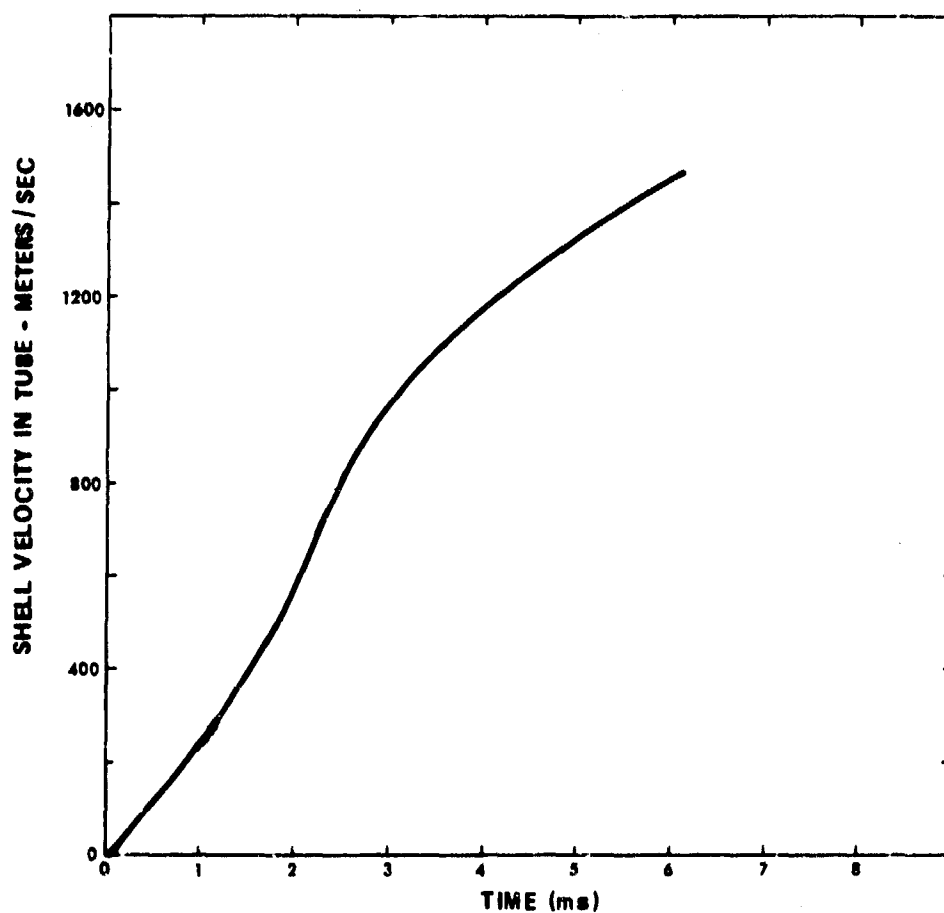


FIGURE 12. VELOCITY OF SHELL IN TUBE OF  
105 mm TANK GUN

$$v(t) = 150 t + 50\tau_1 [\exp(t/\tau_1) - 1] \text{ m/sec}$$

$$t \leq 1.7 \text{ ms}$$

$$a(t) = 150 + 50 \exp(t/\tau_1) \text{ m/sec}^2$$

$$v(t) = 1898 - 2360 \exp(-t/\tau_2) \text{ m/sec}$$

$$t \geq 2 \text{ ms}$$

$$a(t) = 860 \exp(-t/\tau_2) \text{ m/sec}^2$$

The time constants are  $\tau_1 = 0.983 \text{ ms}$  and  $\tau_2 = 2.754 \text{ ms}$ . These expressions closely approximate the measured velocity and derived acceleration over the time intervals indicated.

When these expressions are substituted into Eqs. (5) and (4), respectively, normalized forcing functions acting along the X- and Y-axes can be evaluated. The result for the X-axis is given in Figure 13 and shows that the force is quasi-periodic, with a period in the range 0.9 to 1.1 ms, in close agreement with the period of observed muzzle motion. During the approximately 6 ms between the beginning of round movement and round exit, four to five well-defined oscillations are predicted by this simple analysis. Again, this is in reasonable agreement with the observations.

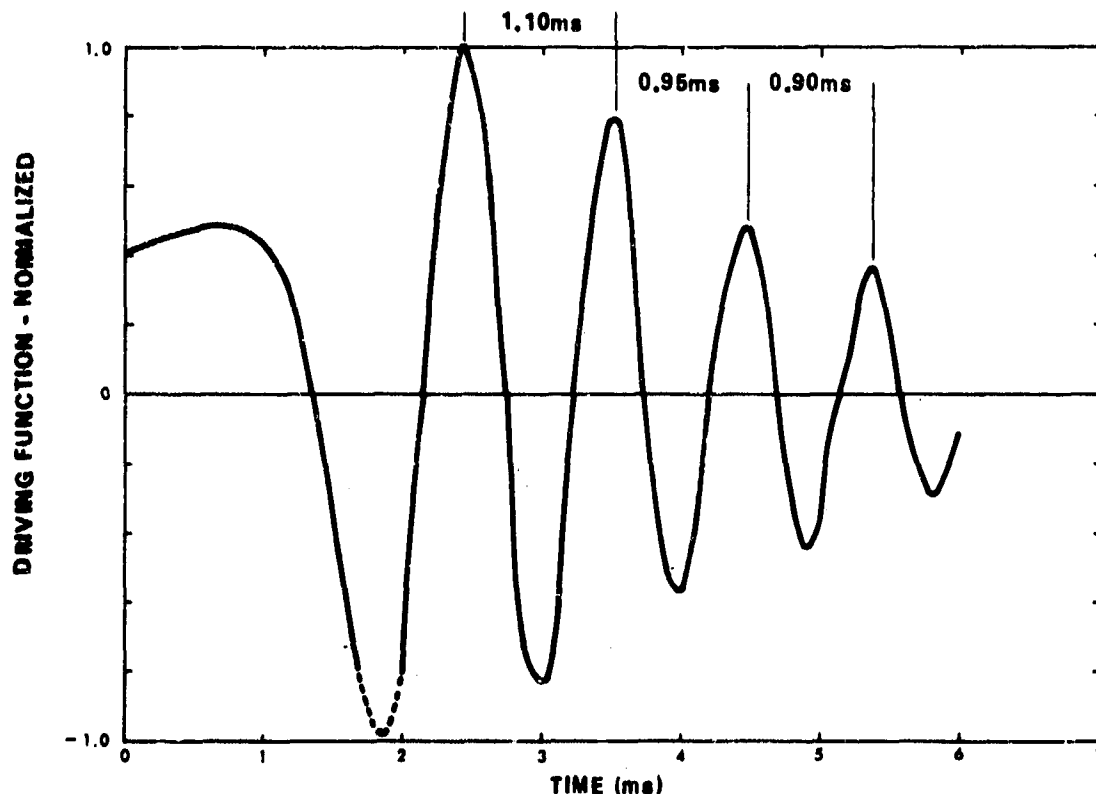


FIGURE 13. NORMALIZED DRIVING FORCE FOR THE TUBE OF A 105 mm TANK GUN BASED ON MEASURED VELOCITY DATA

This result supports the hypothesis that a dominant force on the tube is the reaction to the forced rotation of the accelerating shell and gives rise to a torque on the tube. The time dependence of the axial components of the force has been shown to be the same as the oscillatory motion of the muzzle in the X- and Y-directions. A more comprehensive analysis of the forces generated during firing would be required to show that the proposed mechanism can cause tube bending with the observed amplitude. The results obtained in this study only suggest that this mechanism is an important factor in producing the characteristic muzzle motion. A test of the hypothesis could be made by observing muzzle motion during the firing of M735 APDS, fin-stabilized rounds. In this case one would expect much less energy to be coupled into the tube from the round and consequently less deflection of the muzzle.

Resonant vibration of the muzzle mirror mount could cause the output of the position computer to show oscillations. A design criterion for the mount was that its distortion under maximum muzzle *g*-loading would not change the direction of the reflected beam by more than 0.025 mrad. An analysis of this structure indicates that its resonant frequency is in the neighborhood of 14 kHz. The conclusion is that flexure of the muzzle mirror mount makes no significant contribution to the signal from the position computer, and, therefore, that the observed motion is due to tube bending.

#### Acknowledgement

This work was sponsored by the U. S. Army Ballistic Research Laboratory under Contract No. DAAK 11-77C-0051, while the author was at EG&G, Inc., Albuquerque Operations, Albuquerque, New Mexico.

COX AND HOKANSON

TITLE: Muzzle Motions of the M68 105-mm Gun  
P. A. COX and J. C. HOKANSON

ABSTRACT:

Muzzle motions of the M68 105-mm tank gun which occur during firing were computed and compared to test measurements. Tests were conducted by the Propulsion Division at BRL with the gun secured to the BRL accuracy mount. Motions were calculated in the vertical plane, the horizontal plane, and in torsion using a two-dimensional finite element computer program. Input data for the program were taken from measurements of interior ballistics data. A parameter study was performed to show the effects on muzzle motions and the projectile angular deviation from the line of sight produced by projectile unbalance, breech block eccentricity, and variations in tube support.

BIBLIOGRAPHY:

PRESENT ASSIGNMENT: Senior Engineer, Southwest Research Institute

PAST EXPERIENCE: Pneumatics Engineer, General Dynamics/Astronautics, San Diego, California, 1961-1962; Structural Analyst, General Dynamics, Fort Worth, Texas, 1964-1967; Engineer and Senior Engineer, Southwest Research Institute, 1967-present.

DEGREES HELD: BSME, Texas A&M University, 1961; MSME, Texas A&M University, 1964.



## MUZZLE MOTIONS OF THE M68 105-mm GUN

\*P. A. COX  
JAMES C. HOKANSON  
SOUTHWEST RESEARCH INSTITUTE  
SAN ANTONIO, TEXAS 78284

The paper is based upon work performed for the Propulsion Division of the Ballistic Research Laboratories in the time period November 1974 through June 1977 [1]. In this work, motions of the M68 105-mm weapon produced by a single firing were computed by the finite element method and compared to measured motions. Motions of the gun tube during firing alter the initial pointing vector of the muzzle and impart lateral and angular velocities to the projectile as it exits the tube. The effect of muzzle motions on the projectile exterior ballistics can be gauged by computing the angular momentum of the projectile at muzzle exit and the angular deviation of the projectile flight path relative to the initial line of sight of the muzzle. Changes in these two quantities produced by changes in weapon parameters and in the analytical model were studied. Parameters varied include the projectile unbalance, mass eccentricity of the breech block, and tube support stiffness. Variations in the analytical model included changes in stiffness and in the projectile-tube interaction forces produced by beam shear deflections.

### Analytical Method

The two-dimensional computer program used for calculating muzzle motions is based on a displacement (or compatible) finite element formulation. As outlined by Cook [2], a system of algebraic equations is obtained by minimizing the total potential energy of the system

$$\pi = U + W \quad (1)$$

with respect to kinematically admissible nodal displacements.  $U$  and  $W$  are obtained by summing the strain energy and the potential energy of the external loads over all elements. For uniform beam elements with lateral (bending only) and axial deformations, the element strain energy is given by

$$U_e = \frac{EI}{2} \int_0^l u_{xx}^2 dx + \frac{EA}{2} \int_0^l v_x^2 dx \quad (2)$$

where  $u_{xx}$  is the second derivative of the lateral displacements,  $u$ , with respect to  $x$ , and  $v_x$  is the first derivative of the axial displacements,  $v$ , with respect to  $x$ . The potential energy of external concentrated loads is

$$W_e = \int_0^l [F(x_F) u \delta(x-x_F) + P(x_P) v \delta(x-x_P)] dx \quad (3)$$

where  $\delta(x-x_F)$  and  $\delta(x-x_P)$  are Dirac Delta functions. The above equations reduce to the following form

$$\pi = u^T ku - u^T f \quad (4)$$

which, when minimized with respect to the nodal displacements, gives

$$ku - f = 0 \quad (5)$$

These equations were derived using the Hermite polynomials for interpolation functions within the beam elements.

For the dynamic case, first order differential equations were obtained by employing the well known d'Alembert principle, and introducing the inertia forces as equivalent static loads. Lumped masses were used so that these forces were introduced at the nodes. Interpolation formulas are the same as for the static case. Shear deformations were introduced by deriving the element stiffness matrices using a direct strength of materials approach. The interpolation functions, obtained from the static deformed shape, were used to derive the force vector.

Forcing functions,  $F$  and  $P$  of Eq. (3), include:

- . breech pressure
- . projectile-tube friction
- . forces produced by projectile unbalance
- . forces produced by projectile-tube motions
- . forces produced by reactions within the recoil mechanism

The forces produced by projectile-tube motions couple with beam inertias for the element within which the projectile lies.

The system of equations thus obtained can be written in one of two ways.

$$[M]\{\ddot{U}_N\} + [C]\{\dot{U}_N\} + [K]\{U_N\} = \{F(t, U_N, \dot{U}_N, \ddot{U}_N)\} \quad (6)$$

or

$$[M(t)]\{\ddot{U}_N\} + [C(t)]\{\dot{U}_N\} + [K(t)]\{U_N\} = \{F(t)\} \quad (7)$$

In Eq. (6), the coefficients of the displacements and their derivatives are all constant, and the external forces are functions of time and the instantaneous beam displacements, velocities, and accelerations. The mass matrix  $[M]$  is diagonal as indicated. In Eq. (7), the time dependent coefficients of the forces are combined with the constant coefficients of Eq. (6), which leaves the external forces as functions of time only. The coefficient matrix  $[M(t)]$  is no longer diagonal.

Either system of equations can be solved numerically by marching in a series of time steps,  $\Delta t$ , evaluating accelerations, velocities, and displacements at each step. The procedure used in this work was the average acceleration method described by Timoshenko, et al. [3]. Displacements and velocities are written

$$\{\dot{U}_N\}_t = \{\dot{U}_N\}_{t-\Delta t} + \frac{\Delta t}{2} \left( \{\ddot{U}_N\}_{t-\Delta t} + \{\ddot{U}_N\}_t \right) \quad (8)$$

$$\{U_N\}_t = \{U_N\}_{t-\Delta t} + \frac{\Delta t}{2} \left( \{\dot{U}_N\}_{t-\Delta t} + \{\dot{U}_N\}_t \right) \quad (9)$$

Acceleration at time  $t$  is found from either Eq. (6) or (7). Dropping the distinction between time dependent and constant coefficients, the acceleration at time  $t$  is

$$\{\ddot{U}_N\}_t = [M]_t^{-1} \left( \{F\}_t - [C]_t \{\dot{U}_N\}_t - [K]_t \{U_N\}_t \right) \quad (10)$$

Equations (8) and (9), when substituted into Eq. (10), give the acceleration at time  $t$  in terms of tube displacements and motions at  $t - \Delta t$ .

$$\begin{aligned} \{\ddot{U}_N\}_t = & \left( [M] + \frac{\Delta t}{2} [C] + \frac{\Delta t^2}{4} [K] \right)_t^{-1} \left( \{F\}_t - [C]_t \left( \{\dot{U}_N\}_{t-\Delta t} + \frac{\Delta t}{2} \right. \right. \\ & \left. \left. \times \{\dot{U}_N\}_{t-\Delta t} \right) - [K]_t \left( \{U_N\}_{t-\Delta t} + \Delta t \{\dot{U}_N\}_{t-\Delta t} + \frac{\Delta t^2}{4} \{\ddot{U}_N\}_{t-\Delta t} \right) \right) \end{aligned} \quad (11)$$

Equation (11) is usually written

$$\{\ddot{U}_N\}_t = [\bar{M}]_t^{-1} \{R\}_t \quad (12)$$

For linear systems with constant coefficients, the matrix  $[\bar{M}]^{-1}$  must be assembled and inverted only once. Also, if  $R$  is a prescribed function of time only, then Eqs. (8), (9), and (12) give the displacement history directly without iterations. Even if the matrix  $[\bar{M}]$  is a function of time, the displacement history can be found without iterations, but the matrix  $[\bar{M}]$  must be reformulated and inverted at each time step. This can be very costly in terms of computation time.

A simpler approach, and the one employed in this work, is to solve Eq. (6) using an iterative procedure. For this solution, it is convenient to use Eqs. (6), (8), and (9) directly and avoid the assembly and inversion of the matrix  $[\bar{M}]$ . The general procedure is as follows:

Initial conditions:

1.  $\{U_N\}$ ,  $\{\dot{U}_N\}$ , and  $\{F\}$  must be known at  $t = 0$ . (Call this  $t - \Delta t$  for convenience.)

Predictor:

2. Compute  $\{\ddot{U}_N\}_{t-\Delta t}$  from Eq. (6).
3. Set  $\{\dot{U}_N\} = \{\ddot{U}_N\}_{t-\Delta t}$ .
4. Compute  $\{\dot{U}_N\}_t$  and  $\{U_N\}_t$  from Eqs. (8) and (9).
5. Determine  $\{F\}_t$  using the predicted values of  $\{U_N\}_t$ ,  $\{\dot{U}_N\}_t$ , and  $\{\ddot{U}_N\}_t$ .
6. Compute  $\{\ddot{U}_N\}_t$  from Eq. (6).

Corrector:

7. Repeat Steps, 4, 5, and 6.
8. Compute at time  $t$  for lateral, axial, and rotational displacements, separately

$$R_k = \frac{\sum_i |U_{Nj} - U_{Nj-1}|_i}{\sum_i |U_{Nj}|_i} \quad \text{for } k = 1, 2, 3 \quad (13)$$

where  $j$  denotes the current value and  $j-1$  the value from the previous iteration;  $i$  is the summation index which extends over all lateral displacements for  $k = 1$ , axial displacements for  $k = 2$ , and rotations for  $k = 3$ .

9. If  $R_k > \epsilon$  for  $k = 1, 2$  or  $3$ , repeat Steps 4 through 8; otherwise, save current values, increment time, and continue the integration. For these studies,  $\epsilon = 10^{-6}$ .

Because the  $[M]$  matrix is not formed and inverted in the iterative scheme, this approach is suitable for nonlinear problems which require periodic updating of the  $[M]$ ,  $[K]$ , or  $[C]$  matrices. Because the matrix  $[M]$  is still diagonal, its inversion is trivial.

This same basic iterative approach also can be used with Eq. (7). For this case, Step 5 would call for updating and inverting the time dependent, nondiagonal mass matrix. Leaving the time dependent coefficients in the force vector is more efficient.

#### Finite Element Model

The finite element model (F.E. model) of the weapon for the vertical plane is given in Figure 1. A cross-section through the weapon which includes essential features of the tube, cradle, and BRL accuracy mount is also shown. A legend identifies the parts of the model. In this F.E. model the tube is completely uncoupled from the cradle and the mount. Tube support was altered by varying damping and stiffness for members 20 and 22. Stiffness and damping in member 21 were zero for all calculations. The tube support sleeve is undercut in the center, and calculations of tube motions in this region indicate that contact between the tube and the tube support sleeve at node 16 will not occur. Members 20, 21, and 22 have zero bending stiffness so that axial motions are reacted totally by the spring between node 18 and ground.

The tube has been represented by 18 beam elements and 57 degrees-of-freedom. Up to 38 lateral modes could be calculated from this model. It should give an accurate representation of at least the first ten lateral modes. Joint No. 1 is located 38 mm aft of the muzzle so as to correspond to transducer locations used in the BRL test program. Although not indicated in the model, the tube is given an initial droop. Droop is caused by gravitational forces and is input to the program as a slight offset from the X-axis in the negative Y direction for nodal points 1 through 14. Initial tube offsets produced by manufacturing or solar heating have been ignored. The breech mass also has an initial offset below the X-axis which is associated with the breech block eccentricity.

Input data for the F.E. model were taken from production drawings of the M68 weapon, from physical measurements on weapon parts, and from transducer recordings made during firing. Table I summarizes the input data used for the majority of the calculations. These data correspond to a test identified as IDENT 06 from a firing program conducted by the Propulsion Division of BRL. All parameter studies reported are made for interior ballistics data measured during this test. Test results and the corresponding calculations for tests IDENT 08 and 10 are

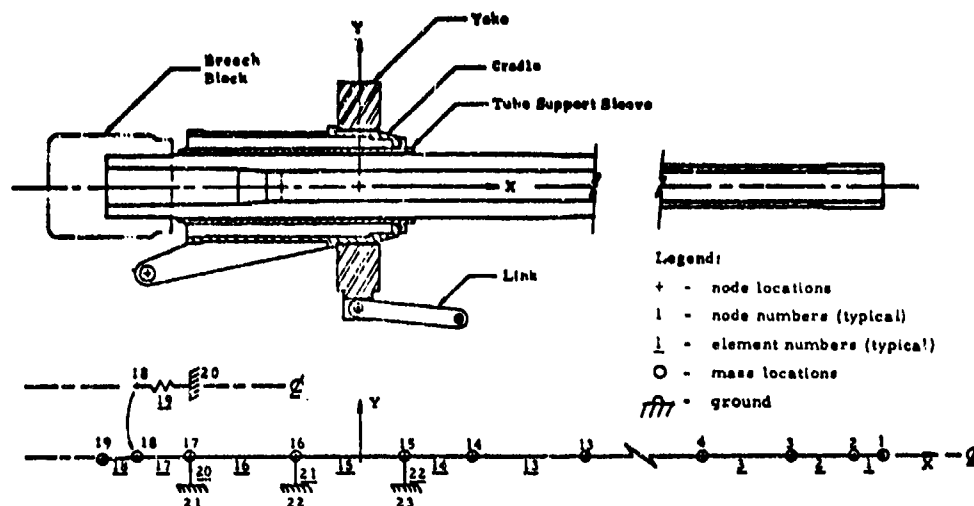


FIGURE 1. FINITE ELEMENT MODEL OF THE TUBE

TABLE I. INPUT DATA FOR IDENT 06: STANDARD SET

Input	Data and Source
Mass and stiffness of tube	Computed from production drawings
Breech block eccentricity	8.911 mm below tube $Q_c$ (measured)
Chamber pressure	Measured during firing (Figure 2)
Projectile axial motions	Displacement measured during firing velocity and acceleration computed from displacement vs time (Figure 3)
Projectile eccentricity	0.35 mm - initially oriented along + y-axis in Figure 1 (measured)
Projectile mass	5.72 kg (measured)
Initial tube drop	Maximum of - 2.5 mm at Node 1 (calculated)
Breech force	Given by Figure 4e (calculated from torsional response of the tube)

\*COX & HOKANSON

given only for comparison with those of IDENT 06.

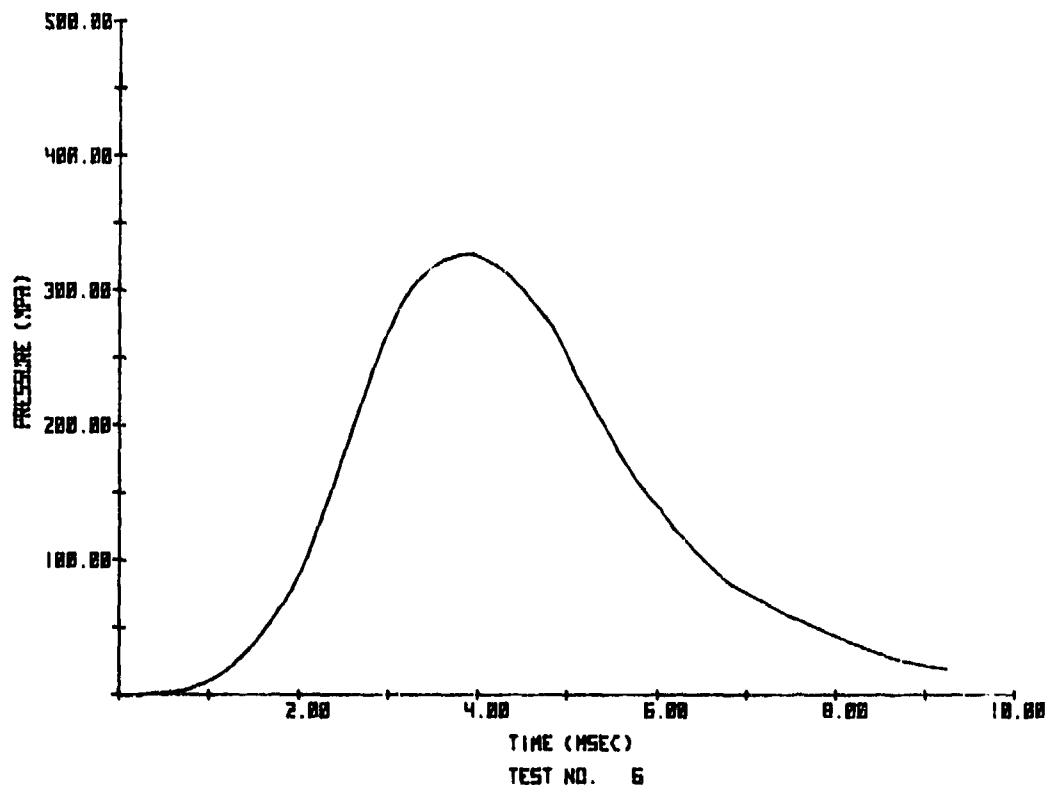


FIGURE 2. CHAMBER PRESSURE INPUT DATA

#### Forcing Functions

The time-dependent forces applied to the model of Figure 1 are given in Figure 4. These include the axial forces produced by breech pressure and projectile-tube friction, lateral forces produced by projectile unbalance coupled with projectile spin velocities and acceleration and a lateral breech force produced by reactions between the breech and the torque bracket. Projectile exit from the muzzle is indicated by the light horizontal and vertical lines which intersect the curves in this figure. Similar lines will be used throughout the

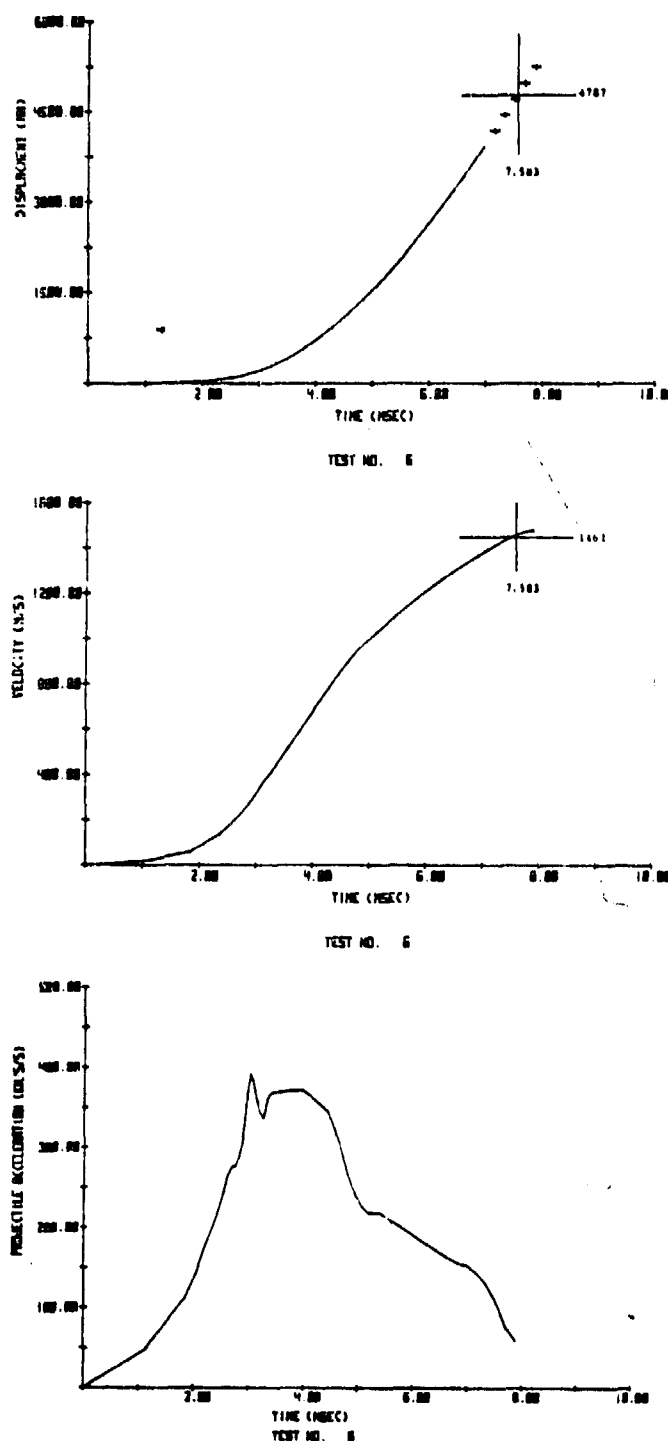


FIGURE 3. PROJECTILE MOTION DATA

paper to denote projectile exit. The so called "Bourdon forces" were omitted.

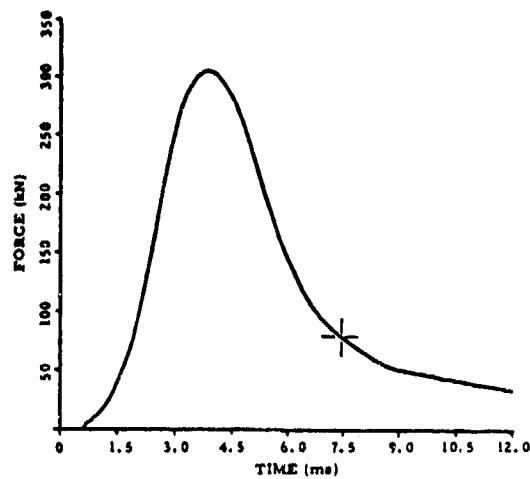
Note that the forces produced by friction and the breech pressure are zero for some finite time after  $t = 0$ . The reason for this delay is that neither the breech pressure nor friction was applied to the tube until the breech pressure overcame that produced by the recoil spring preload and projectile-tube friction.

Motion dependent forcing functions also occur as a result of projectile-tube motions and will differ from run to run unless conditions are identical. These forces are called "moving mass effects" and are inertia forces produced by coupling which occurs between projectile axial motions and tube lateral displacements and motions. An example of these forces is given in Figure 5. The run number in the figure caption refers to numbers which will appear in the table of results. Derivation of these forces is given by Simkins [4] and by Cox and Hokanson [1].

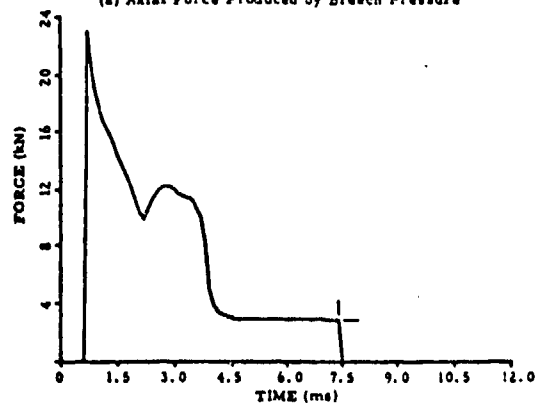
#### Parameter Study

This parameter study was conducted to investigate specifically the effect of projectile unbalances, breech eccentricity, and tube support stiffness

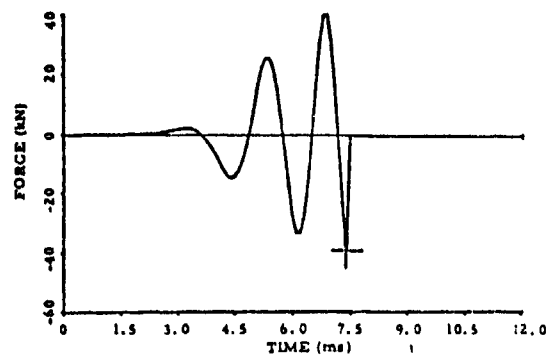




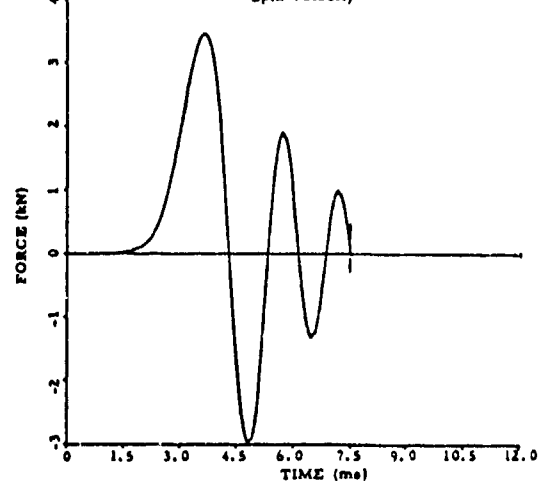
(a) Axial Force Produced by Breach Pressure



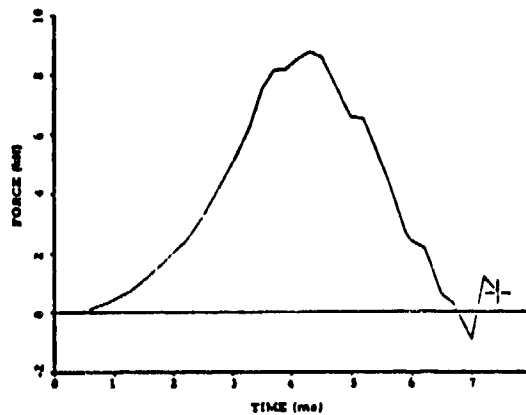
(b) Projectile-Tube Axial Friction Force



(c) Centrifugal Force Produced by Projectile Unbalance and Spin Velocity



(d) Force Produced by Projectile Unbalance and Spin Acceleration



(e) Force Produced by the Torque Reaction

FIGURE 4. TIME-DEPENDENT FORCES APPLIED TO THE F.E. MODEL

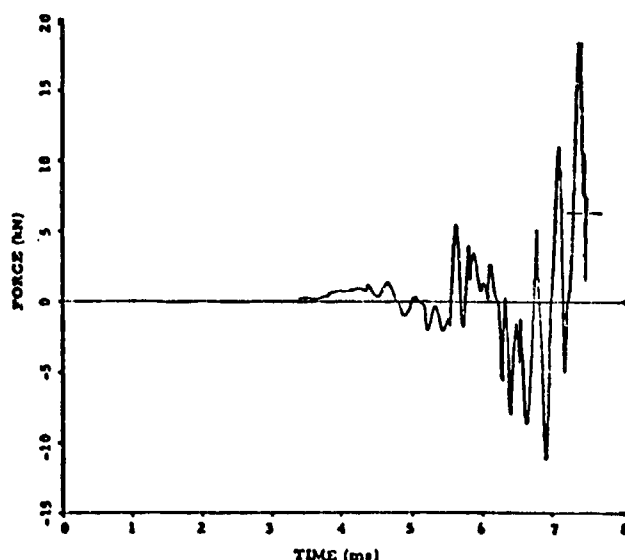


FIGURE 5. TYPICAL MOTION DEPENDENT FORCES (RUN 60.22)

upon muzzle motions. Additional studies were made to examine the effect of certain variations in the analytical model on the calculated muzzle motions. One such variation was the inclusion of shear deformations. Throughout the study, calculated and measured results were compared to assess the accuracy of the calculations.

Included in Figure 6 are the muzzle motions measured on the M68 weapon for test IDENT 06. Calculated motions from the parameter studies will be compared to these values in both magnitude and sig-

nature. The time axis on the graph is labeled in fiducial time (time measured relative to a timing mark). Ignition of the propellant corresponds to about 20.6 ms in fiducial time. The number in parentheses above the time scale is measured from propellant ignition and corresponds to the time scale used for the calculated results.

Forty-two different computer runs were made in the parameter study. Entries in Table II are keyed to computer runs, and these run numbers are also given on figures which will be used to show some of the results graphically. Runs omitted from the table did not contribute to the study.

The parameter variations are identified as column headings. Parameters varied include the integration time-step, projectile eccentricity, breech eccentricity, projectile-tube interaction forces, breech reaction, shear deformations, and the tube support conditions (columns headed by "AJ" and "CA"). The column headed "Moving Mass" is used to denote the inclusion or exclusion of moving mass effects; the breech reaction is the force in Figure 4, discussed previously; "Shear Deformations" refers to the inclusion or exclusion of these effects when computing beam stiffness and the beam deformed shape; the symbols AJ20 and CA20 denote the cross-sectional area and damping, respectively, of member 20 of Figure 1 (it is the member which supports the rear of the tube); and AJ22 and CA22 denote member properties at the front tube support. Also in Table II, the letter "N" denotes "Standard Values" as given in Table I; otherwise, the values are either zero, a reversal of the standard value (-N), or some multiple of the standard value.

TABLE II. SUMMARY OF CALCULATIONS PERFORMED IN THE VERTICAL PLANE WITH THE SMALL MODEL

Run No.	Parameter Variations							Results		
	AT (sec)	Proj. Ecc.	Breach Ecc.	Moving Mass	Breach Reaction	Shear Deformations	$AJ_{20}$ ( $\frac{N \cdot m}{m^2}$ )	$CA_{20}$ ( $\frac{N \cdot m}{m^2}$ )	$AJ_{22}$ ( $\frac{N \cdot m}{m^2}$ )	$CA_{22}$ ( $\frac{N \cdot m}{m^2}$ )
60.01	SE-6	N	N	No	0	Yes	3E-1	SE5	3E-1	SE5
60.06	1E-5			No	0					
60.07	1E-5			Yes	0					
60.10	1E-5				0					
60.11	SE-6				M			SE4		
60.12	1E-6						3E-3			
60.13	SE-6						3E-4			
60.14							3E-5			
60.15							3E-5			
60.16							3E-6			
60.17							3E-6			
60.18							3E-7			
60.19							3E-7			
60.20							3E-7			
60.21							3E-7			
60.22							3E-7			
60.23							3E-7			
60.24							3E-7			
60.25							3E-7			
60.26							3E-7			
60.27							3E-7			
60.28							3E-7			
60.29							3E-7			
60.30							3E-7			
60.31							3E-7			
60.32							3E-7			
60.33							3E-7			
60.34							3E-7			
60.35							3E-7			
60.36							3E-7			
60.37							3E-7			
60.38							3E-7			
60.39							3E-7			
60.40							3E-7			
60.41							3E-7			
60.42							3E-7			

\* Included projectile weight in all subsequent runs.

\*\* Changed interpolation functions to include shear deformations.

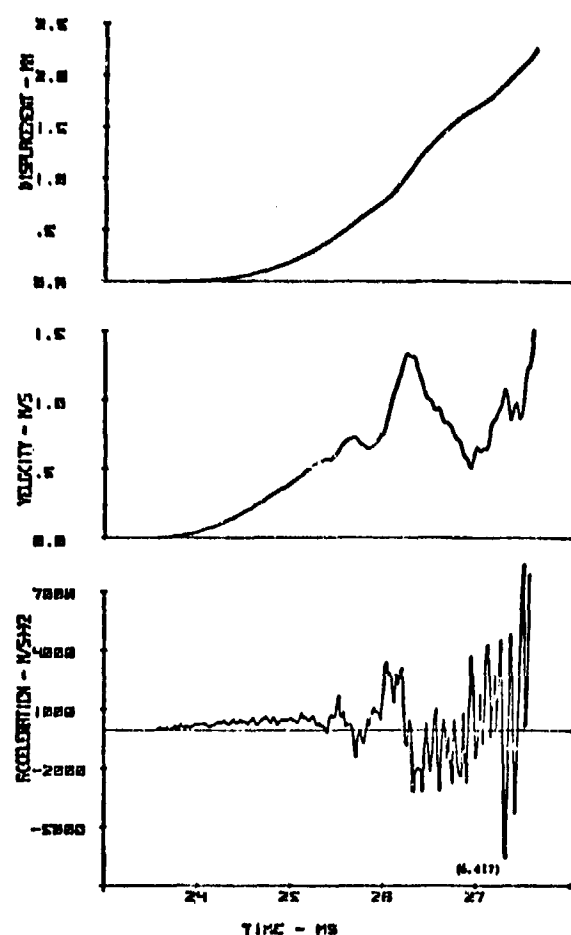


FIGURE 6. MEASURED MUZZLE MOTIONS IN THE VERTICAL PLANE FOR IDENT 06

Results in the table include the lateral displacement calculated at a position 38 mm behind the muzzle; the projectile linear momentum, which is normal to the original line of fire; the projectile angular momentum; and the angular deviation in mils. Angular deviation is simply the angle of flight relative to the original line of fire computed from the projectile linear momentum. The results given correspond to the time of projectile exit from the tube. This time is nominally 7.435 ms.

Selected parameter variations of Table II are discussed. Initial runs (60.01 through 60.12) were made to select an integration time step and to show the effect of including moving mass effects. These will not be discussed further except by comparison with other results. The discussion includes "moving mass effects" produced by the coupling which occurs between projectile axial motions and tube lateral motions, and are based on calculations performed with the same integration time step.

### Tube Support Stiffness

Variations in support stiffness included changes to both the area (stiffness) and damping of members 20 and 22 of Figure 1. Values of AJ above  $0.03 \text{ m}^2$  are considered as firm support, regardless of the damping value. Minor changes in results were produced by increasing the support area above this value. Alternately, the tube behaved essentially as a free-free beam for area and damping values of  $3 \times 10^{-7} \text{ m}^2$  and  $5 \times 10^3 \text{ N-s/m}$ , respectively. Lower values of AJ and CA produced no significant change in the results.

Muzzle motions computed for a firmly supported tube are presented in Figures 7 and 8. Figure 7 gives results for a balanced projectile (zero eccentricity of the projectile mass). For the balanced

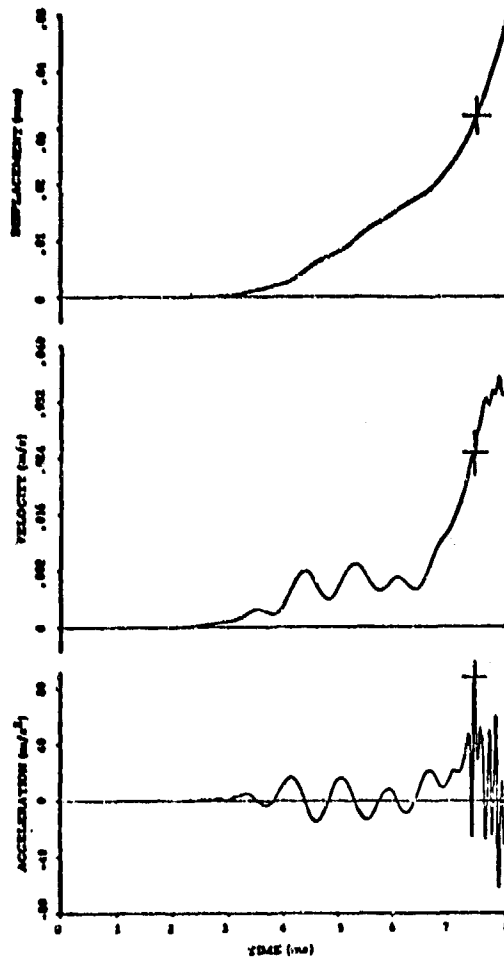


FIGURE 7. MUZZLE MOTIONS IN THE VERTICAL PLANE FOR A FIRMLY SUPPORTED TUBE (RUN 60.30)

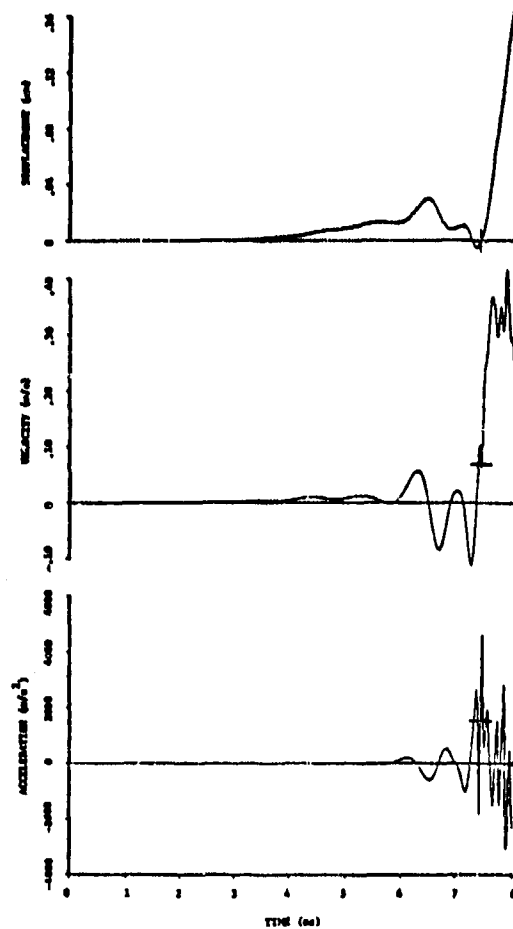


FIGURE 8. MUZZLE MOTIONS COMPUTED WITH CONSISTENT SHEAR DEFORMATIONS FOR A FIRMLY SUPPORTED TUBE (RUN 60.40)

round, the forces shown in Figure 4c and 4d are zero. Otherwise, standard input data given in Table I for IDENT 06 were used. These results match well with the signature of the experimental data, but magnitudes of the displacement, velocity, and acceleration are low by a factor of 50 to 100. Including projectile eccentricity in the calculations produces the muzzle motions of Figure 8. The magnitude of the displacement prior to projectile exit has changed very little, although there is a sharp increase in displacement immediately thereafter. Maximum velocities are now within a factor of 3 to 4 of measured values, and the magnitude of the calculated acceleration is about 64% of the measured acceleration.

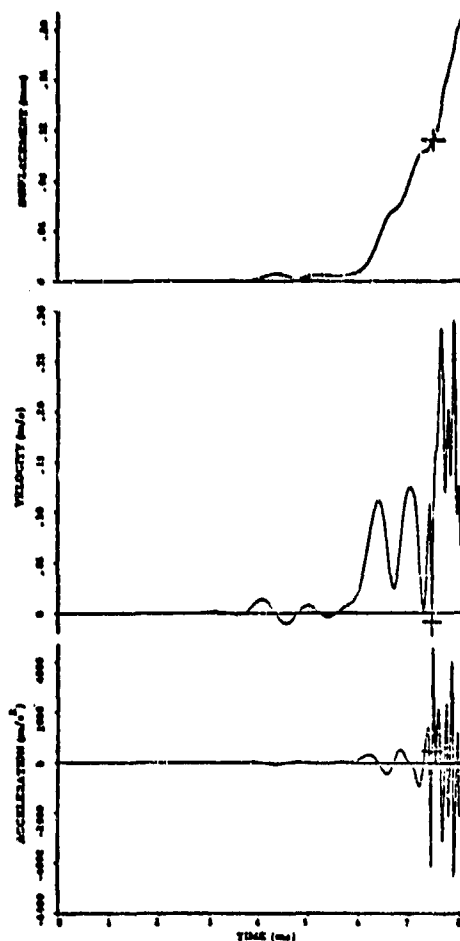


FIGURE 9. MUZZLE MOTIONS COMPUTED WITH SHEAR DEFORMATIONS WITH THE TUBE WEAKLY SUPPORTED (RUN 60.41)

"steady" force acting in the vertical direction produces the additional displacement. A differential force on the tube produced by tube curvature and initial pressure (the so called Bourdon force) might produce the observed result.

#### Projectile Unbalance

Figures 7, 8, and 9 show the effect of projectile unbalance (mass eccentricity from the tube centerline) on a firmly supported tube. Figure 8 indicates that, for the unbalance of the projectile in the IDENT 06 test, muzzle motions produced by the unbalance will be obscured by overall tube motions even smaller than those measured. Thus, projectile unbalance will not be noticeable in the measured displacements;

Freeing the tube produces the results of Figure 9. Except for the support parameters, input data are identical to those used to produce the results of Figure 8. Only the magnitude and character of the displacement have changed significantly. Displacements have increased fourfold, but are still about 1/20-th of measured values. Several observations can be made from these comparisons:

- (1) Calculated displacements in the vertical plane are much lower than measured displacements.
- (2) Analyzing the tube with boundary conditions which closely approximate a free-free beam gives muzzle displacements that best match measured displacements in both magnitude and signature.
- (3) Muzzle oscillations produced by projectile unbalance are small and are probably obscured by motions of the magnitude measured.
- (4) Because calculated and measured velocities and accelerations are much closer in magnitude than the displacements, it may be that some

however, it does have a pronounced effect on the muzzle velocity and acceleration and upon the projectile momentum at muzzle exit. By comparing results in Table II for Runs 60.28 and 60.41, projectile eccentricity reduces the magnitude of projectile momentum for the weakly supported tube. For firm support (compare Runs 60.30 and 60.38), projectile eccentricity increases the projectile momentum.

Increasing projectile eccentricity to twice the value used in test IDENT 06 does not significantly change the peak displacement up to muzzle exit, but it does sharply increase the projectile momentum at muzzle exit. This is shown by Runs 60.27 and 60.31 for both weak and firm tube support. For these two cases, the maximum calculated velocity and acceleration increased to  $-0.281 \text{ m/s}$  and  $9.235 \text{ m/s}^2$ , respectively. This is substantially above measured values.

#### Breech Block Eccentricity

The results of Runs 60.22 and 60.26 show the effects of breech block eccentricity on muzzle motions for a "weakly" supported tube. In these runs, the breech block eccentricity was varied from zero to twice its normal value. Muzzle displacements for the two extremes are shown in Figure 10. Part (a) gives results for a balanced breech, and part (b) for twice normal breech eccentricity. Muzzle displacements are small for the balanced breech, on the same order as displacements calculated for a firmly supported tube. Muzzle motions caused by projectile eccentricity are apparent. When the breech eccentricity is doubled (the normal eccentricity is  $8.911 \text{ mm}$  below the X-axis), muzzle displacements increase substantially. Now muzzle motions produced by projectile eccentricity are completely masked by the larger motions produced by the breech unbalance. Still, muzzle motions are far short of measured values.

#### Shear Deformations

All calculations performed in Runs 60.01 through 60.35 included shear deformations in the evaluation of the beam element stiffness matrices; however, shear deformations were not included in the interpolation functions. Neglecting shear deformations in the interpolation functions affects the magnitude and distribution of the element forces, including "moving mass effects." A more consistent finite element formulation is obtained when shear deformations are included (or neglected) in all terms.

Results in Figures 8 and 9 (Runs 60.40 and 60.41) were obtained with shear deformations in the finite element formulation. When shear deformations are omitted for a weakly supported tube, the results of Figure 11 are obtained. Except for the omission of shear, the run is identical to that of Figure 9. The effect of shear deformation is to stiffen the tube and create higher frequency oscillations at the muzzle. Displacements and velocity change only slightly in magnitude, but accelerations are increased by about 50%.

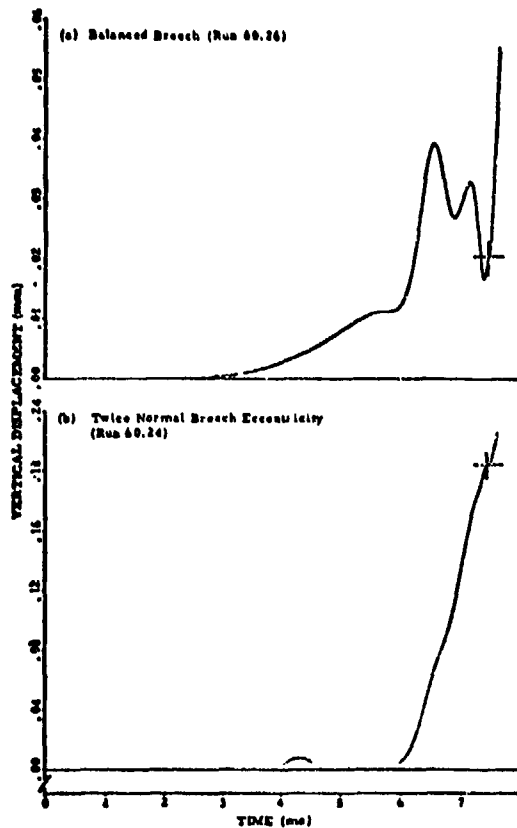


FIGURE 10. EFFECT ON MUZZLE DISPLACEMENTS OF BREECH UNBALANCE

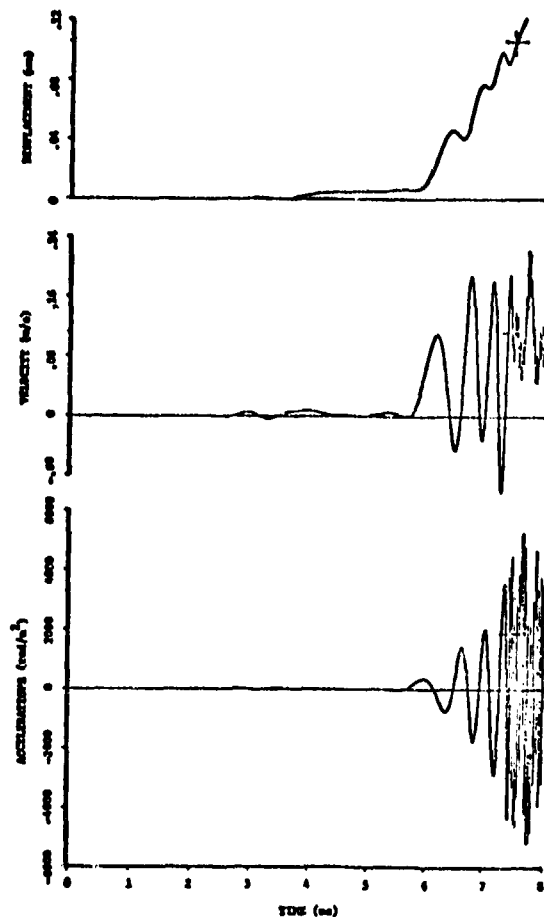


FIGURE 11. MUZZLE MOTIONS COMPUTED WITHOUT SHEAR DEFORMATIONS WITH THE TUBE WEAKLY SUPPORTED (RUN 60.42)

An increase in acceleration is produced by higher forces. The net lateral force between the projectile and the tube is given in Figure 12. Permitting shear deformations in the tube "smooths" the lateral force between the projectile and the tube and reduces the amplitude of the peak by about 50%. From Table II, the angular deviation of the projectile from the initial line of fire is increased in magnitude by a factor of about 2.5.

#### Discussion of Results

In addition to the parameter studies performed for test IDENT 06 in the vertical plane of motion, parameter studies were performed for motions in the horizontal plane and in torsion. Also, muzzle motions were calculated for tests IDENT 08 and 10.



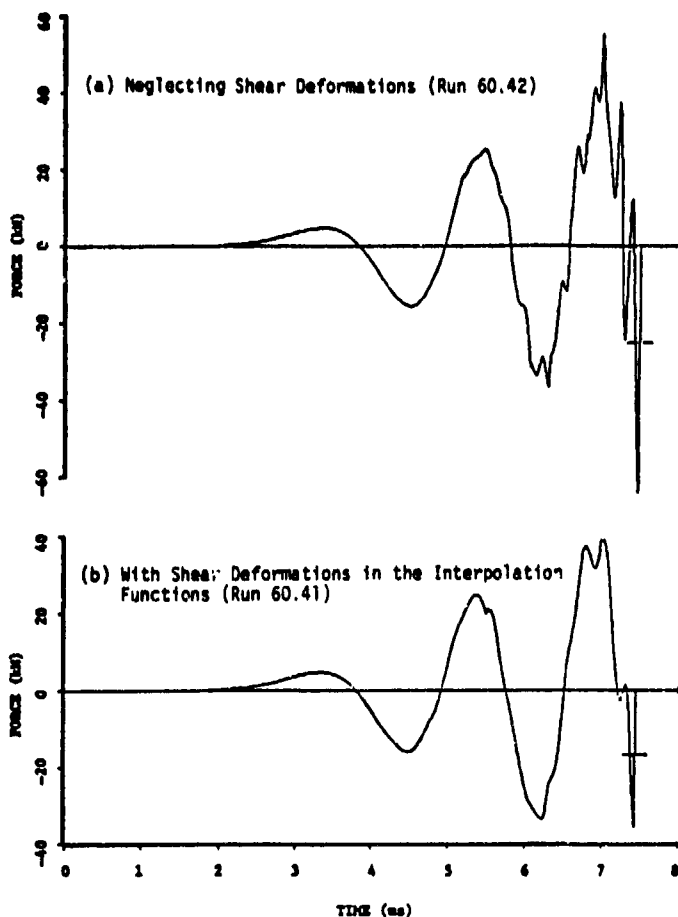


FIGURE 12. NET LATERAL FORCE BETWEEN THE PROJECTILE AND THE TUBE

Analytical and experimental results for the three tests are summarized in Table III. Except as noted, all results are for the tube supported on weak springs (essentially a free-free beam). Peak values of muzzle displacement, velocity, and acceleration are given for two different time intervals labeled as:

$$\text{time} \leq T_m$$

and

$$\text{time} \leq T_{me}$$

$T_m$  is the time at which the experimental data end. It is given in both fiducial time, which corresponds to the time scale for the experimental data, and in time which starts at zero when the propellant is ignited. Zero time was established by the first detectable rise in chamber pressure.

$T_{me}$  denotes projectile exit from the tube. This value was calculated from the tube length, calculated recoil displacements, and measured projectile motions. Because experimental data did not extend to projectile exit, only calculated results are given in the second time interval.

Peak values were determined according to magnitude. A sign is given to show whether it peaked in the positive or negative direction. Because the muzzle accelerations oscillate about zero, both a negative peak and a positive peak are given. Both positive and negative peaks are also given for velocity if they were significant. For vertical motions, positive is up; for horizontal motions, positive is to the right while looking down the tube. Torsion follows the right hand rule with the positive axis pointing down the tube.

TABLE III. COMPARISONS BETWEEN MEASURED AND CALCULATED MUZZLE MOTIONS FOR IDENTs 06, 08, AND 10

Test No. and Direction	T <sub>m</sub> , Time at End of Measured Data (ms)	T <sub>me</sub> <sup>40</sup> , Time of Projectile Exit (ms)	For Time ≤ T <sub>m</sub>			For Time ≤ T <sub>me</sub>					
			Measured			Calculated					
			Peak Disp. (mm or rad.)	Peak Vel. (m/s or rad/s)	Peak Accel. (m/s <sup>2</sup> or rad/s <sup>2</sup> )	Peak Disp. (mm or rad.)	Peak Vel. (m/s or rad/s)	Peak Accel. (m/s <sup>2</sup> or rad/s <sup>2</sup> )			
Ident 06											
	Vertical	27.6/7.02 <sup>0</sup>	2.25	1.5	+8,400 -6,500	0.0833	0.124	+500 -467	0.116	0.124	+1,430 -4,000
	Horizontal	26.3/5.72	0.25	0.28	+2,300 -2,700	-0.0011	-0.009	+0 -90	0.0833	0.481	+5,300 -630
	Torsion	26.3/5.72		0.0091	15.5	+40,000 -35,000	0.005	3.0	+10,000 -10,000	0.0124	7.0
Ident 08											
	Vertical	28.2/6.77	-2.1	-2.2	+5,500 -6,500	0.094	0.13	+500 -500	0.1427	0.23	+2,910 -1,900
	Horizontal	27/5.57	0.39	0.42	+4,600 -3,600	-0.0034	-0.0005	-0	0.0881	0.428	+1,350 -540
	Torsion	27/5.57	-0.0016	-6.1	+17,500 -65,000	0.0018	1.6	+10,000 -10,000	0.0032	+3.16 -4.53	+34,300 -140,900
Ident 10											
	Vertical	25.9/6.84	-1.4	-1.8	+4,000 -4,600	0.11 0.0084	0.15	+670 -550	0.1584	0.156	+3,230 -2,290
	Horizontal	24.5/5.54	+0.66	0.65	+4,900 -4,900	-0.0032	-0.005	+34 -64	0.1131	0.487	+5,450 -610
	Torsion	24.5/5.54	-0.0095	-7.3	+55,000 -56,000	0.0017	1.3	+10,000 -15,000	0.00424	+4.0 -2.4	+55,000 -298,000

<sup>a</sup> Fiducial time/time zero at first detectable pressure rise in the chamber (corresponds to time used in calculations).

\* Calculated with reduced torsional restraint between the breech and the torque bracket--torsional motions for Idents 08 and 10 calculated for firm support.

<sup>a</sup>Calculated using measured projectile displacement and calculated tube recoil-  
for tests 9B and 10 calculated for firm support.

Most of the observations made when comparing measured and calculated values for IDENT 06 also hold when comparing with IDENTs 08 and 10. These include:

- . Calculated motions lag measured values. This is true in every case for time  $\leq T_m$  except perhaps for torsional motions of IDENT 08. Here the magnitude of the calculated displacement exceeds the measured value, but velocity and acceleration are low. The "lagging" of calculated motions behind measured values is most pronounced in the horizontal plane. In the horizontal plane, the breech lies on the axis and no initial tube deflections were considered. Because of this, calculated motions of the muzzle are very small until the projectile nears muzzle exit, at which time abrupt motions occur.
- . If calculated values out to projectile exit are compared to available experimental data, the magnitudes of calculated displacements in the vertical plane are still much too low. For this comparison, the ratios of measured to calculated muzzle displacements are:

19.4 for IDENT 06  
-14.7 for IDENT 08  
- 8.84 for IDENT 10

Muzzle velocities are low by an equal or greater factor, but accelerations are low by a factor less than two.

- . Comparing calculated motions in the horizontal plane (for time  $\leq T_{me}$ ) with the measured data, better agreement is found between analysis and experiment than for the vertical plane. This comparison gives, for the ratio of measured to calculated muzzle displacements:

3.0 for IDENT 06  
4.4 for IDENT 08  
7.6 for IDENT 10

Magnitudes of calculated velocities and accelerations agree well.

- . Magnitudes of calculated and measured torsional motions are in good agreement. Calculated results for IDENTs 08 and 10 are for firm torsional support; even so, magnitudes of the displacements agree fairly well. Velocities are underestimated and accelerations are overestimated, if calculated results out to  $T_{me}$  are compared to measured values.

New observations can also be made when the results for IDENTs 08 and 10 are included in the comparisons. For IDENT 06, calculated

and measured displacements agreed in sign for vertical, horizontal, and torsional motions. For IDENTs 08 and 10, measured displacements in the vertical plane and in torsion are reversed in sign relative to both the calculated values and to measured values for IDENT 06. Calculated torsional displacements at the muzzle were produced by the torque from projectile spin-up. This torque would reverse in sign only for reversed rifling. Thus, additional torques, omitted in the analysis, are necessary to cause a reversal in torsional displacements.

Torques can be produced by the recoil spring and by the interaction of the breech and the torque bracket. These torques would have to exceed those produced by projectile spin-up to reverse the torsional motions at the muzzle. Also, these "additional torques" must act during some firings and not others. Because clearances do exist between the breech and the torque bracket, the direction of the net torque and thus the direction of tube rotation may depend upon the position of the breech lug in the slot in the torque bracket prior to firing. If the lug rests against the counterclockwise (CCW) side of the slot (facing the muzzle), then clockwise (CW) rotations are permitted (produced by torque from projectile spin-up). If the lug rests against the CW side of the slot, then CW rotations are not permitted, and perhaps a torque introduced into the breech by the torque bracket produces CCW motions.

Calculated vertical muzzle displacements were produced principally by breech eccentricity and initial tube droop. Other forces, aside from these, which were not treated in the analysis, are necessary to cause the reversal in calculated muzzle displacements. As for the torques, these forces may arise from the recoil spring (eccentricity in the restoring force) or from interactions between the breech and the torque bracket.

We have examined the effect of lateral forces on the breech produced by torque reactions. Variations of the breech force from -8700 n to +8700 n produced only a small change in muzzle motions for a tube which was weakly supported. The force applied in these studies was determined from the torque produced in the torque bracket. This torque was computed with conditions of zero "torsional clearance" in the weapon (firm support).

Subsequent calculations for IDENTs 08 and 10 showed that the breech reaction computed for IDENT 06 was low by a factor of 4.35. A systematic study of the effect produced by the larger breech forces was not made; however, calculations for IDENT 08 and 10 include the larger forces, and the results in Table III are not substantially different from those of IDENT 06. Although the effect of the larger breech force cannot be predicted with confidence from these comparisons, we suspect that it is still relatively minor. Thus, it seems unlikely that breech reactions will reverse the muzzle displacements.

Additional comparisons between analysis and experiment are needed to resolve the discrepancies which have been observed. Recommendations for further work are included in the next section.

### Conclusions and Recommendations

#### Conclusions

Based on the work documented in this paper, we can draw the following conclusions:

- . Tube support stiffness has a significant effect on muzzle motions up to shot ejection.
- . If measured motions are correct, the gun tube behaves essentially as a free-free beam up to times very near projectile exit.
- . Moving mass effects, that is, the coupling of projectile axial motions and tube lateral motions, are significant at times near projectile exit. Response of the muzzle near projectile exit is altered by the moving mass effects, but is changed very little at earlier times.
- . Measured muzzle motions do not show the higher frequency oscillations in displacements which have been calculated. Although measurements do not extend to muzzle exit, it appears that these motions are caused by the overturning moments produced by breech eccentricity, initial tube droop, and perhaps other forces such as the "Bourdon force" which were not considered. The magnitude of these motions obscures smaller muzzle motions produced by projectile eccentricity. These effects were observed analytically when comparing muzzle motions for a weakly supported and firmly supported tube.
- . Forces at the breech caused by the interaction between the breech lug and the torque bracket do not have a significant effect on lateral muzzle motions.
- . Shear deformations have a significant effect on muzzle motions as the projectile is passing through the muzzle region.

#### Recommendations

The studies performed and conclusions drawn indicate a need for additional research in several areas. Our recommendations for future research are as follows:

- . For better comparisons of analytical results, tube motions should be measured at additional points along the length of

the tube and perhaps on the cradle. In addition, these measurements must extend to times past muzzle exit.

- . A definition of the interaction forces between the tube and the cradle is necessary. If a continuous oil film exits between the tube and tube support sleeve, one approach to the problem would be to define the nonlinear viscous forces produced by the oil film. Lubrication theory for radial motion of two concentric cylinders indicates that, with an oil film present, contact between the tube and the tube support sleeve should never occur. The damping forces will increase rapidly as the two components approach each other, but high contact forces may be avoided.
- . A more accurate treatment of projectile release from the muzzle is needed. This should include the transition region between bourrelet exit and exit of the aft rotating band.
- . The study of gun tube motions should be extended to include a three-dimensional model. With the three-dimensional model, certain effects which must be omitted in two-dimensional ones can be treated. These include: (1) possible coupling between tube torsion and lateral bending, (2) representation of clearances in the weapon as annular spaces rather than as one-dimensional variables, (3) more exact representation of projectile motions at exit, and (4) gyroscopic moments on the projectile produced by out-of-plane motions. The significance of these effects will not be known until a three-dimensional study is undertaken.
- . Further model development should be supported by experimentation on a scale physical model that can be varied to establish precisely known boundary and initial conditions rather than continuing on a set tactical system. Particularly, control and accurate determination of mount and recoil conditions are required. Measurements should include: (1) lateral and angular motions at several points along the tube and in the receiver area, (2) projectile axial, lateral, and angular motions in bore and during exit from the tube, (3) recoil motions, and (4) chamber and projectile base pressures.

#### References

1. P. A. Cox and J. C. Hokanson, "Muzzle Motions of the M68 105-mm Gun," Final Technical Report prepared for Propulsion Division, Ballistic Research Laboratories, Aberdeen Proving Ground, MD, by Southwest Research Institute, June 1977 (in publication).

\*COX & HOKANSON

2. R. D. Cook, Concepts and Applications of Finite Elements Analysis, John Wiley & Sons, Inc., New York, 1974.
3. S. Timoshenko, D. H. Young, and W. Weaver, Jr., Vibration Problems in Engineering, John Wiley & Sons, Inc., New York, 1974.
4. T. E. Simkins, "Radial and Transverse Response of Gun Tubes by Finite Element Methods," Proceedings, First Conference on Dynamics of Precision Gun Systems, Rock Island, IL, January 1977.

LANGHAAR, MILLER AND  
BORESI

TITLE: Excitation of a Gun Barrel Due to Firing.  
HENRY L. LANGHAAR, R. E. MILLER and A. P. BORES  
UNIVERSITY OF ILLINOIS, Urbana-Champaign  
Urbana, Illinois 61801

ABSTRACT:

A finite-element approach is used to analyze the dynamic response of a gun barrel due to firing. A piecewise cubic approximation of the deflection ensures continuity of deflections and slopes at the net points. Initially, at all net points, linear and angular displacements and velocities are prescribed. This arbitrariness in the initial conditions allows for initial residual motions from the preceding shot. A digital computer program based upon the analysis has been developed. The program may be used for the period during which the projectile is in the barrel and also for the period after the projectile leaves the muzzle by setting terms pertaining to the projectile and the gas pressure equal to zero. Horizontal transverse vibrations of the barrel may be treated by discarding the acceleration of gravity. The projectile is treated as a point mass. Consequently, balloting is not covered by the theory. The effects of a gun-barrel tuning mass, eccentricity of the breech, and eccentricity of the recoil mechanism are included.

The differential-difference equations are linear, and of second order. They are solved numerically for the displacements, slopes, velocities and acceleration at all net points. The slope and the lateral velocity at the muzzle are particularly important because of their influence on the accuracy of the shot. Numerous numerical results have been obtained. An interesting result is the effect of eccentricity of the recoil mechanism.

BIOGRAPHY:

PRESENT EXPERIENCE: Professor of Theoretical and Applied  
Mechanics, University of Illinois, Urbana-Champaign, Illinois.

PAST EXPERIENCE: Engineer, Convair Aircraft Corporation, San  
Diego, California, 1941-1947.

DEGREES HELD: Bachelor of Science, Master of Science, Ph. D.,  
Lehigh University, Bethlehem, Pennsylvania.



## EXCITATION OF A GUN BARREL DUE TO FIRING

HENRY L. LANGHAAR, PROFESSOR  
ROBERT E. MILLER, PROFESSOR  
\*ARTHUR P. BORESI, PROFESSOR  
UNIVERSITY OF ILLINOIS  
URBANA, ILLINOIS 61801

1. DESCRIPTION OF THE MATHEMATICAL MODEL. Figure 1 represents a gun barrel with mass  $M$  and elevation angle  $\alpha$ . Axes  $(x, y)$  move axially with the barrel as it recoils, but they undergo no lateral displacement. The projectile is regarded as a point mass  $m$ . Balloting is not considered. A short time  $t$  after firing, the projectile lies in the barrel point  $x = \xi(t)$ , as shown in Fig. 1. The axial velocity of the projectile relative to the breech is  $v(t) = \dot{\xi}$ . The axial frictional force of the projectile on the barrel is  $F(t)$ . The gas pressure driving the projectile is  $p(t)$ . There is a tuning mass  $m_T$  with constant coordinate  $\eta$ . Its center of mass is considered to lie on the axis of the barrel. Its moment of inertia about a transverse axis through its center of mass is  $I_T$ . The breech is regarded as a rigid block with mass  $\bar{M}$

and moment of inertia  $\bar{I}$  about a transverse axis through its center of mass. The location of the center of mass of the breech is defined by two lengths,  $e$  and  $d$ , shown in Fig. 1. The axial recoil displacement is  $u(t)$ . The recoil spring and the recoil dashpot are assumed to be linear. Their constants are  $(a_B, \mu_B)$ , and their eccentricities are  $(e', e'')$ , as shown in Fig. 1.

If there is initial bending of the barrel due to weight, unsymmetrical thermal gradients, or manufacturing tolerances, the bending is aggravated by inertial interaction between the barrel and the projectile. Axial friction  $F(t)$  also excites motion of the barrel. Another disturbance comes from the so-called Bourdon effect, which arises because, in the bent barrel, the area of the bore above the neutral plane, on which the gas pressure acts, is slightly greater than the area below the neutral plane. Still another effect contributing to bending of the barrel is axial inertia of the recoiling barrel and breech. This is especially influential if the breech is eccentric. (See Ref. 1).

The barrel is regarded as a tapered elastic beam, having strain energy per unit length proportional to the square of the curvature. The origin  $x = y = 0$ , lies at the breech. The barrel is divided into intervals by points  $x_0 = 0, x_1, x_2, \dots, x_n$ , where  $x_n$  is the coordinate of the muzzle (Fig. 1). These points need not be equally spaced. In the  $j$ 'th interval  $(x_{j-1}, x_j)$ , we approximate the deflection by a cubic function:

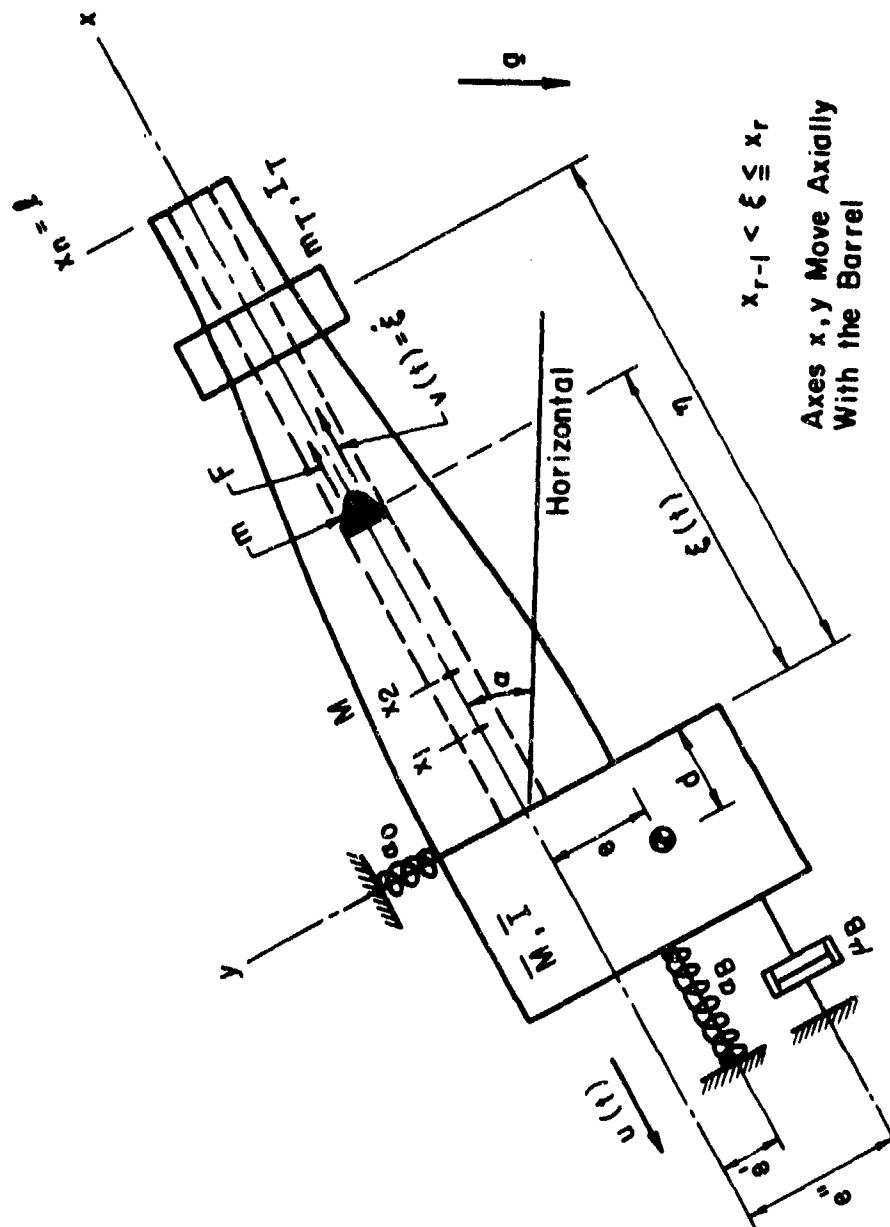


Figure 1

$$y = a_0^j + a_1^j x + a_2^j x^2 + a_3^j; \quad x_{j-1} \leq x \leq x_j \quad (1)$$

$$a_a^j = A_a^j y_{j-1} + B_a^j y_j + C_a^j \theta_{j-1} + D_a^j \theta_j \quad (2)$$

where  $\theta_j = y'_j$ , in which the prime denotes the derivative with respect to  $x$ . The coefficients  $A_a^j, B_a^j, C_a^j, D_a^j$  are chosen so that  $y$  and  $y'$  are everywhere continuous. The structure supporting the barrel and the breech is regarded as a set of independent linear translational and rotational springs and dashpots at all net points. These elements are assumed to be attached to an immovable bed. The spring constants and the damping constants for the translational and rotational springs and dashpots at point  $x_j$  are respectively  $(a_j, a'_j)$  and  $(\mu_j, \mu'_j)$ . At a node where there is actually no supporting spring or dashpot, the spring constants and/or dashpot constants are set equal to zero in the computer program. Spring and dashpot supports are not shown in Fig. 1, except for one lateral spring at the breech, with constant  $a_0$ . For more detail on the breech effect, see Ref. 1.

2. METHOD OF ANALYSIS. An initial-value problem is considered. At time  $t = 0$ , the projectile lies at point  $x_0$ ; i.e.,  $\xi(0) = 0$ . Also,  $v(0) = 0$ , where  $v$  is the axial speed of the projectile. At all net points  $x_j$ , the linear and angular displacements  $(y_j, \theta_j)$  and the linear and angular velocities  $(\dot{y}_j, \dot{\theta}_j)$  are prescribed for time  $t = 0$ . This arbitrariness in the initial conditions allows for initial residual motions from the preceding shot in a rapid-fire gun.

The generalized coordinates are the deflections  $y_j$  and the rotations  $\theta_j$  at the net points. Also, the recoil displacement  $u$  and the projectile coordinate  $\xi$  may be regarded as generalized coordinates. Alternatively,  $u$  and  $\xi$  may be regarded as known functions of  $t$ . The components of generalized force are the coefficients in the expression for the virtual work  $\delta W$ . Contributions to  $\delta W$  come from the action of gravity on the breech, barrel, and projectile, from axial friction  $F(t)$  on the barrel, from the Bourdon effect, from the axial inertia of the recoiling barrel and breech, and from the strain energy of bending of the barrel. The complete expression for  $\delta W$  (which is too lengthy to write here) provides all components of generalized force. (See Ref. 2).

The kinetic energy  $T$  of the system is the sum of the kinetic energies of translation and rotation of the breech, the segments of the barrel, the projectile, and the tuning mass. Hamilton's principle,

$$\int_{t_0}^{t_1} (\delta T + \delta W) dt = 0 \quad (3)$$

yields the Lagrangian equations of motion for the system. With this approach, conservatism of the forces is not demanded. Discontinuities occur at the instantaneous location of the projectile, since, for example, the gas pressure behind the projectile, causing the Bourdon effect, terminates there. However,

discontinuities do not obstruct the finite-element method that is used. This is an advantage over the traditional approach via the differential equation of beams, since, with the latter formulation, the action of the projectile is described by a Dirac delta function or a Heaviside step function. These anomalies are avoided by the finite-element treatment.

The Lagrange equations are linear, second-order, differential-difference equations for the unknown functions  $y_j(t)$  and  $\theta_j(t)$ . A computer program based on Newmark's beta method has been devised for solving them with arbitrary initial values  $y_j(0)$ ,  $\theta_j(0)$  and  $\dot{y}_j(0)$ ,  $\dot{\theta}_j(0)$ . (See Ref. 3).

Vertical bending and lateral bending of the barrel are decoupled in a linear theory. Both of these types of deformation are covered by the program. For lateral motion, there is no gravitational effect.

The program provides the history of the motion of the barrel from the initial instant  $t = 0$  until the projectile leaves the muzzle. Also, it may be used for the period after the projectile has left the muzzle. In that case,  $p = 0$ ,  $F = 0$ , and all other terms pertaining to the projectile are dropped.

To implement the program, we must know the recoil displacement  $u(t)$ , the projectile displacement  $\xi(t)$ , the base pressure on the projectile  $p(t)$ , and the frictional force  $F(t)$ . If  $\xi(t)$  and  $p(t)$  are known,  $F(t)$  is determined by applying Newton's law to the axial motion of the projectile. In applying the program to an actual gun, we must estimate the spring constants  $(a_j, a'_j)$  and the damping constants  $(\mu_j, \mu'_j)$  of the supporting structure. Because of the complicated nature of the structure and the peculiar damping devices in use, this may be difficult.

Of especial significance for the accuracy of shooting are the muzzle slope  $\theta_n$  and the muzzle velocity  $\dot{y}_n$  at the instant when the projectile leaves the barrel. The program permits a study of these quantities corresponding to various motions and deflections of the barrel at the instant of firing.

3. EXAMPLES OF DATA AND RESULTS. Some results have been obtained for an approximate model of the Rarden gun. The following data were used: (See Fig. 1):  $l = 96$  inches (the first 21 inches tapered and the remaining 75 inches uniform; the bore is 30 mm with outside diameter of the uniform section taken as 1.70 inches). The barrel was modeled by ten finite elements. The effects of the breech and flash hider were included. The barrel is taken to be supported laterally by two springs, one located at the breech and the other at a bearing 21 inches from the breech. The exact stiffnesses of the two lateral springs are not known. Hence, a range of values was used  $k = 10^4, 10^5, 10^6$  (lb/in.). In addition, there is a pad arrangement located at 54 inches from the breech. The pads are modeled by a spring and dashpot. The data shown in Table 1 give values of the displacement and slope of the muzzle for the time at which the projectile exits (3.6 millisecon) and also for a later time (10 millisecon). Results are given for cases with pads and without pads (that is, without spring and dashpot).

In Table 2, natural frequencies for the Rarden model are given with and without pads and for the same values of  $k$ .

In general, we note from Table 1 that the deflections at 10 millisecons are two orders of magnitude larger than that at projectile exit. The

slopes are also larger by a factor of 5 or more. Without pads the deflections and slopes at 10 milliseconds are approximately twice the muzzle deflections and slopes with pads. The deflections at projectile exit are of the same order with or without pads. However, the muzzle slopes at projectile exit are roughly twice as large for the case without pads.

From Table 2, we note that a change in support stiffness  $k$  from  $10^4$  lb/in. to  $10^5$  lb/in. results in a large change in frequencies (except for the first mode). However, a change of  $k$  from  $10^5$  lb/in. to  $10^6$  lb/in. produces little change in the first three frequencies. Seemingly, only the first two frequencies are affected greatly by the pads.

TABLE 1. DEFLECTION AND SLOPE AT MUZZLE OF RARDEN GUN FOR VARIOUS VALUES OF SUPPORT STIFFNESS, WITH AND WITHOUT PADS

With Pads				
$k$ (lb/in.)	$t = .0036$ sec.		$t = .0100$ sec.	
	Defl. (in.)	Slope	Defl. (in.)	Slope
$10^4$	$-1.58 \times 10^{-5}$	$5.29 \times 10^{-6}$	$-157 \times 10^{-5}$	$-116 \times 10^{-6}$
$10^5$	$-1.27 \times 10^{-5}$	$5.95 \times 10^{-6}$	$-102 \times 10^{-5}$	$-37.7 \times 10^{-6}$
$10^6$	$-1.29 \times 10^{-5}$	$5.75 \times 10^{-6}$	$-96.9 \times 10^{-5}$	$-24.9 \times 10^{-6}$
Without Pads				
$k$ (lb/in.)	$t = .0036$ sec.		$t = .0100$ sec.	
	Defl. (in.)	Slope	Defl. (in.)	Slope
$10^4$	$+ .582 \times 10^{-5}$	$17.1 \times 10^{-6}$	$-397 \times 10^{-5}$	$-297 \times 10^{-6}$
$10^5$	$-1.19 \times 10^{-5}$	$13.7 \times 10^{-6}$	$-222 \times 10^{-5}$	$-87.4 \times 10^{-6}$
$10^6$	$-1.51 \times 10^{-5}$	$12.1 \times 10^{-6}$	$-212 \times 10^{-5}$	$-69.7 \times 10^{-6}$

TABLE 2. NATURAL FREQUENCIES OF RARDEN GUN

With Pads			
$\begin{matrix} \overrightarrow{k \text{ (lb/in.)}} \\ f(\text{hz}) \end{matrix}$	$10^4$	$10^5$	$10^6$
$f_1$	12.0	12.0	12.0
$f_2$	50.8	59.3	60.4
$f_3$	76.0	148.0	154.0
$f_4$	114.1	225.4	308.4
$f_5$	206.0	289.0	449.3
$f_6$	340.5	425.4	530.9

Without Pads			
$\begin{matrix} \overrightarrow{k \text{ (lb/in.)}} \\ f(\text{hz}) \end{matrix}$	$10^4$	$10^5$	$10^6$
$f_1$	6.67	7.40	7.49
$f_2$	42.8	51.3	52.5
$f_3$	75.9	148.0	153.9
$f_4$	113.8	225.4	307.0
$f_5$	205.3	287.7	449.2
$f_6$	339.6	425.3	530.8

#### REFERENCES

1. "The Development and Implementation of a Methodology of Analyzing the Effects of an Eccentric Breech on Gun Firing Accuracy," by A. P. Boresi, Final Technical Report, Contract DAAK 10-77-M-1326, Department of the Army, U. S. Army Armament Research and Development Command, Dover, New Jersey, February 1978.

2. "Excitation of a Gun Barrel before the Projectile Leaves the Muzzle," by H. L. Langhaar and A. P. Boresi, First Technical Report, Grant No. DAAG 29-77-G-0074, ARO, Durham, N. C., July, 1977.
3. "A Computer Program for the Analysis of a Gun Barrel Motion before the Projectile Leaves the Muzzle," by R. E. Miller, Second Technical Report, Grant No. DAAG 29-77-G-0074, ARO, Durham, N. C., September, 1977.

**SIMKINS**

**TITLE:** Transverse Response of Gun Tubes to Curvature-Induced Load Functions

THOMAS E. SIMKINS,

US ARRADCOM

Benet Weapons Laboratory, LCWSL

Watervliet Arsenal, Watervliet, NY 12189

**ABSTRACT:**

This study investigates transverse tube loadings induced by initial curvature of the tube. Several load functions are derived, two of which are investigated in detail in connection with the 105 mm, M-68 tank gun. Displacement, velocity and slope of the muzzle are given as functions of time through shot ejection. Calculations are based on a Galerkin procedure using as basis functions, ten splined eigenvectors computed using the NASTRAN finite element code. In general it is found that the recoil of a curved gun tube in the absence of strong supports, yields the greatest response at the muzzle compared with that due to the traveling asymmetric pressure and the moving mass projectile mass. The latter exhibit important wavelike characteristics, however, and may point the way for further research.

**BIOGRAPHY:**

**PRESENT ASSIGNMENT:** Research Mechanical Engineer, Benet Weapons Laboratory, Watervliet Arsenal, Watervliet, NY 12189.

**PAST EXPERIENCE:** Research Assistant, Rensselaer Polytechnic Institute, Troy, NY, 1961-63.

**DEGREES HELD:** Bachelor of Science - Mechanical Engineering, Northeastern University, Boston, Mass., 1961; Master of Science, Rensselaer Polytechnic Institute, Troy, NY, 1963; Ph.D., Rensselaer Polytechnic Institute, Troy, NY, 1968.



SIMKINS

## TRANSVERSE RESPONSE OF GUN TUBES TO CURVATURE-INDUCED LOAD FUNCTIONS

THOMAS E. SIMKINS, PHD.  
BENET WEAPONS LABORATORY  
WATERVLIET ARSENAL, WATERLVIET, NY

### INTRODUCTION

The work which follows shows how transient bending vibrations may arise during firing due to tube curvature. Tube motions predicted at the muzzle are of sufficient magnitude to explain a portion of the error realized at the target. Three sources of curvature-induced vibration (1) are treated in detail.

An appreciable effort has been made in the interest of realism. Highly detailed tube geometries and interior ballistic curves of pressure and projectile travel have been included in the analysis. Wherever possible, use has been made of the large, widely accepted, NASTRAN (Nasa STRuctural ANALysis) finite element computer code. Though NASTRAN is quite versatile, it is not particularly well suited for handling curvature-induced load functions which require special programming.

### TRANSVERSE (BENDING) MOTION OF GUN TUBES - CURVATURE INDUCED LOADS

In 1959, measurements by Gay and Elder of the US Army Ballistics Laboratory (2) showed that the muzzle motions of a 90 mm tank gun at the time of shot ejection are very small but yet significant in explaining a portion of the error realized at the target. Typical rotations and displacements at the muzzle, for example, were of the order of  $10^{-1}$  milliradians and  $10^{-2}$  inches, respectively. The theory of gun tube motion by which explanations were sought for these observations assumed that the motion was due solely to a mass eccentricity at the breech which produced a sudden inertial moment upon recoil. The theoretically predicted motion, however, was often much smaller in magnitude than that observed. In the work that follows it will be shown that loads resulting from the initial curvature of the M-68, 105 mm gun tube can also produce muzzle motions of these magnitudes and should therefore be included in future analysis.

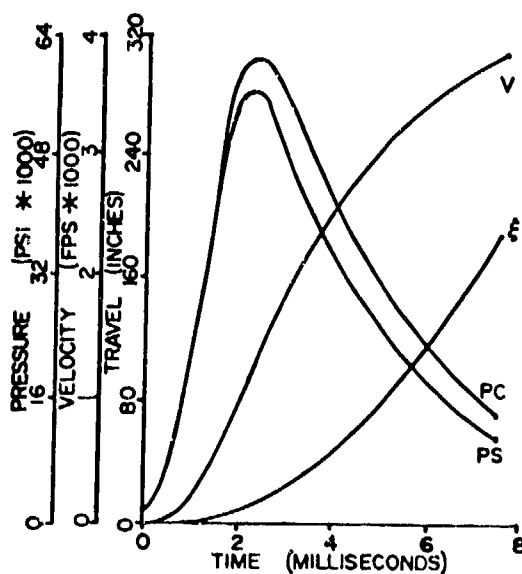


Figure 1 - Internal Ballistic Curves for the M-68.

Each of the loads induced by the curvature of the M-68 depend in one or more ways upon the ballistic pressure and projectile travel versus time. The Recoil Load function, for example, requires either the knowledge of the chamber pressure (PC vs.  $t$ ) and the recoiling mass or, more directly, the deviative of the velocity,  $V(t)$ . On the other hand the 'Bourdon' load function requires the ballistic pressure distribution to the rear of the projectile for which an average of the chamber pressure PC, and the pressure at the base of the projectile PS, is used. The necessary information for these calculations is shown in Figure 1.

#### Recoil Loads

During the recoil of a gun tube there results an axial load per unit length which is equal to the product of the recoil acceleration,  $\alpha(t)$ , and the mass per unit length of the tube  $\rho(x)$ ; i.e.,

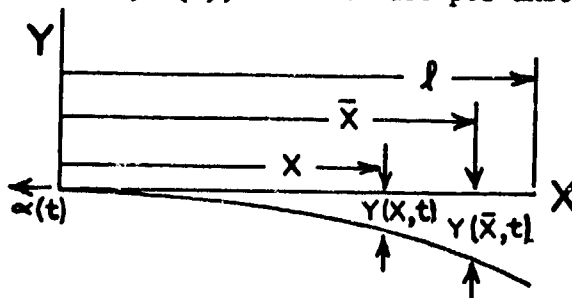


Figure 2 - Inertial Moment Due to Recoil.

$$w(x,t) = -\rho(x)\alpha(t) \quad (1)$$

When the tube is curved, this load creates a moment at any location  $x$ , along the tube. Referring to Figure 2, the total moment is given by the integral:

$$M(x,t) = \int_x^l -w(\bar{x},t)[y(\bar{x},t) - y(x,t)]d\bar{x} \quad (2)$$

Differentiating twice with respect to the space variable  $x$  gives the resultant transverse load intensity due to recoil:  $[ (') = \partial/\partial x ]$

$$f_1(x,y'y'',t) = \alpha(t)\{\rho(x)y'(x,t) - y''(x,t)\int_x^l \rho(\xi)d\xi\} \quad (3)$$

## SIMKINS

### 'Bourdon' Load

If a gun tube is curved, the bore surface area becomes asymmetrically distributed about the central axis owing to the relative extension and contraction of the material. From the geometry of Figure 3 one can verify that the net difference in area is given by the integral:

$$\int_0^{2\pi} \left(\frac{a}{R} \sin\theta + 1\right) a \sin\theta d\theta dx = -\pi a^2 y'' dx \quad (4)$$

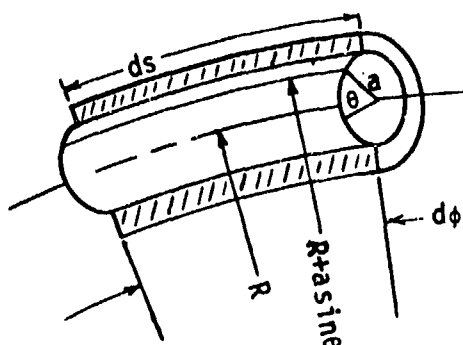


Figure 3 - Curved Section of Tube.

bore. ( $f_2$  has been called the 'Bourdon' Load because of its similarity to a straightening Bourdon tube upon pressurization. Actually, the two effects are completely different and the term 'Bourdon' Load is a misnomer.)

where  $R^{-1}$  has been replaced by  $-y''$ . The applied ballistic pressure therefore produces a resultant transverse load intensity:

$$f_2(x, y'', t) = -p(x, t) \pi a^2 y''(x, t) \quad (5)$$

$p(x, t)$  is a traveling ballistic pressure function, i.e.,

$$p(x, t) = P_0(t) H(\xi - x)$$

$H(z)$  is the Heaviside unit step function and  $\xi(t)$  represents the distance traveled by the projectile along the

### Projectile Loads

If the projectile is assumed to be a point mass  $m_p$ , traveling a curved bore axis which changes in time, it can be shown (3) that there results a transverse load function containing Coriolis, centrifugal and transverse accelerations, i.e.,  $[(\cdot) = \partial/\partial t]$

$$f_3 = -m_p [\ddot{y} + 2V\dot{y}' + V^2 y'' + g] \delta(x - \xi(t)) \quad (6)$$

where  $\delta(z)$  is the Dirac function and  $\xi(t) = \int_0^t V dt$ , where  $V(t)$  is the projectile velocity.  $g$  is the gravitational constant.

### Equation of Motion

Using Euler-Bernoulli beam theory, the displacement  $y(x, t)$  from the undeformed (straight) neutral axis of the tube must satisfy the partial differential equation:

$$(EI y'')'' + \rho(x) \ddot{y} - f_k - (EI y'')'' = 0 \quad (7)$$

## SIMKINS

where  $I(x)$  is the area cross section moment of inertia and  $E$  is Young's Modulus of Elasticity. The last term on the right hand side of (7) represents the static load intensity corresponding to an initial deformation  $Y(x)$ .

The initial conditions are:  $y(x,0) = Y(x)$  and  $\dot{y}(x,0) = 0$  (8)

The load functions  $f_k$  ( $k = 1-3$ ) will be considered in turn. It is to be noted, however, that the beam motions due to each load function may not be superposed as the linear operators involved vary with the particular load function considered.

It is convenient to first define  $\bar{y}(x,t)$  as the displacement as measured from the initial curve  $Y(x)$ . Thus (7) becomes:

$$(EI\bar{y}''')'' + \rho(x)\ddot{\bar{y}} - f_k = 0 \quad (9)$$

It is to be noted that  $(\bar{y}+Y)$  now replaces the variable  $y$  in each of the  $f_k$ . The initial conditions in terms of  $\bar{y}$  are homogeneous:

$$\bar{y}(x,0) = \dot{\bar{y}}(x,0) = 0 \quad (10)$$

### Static and Dynamic Support Conditions

The support (boundary) conditions which prevail prior to firing may not be appropriate during the interior ballistic cycle. For the purpose of calculating the initial static gravitational deformation  $Y(x)$ , the M-68 tube is assumed to be cantilevered from its two mounting points near the breech. Actual vibration records indicate that the mount connections are far from rigid, however. In fact, good agreement between calculated and experimentally observed natural frequencies is obtained only if the tube is regarded as virtually unsupported during the ballistic cycle. The dynamic boundary conditions are therefore assumed to be free.

The partial differential equation (9) can be transformed into a set of  $N$  - ordinary differential equations in time via the Galerkin procedure (4) in which the basis functions are chosen to be the natural modes of vibration of the unsupported M-68 tube. Using the NASTRAN finite element program, these mode shapes,  $W_i(x)$  - as well as the initial gravitational deformation function  $Y(x)$  - are determined at nineteen points along the tube. Between these points the shapes are interpolated by cubic spline functions. The approximation for  $\bar{y}$  in terms of the mode shapes may be written:

$$\bar{y}(x,t) = \sum_{i=1}^N a_i(t)W_i(x) \quad (11)$$

# SIMKINS

The Galerkin procedure, in variational form, consists of multiplying the differential equation (9) by  $\delta\bar{y}$ , the variation of  $\bar{y}$ , and integrating over the length of the tube:

$$\int_0^l \{ (EI\bar{y}''')'' + \rho(x)\ddot{\bar{y}} - f_k \} \delta\bar{y} dx = 0 \quad (12)$$

Substituting the expression for  $\bar{y}$  from (11):

$$\int_0^l \left\{ \sum_{i=1}^N [a_i(t)(EIW_i''')'' + \rho(x)\ddot{a}_i W_i] - f_k \right\} \cdot \sum_{j=1}^N W_j \delta a_j dx = 0 \quad (13)$$

The  $W_i$  are orthogonal with respect to the density function  $\rho(x)$ :

$$\int_0^l \rho(x) W_i W_j dx = \delta_{ij} \quad (14)$$

and since the  $W_i$  are eigenfunctions of the free vibration problem:

$$(EIW_i''')'' = \rho(x)\omega_i^2 W_i(x) \quad (15)$$

where  $\delta_{ij}$  is the Kronecker delta, vanishing unless  $i = j$  whereupon it has unit value, and the  $\omega_i$  are the natural frequencies of the unsupported tube.

Substituting (14) and (15) into equation (13) results in  $N$  ordinary differential equations of the form:

$$\ddot{a}_i + \omega_i^2 a_i - \int_0^l f_k W_i dx = 0 \quad (16)$$

From (10) it is clear that the initial conditions on the  $a_i(t)$  are homogeneous, i.e.:

$$a_i(0) = \dot{a}_i(0) = 0 \quad (17)$$

(a) Recoil Load Function ( $k=1$ ) -

In this case (16) becomes:

$$\ddot{a}_i + \omega_i^2 a_i + \sum_{j=1}^N [A_{ij}(t) - B_{ij}(t)] a_j = C_i(t) \quad (16a)$$

$i = 1 \text{ to } N$

## SIMKINS

$A_{ij}$  derives from the  $\bar{y}''$  terms in (9) while  $B_{ij}(t)$  reflects the slope dependency,  $\bar{y}'$ .  $C_i(t)$  is due to terms in the initial deformation function  $Y(x)$ .

### (b) Bourdon Load Function (k=2) -

For this case (16) becomes:

$$\ddot{a}_i + \omega_i^2 a_i + \pi a^2 P_o(t) \sum_{j=1}^N D_{ij}(t) a_j = -\pi a^2 P_o(t) E_i(t) \quad (16b)$$

$i = 1 \text{ to } N$

$D_{ij}(t)$  derives from the  $\bar{y}''$  term in the 'Bourdon' Load function while  $E_i(t)$  is due to the initial deformation  $Y(x)$ .

### (c) Projectile Load Function (k=3) -

$$\sum_{j=1}^N \{A_{ij}(\xi(t)) \ddot{a}_j + Z_{ij}(\xi(t)) \dot{a}_j + S_{ij}(\xi(t)) a_j\} + \ddot{a}_i + \omega_i^2 a_i = Q_i(\xi(t), t) \quad (16c)$$

The  $A_{ij}$  are coefficients deriving from the transverse acceleration of the tube at the projectile position  $\xi(t)$ . The  $Z_{ij}$  derives from the Coriolis acceleration of the projectile at  $\xi$  and  $S_{ij}$  from the centrifugal acceleration.  $Q_i$  is a linear combination of three terms representing the centrifugal force of the projectile solely due to its traversing the initial curve  $Y(x)$  plus the moving weight of the projectile,  $m_p g \delta(x-\xi)$ .

The systems represented by equations (16) and (17) for  $k = 1$  through 3 were each solved numerically using 4th order, variable time step Runge-Kutta integration.\* In practice a value of  $N = 10$  gave satisfactory convergence. These included two rigid body modes ( $\omega_1 = \omega_2 = 0$ ) representing plane rotation and translation and eight vibration modes of finite frequency.

\*While there are many algorithms requiring less computation time, none has been found more accurate or trustworthy. In fact, the Runge-Kutta algorithm is often chosen as a standard for comparison.

## RESULTS AND DISCUSSION

Figures 4 through 6 represent the responses of the M-68 gun tube to recoil, asymmetric ballistic pressure (the 'Bourdon' effect), and the moving projectile. The magnitudes shown in each of the figures are comparable with those predicted by Gay and Elder (5) in connection with eccentric breech inertia in the T-139 tank gun. This indicates that curvature-induced loads should be included in any theory of gun tube motion during firing.

A fundamental difference is apparent between figures 4 and 5, and is especially obvious in comparing the time histories of the tube shapes, i.e., figures 4a and 5a. Whereas in 4a the motion is well developed along the entire tube length, the motion in 5a is much more wavelike and muzzle displacements remain comparatively small through shot ejection. This difference is due to the fact that the recoil inertia load acts instantaneously\* over the entire tube length whereas development of the 'Bourdon' load proceeds at projectile velocity. Moreover, the recoil loading consists of two parts (cf. equation 3). If evaluated near time zero, these two parts consist of a downward load proportional to the initial curvature ( $Y''$ ) and therefore stronger near the supports, and an upward load proportional to the initial slope ( $Y'$ ) more intense near the muzzle. The two act in unison to encourage a rotation of the entire tube. The large mass at the breech, however, tends to anchor that end of the tube. The result is the deformation shown in figure 4a. The Bourdon load, on the other hand, consists of only one part (cf. equation 5). This part, being proportional to curvature is greatest near the supports and trails off to practically zero value by mid-length of the tube. Muzzle displacement must therefore await the arrival of a disturbance originating from the support end of the tube.

A similarity is also apparent comparing figures 4 and 5. The time histories of the slopes at the muzzle - probably the most important of all the response curves - show a definite similarity in that little muzzle rotation occurs during the first half of the ballistic cycle. This delay represents the propagation time for a disturbance established near the supports (where  $Y'$  is largest) to reach the muzzle.

Figure 6 shows that the moving projectile definitely produces tube motions of higher frequency though in general these reach the muzzle superposed on the same mode shapes as that on which the 'Bourdon' response progresses (cf. figures 5a and 6a). Figures 6b, c show clearly the higher frequency realized at the muzzle. A 'peak-to-peak' measurement indicates this frequency is very nearly 1 kHz. The amplitudes displayed in figure 6 are almost equal to those of figure 5, both being considerably less than those of figure 4.

\*The tube is assumed axially rigid in the analysis.

SIMKINS

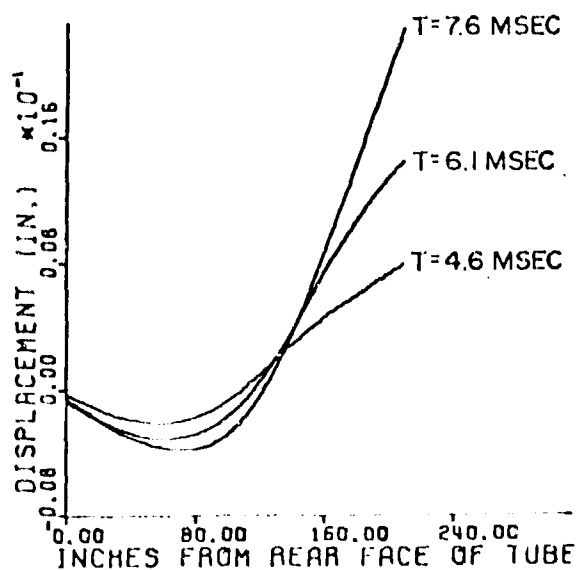


Figure 4a - Displacement of Tube Axis from Initial Position.

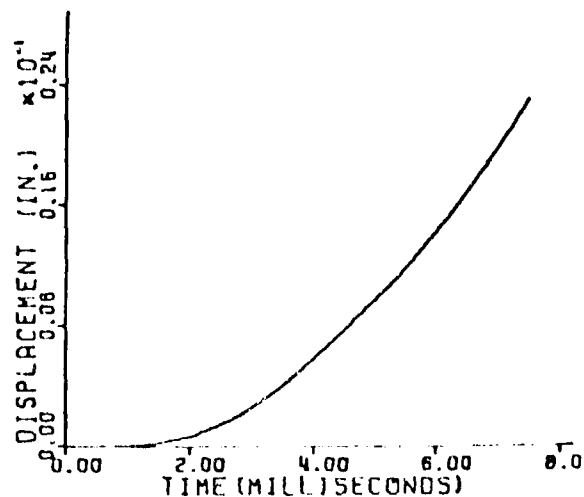


Figure 4b - Muzzle Displacement.

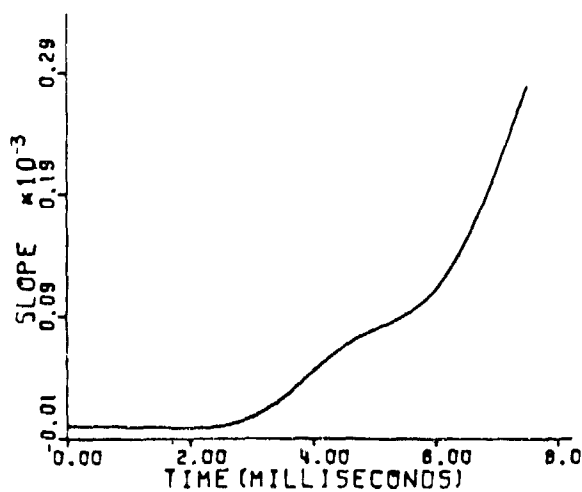


Figure 4c - Muzzle Slope (Rotation).

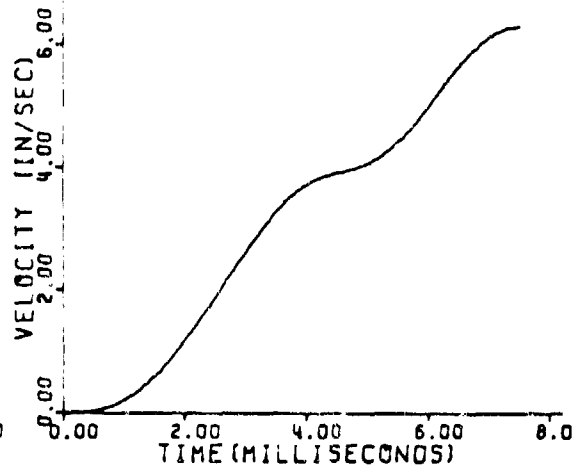


Figure 4d - Transverse Velocity of Muzzle.

Figure 4 - Transverse Response of the M-68 Gun Tube to Recoil Inertia.



SIMKINS

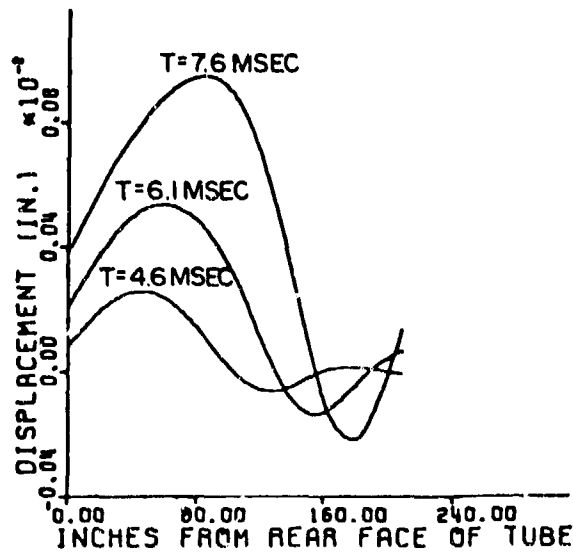


Figure 5a - Displacement of Tube Axis from Initial Position.

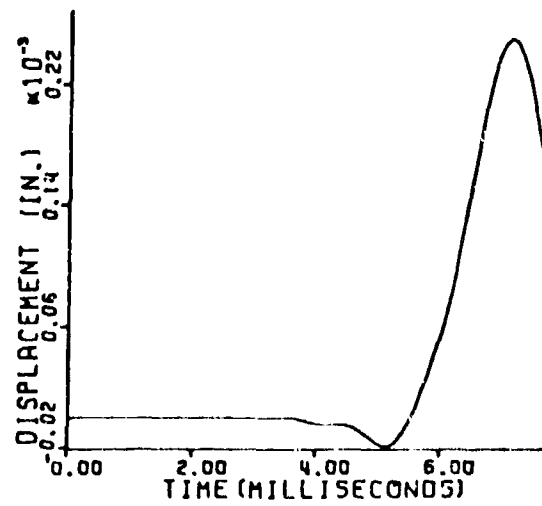


Figure 5b - Muzzle Displacement.

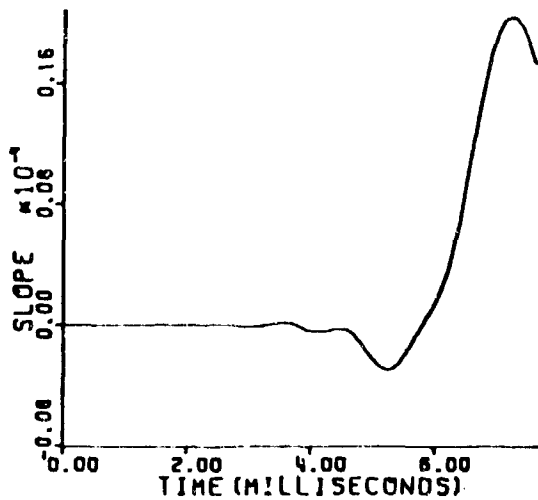


Figure 5c - Muzzle Slope (Rotation).

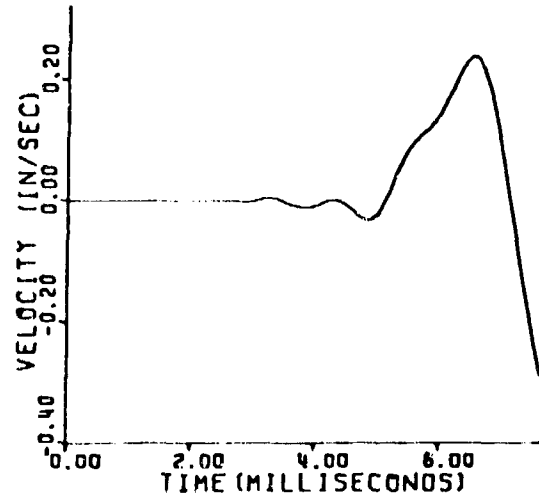


Figure 5d - Transverse Velocity of Muzzle.

Figure 5 - Transverse Response of the M-68 Gun Tube to Traveling Bourdon Pressure.

SIMKINS

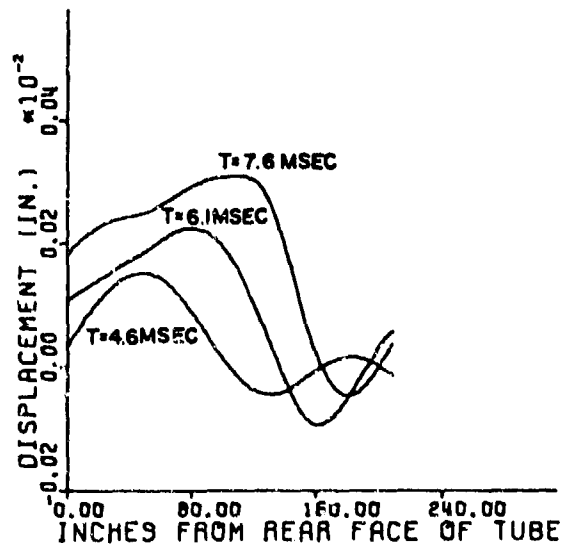


Figure 6a - Displacement of Tube Axis from Initial Position.

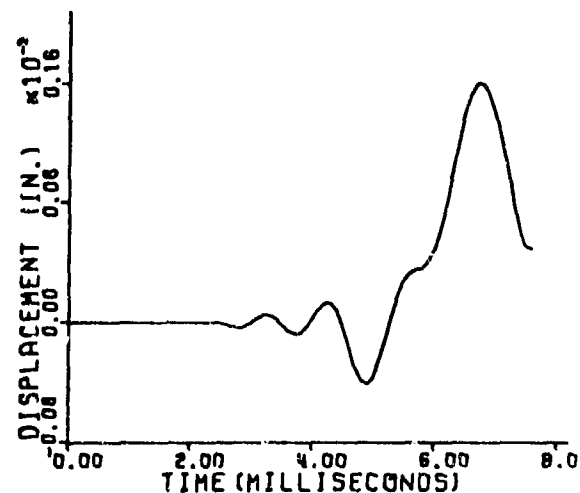


Figure 6b - Muzzle Displacement.

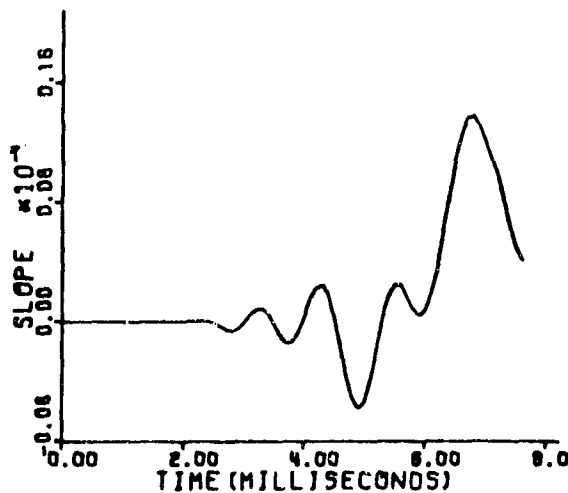


Figure 6c - Muzzle Slope (Rotation).

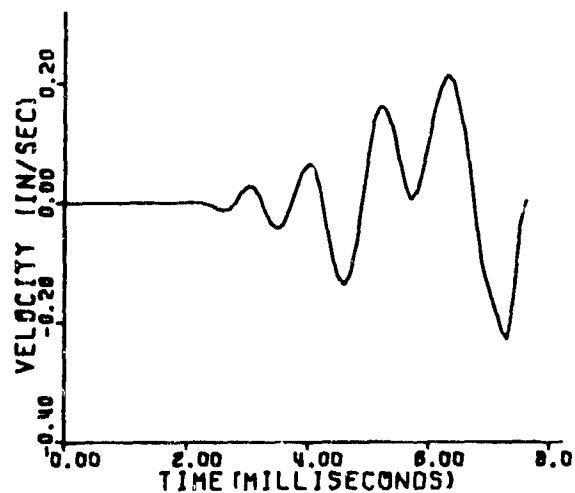


Figure 6d - Transverse Velocity of Muzzle.

Figure 6 - Transverse Response of the M-68 Gun Tube to Traveling Projectile Mass.

## CONCLUSION

To completely account for the motions of a gun tube prior to shot ejection several effects must be considered, among them the effects of tube curvature. Of particular significance is the muzzle slope at the time the projectile arrives. Slope values are particularly sensitive to sudden disturbances which originate near the support or breech end of the tube and propagate in wavelike fashion reaching the muzzle prior to shot ejection. This is exemplified in the case of the Bourdon load and strongly suggests an opportunity for further study as the supports themselves may create strong forces as clearances are abruptly taken up during the initial phases of recoil. The result may significantly strengthen rotations of the muzzle at shot ejection.

The capability of introducing high frequencies of vibration is probably the most important consequence of the projectile load function. It is possible that this effect may be amplified considerably when projectile spin as well as projectile imbalance is taken into account.

## ACKNOWLEDGEMENT

The author thanks Mr. Richard Haggerty of the Benet Weapons Computer Science Laboratory and Ms. Ellen Fogarty for their invaluable assistance.

## REFERENCES

- (1) Simkins, T., Pflegl, G., and Scanlon, R., "Dynamic Response of the M113 Gun Tube to Travelling Ballistic Pressure and Data Smoothing as Applied to XM150 Acceleration Data," Appendix B, Benet Weapons Lab Tech Report No. WVT-TR-75015, ADA010662 (1975).
- (2) Gay, H., and Elder, A., "The Lateral Motion of a Tank Gun and Its Effect on the Accuracy of Fire," Ballistic Research Lab Report No. 1070 (1959), AD217657.
- (3) Simkins, T., "Structural Response to Moving Projectile Mass by the Finite Element Method," Benet Weapons Lab Tech Report No. WVT-TR-75044, (1975).
- (4) Kantorovich, L. V. and Krylov, V. I., Approximate Methods of Higher Analysis, 3rd ed. (Interscience), pp. 258-262.
- (5) Ref. (2), p. 16, Table I.

EHLE, HUANG, AND HAUG

TITLE: Dynamic Analysis and Design of Weapon Mechanisms with Intermittent Motion.

PAUL E. EHLE, U.S. Army Armament Research and Development Command, Dover, N.J. 07807.

RAY C. HUANG, and EDWARD J. HAUG, College of Engineering, The University of Iowa, Iowa City, Iowa 52242.

ABSTRACT:

Automatic weapon mechanisms are characterized by numerous complex mechanical activities that take place. A bolt is unlocked from the barrel, a cartridge is ejected, the hammer is driven back and cocked, buffers are engaged, and parts are cammed relative to each other. This multiplicity of functions is accomplished periodically, with a rate varying from one cycle per second to more than 2000 cycles per second. Each cycle of this motion may be divided into a sequence of time intervals, in each of which a distinct system of differential equations governs the motion. This dynamic behavior is called intermittent motion. Distribution theoretic techniques are used to develop a unified method for analysis of automatic mechanisms with intermittent motion. An idealized model is first studied to illustrate the formulation of system dynamics with intermittent motion. A method of design sensitivity analysis that is compatible with this modeling approach is then presented. The validity of representative sequence approximations is verified, using distribution theoretic analysis. Finally, application of the method to a realistic model of an automatic rifle is presented.

BIOGRAPHY:

PRESENT ASSIGNMENT: Mechanical Engineer, Fire Control and Small Caliber Weapon Systems Laboratory, U.S. Army Armament Research and Development Command.

PAST EXPERIENCE: Mechanical Engineer, U.S. Army Weapons Command, 1968-1969; Capt. U.S.A.R., Serving in Viet Nam, 1969-1970; Mechanical Engineer, R & D Laboratory, U.S. Army Weapons Command, 1970-1973; Mechanical Engineer, Concepts and Technology Division, U.S. Army Armament Command, 1973-1977; Leader, Mechanisms Technology, Fire Control and Small Caliber Weapon System Laboratory, U.S. Army Armament Research and Development Command.

DEGREES HELD: B.S., Johns Hopkins University, 1964; M.S., University of Pennsylvania, 1965.

DYNAMIC ANALYSIS AND DESIGN OF  
WEAPON MECHANISMS WITH INTERMITTENT MOTION

\*PAUL E. EHLE, MECHANICAL ENGINEER  
US ARMY ARMAMENT RESEARCH AND DEVELOPMENT COMMAND  
DOVER, N.J. 07807  
RAY C. HUANG, ASSISTANT PROFESSOR  
EDWARD HAUG, PROFESSOR  
MATERIALS DIVISION, COLLEGE OF ENGINEERING  
THE UNIVERSITY OF IOWA, IOWA CITY, IA. 52242

1. INTRODUCTION

Automatic weapon mechanisms represent a unique class of mechanical systems in which numerous complex mechanical activities take place. A bolt is unlocked from the barrel, a cartridge is ejected, the hammer is driven back and cocked, buffers are engaged, and parts are cammed relative to each other. This multiplicity of functions is accomplished periodically, with a rate varying from one cycle per second to more than 2000 cycles per second. Each cycle of this motion may be divided into a sequence of time intervals, in each of which a distinct system of differential equations governs the motion. Since the geometry of the mechanism and the number of masses moving in any particular time interval vary, the dimension of the state variable (the positions and velocities of the moving parts) varies as the motion proceeds. At those instants when the state equations change, jump conditions are defined that play the role of a set of initial conditions for the next time interval, based on the motion that occurred in the preceding time interval; e.g., a momentum balance due to impact that occurs at the transition time. Further, these transition times are variable, depending upon past states of motion of the mechanism and upon variations of loading impulse, friction within the mechanism, and many other factors.

The academic literature on dynamics of mechanisms with intermittent motion is extremely limited. The peculiar nature of Army automatic mechanisms dictates that the rather extensive defense literature on this subject be heavily utilized. References 1 and 2 are cited as illustrative of the type of automatic mechanisms to be

\*EHLE, HUANG, AND HAUG

considered. A comprehensive and simplified analysis of automatic mechanisms (including blow back operated, recoil operated, gas operated, revolver, and multibarrel externally powered) is presented in Ref. 3. The representation of mechanism dynamics is, however, adequate for only first order analysis. As one might expect, a rather comprehensive literature exists on mechanism dynamics of the M16A1, as reflected by Refs. 4 through 8. Supporting these M16A1 analyses are a number of specialized analyses, such as Refs. 9 through 11. Analysis of extremely high rate mechanisms includes Refs. 12 through 14.

Given the capability to analytically describe the dynamic performance of such multi-state systems, the problem becomes one of design sensitivity analysis and optimization. The designer wishes to know what the effect will be of his systematic variation of design parameters; e.g., spring constants, cam position, cam shape, component mass, mechanism geometry, and mechanism dimensions. He must also be able to predict the effect of variation in parameters, over which he has little control; e.g., friction, variation in gas port performance, variation in temperature, and variation of geometry. First order sensitivity analyses have been performed using preliminary models by direct parametric variation techniques [4, 8, 15]. While these studies are valuable first steps in developing sensitivity analysis and design techniques, they lack the accuracy to be applicable in development of advanced sensitivity analysis and design optimization techniques. An in-depth treatment of sensitivity analysis and optimization of the ARPA 75 mm automatic mechanism was reported in the first symposium on gun dynamics [16] and in Ref. 17. The method developed in these references employs optimization techniques [18] that have been developed for mechanical system design. Encouraging as these results are, the methods used are not well-suited for large scale problems.

Distribution theoretic techniques that have recently appeared in the literature [19] for mechanical system dynamic analysis are used here to develop a unified method for analysis of automatic mechanisms with intermittent motion. Section 2 uses an idealized model to illustrate formulation of system dynamics with intermittent motion. A method of design sensitivity analysis that is compatible with this modeling approach is presented in Section 3. The validity of representative sequence approximations is verified, using distribution theoretic analysis, in Section 4. Finally, application of the method to a realistic model of an automatic rifle is presented in Section 5.

## 2. DISTRIBUTION THEORETIC METHODS IN DYNAMIC ANALYSIS

The principal tool employed in the method presented in this paper is representative sequence approximations of distributions. The well-known Heaviside-step function, the Dirac  $\delta$  function, and the unit doublet that are employed in various areas of mechanics are approximated by smoothly varying functions that provide the effect of

\*EHLE, HUANG, AND HAUG

the distributions in the limit. Illustrations of these approximating functions are shown in Fig. 1. It is shown in the following section that one can replace the distributions in representation of the dynamic system by the smoother representative sequences and achieve as high a degree of precision in the approximation as desired.

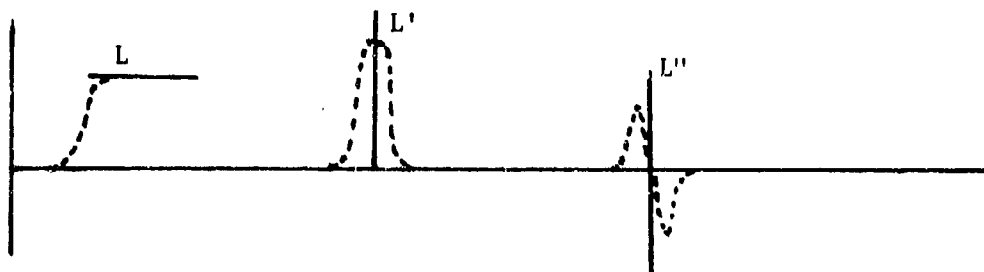


Figure 1. Heaviside-step, Dirac-  $\delta$ , Unit Doublet, and Their Representative Sequence Approximations.

To illustrate use of distributions in dynamic analysis, consider the idealized schematic of Fig. 2. Here, one envisions a bolt mass  $m_1$  which is driven by a drive spring  $k_1$  and which encounters a cartridge located initially at rest at position  $x_a$ . These two masses are subsequently locked together during continued motion and seating of the round. At position  $x_b$ , the pair of masses encounters resistance at the bolt face, represented by a stiff spring  $k_2$ . The conventional logical time modeling of this system would require the following system of pieced differential equations, which are valid only in separate intervals of time:

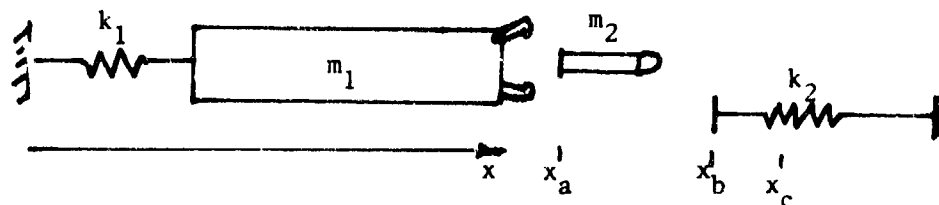


Figure 2. Idealized Mechanism Schematic.

\*EHLE, HUANG, AND HAUG

$$m_1 \ddot{x} + k_1(x - \ell_0) = 0, \quad x < x_a \quad (1,a)$$

$$(m_2 + m_1) \ddot{x} + k_1(x - \ell_0) = 0, \quad x_a < x < x_b \quad (1,b)$$

$$(m_1 + m_2) \ddot{x} + k_1(x - \ell_0) + k_2(x - x_b) = 0, \quad x > x_b \quad (1,c)$$

Equations 1 clearly indicate the discontinuous nature of mass and the variable form of applied forces, even for an extremely simple idealization of three elements of a weapon mechanism. In addition to these equations, certain balance conditions must be imposed to provide modification of initial conditions and the logical time at which  $x(t) = x_a$ . Specifically, momentum before impact must equal momentum after impact, which is  $m_1 \dot{x}(t_a^-) = (m_1 + m_2) \dot{x}(t_a^+)$ . This condition allows the analyst to integrate the equation of motion (1,a) up to the point  $x = x_a$ , to stop the integration process, and to restart using initial conditions  $x(t_a^+) = x(t_a^-)$  and  $\dot{x}(t_a^+) = m_1 \dot{x}(t_a^-) / (m_1 + m_2)$ . As the number of mechanical elements making up a system grows, the number of possible logical behavior conditions grows rapidly. Thus, analysis using logical times becomes quite cumbersome.

As an alternative to this piecewise analysis, one can formally write the equations of motion using the Heaviside function  $L$  of Fig. 1, to obtain the single equation of motion

$$\frac{d}{dt} \left[ \{m_1 + L(x - x_a)m_2\} \dot{x} \right] + k_1(x - \ell_0) + k_2(x - x_b)L(x - x_b) = 0 \quad (2)$$

It is important to note that when variable mass occurs, Newton's equations of motion must be written in the form "rate of change of momentum equals applied force", as in Eq. 2. Even if one employs the strictly discontinuous nature of the Heaviside-step function in Eq. 2, he must implement additional computer simulation that effectively reduces to Eqs. 1. However, using the representative sequence smooth approximation of the Heaviside-step function as illustrated in Fig. 1, one can use a standard numerical integration code to directly integrate Eq. 2. This approach is intuitively appealing, but raises questions concerning the validity of numerical approximation. The analysis of Section 4 of this paper illustrates that replacing the Heaviside-step function and other distributions by smooth approximating sequences is completely valid and that arbitrarily fine precision can be achieved. Thus, one reduces the essentially discontinuous problem to a problem involving only smooth functions. A major advantage of this is that numerical integration can proceed without the logical requirement to stop and reformulate equations of motion and initial conditions. This operation is accomplished automatically by the representative sequence problem



\*EHLE, HUANG, AND HAUG

formulation.

A second attractive feature of the distribution theoretic approach is the ability to represent the time at which a certain event occurs in the integral form

$$t_c = \int_0^{\tau} t L'(x - x_c) \dot{x} dt \quad (3)$$

where  $\tau$  is the total time interval and is greater than the time  $t_c$  at which  $x(t_c)$  equal  $x_c$ . The function  $L'$  here is the formal derivative of the Heaviside-step function, hence it is the  $\delta$ -function. If the pure distribution theoretic interpretation of  $L'$  is used, no computational advantage accrues. However, if the smooth representative sequence approximation of  $L'$  shown in Fig. 1 is employed, then numerical computation can allow evaluation of the event time  $t_c$  by Eq. 3. This formulation fits in nicely with the distribution theoretic model outlined in the foregoing and provides the designer with a method of evaluating and controlling such things as cycle time, time available to feed, and other time variables that play an important role in performance of an automatic weapon.

### 3. DESIGN SENSITIVITY ANALYSIS

The designer of weapon mechanisms would be greatly aided in his work if he knew how sensitive the behavior of a proposed mechanism is to variations in design parameters such as masses, spring constants, dimensions, damping coefficients, and moments of inertia. For analysis, the behavior characteristic to be examined must be expressed as a mathematically definitive quantity, such as time between events, maximum displacement, maximum force, stress, and maximum velocity. The quantities that the designer needs are sensitivity coefficients, defined as the change in the behavior functional due to a small change in design parameters. The presence of intermittent motion greatly complicates the determination of these coefficients, as well as the analysis of time histories of displacement, velocity, and force.

Weapon mechanism performance is subject to certain constraints that restrict the selection of design parameters. For example, total weight cannot be more than a given value or rearward travel of the bolt must be no less than a certain amount if a new round is to be fed. Thus, the designer would also like to know how sensitive the constraint relation is to changes in design parameters. For example, will a small reduction in round impulse greatly affect the ability of the mechanism to meet its constraint on minimum rearward travel of the bolt?

Design derivatives of these behavior characteristics and constraints can be put into the form

$$\ell^{0T} = \frac{\partial \psi_0}{\partial b} \equiv \frac{\partial}{\partial b} \left[ \int_0^{\tau} h_0(t, x(t), b) dt \right] \quad (4)$$

\*EHLE, HUANG, AND HAUG

subject to the equation of motion

$$\frac{dx}{dt} = f(t, x, b), \quad 0 \leq t \leq \tau \quad (5)$$

and equality/inequality constraints

$$\psi_{\alpha} = \int_0^{\tau} h_{\alpha}(t, x, b) dt \begin{cases} = 0, & \alpha = 1, \dots, r' \\ \leq 0, & \alpha = r' + 1, \dots, r \end{cases} \quad (6)$$

where  $b \in R^m$ ,  $x \in R^n$ , and matrix calculus notation [18] is used. Design sensitivity analysis methods are developed in great detail in Refs. 18 and 20. These methods are presented here only in summary form.

Due to a design change  $\delta b$ , the state of the system  $x(t)$  will change by an amount  $\delta x(t)$  that is determined by a linearized form of Eq. 5

$$\frac{d}{dt} \delta x = \frac{\partial f}{\partial x} \delta x + \frac{\partial f}{\partial b} \delta b, \quad \delta x(0) = 0 \quad (7)$$

One may also linearize Eq. 6 to obtain

$$\delta \psi_{\alpha} = \int_0^{\tau} \left( \frac{\partial h_{\alpha}}{\partial x} \delta x + \frac{\partial h_{\alpha}}{\partial b} \delta b \right) dt \quad (8)$$

To write Eq. 8 explicitly in terms of  $\delta b$ , one introduces the adjoint equation

$$\dot{\lambda} = - \frac{\partial f^T}{\partial x} \lambda - \frac{\partial h_{\alpha}^T}{\partial x}, \quad \lambda(\tau) = 0 \quad (9)$$

which is integrated from  $t = \tau$  back to  $t = 0$ . Integrating the identity  $\frac{d}{dt} (\delta x^T \lambda) = \delta \dot{x}^T \lambda + \delta x^T \dot{\lambda}$  from  $t = 0$  to  $t = \tau$  and using Eqs. 7 and 9 one has

$$0 = \int_0^{\tau} \left\{ \delta x^T \frac{\partial f^T}{\partial x} \lambda + \delta b^T \frac{\partial f^T}{\partial b} \lambda - \delta x^T \frac{\partial f^T}{\partial x} \lambda - \delta x^T \frac{\partial h_{\alpha}^T}{\partial x} \right\} dt$$

or

$$\int_0^{\tau} \frac{\partial h_{\alpha}}{\partial x} \delta x dt = \int_0^{\tau} \lambda^T \frac{\partial f}{\partial b} \delta b dt$$

Substituting this into Eq. 8 yields the desired relation for  $\delta \psi_{\alpha}$

$$\delta \psi_{\alpha} = \int_0^{\tau} \left( \lambda^T \frac{\partial f}{\partial b} \delta b + \frac{\partial h_{\alpha}}{\partial b} \delta b \right) dt$$

Since  $\delta b$  does not depend on time, this is

$$\delta \psi_{\alpha} = \left[ \int_0^{\tau} \left( \lambda^T \frac{\partial f}{\partial b} + \frac{\partial h_{\alpha}}{\partial b} \right) dt \right] \delta b \equiv \kappa^{\alpha T} \delta b \quad (10)$$

\*EHLE, HUANG, AND HAUG

The designer can now calculate design derivatives of response measures by evaluating the vector  $\ell^\alpha$ ,  $\alpha = 0, 1, \dots, r$ , of sensitivity coefficients. The only calculations required are to solve the adjoint problem of Eq. 9 and evaluate the integrals in Eq. 10. These calculations have been carried out for large classes of control and design problems [18,20], with reliable results. Here the method is applied to the intermittent motion mechanism problem, as represented by the distribution theoretic (logical function) approach of Section 2. Theoretical justification for this approach is presented in the following section and a large scale application is presented in Section 5.

#### 4. CONVERGENCE OF THE APPROXIMATION FOR A SIMPLIFIED MODEL

To illustrate sensitivity analysis by the distribution theoretic approach described in the previous sections, the mass capture model of Fig. 3 is considered in detail. The convergence of the method is proved here for this simple system and is treated for a broader class of systems in Ref. 20.

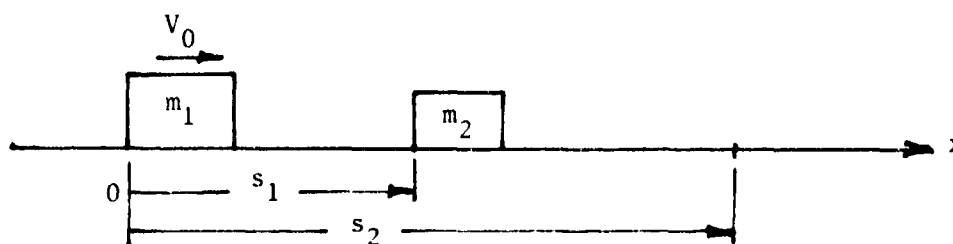


Figure 3. Mass Capture Model.

Let mass  $m_1$  move with constant velocity  $v_0$  from  $x = 0$  and seize mass  $m_2$  at  $x = s_1$ . Let  $t_1$  and  $t_2$  be the times when mass  $m_1$  reaches  $x = s_1$  and  $x = s_2$ , respectively. Suppose that  $(m_1, m_2, s_1, s_2)^T$  is the vector of design parameters and one wishes to find sensitivity coefficients that relate changes in the design parameters to corresponding changes in the functional

$$\psi = t_2 \quad (11)$$

An outline of the sensitivity analysis for this model, by a discontinuous logical time approach is given in Appendix A. This result serves as a limiting case that may be used to test the validity of the distribution theoretic approach.

By using the  $\theta$ - and  $\bar{\delta}$ -representative sequences defined in Appendix B, discontinuities in the analysis, such as the discontinuity of velocity of mass  $m_1$  at  $t = t_1$ , are removed. All variables employed in the dynamic and adjoint analyses are smooth.

\*EHLE, HUANG, AND HAUG

One now approximates the equations of motion by using the  $\theta$ -representative sequence as

$$\frac{d}{dt} \left\{ [m_1 + L_i(x - s_1)m_2] \dot{x} \right\} = 0 \quad (12,a)$$

with initial conditions

$$x(0) = 0, \quad \dot{x}(0) = V_0 \quad (12,b)$$

Let  $x^{(i)}$  be the solution of Eq. 12, where the index  $i$  is associated with the function  $L_i$ . It is shown in Ref. 20 that as  $i$  approaches  $\infty$ ,  $x^{(i)}$  converges to the solution of the ideal discontinuous model given in Appendix A. For simplicity, the dynamic analysis in this section is carried out with approximate functions  $L_i$  in Eq. 12,a, but the index  $i$  in  $x^{(i)}$  will be suppressed for notational convenience.

In order to put the equations of motion in standard first order form, define

$$z_1 = x, \quad z_2 = [m_1 + L_i(z_1 - s_1)m_2] \dot{x} \quad (13)$$

$$\begin{cases} \dot{z}_1 = \frac{z_2}{m_1 + L_i(z_1 - s_1)m_2} \equiv f_1 \\ \dot{z}_2 = 0 \equiv f_2 \end{cases} \quad (14,a)$$

$$z_1(0) = 0, \quad z_2(0) = m_1 V_0 \quad (14,b)$$

By Eqs. 3 and 13, the functional  $\psi$  in Eq. 11 is written as

$$\psi = \int_0^\tau t \frac{L'_n(z_1 - s_2)}{[m_1 + L_i(z_1 - s_1)]} \frac{z_2}{dt} dt = \int_0^\tau h_0 dt \quad (15)$$

where  $\tau > t_2$  and the functions  $L_i$  and  $L_n$  are shown schematically in Fig. 4.

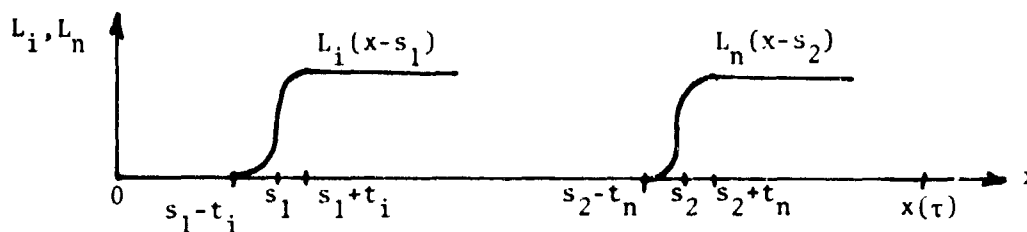


Figure 4.  $\theta$ - Representative Sequences.

\*EHLE, HUANG, AND HAUG

The adjoint equation 6 is now written as

$$\begin{cases} \frac{d\lambda_1}{dt} = \frac{m_2 z_2 L'_1(z_1 - s_1)}{[m_1 + L_1(z_1 - s_1)m_2]^2} \lambda_1 - t L''_n(z_1 - s_2) \frac{z_2}{[m_1 + L_1(z_1 - s_1)m_2]} \\ \frac{d\lambda_2}{dt} = \frac{-\lambda_1}{m_1 + L_1(z_1 - s_1)m_2} - \frac{t L'_n(z_1 - s_2)}{[m_1 + L_1(z_1 - s_1)m_2]} \end{cases} \quad (16.a)$$

$$\lambda_1(\tau) = 0, \quad \lambda_2(\tau) = 0 \quad (16.b)$$

Equations 16 are highly involved ordinary differential equations. By using the properties of the functions  $L_1$  and  $L_n$ , one can solve them over subintervals of the variable  $x$ ,  $(0, s_1 - \epsilon_i)$ ,  $(s_1 - \epsilon_i, s_1 + \epsilon_i)$ ,  $(s_1 + \epsilon_i, s_2 - \epsilon_n)$ ,  $(s_2 - \epsilon_n, s_2 + \epsilon_n)$ , and  $(s_2 + \epsilon_n, x(\tau))$ , separately. Let the corresponding time intervals be  $(0, t_1 - \hat{\epsilon}_{j\ell})$ ,  $(t_1 - \hat{\epsilon}_{i\ell}, t_1 + \hat{\epsilon}_{iu})$ ,  $(t_1 + \hat{\epsilon}_{iu}, t_2 - \hat{\epsilon}_{n\ell})$ ,  $(t_2 - \hat{\epsilon}_{n\ell}, t_2 + \hat{\epsilon}_{nu})$ , and  $(t_2 + \hat{\epsilon}_{nu}, T)$ . Note that  $\hat{\epsilon}_{i\ell}, \hat{\epsilon}_{iu}, \hat{\epsilon}_{n\ell}, \hat{\epsilon}_{nu} \rightarrow 0$  as  $i, n \rightarrow \infty$ . The solutions for the adjoint equations over each of these intervals are:

(a) For  $s_2 + \epsilon_n < x < x(\tau)$ 

$$\lambda_1(t) = 0, \quad \lambda_2(t) = 0 \quad (17)$$

(b) For  $s_2 - \epsilon_n < x < s_2 + \epsilon_n$ 

$$\lambda_1(t) = - \int_0^{t_2 + \hat{\epsilon}_{nu}} L'_n(z_1 - s_2) d\zeta + \int_0^t L'_n(z_1 - s_2) d\zeta - t L'_n(z_1 - s_2) \quad (18.a)$$

$$\begin{aligned} \lambda_2(t) = & \frac{t}{(m_1 + m_2)} \int_0^{t_2 + \hat{\epsilon}_{nu}} L'_n(z_1 - s_2) d\zeta \\ & - \frac{1}{(m_1 + m_2)} \int_0^{t_2 + \hat{\epsilon}_{nu}} L'_n(z_1 - s_2) d\zeta \\ & - \frac{t}{(m_1 + m_2)} \int_0^t L'_n(z_1 - s_2) d\zeta + \frac{1}{(m_1 + m_2)} \int_0^t \zeta L'_n(z_1 - s_2) d\zeta \end{aligned} \quad (18.b)$$

(c) For  $s_1 + \epsilon_i < x < s_2 - \epsilon_n$ 

$$\lambda_1(t) = \lambda_1(t_2 - \hat{\epsilon}_{n\ell}) \quad (19.a)$$

$$\lambda_2(t) = - \frac{\lambda_1(t_2 - \hat{\epsilon}_{n\ell})}{(m_1 + m_2)} t + \frac{(t_2 - \hat{\epsilon}_{n\ell})}{(m_1 + m_2)} \lambda_1(t_2 - \hat{\epsilon}_{n\ell}) \quad (19.b)$$

(d) For  $s_1 - \epsilon_i < x < s_1 + \epsilon_i$ 

$$\lambda_1(t) = \frac{\lambda_1(t_2 - \hat{\epsilon}_{n\ell})}{(m_1 + m_2)} [m_1 + L_1(z_1 - s_1)m_2] \quad (20.a)$$

\*EHLE, HUANG, AND HAUG

$$\lambda_2(t) = - \frac{\lambda_1(t_2 - \hat{\epsilon}_{nl})}{(m_1 + m_2)} (t - t_2 + \hat{\epsilon}_{nl}) \quad (20.b)$$

(e) For  $0 < x < s_1 - \epsilon_i$ 

$$\lambda_1(t) = \frac{m_1}{(m_1 + m_2)} \lambda_1(t_2 - \hat{\epsilon}_{nl}) \quad (21.a)$$

$$\lambda_2(t) = - \frac{\lambda_1(t_2 - \hat{\epsilon}_{nl})}{(m_1 + m_2)} (t - t_2 + \hat{\epsilon}_{nl}) \quad (21.b)$$

Thus, the adjoint variables have been solved.

Next one wishes to find the sensitivity coefficients. For the purpose of illustration, the sensitivity coefficient for the mass  $m_1$  is given and a proof of convergence for it is presented. Sensitivity coefficients for other design parameters and the proof of convergence can be done in a similar fashion [20].

Let  $\ell_{m_1, in}^\psi$  be the sensitivity coefficient of  $m_1$  with respect to the functional  $\psi$  associated with the approximate functions  $L_i$  and  $L_n$  in the dynamic equation and the functional, respectively. By techniques developed in Refs. [17], and [18], one has

$$\ell_{m_1, in}^\psi = \lambda_2(0^+)V_0 + \int_0^\tau \left[ \frac{\partial f_0}{\partial m_1} + \lambda_1 \frac{\partial f_1}{\partial m_1} \right] dt \quad (22)$$

By Eqs. 14, 15, and 17 to 21, Eq. 22 can be written as

$$\begin{aligned} \ell_{m_1, in}^\psi = \lambda_2(0^+)V_0 + \int_0^\tau \left\{ \frac{-tz_2 L'_n(z_1 - s_2)}{[m_1 + m_2 L_i(z_1 - s_1)]} \right. \\ \left. + \frac{-z_2 \lambda_1(t)}{[m_1 + L_i(z_1 - s_1)m_2]^2} \right\} dt \end{aligned} \quad (23)$$

or more explicitly

$$\begin{aligned} \ell_{m_1, in}^\psi = \lambda_2(0^+)V_0 + \int_0^{t_1 - \hat{\epsilon}_{il}} \frac{-\lambda_1(t_2 - \hat{\epsilon}_{nl})}{(m_1 + m_2)} dt \\ + \int_{t_1 - \hat{\epsilon}_{il}}^{t_2 + \hat{\epsilon}_{iu}} \frac{[-\lambda_1(t_2 - \hat{\epsilon}_{nl})]}{(m_1 + m_2)} \dot{z} dt \\ + \int_{t_1 + \hat{\epsilon}_{iu}}^{t_1 - \hat{\epsilon}_{nl}} [-\lambda_1(t_2 - \hat{\epsilon}_{nl})] \frac{\dot{z}}{m_1 + m_2} dt \end{aligned}$$

\*EHLE, HUANG, AND HAUG

$$\begin{aligned}
& + \int_{t_2 - \hat{t}_{nl}}^{t_2 + \hat{t}_{nu}} \left[ - \int_0^{t_2 + \hat{t}_{nu}} L'_n(z_1 - s_2) dt + \right. \\
& + \left. \int_0^t L'_n(z_1 - s_2) d\tau - t L'_n(z_1 - s_2) \right] dt \\
& + \int_{t_2 - \hat{t}_{nl}}^{t_2 + \hat{t}_{nu}} \frac{[-t L'_n(z_1 - s_2) \dot{z}_1]}{(m_1 + m_2)^2} dt \quad (24)
\end{aligned}$$

Letting  $n \rightarrow \infty$  and  $i \rightarrow \infty$ , one has

$$\begin{aligned}
\lim_{i \rightarrow \infty} \lim_{n \rightarrow \infty} \psi_{m_1, in} &= \frac{-t_2}{m_1 V_0} V_0 + \int_0^{t_1^-} \frac{1}{m_1 V_0} dt \\
&+ \int_{t_1^+}^{t_2^-} \frac{1}{m_1 + m_2} dt = - \frac{(s_2 - s_1)m_2}{m_1^2 V_0} \quad (25)
\end{aligned}$$

Note that this is precisely the same as the sensitivity coefficient of Eq. A-15, which was obtained by the discontinuous approach!

Thus the convergence of the sensitivity analysis by the distribution theoretic approach for the model is justified.

The significance of this result is felt in large scale practical problems, in which analysis by the ideal discontinuous approach is intractable. As an example of the complexities encountered in carrying out sensitivity analysis by the discontinuous approach the reader is referred to Ref. 17 where a 75mm automatic weapon is treated. To illustrate the power and potential of the foregoing distribution theoretic approach, a realistic model of a rifle is treated in the next section.

## 5. OUTLINE OF A COMPLEX (AUTOMATIC RIFLE) EXAMPLE

### A. Problem Definition

The example shown schematically in Fig. 5 is chosen to demonstrate the applicability of the preceding distributional or logical function method for complex problems. This mechanism is, in general form and complexity, typical of a variety of small caliber weapons such as the M16A1 rifle. In this particular model, only the bolt is allowed to rotate; all other motions are in the direction of the bore axis. The position of each mass is described by a state variable whose coordinate system is chosen for convenience. The origins are different, but all are located to the rear of the weapon.

The following is a description of weapon operation incorporated in Fig. 5. At time  $t = 0$ , all operating parts except hammer  $m_7$  and buffer weight  $m_3$  are in battery (forward), a round is in the chamber and the hammer is cocked. The stiff spring at the end of the bolt

\*EHLE, HUANG, AND HAUG

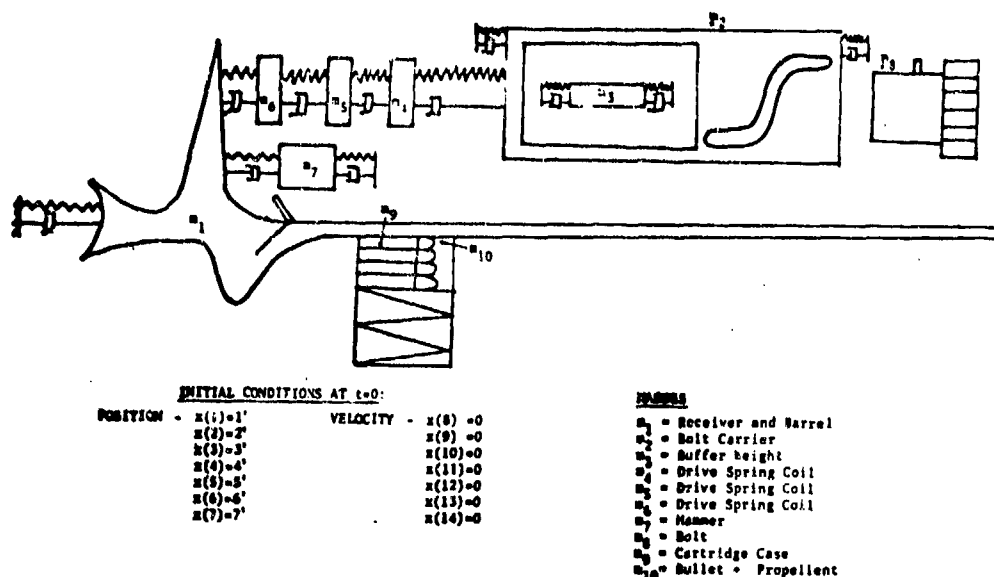


Figure 5. Automatic Rifle Model.

carrier  $m_2$  assures equilibrium of the preloaded drive spring system represented by masses  $m_4$ ,  $m_5$ , and  $m_6$ . At  $t = 0$ , the hammer is released and begins to move forward. When the stiff spring on its forward end strikes the bolt carrier  $m_2$ , the breech force begins to act on the receiver  $m_1$  and the gas force begins to act on  $m_2$ . Also at this time,  $m_1$  loses the mass of the projectile and propellant  $m_{10}$  of the chambered round. Under the action of the gas force,  $m_2$  moves rearward. This motion causes the bolt  $m_8$  to twist. When the forward end of the cam path is reached by the cam pin,  $m_8$  and  $m_9$  are captured by  $m_2$  and released by  $m_1$ . During this period, the rotational moment of inertia of  $m_8$  is that of the bolt plus the empty case. The bolt carrier continues to move rearward, until at a predetermined point it loses the mass of the empty case  $m_9$  through ejection. During the rearward motion of  $m_2$ , the hammer  $m_7$  is driven rearward by  $m_2$ . Chattering takes place between these two masses, because of the stiff elastic contact between them. Next, the buffer spring on  $m_2$  strikes the back of  $m_1$ . During rebound, a mass chosen equal to  $m_8$  plus  $m_9$  is added to  $m_1$  to simulate some of the complex shooter body influence. At a predetermined point in the counter-recoil cycle, the hammer is suddenly latched to  $m_1$ . The mass  $m_2$  continues forward to capture a new round  $m_9$  plus  $m_{10}$ , which is simultaneously released from  $m_1$ . The locking force is activated between  $m_1$  and  $m_2$  and continues until the forward spring on  $m_2$  strikes  $m_1$ . During this period the moment of inertia of  $m_8$  is increased by that of the complete round. The point is reached where the bolt and new round begin to become part of  $m_1$ , and the analysis is termin-



\*EHLE, HUANG, AND HAUG

ated. Throughout this cycle,  $m_3$  has been continually impacting  $m_2$ , and the spring coil masses  $m_4$ ,  $m_5$ , and  $m_6$  have been in motion. In addition,  $m_1$  has been moving under the influence of a flexible mount.

The problem to be solved for this mechanism is twofold:

1. Predict the displacement, velocity, acceleration, force, and event histories associated with each mass in the system.
2. Predict the variation in time required by the mechanism to reach a given event, due to variations in the design parameters. That is, calculate the vector of sensitivity

coefficients  $\ell^J \equiv \frac{\partial t_e}{\partial b}$ , where  $t_e$  is the time at which the event occurs, and  $b$  is the vector of design parameters.

For this paper, the following specific case is examined:

<u>Objective functional</u>	$t_e$ = time at which stripping of a new round from the magazine is begun
<u>Design parameters</u>	$b(1) = m_1$ Receiver and barrel mass $b(2) = m_2$ Bolt carrier mass $b(3) =$ drive spring constant $b(4) =$ hammer spring constant

#### B. Motion Analysis

(1) State Equations: By direct application of Newton's law, equating the net force on a body to the rate of change of linear momentum of that body, one can write the following equations of motion that incorporate all logic conditions discussed in the description of weapon operation in Section 5.A as

$$\begin{aligned}
 & \frac{d}{dt} [(EM(1) + NROUND*(EM(9) + EM(10)) - ELG(1)*(EM(9) + EM(10)) \\
 & \quad + (1. - ELG(7))*EM(7) - ELG(2)*EM(10) + ELG(3)*(EM(8) \\
 & \quad + EM(9) + EM(10)) - ELG(4)*(EM(8) + EM(9)))*X(8)] \\
 & = - ELG(5)*FGAS + F16 + FMOUNT + ELG(7)*F17 + ELG(8)*F12BAR \\
 & \quad + ELG(16)*F12BB + ELG(6)*\left\{\frac{d}{dt} [F4*X(8) + F5*X(9)] + E\right\}*F3 \\
 & \frac{d}{dt} [(EM(2) + ELG(9)*EM(8) + ELG(10)*EM(9) + (ELG(11) \\
 & \quad - ELG(3))*(EM(9) + EM(10)))*X(9)] \\
 & = [ELG(13)*F23 + ELG(14)*F23BAR + ELG(15)*F27 + ELG(8)*F21BAR \\
 & \quad + ELG(16)*F21BB + F24] - ELG(5)*PERCEN*FGAS \\
 & \quad + (-ELG(12))*\left\{\frac{d}{dt} [F4*X(8) + F5*X(9)] + E\right\}*F3 \\
 & \frac{d}{dt} [EM(3)*X(10)] = ELG(13)*F32 + ELG(14)*F32BAR \\
 & \frac{d}{dt} [EM(4)*X(11)] = F42 + F45
 \end{aligned}$$

\*EHLE, HUANG, AND HAUG

$$\frac{d}{dt} [EM(5)*X(12)] = F54 + F56$$

$$\frac{d}{dt} [EM(6)*X(13)] = F65 + F61$$

$$\frac{d}{dt} [EM(7)*X(14)] = ELG(7)*F71 + ELG(15)*F72$$

Note that these equations are written in first-order form, where  $x(1)$  through  $x(7)$  represent the positions of masses  $m_1$  through  $m_7$  and  $x(8)$  through  $x(14)$  represent the corresponding velocities. The  $F_{ij}$  ( $i, j = 1, 7$ ) are the forces on mass  $m_i$  from mass  $m_j$ .  $EM(I)$  is the computer-program variable for  $m_i$ .  $F4$ ,  $F5$ , and  $E$  are terms arising from the cam path constraint forces.  $ELG(I)$  are logical groups described below.

(2) Logical Function: Algebraic combinations of one or more logical functions (representative sequences for the Heaviside-step function) are termed "logical groups". These appear in the equations of motion to switch in and out various forces and masses. They are described below in terms of their dependence on the logical functions and in terms of the physical conditions that cause them to jump between zero and one. Note that the engineering and computer symbols  $LG_I$  and  $ELG(I)$  as well as  $L_I$  and  $EL(I)$ , are used interchangeably, where  $I$  is an integer. The logical groups are:

$$LG_1 = L_1 \quad m_1 \text{ loses } m_9 + m_{10}$$

$$LG_2 = L_2 \quad m_1 \text{ loses } m_{10}$$

$$LG_3 = L_3 L_1 \quad m_1 \text{ gains } m_8 + m_9 + m_{10}$$

$$LG_4 = L_{19} L_{20} \quad m_1 \text{ loses } m_8 + m_9 \text{ on extraction. } m_8 + m_9 \text{ is added to } m_1 \text{ after rebound of } m_2$$

$$LG_5 = ELG(2)$$

$$LG_6 = L_7 L_8 - L_9 L_{10} + L_{11} L_{12} - L_{13} L_{14} \quad \text{Cam force between } m_1 \text{ and } m_2 \text{ is active}$$

$$LG_7 = 1 - L_1 \quad \text{Hammer is tending to push } m_1 \text{ rearward}$$

$$LG_8 = L_{18} \quad \text{Buffer spring acts between } m_1 \text{ and } m_2$$

$$LG_9 = L_{19} \quad m_2 \text{ gains bolt mass } m_8 \text{ at end of unlocking and loses } m_8 \text{ on start of locking}$$

$$LG_{10} = L_{(20)} (LG_9 - L_{21}) \quad m_2 \text{ gains } m_9 \text{ on extraction but } m_2 \text{ loses } m_9 \text{ on ejection}$$

$$LG_{11} = LG_1 \quad m_2 \text{ gains } m_9 + m_{10} \text{ on round pick-up}$$

$$LG_{12} = LG_6 \quad \text{Cam force between } m_1 \text{ and } m_2 \text{ is active}$$

$$LG_{13} = L_{22} \quad \text{Buffer weight force between } m_2 \text{ and } m_3 \text{ is active (forward)}$$

\*EHLE, HUANG, AND HAUG

- $LG_{14} = L_{23}$  Buffer weight force between  $m_2$  and  $m_3$  is active (rear)  
 $LG_{15} = (LG_7)(L_{24})$  Hammer is in contact with  $m_2$   
 $LG_{16} = L_{15}$  Forward spring on  $m_2$  is in contact with  $m_1$   
 $LG_{17} = L_{25}L_{27}$  Position and velocity criteria for  $LG_1(t)$   
 $LG_{18} = L_{26}L_{28}$  Position and velocity criteria for  $LG_2(t)$ ,  $LG_5(t)$

The state variable and time dependencies of the individual logical functions and the physical conditions under which they make the transition from zero to one are as follows:

- EL (1) =  $L_1(t, t')$  where  $t' = t'(x_2 - x_1, x_9 - x_8)$  Round is picked up from magazine at time when  $m_2$  is 3.25" from battery  
 EL (2) =  $L_2(t, t'')$  where  $t'' = t''(x_7 - x_2, x_{14} - x_9)$  Gas force turns on at time when  $\Delta(x_2 - x_7) = 2''$   
 EL (3) =  $L_3(x_2 - x_1)$  Bolt hits locking lugs on receiver when  $\Delta(x_2 - x_1) = 1''$   
 EL (7) =  $L_7(x_2 - x_1)$  Locking begins when  $\Delta(x_1 - x_2) = 1''$   
 EL (8) =  $L_8(x_9 - x_8)$  Locking begins when  $\dot{x}_2 - \dot{x}_1 > 0$   
 EL (9) =  $L_9(x_2 - x_1)$  Locking stops when  $\Delta(x_1 - x_2) = .1''$   
 EL (10) =  $L_{10}(x_9 - x_8)$  Locking stops when  $\dot{x}_2 - \dot{x}_1 > 0$   
 EL (11) =  $L_{11}(x_1 - x_2)$  Unlocking begins when  $\Delta(x_1 - x_2) = .1''$   
 EL (12) =  $L_{12}(x_8 - x_9)$  Unlocking begins when  $\dot{x}_2 - \dot{x}_1 < 0$   
 EL (13) =  $L_{13}(x_1 - x_2)$  Unlocking ends when  $\Delta(x_2 - x_1) = 1''$   
 EL (14) =  $L_{14}(x_8 - x_9)$  Unlocking ends when  $\dot{x}_2 - \dot{x}_1 < 0$   
 EL (15) =  $L_{15}(x_2 - x_1)$  Forward spring on  $m_2$  hits  $m_1$  when  $\Delta(x_2 - x_1) \geq 0$   
 EL (18) =  $L_{18}(x_1 - x_2)$  Buffer spring force is on if  $\Delta(x_2 - x_1) = 4''$   
 EL (19) =  $L_{19}(x_1 - x_2)$  Bolt and round are picked up by  $m_2$  when  $\Delta(x_2 - x_1) > 1$  Bolt and round are attached to receiver when  $\Delta(x_2 - x_1) < 1''$   
 EL (20) =  $L_{20}(x_8 - x_9)$  Empty case part of  $m_1$  until extraction if  $\dot{x}_2 - \dot{x}_1 < 0$   
 EL (21) =  $L_{21}(x_1 - x_2)$  Empty case is ejected when  $\Delta(x_2 - x_1) = 2.5''$   
 EL (22) =  $L_{22}(x_3 - x_2)$  Buffer weight hits forward part of  $m_2$  when  $\Delta(x_3 - x_2) = .2''$

\*EHLE, HUANG, AND HAUG

- EL (23) =  $L_{23}(x_3 - x_2)$  Buffer weight hits forward part of  $m_2$   
when  $\Delta(x_3 - x_2) = .2''$
- EL (24) =  $L_{24}(x_7 - x_2)$  Force between hammer and  $m_2$  on when  
 $\Delta(x_2 - x_7) = 2''$  (See EL (2))
- EL (25) =  $L_{25}(x_2 - x_1)$  Round is picked up from magazine at  
position where  $m_2$  is  $3.25''$  from battery (See EL (1))
- EL (26) =  $L_{26}(x_7 - x_2)$  Gas force is turned on at position  
where  $\Delta(x_2 - x_7) = 2''$  (See EL (2))
- EL (27) =  $L_{27}(x_9 - x_8)$  Round is picked up from magazine when  
 $\dot{x}_2 - \dot{x}_1 > 5$  (see EL (1))
- EL (28) =  $L_{28}(x_{14} - x_9)$  Gas force is turned on when  $\dot{x}_7 - \dot{x}_2 > 5$   
(See EL (2))
- EL (29) =  $L_{29}(t, t'')$  Simulation of gas force

The notation  $\Delta(x_i - x_j)$  above denotes the "change in  $|x_i - x_j|$  from its value at  $t = 0$ .

The representative sequence used here to represent the Heaviside-step function is

$$L = \frac{1}{2} \frac{|Q|^{2n+1} + Q^{2n+1}}{|Q|^{2n+1} + |Q - \epsilon|^{2n+1} - (Q - \epsilon)^{2n+1}}$$

where  $Q \equiv x(I) - x(J) - YA$ . For some integers,  $I$ ,  $J$ , and constant  $YA$ . A graph of this function is shown in Fig. 6.

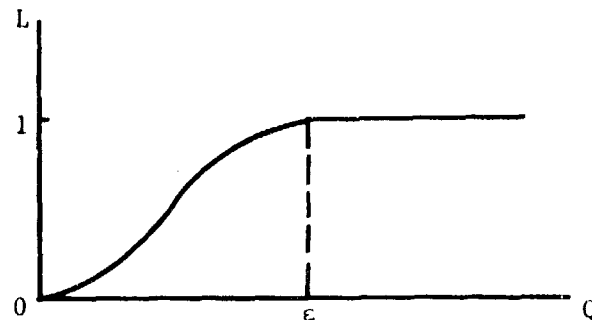


Figure 6. Approximation of Heaviside-step Function.

\*EHLE, HUANG, AND HAUG

The existence of any derivative of order  $d$  is assured everywhere if  $2n+1 > d$ . This form is a single expression that is valid in the regions where  $L = 0$ , where transition occurs, and where  $L = 1$ . Other simpler pieced polynomials may also be used. However, it is important to choose a representative sequence that is precisely zero to the left of the transition and precisely one to the right. Most conventional representations do not have this property.

A number of types of logical functions can be used to control the logic in a given problem. In the current example, logical functions are based on transition at a predetermined displacement or velocity. Other possibilities are predetermined acceleration, time, force, and combinations. It is also possible to develop a logical function (not used here) based on transition at a given number of repetitions of a logical event. A special type of logical function that is used in this example is referred to as a "locked-on" logical function. Here the argument of  $L$  is  $t - t'$ , where  $t'$  is determined by displacement and velocity criteria. The development of the lock-on logical function is motivated by experience. It is convenient to have a logical function available that will lock forever in the "on" position after certain displacement and/or velocity criteria are met and will not be affected by subsequent repeated satisfaction of these criteria.

Let  $L_x$  be a logical function based on position that makes its transition<sup>x</sup> from zero to one when a certain displacement condition is met and let  $L_{\dot{x}}$  be a similar logical function for velocity. TMAX is defined to be<sup>x</sup> a time greater than the maximum time over which the analysis is conducted. Consider the following definition for  $t'$ :

$$t' = TMAX \left[ 1 - \int_0^t L'_x L_{\dot{x}} \dot{x} d\zeta \right] + \int_0^t \zeta L'_x L_{\dot{x}} \dot{x} d\zeta$$

The term  $TMAX \left[ 1 - \int_0^t L'_x L_{\dot{x}} \dot{x} d\zeta \right] \equiv A$  insures that  $L(t - t')$  will not change value until  $x$  is at the appropriate position, since before that point is reached,  $t' = TMAX > t$  and the argument of  $L$  is negative. After transition has occurred,  $A = 0$ . If  $L_x$  and/or  $L_{\dot{x}}$  later change to zero, both of the above integrals will remain unchanged. If they later change to zero and then switch back on,  $A$  will become a large negative number. In this case,  $t'$  will be progressively decreased by an amount equal to TMAX and increased by an amount less than TMAX each time  $L_x L_{\dot{x}}$  is switched on. Hence with this definition,  $t'$  will always be less<sup>x</sup> than  $t$  once the criteria for position and velocity have been satisfied for the first time, the argument of  $L$  will remain positive, and  $L$  will remain "locked on". The terms in the definition of  $t'$  can be collected as  $t' = TMAX + \int_0^t (\zeta - TMAX) L'_x L_{\dot{x}} \dot{x} d\zeta$ . In order to calculate  $t'$ , the integral relation is converted to a differential equation  $\frac{dt'}{dt} = (t - TMAX) L'_x L_{\dot{x}} \dot{x}$  with  $t(0) = TMAX$  and is solved along

\*EHLE, HUANG, AND HAUG

with the other state equations. Thus  $t'$  becomes essentially another state variable with its own associated adjoint variable for sensitivity analysis. The variables  $EL(1)$  and  $EL(2)$  in the current problem are locked-on logical functions.

(3) Forces: The breech and gas forces are assumed to be impulses that are simulated by constant multiples of time-based representative sequences for the deta function. The spring forces are as follows:

$$\begin{aligned}
 F_{16} &= 76.8(x_6 - x_1 - 5.08425) - \text{DAMPDR}(\dot{x}_1 - \dot{x}_6) = \text{SPDRIK}(x_1 - x_6 \\
 &\quad + \text{DDR}) - \text{DAMPDR}(\dot{x}_1 - \dot{x}_6) \\
 F_{\text{MOUNT}} &= -300(x_1 - 1) - 9.43\dot{x}_1 = \text{SOJNTK}(x_1 - D_{\text{MOUNT}}) - \text{DAMPMO}(\dot{x}_1) \\
 F_{12\text{BB}} &= 20,000(x_2 - x_1 - .9996749) + 25(\dot{x}_1 - \dot{x}_2) = \text{FORWSK}(x_2 - x_1 \\
 &\quad + \text{DFOR}) + \text{DAMPFO}(\dot{x}_1 - \dot{x}_2) \\
 F_{24} &= 76.8(x_4 - x_2 - 1.91575) - .01(\dot{x}_2 - \dot{x}_4) = -\text{BCSK}(x_2 - x_4 + \text{BCSD}) \\
 &\quad - \text{BCSDAM}(\dot{x}_2 - \dot{x}_4) \\
 F_{45} &= 76.8(x_5 - x_4 - .91575) - .01(\dot{x}_4 - \dot{x}_5) = -\text{FSMK}(x_4 - x_5 + \text{DFSM}) \\
 &\quad - \text{DAMFSM}(\dot{x}_4 - \dot{x}_5) \\
 F_{56} &= 76.8(x_6 - x_5 - .91575) - .01(\dot{x}_5 - \dot{x}_6) = -\text{RMSK}(x_5 - x_6 + \text{RSD}) \\
 &\quad - \text{DAMRS}(\dot{x}_5 - \dot{x}_6) \\
 F_{17} &= -20(x_1 - x_7 + 6.5) - \text{HAMDAM}(\dot{x}_1 - \dot{x}_7) = -\text{HAMSPK}(x_1 - x_7 + \text{DHAM}) \\
 &\quad - \text{HAMDAM}(\dot{x}_1 - \dot{x}_7) \\
 F_{12\text{B}} &= 10000(x_2 - x_1 - .66667) + .13(\dot{x}_2 - \dot{x}_1) = \text{BUFFK}(x_2 - x_1 \\
 &\quad + \text{BUFDAM}(\dot{x}_1 - \dot{x}_2) \\
 F_{23} &= -20000(x_2 - x_3 + 1.01666) - 15(\dot{x}_2 - \dot{x}_3) = -\text{BWK}(x_2 - x_3 + \text{DBW}) \\
 &\quad - \text{BWDAM}(\dot{x}_2 - \dot{x}_3) \\
 F_{23\text{B}} &= 20000(x_2 - x_3 - .98333) - 15(\dot{x}_2 - \dot{x}_3) = \text{BWRK}(x_2 - x_3 + \text{DBWR}) \\
 &\quad - \text{BWDAM}(\dot{x}_2 - \dot{x}_3) \\
 F_{27} &= -20000(x_2 - x_7 + 5.16667) - 9(\dot{x}_2 - \dot{x}_7) = \text{HBK}(x_2 - x_7 + \text{HBD}) \\
 &\quad - \text{HBDAM}(\dot{x}_2 - \dot{x}_7)
 \end{aligned}$$

The axial component of the constraint force between the bolt carrier and the bolt that causes the bolt to rotate in accordance with the cam path is

$$F_{12} = I_{\text{BOLT}} \ddot{\theta} \frac{d\theta}{dx} = I_{\text{BOLT}} \frac{d\theta}{dx} \left( \frac{d^2\theta}{dx^2} x^2 + \frac{d\theta}{dx} \ddot{x} \right)$$

where  $\theta$  is the rotation angle,  $I_{\text{BOLT}}$  the mass moment of inertia of the bolt, and  $x$  the relative position between bolt and bolt carrier.

\*EHLE, HUANG, HAUG

This expression can be reformulated for the state equations as  $F_{12} = F3 \left\{ \frac{d}{dt} [(F4)x(8) + (F5)x(9) + E] \right\}$ , with appropriate definitions for  $F3$ ,  $F4$ ,  $F5$ , and  $E$ .

Note that this expression for  $F_{12}$  introduces coupling in the highest order derivatives in the first two state equations. The integration algorithm used requires that these equations be in standard form  $\frac{dx}{dt} = f$ . The process of converting the first two equations to this  $\frac{dx}{dt}$  form leads to the undesirable appearance of the delta function, which has relatively high derivative values. However, it is likely that only step functions need be considered in the dynamic analysis if a mixed algorithm for differential and algebraic (constraint) equations is used. The desired algorithms do exist that will solve mixed equations in the form  $f(x, \dot{x}, t) = 0$ . However, in this problem, the equations were put in standard form. The first two equations have the original form

$$\frac{d}{dt}[F1\dot{x}_1] = F2 + F3 \frac{d}{dt} [F4\dot{x}_1 + F5\dot{x}_2]$$

$$\frac{d}{dt}[F6\dot{x}_2] = F7 + F8 \frac{d}{dt} [F9\dot{x}_1 + F10\dot{x}_2]$$

and these are manipulated so as to become

$$\frac{d\dot{x}_1}{dt} = \frac{\alpha_3\alpha_5 - \alpha_2\alpha_6}{\alpha_1\alpha_5 - \alpha_2\alpha_4}$$

$$\frac{d\dot{x}_2}{dt} = \frac{\alpha_1\alpha_6 - \alpha_3\alpha_4}{\alpha_1\alpha_5 - \alpha_2\alpha_4}$$

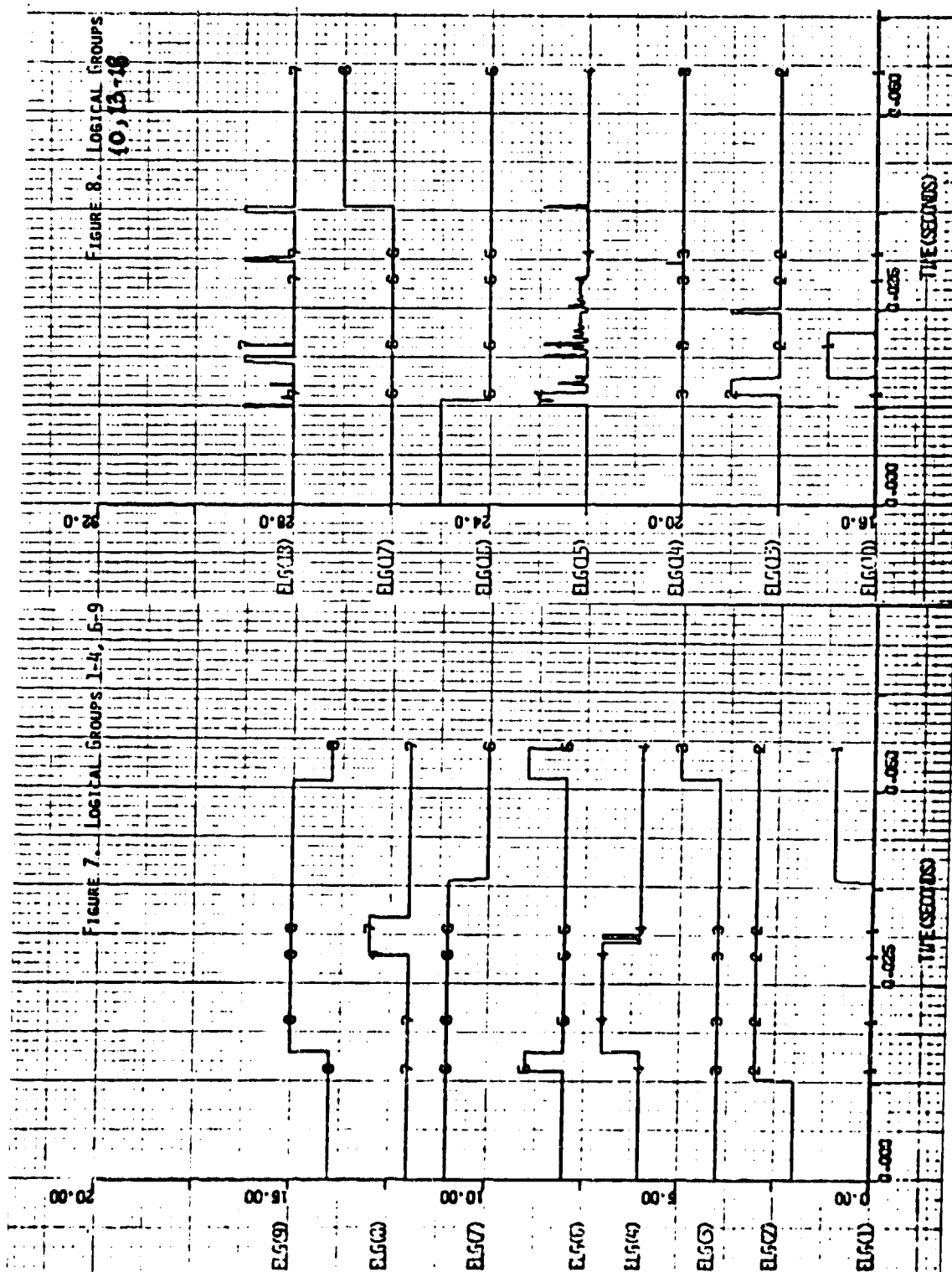
where the alpha's are algebraic equations involving step functions, delta functions, state variables, and time.

(4) Integration Algorithm: The fourth order Runge-Kutta algorithm was used to solve the state equations. No error control was used, except that each logical function transition region was divided into a specified minimum number of parts. The objective was at this stage to "brute force" a solution and not relinquish control to an automatic integration scheme. With large programming inefficiencies, the CPU time for the CDC 6600 computer was 77 seconds for a problem real time of .039 seconds. The accuracy was not quantifiable, but appeared to be satisfactory. No instabilities were apparent, even with the explicit appearance of the delta functions.

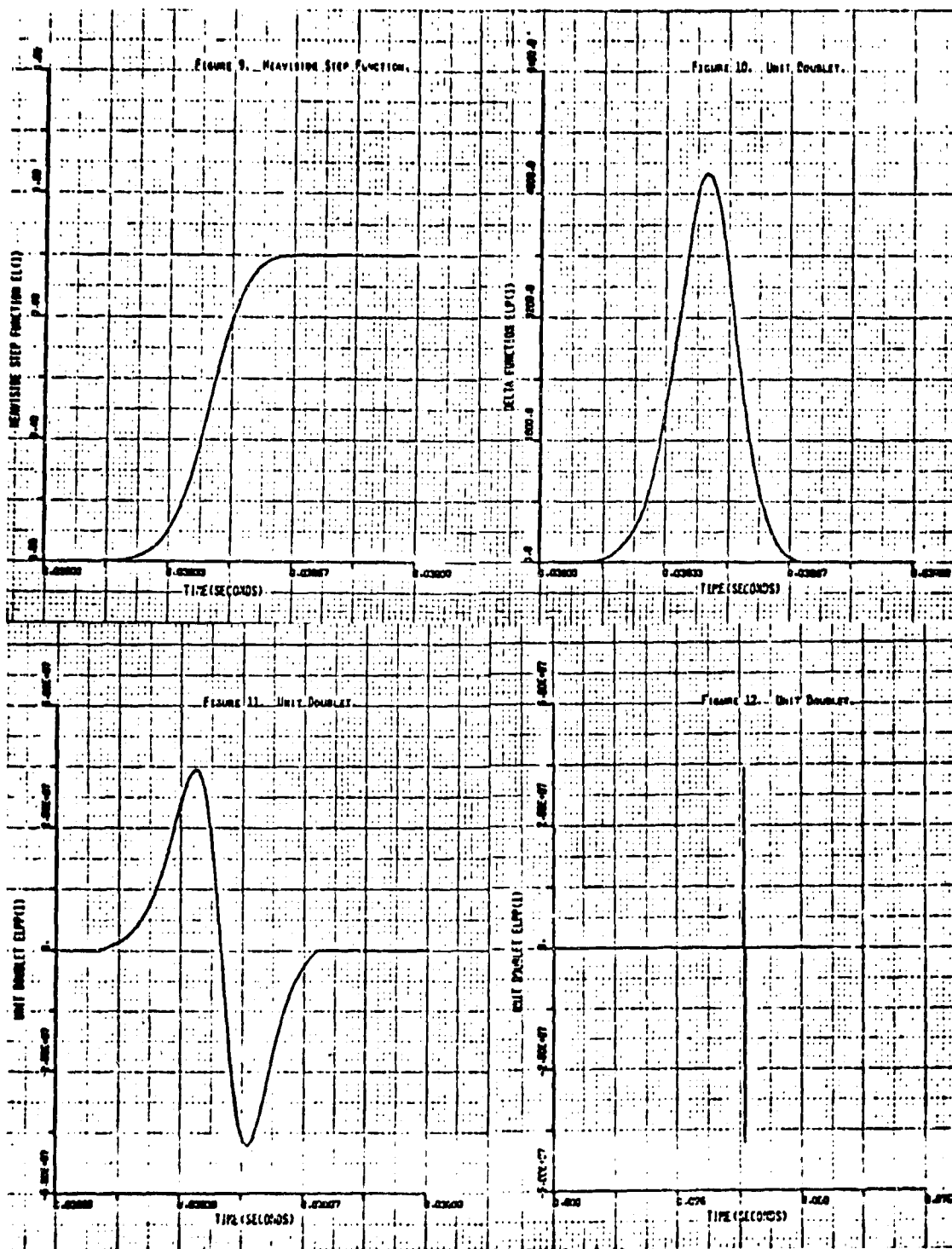
(5) Results: Plots of the logical groups are shown in Figs. 7 and 8. Sample plots of a typical logical function and its derivatives are shown in Figs. 9-12. Various computed motions as a function of time are shown in Figs. 13. through 20. Fig. 21 shows a typical force history.

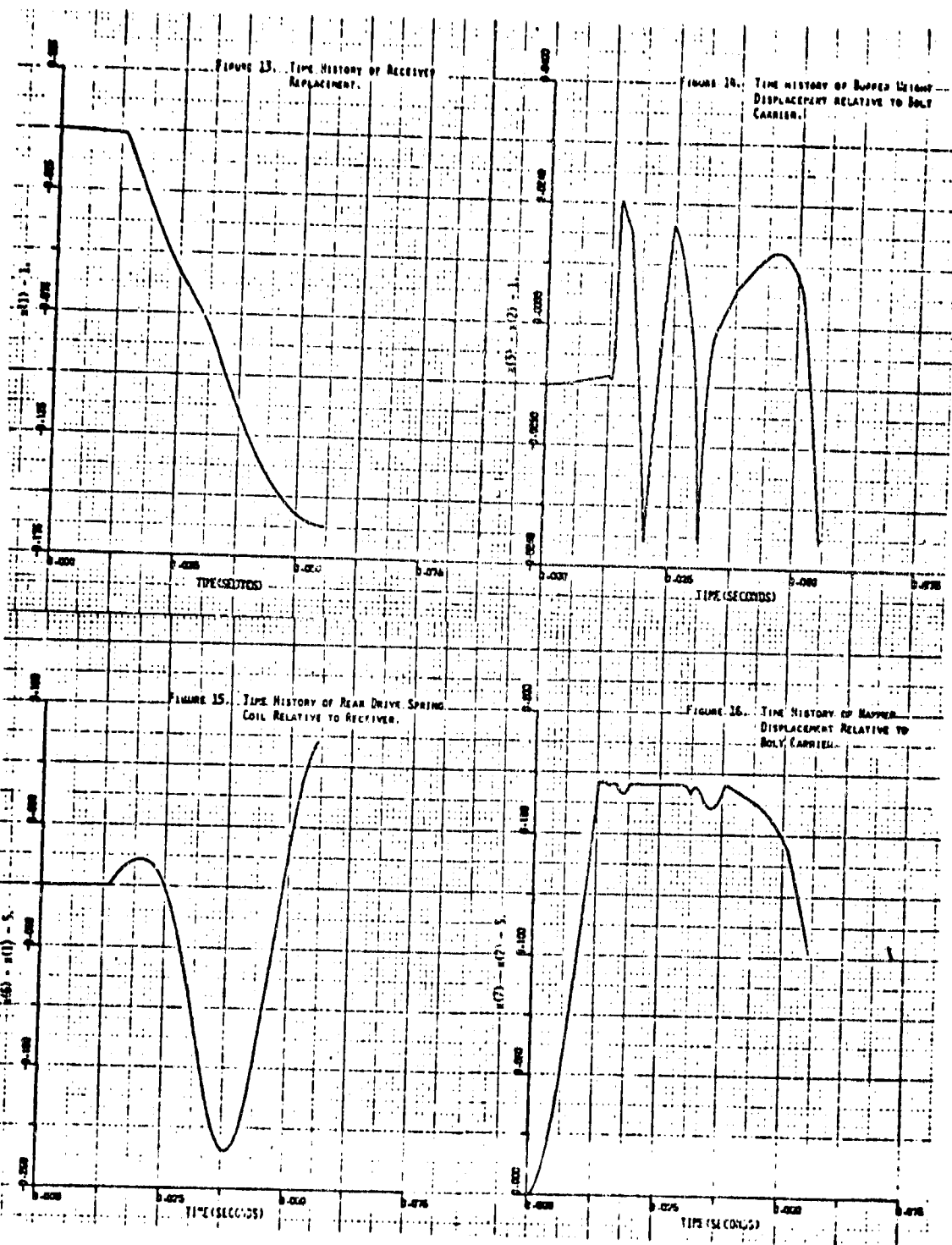
### C. Sensitivity Analysis

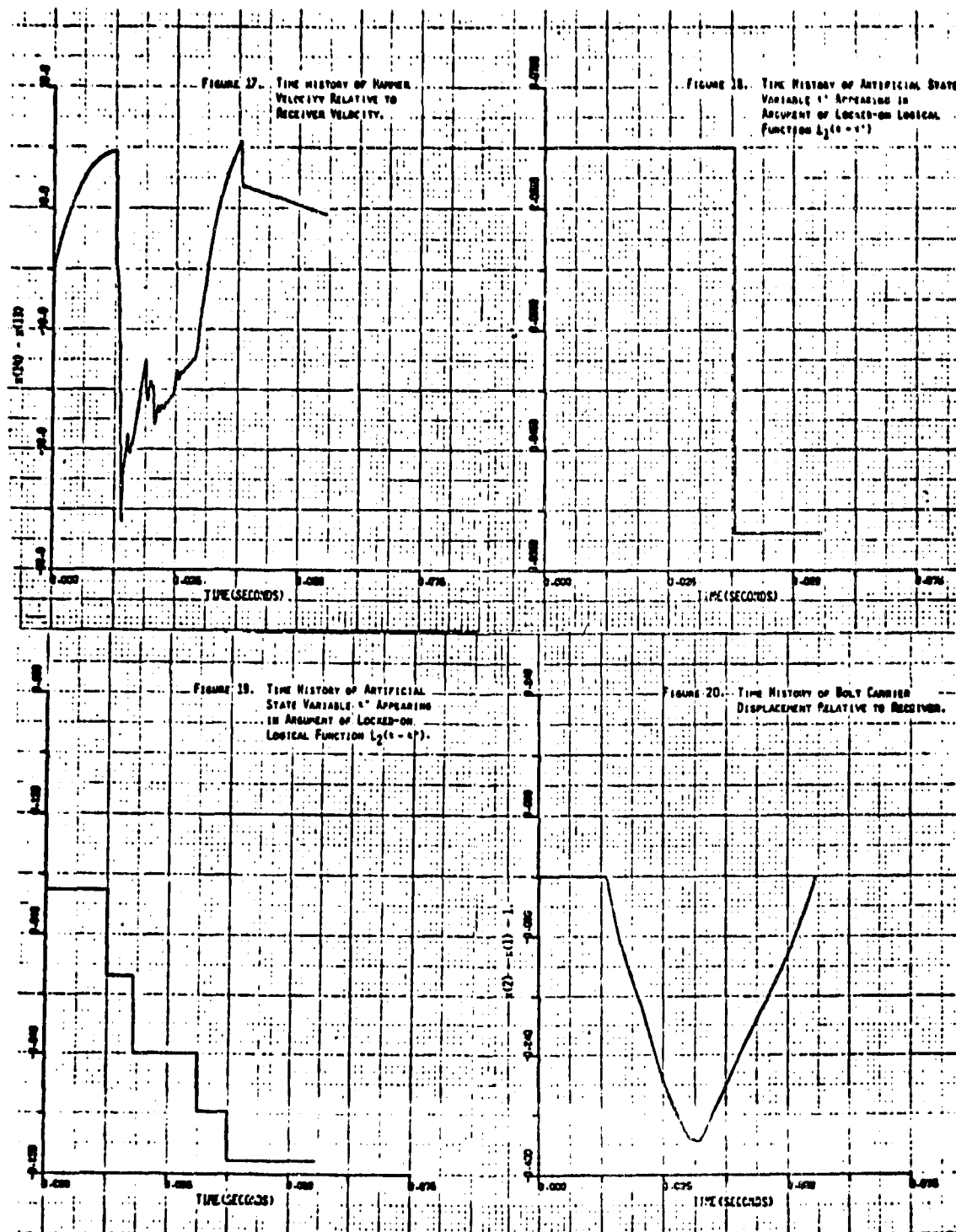
Application of the logical function method to sensitivity











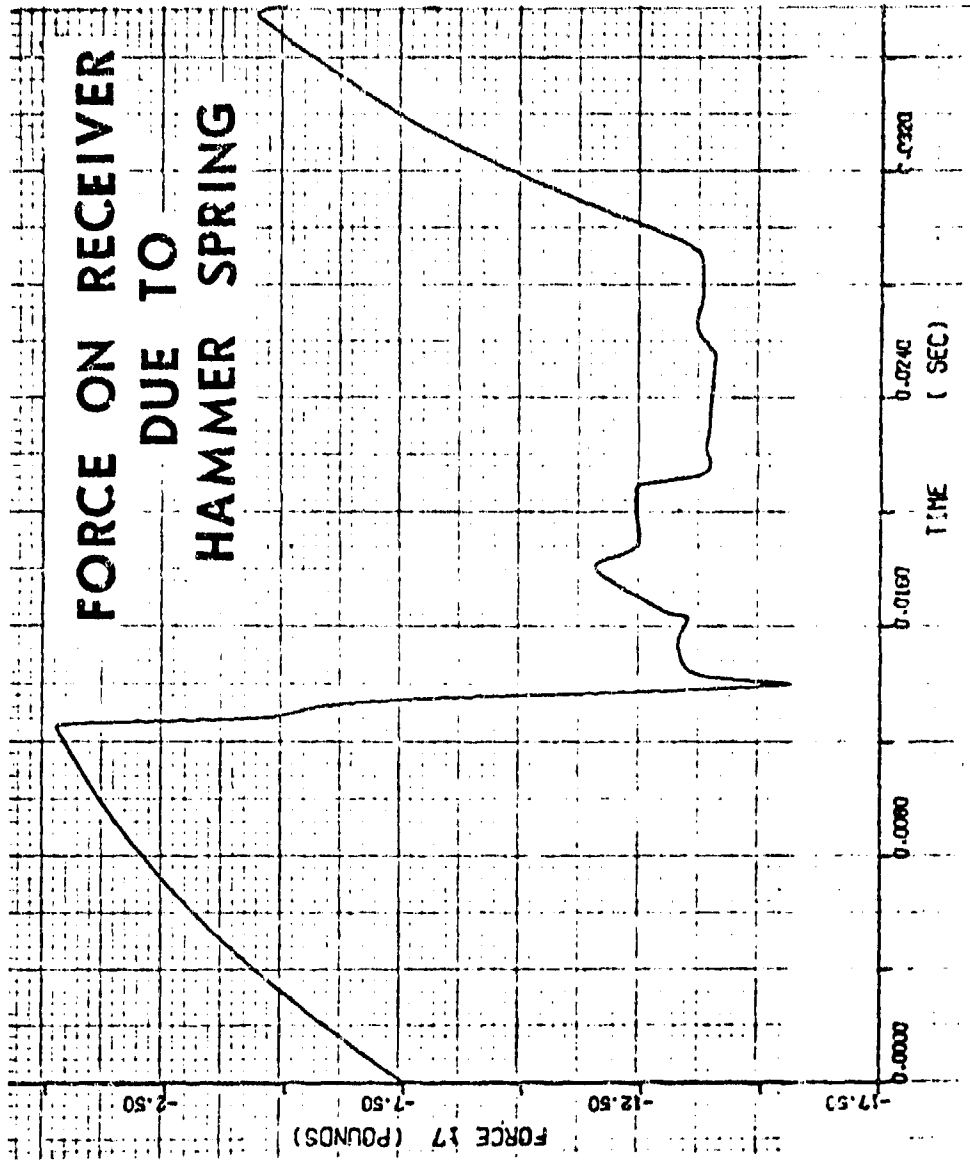


Figure 21. Typical Force History.

\*EHLE, HUANG, AND HIAUG

analysis permits the solution of complex problems that are not currently solvable by existing methods. The lack of any requirement for a prior knowledge of the sequence of events, the capability to treat chatter, and the generalization of logical control are important characteristics for sensitivity analysis of complex systems.

The sensitivity analysis problem for this example was stated in Section 5.A. Note that solutions of the state equations are required as input for this analysis. Recall that the matrix  $\partial f/\partial x$  appears in the adjoint equations. Analytically, this is a very lengthy and tedious calculation, so the details will be omitted here. Recall also that delta functions introduced as a result of the cam path and the requirement of standard-form equations with the Runge-Kutta algorithm appear in the "f" expressions in the state equations. Therefore, the calculation of  $\partial f/\partial x$  leads to the appearance of the unit doublet. Since  $h_0$  contains the  $\delta x$  delta function, the  $\partial h_0/\partial x$  term in the adjoint equations also gives rise to the unit doublet. The doublet arising from  $\partial f/\partial x$  may be eliminated by the use of the algorithm for differential and algebraic equations. It can be shown that the doublet resulting from the objective functional can always be eliminated if that functional contains no derivatives of  $L$  higher than that first, which will be the case for virtually all problems. However, for the present example, no attempt to eliminate the doublet was made.

Again, the Runge-Kutta fourth order algorithm without error control was used to demonstrate that stable solutions could be obtained, even with the occurrence of the extremely rapidly varying doublet. For convenience in demonstrating feasibility, very large inefficiencies in the lengthy calculation of  $\partial f/\partial x$  were allowed. The results obtained for  $\lambda_i^0 \equiv \frac{\partial t'}{\partial b(i)}$ , where  $t'$  is the time for stripping of a new round from the magazine and  $b(1) = m_1$ ,  $b(2) = m_2$ ,  $b(3) =$  drive spring constant, and  $b(4) =$  hammer spring constant, are as follows:

$$\begin{array}{cccc} \lambda_1^0 & \lambda_2^0 & \lambda_3^0 & \lambda_4^0 \\ \hline -.0086 & .61 & .35 \times 10^{-4} & -1.4 \times 10^{-4} \end{array}$$

approximate values from finite variations:

$$-.013 \quad .92 \quad .53 \times 10^{-4} \quad -1.3 \times 10^{-4}$$

Confidence in the approximate values from finite variations is limited to order of magnitude and algebraic sign. They are obtained from solving the state equations for different values of  $b$  and calculating  $\Delta t'/\Delta b$ . However, reasonable changes in  $b$  for which approximate linearity might be expected result in changes in  $t'$  on the order of one time step in the integration process; so  $\Delta t'$  is not highly reliable. The error analysis problem is complicated by the fact that both the size of  $\epsilon$  and the integration step size control the error. Additional study of this interaction is desirable.

\*EHLE, HUANG, AND HAUG

#### D. Future Work

Now that basic feasibility has been shown, the next step is the introduction of efficiency. A recent variable order variable step size integration code by Shampine and Gordon will be used to replace the Runge-Kutta algorithm. The calculation of  $\partial f / \partial x$  will be streamlined to provide perhaps the greatest gain in efficiency. Then a reasonable estimate of the computation time inherent in this method can be determined. Next, the appearance of the delta function in the state equations and of the unit doublet in the adjoint equations will be eliminated. This step should also increase efficiency. Next an analytical basis for the determination of the transition width will be established for optimum accuracy and efficiency. Finally, the logical function method will be introduced into the ADAMS 2-D generalized mechanism analysis code.

#### REFERENCES

- [1] Brown, P.M., and Skoro, V., "XM140 Propellant Compatability Test and Evaluation Program", Philco-Ford Corporation, Newport Beach, California, August 1972.
- [2] Vrana, N., and Baren, A., "A Hybrid Computer Model of the 30mm XM140 Automatic Weapon System", BRL Report No. 1637, Ballistics Research Laboratories, Aberdeen, Maryland, March 1973.
- [3] "Automatic Weapons", AMCP 706-260, Engineering Design Handbook, Headquarters U.S. Army Materiel Command, Washington, D.C., February 1970.
- [4] Ehle, P.E., and Rahe, A.D., "Theory and Application of Mathematical Modeling of Shoulder Fired Weapons, Part I: M16A1 Rifle", Rodman Laboratory Technical Report, R-TR-75-010, Rock Island, Illinois, November 1972.
- [5] Grandy, A.J., Duffy, J.A., Horchler, M.H., and Ehle, P.E., "Investigation of Bolt/Bolt-Carrier Clearances in the M16A1 Rifle", Technical Note TN-1159, Frankford Arsenal, Philadelphia, Pennsylvania, May 1971.
- [6] Gay, H.P., and Wineholt, E.M., "Analog Simulation of the Mechanism of the M16A1 Rifle", BRL Report No. 1596, Aberdeen Proving Ground, Maryland, June 1972.
- [7] Brosseau, T.L., "Kinematic Study of the M16A1 Rifle", Ballistic Research Laboratories Report No. 2153, Aberdeen Proving Ground, Maryland, January 1972.
- [8] Gerber, N., "Sensitivity Study of Rifle Gas Systems", BRL Report No. 1524, Aberdeen Proving Ground, Maryland, January 1971.
- [9] Gay, H.R., and Wineholt, E.H., "Analog Simulation of Ring Spring Recoil Systems", BRL Memorandum Report No. 1826, March 1967.

\*EHLE, HUANG, AND HAUG

- [10] Gay, H.P., "The Dynamics of Cam Systems for Gun Mechanisms" BRL Memorandum Report No. 2177, March 1972, AD741360.
- [11] Means, E.W., "Weapon Dynamics - Gas Dynamics Study", WECOM Report SWERR-TR-72-79, Contract DAAF03-70-C033, June 1971.
- [12] Vrana, N.M., "A Hybrid Computer Model of the XM19 Weapon", BRL MR No. 2312, July 1973.
- [13] "High Rate of Fire Rifle Mechanism", General Electric Contract Report, No. 72 APB551, November 1972.
- [14] Belliat, A.R., "A Theoretical Analysis of the Cyclic Rate of Fire and Recoil System of an Experimental Automatic Rifle", AMSAA TM 22, February 1969.
- [15] Stone, C.R., "Math Model-Evaluation of a Mechanical Spring in the XM207 Machine Gun Mechanisms to Reduce Weapon Cycle Rate Sensitivity to Ammunition", SWERR-TR 72-31, December 1971.
- [16] Huang, R.C., Haug, E.J., and Andrews, J.G., "Sensitivity Analysis and Optimal Design of the 75mm Automatic Cannon Mechanism", Proceedings, First US Army Conference on Dynamics of Precision Gun Weapons, Rock Island, Illinois, January 1977, pp.258-304.
- [17] Huang, R.C., Haug, E.J., and Andrews, J.G., "Sensitivity Analysis and Optimal Design of Mechanical Systems with Intermittent Motion", to appear ASME Journal of Engineering for Industry, 1978.
- [18] Haug, E.J., Computer Aided Design of Mechanical Systems, AMCP 706-192, Army Materiel Command, Washington, D.C., 1973.
- [19] Kec, W., and Teodorescu, P.P., Applications of the Theory of Distributions in Mechanics, Editura Acedemica, Romania, 1970.
- [20] Huang, R.C., and Haug, E.J., "A Distributional Approach to Sensitivity Analysis of Mechanical Systems with Intermittent Motion", Technical Report No. 42, Division of Materials Engineering, University of Iowa, Iowa City, Iowa, July, 1978.

APPENDIX A: Sensitivity Analysis of the Mass Capture Model by a Discontinuous Approach

In this appendix, sensitivity analysis of the mass capture model (shown in Fig. 2) by the discontinuous approach, is given. The results of the adjoint solution and sensitivity coefficients by this method serve as the limiting case for the solution by the distributional approach. Here, only the formulation and results are presented. A detailed derivation is given in [20].

Let  $z_1 = x$  and  $z_2 = m\dot{x}$ . As defined in Section 4, let  $t_1$  and  $t_2$  be the times when mass  $m_1$  reaches  $x = s_1$  and  $s_2$ , respectively. Let the functional to be considered be defined as

$$\psi = t_2 \quad (A-1)$$

\*EHLE, HUANG, AND HAUG

(a) Equations of motion

$$z_1(0) = 0, \quad z_2(0) = m_1 v_0 \quad (\text{A-2})$$

$$\begin{cases} \dot{z}_1 = \frac{z_2}{m_1} \\ \dot{z}_2 = 0 \end{cases} \quad 0 < t < t_1 \quad (\text{A-3})$$

$$z_1(t_1^+) = s_1, \quad z_2(t_1^+) = z_2(t_1^-) \quad (\text{A-4})$$

$$\begin{cases} \dot{z}_1 = \frac{z_2}{(m_1 + m_2)} \\ \dot{z}_2 = 0 \end{cases} \quad t_1 < t < t_2 \quad (\text{A-5})$$

(b) Special time definitions

$$z_1(t_1) = s_1 \quad (\text{A-6})$$

$$z_2(t_2) = s_2$$

(c) Adjoint equations

$$\begin{cases} \frac{d\lambda_1}{dt} = 0 \\ \frac{d\lambda_2}{dt} = -\frac{1}{m_1} \lambda_1 \end{cases} \quad 0 < t < t_1 \quad (\text{A-7})$$

$$\lambda_1(t_1^-) = -\frac{1}{\dot{x}(t_1^-)}, \quad \lambda_2(t_1^-) = \lambda_2(t_1^+) \quad (\text{A-8})$$

$$\begin{cases} \frac{d\lambda_1}{dt} = 0 \\ \frac{d\lambda_2}{dt} = -\frac{1}{(m_1 + m_2)} \lambda_1 \end{cases} \quad t_1 < t < t_2 \quad (\text{A-9})$$

$$\lambda_1(t_2^-) = -\frac{1}{\dot{x}(t_2^-)}, \quad \lambda_2(t_2^-) = 0 \quad (\text{A-10})$$

(d) Solution of the equations of motion

$$\begin{cases} z_1(t) = v_0 t \\ z_2(t) = m_1 v_0 \end{cases} \quad 0 < t < t_1 \quad (\text{A-11})$$



\*EHLE, HUANG, AND HAUG

$$\begin{cases} z_1(t) = \frac{m_1 V_0}{(m_1 + m_2)} (t - t_1) + s_1 \\ z_2(t) = m_1 V_0 \end{cases} \quad t_1 < t < t_2 \quad (\text{A-12})$$

(e) Solution of the adjoint equations

$$\begin{cases} \lambda_1(t) = -\frac{1}{\dot{x}(t_2^-)} \\ \lambda_2(t) = \frac{1}{(m_1 + m_2)\dot{x}(t_2^-)} (t - t_2) \end{cases} \quad t_1 < t < t_2 \quad (\text{A-13})$$

$$\begin{cases} \lambda_1(t) = -\frac{1}{\dot{x}(t_1^-)} \\ \lambda_2(t) = \frac{-t_2}{m_1 \dot{x}(t_1^-)} \end{cases} \quad (\text{A-14})$$

(f) Sensitivity coefficient of mass  $m_1$  with respect to the functional  $\psi$ ,  $\ell_J^\psi$ :

$$\ell_J^\psi = -(s_2 - s_1) \frac{m_2}{m_1 V_0} \quad (\text{A-15})$$

Sensitivity coefficients of other parameters  $m_2$ ,  $V_0$ ,  $s_1$ , and  $s_2$  are given in [20].APPENDIX B: Definition of a  $\theta$ -Representative SequenceLet a  $\theta$ -representative sequence  $\{L_n(z)\}$  be defined as follows:

- (a)  $L_n(z) \in C^m$  for some prechosen integer  $m$ ,
- (b)  $L_n(z)$  is monotone increasing, and  $L_n(z) = 0$  if  $z \leq -\epsilon_n$ , and  $L_n(z) = 1$  if  $z \geq \epsilon_n$ , where  $\epsilon_n$  is a positive and  $\epsilon_n \rightarrow 0$  as  $n \rightarrow \infty$ ,
- (c)  $L_{n+1}(z) \geq L_n(z)$ , for all  $n$ .

With this definition, one can show that  $\{L'_n(z)\}$  is a  $\bar{\delta}$ -representative sequence [19].

HAUG AND HUANG

TITLE: Design Sensitivity Analysis of A Recoiling Gun On Elastic Supports.

EDWARD J. HAUG and RAY C. HUANG  
College of Engineering, The University of Iowa,  
Iowa City, Iowa 52242

ABSTRACT:

Dynamic and design sensitivity analysis of a gun barrel that recoils in automatic fire on two supports is considered. The equations of motion for the gun barrel under the above conditions are solved by a Picard iteration method to determine gun barrel dynamic response during a firing cycle. To optimize system precision, a design sensitivity analysis is first formulated to determine the effect of design changes of system components on dynamic response of the muzzle at shot exit. To develop the sensitivity analysis, an adjoint equation for a general performance functional is defined and design sensitivity coefficients for the functional are found. The sensitivity coefficients provide trend information directly to the designer to predict the effect of changes in system components on precision. In this paper, the masses of the projectile and the flash suppressor and the location of supports are taken as design parameters.

BIOGRAPHY:

PRESENT ASSIGNMENT: Professor of Mechanical Engineering,  
The University of Iowa.

PAST EXPERIENCE: Mechanical Engineer, U.S. Army Weapons Command, 1966-1969. Chief, Systems Analysis Directorate, U.S. Army Weapons Command, 1969-1971. Chief, Systems Research Division, U.S. Army Weapons Command, 1971-1973. Chief, Concepts and Technology Division, U.S. Army Armament Command, 1973-1976.

DEGREES HELD: Bachelor of Science, University of Missouri at Rolla, 1962; M.S., 1964, and Ph.D., 1966, Kansas State University.

## DESIGN SENSITIVITY ANALYSIS OF A RECOILING GUN ON ELASTIC SUPPORTS

E.J. HAUG\* PROFESSOR  
R.C. HUANG, ASSISTANT PROFESSOR  
MATERIALS DIVISION, COLLEGE OF ENGINEERING  
THE UNIVERSITY OF IOWA, IOWA CITY, IOWA 52242

### 1. INTRODUCTION

A gun barrel that recoils in automatic fire on two supports is considered, see Fig. 1. The derivation of the equations of motion for the gun barrel under the above conditions can be found in [1]. In this reference, Simkins used NASTRAN to solve for the dynamic response of an M113 gun tube. Feng and Hung [2] applied a finite element method, modal analysis, and the Picard iteration method to determine 60mm gun barrel dynamic response during a firing cycle.

To optimize system precision, one must first determine the effect of design changes of system components on dynamic response of the muzzle at shot exit. To date, no systematic sensitivity analysis has been attempted to deal with this precision model. It is the purpose of this paper to carry out such a sensitivity analysis. The main tools used are the calculus of variations, the theory of distributions, and a sensitivity analysis technique developed in [3,4].

In developing the sensitivity analysis, one first constructs an adjoint equation for a general performance functional and finds the design sensitivity coefficients for the functional. These coefficients may be interpreted as partial derivatives of the performance functional. This general formulation can then be applied to both the cost and constraint functionals in the design process. The sensitivity coefficients provide trend information directly to the designer to predict the effect of changes in system components on precision, or they can be used to implement an optimal design algorithm.

In this paper, the masses of the projectile and the flash suppressor and the location of supports are taken as design parameters. Any other system components can be described by design parameters and treated in a similar way. Section 2 gives the equations of motion and a method of solution. This method can also be applied for the solution of the adjoint equations, which is an important consideration for numerical efficiency. In Section 3, a sensitivity analysis for the system is carried out, with a general form of performance functional. A formulation for design sensitivity coefficients and the associated adjoint equations and terminal and boundary condition are given. In Section 4, a numerical example is treated. Finally,

\*HAUG AND HUANG

a summary and discussion is presented in Section 5.

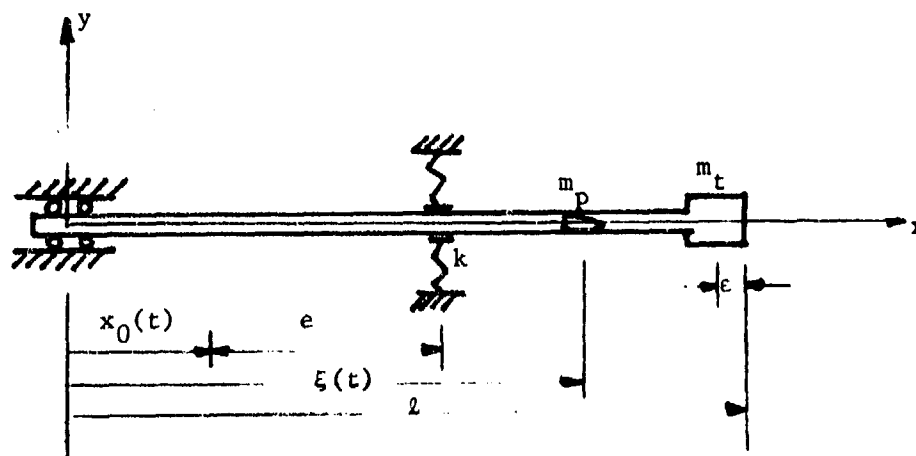


Figure 1. Mechanism of a Moving Gun Barrel with Two Supports.

## 2. EQUATIONS OF MOTION

The system shown in Fig. 1 is a model of a recoiling gun barrel with two supports fixed in an inertial frame. The coordinate system  $Oxy$  is embedded in the barrel and  $x_0(t)$  is the distance from the left end of the barrel to the flexible support, which varies in time as the gun barrel recoils.

The projectile and the flash suppressor are considered as point masses. The differential equation of motion was derived in [1] as

$$By = f \quad (1)$$

where

$$B \equiv \frac{\partial^2}{\partial x^2} \left[ EI(x) \frac{\partial^2}{\partial x^2} \right] + \rho A(x) \frac{\partial^2}{\partial t^2} \quad (2)$$

and

$$\begin{aligned} f \equiv & -\rho g A(x) \cos \alpha - p(x, t) \pi a^2 y''(x, t) \\ & + \rho g A(x) \left( \frac{\ddot{x}_0}{g} + \sin \alpha \right) y'(x, t) \\ & - \rho g \left( \frac{\ddot{x}_0}{g} + \sin \alpha \right) y''(x, t) \int_{x_0}^l A(\bar{x}) d\bar{x} - ky(x(t), t) \delta(x - x_0(t)) \\ & - [V^2(t) y''(x, t) + 2V(t) \dot{y}'(x, t) + \ddot{y}(x, t)] \quad (\text{Eq. cont'd}) \end{aligned}$$

\*HAUG, AND HUANG

$$\begin{aligned}
 & + \dot{V}(t)y'(x,t) + g \cos \alpha] m_p \bar{\delta}(x - \epsilon(t)) \\
 & - m_c [\ddot{y}(x,t) + g \cos \alpha] \bar{\delta}(x - \ell + \epsilon)
 \end{aligned} \quad (3)$$

The parameters and variables in these equations are defined in detail in Appendix A. The variable  $y(x,t)$  is the lateral displacement of the barrel. The first term in the expression of  $f$  (Eq. 3) represents the effect of gravity. The second term is due to the Bourdon pressure load and  $p(x,t)$  is bore pressure. The third and fourth terms represent the combined effects of recoil and counter-recoil inertia and the lateral motion of the gun barrel. The last two terms in Eq. 3 are due to the concentrated mass of the moving projectile and the fixed flash suppressor, respectively.

Since there is no concentrated moment applied on the barrel, the state variable  $y$  is twice continuously differentiable with respect to the variable  $x$ . A simple calculation shows that the speeds of the stress waves in the tube are much faster than the speed of the projectile. Hence, the state variable  $y$  is assumed to be twice continuously differentiable with respect to the time variable  $t$ .

The initial conditions are taken in the general form

$$y(x,0) = y_0 \quad (4.a)$$

$$\dot{y}(x,0) = \dot{y}_0 \quad (4.b)$$

and the boundary conditions are

$$y(0,t) = 0 \quad (5.a)$$

$$y'(0,t) = 0 \quad (5.b)$$

$$(EIy'')(l^-,t) = 0 \quad (5.c)$$

$$(EIy'')'(l^-,t) = 0 \quad (5.d)$$

The terms involving the second and third derivations in Eq. 5 represent conditions on bending moment and shear force on the gun barrel. For example, Eqs. 5.c and 5.d give the free end condition of the barrel.

To solve this complicated initial-boundary-value problem, a Galerkin method [5,6] is applied to develop a finite element formulation. In this paper quintic polynomials are chosen as the coordinate functions. Consider the  $i$ th nodal point of the discretized barrel, shown in Fig. 2. The coordinate functions associated with this node are  $\psi_i(x)$ ,  $\phi_i(x)$  and  $\omega_i(x)$  which are defined in Appendix A. An approximate solution is of the form

$$U_n(x,t) = \sum_{i=1}^n [a_{3i-2}(t) \psi_i(x) + a_{3i-1}(t) \phi_i(x) + a_{3i}(t) \omega_i(x)] \quad (6)$$

where the functions  $a_{3i-2}(t)$ ,  $a_{3i-1}(t)$  and  $a_{3i}(t)$  are the displacement, slope, and the second  $x$ -derivative of the barrel at the  $i$ th

\*HAUG, AND HUANG

nodal point, which are to be determined.

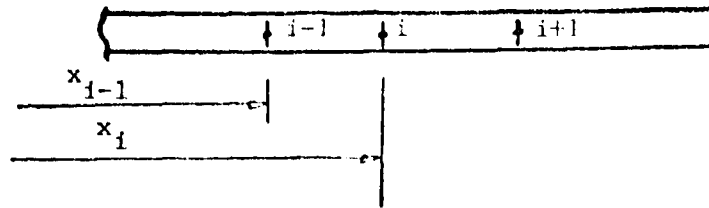


Figure 2. Finite Element Nodes.

By the modified Bubnov-Galerkin method [6], the residues are formed as

$$(EI U_n'', \psi_i'') + (\rho A \ddot{U}_n, \psi_i) = (f, \psi_i) \quad (7)$$

$$(EI U_n'', \phi_i'') + (e A \ddot{U}_n, \phi_i) = (f, \phi_i) \quad (8)$$

$$(EI U_n'', \omega_i'') + (\rho A \ddot{U}_n, \omega_i) = (f, \omega_i) \quad (9)$$

Since  $i=1,2,\dots,n$ , this is a system of  $3n$  ordinary differential equations for the  $a_j(t)$ ,  $j=1,\dots,3n$  and where

$$(f,g) \equiv \int_0^l f(x)g(x)dx \quad (10)$$

One may write this system of  $3n$  second order differential equations in matrix form as

$$Ka + M\ddot{a} = F(\dot{a}, \ddot{a}, V(t), x_0(t)) \quad (11)$$

with initial conditions

$$\begin{aligned} a(0) &= a_0 \\ \dot{a}(0) &= \dot{a}_0 \end{aligned} \quad (12)$$

Here the matrices  $M$  and  $K$  are constant, while the vector  $F$  is a function of time. These matrices can be constructed and evaluated by finite element computer programs. A combination of modal analysis and Picard iteration is used to solve the equations. The convergence of the Picard iteration will be presented in Section 4.

### 3. SENSITIVITY ANALYSIS

In this section, a general performance functional  $\psi$ , which can arise as a constraint or as the cost functional, is considered. Also, an adjoint variable  $\lambda(x,t)$  that is associated with the functional  $\psi$  is introduced. The sensitivity coefficients with respect to the design

\*HAUG AND HUANG

variables and design parameters are then developed, using techniques developed in [3] and the theory of distributions.

Consider a functional of the form

$$\psi = \int_0^\tau \int_0^\ell L(x, t, y, \dot{y}, y', b) dx dt \quad (13)$$

where  $b$  is a vector of scalar design parameters. Taking the first variation of the functional  $\psi$ , one has

$$\delta \psi = \int_0^\tau \int_0^\ell \left[ \left( \frac{\partial L}{\partial y} - \frac{\partial^2 L}{\partial x \partial y'} - \frac{\partial^2 L}{\partial t \partial \dot{y}} \right) \delta y + \frac{\partial L}{\partial b} \delta b \right] dx dt + G \quad (14)$$

where

$$G \equiv \int_0^\tau \left\{ - \frac{\partial L}{\partial y} \delta y \Big|_{x=0} + \frac{\partial L}{\partial y'} \delta y \Big|_{x=\ell} \right\} dt + \int_0^\ell \frac{\partial L}{\partial \dot{y}} \delta y \Big|_0^\tau dt \quad (15)$$

Now one is in a position to introduce the adjoint variable  $\lambda(x, t)$  and to construct the adjoint equation associated with the functional  $\psi$ . For simplicity of notation, let

$$S(x) = \int_x^\ell A(\bar{\xi}) d\bar{\xi} \quad (16)$$

Multiplying Eq. 1 by the adjoint variable  $\lambda$  and integrating over the domain  $(0, \ell) \times (0, \tau)$ , one has the identity

$$\begin{aligned} \int_0^\tau \int_0^\ell \lambda \left\{ (EI(x)y'') + \rho A(x)\ddot{y} + \rho g A(x) \cos \alpha + p(x, t)\pi a^2 y'' \right. \\ \left. - y'(x, t)\rho g A(x) \left( \frac{\ddot{x}_0}{g} + \sin \alpha \right) + y'' \rho g \left( \frac{\ddot{x}_0}{g} + \sin \alpha \right) S(x) \right. \\ \left. + \lambda(x, t)y(x, t)k\bar{\delta}(x - x_0(t) - e) + m_p(\ddot{y} + 2V\dot{y}' + \dot{V}y' + V^2y'' \right. \\ \left. + g \cos \alpha)\bar{\delta}(x - \xi) + m_t(\ddot{y} + g \cos \alpha)\bar{\delta}(x - \ell + \varepsilon) \right\} dx dt = 0 \end{aligned} \quad (17)$$

Integrating Eq. 17 by parts, one obtains

$$\begin{aligned} \int_0^\tau \left\{ [\lambda(EIy'')] - \lambda'(EIy'') + (EI\lambda'')y' - (EI\lambda'')'y \right. \\ \left. + [\lambda p(x, t)\pi a^2 y' - (\lambda p(x, t))'\pi a^2 y] - \left[ \rho g \left( \frac{\ddot{x}_0}{g} + \sin \alpha \right) A(x)\lambda y \right] \right. \\ \left. + \left[ \lambda \rho g S(x) \left( \frac{\ddot{x}_0}{g} + \sin \alpha \right) y' - \rho g \left( \frac{\ddot{x}_0}{g} + \sin \alpha \right) (\lambda S)' y \right] \right\} dt \\ + \int_0^\tau \int_0^\ell \left[ (EI\lambda'')'' + \pi a^2 (\lambda p)'' + \rho g \left( \frac{\ddot{x}_0}{g} + \sin \alpha \right) (A\lambda)' \right. \\ \left. + \rho g \left( \frac{\ddot{x}_0}{g} + \sin \alpha \right) (\lambda S)'' \right] y dx dt + \int_0^\ell \left[ \lambda p A \dot{y} \Big|_0^\tau - \dot{\lambda} p A y \Big|_0^\tau \right] dx \\ + \int_0^\tau \int_0^\ell \rho A \ddot{\lambda} y dx dt + \int_0^\tau \lambda(z_0, t)y(z_0, t)k dt + m_p \lambda(\xi, t)\dot{y}(\xi, t) \\ - m_p \dot{\lambda}(\xi, t)y(\xi, t) + \int_0^\tau m_p \ddot{\lambda}(\xi, t)y(\xi, t) dt \quad (\text{Eq. cont'd}) \end{aligned}$$

where  $|_{\Gamma}$  denotes evaluation at the end points  $\{0^+, l^-\}$  and  $z_0 = x_0 + e$ . Taking the first variation of Eq. 18 with respect to the state variable  $y$  and design parameter  $b$ , one obtains the identity

II-37



\*HAUG, AND HUANG

$$\begin{aligned}
& + \int_0^\tau \left\{ \lambda(\xi, t) V^2(t) y''(\xi, t) dt + \int_0^\tau \lambda(\xi, t) g \cos \alpha dt \right\} \\
& + (\delta m_t) \left\{ \lambda(\ell - \epsilon, \tau) \dot{y}(\ell - \epsilon, \tau) - \dot{\lambda}(\ell - \epsilon, \tau) y(\ell - \epsilon, \tau) \right. \\
& \left. + \int_0^\tau \ddot{\lambda}(\ell - \epsilon, t) y(\ell - \epsilon, t) dt + \int_0^\tau \lambda(\ell - \epsilon, t) g \cos \alpha dt \right\} = 0
\end{aligned} \quad (19)$$

Note that the variation of the first two terms in the boundary integral of Eq. 19 are left as  $\lambda(EIY'')$  and  $\lambda'(EIY')$ , rather than expanding to include variations in EI as a function of design parameters. Retaining the terms in this form allows one to interpret  $(EIY'')$  as shear and  $(EIY')$  as moment. Thus, if a shear or moment is specified, such as at the free end of the gun tube, then the total variation of shear or moment must be zero. Now consider the following terms in Eq. 19:

$$\begin{aligned}
& \int_0^\tau 2m_p \left\{ \frac{\partial}{\partial t} [\lambda(\xi, t) V(t)] \right\} \delta y'(\xi, t) dt \\
& \int_0^\tau m_p \dot{V}(t) \lambda(\xi, t) \delta y'(\xi, t) dt \\
& \int_0^\tau m_p \lambda(\xi, t) V^2(t) \delta y''(\xi, t) dt
\end{aligned}$$

By the theory of distributions [7,8],

$$\begin{aligned}
& \int_0^\tau 2m_p \left\{ \frac{\partial}{\partial t} [\lambda(\xi, t) V(t)] \right\} \delta y'(\xi, t) dt \\
& = - \int_0^\tau \int_0^\ell 2m_p \left\{ \frac{\partial}{\partial t} [\lambda(x, t) V(t)] \right\} y'(x, t) \bar{\delta}(x - \xi) dt \\
& = - \int_0^\tau \int_0^\ell \left\{ 2m_p \left[ \frac{\partial^2}{\partial x \partial t} (\lambda(x, t) V(t)) \right] \bar{\delta}(x - \xi) \right. \\
& \quad \left. + 2m_p \left[ \frac{\partial}{\partial t} (\lambda(x, t) V(t)) \right] \bar{\delta}'(x - \xi) \right\} \delta y(x, t) dx dt \quad (20)
\end{aligned}$$

In the last equality of Eq. 20, the product rule of distributional derivatives has been used. Similarly, one has

$$\begin{aligned}
& \int_0^\tau m_p \dot{V}(t) \lambda(\xi, t) \delta y'(\xi, t) dt = \int_0^\tau \int_0^\ell m_p \dot{V}(t) \lambda(x, t) \delta y'(x, t) \\
& \quad \cdot \bar{\delta}(x - \xi) dx dt \\
& = - \int_0^\tau \int_0^\ell m_p \dot{V}(t) [\lambda'(x, t) \bar{\delta}(x - \xi) + \lambda(x, t) \bar{\delta}'(x - \xi)] \delta y(x, t) dx dt
\end{aligned} \quad (21)$$

and

$$\begin{aligned}
& \int_0^\tau m_p \lambda(\xi, t) V^2(t) \delta y''(\xi, t) dt = \int_0^\tau \int_0^\ell m_p \lambda(x, t) V^2(t) \delta y''(x, t) \bar{\delta}(x - \xi) \\
& \quad dx dt \\
& = - \int_0^\tau \int_0^\ell m_p V^2(t) [\lambda'(x, t) \bar{\delta}(x - \xi) + \lambda(x, t) \bar{\delta}'(x - \xi)] y'(x, t) dx dt
\end{aligned}$$

(Eq. cont'd)

\*HAUG, AND HUANG

$$= \int_0^\tau \int_0^l m_p V^2(t) [\lambda''(x,t) \bar{\delta}(x-\xi) + 2\lambda'(x,t) \bar{\delta}'(x-\xi) + \lambda(x,t) \bar{\delta}''(x-\xi)] \delta y(x,t) dx dt \quad (22)$$

For notational simplification, define

$$B_1(x,t) \equiv EI\lambda'' + \pi a^2 \lambda p(x,t) + \lambda \rho g S(x) \left( \frac{\ddot{x}_0}{g} + \sin \alpha \right) \quad (23)$$

$$B_2(x,t) \equiv (EI\lambda'')' + \pi a^2 (\lambda p)' + \rho g A \lambda \left( \frac{\ddot{x}_0}{g} + \sin \alpha \right) + \rho g (\lambda S)' \left( \frac{\ddot{x}_0}{g} + \sin \alpha \right) \quad (24)$$

Expanding over the end points, using Eqs. 20, 21, and 22 and the variational conditions of the initial and boundary conditions given in Appendix B, Eq. 19 becomes

$$\begin{aligned} & \int_0^\tau \int_0^l \left\{ (EI\lambda'')'' + \rho A \ddot{\lambda} + \pi a^2 (p\lambda)'' + \rho g \left( \frac{\ddot{x}_0}{g} + \sin \alpha \right) [(\lambda\lambda)'] \right. \\ & \quad + (\lambda S)'' + m_p [\ddot{\lambda}(x,t) + 2 \frac{\partial^2}{\partial x \partial t} (\lambda(x,t)V(t)) \\ & \quad - \dot{V}(t)\lambda'(x,t) + V^2(t)\lambda''(x,t)] \bar{\delta}(x-\xi) + m_p [2 \frac{\partial}{\partial t} (\lambda(x,t)V(t)) \\ & \quad - \dot{V}(t)\lambda(x,t) + 2V^2(t)\lambda'(x,t)] \bar{\delta}'(x-\xi) + m_p V^2(t)\lambda(x,t) \bar{\delta}''(x \\ & \quad - \xi) + m_t \ddot{\lambda}(x,t) \bar{\delta}(x-l+\epsilon) + \lambda(x,t) k \bar{\delta}(x-z_0) \left. \right\} \delta y(x,t) dx dt \\ & + Q_1 + Q_2 + Q_3 + Q_4 + Q_5 = 0 \quad (25) \end{aligned}$$

where

$$\begin{aligned} Q_1 \equiv & \int_0^\tau \left\{ [\ddot{\lambda}(\xi,t)y(\xi,t) + 2y'(\xi,t) \frac{\partial}{\partial t} [\lambda(\xi,t)V(t)] \right. \\ & + \dot{V}(t)\lambda(\xi,t)y'(\xi,t) + \lambda(\xi,t)V^2(t)y''(\xi,t) + \lambda(\xi,t)g \cos \alpha] \delta m_p \\ & + [\ddot{\lambda}(l-\epsilon,t)y(l-\epsilon,t) + \lambda(l-\epsilon,t)g \cos \alpha] \delta m_t \\ & \left. + \lambda(z_0,t)y(z_0,t)\delta k - \lambda(z_0,t)y(z_0,t)k\delta\epsilon \right\} dt \quad (26) \end{aligned}$$

$$\begin{aligned} Q_2 \equiv & \int_0^\tau \left\{ -\lambda \delta(EIy'')' \Big|_{0^+} + \lambda' \delta(EIy'') \Big|_{0^+} + [B_1(l^-,t)\delta y'(l^-,t) \right. \\ & \left. - B_2(l^-,t)\delta y(l^-,t)] \right\} dt \quad (27) \end{aligned}$$

$$\begin{aligned} Q_3 \equiv & [\lambda(\xi,\tau)\dot{y}(\xi,\tau) - \dot{\lambda}(\xi,\tau)y(\xi,\tau)] \delta m_p + [\lambda(l-\epsilon,\tau)\dot{y}(l-\epsilon,\tau) \\ & - \dot{\lambda}(l-\epsilon,\tau)y(l-\epsilon,\tau)] \delta m_t \quad (28) \end{aligned}$$

$$Q_4 \equiv 2m_p \lambda(\xi,\tau)V(\tau)\delta y'(\xi,\tau) \quad (29)$$

\*HAUG, AND HUANG

$$Q_5 \equiv \int_0^{\ell} \{ [\rho A(x) \lambda(x, \tau) + m_p \lambda(x, \tau) \bar{\delta}(x - \tau) + m_t \lambda(x, \tau) \bar{\delta}(x - \ell + \epsilon)] \delta \dot{y}(x, \tau) - [\rho A(x) \dot{\lambda}(x, \tau) + m_p \dot{\lambda}(x, \tau) \bar{\delta}(x - \xi) + m_t \dot{\lambda}(x, \tau) \bar{\delta}(x - \ell + \epsilon)] \delta y(x, \tau) \} dx \quad (30)$$

Requiring  $\lambda$  to satisfy the differential equation

$$\begin{aligned} (EI \lambda'')'' + \rho A \ddot{\lambda} + \pi a^2 (p \lambda)'' + \rho g \left( \frac{\ddot{x}_0}{g} + \sin \alpha \right) [(\lambda \lambda)' + (\lambda S)'] \\ + m_p [\ddot{\lambda}(x, t) + 2 \frac{\partial^2}{\partial x \partial t} (\lambda(x, t) V(t)) - \dot{V}(t) \lambda'(x, t) \\ + V^2(t) \lambda''(x, t)] \bar{\delta}(x - \xi) + m_p [2 \frac{\partial}{\partial t} (\lambda(x, t) V(t)) \\ - \dot{V}(t) \lambda(x, t) + 2 V^2(t) \lambda'(x, t)] \bar{\delta}'(x - \xi) \\ + m_p V^2(t) \lambda(x, t) \bar{\delta}''(x - \xi) + m_t \ddot{\lambda}(x, t) \bar{\delta}(x - \ell + \epsilon) \\ + \lambda(x, t) k \bar{\delta}(x - z_0) = \frac{\partial L}{\partial y} - \frac{\partial^2 L}{\partial x \partial y} - \frac{\partial^2 L}{\partial t \partial y} \end{aligned} \quad (31)$$

equation 25 becomes

$$\int_0^{\tau} \int_0^{\ell} \left( \frac{\partial L}{\partial y} - \frac{\partial^2 L}{\partial x \partial y} - \frac{\partial^2 L}{\partial t \partial y} \right) \delta y \, dx \, dt = - (Q_1 + Q_2 + Q_3 + Q_4 + Q_5) \quad (32)$$

Substituting Eq. 32 into Eq. 14, one has

$$\delta \psi = \int_0^{\tau} \int_0^{\ell} \frac{\partial L}{\partial b} \delta b \, dx \, dt - (Q_1 + Q_2 + Q_3 + Q_4 + Q_5) + G \quad (33)$$

One now defines

$$\bar{Q}_1 \equiv -Q_1 + \int_0^{\tau} \int_0^{\ell} \frac{\partial L}{\partial b} \delta b \, dx \, dt \quad (34)$$

$$\bar{Q}_2 \equiv -Q_2 + \int_0^{\tau} \left[ -\frac{\partial L}{\partial y} \delta y \Big|_{0^+} + \frac{\partial L}{\partial y} \delta y \Big|_{\ell^-} \right] dt \quad (35)$$

With these notations, one may write Eq. 33 as

$$\delta \psi = \bar{Q}_1 + \bar{Q}_2 - (Q_3 + Q_4 + Q_5) \quad (36)$$

Only variations of the design variables and the design parameters are involved in  $\bar{Q}_1 + Q_3$  and only variations of the state variable are involved in  $\bar{Q}_2 + Q_4 + Q_5$ .

Choosing initial and boundary conditions for the adjoint variable, one is able to cause  $\bar{Q}_2 = 0$  and  $Q_5 = 0$ . To achieve this, one requires that

$$\begin{aligned} \rho A \lambda(x, \tau) + m_p \lambda(\xi, \tau) \bar{\delta}(x - \xi) + m_t \lambda(\ell - \epsilon, \tau) \bar{\delta}(x - \ell + \epsilon, \tau) &= 0 \\ \rho A \dot{\lambda}(x, \tau) + m_p \dot{\lambda}(\xi, \tau) \bar{\delta}(x - \xi) + m_t \dot{\lambda}(\ell - \epsilon, \tau) \bar{\delta}(x - \ell + \epsilon, \tau) &= 0 \end{aligned} \quad (37)$$

\*HAUG, AND HUANG

It can be proved [9] that Eq. 37 implies  $\lambda(x, \tau) = 0$ ,  $\lambda(\xi, \tau) = 0$ ,  $\lambda(l - \epsilon, \tau) = 0$ ,  $\dot{\lambda}(x, \tau) = 0$ ,  $\dot{\lambda}(\xi, \tau) = 0$ , and  $\dot{\lambda}(l - \epsilon, \tau) = 0$ ; or in a more concise form,

$$\left. \begin{aligned} \lambda(x, \tau) &= 0 \\ \dot{\lambda}(x, \tau) &= 0 \end{aligned} \right\} \quad (38)$$

Eq. 38 gives the terminal condition on the adjoint variable  $\lambda(x, t)$ .

Also one chooses the following boundary conditions for the adjoint variable,

$$\lambda(0^+, t) = 0 \quad (39.a)$$

$$\lambda'(0^+, t) = 0 \quad (39.b)$$

$$B_1(l^-, t) = 0 \quad (39.c)$$

$$B_2(l^-, t) + \frac{\partial L}{\partial y}(l^-, t) = 0 \quad (39.d)$$

where the functions  $B_1$  and  $B_2$  are defined in Eqs. 23 and 24.

By the chosen terminal and boundary conditions on the adjoint variable  $\lambda(x, t)$ , one has  $Q_3 = 0$  and  $Q_4 = 0$ . Thus,

$$\delta\psi = \bar{Q}_1 \quad (40)$$

Using Eqs. 26 and 34, Eq. 40 is written explicitly as

$$\begin{aligned} \delta\psi = & \int_0^\tau \left\{ -[\ddot{\lambda}(\xi, t)y(\xi, t) + 2y'(\xi, t)\frac{\partial}{\partial t}(\lambda(\xi, t)V(t)) \right. \\ & + \dot{V}(t)\lambda(\xi, t)y'(\xi, t) + \lambda(\xi, t)V^2(t)y''(\xi, t) \\ & + \lambda(\xi, t)g \cos \alpha] \delta m_p - [\ddot{\lambda}(l - \epsilon, t)y(l - \epsilon, t) \\ & + \lambda(l - \epsilon, t)g \cos \alpha] \delta m_t - \lambda(z_0, t)y(z_0, t)\delta k \\ & \left. + \lambda(z_0, t)y(z_0, t)k\delta e \right\} dt + \int_0^\tau \int_0^l \frac{\partial L}{\partial b} \delta b dx dt \end{aligned} \quad (41)$$

In a more compact form, Eq. 41 is

$$\delta\psi = \ell^\psi \delta b \quad (42)$$

where  $\ell^\psi$  is the desired sensitivity coefficient vector with respect to the design parameter vector. Let  $b = [m_p, m_t, k, e]^T$ . Then the  $\ell^\psi_i$  are

$$\begin{aligned} \ell^\psi_1 = & \int_0^\tau \left\{ -[\ddot{\lambda}(\xi, t)y(\xi, t) + 2y'(\xi, t)\frac{\partial}{\partial t}(\lambda(\xi, t)V(t)) \right. \\ & + \dot{V}(t)\lambda(\xi, t)y'(\xi, t) + \lambda(\xi, t)V^2(t)y''(\xi, t) + \lambda(\xi, t)g \cos \alpha] dt \\ & \left. + \int_0^\tau \int_0^l \frac{\partial L}{\partial b_1} dx dt \right\} \end{aligned} \quad (43.a)$$

$$\begin{aligned} \ell^\psi_2 = & \int_0^\tau \left\{ -[\ddot{\lambda}(l - \epsilon, t)y(l - \epsilon, t) + \lambda(l - \epsilon, t)g \cos \alpha] dt \right. \\ & \left. + \int_0^\tau \int_0^l \frac{\partial L}{\partial b_2} dx dt \right\} \end{aligned} \quad (43.b)$$

$$\ell^\psi_3 = \int_0^\tau \left\{ [-\lambda(z_0, t)y(z_0, t)] dt + \int_0^\tau \int_0^l \frac{\partial L}{\partial b_3} dx dt \right\} \quad (43.c)$$

\*HAUG, AND HUANG

$$\begin{aligned} \ell_4^\psi = & - \int_0^\tau k[\lambda'(z_0, t)y(z_0, t) + \lambda(z_0, t)y'(z_0, t)]dt \\ & + \int_0^\tau \int_0^\ell \frac{\partial L}{\partial b_4} dxdt \end{aligned} \quad (43.d)$$

With these sensitivity coefficients, one can proceed to carry out design sensitivity analysis and optimal design. An algorithm for digital computer calculation of the sensitivity coefficients is summarized as follows:

- (1) With estimated values of the design parameters  $b_1$ , solve Eqs. 1, 4, and 5 for the state variable  $y(x, t)$ .
- (2) Using the solution  $y(x, t)$  from step (1), along with  $b_1$ , solve Eqs. 31, 38, and 39 for the adjoint variable  $\lambda(x, t)$ .
- (3) Use the values of  $b_1$  and  $y(x, t)$  from step (1) and  $\lambda(x, t)$  from step (2) to calculate the sensitivity coefficients  $\ell_1^\psi$  in Eq. 43.

#### 4. NUMERICAL RESULT FOR DYNAMIC RESPONSE ANALYSIS

To illustrate the dynamic analysis technique developed in the previous sections, a numerical example of the recoil system shown in Fig. 3 is treated and its dynamic solution is presented.

The recoil motion  $x_0(t)$  of the gun tube is given in Fig. 4. The projectile motion  $\xi(t)$  relative to the gun is shown in Fig. 5. The pressure function  $p(x, t)$  is given as

$$p(x, t) = p_0(t) \left[ 1 - \frac{m_c}{\frac{m_c}{2} + m_p} \frac{1}{2} \left( \frac{x}{\xi} \right)^2 \right],$$

where  $p_0(t)$  is given in Fig. 5 and  $m_c = 5.22661b.$  is the mass of the charge. The gun tube is discretized by 13 equally spaced nodes with a total of 36 degrees of freedom, 3 for each nodal point except those two at the boundary.

Modal analysis and Picard iteration are applied to solve the differential equations (2.11) and (2.12), with 9 used in the eigenfunction expansion. The eigenvalues and eigenvectors are determined by Jacobi method. Dynamic analysis is performed from  $t = 0$  to  $t = 5.6 \times 10^{-3}$  secs. (projectile exit).

The Picard iteration method can be applied in two ways, namely (a) by taking the whole time interval as an iteration time period and (b) by iterating over subintervals  $[t_i, t_i + \Delta T]$  successively. For each time step, only the gravity force is taken into consideration in the first iteration, as the forcing function  $f$  in Eq. (2.3). The result is then used to evaluate an estimate for the forcing function.

This process is repeated until the convergence criterion is met

\*HAUG AND HUANG

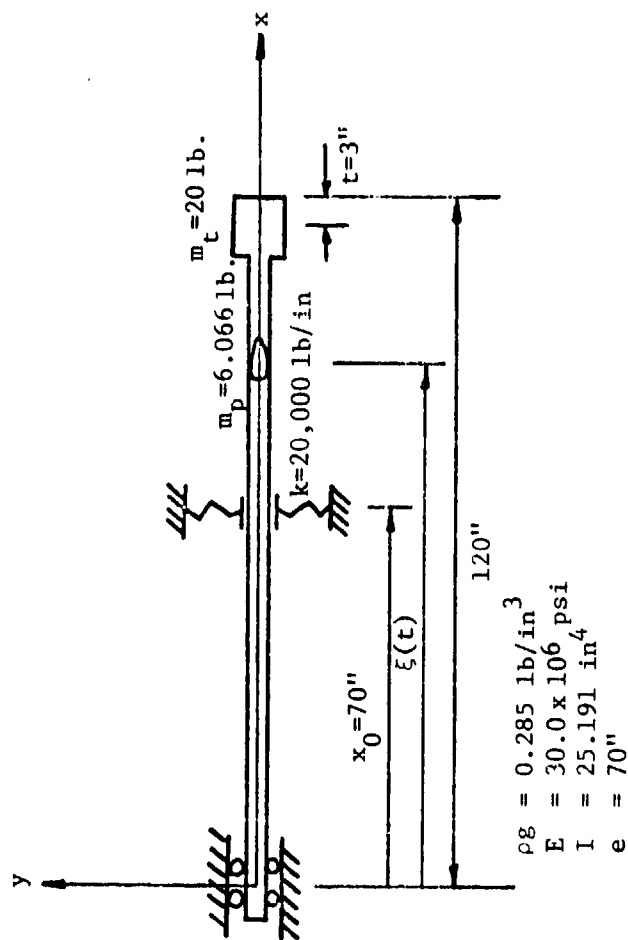


Figure 3. Data for the Recoil System.

\*HAUG, AND HUANG

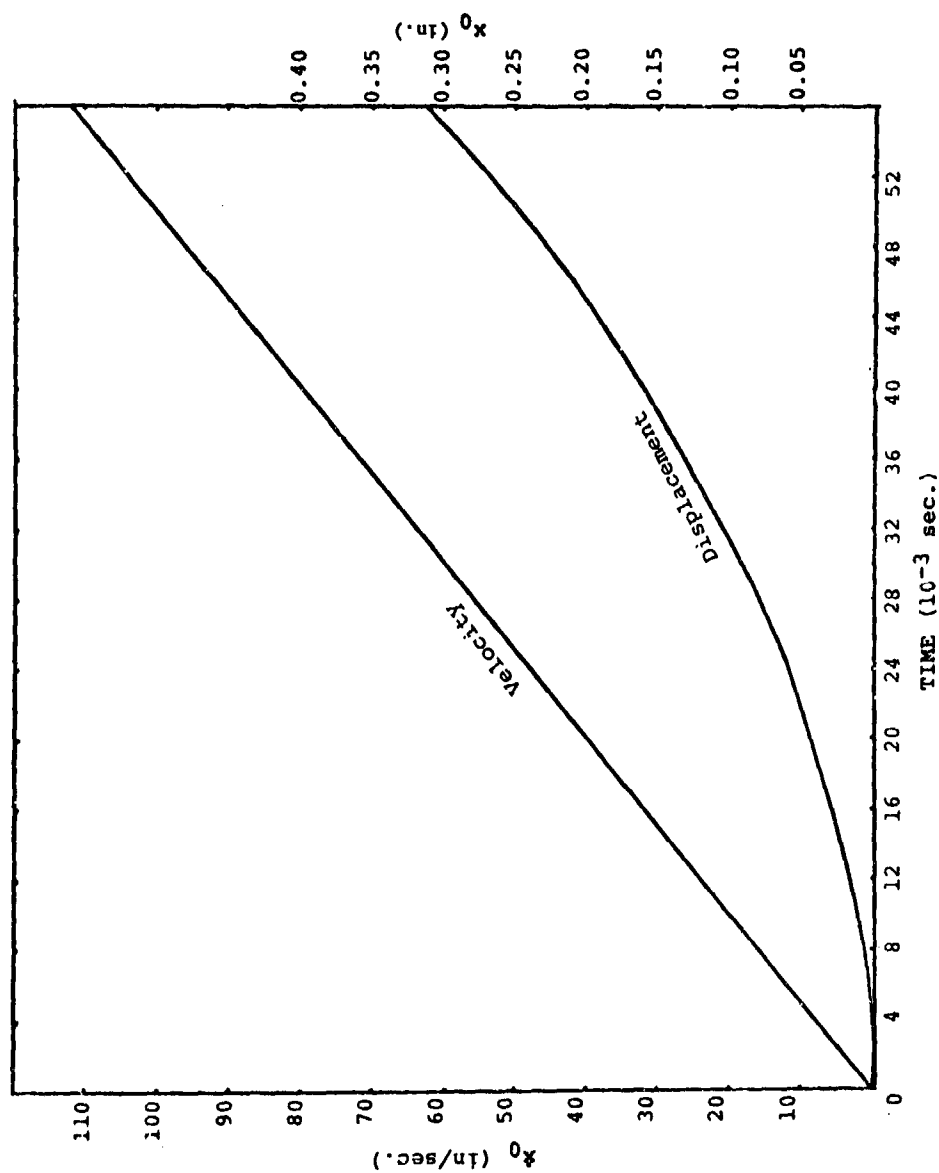


Figure 4. Recoil Velocity and Displacement.

\*HAUG, AND HUANG

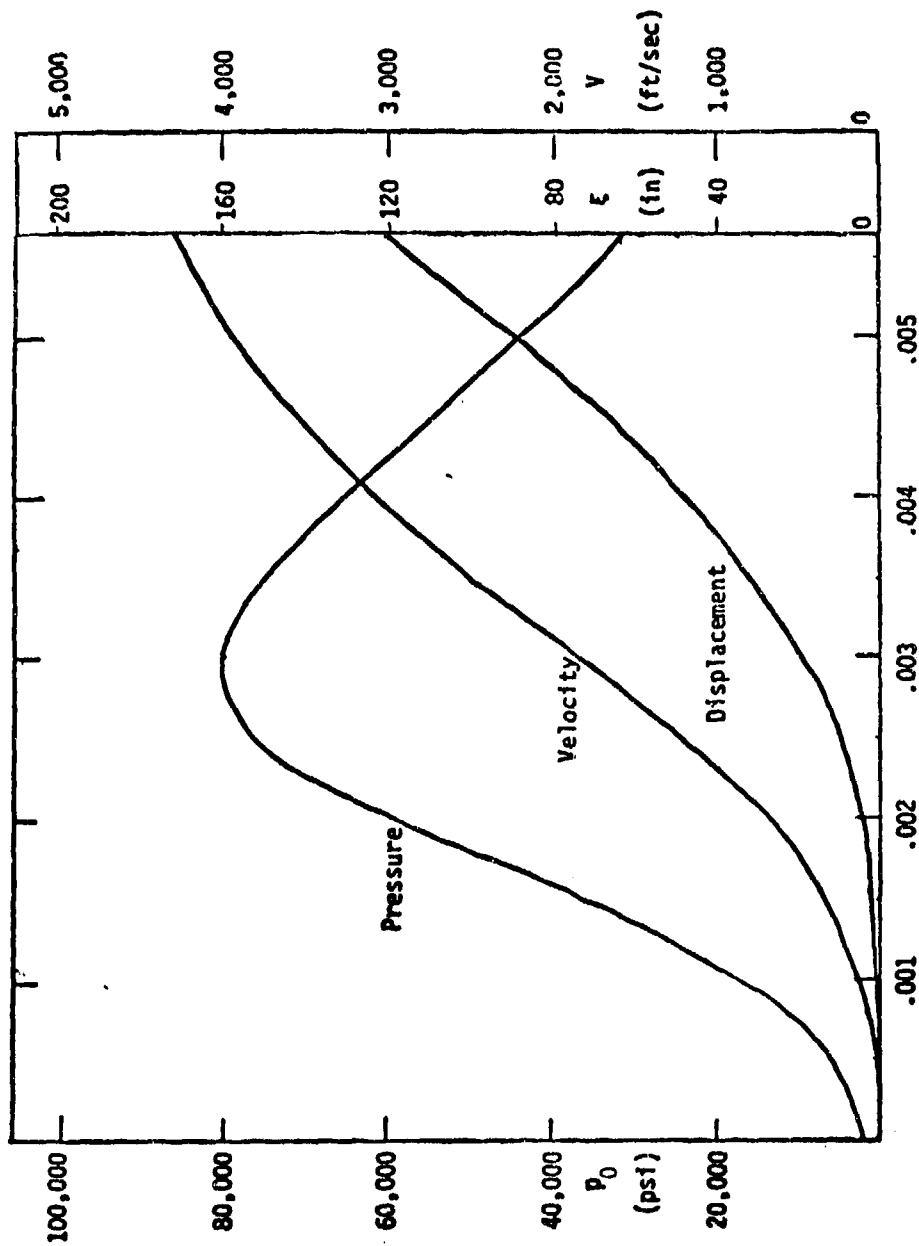
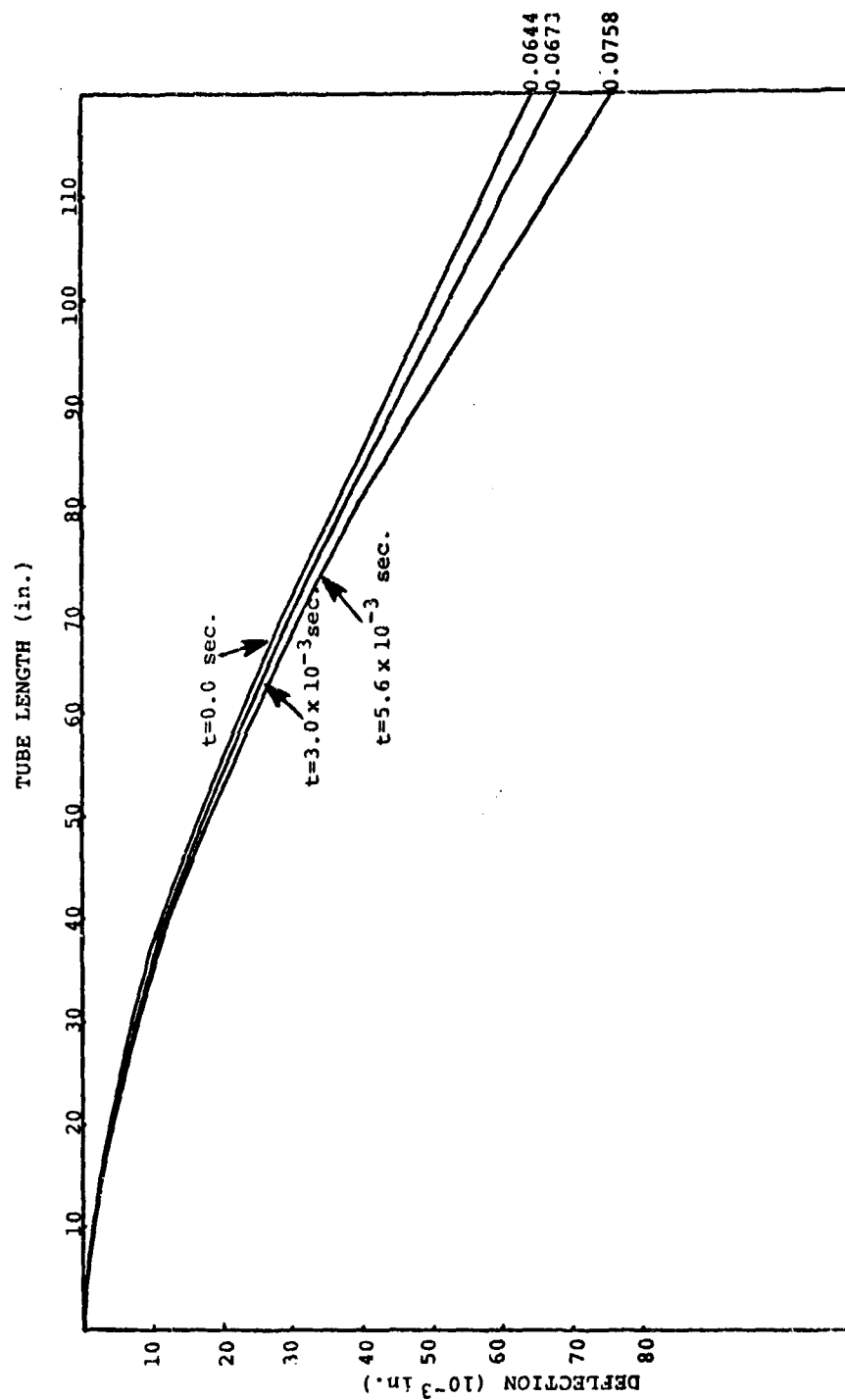


Figure 5. Breech Pressure and Projectile Velocity and Displacement.



\*HAUG AND HUANG

Figure 6. Dynamic Solution with Picard Iteration Taken Over Time Interval  $[0., 5.6 \times 10^{-3}]$

\*HAUG, AND HUANG

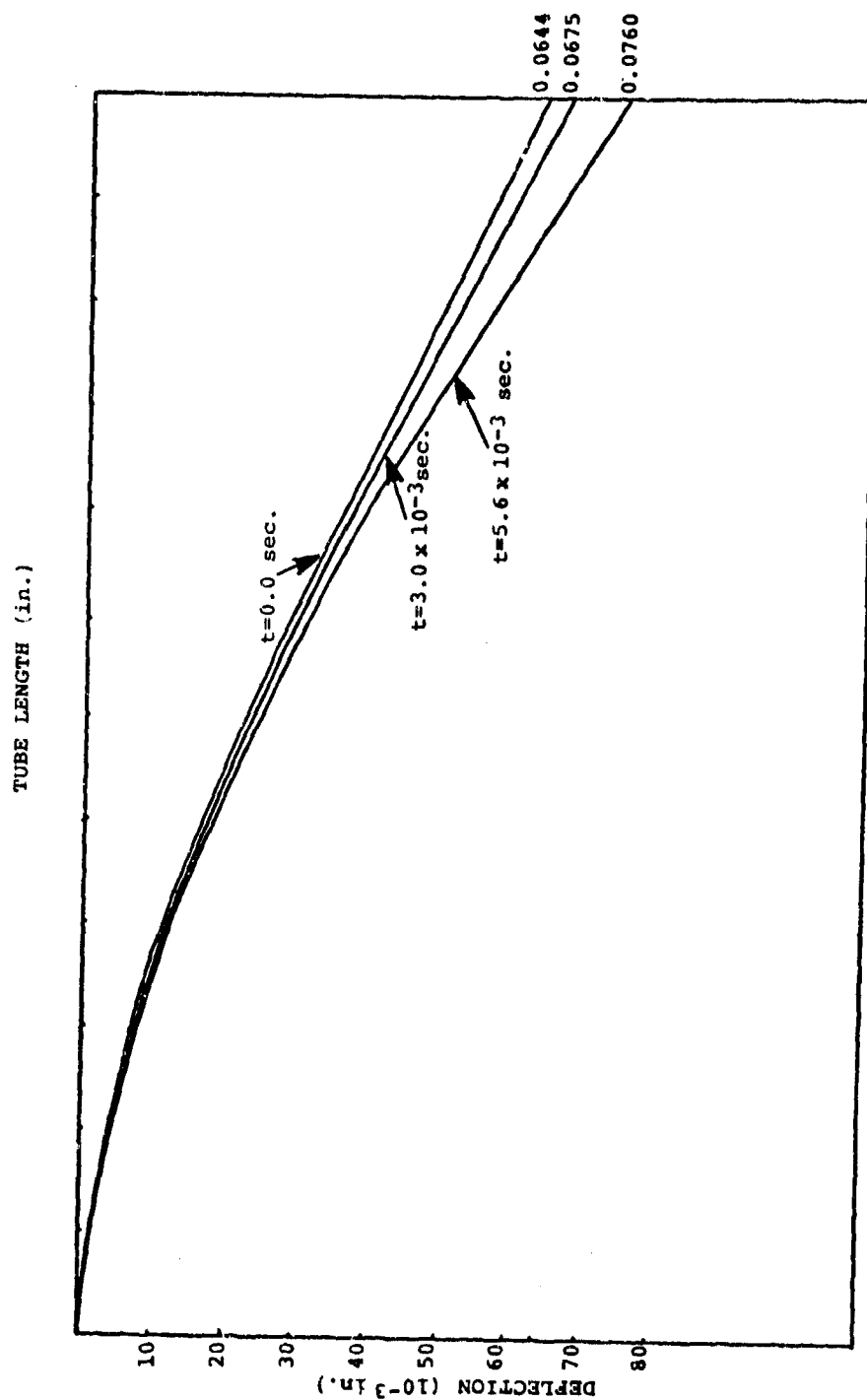


Figure 7. Dynamic Solution with Picard Iteration Taken Over Time Interval  $\Delta T = 0.4 \times 10^{-3}$  sec. Successively.

\*HAUG, AND HUANG

Table 1. Convergence History of the Picard Iteration  
Taken Over Time Subintervals Successively.

Time ( $10^{-3}$ sec.)	No. of Time Grid Points	No. of Iterations	Initial $  y  $	Final $  y  $ (in. $10^{-4}$ )
0.4	3	2	1	0.48
0.8	3	1	1	5.05
1.2	3	1	1	4.55
1.6	3	1	1	3.30
2.0	3	1	1	2.79
2.4	3	1	1	2.63
2.8	3	1	1	2.57
3.2	3	1	1	2.22
3.6	3	1	1	2.26
4.0	3	1	1	1.73
4.4	3	1	1	1.87
4.8	3	1	1	2.87
5.2	3	1	1	2.04
5.6	3	1	1	1.73

Table 2. Convergence History of the Picard Iteration  
Taken Over the Whole Time Interval.

Iteration	$  y  $
0	1.00000
1	0.03136
2	0.00590
3	0.00110
4	0.00048

Table 3. Deflection and Slope at the Muzzle End.

Time ( $10^{-3}$ sec.)	Deflection ( $10^{-2}$ in.)	Slope ( $10^{-4}$ rad.)
0.0	6.4420	7.1571
0.5	6.4435	7.0180
1.0	6.4804	7.1394
1.5	6.5526	7.4749
2.0	6.6198	7.6996
2.5	6.6771	7.5302
3.0	6.7501	7.5671
3.5	6.8609	7.6923
4.0	6.9835	7.9321
4.5	7.1174	7.8986
5.0	7.2938	8.1364
5.6	7.6068	9.5140

\*HAUG AND HUANG

or the maximum iteration number allowed is exceeded. The convergence measure is defined as

$$||y|| = \frac{\left[ \int_0^L \int_0^T |y_{k+1} - y_k|^2 dt dx \right]^{\frac{1}{2}}}{\left[ \int_0^L \int_0^T y_{k+1}^2 dt dx \right]^{\frac{1}{2}}}$$

where  $k$  is the iteration number.

With the given data and forcing functions, the dynamic response  $y(x,t)$  of the gun tube is shown in Figs. 6 and 7, for Picard iteration processes (a) and (b), respectively. The convergence criterion used is 0.001 and the number of iterations required to achieve convergence is 4 for process (a) and is never more than 2 for process (b). One may notice from Figs. 6 and 7 that the two iterative schemes yield the same result. The convergence histories are given in Tables 1 and 2. The deflection and the slope of the muzzle end are given in Table 3.

## 5. SUMMARY AND DISCUSSION

(1) A method for dynamic design sensitivity analysis for the moving gun barrel under the effects of the transverse and longitudinal motion of the gun tube, the projectile inertia, and the flash suppressor inertia is developed. In the development, the state variable  $y(x,t)$  and the adjoint variable  $\lambda(x,t)$  are assumed to be twice continuously differentiable with respect to the time variable  $t$ , such that operations with distributions are meaningful in both the equations of motion and in the adjoint equation.

(2) A numerical example for the dynamic response of the system shown in Fig. 3 is given and discussed in Section 4. To carry out this analysis, the Galerkin method, Picard iteration, and modal analysis are applied. Convergence of the iterative procedure is rapid.

(3) The adjoint equation (3.19) is of the same form as of the dynamic equation (2.1), therefore the method of solution used for solving the dynamic equations can be applied to the adjoint equation. For numerical solution, the same program can be used for solving both the dynamic equation and the adjoint equation. Work in this direction is under way.

(4) The functional form considered in Section 3 is general enough to include practical cost and constraint functionals. For example, one may choose the cost function to be

$$\psi = \int_0^T \int_0^L \left[ \phi_1(x) \left( \frac{\partial y}{\partial x} \right)^2 + \phi_2(x) \left( \frac{\partial y}{\partial t} \right)^2 \right] dx dt$$

which can be a measure of the accuracy of projectile launch. In this paper, the masses of the projectile  $m_p$  and the flash suppressor  $m_t$ , the spring constant  $k$ , and the initial distance  $e$  from the left end of the barrel to the spring support are taken as design parameters. Other parameters can be treated in the same way.

## \*HAUG AND HUANG

(5) One may use the  $\delta$ -representative sequences [9] for the distributional delta functions  $\bar{\delta}$  and  $\bar{\delta}'$  in the equations of motion and the adjoint equations.

## 6. REFERENCES

- [1] Simkins, T.E., "Radial and Transverse Response of Gun Tubes by Finite Element Methods", p.373, Proceedings on Dynamics of Precision Gun Weapons, R-TR-77-008, January 1977.
- [2] Feng, T.T., and Hung, T., "Transverse Dynamic Response of Gun Barrel with Time Varying Supports", p.179, Proceedings on Dynamics of Precision Gun Weapons, R-TR-77-008, January 1977.
- [3] Haug, E.J., Jr., Engineering Design Handbook Computer Aided Design of Mechanical Systems, AMC Pamphlet No. 706-192, U.S. Army Materiel Command, Washington, D.C., 1973.
- [4] Huang, R.C., Haug, E.J., Jr., and Andrews, J.G., "Optimal Design of Mechanical Systems with Intermittent Motion", to appear in ASME.
- [5] Haug, E.J., Jr., Analytical Methods in Mechanics, Lecture Notes, College of Engineering, University of Iowa, May 1976.
- [6] Mikhlin, S.G., Variational Methods in Mathematical Physics, McMillan, New York, 1964.
- [7] Adams, R.A., Sobolev Spaces, Academic Press, New York, 1975.
- [8] Schwartz, L., Mathematics for the Physical Sciences, Addison-Wesley Publishing Co., Palo Alto, 1966.
- [9] Kec, W., and Teodorescu, P.P., Applications of the Theory of Distributions in Mechanics, Editura Academiei, 1970.

## 7. APPENDIX A: NOTATION

$A(x)$  = cross-sectional area of the barrel  
 $a$  = inner radius of the barrel  
 $b$  = vector of design parameters  
 $e$  = initial distance from the left end of barrel to the spring support  
 $E$  = elastic modulus of the barrel  
 $g$  = gravitational acceleration  
 $I(x)$  = moment of inertia of the cross-sectional area of the barrel  
 $k$  = spring constant  
 $l$  = total length of the barrel  
 $m_p$  = projectile mass  
 $m_t$  = flash suppressor mass  
 $u$  = vector of the design variables  
 $v$  = projectile velocity  
 $\ddot{x}_0$  = recoil and the counter-recoil acceleration  
 $y$  = lateral displacement of the barrel  
 $z_0$  =  $x_0(t) + e$   
 $\alpha$  = inclined angle of the barrel axis

\*HAUG, AND HUANG

$\Delta$  = total variation  
 $\delta$  = variation  
 $\bar{\delta}$  = Dirac delta function  
 $\epsilon$  = small positive number  
 $\xi(t)$  = position of the projectile

In the following expression,  $x_{i-1} \leq x \leq x_{i+1}$  and  $r = \frac{x - x_i}{x_i - x_{i-1}}$

$$\psi_i = \begin{cases} 1 - 10|r|^3 + 15r^4 - 6|r|^5, & |r| \leq 1 \\ 0, & |r| > 1 \end{cases}$$

$$\phi_i = \begin{cases} (x_i - x_{i-1})r(1 - 6r^2 + 8|r|^3 - 3r^4), & |r| \leq 1 \\ 0, & |r| > 1 \end{cases}$$

$$\omega_i = \begin{cases} \frac{(x_i - x_{i-1})^2}{2} r^2(1 - 3|r| + 3r^2 - |r|^3), & |r| \leq 1 \\ 0, & |r| > 1 \end{cases}$$

#### 8. APPENDIX B: VARIATIONS OF THE INITIAL CONDITIONS AND THE BOUNDARY CONDITIONS

Let  $\delta$  denote the total variation of a function. Taking the variation of Eqs. 4 and 5, one has

$$\delta y(x, 0) = 0 \quad (B1)$$

$$\delta \dot{y}(x, 0) = 0 \quad (B2)$$

and

$$\delta y(0, t) = 0 \quad (B3)$$

$$\delta y'(0, t) = 0 \quad (B4)$$

$$\delta(EI y'')(l^-, t) = 0 \quad (B5)$$

$$\delta(EI y''')(l^-, t) = 0 \quad (B6)$$

LOH, HUTCHINGS & KASTEN

TITLE: State Space Design for Helicopter Pointing  
and Tracking Systems  
NAN K. LOH  
Electrical and Computer Engineering  
University of Iowa, Iowa City, Iowa 52242  
THOMAS D. HUTCHINGS  
US Army Armament Research and Development Command  
DRDAR-SCS-M  
Dover, New Jersey 07801  
ROBERT E. KASTEN  
Ware Simulation Division, SARRI-ENW-3900  
Rock Island Arsenal, Rock Island, Illinois 61201

ABSTRACT:

This paper describes the optimal control of a helicopter turret control system with external disturbances of known waveform structure and which has a state variable which is not accessible for online measurement. Design techniques for dealing with the combined problem of optimal control, disturbance accommodation, and estimation of inaccessible state variables are developed. Simulation results providing comparison between the performance of the existing turret and the optimal turret are given.

STATE SPACE DESIGN FOR HELICOPTER  
POINTING AND TRACKING SYSTEMS

NAN K. LOH, Ph.D.  
ELECTRICAL AND COMPUTER ENGINEERING  
UNIVERSITY OF IOWA  
IOWA CITY, IOWA 52242

THOMAS D. HUTCHINGS  
US ARMY ARMAMENT RESEARCH AND DEVELOPMENT COMMAND  
DRDAR-SCS-M  
DOVER, NEW JERSEY 07801

ROBERT E. KASTEN  
WARE SIMULATION DIVISION  
SARRI-ENW-3900  
ROCK ISLAND ARSENAL  
ROCK ISLAND, ILLINOIS 61201

I. INTRODUCTION

One of the most difficult problems encountered in the analysis, design or operation of an engineering system, is the effective accommodation or rejection of unknown disturbances, often describable in terms of environmental parameters with unknown values. Typical examples of disturbances are hull motions and recoil forces encountered by helicopters, terrain variations experienced by surface moving vehicles, electronic and atmospheric noise experienced by communication systems, load torque variations experienced by electromechanical systems, ocean currents experienced by ships, and load fluctuations encountered by electrical power systems. Almost all disturbances encountered in the real world are not known before they occur and begin to cause undesirable effects on the performance of a system. Hence the physical behavior and properties of disturbances, such as their physical waveforms, magnitudes, phases, times of arrival, duration, directions, etc., cannot be predicted precisely before they actually occur. However, whenever a particular type of disturbances is known to exist or is detected in a particular system or a particular class of systems, some suitable methods can often be developed to accommodate or counteract these disturbances.



LOH, HUTCHINGS & KASTEN

An extremely useful and effective disturbance accommodation method is the method which will provide on-line real-time determination of the waveform characteristics and properties of a disturbance function and/or disturbance sequence. This is the waveform mode of disturbance accommodation techniques developed by C.D. Johnson [1-5], see also [6-9]. A large class of physical disturbances exhibit specific waveform structures. Some typical examples are steps of unknown magnitudes ( $w_1(t)$  in Figure 1), steps plus ramps ( $w_2(t)$  in Figure 1), sinusoids of unknown amplitudes ( $w_3(t)$  in Figure 1), exponentials of unknown coefficients, and a complicated combination of these disturbances. From the engineering point of view, knowledge of the possible waveform structure of an expected disturbance is often much more important and useful than its statistical properties. Once the waveform structure of a disturbance is known and/or anticipated, suitable methods may be developed to

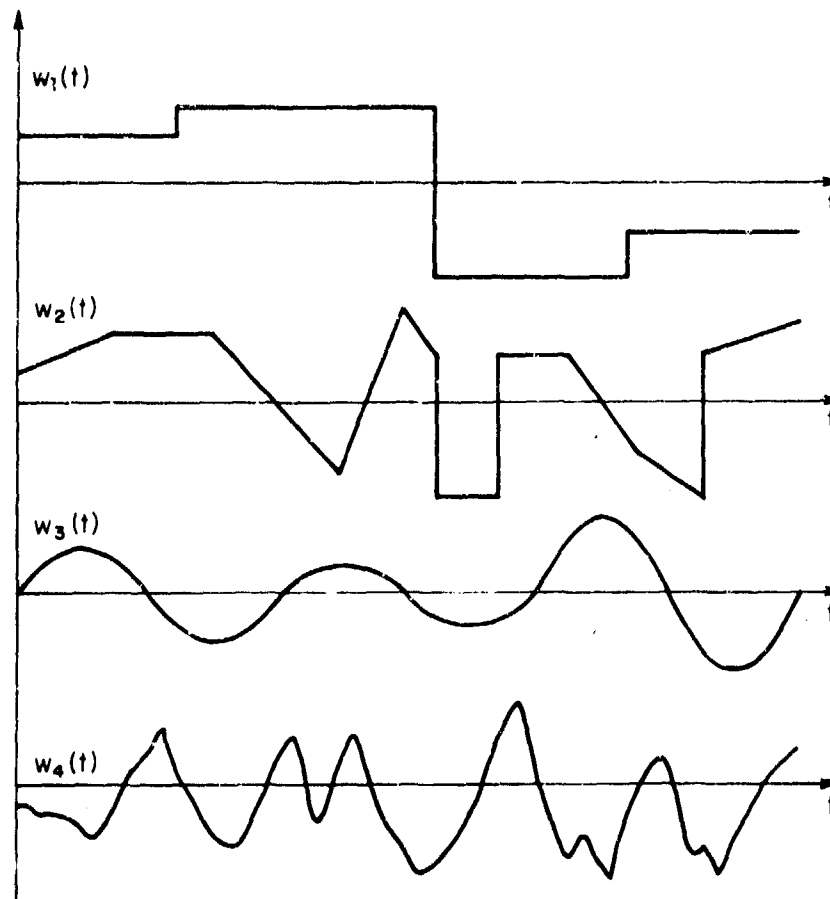


Figure 1 Disturbance  $W(t)$

either accommodate or reject it, such as an integral control designed to accommodate constant off-set and/or constant disturbances [10,11] and a comb filter designed to remove sinusoidal signals of various frequencies [12].

In this paper, the optimal design of a helicopter turret control system is considered. The waveform mode of disturbance accommodation techniques will be used. Furthermore, the helicopter turret control system contains a state variable which is not accessible for on-line measurement. A Luenberger observer [13-16] will be designed to provide the estimated values of the inaccessible state variable and unknown disturbance.

## II. SYSTEM DESCRIPTION

The system under investigation is the turret control system in a helicopter as shown in Figure 2. The turret control system consists of two independent controllers. One controller positions the turret in azimuth and the other elevates and depresses the gun cradle and the gun. The two controllers are functionally similar and so only the elevation channel will be considered [6-9, 17].

Two main disturbances experienced by the turret control system are the hull vibrations of the helicopter and the recoil forces due to firing. In [18], it was found that the hull vibrations are dominated by sinusoids with relatively high frequencies, while the recoil forces exhibit a typical waveform as shown in Figure 3(a).

The gun turret is essentially an inertial load driven by a pulse width modulated, split series DC motor, through a compliant gear box. The existing or "classical" system employs angular position feedback aided by velocity feedback to achieve better system performance (see Figure 2(b)).

A functional block diagram of the elevation channel of the turret control system under investigation is as shown in Figure 2(b). The state variables chosen are as shown, where

- $x_1(t)$  is the gun angular position relative to the hull (radians),
- $x_2(t)$  is the gun angular velocity (radians/second),
- $x_3(t)$  is the angular velocity of the motor (radians/second),
- $x_4(t)$  is the motor torque (foot-pounds)
- $x_5(t)$  is the output of the power amplifier (volts),
- $x_6(t)$  is the output of the low level electronics (volts),
- $x_7(t)$  is the "geared down" shaft angular position (radians),



11-56

$x_8(t)$  is the output of the tachometer feedback loop (volts),  
and

$w(t)$  is the disturbance torque (foot-pounds).

With the state variables chosen as shown in Figure 2(b), it can readily be shown that the turret is described by the following 8-dimensional vector differential equation

$$\dot{\underline{x}}(t) = A\underline{x}(t) + \underline{b}u(t) + \underline{f}w(t) \quad , \quad \underline{x}(0) = \underline{x}_0 \quad (1)$$

with

$$u(t) = r(t) - x_1(t) \quad (2)$$

where  $A$ ,  $\underline{b}$ , and  $\underline{f}$  can be determined from known transfer functions, and  $r(t)$  is the servo-command input.

### III. OPTIMAL TRACKING TURRET WITH INACCESSIBLE STATE VARIABLES AND DISTURBANCE ACCOMMODATION

Consider a completely controllable and completely observable turret control system described by the following general vector differential equation

$$\dot{\underline{x}}(t) = A \underline{x}(t) + B \underline{u}(t) + F \underline{w}(t) \quad , \quad \underline{x}(0) = \underline{x}_0 \quad (3a)$$

$$\underline{z}_c(t) = D_x \underline{x}(t) \quad , \quad (3b)$$

$$\underline{y}(t) = H \underline{x}(t) \quad , \quad (3c)$$

where

- $\underline{x}(t)$  is an  $n_x$ -vector of turret state variables,
- $\underline{u}(t)$  is an  $n_u$ -vector of turret control inputs,
- $\underline{z}_r(t)$  is an  $n_z$ -vector of turret servo-command inputs
- $\underline{w}(t)$  is an  $n_w$ -vector of turret disturbance inputs,
- $\underline{z}_c(t)$  is an  $n_z$ -vector of turret controlled variables,
- $\underline{y}(t)$  is an  $n_y$ -vector of turret output variables,
- $A$  is an  $n_x \times n_x$  constant matrix,
- $B$  is an  $n_x \times n_u$  constant matrix,
- $F$  is an  $n_x \times n_w$  constant matrix,
- $D_x$  is an  $n_z \times n_x$  constant matrix, and

# LOH, HUTCHINGS & KASTEN

$H$  is an  $n_y \times n_x$  constant matrix.

The turret servo-command input  $\underline{z}_r(t)$  is generated by

$$\underline{\dot{z}}_r(t) = D_r \underline{r}(t) , \quad (4a)$$

$$\underline{\dot{r}}(t) = A_r \underline{r}(t) , \quad \underline{r}(0) = \underline{r}_0 , \quad (4b)$$

where

$\underline{z}_r(t)$  is an  $n_z$ -vector of turret command or reference variables which represent the prescribed values of the turret controlled vector  $\underline{z}_c(t)$ ,

$\underline{r}(t)$  is an  $n_r$ -vector of reference state variables which form  $\underline{z}_r(t)$ ,

$D_r$  is an  $n_z \times n_r$  constant matrix, and

$A_r$  is an  $n_r \times n_r$  constant matrix.

A broad class of realistic command signals, such as steps, ramps, and more complicated functions, can be generated by (4) by the proper choice of  $D_r$  and  $A_r$ .

The turret disturbance input  $\underline{w}(t)$  is generated by

$$\underline{w}(t) = D_v \underline{v}(t) , \quad (5a)$$

$$\underline{\dot{v}}(t) = A_v \underline{v}(t) + \underline{\sigma}(t) , \quad (5b)$$

where

$\underline{v}(t)$  is the  $n_v$ -vector of disturbance state variables,

$\underline{\sigma}(t)$  is the  $n_v$ -vector of impulsive functions which model unknown initial conditions, discontinuities, etc. of  $\underline{v}(t)$ ,

$D_v$  is the  $n_w \times n_z$  constant matrix, and

$A_v$  is the  $n_v \times n_v$  constant matrix.

A broad class of realistic disturbances, such as steps, ramps, sine-waves, and more complicated functions, can be generated by (5) (see [5] for an excellent discussion, see also Figure 1).

The design objective is to formulate a control input  $\underline{u}(t)$  to drive the turret control system, which is operating under the influence of the disturbance  $\underline{w}(t)$ , in such a way that the controlled vector  $\underline{z}_c(t)$  will follow the servo-command vector  $\underline{z}_r(t)$  accurately in some suitable sense.

Consider the performance measure

$$J = \int_0^T \{ [\underline{z}_c(t) - \underline{z}_r(t)]^T Q [\underline{z}_c(t) - \underline{z}_r(t)] + \underline{u}^T(t) R \underline{u}(t) \} dt, \quad (6)$$

where  $Q$  and  $R$  are, respectively,  $n_z \times n_z$  positive-semidefinite and  $n_u \times n_u$  positive definite weighting matrices.

The optimal control which minimizes (6) is given by [5-7]

$$\underline{u}_{opt}(t) = -R^{-1}B^TK_{xx}(t)\underline{x}(t) - R^{-1}B^TK_{xr}(t)\underline{r}(t) - R^{-1}B^TK_{xv}(t)\underline{v}(t), \quad (7)$$

where  $K_{xx}(t)$ ,  $K_{xr}(t)$  and  $K_{xv}(t)$  satisfy the matrix Riccati equations

$$-\dot{K}_{xx}(t) = A^TK_{xx}(t) + K_{xx}(t)A - K_{xx}(t)BR^{-1}B^TK_{xx}(t) + D_x^TQD_x, \quad (8)$$

$$-\dot{K}_{xr}(t) = [A - BR^{-1}B^TK_{xx}(t)]^TK_{xr}(t) + K_{xr}(t)A_r - D_x^TQD_r, \quad (9)$$

$$-\dot{K}_{xv}(t) = [A - BR^{-1}B^TK_{xx}(t)]^TK_{xv}(t) + K_{xv}(t)A_v + K_{xx}(t)FD_v, \quad (10)$$

with boundary conditions  $K_{xx}(T) = 0$ ,  $K_{xr}(T) = 0$  and  $K_{xv}(T) = 0$ .

The implementation of the optimal control,  $\underline{u}_{opt}(t)$ , requires knowledge of the exact values of every component of the turret state vector  $\underline{x}(t)$ , the turret reference state vector  $\underline{r}(t)$ , and the turret disturbance state vector  $\underline{v}(t)$  at every instant of time  $t \geq 0$ . In almost all practical situations, however, not all the turret state variables and disturbances are accessible for on-line measurement, nor is it economical to measure all the state variables and disturbances involved. Hence, in practical situations, (7) may be implemented as\*

$$\begin{aligned} \underline{u}_{opt}(t) = & -R^{-1}B^TK_{xx}(t) \begin{bmatrix} \underline{x}_1(t) \\ \hat{\underline{x}}_2(t) \end{bmatrix} - R^{-1}B^TK_{xr}(t)\underline{r}(t) \\ & - R^{-1}B^TK_{xv}(t)\hat{\underline{v}}(t), \end{aligned} \quad (11)$$

\* It is assumed that  $\underline{r}(t)$  is given.

LOH, HUTCHINGS & KASTEN

where  $\underline{x}_1(t)$  is a subset of  $\underline{x}(t)$  accessible for on-line measurement,  $\underline{x}_2(t)$  is a subset of  $\underline{x}(t)$  inaccessible for on-line measurement, and  $\underline{x}_2(t)$  and  $\underline{\hat{v}}(t)$  are estimates of  $\underline{x}_2(t)$  and  $\underline{v}(t)$ , respectively.

In order to generate the estimates,  $\hat{\underline{x}}_2(t)$  and  $\hat{\underline{v}}(t)$  required by (11), a suitable estimator will be required. An effective estimator is the Luenberger observer given by [16].

#### IV. DESIGN OF THE LUENBERGER OBSERVER

To solve the estimation problem associated with the inaccessible turret state variables and unknown disturbances, consider the following augmented state equation obtained by combining (3a) and (5b),

$$\begin{bmatrix} \dot{\underline{x}}_1(t) \\ \dot{\underline{x}}_2(t) \\ \dot{\underline{v}}(t) \end{bmatrix} = \begin{bmatrix} A_{11} & A_{12} & D_{11} \\ A_{21} & A_{22} & D_{21} \\ 0 & 0 & A_v \end{bmatrix} \begin{bmatrix} \underline{x}_1(t) \\ \underline{x}_2(t) \\ \underline{v}(t) \end{bmatrix} + \begin{bmatrix} B_{11} \\ B_{21} \\ 0 \end{bmatrix} \underline{u}(t) + \begin{bmatrix} 0 \\ 0 \\ I \end{bmatrix} \underline{\sigma}(t) \quad (12)$$

where  $\underline{x}_1(t)$  is an  $n_1$ -vector of the turret state variables accessible for measurement,  $\underline{x}_2(t)$  is an  $n_2$ -vector of inaccessible state variables ( $n_1 + n_2 = \underline{n}$ ),  $A_{11}$ ,  $A_{12}$ ,  $A_{21}$ , and  $A_{22}$  are partitioned matrices of appropriate dimensions, and

$$\begin{bmatrix} D_{11} \\ D_{21} \end{bmatrix} \triangleq FD_v, \quad \begin{bmatrix} B_{11} \\ B_{21} \end{bmatrix} \triangleq B.$$

Without loss of generality, the turret output  $\underline{y}(t)$  may be expressed as

$$\underline{y}(t) = H\underline{x}(t) = [I \quad 0] \begin{bmatrix} \underline{x}_1(t) \\ \underline{x}_2(t) \end{bmatrix} = \underline{x}_1(t). \quad (13)$$

Based on the measurements  $\underline{y}(t)$ , we wish to estimate the unknown values of  $\underline{x}_2$  and  $\underline{v}(t)$ . A suitable Luenberger observer is given by [16,19],

$$\begin{bmatrix} \hat{\underline{x}}_2(t) \\ \hat{\underline{v}}(t) \end{bmatrix} = \underline{p}(t) + L\underline{y}(t) \quad (14a)$$

$$\begin{aligned}
\dot{\underline{p}}(t) = & \left\{ \begin{bmatrix} A_{22} & D_{21} \\ 0 & A_v \end{bmatrix} - L[A_{12} \quad D_{11}] \right\} \underline{p}(t) \\
& + \left\{ \begin{bmatrix} B_{21} \\ 0 \end{bmatrix} - LB_{11} \right\} \underline{u}(t) + \left\{ \left( \begin{bmatrix} A_{21} \\ 0 \end{bmatrix} - LA_{11} \right) \right. \\
& \left. + \left( \begin{bmatrix} A_{22} & D_{21} \\ 0 & A_v \end{bmatrix} - L[A_{12} \quad D_{11}] \right) L \right\} \underline{y}(t)
\end{aligned} \tag{14b}$$

with initial condition

$$\underline{p}(0) = \begin{bmatrix} \hat{\underline{x}}_2(0) \\ \hat{\underline{v}}(0) \end{bmatrix} - L\underline{y}(0), \tag{14c}$$

where  $\hat{\underline{x}}_2(t)$  and  $\hat{\underline{v}}(t)$  are the estimates of  $\underline{x}_2(t)$  and  $\underline{v}(t)$ , respectively,  $\hat{\underline{x}}_2(0)$  and  $\hat{\underline{v}}(0)$  may be chosen arbitrary,  $\underline{p}(t)$  is an  $(n_2 + n_v)$ -vector, and  $L$  is an  $(n_2 + n_v) \times n_1$  matrix chosen such that  $\hat{\underline{x}}_2(t) \rightarrow \underline{x}_2(t)$  and  $\hat{\underline{v}}(t) \rightarrow \underline{v}(t)$  "sufficiently fast". In general,  $L$  is chosen such that the  $(n_2 + n_v) \times (n_2 + n_v)$  matrix

$$M \triangleq \begin{bmatrix} A_{22} & D_{21} \\ 0 & A_v \end{bmatrix} - L[A_{12} \quad D_{11}] \tag{15}$$

is asymptotically stable, i.e., the eigenvalues of  $M$  have negative real parts. In order to ensure that there exists a matrix  $L$  such that  $M$  is asymptotically stable, the matrix pair

$$\tilde{A}_{22} \triangleq \begin{bmatrix} A_{22} & D_{21} \\ 0 & A_v \end{bmatrix}, \quad \tilde{A}_{12} \triangleq [A_{12} \quad D_{11}] \tag{16}$$



LOH, HUTCHINGS & KASTEN

must be completely observable, i.e.,

$$\text{rank} \begin{bmatrix} \tilde{A}_{12}^T & \tilde{A}_{22}^T \tilde{A}_{12}^T & \dots & (\tilde{A}_{22}^{m-1})^T \tilde{A}_{12}^T \end{bmatrix} = m \quad (17)$$

where  $m \triangleq (n_2 + n_v)$ , and  $\text{rank} [\cdot]$  denotes the rank of  $[\cdot]$ .

## V. OPTIMAL DESIGN OF HELICOPTER TURRET CONTROL SYSTEM

Now to develop an optimal controller for the elevation channel of the helicopter turret control system under investigation, the state variables are chosen as shown in Figure 2(b), less the dashed feedback lines, i.e.,  $x_8(t)$  is not part of the optimal system. The measured variables are

$$\underline{y}^T(t) = \underline{x}_1^T(t) = [x_1(t), x_2(t), x_3(t), x_4(t), x_5(t), x_6(t)] \quad (18)$$

We have two major design objectives, namely, to make  $x_1(t)$  follow the command input  $z_r(t)$  as closely as possible and to keep the system operating in the linear region (see below). In order to meet these objectives, we use a performance measure as follows

$$J = \int_0^\infty \{q_{11}[x_1(t) - z_r(t)]^2 + q_{55}x_5^2(t) + r_{11}u^2(t)\}dt \quad (19)$$

where  $q_{11}$ ,  $q_{55}$ , and  $r_{11}$  are positive constants. The first term in (19) is assigned to regulate the error  $[x_1(t) - z_r(t)]$  between the desired angular position  $z_r(t)$  and the actual angular position  $x_1(t)$ , the second term to restrict large amplifier output voltage  $x_5(t)$ , and the third term to regulate the control input  $u(t)$ . There is no optimal choice for  $q_{11}$ ,  $q_{55}$ , and  $r_{11}$ , so these relative values must be determined by trial and error. The inclusion of the second term in the performance measure is motivated by the fact that the maximum value of  $x_5(t)$  is limited to  $\pm 40$  volts (saturation nonlinearity).

For the elevation channel under investigation, the state variable  $x_7(t)$  and the disturbance  $w(t) = D_v v(t)$  are not accessible for on-line measurement. Hence

$$\underline{x}_2(t) = [x_7(t)] \quad (20)$$

Using Eq. (11), the optimal control  $u_{\text{opt}}(t)$  in the present case is given by

$$u_{\text{opt}}(t) = -r_{11}^1 b^T K_{xx} \begin{bmatrix} \underline{x}_1(t) \\ \hat{\underline{x}}_2(t) \end{bmatrix} - r_{11}^1 b^T K_{xr} r(t) - r_{11}^1 b^T K_{xv} \hat{v}(t), \quad (21)$$

where  $K_{xx}$ ,  $K_{xr}$ , and  $K_{xv}$  are constant matrices and are the steady state values of  $K_{xx}(t)$ ,  $K_{xr}(t)$ , and  $K_{xv}(t)$  given by (8), (9) and (10) respectively. The dimension of  $K_{xx}$  in the present case is  $7 \times 7$ , whereas those of  $K_{xr}$  and  $K_{xv}$  are  $7 \times n_r$  and  $7 \times n_v$ , respectively, depending on the type of servo-command input  $z_r(t)$  and the waveform structure of the disturbance  $w(t)$ ; for example, for step commands and disturbances,  $n_r = n_v = 1$ , while for step-plus-ramp commands and disturbances and for sinusoidal commands and disturbances,  $n_r = n_v = 2$ .

## VI. NUMERICAL STUDIES

Numerical studies of the response of the elevation channel of the optimal helicopter turret control system with disturbance accommodation are carried out by assigning numerical values to  $q_{11}$ ,  $q_{55}$  and  $r_{11}$  as  $q_{11} = 50,000$ ,  $q_{55} = 0.001$ , and  $r_{11} = 1.0$ . The servo-command input is assumed to be a step command given by

$$z_r(t) = r(t) = r_0 \text{ radians}$$

which corresponds to  $A_r = 0$  and  $D_r = 1$  in (4).

Two cases of disturbances are considered and are described below.

### Case 1

In this case, the actual disturbance  $w(t)$  is generated by

$$w(t) = \begin{cases} 1800 \cos(16\pi t) & , \quad \text{for all } 0 \leq t \leq 0.25 & , \quad (22a) \\ 1800 \cos(16\pi t) + 5000 e^{-40(t-t_i)} \sin[32\pi(t-t_i)] & , \end{cases}$$

$$\text{for } t_i \leq t < t_{i+1}$$

$$\text{and } t_i = i \times 0.125 + 0.25$$

$$i = 0, 1, \dots, 9 \quad . \quad (22b)$$

Equation (22a) simulates the hull disturbance torque of amplitude 1800 foot-pounds and frequency 8 Hz, while (22b) simulates the combined disturbance torque produced by the hull vibrations and the recoil force during the firing period  $(t_{i+1} - t_i)$ . The second term in (22b) simulates the disturbance torque caused by the recoil force of firing and is plotted as shown in Figure 3(a) for  $t_i < t < t_{i+1}$ . It was found that the disturbance waveform shown in Figure 3(a) corresponds to many recoil forces produced by various firing configurations. A 10-shot burst for a 480-round per minute experiment is simulated. The combined disturbance torque  $w(t)$  is as shown in Figure 3(b). Note that the first round of burst starts at  $t = 0.25$  second.

In implementing the Luenberger observer given by (14) to produce the required estimates  $\hat{x}_7(t)$  and  $\hat{v}(t)$ , the  $A_v$  and  $D_v$  matrices in (5) are taken as

$$A_v = \begin{bmatrix} 0 & 1 \\ -(2\pi \times 8)^2 & 0 \end{bmatrix}, \quad D_v = \begin{bmatrix} 1 & 0 \end{bmatrix}, \quad (23)$$

so that  $w(t)$  given by (22) before firing and during firing is approximated as a sinusoid with unknown amplitudes but with known frequency  $f = 8$  Hz, i.e.,  $w(t) = W \sin(16\pi t)$  where  $W$  is unknown.

Let the eigenvalues of the Luenberger observer given by (14), i.e., the eigenvalues of  $M$  given by (15), be chosen as  $\lambda_1 = -50$ ,  $\lambda_2 = -50 + j50$ , and  $\lambda_3 = -50 - j50$ . A suitable  $M$  (non-unique) is given by

$$M = \begin{bmatrix} -50.0 & 0.0 & 0.0 \\ 0.0 & -100.0 & 1.0 \\ 0.0 & -5000.0 & 0.0 \end{bmatrix}.$$

The corresponding  $L$  matrix is determined as (non-unique)

$$L = \begin{bmatrix} 0.0 & 0.0 & -1.92 \times 10^{-5} & 0.0 & 0.0 & 0.0 \\ 0.0 & 1.60 \times 10^3 & 1.92 \times 10 & 0.0 & 0.0 & 0.0 \\ 0.0 & 4.00 \times 10^4 & 4.80 \times 10^2 & 0.0 & 0.0 & 0.0 \end{bmatrix}.$$

With such a choice of  $L$ , the estimated disturbance torque  $\hat{w}(t) = \hat{v}_1(t)$  is as given in Figure 3(b). The estimation errors are small so that the approximation given by (23) is acceptable.

The performance of the optimal turret with disturbance

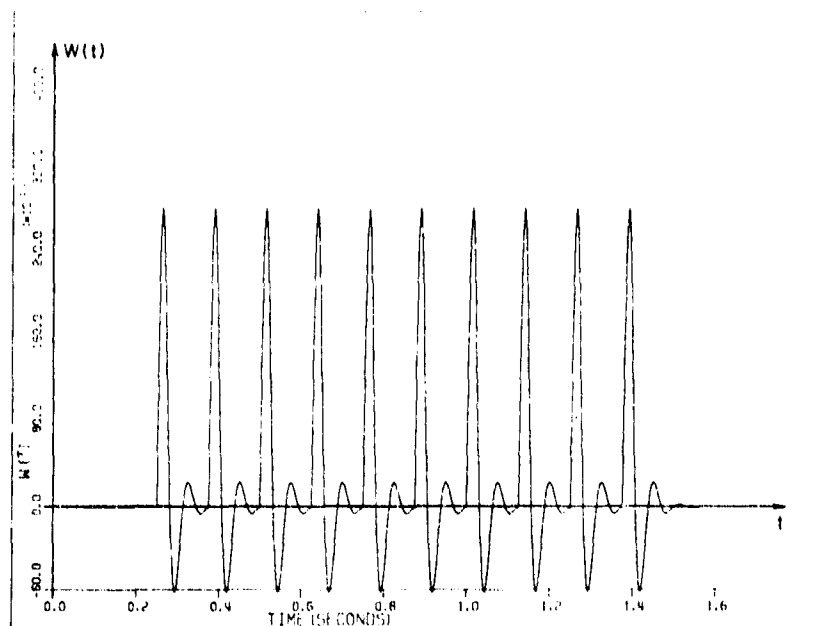


Figure 3(a) Disturbance Torque Produced by Recoil Force of Firing

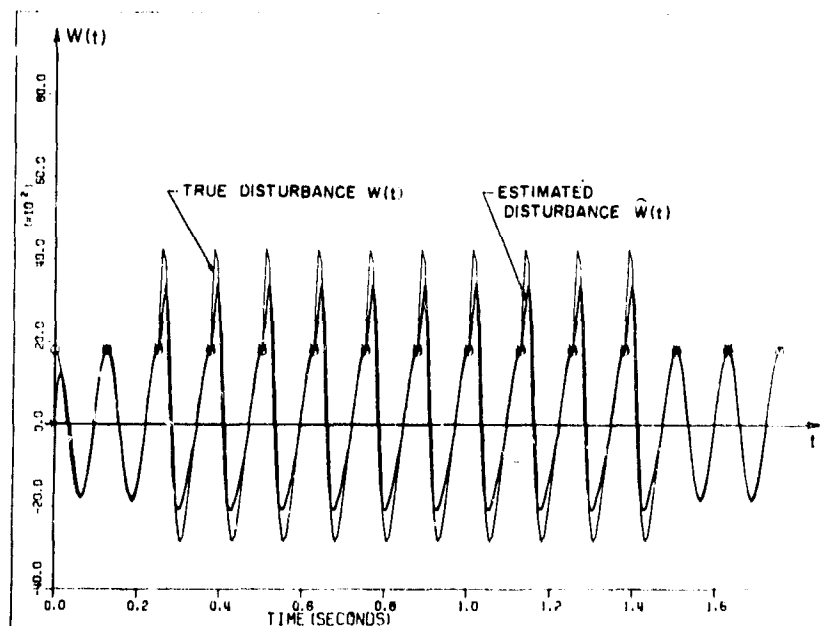


Figure 3(b) Combined Disturbance Produced by Hull Motion and Recoil Force

## LOH, HUTCHINGS & KASTEN

accommodation and the existing turret is compared. The step response for  $x_1(t)$  with  $z_1(t) = 0.0$  radian is as given in Figure 4. The error of firing for each round is approximately 1.2 milliradians for the optimal turret and 8.5 milliradians for the existing turret. Hence the tracking accuracy of the optimal turret control system with disturbance accommodation is more than 7 times better than that of the existing turret designed under the classical design techniques.

### Case 2

In this case, the experimental data of the disturbance  $w(t)$  is provided by Mr. T. Hutchings of [18]. This data represents the combined disturbance produced by the hull vibrations and the recoil force caused by a 20-round burst for a 669-round per minute experiment.

In implementing the Luenberger observer given by (14), the  $A_V$  and  $D_V$  matrices are taken as  $A_V = 0$  and  $D_V = 1$ . This means that  $w(t) = v(t)$  is assumed to be a random step function of unknown amplitudes. This assumption turns out to be quite satisfactory.

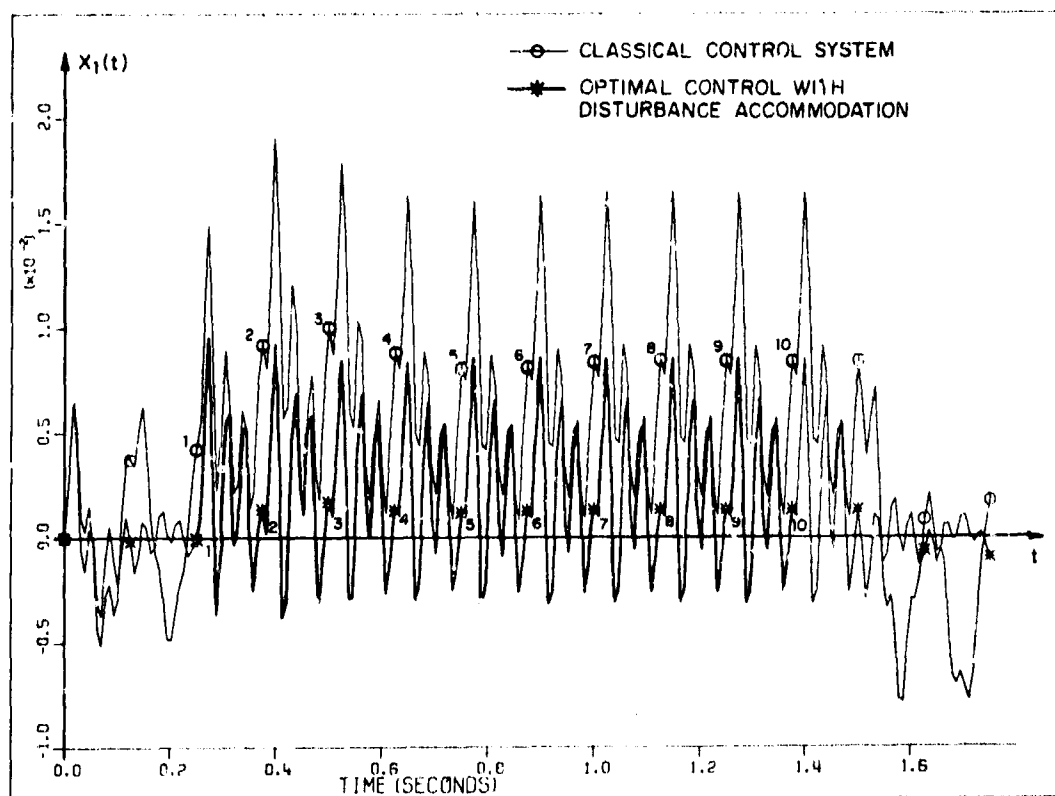


Figure 4 Response of  $x_1(t)$  During Firing

LOH, HUTCHINGS & KASTEN

The eigenvalues for the Luenberger observer given by (14) are chosen as  $\lambda_1^o = -50$  and  $\lambda_2^o = -100$ . A suitable  $M$  (non-unique) is given by

$$M = \begin{bmatrix} \lambda_1^o & 0 \\ 0 & \lambda_2^o \end{bmatrix} = \begin{bmatrix} -50 & 0 \\ 0 & -100 \end{bmatrix}.$$

The corresponding  $L$  matrix is determined as (non-unique)

$$L = \begin{bmatrix} 0.0 & 0.0 & -1.92 \times 10^{-5} & 0.0 & 0.0 & 0.0 \\ 0.0 & 1.60 \times 10^3 & 1.92 \times 10 & 0.0 & 0.0 & 0.0 \end{bmatrix}.$$

The performance of the optimal and existing turrets is compared with a servo-command input of  $z_r(t) = 0.2$  radian. The response of the optimal turret with disturbance accommodation is found to be much faster with little overshoot than that of the existing turret.

#### REFERENCES

- [1] C.D. Johnson, "Accommodation of external disturbances in linear regulator and servomechanism problems," IEEE Trans. Automat. Contr., vol. AC-16, pp. 635-644, December 1971.
- [2] C.D. Johnson, "Accommodation of disturbances in optimal control problems," Int. J. Contr., vol. 15, no. 2, pp. 209-231, 1972.
- [3] C.D. Johnson, "Algebraic solution of the servomechanism problem with external disturbances," ASME Trans. J. Dynamic Systems, Measurements, and Control, pp. 25-35, March 1974.
- [4] C.D. Johnson, "Control of dynamical systems in the face of uncertain disturbances," in Stochastic Problems in Mechanics. Ontario, Canada: University of Waterloo Press, 1974.
- [5] C.D. Johnson, "Theory of disturbance-accommodation controllers," in Control and Dynamic Systems, C.T. Leondes, Ed., New York: Academic Press, 1976.
- [6] N.K. Loh, "Disturbance accommodation techniques with applications to control systems," Research report submitted to Rodman Laboratory, Rock Island Arsenal, Illinois and U.S. Army Armament Research and Development Command, New Jersey, December 1976.
- [7] N.K. Loh and A. Hauser, "Optimal control of systems with inaccessible state variables and with disturbance rejection," in Proceedings of the First International Conference on Information Sciences and Systems, Greece, pp. 32-36, 1976.

LOH, HUTCHINGS & KASTEN

- [8] N.K. Loh and A. Hauser, "Accommodating disturbances of known waveform in discrete-time optimal control systems," in Proceedings of the Eighth Annual Pittsburgh Conference on Modeling and Simulation, vol. 8, pp. 331-335, 1977.
- [9] R.E. Kasten and N.K. Loh, "Precision pointing and stabilization of low dispersion automatic cannon system," Rodman Laboratory Research Report, Rock Island Arsenal, Illinois, April 1977.
- [10] P. Harriott, Process Control. New York: McGraw-Hill, 1964.
- [11] J.J. D'Azzo and C.Y. Houpis, Feedback Control System Analysis and Synthesis. New York: McGraw-Hill, 1966.
- [12] B. Gold and C.M. Rader, Digital Processing of Signals. New York: McGraw-Hill, 1969.
- [13] D.G. Luenberger, "Observing the state of a linear system," IEEE Trans. Mil. Electron., vol. MIL-8, pp. 74-80, April 1964.
- [14] D.G. Luenberger, "Observers for multivariable systems," IEEE Trans. Automat. Contr., vol. AC-11, pp. 190-197, April 1966.
- [15] D.G. Luenberger, "An introduction to observers," IEEE Trans. Automat. Contr., ol. AC-16, pp. 596-602, December 1971.
- [16] B. Gopinath, "On the control of linear multiple input-output systems," Bell Syst. Tech. J., vol. 50, pp. 1063-1081, March 1971.
- [17] N.K. Loh, A. Hauser, R.E. Kasten, J. Mirdock and R.B. Walljasper, "Helicopter turret control with inaccessible state variables," in Proceedings of Seventh Pittsburgh Conference on Modeling and Simulation, vol. 7, pp. 344-349, 1976.
- [18] T.D. Hutchings and A.R. Zak, "The investigation of dynamic gun pointing errors for helicopter mounted automatic cannon systems," Report No. R-TR-TR-76-042, Rodman Laboratory, Rock Island Arsenal, Illinois, November 1976.
- [19] G.W. Carlock and A.P. Sage, "VTOL flight-control system design using sensitivity analysis," IEEE Trans. Aerospace and Electronic Systems, vol. AES-11, pp. 155-161, March 1975.

\*NASH AND STOCKTON

Application of the Method of Characteristics  
to Gun Tube Problems

WILLIAM A. NASH, and F.D. STOCKTON

Department of Civil Engineering  
University of Massachusetts  
Amherst, Massachusetts 01003

ABSTRACT:

The problem of elastic behavior of a thick-walled tube whose internal surface is loaded by a band of transient normal pressure is investigated by the method of characteristics. It is demonstrated that the method is well-suited to this type of transient problem. The technique leads to finite-difference evaluation of displacements and stresses along the bicharacteristic curves of the system. This evaluation is readily carried out with minimal digital computer effort.

BIOGRAPHY:

PRESENT ASSIGNMENT: Professor of Civil Engineering, University of Massachusetts, Amherst, Massachusetts 01003.

PAST EXPERIENCE: David W. Taylor Model Basin, Navy Department, Washington, D.C., 1950-1954. Professor of Engineering Mechanics, University of Florida, Gainesville, Florida, 1954-1967. Professor of Civil Engineering, University of Massachusetts, 1967-date.

DEGREES HELD: B.S. in C.E., Illinois Institute of Technology, 1944, M.S. in Mechanics, Illinois Institute of Technology, 1946, Ph.D. University of Michigan, 1949.



## APPLICATION OF THE METHOD OF CHARACTERISTICS TO GUN TUBE PROBLEMS

\*WILLIAM A. NASH, DR.  
FREDERICK D. STOCKTON, DR.  
DEPARTMENT OF CIVIL ENGINEERING  
UNIVERSITY OF MASSACHUSETTS  
AMHERST, MASSACHUSETTS 01003

The problem of elastodynamics of thick-walled tubes has received only limited attention by investigators in the area of solid mechanics, primarily because of the severe mathematical difficulties associated with three-dimensional elasticity. Exactly a century ago, L. Pochhammer gave the solution for flexural and extensional vibrations and waves in an infinitely long solid circular cylinder. Several surveys indicate advancements made during the period between Pochhammer's work and 1960 [1], [2].

In 1965 C.K. Liu and C.H. Chang [3] presented the solution of the problem of an infinitely long hollow elastic tube subject to internal axisymmetric blast together with a sudden change of temperature. C.K. Liu and T.N. Lee later considered the dynamic response of an infinitely long elastic cylinder subject to asymmetric pressure on its lateral surface [4]. The solution for radial and circumferential displacements was presented in terms of Bessel functions of the first kind with the order depending on the manner in which pressure is distributed around the circumference.

In 1971 J. Zemanek [5] applied digital computer techniques to the solution of the Pochhammer equation and carried out experiments on aluminum cylinders. Zemanek also presented an analysis of displacements in a cylinder of semi-infinite length. In 1972 R. Kumar and R.W.B. Stephens [6] presented a parametric study which indicated the effect of wall thickness on flexural wave effects in thick tubes. Also in 1972 A.S.D. Wang and A. Ertepinar [7] investigated vibrations of very thick-walled tubes subject to normal pressure. Their results even apply to neo-Hookean materials. A recent investigation by J.L. Rose, S.C. Chou, and P.C. Chou [8] of wave propagation effects in hollow spheres and cylinders yielded information pertinent to the

## \*NASH AND STOCKTON

number of wave reflections off the inner and outer surfaces for various wall thicknesses. Fundamental frequencies of thick tubes were presented in a form useful to a designer.

All of the above treatments pertain to elastodynamics of *straight* thick-walled tubes. To the best of the knowledge of the present authors no analytical solution for transient effects in initially *curved* thick-walled tubes has ever been presented. However, a finite element approach to the problem of travelling ballistic pressures in a slightly curved gun tube (the curvature arising from the dead weight of the system) has been presented by T.E. Simkins, G. Pflegl, and R. Scanlon [9] and later refined by T.E. Simkins [10].

Computational methods available for the solution of two- and three-dimensional wave propagation problems in elastic solids include (a) complex variables, (b) artificial viscosity concepts coupled with finite differences, (c) the ray method, and (d) the method of characteristics. The complex variable approach is based upon integral transform techniques and is limited to relatively simple configurations. In (b), the basic differential equations are replaced by their finite difference analogs and the resulting algebraic equations solved step-wise with respect to time. This approach usually leads to excessive amounts of digital computer effort. The ray method was originally developed by B. van der Pol and H. Bremmer [11] to investigate the propagation of radio waves around the earth. It was extended to the case of pulses in a layered, elastic solid by Y.H. Pao and R. Gajewski [12] as well as pulses in a thick-walled sphere by Y.H. Pao and A.N. Ceranoglu [13] in 1978.

The ultimate objective of the present investigation is to present a new approach to the elastodynamics of thick-walled tubes having slight initial curvature and subject to transient internal pressures. The method of characteristics promises to be the most accurate and least demanding of computer time and will be used to accomplish this objective. The method will be outlined in the following section.

### The Method of Characteristics

Wave propagation problems are essentially initial value problems that have an unsteady state or transient nature. Propagation of stresses and displacements in elastic systems, propagation of pressure waves in a fluid, propagation of heat and many other phenomena are examples of such transient systems. Governing differential equations for such systems are either parabolic or hyperbolic.

Let us consider the second-order equation

$$au_{xx} + bu_{xy} + cu_{yy} = f \quad (1)$$

\*NASH AND STOCKTON

where  $a$ ,  $b$ ,  $c$ , and  $f$  are functions of  $x$ ,  $y$ ,  $u$ ,  $u_x$ , and  $u_y$ . Assume that the solution for  $u$  and  $v$  is known from the initial state on some curve  $\Gamma$ . At any point  $P$  on this curve we know the values of  $u$  and  $v$  as well as their directional derivatives. We seek the conditions under which a knowledge of  $u$ ,  $u_x$ , and  $u_y$  on  $\Gamma$  serves to determine  $u_{xx}$ ,  $u_{xy}$ , and  $u_{yy}$  uniquely so that (1) is satisfied. If these derivatives exist we must have

$$\begin{aligned} d(u_x) &= u_{xx}dx + u_{xy}dy \\ d(u_y) &= u_{xy}dx + u_{yy}dy \end{aligned} \quad (2)$$

The solution for  $u_{xx}$ ,  $u_{xy}$ , and  $u_{yy}$  exists and is unique unless the determinant of the coefficient matrix vanishes, i.e.

$$a(dy)^2 - b(dx)(dy) + c(dx)^2 = 0 \quad (3)$$

This is the characteristic equation, which is a quadratic in  $dy/dx$ . Equation (1) is hyperbolic if  $b^2 - 4ac > 0$ , parabolic if  $b^2 - 4ac = 0$ , and elliptic if  $b^2 - 4ac < 0$ . The directions specified by (3) are called characteristic directions. In the case of a hyperbolic equation these are two real characteristic curves. The higher order derivatives are indeterminate along these curves and thus these curves provide paths for propagation of discontinuities. This feature is of particular value in shock wave investigations.

The characteristics are essentially the natural coordinates of the system. The attractive feature of the use of characteristics is that, by an appropriate choice of coordinates, the original system of hyperbolic equations can be replaced by a system whose coordinates are the characteristics. When (3) holds there is no solution at all unless the other determinants of the system also vanish, so as one possibility we may have

$$\begin{bmatrix} a & f & c \\ dx & d(u_x) & 0 \\ 0 & d(u_y) & dy \end{bmatrix} = 0 \quad (4)$$

or

$$ad(u_x)dy - fdxdy + cdx d(u_y) = 0 \quad (5)$$

Let us divide (5) by  $dx$  and identify the characteristics as  $dy = \alpha dx$ ,  $dy = \beta dx$ . Then (5) becomes, respectively

$$\begin{aligned} a\alpha d(u_x) + c d(u_y) - f(dy) &= 0 \\ a\beta d(u_x) + c d(u_y) - f(dy) &= 0 \end{aligned} \quad (6)$$

Equations (6) specify conditions which the solutions must satisfy along the characteristics. The desired solution is obtained by solution of

\*NASH AND STOCKTON

(3) and (6) in a step-by-step numerical integration along the characteristics. This process simultaneously constructs the characteristic grid and the solution of the equation (1) at the grid points.

There has been extensive engineering usage of the method of characteristics in many fields concerned with problems involving two independent variables. One of the earliest of these is due to L. Prandtl and A. Busemann (1929) in application to compressible flow problems. The 1947 text of H.W. Liepmann and A.E. Puckett [14] gives many applications of the technique to problems involving flows along curved walls, nozzle design, and others.

Application of characteristics to solid mechanics problems followed somewhat later. Perhaps the first use is due to R.W. Leonard and B. Budiansky [15] who investigated a Timoshenko beam in 1954. In 1958 W.E. Jahsman [16] derived characteristic equations for circular sheets and plates under very general loading conditions at an inner hole. He obtained the relations between stresses and displacements at the wave fronts due to abrupt step-function type inputs. H.G. Hopkins [17] formulated the characteristic equations for spherical elastic and plastic waves, including shock waves in the plastic region, but did not carry out the solution for any specific problem. More recently, P.C. Chou and H.A. Koenig [18] applied characteristics to investigate the propagation of cylindrical and spherical dilatational waves in elastic media. Examples pertinent to sheets and spheres subject to step-function loadings indicated excellent agreement with existing solutions. S.C. Chou and R. Greif [19] applied characteristics to investigate transient elastic stresses in cylindrical and spherical bodies subject to radially symmetric transient normal pressure at a boundary for the case of multilayered media having different elastic characteristics in each layer. Later, these same authors [20] considered the transient response of an anisotropic thick-walled cylinder to axially symmetric time-dependent pressure at an internal or external surface.

The application of characteristics to two-dimensional elastodynamics problems has also been discussed by P.C. Chou and P.F. Gordon [21] and M. Ziv. Ziv was particularly concerned with (a) a circular cylindrical cavity in an infinite elastic solid subjected to a uniform radial load applied to the cavity wall [22], and (b) a line load suddenly applied to a half-space [23].

One of the most attractive methods for numerical solution of hyperbolic systems of partial differential equations in three independent variables is due to D.S. Butler [24]. Bicharacteristic relations for three-variable problems are weaker than the corresponding characteristic relations for two-variable problems because they imply derivatives in two directions instead of only one. Butler, however, derived an approach based upon a linear combination of relations among bicharacteristics through a point to yield two independent relations

involving only derivatives in the bicharacteristic directions at that point. These directions, together with that corresponding to still another curve through the point (with form fixed by the bicharacteristic conditions) permit step-by-step numerical solution of the hyperbolic system involving three independent variables. Butler offered an example involving steady supersonic flow over a delta-shaped body.

An application of the Butler technique is due to P.F. Sabodash and R.A. Cherednichenko [25]. These investigators examined a general class of axially symmetric dynamic problems of elasticity by transforming the equations of axially symmetric motions of a three-dimensional elastic solid to a larger system of first order equations by introducing additional dependent variables. A characteristic surface of the system was obtained, and the bicharacteristics determined. A difference method (together with a digital computer) was employed to integrate along each of the bicharacteristics for the particular problem of a semi-infinite solid cylindrical rod, the end points of which are given an initial axial velocity.

In 1973 Y. Beyd [26] applied the Butler technique of integrating along bicharacteristic lines to investigate the problem of two-dimensional elasto-plastic wave propagation in a nonhardening media. In that same year G.I. Bykovtsev, N.D. Vervevko, and N.M. Zinovyev [27] considered the problem of a stepped load applied at supersonic speed to an elasto-viscoplastic half space and treated the hyperbolic system of equations having five characteristics to obtain all information pertinent to shear and pressure waves. Numerical integration along bicharacteristics was carried out on a computer.

#### Formulation of Problem

The problem under consideration represents a first approach to the gun tube problem. We are considering a thick-walled elastic tube having an initially straight geometric axis, with the tube being of semi-infinite length. Let us introduce a coordinate system at the end of the tube such that a radial coordinate is designated by  $r$ , the coordinate along the tube axis by  $z$ , the inner radius of the tube by  $R_i$  and the outer by  $R_o$ . The loading consists of a Heaviside unit step function which describes the axisymmetrically applied radial loading applied at  $t = 0$  at  $R_i$ , with the loading extending over the finite axial band designated by  $z = z_1$  and  $z = z_2$ . The stress distribution and particle velocities are sought for the entire hollow tube. The dynamically applied load gives rise to waves originating from the inner boundary and later being reflected from both the outer circular boundary  $R_o$  as well as the flat end  $z = 0$ . The tube is taken to be of semi-infinite length at this stage of the investigation to avoid the mathematical complication of waves being reflected from the remote end of a finite length tube. However, this problem will of course be attacked after solution of the semi-infinite length tube has been completed.

\*NASH AND STOCKTON

The time-dependent normal stress components are designated by  $\sigma_{rr}$ ,  $\sigma_{\theta\theta}$  and  $\sigma_{zz}$  in the radial, circumferential, and axial directions, respectively. The shear stress component is denoted by  $\sigma_{rz}$ . Further,  $U_r$  and  $U_z$  denote particle velocities in the radial and axial directions respectively. Lastly,  $\lambda$  and  $\mu$  denote Lamé's constants for the material, and  $\rho$  is the mass density of the material. The equations describing elastic motion of the thick-walled tube are

$$\frac{\partial \sigma_{rr}}{\partial r} + \frac{\partial \sigma_{rz}}{\partial z} + \frac{1}{r}(\sigma_{rr} - \sigma_{\theta\theta}) = \rho \frac{\partial U_r}{\partial t} \quad (7)$$

$$\frac{\partial \sigma_{rz}}{\partial r} + \frac{\partial \sigma_{zz}}{\partial z} + \frac{\sigma_{rz}}{r} = \rho \frac{\partial U_z}{\partial t} \quad (8)$$

The constitutive equations for a linear elastic, homogeneous, isotropic material are

$$\frac{\partial \sigma_{rr}}{\partial t} = (\lambda + 2\mu) \frac{\partial U_r}{\partial r} + \lambda \left( \frac{U_r}{r} + \frac{\partial U_z}{\partial z} \right) \quad (9)$$

$$\frac{\partial \sigma_{zz}}{\partial t} = (\lambda + 2\mu) \frac{\partial U_z}{\partial z} + \lambda \left( \frac{U_r}{r} + \frac{\partial U_r}{\partial r} \right) \quad (10)$$

$$\frac{\partial \sigma_{\theta\theta}}{\partial t} = (\lambda + 2\mu) \frac{U_r}{r} + \lambda \left( \frac{\partial U_r}{\partial r} + \frac{\partial U_z}{\partial z} \right) \quad (11)$$

$$\frac{\partial \sigma_{rz}}{\partial t} = \mu \left( \frac{\partial U_z}{\partial r} + \frac{\partial U_r}{\partial z} \right) \quad (12)$$

The dependent variables (particle velocities, stresses, etc) corresponding to a material particle at the point  $(r, z, t)$  are evaluated by consideration of the bicharacteristic curves which are the integration paths corresponding to a plane  $r = \text{constant}$  as well as an orthogonal plane corresponding to  $z = \text{constant}$ . These plane intersect along the time axis. Various straight lines in these planes characterize the formulation of the characteristics. For example, in the  $z = \text{constant}$  plane along  $dr = d\tau$  the characteristics formulation is:

$$d\sigma_{rr} - dU_r = \left\{ \alpha \left( \frac{\partial U_z}{\partial z} + \frac{U_r}{r} \right) - \frac{\partial \sigma_{rz}}{\partial z} + \frac{\sigma_{\theta\theta} - \sigma_{rr}}{r} \right\} d\tau \quad (13)$$

Comparable descriptions exist along  $dr = -d\tau$ ,  $dr = \beta d\tau$ , etc where  $\alpha$  and  $\beta$  are functions of the lame constants. Similarly in the plane  $r = \text{constant}$  along  $dz = d\tau$  we have

$$d\sigma_{zz} - dU_z = \left\{ \alpha \left( \frac{\partial U_r}{\partial r} + \frac{U_r}{r} \right) - \frac{\partial \sigma_{rz}}{\partial r} - \frac{\sigma_{rz}}{r} \right\} d\tau \quad (14)$$

## \*NASH AND STOCKTON

Likewise, along  $dr = dz = 0$  we have, for example:

$$d\sigma_{rz} = \beta^2 \left( \frac{\partial U_z}{\partial r} + \frac{\partial U_r}{\partial z} \right) d\tau \quad (15)$$

There are fourteen such relations but no more will be given here for the sake of brevity.

The relations (13), (14), (15) and their other eleven counterparts must be modified slightly to account for the effect of waves across which discontinuities occur in the dependent variables. For example, (13) becomes

$$\begin{aligned} d[\sigma_{rr}] - d[U_r] = & \{ \alpha([U_{z;z}] + \frac{[U_r]}{r} - [\sigma_{rz;z}] \\ & + \frac{[\sigma_{\theta\theta}] - [\sigma_{rr}]}{r} ) d\tau \end{aligned} \quad (16)$$

which characterizes impulsive reflected spherical waves. Likewise other equations characterize cylindrical waves which approach the free surface. Equation (16) as well as its counterparts may be readily expressed in finite difference form. Stresses and particle velocities are obtainable by direct step-by-step integration along appropriate bicharacteristic curves. Numerical work on this aspect of the problem is now in progress.

## References

1. Abramson, H.N., Plass, H.J., and Ripperger, E.A., "Stress Wave Propagation in Rods and Beams," Advances in Applied Mechanics, Vol. 5, Academic Press, 1958, pp. 111-194.
2. Miklowitz, J., "Recent Developments in Elastic Wave Propagation," Applied Mechanics Reviews, Vol. 13, 1960, pp. 864-878.
3. Liu, C.K., and Change, C.H., "Thermal and Dynamic Response of an Infinite Hollow Cylinder," Developments in Theoretical and Applied Mechanics, Vol. 2, Pergamon Press, 1965, pp. 487-501.
4. Liu, C.K., and Lee, T.N., "Dynamic Response of an Infinite Cylinder to Asymmetric Pressure on its Lateral Surface," Developments in Theoretical and Applied Mechanics, Vol. 3, 1967, Pergamon Press, pp. 447-464.
5. Zemanek, J., "An Experimental and Theoretical Investigation of Elastic Wave Propagation in a Cylinder," Journal of the Acoustical Society of America, Vol. 51, No. 1, Part 2, 1972, pp. 265-283.
6. Kumar, R., and Stephens, R.W.B., "Dispersion of Flexural Waves in Circular Cylindrical Shells," Proceedings of the Royal Society of

\*NASH AND STOCKTON

London, Series A, Vol. 329, 1972, pp. 283-297.

7. Wang, A.S.D., and Ertepinar, A., "Stability and Vibrations of Elastic Thick-Walled Cylindrical and Spherical Shells Subject to Pressure," International Journal of Non-Linear Mechanics, Vol. 7, No. 5, 1972, pp. 539-556.
8. Rose, J.L., Chou, S.C., and Chou, P.C., "Vibration Analysis of Thick-Walled Spheres and Cylinders," Journal of the Acoustical Society of America, Vol. 53, No. 3, 1973, pp. 771-776.
9. Simkins, T., Pflegl, G., and Scanlon, R., "Dynamic Response of the M113 Gun Tube to Travelling Ballistic Pressure and Data Smoothing as Applied to XM150 Acceleration Data," Watervliet Arsenal, Report WVT-TR-75015, April 1975.
10. Simkins, T.E., "Structural Response to Moving Projectile Mass by the Finite Element Method," Watervliet Arsenal, Report WVT-TR-75044, July 1975.
11. Van der Pol, B., and Bremmer, H., "The Propagation of Radio Waves Over a Finitely Conducting Spherical Earth," Philosophical Magazine, Vol. 25, p. 817, 1938.
12. Pao, Y.H., and Gajewski, R., "The Generalized Ray Theory and Transient Elastic Waves in Layered Media," Physical Acoustics, Vol. 13, ed. by W. Mason and R. Thurston, Academic Press, 1977, pp. 183-265.
13. Pao, Y.H. and Ceranoglu, A.N., "Determination of Transient Responses of a Thick-Walled Spherical Shell by the Ray Theory," Journal of Applied Mechanics, Transactions of the ASME, Vol. 45, March 1978, pp. 114-122.
14. Liepmann, H.W., and Puckett, A.E., Introduction to Aerodynamics of a Compressible Fluid, John Wiley & Sons, 1947.
15. Leonard, R.W. and Budiansky, B., "On Travelling Waves in Beams," NACA Report 1173, 1954.
16. Jahsman, W.E., "Propagation of Abrupt Circular Wave Fronts in Elastic Sheets and Plates," Proceedings of the Third National Congress of Applied Mechanics, pp. 195-202, 1958.
17. Hopkins, H.G., "Dynamic Expansion of Spherical Cavities in Metals," Progress in Solid Mechanics, Vol. I, North-Holland Publishing Co., Amsterdam, 1960.
18. Chou, P.C., and Koenig, H.A., "A Unified Approach to Cylindrical and Spherical Elastic Waves by Method of Characteristics,"



\*NASH AND STOCKTON

Journal of Applied Mechanics, March 1966, pp. 159-167.

19. Chou, S.C., and Grief, R., "Numerical Solution of Stress Waves in Layered Media," AIAA Journal, pp. 1067-1074, Vol. 6, No. 6, 1968.
20. Grief, R., and Chou, S.C., "The Propagation of Radially Symmetric Stress Waves in Anisotropic Nonhomogeneous Elastic Media," Journal of Applied Mechanics, March 1971, pp. 51-57.
21. Chou, P.C., and Gordon, P.F., "Radial Propagation of Axial Shear Waves in Nonhomogeneous Elastic Media," Journal of the Acoustical Society of America, Vol. 42, No. 1, pp. 36-41, July 1967.
22. Ziv, M., "Two-Spatial Dimensional Elastic Wave Propagation by the Theory of Characteristics," International Journal of Solids and Structures, Vol. 5, No. 10, 1969, pp. 1135-1152.
23. Ziv, M., "The Decay of Leading Elastic Waves by the Theory of Characteristics," International Journal of Engineering Science, Vol. 8, 1960, pp. 483-497.
24. Butler, D.S., "The Numerical Solution of Hyperbolic Systems of Partial Differential Equations in Three Independent Variables," Proceedings of the Royal Society of London, Series A, Vol. 255, No. 1281, pp. 232-252, 1960.
25. Sabodash, P.F., and Cherednichenko, R.A., "Application of the Method of Spatial Characteristics to the Solution of Axially Symmetric Problems Relating to the Propagation of Elastic Waves," Zhurnal Prikladnoi Mekhaniki i Tekhnicheskoi Fiziki, No. 4, 1971, pp. 101-109 (in Russian). Available in English as Journal of Applied Mechanics and Engineering Physics, Plenum Press, 1972, pp. 571-577.
26. Beyd, Y., "Two-Dimensional Elastic-Ductile Plastic Waves," Propagation of Elastic and Elastoplastic Waves-Materials of the Vth All-Union Symposium, (in Russian). Available in English as FTD-MT-24-1152-75, pp. 204-218.
27. Bykovstev, G.I., Vervevko, N.D., and Zinovyev, N.M., "Application of the Method of Characteristics to the Solution of the Problem of the Motion of a Stepped Load," Propagation of Elastic and Elastoplastic Waves-Materials of the Vth All-Union Symposium, (in Russian). Available in English as FTD-MT-24-1152-75, pp. 219-250.

\*NASH AND STOCKTON

Acknowledgement

This investigation is sponsored by the U.S. Army Research Office under Grant DAAG29-77-G-0095. The authors express their thanks for this support.

WU

**TITLE:** Gun Dynamic Analysis by the Use of Unconstrained,  
Adjoint Variational Formulations  
**JULIAN J. WU**  
U.S. Army Armament Research and Development Command  
Benet Weapons Laboratory  
Watervliet Arsenal, Watervliet, NY 12189

**ABSTRACT:**

This paper is concerned with the establishment of a basis of a unified numerical solution-formulation to the complicated problem of gun dynamics. The lateral movement of a gun tube is modeled by an Euler-Bernoulli beam at the present time. However, the effects due to recoil force, curvature-induced load, moving mass of a projectile and gravitational forces have been incorporated into the equation. The difficulties of obtaining solutions to this problem can be seen from the following: 1. it is both a boundary- and an initial-value problem; 2. it is a nonself-adjoint problem due to the time-dependency and the recoil force; 3. there are loads of severe discontinuities due to the travelling pressure and the moving projectile mass; and 4. the support conditions can also be time-dependent. It is shown in this paper that all of these difficulties can be handled easily and in a routine fashion through the use of an unconstrained, adjoint variational formulation. First, an adjoint variational principle is established which is shown to be equivalent to the given differential equation. An adjoint field variable must be introduced to accommodate the nonsymmetry of the problem. Due to the fact that the variational principle requires no constraint conditions on either the original, or the adjoint field variable, the approximate solutions of the original variable are shown to be obtainable without solving for the adjoint problem. In the framework of the finite element discretization, the unified approach to initial conditions and boundary conditions is then demonstrated. It is also shown that the inclusion of various discontinuous load functions, moving mass and moving supports does not present any difficulty in this solution formulation.

**BIOGRAPHY:**

**PRESENT ASSIGNMENT:** Research Mathematician, Benet Weapons Laboratory, Watervliet Arsenal, Watervliet, NY.

**PAST EXPERIENCE:** Research Associate with Rensselaer Polytechnic Institute, Troy, NY (1970-1971), Project Engineer with Teledyne Material Research, Waltham, Mass. (1967-1968) and Senior Scientist with AVCO, Lowell, Mass. (1966-1967).

**DEGREES HELD:** B.S.C.E. National Taiwan University (1958), M.S.C.E. Rice University, (1962), M.S.M.E. Columbia University (1966), and Ph.D. E.M., Rensselaer, (1970).

WU

## GUN DYNAMIC ANALYSIS BY THE USE OF UNCONSTRAINED, ADJOINT VARIATIONAL FORMULATIONS

JULIAN J. WU  
U.S. ARMY ARMAMENT RESEARCH AND DEVELOPMENT COMMAND  
BENET WEAPONS LABORATORY, LCWSL  
WATERVLIET ARSENAL, WATERVLIET, NY 12189

### 1. INTRODUCTION

The purpose of this paper is to introduce an efficient method, which is quite general and easy to use, to the solution of the dynamic problems of gun system.

The basic concept of unconstrained, adjoint variational formulation for linear problems was described in an earlier paper [1]. Its advantage over constrained methods in obtaining approximate solutions has been demonstrated for both conservative (self-adjoint) and unconservative (nonself-adjoint) problems [2]. In comparison with Galerkin procedure, the unconstrained, adjoint variational formulation has further advantage in the freedom of selecting shape functions which have less requirement on differentiability and which are not required to satisfy any of the end conditions. The same concept was extended to solution formulation of initial value problems [3]. In view of the generality of this approach and its easy adaptability to finite element discretizations, it appears to be quite attractive in seeking solutions to the complicated problems associated with the dynamics of gun systems.

In this paper, the motion of a gun barrel (tube) is considered together with a moving projectile, pressure due the charge detonation, recoil force and various support conditions. The differential equation originally derived by Simkins [4] is described in Section 2. For the convenience of solution formulations and later parametric studies, the equation is nondimensionalized and the dimensionless parameters are given in Section 3. The unconstrained, adjoint variational statement together with a very general set of support and initial conditions are given in Section 4. With solutions in the form of finite element approximations, the matrix equation is obtained formally in Section 5. The specific form of the displacement functions is discussed in Sections 6.

WU

## 2. GOVERNING EQUATIONS

Let us begin with the basic form of the equation of an Euler-Bernoulli beam,

$$(EIy'')'' = -q(x,t,y,y',\dots) \quad (2-1)$$

where  $q = y(x,t)$  is the lateral displacement of the beam from its undeformed position (assumed to be a straight line) as a function of the spatial coordinate  $x$  (measured from the breech end of the gun tube) and the time  $t$  (Figure 1). The letter  $E$  and  $I$  denote the modulus of elasticity of the beam material and the second moment of the cross-section respectively. We shall adopt the notation that a prime ( $'$ ) denotes differentiation with respect to  $x$ ; and a dot ( $\dot{\phantom{x}}$ ), differentiation with respect to  $t$ . The function  $q$  on the right hand side of Eq. (2-1) represent the sum of various lateral distributed load, or the equivalents, acting on the beam. Depending the precise form of  $q$ , Eq. (2-1) can be much more general than the Euler-Bernoulli beam problem usually encountered as it will be shown in the sequel.

Let us consider

$$q(x,t,y,y',\dots) = \sum_{i=1}^N q_i(x,t,y,y',\dots) \quad (2-2)$$

In the following, we shall take  $N = 5$  and discuss each  $q_i$ ,  $i=1,2,\dots,N$  to be included in this analysis.

i. Contribution due to tube inertia.

$$q_1 = \rho A \ddot{y}(x,t) \quad (2-3)$$

where  $\rho$  is the density of the tube material and  $A$ , the cross-sectional area.

ii. Contribution due to curvature-and-pressure induced load.

$$q_2 = \bar{P}(x,t) y''(x,t) H(\bar{x}-x) \quad (2-4)$$

with

$$\bar{P}(x,t) = \pi R^2(x) p(t) \quad (2-5)$$

where  $R(x)$  is the tube inner radius,  $p(t)$ , the travelling pressure,  $H(x)$ , the Heaviside step function and  $\bar{x} = \bar{x}(t)$  is the location of the moving projectile. This expression for  $q_2$  was first derived by Simkins [4].

WU

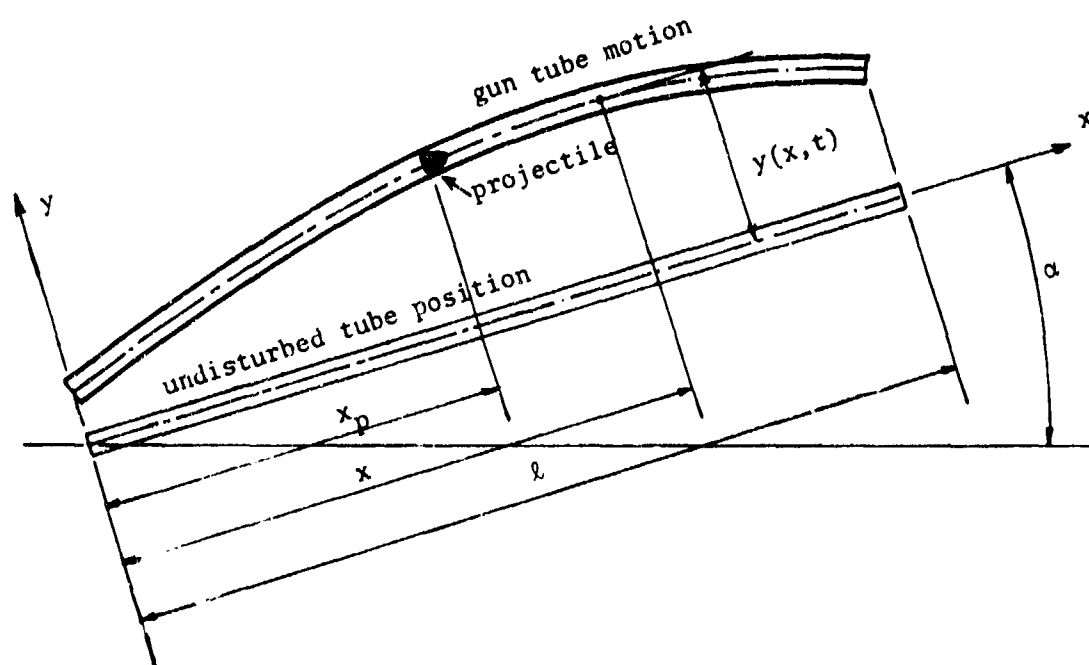


FIGURE 1. A Schematic Drawing of the Problem Configuration.

WU

iii. Contribution due to the moving mass of a projectile.

$$q_3 = \frac{m_p}{l} [\dot{x}^2 y'' + 2\dot{x}\ddot{y}' + \ddot{x}y' + \ddot{y}] \bar{\delta}(\bar{x}-x) \quad (2-6)$$

where  $m_p$  is the projectile mass and  $l$ , the tube length;  $\bar{\delta}(x)$  is the Dirac-delta function.

iv. Contribution due to gravitational on the tube and on the projectile.

$$q_4 = g\rho A \cos\alpha + (g \frac{m_p}{l} \cos\alpha) \bar{\delta}(\bar{x}-x) \quad (2-7)$$

where  $g$  is the gravitational acceleration and  $\alpha$  the elevation angle (Figure 1).

v. Contribution due to axial force  $P(x,t)$ .

$$q_5 = [P(x,t)y']' = P'(x,t)y'(x,t) + P(x,t)y''(x,t) \quad (2-8)$$

with

$$P(x,t) = [-\bar{P}(0,t) + g \sin\alpha \int_0^l \rho A dx] \frac{\int_x^l \rho A dx}{\int_0^l \rho A dx} \quad (2-9)$$

where  $\bar{P}(0,t) = \pi R^2(0)p(t)$  from Eq. (2-5) and is the recoil force at the breech end. The second term in the brackets of Eq. (2-9) is the axial gravitational load of the tube due to the elevation angle  $\alpha$ .

With loading included above, Eq. (2-1) can be written in more specific form:

$$\begin{aligned} (EIy'')'' + [P(x,t)y']' + \rho A \ddot{y} \\ = - \bar{P}(x,t)y''(x,t)H(\bar{x}-x) \\ - \frac{m_p}{l} [\dot{x}^2 y'' + 2\dot{x}\ddot{y}' + \ddot{x}y' + \ddot{y}] \bar{\delta}(\bar{x}-x) \\ - (g \frac{m_p}{l} \cos\alpha) \bar{\delta}(\bar{x}-x) - g\rho A \cos\alpha \end{aligned} \quad (2-10)$$

### 3. NONDIMENSIONAL EQUATIONS AND PARAMETERS

It will be convenient to use nondimensional equations and variables both for the manipulation of the equation and for parametric studies. To this end, one introduces these dimensionless variables

$$y^* = y/l, \quad x^* = x/l, \quad t^* = t/c \quad (3-1)$$

WU

where  $c$  is a constant to be defined in Eq. (3-3) and it has the same physical dimension as the real time  $t$ . Substitute Eqs. (3-1) into (2-10) and multiply both sides of the equation (2-10) by  $\ell^3/E_0 I_0$ , where  $E_0 I_0$  are the  $E$ ,  $I$  at some reference cross-section. One obtains

$$\begin{aligned} & \left[ \frac{EI}{E_0 I_0} y^{*'''} \right]^* + \left[ \frac{P(x,t)\ell^2}{E_0 I_0} y^{*'} \right]' + \frac{\rho A}{\rho_0 A_0} \ddot{y}^* \\ & = - \frac{\bar{P}(x,t)\ell^2}{E_0 I_0} y^{*''} H(\bar{x}^* - x^*) \\ & - \frac{m_p}{\rho_0 A_0 \ell} [\dot{x}^{*2} y^{*''} + 2\dot{x}^* \dot{y}^{*'} + \ddot{x}^* y^{*'} + \ddot{y}^*] \delta(\bar{x}^* - x^*) \\ & - \left( \frac{gc^2}{\ell} \frac{m_p}{\rho_0 A_0 \ell} \cos \alpha \right) \delta(\bar{x}^* - x^*) - \frac{gc^2}{\ell} \frac{\rho A}{\rho_0 A_0} \cos \alpha \end{aligned} \quad (3-2)$$

It should be noted that the prime ( $'$ ) and the dot ( $\dot{\phantom{x}}$ ) now refer to differentiations with respect to  $x^*$  and  $t^*$ , respectively. The constant  $c$  has been defined by

$$c^2 = \frac{\rho_0 A_0 \ell^4}{E_0 I_0} \quad (3-3)$$

Also define the following dimensionless functions and parameters

$$\begin{aligned} a(x) &= \frac{E(x)I(x)}{E_0 I_0} = a^*(x^*) \\ b(x) &= \frac{\rho(x)A(x)}{\rho_0 A_0} = b^*(x^*) \\ m_p^* &= \frac{m_p}{\rho_0 A_0 \ell}, \quad g^* = \frac{gc^2}{\ell} \\ \bar{P}^*(x^*, t^*) &= \frac{\bar{P}(x,t)\ell^2}{E_0 I_0} = \pi R^{*2}(x^*) p^*(t^*) \\ R^*(x^*) &= \frac{R(x)}{\ell}, \quad p^*(t^*) = \frac{p(t)\ell^4}{E_0 I_0} \\ P^*(x^*, t^*) &= \frac{P(x,t)\ell^2}{E_0 I_0} \\ &= [-\bar{P}^*(0, t^*) + g^* \sin \alpha \int_0^1 b^*(x^*) dx^*] \frac{\int_{x^*}^1 b^*(x^*) dx^*}{\int_0^1 b^*(x^*) dx^*} \end{aligned} \quad (3-4)$$



WU

In terms of Eqs. (3-4), one can write Eq. (3-2) as

$$\begin{aligned}
 & [a^*(x^*)y^{*''}]'' + [P^*(x^*, t^*)y^{*'}]' + b^*(x^*)\ddot{y}^* \\
 & = - \bar{P}^*(x^*, t^*)y^{*''} H(\bar{x}^* - x^*) \\
 & = m_p [\dot{\bar{x}}^{*2} y^{*''} + 2\bar{x}^* \dot{y}^{*'} + \ddot{\bar{x}}^* y^{*'} + \ddot{y}^*] \delta(\bar{x}^* - x^*) \\
 & - (g^* m_p \cos \alpha) \delta(\bar{x}^* - x^*) - g^* b^*(x^*) \cos \alpha
 \end{aligned} \tag{3-5}$$

Since all the quantities in the equation are associated with an asterisk (\*), except  $\alpha$ , which is already dimensionless and thus need not to change, we shall drop all the asterisks all together for the sake of simplicity and with the understanding that they are actually those quantities with asterisks defined in Eqs. (3-1) and (3-4). Thus, Eq. (3-5) becomes

$$\begin{aligned}
 & [a(x)y'']'' + [P(x, t)y']' + b(x)\ddot{y} \\
 & = - \bar{P}(x, t)y'' H(\bar{x} - x) \\
 & = m_p [\dot{\bar{x}}^2 y'' + 2\bar{x} \dot{y}' + \ddot{\bar{x}} y' + \ddot{y}] \delta(\bar{x} - x) \\
 & - (g m_p \cos \alpha) \delta(\bar{x} - x) - g b(x) \cos \alpha
 \end{aligned} \tag{3-6a}$$

with

$$P(x, t) = [-\bar{P}(0, t) + g \sin \alpha \int_0^1 b(x) dx] \frac{\int_0^1 b(x) dx}{\int_0^1 b(x) dx} \tag{3-6b}$$

$$\bar{P}(x, t) = \pi R^2(x) p(t) \tag{3-6c}$$

It should be reemphasized that in Eqs. (3-6), all the quantities are those with asterisks defined in Eqs. (3-1) and (3-4).

Eqs. (3-6) will be used in the further study of the general case. For our present solution formulations and computations. We shall further assume that (1) the tube is uniform in cross-sectional properties, (2) the travelling pressure is constant in time, and, (3) the projectile moves in constant acceleration. Thus, one has

WU

$$a(x) = b(x) = 1, \quad R(x) = R = \text{constant}$$

$$p(t) = p = \text{constant}$$

$$\bar{P}(x,t) = \pi R^2 p = \bar{P} = \text{constant} \quad (3-7)$$

$$P(x,t) = [-\bar{P} + g \sin \alpha](1-x)$$

$$\ddot{x} = \beta = \text{constant}, \quad \dot{x} = \beta t, \quad \bar{x} = \frac{1}{2} \beta t^2$$

where  $\beta$  denotes the acceleration of the projectile. With Eqs. (3-7), one can rewrite Eqs. (3-6) as

$$\begin{aligned} y'''' + (-\bar{P} + g \sin \alpha)[(1-x)y']' + \ddot{y} \\ = -\bar{P}y'' H(\bar{x}-x) \\ - m[\beta^2 t^2 y'' + 2\beta t \dot{y}' + \beta y' + \ddot{y}] \delta(\bar{x}-x) \\ - (gm \cos \alpha) \delta(\bar{x}-x) - g \cos \alpha \end{aligned} \quad (3-8a)$$

with

$$\bar{P} = \pi R^2 p \quad (3-8b)$$

In Eqs. (3-8) the subscript  $p$  for the projectile mass  $m_p$  is dropped for simplicity.

#### 4. VARIATIONAL PRINCIPLE AND END CONDITIONS

A variational principle which is equivalent to our pertinent differential equation and boundary and initial conditions will be given in this section. It will also be used as the basis for finite element solutions. The procedure to arrive at such a variational statement is the usual integration-by-parts in the direction of reducing the higher ordered terms in the given differential equation. It will suffice to state such a variational principle and to show that it meets the requirements desired. Hence, let us consider the adjoint variational statement

$$\delta I = 0 \quad (4-1a)$$

with

$$I = \sum_{i=1}^{11} I_i(y, y^*) - \sum_{j=1}^2 J_j(y^*) \quad (4-1b)$$

WU

and

$$I_1 = \int_0^T \int_0^1 y'' y''' dx dt$$

$$I_2 = (\bar{P} - g \sin \alpha) \int_0^T \int_0^1 (1-x) y' y'' dx dt$$

$$I_3 = - \int_0^T \int_0^1 \dot{y} \dot{y}'' dx dt$$

$$I_4 = - \bar{P} \int_0^T \int_0^1 y' y'' H(\bar{x}-x) dx dt$$

$$I_5 = - \bar{P} \int_0^T \int_0^1 y' y'' \bar{\delta}(\bar{x}-x) dx dt$$

$$I_6 = - m \int_0^T \int_0^1 \beta^2 t^2 y' y'' \bar{\delta}(\bar{x}-x) dx dt$$

$$I_7 = - m \int_0^T \int_0^1 \beta^2 t^2 y' y'' \bar{\delta}'(\bar{x}-x) dx dt \quad (4-1c)$$

$$I_8 = 2m\beta \int_0^T \int_0^1 t \dot{y}' y'' \bar{\delta}(\bar{x}-x) dx dt$$

$$I_9 = m\beta \int_0^T \int_0^1 y' y'' \bar{\delta}(\bar{x}-x) dx dt$$

$$I_{10} = - m \int_0^T \int_0^1 \dot{y} \dot{y}'' \bar{\delta}(\bar{x}-x) dx dt$$

$$I_{11} = - m \int_0^T \int_0^1 \dot{y} \dot{y}'' \bar{\delta}'(\bar{x}-x) dx dt$$

$$J_1 = - g \cos \alpha \int_0^T \int_0^1 y'' dx dt$$

$$J_2 = - gm \cos \alpha \int_0^T \int_0^1 y'' \bar{\delta}(\bar{x}-x) dx dt$$

In Eqs. (4-1),  $y^* = y^*(x, t)$  denotes the adjoint field variable. All other quantities have been defined in the previous section. In as far as the problem is linear, one only needs one-half of the variational statement (4-1a). Consider that the original field variable  $y$  is fixed while varying the adjoint variable  $y^*$ . One then has

$$\delta I = (\delta I)_y = \sum_{i=1}^{11} (\delta I_i)_y - \sum_{j=1}^2 (\delta J_j) \quad (4-2)$$

where  $(\delta I_i)_y$  is defined by Eqs. (4-1c) where  $y^*$  is replaced by  $\delta y^*$ . Through integration-by-parts, Eq. (4-2) can be written as

$$\begin{aligned} & \int_0^T \int_0^1 \{ y'''' + (-\bar{P} + g \sin \alpha) [(1-x)y']' + \ddot{y} + \bar{P}y'' H(\bar{x}-x) \\ & \quad + m[\beta^2 t^2 y'' + 2\beta t \dot{y}' + \beta y' + \ddot{y}] \bar{\delta}(\bar{x}-x) \\ & \quad + g \cos \alpha + (mg \cos \alpha) \bar{\delta}(\bar{x}-x) \} \delta y^* dx dt \\ & + \int_0^T \{ y'' \delta y^* - [y''' + (-\bar{P} + g \cos \alpha)(1-x)y' \\ & \quad + \bar{P}y' H(\bar{x}-x) + m\beta^2 y' \bar{\delta}(\bar{x}-x)] \delta y^* \} \Big|_{x=0}^{x=1} dt \\ & - \int_0^1 \{ [\dot{y} + m\dot{y} \bar{\delta}(\bar{x}-x)] \delta y^* \} \Big|_{t=0}^{t=T} dx = 0 \end{aligned} \quad (4-3)$$

Since  $\delta y^*$  is quite independent of  $y$  and it is also quite arbitrary, Eq. (4-3) leads to the original partial differential equation (3-8a) and the following "intrinsic" end conditions (see Ref. [1]):

$$y''(0, t) = 0 \quad (4-4a)$$

$$y''(1, t) = 0 \quad (4-4b)$$

$$\begin{aligned} y'''(0, t) + (-\bar{P} + g \cos \alpha) y'(0, t) + \bar{P} y'(0, t) H\left(\frac{1}{2} \beta t^2\right) \\ + m\beta^2 y'(0, t) \bar{\delta}\left(\frac{1}{2} \beta t^2\right) = 0 \end{aligned} \quad (4-4c)$$

$$\begin{aligned} y'''(1, t) + 0 + \bar{P} y'(1, t) H\left(\frac{1}{2} \beta t^2 - 1\right) \\ + m\beta^2 y'(1, t) \bar{\delta}\left(\frac{1}{2} \beta t^2 - 1\right) = 0 \end{aligned} \quad (4-4d)$$

$$\dot{y}(x, 0) = 0 \quad (4-4e)$$

$$\dot{y}(x, T) = 0 \quad (4-4f)$$

WU

Following the concept introduced in Ref. [3], various support conditions and initial conditions can be easily incorporated into the solution formulation. For our present purpose, we shall add to the functional I the following terms:

$$I_{12} = \int_0^T \{k_1 y(0,t) y^*(0,t) + k_2 y'(0,t) y^{*'}(0,t) + k_3 y(1,t) y^*(1,t) + k_4 y'(1,t) y^{*'}(1,t) + k_5 y(x_s,t) y^*(x_s,t) + k_6 y'(x_s,t) y^{*'}(x_s,t)\} dt \quad (4-5a)$$

$$I_{13} = k_7 \int_0^1 y(x,0) y^*(x,T) dx \quad (4-5b)$$

$$J_3 = k_7 \int_0^1 Y(x) y^*(x,T) dx \quad (4-5c)$$

so that

$$I_{13} - J_3 = k_7 \int_0^1 [y(x,0) - Y(x)] y^*(x,T) dx \quad (4-5d)$$

With  $I_{12}$ ,  $I_{13}$  and  $(-J_3)$  added to I in Eqs. (4), it is readily seen that the differential equation and end conditions now become

$$\begin{aligned} y'''' + (-\bar{P} + g \sin \alpha) [(1-x)y']' + \ddot{y} + \bar{P} y'' H(\bar{x}-x) \\ + m[\beta^2 t^2 y'' + 2\beta t \dot{y}' + \beta y' + \ddot{y}] \bar{\delta}(\bar{x}-x) \\ + k_5 y(x,t) \bar{\delta}(x_s) - k_6 [y''(x,t) \bar{\delta}(x_s) + y'(x,t) \bar{\delta}'(x_s)] \\ + g \cos \alpha + (mg \cos \alpha) \bar{\delta}(\bar{x}-x) = 0 \end{aligned} \quad (4-6)$$

and

$$y''(0,t) - k_2 y'(0,t) = 0 \quad (4-7a)$$

$$y''(1,t) + k_4 y'(1,t) = 0 \quad (4-7b)$$

$$\begin{aligned} y'''(0,t) + k_1 y(0,t) \\ + (-\bar{P} + g \cos \alpha) y'(0,t) + \bar{P} y'(0,t) H(\frac{1}{2} \beta t^2) \\ + m\beta^2 y'(0,t) \bar{\delta}(\frac{1}{2} \beta t^2) = 0 \end{aligned} \quad (4-7c)$$

WU

$$y'''(1,t) - k_3 y(1,t) + \bar{P} y'(1,t) H\left(\frac{1}{2} \beta t^2 - 1\right) + m \beta^2 y'(1,t) \delta\left(\frac{1}{2} \beta t^2 - 1\right) = 0 \quad (4-7d)$$

$$\dot{y}(x,0) = 0 \quad (4-7e)$$

$$\dot{y}(x,T) \left[1 + m \delta\left(\frac{1}{2} \beta T^2 x\right)\right] + k_7 [y(x,0) - Y(x)] = 0 \quad (4-7f)$$

The parameters first introduced in Eqs. (4-5) are now given the meanings. The constants  $k_1$  and  $k_2$  are the nondimensionalized spring constants of deflection and rotation, respectively, at  $x = 0$ ;  $k_3$ ,  $k_4$  are the same at  $x = 1$ ; and,  $k_5$ ,  $k_6$ , at  $x = x_s$ . If we allow  $x_s$  to be a function of time, the case of a moving support would have been included. It is noted that  $k_i$ ,  $i = 1$  through  $i = 6$ , can assume any value from zero to infinite.  $k_i = 0$  corresponds to no spring and  $k_i = \infty$ , to a rigid support. However, the constant  $k_7$  in Eq. (4-5b) is infinity in theory and is to assume a very large number compared with unity so that the end condition Eq. (4-7f) reduces to that the initial shape of  $y(x,t)$  is  $Y(x)$ .

The last task in this section is to normalize the time variable  $t$  so that the solution for any time range can be simplified. To this end, one replaces the variable  $t$  with  $Tt$  and the final equation become:

$$\delta I = (\delta I)_y = \sum_{i=1}^{13} (\delta I_i)_y - \sum_{j=1}^3 (\delta J_j) = 0 \quad (4-8a)$$

with

$$\begin{aligned} I_1 &= \int_0^1 \int_0^1 y'' y''' dx dt \\ I_2 &= T(\bar{P} - g \sin \alpha) \int_0^1 \int_0^1 (1-x) y' y'' dx dt \\ I_3 &= -\frac{1}{T} \int_0^1 \int_0^1 \ddot{y} y'' dx dt \\ I_4 &= -T \bar{P} \int_0^1 \int_0^1 y' y'' H(\bar{x} - x) dx dt \\ I_5 &= -T \bar{P} \int_0^1 \int_0^1 y' y'' \delta(\bar{x} - x) dx dt \end{aligned} \quad (4-8b)$$

$$I_6 = -\frac{m\beta^2}{T} \int_0^1 \int_0^1 t^2 y' y^{*'} \bar{\delta}(\bar{x}-x) dx dt$$

$$I_7 = -\frac{m\beta^2}{T} \int_0^1 \int_0^1 t^2 y' y^{*'} \bar{\delta}'(\bar{x}-x) dx dt$$

$$I_8 = \frac{2m\beta}{T} \int_0^1 \int_0^1 t \dot{y}' y^{*'} \bar{\delta}(\bar{x}-x) dx dt$$

$$I_9 = \frac{m\beta}{T} \int_0^1 \int_0^1 y' y^{*'} \bar{\delta}(\bar{x}-x) dx dt$$

$$I_{10} = -\frac{m}{T} \int_0^1 \int_0^1 \dot{y} \dot{y}^{*'} \bar{\delta}(\bar{x}-x) dx dt \quad (4-8b)$$

$$I_{11} = -\frac{m}{T} \int_0^1 \int_0^1 \dot{y} y^{*'} \bar{\delta}(\bar{x}-x) dx dt$$

$$I_{12} = T \int_0^1 \{ k_1 y(0,t) y^{*'}(0,t) + k_2 y'(0,t) y^{*'}(0,t) \\ + k_3 y(1,t) y^{*'}(1,t) + k_4 y'(1,t) y^{*'}(1,t) \\ + k_5 y(x_s,t) y^{*'}(x_s,t) + k_6 y'(x_s,t) y^{*'}(x_s,t) \} dt$$

$$I_{13} = k_7 \int_0^1 y(x,0) y^{*'}(x,1) dx$$

$$J_1 = -Tg \cos \alpha \int_0^1 \int_0^1 y^{*'} dx dt$$

$$J_2 = -Tgm \cos \alpha \int_0^1 \int_0^1 y^{*'} \bar{\delta}(\bar{x}-x) dx dt \quad (4-8c)$$

$$J_3 = k_7 \int_0^1 Y(x) y^{*'}(x,1) dx$$

## 5. SOLUTION FORMULATION BY FINITE ELEMENTS

With the variational statement established in the previous section, one is now ready to formulate the finite element matrix equation. The normalized region of a unit square is divided into  $K$  by  $L$  sub-rectangulars (elements, Figure 2). In each  $(i,j)$ -th element, the field variables are assumed to be in the form of

$$y^{(i,j)}(\xi, \eta) = \underline{a}^T(\xi, \eta) \underline{Y}^{(i,j)} \quad (5-1)$$

$$y^{*(i,j)}(\xi, \eta) = \underline{a}^T(\xi, \eta) \underline{Y}^{*(i,j)}$$

where  $\xi, \eta$  are local coordinates of space and time and are related to  $x$  and  $t$  by the following transformations:

$$\begin{aligned} \xi &= \xi^{(i)} = Kx - i + 1 \\ \eta &= \eta^{(j)} = Lt - j + 1 \end{aligned} \quad (5-2a)$$

or,

$$\begin{aligned} x &= \frac{1}{K} \{\xi + i - 1\} \\ t &= \frac{1}{L} \{\eta + j - 1\} \end{aligned} \quad (5-2b)$$

The vector function  $\underline{a}(\xi, \eta)$  is the two dimensional displacement function and  $\underline{Y}^{(i,j)}$ ,  $\underline{Y}^{*(i,j)}$  are the generalized coordinates vector - their specific form and meaning are to be given later. If one substitutes Eqs. (5-1) into (4-8), he can write,

$$\delta I = (\delta I)_y = \sum_{m=1}^{13} (\delta I_m)_y - \sum_{n=1}^3 (\delta J_n) = 0 \quad (5-3a)$$

with

$$(\delta I_m)_y = \sum_{i=1}^K \sum_{j=1}^L \delta \underline{Y}^{*(i,j)T} \underline{A}_m^{(i,j)} \underline{Y}^{(i,j)} \quad (5-3b)$$

$$(\delta J_n) = \sum_{i=1}^K \sum_{j=1}^L \delta \underline{Y}^{*(i,j)T} \underline{B}_n^{(i,j)} \quad (5-3c)$$



WU

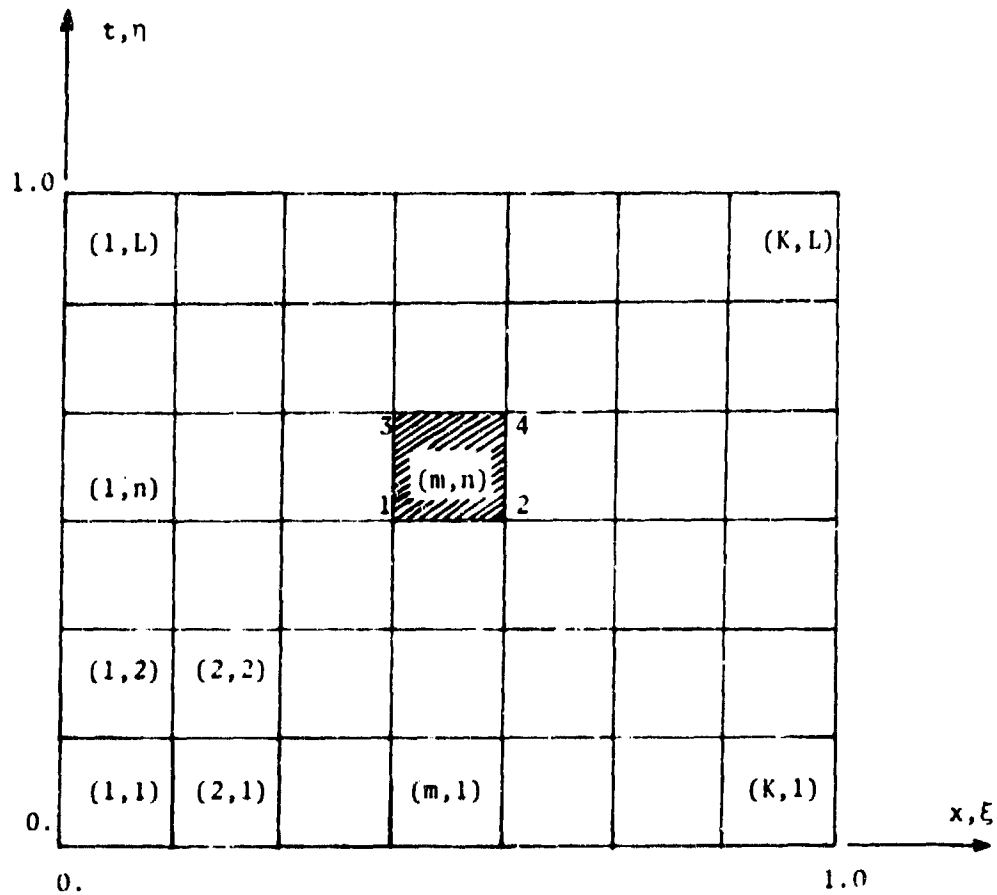


**FIGURE 2.** Finite Element Grid Scheme in Space- and Time-Coordinates. Also shown: Node Point Ordering in a Typical Element  $(m,n)$ .

WU

where  $A_m^{(i,j)}$  is a local square matrix and  $B_m^{(i,j)}$ , a local column vector. They are defined in the following equations:

$$\begin{aligned}
 A_1^{(i,j)} &= \left(\frac{K^2 T}{L}\right) \int_0^1 \int_0^1 \underline{\underline{a''a''}}^T d\xi d\eta \\
 A_2^{(i,j)} &= \left(\frac{i}{L}\right) (\bar{P} - g \sin \alpha) [(K-i+1) \int_0^1 \int_0^1 \underline{\underline{a'a'}}^T d\xi d\eta - \int_0^1 \int_0^1 \xi \underline{\underline{a'a'}}^T d\xi d\eta] \\
 A_3^{(i,j)} &= - \left(\frac{L}{KT}\right) \int_0^1 \int_0^1 \underline{\underline{aa}}^T d\xi d\eta \\
 A_4^{(i,j)} &= - \left(\frac{TPK}{L}\right) \int_0^1 \int_0^1 \underline{\underline{a'a'}}^T T_H^{(i,j)} (\bar{\xi} - \xi) d\xi d\eta \\
 A_5^{(i,j)} &= - \left(\frac{TP}{L}\right) \int_0^1 \int_0^1 \underline{\underline{aa}}^T T_{\bar{\delta}}^{(i,j)} (\bar{\xi} - \xi) d\xi d\eta \\
 A_6^{(i,j)} &= - \left(\frac{m\beta^2 K}{TL^3}\right) [(j-1)^2 \int_0^1 \int_0^1 \underline{\underline{a'a'}}^T \bar{\delta}^{(i,j)} (\bar{\xi} - \xi) d\xi d\eta \\
 &\quad + 2(j-1) \int_0^1 \int_0^1 \eta \underline{\underline{a'a'}}^T \bar{\delta}^{(i,j)} (\bar{\xi} - \xi) d\xi d\eta \\
 &\quad + \int_0^1 \int_0^1 \eta^2 \underline{\underline{a'a'}}^T \bar{\delta}^{(i,j)} (\bar{\xi} - \xi) d\xi d\eta] \\
 A_7^{(i,j)} &= - \left(\frac{m\beta^2 K}{TL^3}\right) [(j-1)^2 \int_0^1 \int_0^1 \underline{\underline{aa}}^T T_{\bar{\delta}}^{(i,j)'} (\bar{\xi} - \xi) d\xi d\eta \\
 &\quad + 2(j-1) \int_0^1 \int_0^1 \eta \underline{\underline{aa}}^T T_{\bar{\delta}}^{(i,j)'} (\bar{\xi} - \xi) d\xi d\eta \\
 &\quad + \int_0^1 \int_0^1 \eta^2 \underline{\underline{aa}}^T T_{\bar{\delta}}^{(i,j)'} (\bar{\xi} - \xi) d\xi d\eta]
 \end{aligned}
 \tag{5-4a}$$

WU

$$\begin{aligned} A_8^{(i,j)} = & \left( \frac{2m\beta}{TL} \right) \left[ (j-1) \int_0^1 \int_0^1 \underline{\underline{a}} \underline{\underline{a}}', T_{\delta}^{-}(i,j) (\bar{\xi}-\xi) d\xi d\eta \right. \\ & \left. + \int_0^1 \int_0^1 \eta \underline{\underline{a}} \underline{\underline{a}}', T_{\delta}^{-}(i,j) (\bar{\xi}-\xi) d\xi d\eta \right] \end{aligned}$$

$$A_9^{(i,j)} = \left( \frac{m\beta}{TL} \right) \int_0^1 \int_0^1 \underline{\underline{a}} \underline{\underline{a}}', T_{\delta}^{-}(i,j) (\bar{\xi}-\xi) d\xi d\eta$$

$$A_{10}^{(i,j)} = \left( \frac{mL}{TK} \right) \int_0^1 \int_0^1 \underline{\underline{a}} \underline{\underline{a}}', T_{\delta}^{-}(i,j) (\bar{\xi}-\xi) d\xi d\eta$$

$$A_{11}^{(i,j)} = - \left( \frac{mL}{TK} \right) \int_0^1 \int_0^1 \underline{\underline{a}} \underline{\underline{a}}', T_{\delta}^{+}(i,j) (\bar{\xi}-\xi) d\xi d\eta$$

$$(\delta I_{12})_y = \sum_{j=1}^L \delta Y^{*}(1,j) \frac{k_1 T}{KL} \int_0^1 \underline{\underline{a}}(0,\eta) \underline{\underline{a}}^T(0,\eta) d\eta \underline{\underline{Y}}^{(1,j)} \quad (5-4b)$$

$$+ \sum_{j=1}^L \delta Y^{*}(K,j) \frac{k_3 T}{KL} \int_0^1 \underline{\underline{a}}(1,\eta) \underline{\underline{a}}^T(1,\eta) d\eta \underline{\underline{Y}}^{(K,j)}$$

$$+ \sum_{j=1}^L \delta Y^{*}(i_s,j) \frac{k_5 T}{KL} \int_0^1 \underline{\underline{a}}(\xi_s,\eta) \underline{\underline{a}}^T(\xi_s,\eta) d\eta \underline{\underline{Y}}^{(i_s,j)}$$

$$+ \sum_{j=1}^L \delta Y^{*}(1,j) \frac{k_2 K T}{L} \int_0^1 \underline{\underline{a}}'(0,\eta) \underline{\underline{a}}'^T(0,\eta) d\eta \underline{\underline{Y}}^{(1,j)}$$

$$+ \sum_{j=1}^L \delta Y^{*}(K,j) k_4 \frac{TK}{L} \int_0^1 \underline{\underline{a}}'(1,\eta) \underline{\underline{a}}'^T(1,\eta) d\eta \underline{\underline{Y}}^{(K,j)}$$

$$+ \sum_{j=1}^L \delta Y^{*}(i_s,j) k_6 \frac{TK}{T} \int_0^1 \underline{\underline{a}}'(\xi_s,\eta) \underline{\underline{a}}'^T(\xi_s,\eta) d\eta \underline{\underline{Y}}^{(i_s,j)}$$

WU

$$\begin{aligned}
 (\delta I_{13})_y &= \sum_{i=1}^K \delta Y^*(i, L) \frac{k_7}{K} \int_0^1 \tilde{a}(\xi, 1) \tilde{a}^T(\xi, 0) d\xi \tilde{Y}(i, 1) \\
 B_1(i, j) &= - \frac{Tg \cos \alpha}{KL} \int_0^1 \int_0^1 \tilde{a}(\xi, \eta) d\xi d\eta \\
 B_2(i, j) &= - \frac{Tgm \cos \alpha}{KL} \int_0^1 \int_0^1 \tilde{a}(\xi, \eta) \delta^{(i, j)} (\tilde{\xi} - \xi) d\xi d\eta \\
 (\delta J_3) &= \sum_{i=1}^K \delta Y^*(i, L) \frac{k_7}{K} \int_0^1 Y^{(i)}(\xi) \tilde{a}(\xi, 1) d\xi
 \end{aligned} \tag{5-4c}$$

The local matrices defined in Eqs. (5-4) can be assembled into a global equation. Thus Eq. (5-3a) can be written as

$$\delta \tilde{Y}^* T_{KY} = \delta \tilde{Y}^* T_F \tag{5-5}$$

where  $\tilde{Y}$  and  $\tilde{Y}^*$  are the generalized coordinates in the global system;  $K$  and  $F$  are global "stiffness" matrix and "force" vector respectively assembled from the local matrix equations of Eqs. (5-4). Since  $\delta \tilde{Y}^*$  in Eq. (5-5) is not constrained in anyway, the equation reduces to the algebraic matrix equation to be solved

$$KY = F \tag{5-6}$$

## 6. DISPLACEMENT FUNCTIONS

In dealing with one dimensional problems using finite elements, excellent results have been obtained with cubic polynomials as displacement functions [2]. For the present problem with two independent variables we choose it to be the product of two cubic polynomials, each for one independent variable. This choice also provides some advantage in algebraic manipulations and integrations as it will become evident in the sequel. Hence the vector function in Eqs. (5-1) is assumed to have the form

$$\tilde{a}^T(\xi, \eta) = [a_1(\xi, \eta), a_2(\xi, \eta), \dots, a_k(\xi, \eta), \dots, a_{16}(\xi, \eta)] \tag{6-1}$$

WU

where

$$a_k(\xi, \eta) = b_i(\xi)b_j(\eta), \quad k = 1, 2, \dots, 16 \quad (6-2)$$

$$i, j = 1, 2, 3, 4$$

The function  $b_1(\xi)$ , as mentioned earlier, is taken to be the one-dimensional shape function of a cubic polynomial, i.e.,

$$\begin{aligned} b_1(\xi) &= 1 - 3\xi^2 + 2\xi^3 \\ b_2(\xi) &= \xi - 2\xi^2 + \xi^3 \\ b_3(\xi) &= 3\xi^2 - 2\xi^3 \\ b_4(\xi) &= -\xi^2 + \xi^3 \end{aligned} \quad (6-3)$$

Now the correspondence between  $k$  and the pair  $(i, j)$  in Eq. (6-2) can be established by giving specific definitions to the local generalized coordinates in  $\underline{Y}^{(m, n)}$  identifies the element considered. Hence, if we let

$$\begin{aligned} \underline{Y} &= \underline{Y}^{(m, n)} \\ &= \{(y_{y, \xi} \ y_{y, \eta} \ y_{y, \xi \eta})_1 \ (y_{y, \xi} \ y_{y, \eta} \ y_{y, \xi \eta})_2 \\ &\quad (y_{y, \xi} \ y_{y, \eta} \ y_{y, \xi \eta})_3 \ (y_{y, \xi} \ y_{y, \eta} \ y_{y, \xi \eta})_4\}^{(m, n)} \end{aligned} \quad (6-4)$$

with points 1, 2, 3, 4 shown in Figure 2, the following correspondence between  $k$  and  $(i, j)$  can be easily shown:

$k$	$(i, j)$	$k$	$(i, j)$
1	(1, 1)	9	(1, 3)
2	(2, 1)	10	(2, 3)
3	(1, 2)	11	(1, 4)
4	(2, 2)	12	(2, 4)
5	(3, 1)	13	(3, 3)
6	(4, 1)	14	(4, 3)
7	(3, 2)	15	(3, 4)
8	(4, 2)	16	(4, 4)

## 7. CONCLUSIONS AND FUTURE WORK

In this paper, we have presented the complete formulation of a gun dynamics formulation in conjunction with finite element discretization. The effect of projectile moving mass, recoil force, travelling pressure and curvature induced loads and support conditions have all been included in the formulation. It has also been observed that time dependent or moving support conditions can be conveniently

WU

included. The computer algorithms have been completed. Our task in the immediate future is to carry out a comprehensive parametric study to investigate the relative significance of various terms on the gun motions in general and muzzle motions in particular. It is hoped that these data will be made available in the near future.

#### REFERENCES

1. J. J. Wu, 1975 Journal of Sound and Vibration, 39, pp. 195-206.  
On adjoint operators associated with boundary value problems.
2. J. J. Wu, 1974 Journal of Sound and Vibrations, 37, pp. 349-358.  
On the numerical convergence of matrix eigenvalue problems due to constraint conditions.
3. J. J. Wu, 1977 Journal of Sound and Vibration, 53, pp. 341-356.  
Solutions to initial value problems by use of finite-elements-unconstrained variational formulations.
4. T. E. Simkins, 1977 Proceedings of First Conference on Dynamics of Precision Gun Weapons, pp. 373-469. Radial and transverse response of gun tubes by finite element methods.

## ABSTRACT

\*Chen, Macagno, Chang & Lin

TITLE: A Study of Orifice Area and Orifice Discharge Coefficient in Recoil Mechanisms.  
C. J. Chen, E. O. Macagno, K. Y. Chang and S. C. Lin  
Energy Division & Iowa Institute of Hydraulic Research  
The University of Iowa, Iowa City, IA 52242

### ABSTRACT:

A procedure of determining orifice clearance area and orifice discharge coefficient is given. It is shown that by requiring the resistance offered by recoil mechanism to have a small peak resistance, an orifice design criterion may be defined. This criterion provides decoupling of fluid motion with recoil motion. The recoil motion is first solved. Then the orifice clearance area is determined in terms of recoil velocity and required resistance. A variable orifice discharge coefficient is introduced to account for one-dimensional assumption and pressure drop for fluid throttling through the orifice due to friction loss. Factors affecting the determination of orifice discharge coefficient are discussed. A method of determining variable orifice coefficient is proposed.

### BIOGRAPHY:

PRESENT ASSIGNMENT: Professor of Engineering, The University of Iowa, Iowa City, Iowa.

PAST EXPERIENCE: 1967-1970 Assistant Professor; 1970-1977 Associate Professor; 1977 Professor, The University of Iowa. 1973 Summer U. S. Army Scientific Advisor, Rock Island Arsenal; 1974-1975 U. S. Senior Scientist Award, University of Karlsruhe, West Germany.

DEGREES HELD: Bachelor of Engineering, Mechanical Engineering (ME), Institute of Technology, Taipei, Taiwan, 1957; Master of Science (ME), Kansas State University, Manhattan, Kansas, 1962; Ph.D. (ME), Case-Western Reserve University, Cleveland, Ohio, 1967.

\*Chen, Macagno, Chang & Lin

A STUDY OF ORIFICE AREA AND ORIFICE DISCHARGE  
COEFFICIENT IN RECOIL MECHANISMS

\*Ching Jen Chen, Professor  
Enzo O. Macagno, Professor  
King Y. Chang, Research Assistant  
Shyi J. Lin, Research Assistant  
Energy Division and Iowa Institute of Hydraulic Research  
The University of Iowa  
Iowa City, Iowa 52242

I. Introduction

The recoil mechanism is a component of the recoil system which provides a retarding force acting on the gun so as to brake the rearward motion in the firing cycle. The counter-recoil mechanism is also a component of the recoil mechanisms which stores the energy during the recoil and dispenses it during the counter-recoil phase so as to bring the gun back into its in-battery position. Without a recoil system the force acting on the gun and its mounts induced by firing the charge is so large that damages to the gun often immediately result. An improperly designed recoil mechanism can also affect the accuracy of the gun in hitting the target and reduce the life of the gun. Therefore, the recoil system is one of the most important components of a gun system.

Frequent failure and the undesirable characteristic of many springs used in the recoil mechanism prompted recent designers of a gun system to adopt more fluid-type recoil mechanisms (hydropneumatic) or the combination of fluid and spring type recoil mechanisms (hydrospring). The fluid recoil mechanism is essentially a fluid shock absorber. The fluid in the mechanism, gas or liquids, is throttling during a firing cycle through an orifice which divides the recoil mechanism into two or more chambers. The difference in the pressure between the chambers thus provides the retarding force for braking action. The retarding force and the counter-recoiling force are thus functions of the fluid motion, the type of fluids, and the orifice geometry of recoil mechanisms. Therefore, the knowledge of fluid mechanics of the recoil mechanism is an indispensable part of the weapon design.

The aim of this paper is to provide the fundamental description of fluid mechanics for recoil mechanisms and to present an approximate determination of orifice area.



## II. Criterion of Orifice Design

A recoil mechanism may be designed to operate on incompressible or compressible principle. For incompressible type, the total volume of the recoil cylinder will remain the same during recoil motion since the fluid is treated as incompressible. For the compressible type the volume may be decreased in the recoil motion. The fluid used in the recoil mechanisms may be gas or liquid such as air, nitrogen, hydraulic or silicone oil. In both cases, the orifice must be properly designed to achieve desired characteristics of retarding force for recoil mechanism.

Before one calculates the fluid motion and the pressure distribution in a recoil mechanism, design characteristics of recoil mechanisms should be first defined so that the required geometry of the orifice can be determined.

Generally all recoil mechanisms work on some combination of the same basic principles; that of providing a controlled resistance over a set distance to check the motion of the recoiling parts, then returning them to the firing position and providing a sufficient restraint to hold them in that position at a given elevation. A basic requirement for a recoil mechanism is that the resistance to recoil should be nearly constant for a prescribed recoil distance, since this will produce the smallest possible force on the gun structure. A typical recoil force versus recoil distance relation is given in Fig. 1. The area under the recoil force-time curve represents recoil impulse to be dissipated by the recoil mechanism. Clearly, a rectangular curve will yield the lowest retarding force for a given recoil motion. However, a rectangular curve is not applicable at the beginning because the recoil resistance  $K(t)$  should not exceed the recoil force  $B(t)$  created by the propellant gas.

The total resistance force  $K(t)$  is a combination of a hydraulic force  $F_0(t)$ , a spring force if a spring is used with fluid and friction of moving mechanism. Whichever the type of recoil mechanism is used, this force works as a unit.

In general, the recoil force  $B(t)$  is offset largely by the hydraulic resistance  $F_0(t)$  offered by throttling the fluid through the controlling orifice and by the spring force. Thus design of the control orifice is a vital part of the recoil mechanisms.

We now consider a basic recoil mechanism as shown in Fig. 2 that a recoiling mass  $M$  is subjected to a time dependent recoil force,  $B(t)$ , from the discharge in the breech of a gun creating an acceleration of  $X$  in the  $x$  direction. Here  $X = 0$  is taken as the orifice plane before the recoil motion. The recoil motion of mass  $M$  forces the fluid to flow from Chamber (1) to Chamber (2) if the orifice installed between the two chambers restricts the flow from Chamber (1) to (2) so as to create a pressure difference between the two chambers. This differential pressure acts on the wall of recoiling orifice  $A_1$  and  $A_2$  to control the recoiling speed and motion. The force balance for the recoil motion can be written as

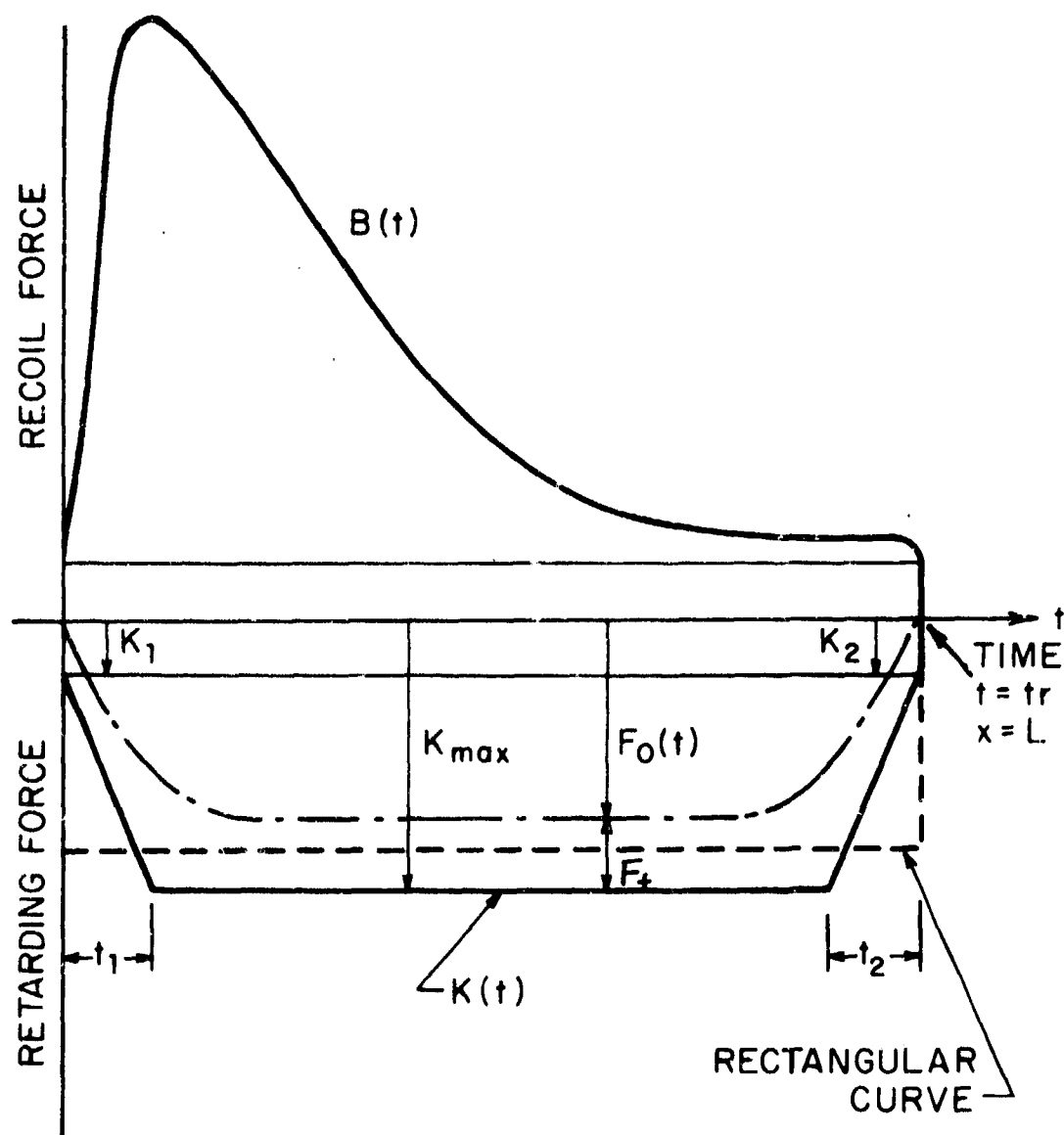


Figure 1. Recoil Force and Retarding Force of Recoil Mechanisms

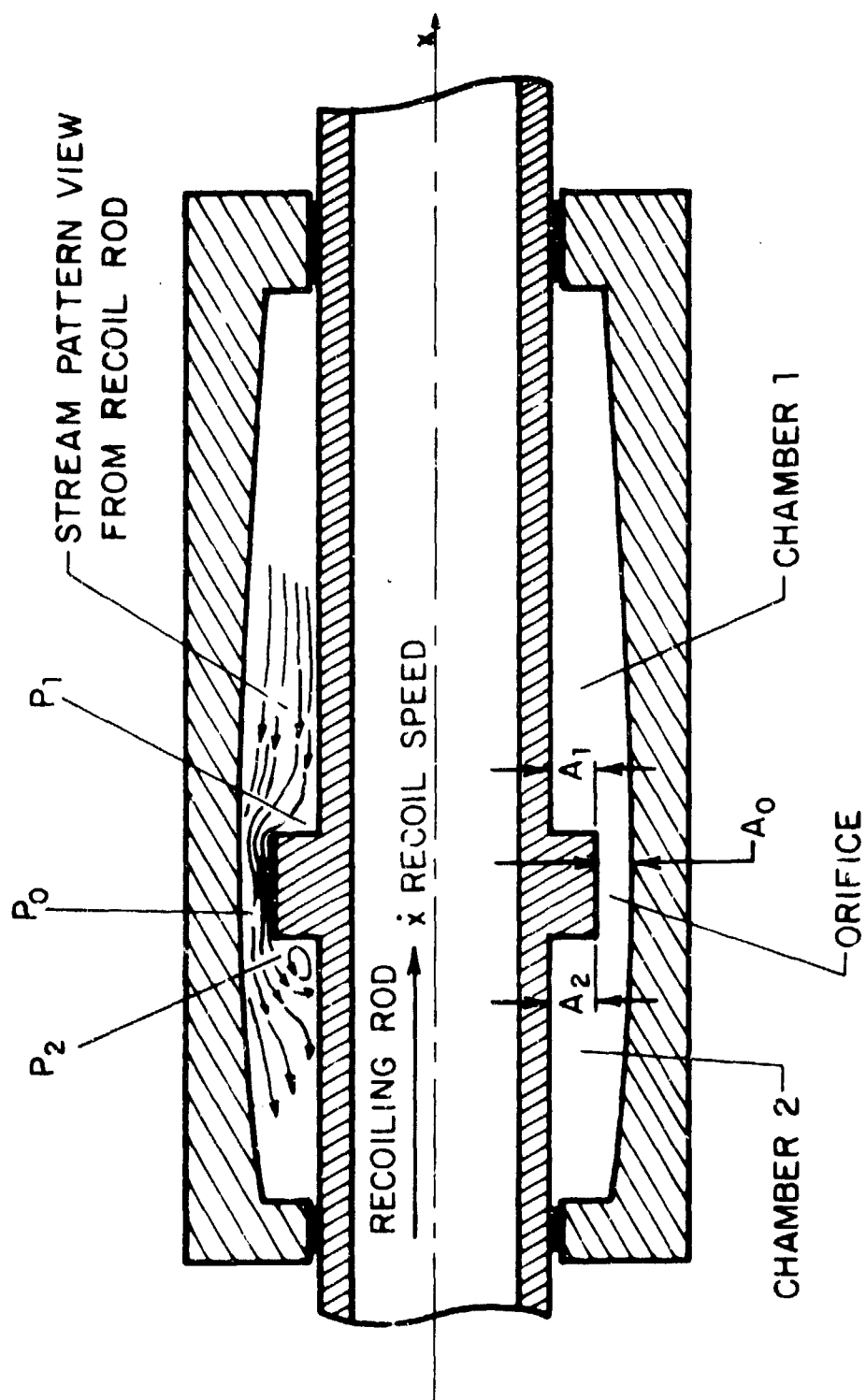


Figure 2. Typical Recoil Mechanism

\*Chen, Macagno, Chang & Lin

$$M\ddot{X} = B(t) - K(t) + M g \sin \theta \quad (1)$$

$$K(t) = \int_{A_1} P_1 dA_1 - \int_{A_2} P_2 dA_2 + F_f = F_o(t) + F_f$$

where  $P_1$  and  $P_2$  are respectively the pressure distributed on the orifice surface facing Chamber (1) and Chamber (2).  $A_1$  and  $A_2$  are area of the orifice facing Chambers (1) and (2). Here  $A_1 = A_2$  is for incompressible type and  $A_1 > A_2$  for compressible type.  $F_f$  is the frictional resistance force from seal, various moving parts and, if any, recuperator. The last term of Eq. (1) is the contribution of the gravitational force with  $\theta$  being the inclined angle of the recoil mechanism with respect to horizontal plane. The dot on  $X$  denotes the time derivative. In Eq. (1) the mass  $M$ , the retarding force from breech  $B(t)$ , two areas  $A_1$  and  $A_2$  and frictional resistance force,  $F_f$ , are assumed known but distribution of pressures  $P_1$  and  $P_2$  acting on the surface  $A_1$  and  $A_2$  are unknown and must be solved associated with the fluid motion induced by the motion of recoiling parts. In general both  $P_1$  and  $P_2$  must be integrated from the pressure distribution respectively on their surfaces  $A_1$  and  $A_2$ .

Now the pressure distribution on the orifice surface and their time variations must be determined by solving the fluid motion in the recoil fluid chambers. This creates the coupling between the recoiling force, and the fluid motion. It should also be pointed out here that the designer has very little control over the resistance force,  $F_f$ , from the friction and recuperator and the gravitational force,  $Mg$ , but he can control the resistance offered by the pressure force from the two chambers by properly designing the orifice such that the total resistance to the recoil force is sufficient to arrest the rearward motion of the gun in a specific recoil length allowed in the design.

One is now faced with the question of what orifice design will provide the lowest peak resistance force for a given mechanism. To set up the criterion for the orifice design let us consider Eq. (1) for recoil motion again.  $K(t)$  is the total resistance force including frictional forces  $F_f$  and pressure forces  $F_o$  created from the fluid throttling through the orifice. As the design characteristic of recoil mechanisms requires that the total resistance  $K(t)$  to recoil should be nearly constant for a prescribed recoil length, a trapezoidal shape for  $K(t)$  such as in Fig. 1 is normally adopted.

Since Eq. (1) is a second order ordinary differential equation, one needs two initial conditions to obtain a unique solution. These two may be taken as

$$t = 0 \quad X = 0 \quad (2)$$

$$t = 0 \quad \dot{X} = 0 \quad (3)$$

\*Chen, Macagno, Chang & Lin

That is initially the recoil mechanism is at rest. However, if the total resistance  $K(t)$  is not specified there will be infinite many solutions of  $X(t)$  to Eqs. (1), (2) and (3). To determine  $K(t)$ , we need additional design constraints. They are:

- (1) the velocity of recoil  $\dot{X}_0$  is zero at the end of the recoil,  
 $t = t_r$ , or

$$t = t_r \quad \dot{X}(t_r) = 0 \quad (4)$$

- (2) the total length of recoil allowed is  $L$ , which must be achieved in a duration of  $t_r$ , or

$$t = t_r \quad X(t_r) = L \quad (5)$$

While the recoil length may normally be specified, the time duration,  $t_r$ , to arrest the rearward motion of the recoil is dictated by the resistance force  $K(t)$  and is not known normally a priori. Indeed,  $t_r$  must be solved with  $K(t)$  together. To determine the function  $K(t)$  we reason as follows.

First, at the beginning of recoil,  $t = 0$ , and at the end of recoil,  $t = t_r$ , the mechanism is at rest and zero acceleration  $\ddot{X} = \ddot{X} = 0$  and meantime the breech force is zero or  $B(0) = B(t_r) = 0$ . We thus require from Eq. (1)

$$K_1 = K(0) = Mg \sin \theta \quad (6)$$

$$K_2 = K(t_r) = Mg \sin \theta \quad (7)$$

Here  $K_1$  and  $K_2$  are the resistance at the beginning and at the end of recoil motion.

Secondly, integrating Eq. (2) twice and with the initial conditions (3) and (4), we obtain

$$M\dot{X} = \int_0^t B(\tau) d\tau - \int_0^t K(\tau) d\tau + Mg \sin \theta t \quad (8)$$

$$MX = \int_0^t \int_0^t B(\tau) d\tau dt - \int_0^t \int_0^t K(\tau) d\tau dt + Mg \sin \theta \frac{t^2}{2} \quad (9)$$

Now with additional design constraints (4) and (5), Eqs. (8) and (9) become

$$0 = \int_0^{t_r} B(t) dt - \int_0^{t_r} K(t) dt + Mg \sin \theta t_r \quad (10)$$

and

\*Chen, Macagno, Chang & Lin

$$ML = \int_0^{t_r} \int_0^t B(\tau) d\tau dt - \int_0^{t_r} \int_0^t K(\tau) d\tau dt + Mg \sin \theta \frac{t_r^2}{2} \quad (11)$$

Integral Eqs. (10) and (11) thus provide us with a means of determining the recoil time duration  $t_r$  and the total resistance force  $K(t)$ . Since the total resistance force  $K(t)$  is generally desired to be of trapezoidal shape as shown in Fig. 1, if the initial and final periods,  $t_1$  and  $t_2$ , of the variable resistance force are specified then Eqs. (10) and (11) determine uniquely the time  $t_r$  and the maximum total resistance for  $K_{\max}$ .

Either the moment area method or a trial-and-error procedure, as discussed by Arora and Haug [1] and Coberly [2], may be used to solve Eqs. (10) and (11). Readers are referred to the above references for more details. The total resistance function  $K(t)$  thus can be used as the criterion of orifice design.

When the total resistance function  $K(t)$  is determined one may substitute the  $K(t)$  function into Eqs. (8) and (9) to obtain the recoil velocity  $\dot{X}(t)$  and the recoil displacement  $X(t)$  as a function of time. The recoil velocity and displacement in turn become the boundary conditions for the solution of fluid flow in the recoil mechanism. For the recoil mechanism shown in Fig. 2, the orifice now must move with  $\dot{X}$  velocity in the recoiling phase.

The fluid throttling through the orifice must produce a resistance force such that when combined with other frictional resistance from seals and other rubbing parts,  $F_f$ , it is equal to the desired total resistance force,  $K(t)$ . It is a difficult task for a designer to design such an orifice, since he must solve or know how the pressure force is generated when the fluid is throttling through the orifice. What is more difficult, the orifice clearance area in general is variable at different locations; the flow is unsteady and may be in both laminar and turbulent regions.

### III. Quasi-Steady One-Dimensional Solution

The fluid motion and the pressure distribution on the orifice surface are governed by the mass conservation equation, the equation of state, the Navier-Stokes equation and energy equation for unsteady compressible fluid. In principle, the continuity equation, momentum equation, equation of state and energy equation - total of six equations - provide the solution of pressure, density, temperature and three velocity components. These equations, however, are coupled with Eq. (1) through the moving boundary condition of  $\dot{X}(t)$ . Thus the fluid motion must be solved with the piston moving at a speed of  $\dot{X}(t)$ .

The initial condition for the flow problem may be assumed to be at rest. Thus, the velocity is zero everywhere. The initial density and pressure in the recoil mechanism is uniform.

After the gun is fired, the boundary condition for the fluid motion requires that the fluid on the recoil rod assumes the recoil velocity  $\dot{X}(t)$  and is at rest on the stationary cylinder surface. Now the orifice cross section must be designed so that the pressure forces,

$F_o$ , created by the throttling of fluid between the two chambers plus other resistance forces,  $F_f$ , is equal to the required design characteristic of the total resistance force  $K(t)$ . At present no such general solution of fluid motion exists even for the simplest recoil mechanism.

We consider a simple fluid dynamic model for the recoil mechanism. This model in many applications does not provide an accurate description of the flow pattern in the recoil mechanism but it provides the first approximate design of the control orifice. This method also provides a basis for further modifications in cases of complex geometries and compressible liquids and gases. We assume that the flow is quasi-steady incompressible flow and the flow is one dimensional. The assumption of a quasi-steady flow is equivalent to the assumption that the flow is instantaneously steady and that the force due to the acceleration and deceleration of fluid in the recoil is negligible. The one dimensional assumption implies that the pressure is uniform in the radial section of the mechanism. The resistance force offered by the orifice in Eq. (1) thus may be written as

$$F_o(t) = K(t) - (K_a + K_f + K_p) = P_1 A_1 - P_2 A_2$$

For incompressible type of recoil mechanisms, we have  $A_1 = A_2$  or

$$(P_1 - P_2) = F_o(t)/A_1 \quad (12)$$

The continuity equations for one-dimensional steady incompressible flow is approximately (see Figure 2)

$$A_o U_o = (A_1 + A_o) U_1 \quad (13)$$

Here  $A_o$  and  $A_1$  are respectively the orifice clearance area and orifice surface area facing Chamber (1).  $U_1$  is the average velocity in Chamber (1) relative to orifice velocity. From the boundary condition, we have

$$U_1 = \dot{x}(t) \quad (14)$$

The momentum equation under quasi-steady, one-dimensional assumption may be integrated from the Chamber (1) to the rear end of the orifice as

$$\frac{U_1^2}{2} + \frac{P_1}{\rho} = \frac{U_o^2}{2} + \frac{P_o}{\rho} + \Delta H_f \quad (15)$$

where  $\Delta H_f$  represents the loss of kinetic energy due to viscous friction and, if the flow becomes turbulent, turbulent shear. There are six unknowns,  $P_1$ ,  $P_2$ ,  $P_o$ ,  $U_1$ ,  $U_o$ , and  $A_o$ , in four Eqs. (12), (13), (14) and (15). To facilitate the solution for orifice clearance area  $A_o$ , we assume that the pressure  $P_2$  on the rear orifice surface is

approximately equal to the pressure at the end of orifice  $P_0$  or

$$P_2 \doteq P_0 \quad (16)$$

The reason for adopting this approximation is as follows. As shown in Fig. 2, the one-dimensional approximation is perhaps invalid immediately behind the orifice because from experiments conducted by Chen et al. [7] as shown in Fig. 3 we recognized that the flow always separates at the rear side of orifice except at the start of recoil motion. Therefore, for one-dimensional assumption to remain valid at the end of orifice, the flow should be considered like a jet (see Fig. 3) and separates at the rear end corner of the orifice. Under this condition the pressure in jet portion of the flow will remain approximately  $P_0$ . Thus for no other means of determining the pressure on the rear surface of orifice,  $P_2$ , we equal  $P_2$  to  $P_0$  on the same cross section which is the closest pressure available under one-dimensional assumption.

Furthermore, the loss of kinetic energy due to friction,  $\Delta H_f$ , is normally proportional to the pressure difference  $(P_1 - P_2)/\rho$  or

$$\Delta H_f \sim (P_1 - P_2)/\rho \quad (17)$$

Thus combining Eqs. (13), (14), (15), (16) and (17), the orifice velocity  $U_0$  can be written as

$$U_0 = C_D \sqrt{2(P_1 - P_2) / \left[ 1 - \left( \frac{A_0}{A_1 + A_0} \right)^2 \right] \rho} \quad (18)$$

Here the orifice discharge coefficient  $C_D$  is introduced to account for the frictional loss and also to serve as a correction factor for the assumptions made, namely, one-dimensional quasi-steady flow and the assumptions that lead to Eqs. (16) and (17). More discussions on the coefficient  $C_D$  are given in Section IV.

Now from Eqs. (13) and (14) we also have

$$A_0 = A_1 / \left( \frac{U_0}{\dot{X}} - 1 \right) \quad (19)$$

We thus can solve the orifice clearance area  $A_0$  from Eqs. (18), (19) and (12) as

$$\frac{A_0}{A_1} = \left[ \sqrt{\frac{C_D^2}{\dot{X}^2} \frac{(P_1 - P_2)^2}{\rho} + 1} - 1 \right]^{-1}$$

or



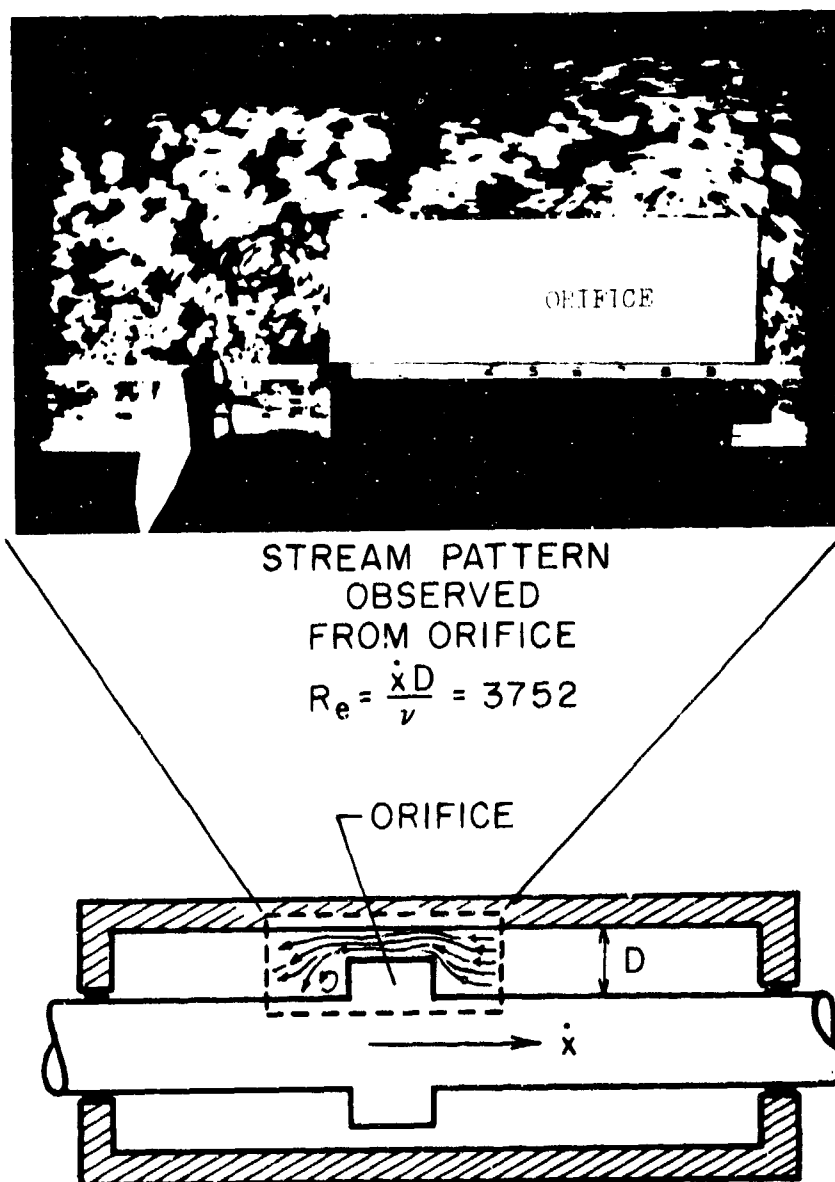


Figure 3. Flow Pattern Near Orifice

$$\frac{A_o}{A_1} = \left[ \sqrt{\frac{C_D^2 F_o(t)^2}{\dot{X}^2 \rho A_1}} + 1 - 1 \right]^{-1} \quad (20)$$

Equation (20) thus provides an approximate way of predicting the orifice clearance area for recoil mechanisms. It should be noted that the orifice area  $A_o$  is a function of orifice surface area  $A_1$ , recoiling speed  $\dot{X}$ , fluid density,  $\rho$ , orifice discharge coefficient,  $C_D$ , and the resistant force  $F_o(t)$  required from the criterion established for the orifice design. Since both  $F_o(t)$  and  $\dot{X}$  are time dependent and the orifice moves with  $\dot{X}$ , the orifice area  $A_o$  must in general vary with the recoil distance  $X$ . The orifice area  $A_o$  can now be predicted if the orifice discharge coefficient  $C_D$  is known.

#### IV. Orifice Discharge Coefficient $C_D$

The orifice discharge coefficient  $C_D$  was originally introduced to account for the pressure loss in a steady flow through an orifice. Customarily, it is treated as a constant. However, in case of recoil mechanisms  $C_D$ , it certainly is not a constant for the following reasons. First the recoil rod starts with zero speed and is accelerated to a high speed flow. Then it decelerates to zero speed and reverses the direction of motion in the counter-recoil motion. In the process the flow starts from laminar motion to turbulent flow and then back to laminar motion again. The instantaneous Reynolds number based on upstream gap and average velocity may vary from zero to an order of  $10^4$ . The orifice discharge coefficient certainly should vary since Reynolds number varies over such a wide range. In addition, in order to create a desirable characteristic of the recoil motion the orifice clearance area  $A_o$  must be designed to vary. In summary, the orifice coefficient  $C_D$  should be dependent of

- A. Geometry of orifice and shape of Chambers (1) and (2).
- B. Time variable.
- C. Laminar and turbulent phenomena.
- D. The average velocity across the orifice and viscosity and linear dimensions of orifice, or the Reynolds number.
- E. Fluid compressibility.

The precise value of orifice discharge coefficient  $C_D$  for recoil mechanisms is not available to date since design of an orifice varies from one gun to another. Even for the same weapon, if a different charge is used the orifice coefficient will be different because different recoil forces produce different recoiling speeds. Although as a rough approximation, constant values of  $C_D$ , between 0.7 ~ 0.9, had been used [3,4] but the resulting resistance forces were not satisfactory. In addition, the resistance force generated by the recoil mechanism was shown by Nerdahl and Frantz [5] and Coberly and Frantz [6] to be sensitive to the change of the value of orifice discharge coefficient. Therefore, a variable orifice discharge coefficient should be used whenever the variable value of  $C_D$  is available. To date

neither experimental correlation nor theoretical prediction for variable  $C_D$  is yet available. Chen and Macagno [7] are currently attempting to solve the detail of fluid motion and thereby to predict the value of  $C_D$  from the numerically prediction pressure distribution. While the progress is being made we suggest the following temporary measure. To determine the variable orifice discharge coefficient, we propose that the value of variable orifice discharge coefficient at any instance during the recoil be the value for steady flow with the flow Reynolds number,  $UD/\nu$ , corresponding to the instantaneous Reynolds number  $\dot{X}D/\nu$ . Here  $D$  is the upstream characteristic length, the diameter in case of tube flow and the gap width in case of annular flow.  $U$  is the average velocity upstream of the orifice. This assumption is consistent with the quasi-steady assumption made in deriving Eq. (20).

Figure 4 shows the experimental correlation [8] of the orifice discharge coefficient,  $C_D$ , versus steady flow Reynolds number  $UD/\nu$  as defined by Eq. (18). In this case  $A_0$  is the orifice hole area  $\pi d^2/4$  and  $(A_1 + A_0)$  is the upstream area or  $\pi D^2/4$ . Although the geometry of orifice in Fig. 4 differs from the one in Fig. 2 for recoil mechanisms, Fig. 4 does illustrate the qualitative variation of orifice discharge coefficient with Reynolds number as well as the geometry. In Fig. 4,  $L$  is the thickness of the orifice. The ratio  $L/D$  seems to have an appreciable effect on  $C_D$  value. For a given Reynolds number  $C_D$  value in general increases with  $L/D$  ratio except at a large Reynolds number over  $10^3$ .

The flow over Reynolds number of  $10^3$  is likely to be turbulent in some region of the flow. Turbulence is likely to be present near both orifice front and rear extruding corners and behind the orifice. The flow near the orifice is very complicated. The flow may separate at the front corner and reattach and then separate at the rear corner again. Even when the upstream flow is steady the separation phenomena may still be unsteady. That is the separation bubble may grow to a certain size and then separate from the corner and is carried downstream. A new separation bubble may follow to form at the front corner again and the phenomenon repeats to give a definite periodic separation. The above mentioned phenomenon was observed by Chen and Macagno [7] in simulation of recoil motion with a similar configuration as shown Fig. 2 at Reynolds number of 3752 based on upstream gap and velocity.

Examining Fig. 4, we may conclude that the orifice discharge coefficient  $C_D$  is less sensitive to the ratio of  $d/D$  in the range 0.04 to 0.25 than to the ratio of  $L/D$ . This has a favorable implication that the  $C_D$  is less dependent on the variable orifice clearance area  $A_0$  required in recoil mechanisms since the ratio  $A_0/(A_0 + A)$  is similar to  $(d/D)^2$  in Fig. 4. This implication will lessen the complication in determining  $C_D$  for recoil mechanism. The variable orifice coefficient  $C_D$  to be used in recoil mechanism is then a strong function of instantaneous Reynolds number and the ratio of orifice thickness to the upstream gap or  $L/D$ .

When the fluid is compressible the orifice coefficient should be modified. This is discussed also in the report by Chen and Macagno [7].

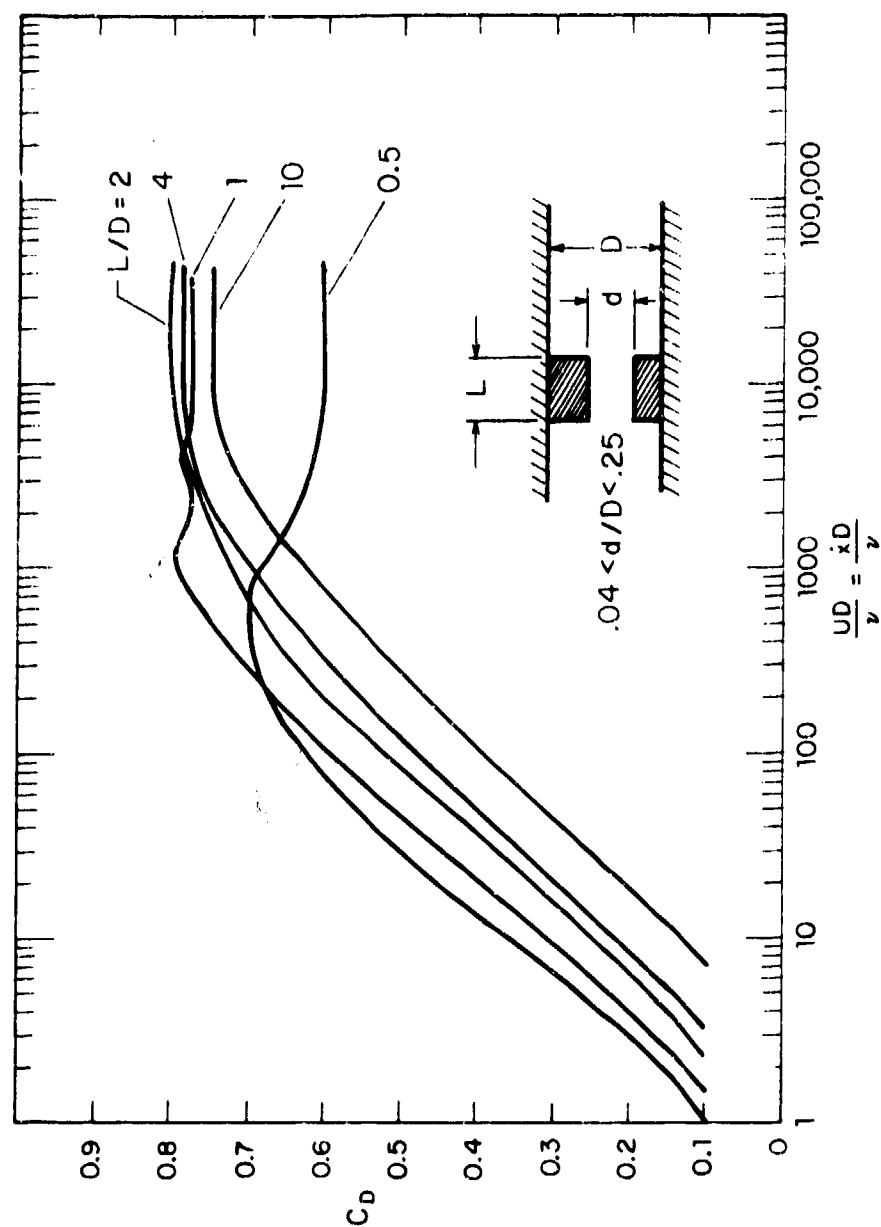


Figure 4. Orifice Coefficient vs. Reynolds Number

\*Chen, Macagno, Chang & Lin

## V. Conclusion and Suggestion

In this paper we show that if the resistance force offered by recoil mechanism is defined, for example, a trapezoidal function in time, then a criterion for orifice design may be reduced from the equation of motion for recoil mechanism. The orifice clearance area  $A_0$  may then be approximately predicted from the quasi-steady one dimensional analysis for incompressible flow. The orifice discharge coefficient,  $C_D$ , is then defined and needed for experimental correlation for determination of orifice area,  $A_0$ , which in general varies with recoil distance. A variable orifice discharge coefficient,  $C_D$ , is proposed and, as a temporary measure, is taken as that of the steady flow with the instantaneous Reynolds number  $\dot{X}D/\nu$  replacing the steady Reynolds number.

For future design of recoil mechanism, unsteady two dimensional analysis of flow motion is proposed so that detail and precise pressure distribution on both sides of the orifice surface may be predicted. Such an analysis may be made quite versatile in that orifice geometry, recoil speed and distance can all be made as input parameters.

## References

- [1] Arora, J. S. and Haug, E. J., Jr., "A Guide to Design of Artillery Recoil Mechanisms," Technical Report, Materials Division, College of Engineering, The University of Iowa, Iowa City, IA., July 1977.
- [2] Coberly, R. H., "Miscellaneous Artillery Problems," RIA Technical Note, No. 68-288, U. S. Army Weapons Command, Rock Island Arsenal, Rock Island, Illinois, 1968, pp. 1-7.
- [3] Moody, B., "Mathematical Computer Simulation of Compressible Fluid Behavior in Recoil Application (Orifice Design)," Army Weapons Command Technical Note SWERR-T-TTN-2-72, April 1972.
- [4] Frantz, J. W., "Design of New Control Orifices for the M109 E1 155 MM Self-Propelled Howitzer," Technical Report RE-71-9, Science and Technology Laboratory, U. S. Army Weapons Command, March 1971.
- [5] Nerdahl, M. C. and Frantz, J. W., "Modeling Effective Fluid Compressibility in a Pateaux Recoil Mechanism," Artillery Weapons Systems Div., SWERR-TR-72-34, Rock Island Arsenal, June 1972.
- [6] Coberly R. H. and Frantz, J. W., "First Approximation of Fluid Flow in Recoil System Specifically Applied to the XM37 Recoil Mechanism," Technical Report No. 16-65, Research and Engineering Division, Rock Island Arsenal, November 1965.

\*Chen, Macagno, Chang & Lin

- [7] Chen, C. J. and Macagno, E., "Fluid and Thermodynamic Characteristics of Compressible Recoil Mechanism," Technical Report, Energy Division, College of Engineering, The University of Iowa, Iowa City, IA., December 1977.
- [8] Lichtarowitz, A, Duggins, R. K. and Markland, E., "Discharge Coefficients for Incompressible Non-Cavitating Flow Through Long Orifice," Journal of Mechanical Engineering Science, Vol. 7, No. 2, 1965, pp. 210-219.

GARDNER

**TITLE: Experimental Design for Evaluating the Dynamics of  
Soil/Mount Interaction**

The difficulties of adequately designing experiments to evaluate the dynamics of soil/mount interactions for modern weapons are discussed. The design of field tests are complicated by the variable operational and environmental conditions that have an effect on weapon performance.

Obviously, what is needed are very carefully controlled laboratory experiments where all the factors effecting the dynamics of soil/mount interaction and the performance of weapon systems can be held constant or varied at the will of the experimenter. Physical simulation technology can be used to provide a firing test fixture that has the same mounting flexibility as the soil. Such a simulator can be constructed to withstand repeated firings and to fit inside a laboratory enclosure.

In any type of laboratory test the question arises as to how carefully does the test replicate actual field conditions. The answer, also discussed in the paper, is to conduct a series of experiments in which the dynamic impedance and the results of firing tests are carefully compared between field and laboratory tests.

**PRESENT ASSIGNMENT:** Chief of Computer Instrumentation Branch, Technical Services Directorate, Army Research and Development Command, Dover, New Jersey 1977-

**PAST EXPERIENCE:** Twenty-seven other years of professional experience including Chief, Aircraft Weapons Laboratory, Army Weapons Command, Rock Island, Illinois, 1968-1977.

**DEGREES HELD:** Bachelor of Science, UCLA, Los Angeles, California, 1951; Master of Science, Golden State University, Los Angeles, California, 1953; Doctor of Science, Golden State University, Los Angeles, California, 1954; Master of Science, Augustana College, Rock Island, Illinois, 1977.

## EXPERIMENTAL DESIGN FOR EVALUATING THE DYNAMICS OF SOIL/MOUNT INTERACTION

LEONARD B. GARDNER, DR.  
US ARMY ARMAMENT RESEARCH AND DEVELOPMENT COMMAND  
DOVER, N. J. 07801

### I. Historical Background

The only effort to develop physical simulation as a technology that can replace a significant number of weapon firing field tests and that facilitates the replication of such field tests under controlled laboratory conditions began in the 1960's as follows.

About this time, the influence of mounting flexibility on weapon operation of helicopter and armored vehicle weapon systems became apparent. The M73 Machine Gun is an example of the class of weapons that did not satisfactorily operate from either a very flexible or a very rigid mount. The effects of mounting flexibility were particularly apparent when the firing rate of the weapon approached the natural frequency of the weapon mount thus forming a resonance condition.

The effects of weapon mount flexibility were first examined by means of theoretical analyses performed at Springfield Armory. Later, the concept of simulation testing was considered as a means by which, without resorting to field tests, experimental firing data regarding mounting sensitivity could be obtained and used to validate the theoretical analyses. This testing technique was envisioned to require less time and to be more economical than conventional field testing. The objectives of simulation testing were as follows:

1. Provide a laboratory facility for validating theoretical analyses of weapon performance by means of carefully controlled experimental firing tests under variable but known mounting impedances.
2. Provide a means for conducting Engineering Design Tests (EDT) of Weapons with utilizing field testing, thereby reducing logistics.

The simulation facility envisioned at that time included the latest applications of engineering sciences for live, full-scale, firing of small and medium caliber weapons. The facility consisted of a one- and six-degree- of-freedom mounts that could re-



present human/ground, ground/vehicle, and air/vehicle mounting characteristics. It provided realistic forcing functions representative of the dynamic conditions of a tactical environment that surrounds weapons, fire control equipment, and accessories.

Specifications were then written for a helicopter gun mount simulator having response in three translational and three rotational degrees-of-freedom. About this time, a proposal in which a suitable device was described based on an extension of the concept for a motion simulator built for United Aircraft Corporation, Franklin Institute Research Laboratories was received. A Determination and Findings signed in December 1969 gave approval to negotiate an individual contract which was awarded (DAAF001-70-C-0406) for \$220,000 on 30 December 1969. The initial phase of this work consisted of a supporting pillar and the basic structure which could be thought of as a holding fixture for the weapon system under test. A second phase effort consisted of the "activation" of the simulator so that the several actuators would be positioned by computer control, the vibration induced into a field-operable weapon system would add those vibrational effects, since the actual boom had to be removed when the helicopter was mounted on the simulator. This was a "tall order" considering that the helicopter/tank had to respond as it would in field operation with an operable stability augmentation system, weapons had to fire from the helicopter/tank mounted on the simulator. The simulator was rather large, consisting of a 16K lb. upper fork, a 30K lb. gimbal, and a 90K lb. support tower. This simulator was installed over several months during the summer of 1973.

Now that the Small Arms mission has been transferred to Rock Island the increased logistics associated with RD personnel at Dover being involved in simulator tests at Rock Island is untenable. Consequently, a five year plan has been conceived whereby the simulation facility at Rock Island will be phased out and the Army Armament Development Testing Simulation Facility for weapon systems will be located at Dover. Only the helicopter gun mount simulator poses special problems, but, since it was assembled on site from component parts, it can be disassembled and then shipped. The support pillar and reaction mass would not be removed.

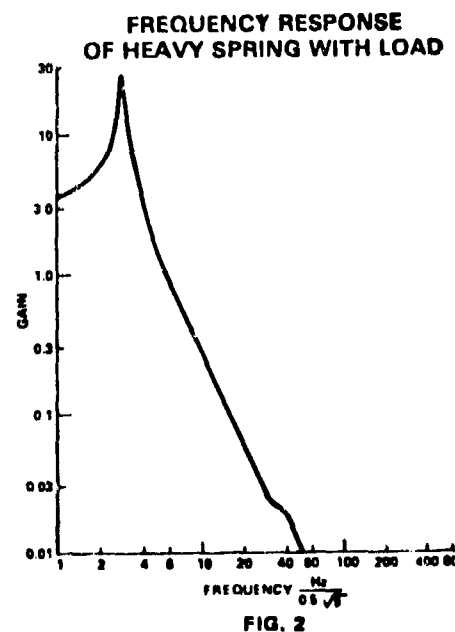
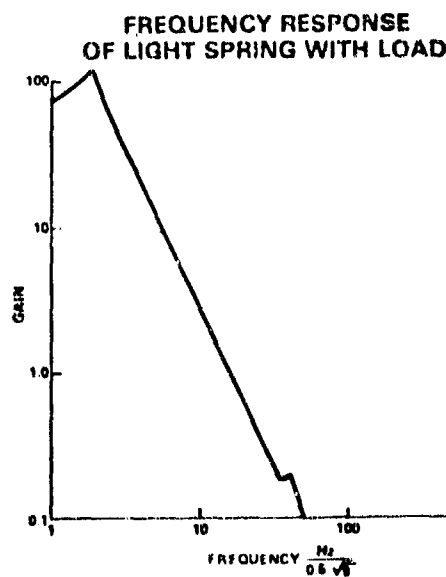
In 1975 personnel from Franklin Institute Laboratories installed automated controls for adjusting the spring rate and damping ration of the six-degree-of-freedom simulator and in 1976/7 the programmable tail-boom simulator-sub-system was installed. In the completed simulator, the triangular actuator pressure-control was automated to maintain a nearby constant vehicle position in somewhat the same manner that a stability aug-

mentation system operates in a real vehicle when a burst is fired from an automatic weapon. The two positioning subsystems in the original simulator were modified to incorporate programmable motion associated with the weapon system and about the nominal pitch-axis of a combat vehicle gunners station. Additional capabilities to replicate engine and rotor vibrations were also added and flexibility of the suspension more nearly replicated the flexibility of a hovering helicopter. After these installations were completed, another series of flight tests were conducted by means of which the simulators were partially validated. Additional mobilization tests still continue at this present date.

As the work continued to be developed, TAARADCOM has become interested in a tank simulator from which weapons could be fired. Discussions concerning such a device have been held between personnel of that organization and those from Reine Metale (in the Federal Republic of Germany) who have developed a tank motion simulator. Although there are many other motion simulators in use or being developed by various DOD organizations these are the only motion simulators known that can also resist the recoil forces of medium caliber weapons.

## II. Experimental Data

The Hispano Suiza 20MM Automatic Gun XM-139, with its recoil adaptor, mounted on the One-Degree-Of-Freedom Variable Flexibility Mount, was simulated on the analogue portion of the EIA 8812 Hybrid Analogue Computer located at Picatinny Arsenal, Dover, New



Jersey. The ODOFVFM consists of a firing platform, to hold the weapon, that is supported by two leaf springs. A hydraulically supported frame can be positioned anywhere along the springs. This frame contains pressure pads clamping the springs to a solid frame bolted to a reaction mass thus proving an adjustable spring rate. Adjustable dash-pot dampers are located between the firing platform and the frame to provide variable damping ratio. The spring may be considered as a vibrating beam. The equation of the beam was solved to find the frequency response of the mount (including the firing platform) under two conditions of spring rate: 18 lb/in and  $14.3 \times 10$  lb/in. The frequency response for the light spring mount with the load of the firing platform is shown in Figure 1. The natural frequency found from this plot is about  $1.08 \text{ Hz}/0.5\sqrt{g}$  and there are no significant higher frequency responses that are apparent. The factor  $1.0/0.5\sqrt{g}$ , where  $g$  is the gravitational constant, enters into the frequency term because weight instead of mass was used in the spring equation and remembering that  $1/g$  is directly proportional to the square of the frequency. The 0.5 part of this term was a convenient scaling factor. From these data, it appears the transfer functions of the simulator has a pair of complex zeros at  $19.8 \text{ Hz}/0.5\sqrt{g}$  and two pairs of complex poles at  $1.02 \text{ Hz}/0.5\sqrt{g}$  and  $22.7 \text{ Hz}/0.5\sqrt{g}$ , respectively. From this data it is possible to evaluate the constant of the transfer function as 2.28 and to estimate the damping constants for all these frequencies to be 0.1. In the case of the heavy spring, only one significant resonant peak was observed at  $2.3 \text{ Hz}/0.5\sqrt{g}$  as is seen in Figure 2. The constant was calculated to be  $1.147 \times 10$  and the damping constant was estimated again to be 0.1. The mechanical impedance  $H(S)$  of the mount at these two spring rates was estimated for the light spring and

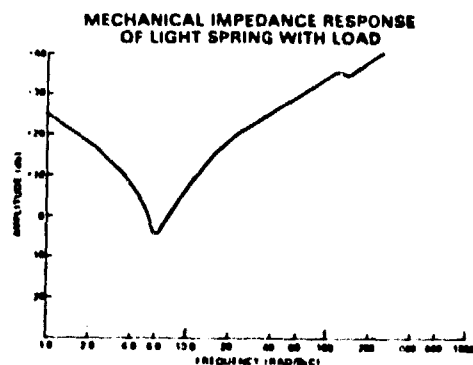


FIG. 3

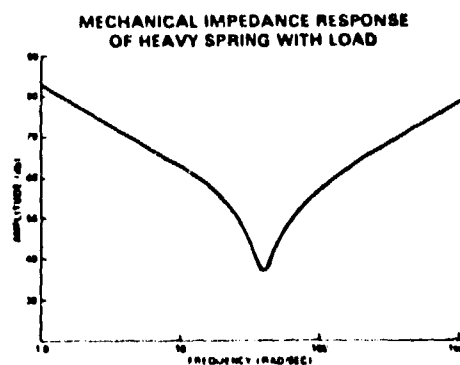


FIG. 4

for the heavy spring. Frequency plots of these mechanical impedances are shown in Figures 3 and 4, respectively. From these figures, it is seen that most of the energy was transferred between the weapon and the mount if the fundamental frequency of this energy (i.e., firing rate) is between 6 and 40 radians/sec (1 and 7 Hz). The purpose of selecting the lighter spring rate for the above analyses was to examine possible higher modes of vibration in the simulator that could impair replication of field test data. As may be seen in Figure 1 and 2 there is a small high frequency resonance but the magnitude about 1/100 that of the main resonance. Since, the magnitude of the higher resonance is so small, the effect of high modes of vibration is negligible. The purpose of selecting the higher spring  $14.3 \times 10$  lb/in was because it approximated some test data we had on the soil-mount dynamics of a lightly emplaced howitzer. The 20MM HS weapon was still used because it was not possible to place a cannon tube on this simulator. We do believe that the mechanical impedance shown in Figure 4 represents an approximation to the soil-mount dynamics of a light howitzer. It illustrates that rapid firing rates become increasingly destructive of the mount. This may be likened to the familiar problem of dynamic loading.

### III. A Modern Simulation Facility

Let's go back and re-examine some of the details of these several equipments. The one-degree-of freedom variable flexibility gun mount simulator is designed to support firing weapons weighing less than 350 pounds and having a muzzle energy of less than 120,000 ft-lb and a muzzle impulse of less than 70 lb-sec. The simulation range has been approved for the firing of no larger than 30mm Class III ammunition or 40mm Class I grenades. The simulator is passive in the sense that it is designed to respond to the recoil forces of the weapon as would an actual mount. The flexibility, characterized by a spring rate and a damping ratio, is readily adjustable by means of a closed loop servocontrol in such a manner that the height of the weapon from the ground is unchanged. The static spring rate is adjustable between 25 lb/in. and 85,000 lb/in. with four sets of leaf springs. The damping ratio is adjustable from 0.05 to 0.8; however, above 0.1 the damping is nonlinear. This simulator includes a firing platform attached to the top ends of the leaf springs with one degree of freedom in the direction of the line of fire. The bottom ends of the leaf springs are bolted to a steel outer structure anchored to a concrete inertia mass. Stiffness of the leaf springs is adjusted by moving of the frame assembly by means of a servocontrolled hydraulic actuator. Hydraulically operate pressure pads are provided to clamp the moving frame assembly to the outer structure at any desired position, and another set of pads are used to clamp the springs to

the moving frame. A change in the cantilevered length of the leaf springs changes the stiffness of the mount. The damping of the leaf springs is accomplished by means of hydraulic dampers and a servocontroller. The piston rods of the two dampers are attached to the leaf springs and the cylinders of these dampers are attached to the outer structure. The damping system is located on the same axis as the gun mount table. At the interconnection of the damper chambers, a precision-ground pin is controlled by an electrohydraulic servosystem.

With this simulator, the flexibility and the damping of the weapon mount may be varied by approximately an order of magnitude within 30 seconds. Four different sets of leaf springs are available by which variation is possible in mount flexibility by over three orders of magnitude. These leaf springs may be changed and the weapon system remounted for additional testing within 2-1/2 hours.

The data acquisition and reduction system of the simulation facility allows processing of information from weapon tests. Transducers are available for measuring a wide range of parameters including pressure, displacement, velocity, acceleration, force, temperature and strain. This system is comprised of 18 units of signal conditioning equipment, a special calibrator under computer control, two analog tape transports, a multiplexer, an analog-to-digital converter, a time code generator, a closed loop TV system and a dedicated digital computer (including digital tape transport, magnetic disk, card reader/punch, line printer and plotter). The special calibrator provides a quick and simple method of system calibration. When in operation, up to 14 transducers are individually disconnected and different steps of known signal level are injected into the system. Three types of calibration may be performed: bridge or charge in five steps and voltage in eight steps. In addition, the system was designed to provide for future expansion. Space exists for additional signal conditioning equipment. The number of recording channels may be increased from 14 to 28 merely by the purchase of additional plug-in electronics and can be increased to 56 channels by some further plug-in additions to the present tape units. In real time, the highest data sampling rate is 20KHz. This would allow for the analysis of a single channel of 4KHz data. However, if 13 channels of data are acquired in real time, the highest frequency component that could be analyzed in each channel is approximately 300Hz. First by the recording of data at 120 ips and then by reproducing the data at 1-7/8 ips, a time base expansion of 64 is realized by which 13 channels of 20KHz data may be analyzed by means of a playback program. In the playback mode, individual channels may be sampled for analysis; thus, 240KHz could be analyzed. At present, the maximum data

bandwidth is limited to 40KHz by the characteristics of the present FM amplifiers.

By means of computer programs, data may be reduced to engineering units. Also, various channels of data may be added or subtracted, and spectral analysis performed. These data, recorded in a standard format, may then be analyzed at larger computer facilities at which more complete analysis programs can be effectively used.

The six-degree-of-freedom simulator consists of a mounting platform suspended by means of six actuators from the gimbal system and attached to a support tower. The support tower is made from 1-inch steel plate and is 6-feet by 10-feet on the base and 16-feet high. It is filled with approximately 30 tons of sand to form part of the reaction mass and it is securely anchored to a 2500 cubic foot concrete base. The purpose of the actuators is to simulate the restoring forces that affect a body under the firing conditions of a mounted weapon system. The gimbal system weighs 15 tons, rotates in yaw, and is also pivoted to permit rotation in pitch by means of an external actuator. Thus, counter-rotation of the suspension is possible in the opposite direction that the weapons are rotated so that the line of fire will remain directed toward a fixed target. The gimbal system is supported by a steel fork structure, shown in Figure 5c, and weighs a total of 30 tons. The building size constrains the motion of the UH-1 helicopter to a pitch of 18 degrees down and 40 degrees up with yaw plus or minus 35 degrees; and sections of the AH-56, with some modification, can be supported with pitch limited between 0 degrees and 20 degrees up and yaw limited to plus or minus 10 degrees. The simulator will support sections of helicopter fuselages and ring turrets that weigh up to 18,000 pounds and that are no larger than eight feet from the bottom of the test item to where it is attached to the mounting platform. The suspension actuators of the system are capable of a stroke of 10 inches with an operating range of plus or minus three inches about center of the actuator stroke and are designed as simple spring damper systems. Oil pressure, which controls the mount flexibility, is adjusted by means of a set of valves located on the operating console. The orifice area between each pair of accumulators, by which the damping is controlled, is adjusted by means of valves located above the mounting platform of the simulator.

III. Simulation for Artillery Acceptance Testing

A simulator Task Group for the acceptance testing of artillery weapons was established by the Commanding General of the Army Weapons Command in July 1969 because of the interest being developed by higher headquarters in this subject. This Group was formed to be responsive to the request of the Chief of Staff of

the Army for information regarding improvements that were possible in the present acceptance testing of artillery weapons. The Group reviewed and evaluated current test methods, identified new projects with the potential for optimization of testing methods, and developed a five year plan with appropriate priorities for the exploitation of improved testing technology. This study identified a 5.1M\$ cost savings over 5 years over and above costs for equipment, facilities, and implementation. Several projects discussed below were considered viable for artillery acceptance testing and are those that could also be of benefit to the R&D community if performed at ARRADCOM, Dover, NJ.

An Artillery Carriage Firing Load Simulator. The concept entails a hydraulic simulator by which repetitive impulses from an actuator attached to the carriage duplicating the trunnion that during field operation of the weapon is applied to the carriage, trails, and support assemblies. The facility is intended primarily to disclose design weaknesses in structures that are too complex for a realistic theoretical stress analysis. Such determinations can presently be made only through the expensive firing of thousands of rounds either during Engineering Design Testing (EDT) or during Engineering Tests and Service Tests (ET/ST). When deficiencies are found during ET/ST, many costs in addition to the test costs may be incurred as a result of program delays while system modifications are accomplished. Other concrete benefits would derive from the provided capability to develop artillery carriages without the delays imposed by slippage in the development of the other components of a weapon.

This is a follow-on effort to extend the capabilities of the helicopter simulator when it is used as a combat vehicle gun turret simulator. It will be capable of mounting the M150 Recoil Mechanism on the Mechanical Recoil Simulator in somewhat the same manner by which the M158 Recoil Mechanism is mounted. The project includes the necessary testing and correlation analysis to verify the adequacy of the simulation that is achieved through the modification. Future Recoil Simulator capabilities exceeding those that are attainable through modification of existing machines, may already be predictable as a result of recent developments in soft-recoil or fire-out-of-battery and fire-on-the-move. If the genesis of recoil simulators continues, simulation continues to be a prerequisite for qualification of the machines as acceptance-testing devices, then a continual increase in the size and complexity of the simulators may also be predictable. However, if recent scientific advances can be exploited, the need for complex simulators may be alleviated. To provide the necessary perspective, it must be observed that at least in principle even the best of the existing simulators has some inherent deficiencies. Mechanical impedance measuring techniques may be used

in a recoil mechanism proof test simulator. This device makes use of shock and vibration analysis principles that, if successfully applied to artillery weapons, would eliminate the necessity for the generation of a precise velocity-time curve in the simulation testing of recoil mechanisms, thus greatly simplifying the simulators. Mechanical impedance analysis is based on the hypothesis that the differential equations of motion for a linear mechanical system can be expressed in terms of the driving force and the acceleration, the velocity, or the displacement of elements of the system. Conversely, if the driving force and one or more of the other parameters can be measured, the measurements may be used to uniquely define the response of the system. The relationship between the driving force and the motion of a system is referred to as mechanical impedance or the inverse thereof, which is called the mobility. Mechanical impedance methods allow a complete analysis of the response of each part of a complex physical system. But, more usefully, the methods include a "black box" concept whereby the forces and motions at a few points of major interest in a system may be used to characterize the system without a complete analysis of the details. These methods define the response of such complicated systems that a complete analysis would otherwise be impractical. Traditionally, the analysis by mechanical impedance methods has been accomplished through the acquisition of response data from a system under sinusoidal excitation. Newer techniques now permit equivalent evaluation of a system under impulsive loading. This technique is called spectrum analysis and is accomplished through equipment known as Real-Time Spectrum Analyzer that automatically reduces the recorded test data. When a weapon is fired, impulsive forces are generated in the mechanical system. These impulses are broken down into a combination of sinewave frequencies and amplitudes. When the firing forces have been thus analyzed, their important characteristics can be synthesized and equivalent forcing functions can be applied for testing weapons or components through the use of electromechanical or electrohydraulic excitation without the weapon being actually fired.

The spectral analysis would completely characterize the quality and performance of artillery recoil mechanisms with the exception of their safety and leakage factors under peak recoil velocities. However, it is believed that the latter aspects can be assured through development of simple hydrostatic test.

The firing simulator device entails a cannon-breech testing-device powered by a propellant charge in somewhat the same manner conceived by Watervliet for the pyrotechnic cannon-breech tester. However, major differences exist between the objectives, hence the features, of the two concepts. In one concept, the breech closure is bored for a shaft that at one end



carries an external flywheel to simulate the moment of inertia of an artillery shell and at the inner chamber end has a pre-engraved disc to engage the cannon-tube rifling or a helical simulation of it. Firing of a power cartridge in the breech chamber accelerates the disc, thus producing torsional rotating-band forces as well as the pressure stresses of proof-firing on the tested breech mechanism and the stub tube. In the second concept, the breechblock is bored for a pretorque insert for simulation of the rotating band torque and driving-edge force, while pressure is again generated by a power cartridge. The concept of both devices is based on a relatively low peak-velocity (50 feet per second) of the forward disc while the torque and driving-edge force are distributed over the length of rifling in the stub tube.

These devices simulate the gas-pressure loading, the motion of the gas-pressure front, the approximate rise-time and duration of gas pressure, the chemical environment (corrosion fatigue conditions), and the net driving-edge pressure exerted by a moving shell. Precise simulation is not achieved for the exact temperature variations, the erosion conditions, the rotating-band engraving loads, the radial band pressure (if in excess of the chamber pressure), the bilateral driving edge pressure, or ballooning of an artillery shell in the tube. Despite the latter omissions, this simulator provides most realistic simulation of test-firing that is presently contemplated. However, owing to the necessity for a special (bored) breechblock, the device is viewed as an engineering development tool rather than as an acceptance-testing device.

There are other devices that could be used for a firing simulator. In one such device, the weapon trails are lifted to simulate evaluation firing. In another current concept, the firing-impulse simulator is mounted on a gantry so that the trails may remain horizontal while the simulator tilts to accommodate the cannon tube in actual elevation. Hydraulic, pneumatic and steam power are currently viewed as strong competitors for eventual selection of an actuation source because these are more amenable to automatic control and might minimize the problems with noise, air pollution, and erosion of operating parts that must be accommodated in propellant-actuated systems. Preliminary studies indicate that a pump or compressor capacity of about 200 horsepower, or a steam boiler capacity of about 10,000 pounds per hour, would be required to produce the 75-inch recoil of a 155mm Howitzer at a simulated firing rate of 5 rounds per minute in the contemplated system. Another concept for an actuation system makes use of a heavy ram accelerated over a relatively long period of time until, at the proper level of kinetic energy,

the ram impacts an impulse programmer comprising of a compressible-liquid-filled elastomer cartridge in the gun tube. The impulse programmer or liquid spring would be designed to transmit the energy of the ram to the gun tube at a rate similar to the one which the breech-force develops during live-firing. The method has been used in a complete-weapon firing-simulator for the endurance testing of the 30mm, XM140, Aircraft Cannon, thus the problems are expected to be mostly those associated with the scaling of effects. The development of an endurance-testing simulator based on this concept is viewed as a relatively straightforward task in engineering design, but a certain amount of innovation would be required to make the system useful for acceptance testing.

Acoustic signatures of cannon tubes can be used to determine structural weakness. The sound emitted by a freely suspended structural member when impacted has long served as a qualitative measure of the homogeneity of the member as in the instance where the tone of a bell may indicate the presence of a crack. Through utilization of the bell-ringing technique, Frankford Arsenal successfully developed equipment for the detection of defective 81mm mortar shell-bodies. The extension of this technology to the acceptance testing of cannon tubes has been proposed in which cannon-tubes will be suspended in the manner of a bell. A hammer or clapper will be provided to strike the tube with a controlled reproducible impact. A microphone or other appropriate transducer will be located in proximity to the tube (and probably opposite to the point of impact) for the acquisition of the acoustic signals that are generated by the clapper. The amplified and recorded sonic response of the tube will be analyzed and metallurgical tests will be conducted on the specimen tubes to determine the level of defects that can be acoustically detected.

#### IV. Validating Physical Simulation

The first step in validating a simulator is to formulate a mathematical model. By means of this model, the performance of the simulator may be understood. Such models are validated experimentally by the firing of a weapon from the simulator, the measurement of the performance characteristics of the weapon during this firing, and the comparison of these data with values predicted by the mathematical model. A validated mathematical model must exist for the weapon selected for this test. Weapon models are validated in a similar manner with firing tests performed with rigidly mounted weapons. This mathematical model is then coupled to the model proposed for the simulator. Since the model for the weapon has already been validated, the only differences between experimental data obtained from firing on the simulator and predicted data obtained from the coupled models must be

caused by inaccuracies in the model of the simulator. This model is then adjusted until a favorable comparison without any serious inaccuracy is achieved.

Two mathematical models of the one-degree-of-freedom simulator have been studied. One contained a continuous model of a cantilever beam, and the other a discrete model of the same beam. This beam provides the variable spring rate for the simulated mount. These models were used to obtain the mechanical impedance (magnitude and phase angle) of the mount which was then compared and adjusted as necessary. A suitable discrete model of the springs is on an analog computer. The model of the springs was combined with models of other essential components of the simulator, for example, the dampers, until a complete model of the simulator formulated.

For validation purposes, the 20mm Automatic Gun (M139) was test fired from the simulator because a mathematical model of this weapon was available. The data from the previous test firing was compared with the data from the combined models for the weapon and the simulator. Sensitivity studies were performed with this model to obtain a more nearly accurate model for the simulator. The model, in conjunction with the mechanical impedance studies of the mount discussed below, provided the information required to adjust the parameters of the simulator so that its mechanical impedance matched that of several field mounts.

Once the impedance of the field mount was obtained, a determination was made of the initial settings of flexibility and damping that must be made on the simulator for the first approximation, the impedance of the simulated mount was determined and compared to that obtained from the field mount. When the impedances were not in agreement, the required adjustments in flexibility, damping and mass of the one-degree-of-freedom gun mount simulator was systematically made to correct the impedance toward agreement with a field mount. Once the impedance techniques were worked out, a study was conducted by which a catalog of variation of mechanical impedance profiles was obtained. By means of tabular data presented in the catalog, the controls of the simulator could be quickly set to represent any particular type of weapon mount. Also, by means of these data, engineers were able to readily determine which of several mounts were suitable for particular weapon applications.

The comparison of the simulator performance during firing of the XM-30 armament subsystem mounted on a section of the UH-1 helicopter suspended from the simulator was compared with actual flight test data obtained by personnel of the Aviation Systems Command.

The method of analysis was similar to that used for the one-degree-of-freedom simulator except that a mathematical model was not attempted. This was because the structure of helicopters is far from rigid with many complex nodes and several sources of vibration. Thus, the analysis was more of a comparison of actual flight test data including firing weapons with the performance of the simulator. Forces and accelerations (that were integrated to obtain velocities) were measured at several "hard-points" of the helicopter and at the points of weapon attachment. From these data crude determinations of mechanical impedance and transfer functions were made. An analog computer program was written based upon the transfer functions together with a driving function corresponding to the recoil force of the weapons. The constants associated with the transfer functions were adjusted until the response of the computer program closely duplicated the response observed during flight test. The flexibility and damping of the simulator were then adjusted to correspond to constants used in the computer program. Such data represent one set of test conditions out of a possible family. As experience with the use of the simulator grew, so does the set of varified constants that could be used repeatedly. Now it is much easier to determine the desired flexibility and damping for each particular configuration of weapon test. The use of these simulators, while not exactly replacing all field tests, since such are never replicated, could replace a majority of them with the advantages of controlled test conditions, greater range-time utilization, reduced cost, and improved logistics.

#### V. Army Armament Simulation Center

A center for the physical simulation of weapon firing conditions is contemplated to be constructed at Dover, NJ to support the research and development requirements of ARRADCOM. The weapon systems now being developed by ARRADCOM fall into four major categories: Land warfare, air defense, miscellaneous artillery and small caliber arms. Typical of these are the following:

XM-1 Tank - 105mm/120mm gun; fire on-the-move capability

IFV/ITV - 25mm automatic cannon, TOW anti-tank missile system and small arms; stabilization system.

VIPER - light anti-tank assault weapon

YAH-64 Helicopter - 30mm chain gun, 2.75 inch rockets

COPPERHEAD - 155 mm semiactive laser guided howitzer round.

PATRIOT - Air defense TVM guidance

#### DIVAD - 35/40mm cannon air defense

In recent years, approximately 200K\$ was spent for a simulation test of VULCAN, a forerunner of DIVAD. Actual flight tests for this work would have cost 10 to 20 times more. Approximately 350K\$ was spent for a simulation test of the MICV with actual tests costing about 1.4 times as much. Simulation testing of combat vehicle hulls could save about 50% for each test. Countless simulation testing of the future rifle, squad automatic weapon system, armor machine gun, automatic grenade launcher, and personal defense weapons have been made at a savings of about 5K\$ per test. In the case of helicopter or tank mounted weapon systems, experience at the Ware Center has shown that simulation testing can save about 50K\$ per test series. Unfortunately, since the mission of ARMCOM was combined into ARRADCOM with the R&D work performed at Dover, the logistic cost increased about 30K\$ over the above saving. All together, when the R&D work was performed at Rock Island, an annual cost savings of 700K\$ was projected in 1975. The one time expenditures of the simulation equipment at the Ware Center was 2.8M\$. Because the equipment only recently became fully operational, the projected cost savings was not fully operational, the projected cost savings was not fully realized and the equipment was just amortized.

The simulation and data reduction equipment at the Ware Center could best be utilized at the new Army Armament Simulation Center at Dover. As such, a large savings in shipping and project engineer travel costs will be realized. Also, the full capability of simulation testing will be realized: the engineers concerned with the test (at Dover) may readily obtain reduced and analyzed test results and modify test conditions between bursts of fire. This is possible because of computer processing and short communication lines.

The Simulation Center could be constructed in a remote section of Picatinny Arsenal that is now used as a short artillery range. It could contain equipment now located at the Ware Center consisting of data reduction equipment, one- and six-degrees-of-freedom simulators and associated equipment (except the support pillar). Franklin Institute Research Laboratories (who designed and fabricated most of the equipment) has estimated the cost of disassembly, crating, moving, and reassembly to be 750K\$ for equipment that is now valued at about 5M\$. Approximately 12 months would be lost during the move. This equipment could be immediately used to support projects concerned with adaptive recoil and stability/control (AH60), high rate mechanisms (AH61), aircraft armament and weapon mount interface (AH19). However, additional new equipment is required to support all of ARRADCOM RD Programs. Included in the FY79 SPE Budget for

the new Simulation Center were the following:

ITEM	ESTIMATED K\$
Mortar Firing Simulator	220
Mechanical Recoil Simulator	510
Breech/Tube Firing Load Simulator	200
Multidegree Stability and Control Simulator	500

Such new equipment could be used to test the XM1 Tank. Col. Apply has suggested its use for initial training of crews in FCM exercises under simulated field conditions. It could be also used to simulate the 105mm bagload operation and to study Tank/Gun/Target interactions. Ltc Solberg has suggested the use of such equipment for RAM studies. The Breech/Tube Simulator could be used in the measurement of pressure curves for the XM198. The Multidegree Simulator could be used to study the interface between the XM230 gun and the Cobra turret. Firing Simulators could be used for wear and erosion hot gas flow studies now being performed in special wind tunnels. The mortar Firing Simulator could evaluate laying, elevation, and setback effects on bare plate design. Additional projects concerned with breech mechanisms and complex loading (AH670), howitzer, scatterable mines, and liquid propellants (AH18) could be more fully supported by physical simulation.

In summary, test and evaluation of weapon systems is a complicated process involving many interacting components and effected by many interacting test conditions. Physical simulation is a useful mechanism for performing tests under conditions that can be made to replicate field conditions. Test by simulation have the advantage of carefully controlling test conditions so that measurements may be more easily repeatable and thereby improve data interpretation. While not replacing DT/ET sequences, simulation technology is cost effective to implement and may be employed to shorten development time. The use of such devices is contemplated in the new Army Armament Simulation Center where the following interfaces in weapon systems will be studied as part of the R&D effort:

- Weapon/Gun Mount
- Gun Mount/Gun Control
- Gun Control/Gun Sight
- Gun Sight/Target
- Target/Weapon
- Weapon/Vehicle
- Vehicle/Gun Mount
- Vehicle/External Force
- Vehicle/Power Plant

Full use will be made of all simulation equipment now at the Ware Center, Rock Island Arsenal. This equipment, having a replacement cost of 5M\$ can be moved to Dover for the Army Armament Center for 0.75M\$. New equipment for the center is estimated to cost about 1.5M\$ and facility cost is estimated to be 2.25M\$. Salary costs associated with the establishment of this center would be about 0.5M\$ for a grand total of 5M\$. An experiment at the Ware Center has shown that physical simulation testing can save between 1.7 and 2M\$/year over the cost of fully instrumented proving ground field tests. Thus the center is cost effective. Location of the center at Dover will place a facility for R&D testing at the location where R&D is being performed, thereby decreasing support costs and increasing utility.

The equipment at this center would be committed to developing better Armament Systems. We are putting simulation technology to work on tomorrows designs - today. Through vision, innovation, and intuitive leaps, testing techniques are being kept abreast of the needs of engineers engaged in development of our country's future armament systems. All of these are achieved and cost effectiveness is realized. Simulation is destined to become a truly fantastic chapter in the future of all test programs.

MONTOYA

TITLE: Counter Recoil System Effects on Projectile  
Velocity in the Naval 5-Inch, 54-Caliber Gun  
ROMAN M. MONTOYA  
Naval Ordnance Station  
Indian Head, Maryland 20640

ABSTRACT:

The paper discusses results of test programs wherein highly instrumented guns were used in an attempt to determine the cause of the historically noted day-to-day effect on ballistics.

These effects appear to be associated with gun mount reaction parameters. The theory is that climatic and gun mount factors cause variations in the work input to the recoil and counter recoil systems. These variations affect the utilization of the available propellant energy, and the resulting kinetic energy of the projectile.

BIOGRAPHY:

PRESENT ASSIGNMENT: Gun Propellant Technologist, Naval Ordnance Station

PAST EXPERIENCE: Manufacture of A-2, and A-3 Polaris casting powders and numerous experimental casting powder formulations 1959-1964. Developed processing techniques to manufacture methyl centralite deterred 20mm propellant resulting in eight fold increase in barrel life of Navy's MK 11 Aircraft Gun, 1965-1966. Designed and developed barrel erosion-reducing propelling charge liners for a number of Navy gun systems, project engineer for 8-Inch Major Caliber Lightweight Gun, developed NC/HMX propellant formulations, designed and developed gun flash suppressant packages, conducted numerous velocity variability studies, 1967-1978.

DEGREES HELD: B.A. Chemical Engineer, New Mexico State University, University Park, New Mexico.



COUNTER RECOIL SYSTEM EFFECTS ON PROJECTILE VELOCITY  
IN THE NAVAL 5-INCH, 54-CALIBER GUN

ROMAN M. MONTOYA, MR.  
NAVAL ORDNANCE STATION  
INDIAN HEAD, MD 20640

INTRODUCTION

The objective of this continuing study is to determine the causes and a possible means of predicting the historically noted day-to-day and hot gun velocity decay effects on gun ballistics. The premise is that day-to-day climatic changes coupled with changing gun mount operating parameters cause variations on the work input level to the recoil and counter recoil systems. These variations, in turn, affect the level of propellant energy available for use as kinetic energy of the projectile.

First, I will present and discuss the data and analyses thereof taken from test programs which led toward the postulation of the stated premise. Subsequently, I will present and discuss test data specifically generated in an effort to prove or disprove the premise.

DISCUSSION

In Figure I we see an example of the random day-to-day effect on mean velocity. Six rounds of each of two master lots were fired on each of five occasions in the same new gun barrel. Charge weights were controlled to within 0.01 pound and bullet weights within 0.1 pound. Note the large and significant mean velocity differential for the third occasion and the nonsignificant differential for the fourth occasion. Had the test for the third occasion been a charge weight verification test, we would have concluded that the charge weight of the NACO master lot had been assessed low; whereas using the data of the fourth occasion we would have concluded that the charge weight had been assessed correctly. This illustrates the importance of finding out the cause of the occasion effect.

MONTTOYA

Figure II shows an example of the hot gun velocity decay effect. The data were generated during gun mount evaluations on the USS TURNER JOY wherein hundreds of rounds were fired each day. Each point is the mean of ten rounds. Outer barrel wall temperatures were measured at several locations on the barrel. There was no significant relationship of barrel temperature and velocity. Also bore measurements showed that this effect was not associated with barrel erosion.

The data from Figure III were also taken from gun mount evaluation tests; that is there was no intent to associate velocity data with counter recoil cylinder wall temperature. These data are also based on ten round means. It would be expected that as the counter recoil gas temperature increases, the static pressure would increase proportionally. If the initial static pressure increases and the change in volume either remains constant or increases (that is the total recoil distance remains constant or increases), the work input to the gas will increase. Theoretically, for the work to remain constant from firing to firing the recoil distance or change in volume must decrease proportionally with an increase in static pressure. The experimental data which I will discuss later shows that the static pressure increases with the number of rounds fired, while the recoil distance is either remaining relatively constant or increasing with the number of rounds fired. Thus, the general trend appears to be that the work input to the gas is increasing with the number of rounds fired resulting in velocity decay. Note the strong negative correlation obtained for the data of Figure III.

There have been some observations where the static pressure initially increases with number of rounds fired and suddenly remains constant. It is felt that changing climatic conditions coupled with changing gun mount temperatures influence heat transfer to the counter recoil gas, the recoil fluid, and to the lubricant used on sliding parts, thereby, affecting the amount of work input to the gas.

For instance in Figure IV we see that as the hydraulic oil used to operate the mount is worked, its temperature increases inputting heat to the counter recoil cylinder causing the gas temperature to increase. Note that here we have a strong positive correlation.

For the USS HEWITT tests shown in Figure V counter recoil gas pressure-time data were taken per my request. Again charge weights and bullet weights were very closely controlled. The pressure-time trace line could only be read to an accuracy of about 25 psi. The change in counter recoil pressure from static to peak was used since it is proportional to the work input to the gas. The data was grouped by means for 25 psi increments and then plotted as shown. A strong negative correlation with velocity was obtained despite the relatively small sample size of the means.

MONTOYA

Figure VI shows that the counter recoil peak pressure for the USS HEWITT tests is increasing with the number of rounds fired as a result of the increasing static pressure.

In Figure VII we see some of the data that were specifically generated to test the premise. These test programs consisted of firing ten rounds in one new gun barrel at each of three different days. Only one lot of propellant was used; charge weight was controlled to an accuracy of 0.01 pound, bullet weight to an accuracy of 0.1 pound and all other propelling charge factors known to affect ballistics were closely controlled. The following ballistic parameters were monitored:

- a. Velocity
- b. Pressure-time
- c. Barrel outer wall temperature
- d. Barrel strain at two locations
- e. Counter Recoil Gas Pressure-time
- f. Ejection Time
- g. High-speed movies of the recoil event and back to battery event.

Efforts were made to synchronize time zero for the counter recoil gas pressure-time data and the high speed movie recoil distance-time data. The objective was to calculate the area under the pressure-volume curve at the conclusion of the recoil event because this is the work input to the counter recoil gas. On the basis of the theory, the work value would be expected to correlate negatively with bullet velocity.

There are only five rounds of data for the first occasion because a leak developed and five rounds of counter recoil pressure-time data were lost. Two of the five data points were affected by this leak and are not grouped with the other three. The two data points are presented because they illustrate that the velocity exhibits the negative correlation with counter recoil pressure even in an atypical instance. Here we see a strong positive correlation of the static pressure to the peak pressure divided by two. This latter value was used because it is expected to be more nearly proportional to the work done to the gas. Of interest is that the single lowest velocity obtained is the highest point and the highest single velocity is the lowest point on the graph. It is obvious that the strong correlation obtained is across population groups (or occasions) and would not be significant on a per occasion basis.

Figure VIII shows a schematic of the recoil and counter recoil systems in the recoil and battery positions. Energy is stored in the counter recoil system in the form of compressed gas. Energy is also stored in the recoil system in terms of a fluid pressure differential, however, this was not monitored.

5  
MONTROYA

Figure IX shows the effect of increasing peak counter recoil pressure on velocity across the three occasions. Again, the first two points of the first occasion are not grouped with the other three because at that point a pressure leak developed. We continue to see that these correlations are only significant across the population groups or occasions.

Figure X shows the relationship of the calculated work input to the counter recoil gas at the conclusion of the recoil event to velocity. The relationship is strongly negative complying with the stated theory and significant to the 99.9 percent confidence level. Further, it was determined that there were three data points which were statistical outliers, the cause of which is, frankly, unknown, which if omitted from the calculation of the correlation coefficient increases the magnitude to  $-0.8708$ .

Figure XI shows some of the pressure-volume curves. As can be noted the largest area obtained corresponded to the lowest velocity and the smallest area obtained corresponded to the highest velocity obtained. A PV curve for an intermediate velocity is also shown. Since the volume displacement or total recoil distance is remaining essentially constant, one can see that the initial static pressure level (shown on the graph) is essentially dictating the area under the curve.

Figure XII shows that the work input is in fact increasing with the number of rounds fired or with increasing static pressure levels.

Future plans will include an attempt to monitor the stored energy in the recoil system and to tie-in the other factors felt to influence the work input to the recoil and counter recoil system; such as changing day-to-day temperature and changing hydraulic oil temperature resulting from working the oil during mount operation.

In summary, it is known that the initial velocity varies from day-to-day, even for so called master propellant, and with continued firing schedules the velocity decays. Tests conducted by the Naval Ordnance Station, Indian Head have shown that one parameter, counter recoil pressure, does reflect a significant relationship with velocity.

These real world effects, such as loss of kinetic energy of the projectile, because of fluctuating counter recoil pressure on velocity, inhibits gun fire accuracy. The paramount concern appears to be the inability to predict the velocity of early rounds and therefore, the accuracy of fire power. It is hoped that our and other efforts in the gun community will lead to the establishment of parameters that if monitored will greatly reduce, if not eliminate these mount related effects.

# MONTOYA

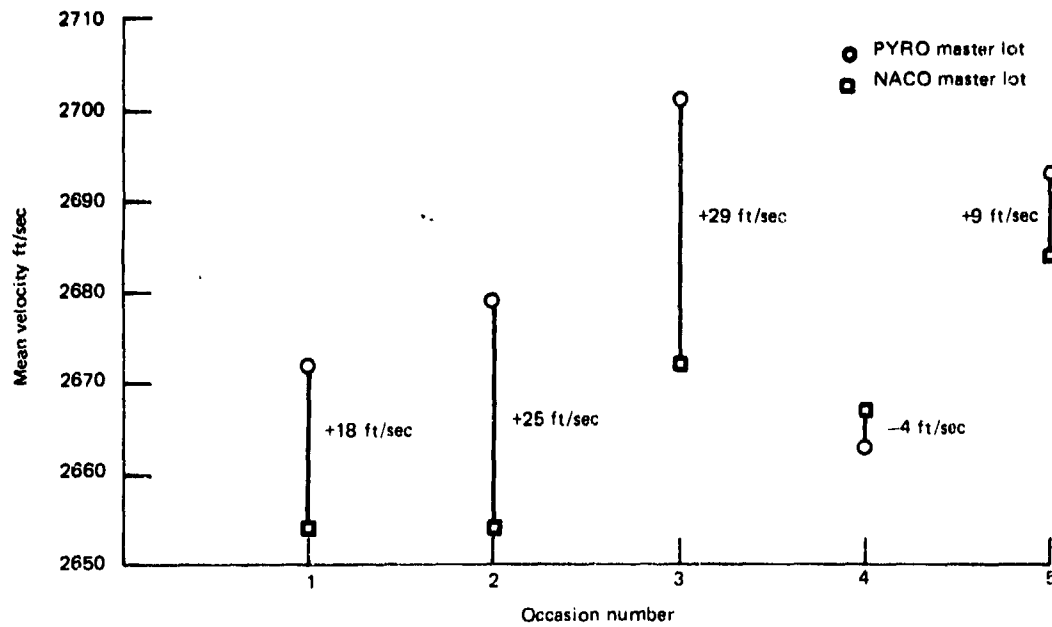


FIGURE I. EXAMPLE OF RANDOM DAY-TO-DAY EFFECT ON MEAN VELOCITY

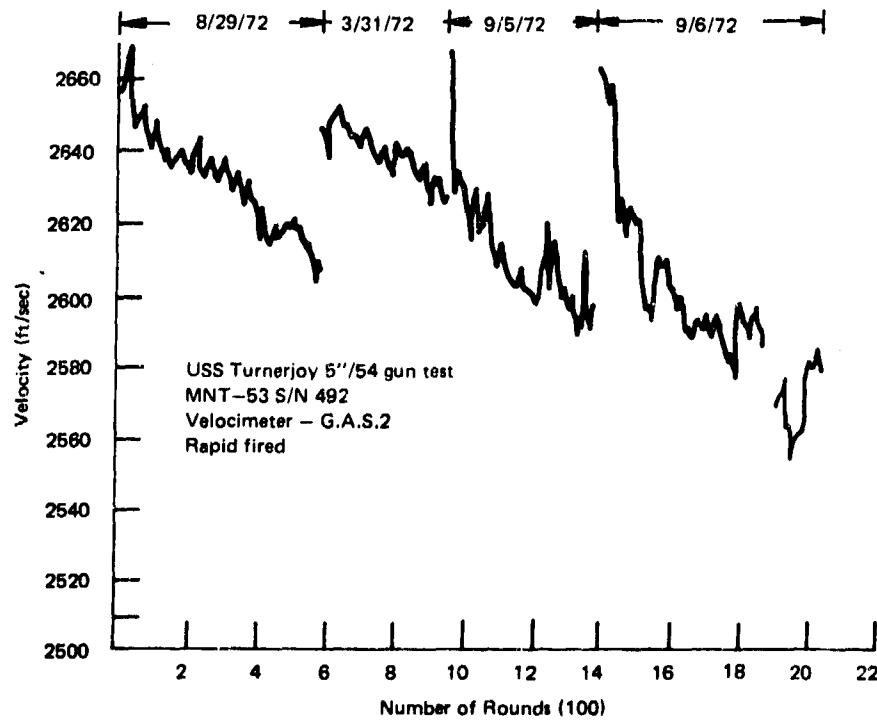


FIGURE II. EXAMPLE OF HOT GUN VELOCITY DECAY

MONTAYA

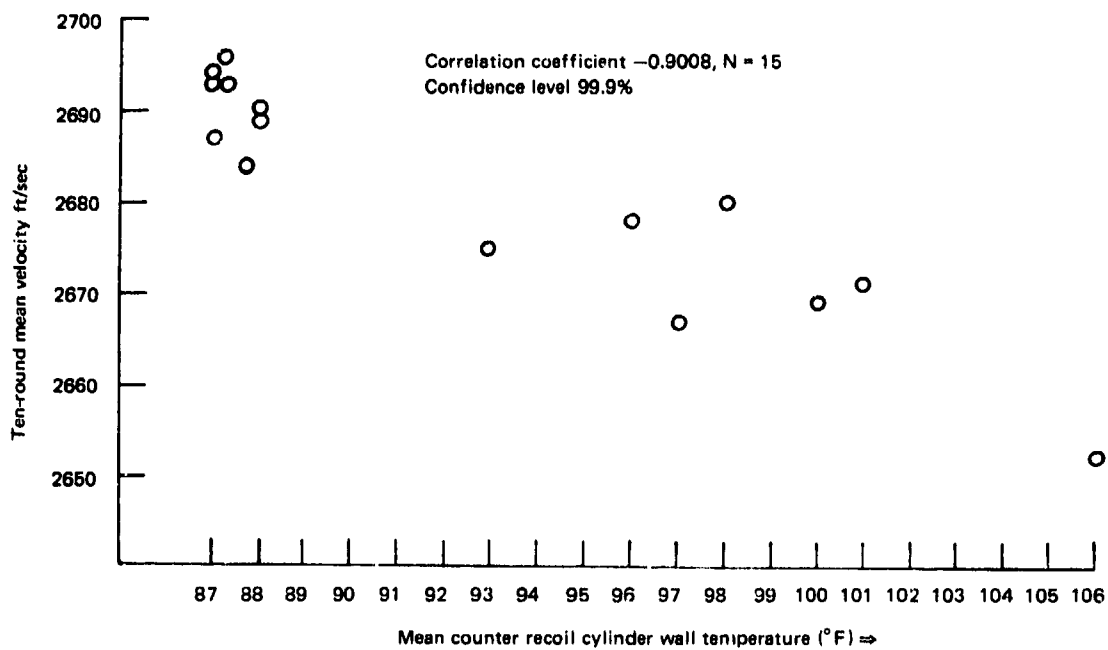


FIGURE III. *USS NORTON SOUND* VELOCIMETER DATA  
TEN ROUND MEANS

MONTROYA

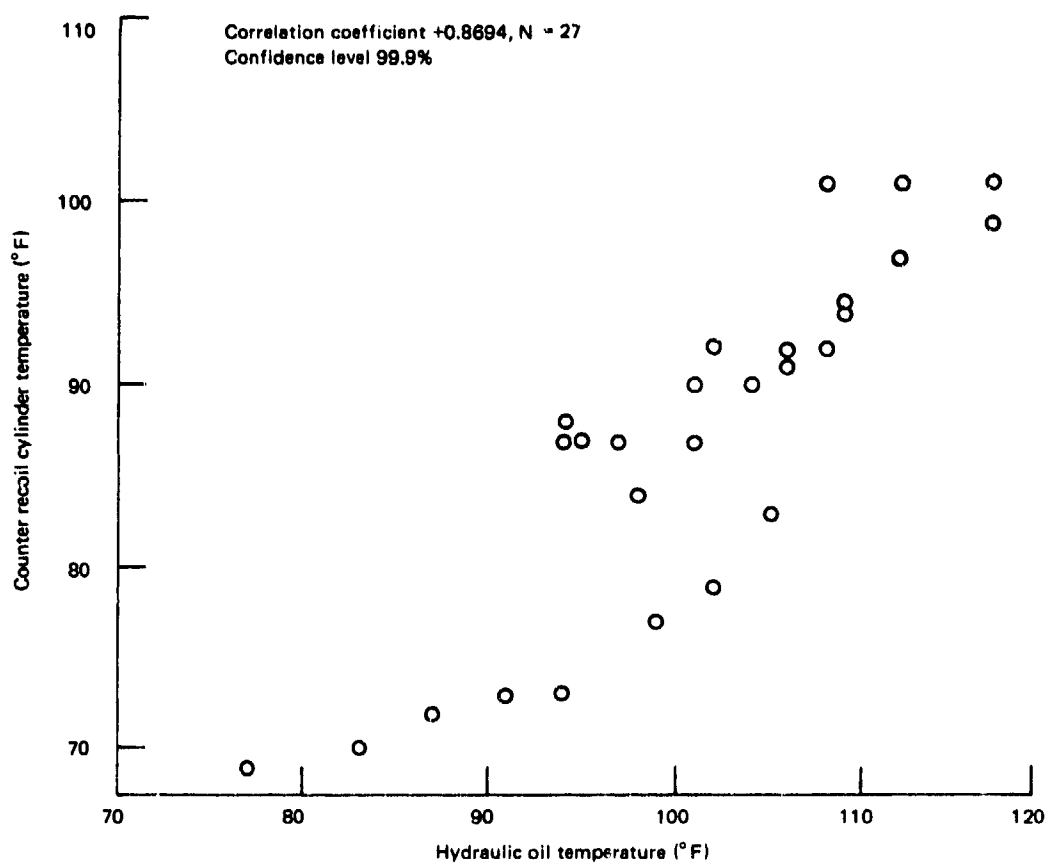


FIGURE IV. *USS NORTON SOUND* INFLUENCE OF OIL TEMPERATURE ON COUNTER RECOIL GAS TEMPERATURE AND PRESSURE

# MONTOYA

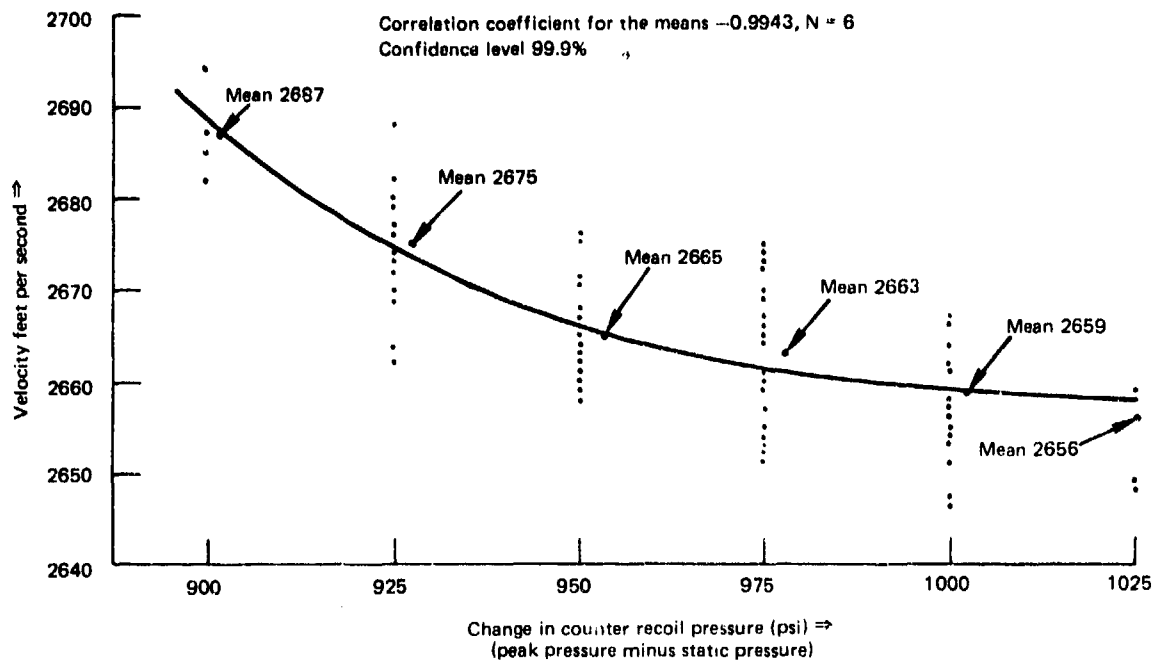


FIGURE V. *USS HEWITT* BALLISTIC TEST DATA

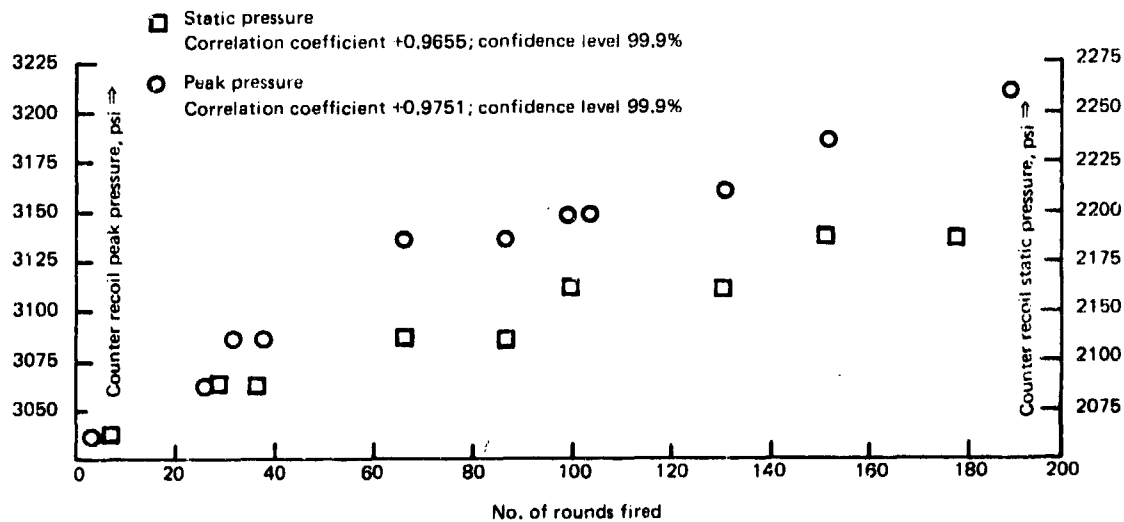


FIGURE VI. *USS HEWITT* TESTS



MONTOYA

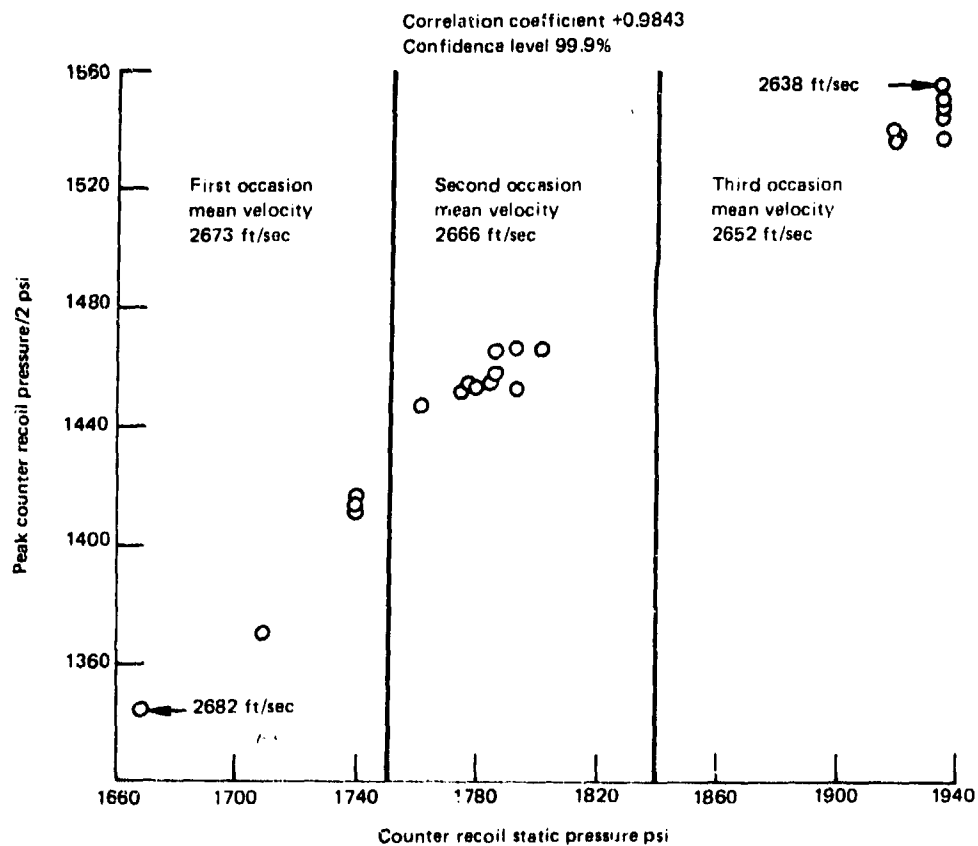
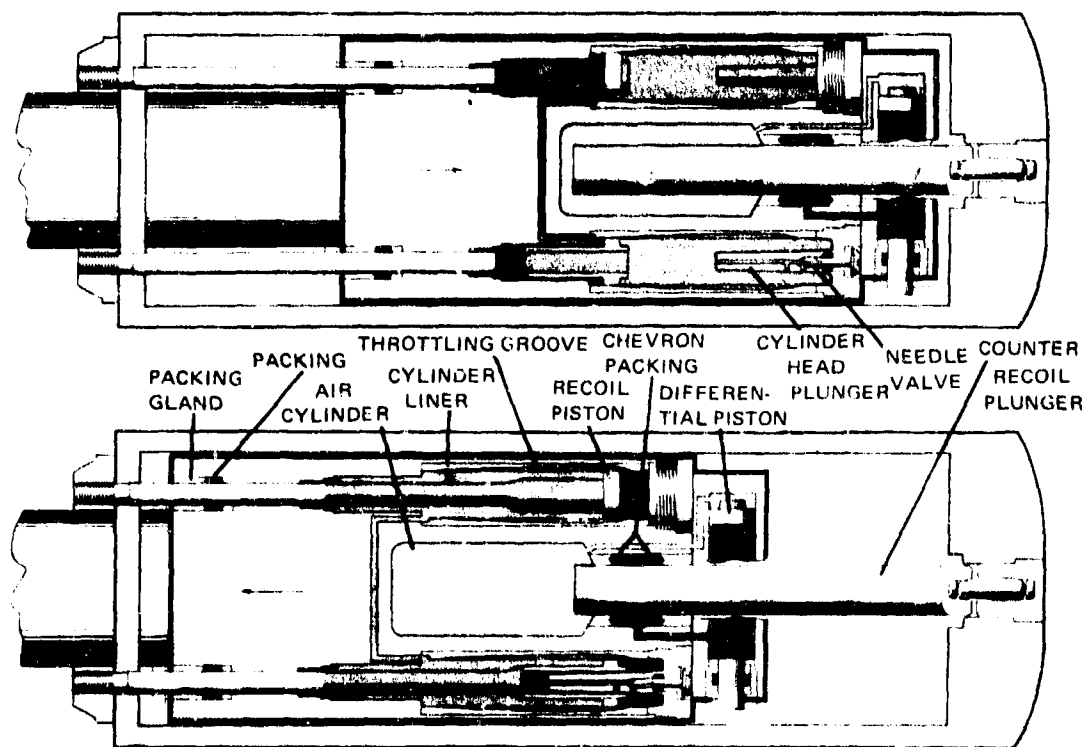


FIGURE VII. SPECIAL TEST PROGRAMS DATA  
EFFECT OF INCREASING COUNTER RECOIL STATIC PRESSURE  
ON PEAK COUNTER RECOIL PRESSURE

MONTOYA



ABOVE -- RECOIL AND COUNTER RECOIL SYSTEMS--  
HOUSING IN RECOIL POSITION

BELOW -- RECOIL AND COUNTER RECOIL SYSTEMS--  
HOUSING IN BATTERY POSITION

RECOIL SYSTEM FLUID - LOW PRESSURE  
 RECOIL SYSTEM FLUID - HIGH PRESSURE  
 COUNTER RECOIL SYSTEM FLUID  
 COUNTER RECOIL SYSTEM AIR

FIGURE VIII. COUNTER RECOIL AND DIFFERENTIAL ASSEMBLIES

# MONTOKA

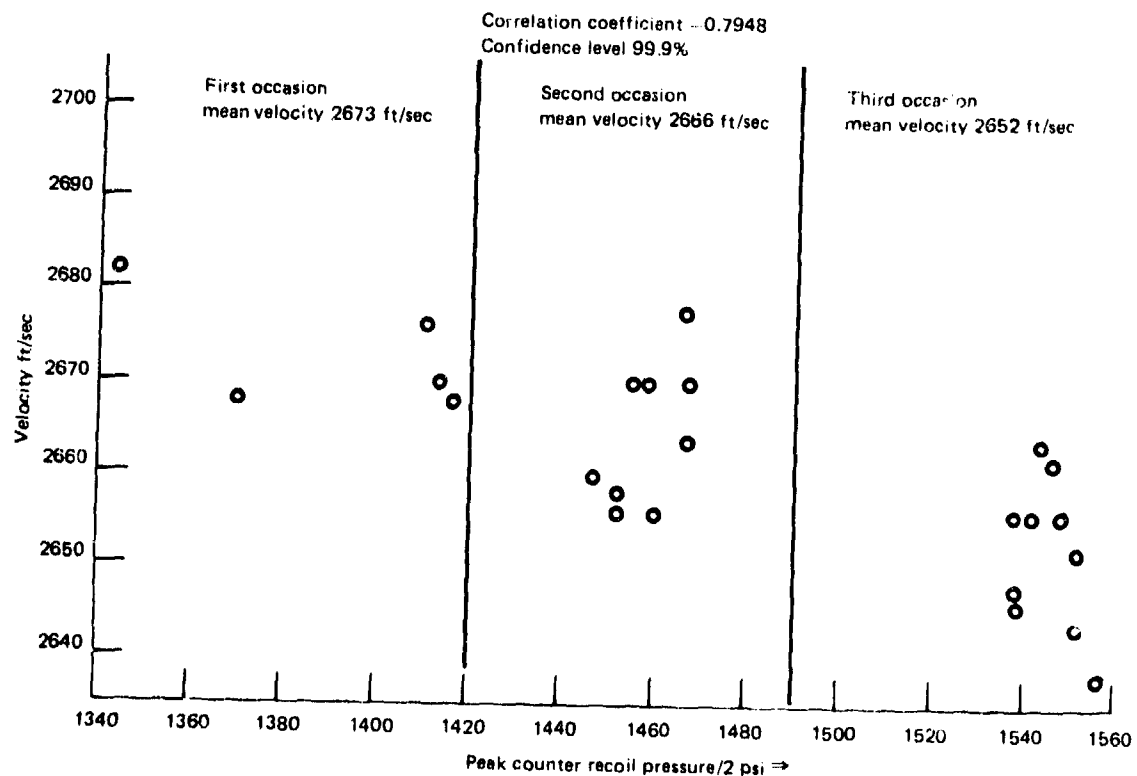


FIGURE IX. EFFECT OF INCREASING PEAK RECOIL PRESSURE ON VELOCITY

MONTTOYA

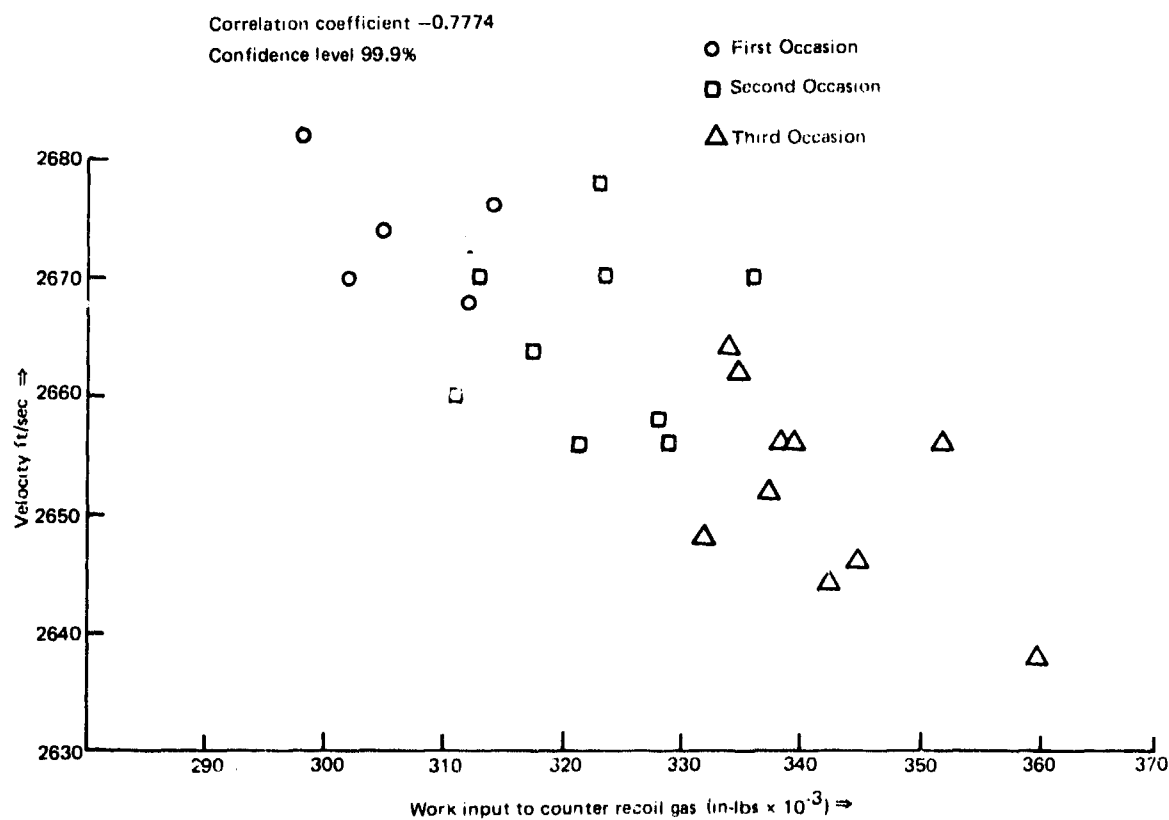


FIGURE X. INFLUENCE OF WORK INPUT TO  
COUNTER RECOIL GAS ON VELOCITY

# MONTOYA

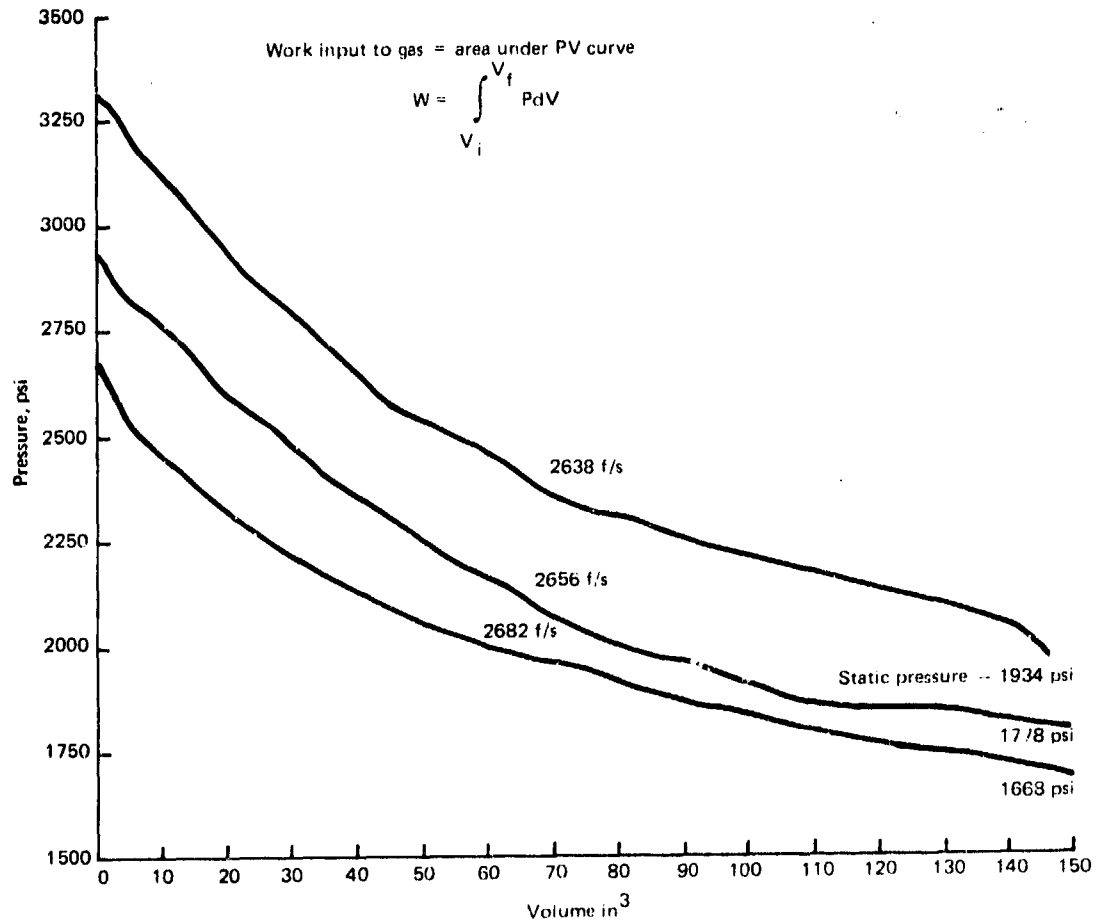


FIGURE XI. PRESSURE VOLUME CURVES

MONTOYA

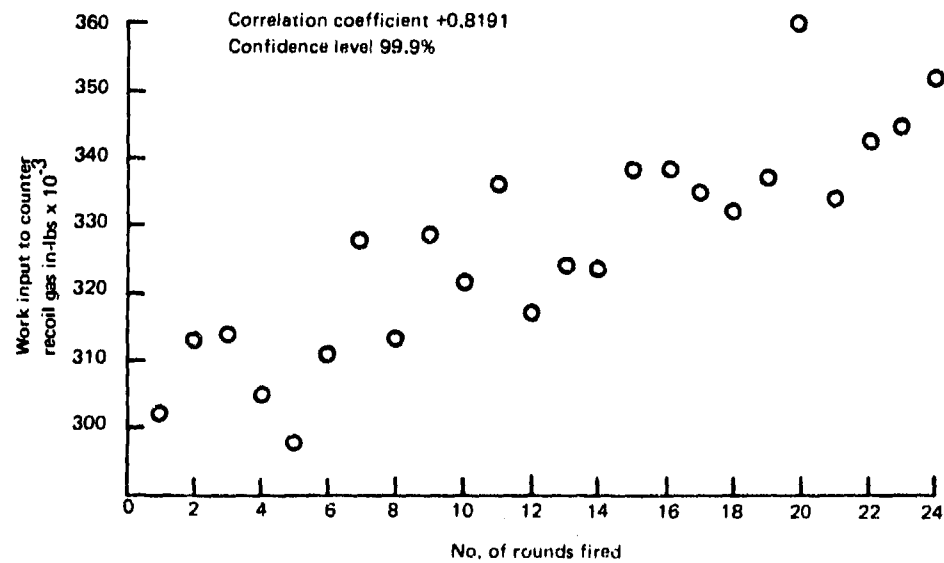


FIGURE XII. WORK INPUT TO GAS INCREASES WITH  
NUMBER OF ROUNDS FIRED

SHEN

**TITLE:** On the Sensitivity Coefficient of Exterior Ballistics and its Potential Matching to Interior Ballistics Sensitivity  
DR. C. N. Shen  
Benet Weapons Laboratory  
Watervliet Arsenal, Watervliet, NY 12189

**ABSTRACT:**

Modern Weapon System development requires a gun to have first round accuracy in hitting its targets. It is desirable to design a passive system capable to adjust some of its parameters in compensating deviations of other uncontrolled variables. One may use the method of matching sensitivity coefficients for the exterior and interior ballistics. The sensitivity for exterior ballistics can be found by setting to zero the deviation of the range, which is equivalent to hitting the target physically. This gives the functional relationship of the elevation angle deviation to the velocity deviation as a function of nominal values of the elevation angle. It is noted that the percentage velocity deviation is unpredictable and is the quantity to be compensated. If the nominal angle is less than an optimal angle as in the case of tank guns with low trajectories the exterior sensitivity coefficient is negative. This shows that a decrease in elevation angle is required for increase of percentage velocity deviation. The gun should thus yield automatically an amount of elevation angle deviation at muzzle if the shell generated a percentage velocity deviation at muzzle. Interior ballistics for a moving shell mass gives a partial differential equation in terms of the deflection of the gun tube. The sensitivity coefficient for the interior ballistics at the muzzle can be found by evaluating from a modified partial differential equation. We will select a design by letting the exterior ballistic coefficient equal to the interior ballistic coefficient. The above sensitivity coefficient matching shows that one can obtain a correct design for passive control of a gun in order to give better accuracy in hitting a target.

**BIBLIOGRAPHY:**

**PRESENT ASSIGNMENT:** Research Mechanical Engineer (Consultant)  
Benet Weapons Laboratory (LCWSL) Watervliet Arsenal; Professor of Mechanical Engineering, Electrical and Systems Engineering Department, Rensselaer Polytechnic Institute, 1958 - present.

**PAST EXPERIENCE:** Visiting Professor of Mechanical Engineering, M.I.T., 1967-68; Assistant Professor of Mechanical Engineering, Dartmouth College, 1954-58.

**DEGREES HELD:** B.S. National Tsing-Hua University, China, 1939; Master of Engineering, University of Minnesota, 1950; Ph.D., University of Minnesota, 1954.

SHEN

ON THE SENSITIVITY COEFFICIENT OF EXTERIOR BALLISTICS AND  
ITS POTENTIAL MATCHING TO INTERIOR BALLISTICS SENSITIVITY

Dr. C. N. Shen  
U. S. Army Armament Research and Development Command  
Benet Weapons Laboratory, LCWSI.  
Watervliet Arsenal, Watervliet, NY 12189

INTRODUCTION

Modern Weapon System development requires a gun to have first round accuracy in hitting its targets. It is desirable to design a passive system capable to adjust some of its parameters in compensating deviations of other uncontrolled variables. In exterior ballistics the range of a projectile can be expressed in terms of the velocity  $v$ , the elevation angle  $\theta$  and the elevation  $y$  of the shell as it leaves the gun. The effect of the velocity term to the accuracy of the gun dynamics is very much pronounced. Moreover, the change of velocity itself is very much uncertain and complicated. Instead of measuring and determining the velocity by any instrumentation one may use the method of matching sensitivity coefficients for the exterior and interior ballistics. The sensitivity for exterior ballistics can be found by setting to zero the deviation of the range, which is equivalent to hitting the target physically. This gives the functional relationship of the elevation angle deviation  $\Delta\theta$  to the velocity deviation  $\Delta v$  as a function of nominal values of the elevation angle  $\theta_0$ . To illustrate the point one may take a simple example using a target in the same elevation with no head wind and no other anomalies. The sensitivity coefficient  $S_{ext}$  for exterior ballistics for this case can be expressed as

$$S_{ext} = \frac{(\Delta\theta)}{(\Delta v)/v} = -\tan 2\theta_0 \quad (1)$$

It is noted that the percentage velocity deviation  $(\Delta v)/v$  is unpredictable and is the quantity to be compensated. By setting the nominal angle  $\theta_0$  greater than  $45^\circ$ , as in the case of firing a howitzer over a hill, the sensitivity coefficient  $S_{ext}$  is positive. This means that for hitting the target an additional elevation angle  $\Delta\theta$  is needed (i.e.  $\theta$  increases) if percentage velocity deviation  $(\Delta v)/v$  is positive. On the other hand, if the nominal angle  $\theta_0$  is less than  $45^\circ$  as in the case of tank guns with low trajectories the sensitivity coefficient  $S_{ext}$  is



SHEN

negative. This shows that a decrease in elevation angle  $\Delta\theta$  is required for increase of percentage velocity deviation  $(\Delta v)/v$ .

#### MATCHING SENSITIVITY COEFFICIENTS

The effect to interior ballistics for gun dynamics from exterior ballistics can be observed by matching the two ballistics so that the sensitivity coefficients become the same, i.e.,

$$S_{int} = S_{ext}. \quad (2)$$

where  $S_{int}$  is the sensitivity coefficient for interior ballistics. The gun should thus yield an amount of  $\Delta\theta$  at muzzle if the shell generated a percentage velocity deviation  $(\Delta v)/v$  at muzzle.

A typical equation for interior ballistics [1] for a moving shell mass gives

$$EIy'''' + \rho A \ddot{y} + m_p (\ddot{y} + 2v\dot{y}' + g + v^2 y'') \delta(x-vt) = 0 \quad (3)$$

where  $y$  is the deflection of the gun tube. Taking partial differentiation with respect to  $v$  and multiplying by  $v$ , we have

$$EIu'''' + \rho A \ddot{u} + m_p (\ddot{u} + 2v\dot{u} + v^2 u'') \delta(x-vt) = -m_p v (2\dot{y}' + 2vy'') \delta(x-vt) \quad (4)$$

$$\text{where } u = v \frac{\partial y}{\partial v} \quad (5)$$

Deviation of deflection due to change of velocity  $\Delta v$  yields

$$\Delta y = \frac{\partial y}{\partial v/v} \left( \frac{\Delta v}{v} \right) = u \left( \frac{\Delta v}{v} \right) \quad (6)$$

The deviation of elevation angle  $\Delta\theta$  at muzzle location is

$$\Delta\theta \Big|_m = \Delta \left( \frac{\partial y}{\partial x} \right) \Big|_m = \frac{\partial}{\partial x} (\Delta y) \Big|_m = \frac{\partial}{\partial x} \left[ u \left( \frac{\Delta v}{v} \right) \right] \Big|_m \quad (7)$$

$$\Delta\theta \Big|_m = \frac{\partial u}{\partial x} \Big|_m \frac{\Delta v}{v} \Big|_m \quad (8)$$

where  $m$  indicate that the location and time of the shell is at the muzzle. The above gives the sensitivity coefficient for the interior ballistics as

$$S_{int} = \frac{\Delta\theta|_m}{(\Delta v)/v|_m} = \frac{\partial u}{\partial x} \Big|_m \quad (9)$$

One can solve for the solution for  $\frac{du}{dx}|_m$  from the PDE in  $u$  with different design parameters, boundary conditions and initial conditions. We will select a design that gives

$$\frac{\partial u}{\partial x}|_m = S_{int} = S_{ext} = -\tan 2\theta_0 \quad (10)$$

The above sensitivity coefficient matching shows that one can obtain a correct design for passive control of a gun in order to give better accuracy in hitting a target. However, this paper investigates the problems concerning the exterior ballistic coefficient  $S_{ext}$  only and leaves the matching to interior ballistic coefficients for future work.

#### STATEMENT OF THE PROBLEM AND THE METHOD OF APPROACH

It is desired to find first the analytic expression of the range for exterior ballistics in terms of the initial velocity  $v_0$  (i.e., muzzle velocity) and the initial elevation angle  $\theta_0$  (i.e., elevation angle at muzzle) for different target slopes  $m$  from the initial firing point to the target point, not necessarily on a horizontal terrain.

(a) The effect of head wind and other drag forces are considered in forming the dynamical equations for the trajectories. These equations are transformed with elevation angle  $\theta$  as independent variables rather than the usual time  $t$ . The principal equation of exterior ballistics is then derived. This differential equation gives the differentiation of the product of velocity  $v$  and the cosine of  $\theta$  with respect to  $\theta$  in terms of the drag  $D$ , the velocity  $v$  and the gravity  $mg$ . With the drag  $D$  expressed in terms of the square of velocity  $v$  the analytic solution for  $v$  can be obtained by further transformation and integration.

(b) After determining  $v$  in terms of  $\theta$  and the initial conditions  $v_0$  and  $\theta_0$ , the differential equations for the horizontal distance  $x$  and the altitude  $y$  are expressed as functions of variables  $v$  and  $\theta$ . Expressions for analytic solutions of the trajectory can be written. The exact solution is determined when no head wind exists. Other analytic solutions may be found if certain approximations are used.

(c) A nondimensional range  $X$  is defined as the range  $(x_i - x_0)$  multiplied by the gravity acceleration  $g$  and divided by the square of initial velocity  $v_0$ . Similarly a nondimensional elevation  $Y$  can also be given. Thus the target slope  $m$  is the nondimensional elevation  $Y$  divided by the nondimensional range  $X$ . With these definitions the nondimensional range  $X$  can be expressed as a function of  $\tan \theta_0$  and  $m$  for the cases where no drag exists. This is a key equation from which the properties of the trajectories can be found. For example,  $X = 0$  at  $\tan \theta_0 = m$ .

SHEN

(d) The maximum nondimensional range  $X_{\max}$  occurs at  $\theta_0^*$  where the target slope  $m^*$  is equal to the negative of  $\cot 2\theta^*$ . The value of the maximum nondimensional range  $X_{\max}$  is equal to  $\cot \theta_0^*$ , which is not unity if  $\theta_0 \neq 45^\circ$ . This needs a further normalizing factor to make the maximum nondimensional range unity. The range ratio  $R$  is defined as the nondimensional range  $X$  divided by its maximum nondimensional range  $X_{\max}$  for the same target slope  $m$ . After this is done any range ratio can be compared to unity in determining the efficiency of using its energy supply.

(e) The error increments in hitting a target may be obtained by taking natural logarithms of the range  $(x_1 - x_0)$  and the elevation  $(y_1 - y_0)$  and then taking their differentials. In order to hit a target these increments  $\Delta(x_1 - x_0)$  and  $\Delta(y_1 - y_0)$  become zeroes. An expression for  $\Delta\theta_0/(\Delta v_0/v_0)$  can be found as a function of  $\tan \theta_0$  and  $m$ . This function is called the sensitivity coefficient  $S$  for exterior ballistics. This is the other key equation from which the properties of the sensitivity can be found. For example  $S = 0$  at  $\tan \theta_0 = m$ . The sensitivity  $S$  becomes infinite at  $m^* = -\cot 2\theta^*$  which is at the same location for maximum range.

#### DYNAMICAL EQUATIONS FOR TRAJECTORIES

For a constant mass travelling in a vertical plane with the drag and velocity vectors contained in the plane of symmetry as shown in Figure 1. The dynamical equations of motion are (2)

$$\frac{dx}{dt} - v \cos \theta = 0 \quad (11)$$

$$\frac{dy}{dt} - v \sin \theta = 0 \quad (12)$$

$$T \cos \epsilon - D - m(g \sin \theta + \frac{dv}{dt}) = 0 \quad (13)$$

and

$$T \sin \epsilon + L - m(g \cos \theta + v \frac{d\theta}{dt}) = 0 \quad (14)$$

where  $m$  = the mass of the projectile  
 $g$  = the acceleration due to gravity  
 $T$  = the thrust, if any  
 $L$  = the lift of the projectile  
 $D$  = the drag of the projectile  
 $v$  = the velocity of the projectile  
 $\theta$  = the path inclination (elevation angle)  
 $x$  = the horizontal distance  
 $y$  = the altitude or vertical distance

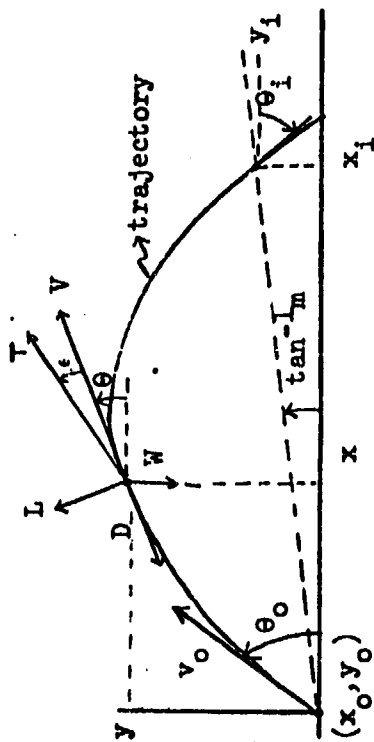


Fig. 1; Forces, Slopes, and Initial and Final Parameters for a Trajectory

III-54

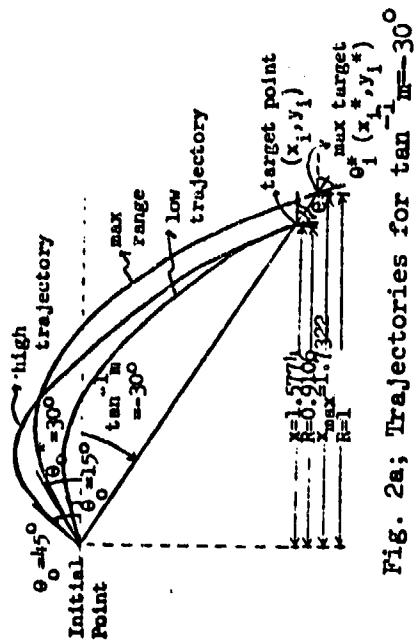


Fig. 2a; Trajectories for  $\tan^{-1} m = -30^\circ$

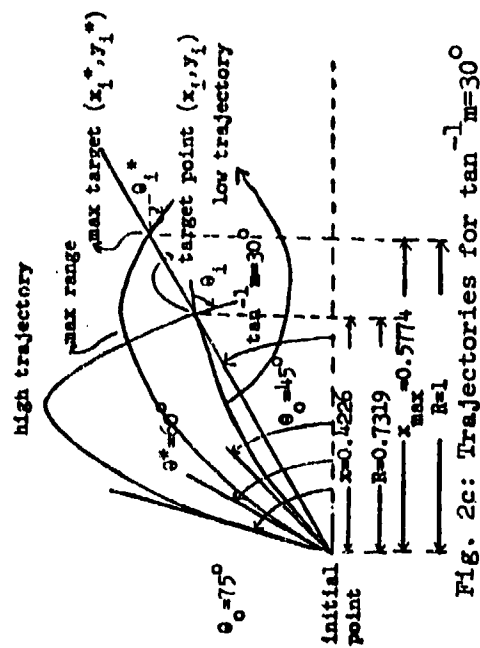


Fig. 2c; Trajectories for  $\tan^{-1} m = 30^\circ$

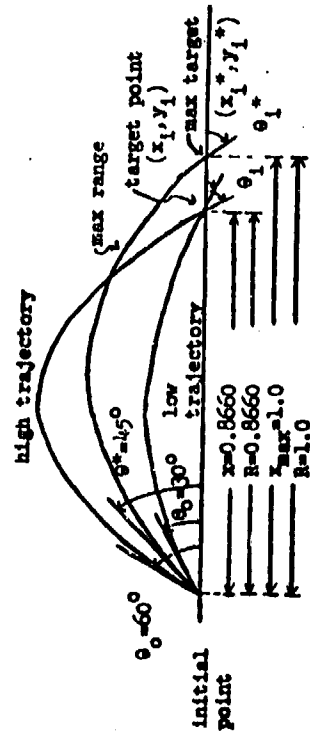


Fig. 2b; Trajectories for  $\tan^{-1} m = 0^\circ$

SHEN

It is noticed that the deviations due to anomalies in the azimuth direction is not considered here.

For the case where the thrust does not exist and the lift is negligible Equations (13) and (14) reduce to

$$g \sin \theta + \frac{dv}{dt} = - \frac{D}{m} \quad (15)$$

$$g \cos \theta + v \frac{d\theta}{dt} = 0 \quad (16)$$

Using Newton's law of motion the accelerations components are derived as

$$\frac{d^2x}{dt^2} = - \frac{D \cos \theta}{m} \quad (17)$$

$$\frac{d^2y}{dt^2} = - \frac{D \sin \theta}{m} - g \quad (18)$$

By differentiating Equation (11) with respect to  $t$  and using Equation (17) we have

$$\frac{d}{dt} (v \cos \theta) = - \frac{D \cos \theta}{m} \quad (19)$$

Solving for  $d\theta/dt$  in Equation (16) one obtains

$$\frac{d\theta}{dt} = \frac{-g \cos \theta}{v} \quad (20)$$

In order to find the solutions of the variables  $v$ ,  $x$  and  $y$  it is easier to obtain analytic expressions in terms of the elevation angle  $\theta$  rather than the time  $t$ . Equations (19), (11) and (12) are divided by Equation (20) in achieving this new transformation as

$$\frac{d(v \cos \theta)}{d\theta} = \frac{Dv}{mg} \quad (21)$$

$$\frac{dx}{d\theta} = - \frac{v^2}{g} \quad (22)$$

$$\frac{dy}{d\theta} = - \frac{v^2}{g} \tan \theta \quad (23)$$

Equation (21) is called the principal equation of exterior ballistics (3). It can be integrated if the drag  $D$  is a known function of velocity  $v$ .

SHEN

# ANALYTICAL SOLUTION FOR VELOCITY FOR HEAD WIND DRAG

If the projectile mass  $m$  is constant in a constant gravitational field  $g$ , the head wind drag force can be expressed as

$$\frac{D}{m} = cv^2 \quad (24)$$

where

$$c = c_w \left( \frac{\pi}{4} d^2 \right) \left( \frac{\rho}{2} \right) \quad (25)$$

$c_w$  = the dimensionless resistance coefficient  
 $d$  = the diameter of the projectile  
 and  $\rho$  = the air density

Thus the principal equation of exterior ballistics (Equation 21) becomes

$$\frac{d}{d\theta} (v \cos\theta) = \frac{cv^3}{g} \quad (26)$$

In order to solve the above equation a further transformation is necessary by letting

$$u = v \cos\theta \quad (27)$$

Equation (26) then becomes separable as

$$\frac{g}{cu^3} du = \frac{d\theta}{\cos^3\theta} \quad (28)$$

If this equation is integrated from the initial conditions  $\theta_0$  and  $u_0 = v_0 \cos\theta_0$ , one obtains

$$\frac{g}{c} \left[ \frac{u^{-2}}{-2} \right]_{u_0}^u = \left[ \frac{1}{2} \frac{\sin\theta}{\cos^2\theta} \right]_{\theta_0}^{\theta} + \frac{1}{2} \int_{\theta_0}^{\theta} \frac{d\theta}{\cos\theta} \quad (29)$$

Substituting the upper and lower limits we have

$$\begin{aligned} - \frac{g}{2c} \left[ \frac{1}{u^2} - \frac{1}{u_0^2} \right] &= \frac{1}{2} \left[ \frac{\sin\theta}{\cos^2\theta} - \frac{\sin\theta_0}{\cos^2\theta_0} \right] \\ &+ \frac{1}{2} \left[ \frac{1}{2} \ln \left( \frac{1 + \sin\theta}{1 - \sin\theta} \right) - \frac{1}{2} \ln \left( \frac{1 + \sin\theta_0}{1 - \sin\theta_0} \right) \right] \end{aligned} \quad (30)$$

One can solve for  $v^2$  by using Equation (27) with the following results

$$v^2 = \frac{v_0^2 \cos^2\theta_0}{\cos^2\theta} \frac{1}{1 + c\phi(v, \theta, v_0, \theta_0)} \quad (31)$$

SHEN

where

$$\phi(\theta, v_0, \theta_0) = K - \frac{v_0^2 \cos^2 \theta_0}{g} \left[ \frac{\sin \theta}{\cos^2 \theta} + \frac{1}{2} \ln \left( \frac{1 + \sin \theta}{1 - \sin \theta} \right) \right] \quad (32)$$

and

$$K = \frac{v_0^2 \cos^2 \theta_0}{g} \left[ \frac{\sin \theta_0}{\cos^2 \theta_0} + \frac{1}{2} \ln \left( \frac{1 + \sin \theta_0}{1 - \sin \theta_0} \right) \right] \quad (33)$$

#### EQUATIONS FOR THE TRAJECTORY IN THE x-y PLANE

If Equations (31) - (33) are substituted into Equations (22) and (23) we have

$$\frac{dx}{d\theta} = - \frac{1}{g} \frac{v_0^2 \cos^2 \theta_0}{\cos^2 \theta} \frac{1}{1 + c\phi(\theta, v_0, \theta_0)} \quad (34)$$

$$\frac{dy}{d\theta} = - \frac{1}{g} \frac{v_0^2 \cos^2 \theta_0}{\cos^2 \theta} \frac{\tan \theta}{1 + c\phi(\theta, v_0, \theta_0)} \quad (35)$$

The variables in these equations are not separable and integrations into analytical form are harder to achieve. However, if the coefficient  $c$  in Equation (24) for the head wind is small one may approximate it by

$$\frac{dx}{d\theta} = - \frac{1}{g} \frac{v_0^2 \cos^2 \theta_0}{\cos^2 \theta} [1 - c\phi(\theta, v_0, \theta_0)] \quad (36)$$

$$\frac{dy}{d\theta} = - \frac{1}{g} \frac{v_0^2 \cos^2 \theta_0 \tan \theta}{\cos^2 \theta} [1 - c\phi(\theta, v_0, \theta_0)] \quad (37)$$

which are relatively easier to solve for the solutions than Equations (34) and (35).

#### EXPRESSIONS FOR ANALYTIC SOLUTIONS OF THE TRAJECTORY

By integrating Equation (36) we have

$$x_i - x_0 = - \frac{v_0^2 \cos^2 \theta_0}{g} [(\tan \theta_i - \tan \theta_0) - c\xi(\theta_i, \theta_0, v_0)] \quad (38)$$

where

$$\xi(\theta_i, \theta_0, v_0) = \int_{\theta_0}^{\theta_i} \frac{\phi(\theta, v_0, \theta_0)}{\cos^2 \theta} d\theta \quad (39)$$

$\theta_i$  = value of  $\theta$  at impact point (target)

and

$x_i$  = value of  $x$  at impact point

SHEN

Similarly by integrating Equation (37) one obtains

$$y_1 - y_0 = - \frac{v_0^2 \cos^2 \theta_0}{2g} [(\tan^2 \theta_1 - \tan^2 \theta_0) - c\eta(\theta_1, \theta_0, v_0)] \quad (40)$$

where

$$\eta(\theta_1, \theta_0, v_0) = \int_{\theta_0}^{\theta_1} \frac{\phi(\theta, v_0, \theta_0)}{\cos^2 \theta} \tan \theta d\theta \quad (41)$$

The integration of Equations (39) and (41) with the aid of Equation (32) involves long expressions. This will be accomplished in the future for extension of this work.

#### THE NONDIMENSIONAL RANGE AND THE MAXIMUM RANGE

For the case with no head wind or drag, the coefficient  $c$  becomes zero in Equations (38) and (40). Solving for  $\tan \theta_1$  in Equation (38) gives

$$\tan \theta_1 = \tan \theta_0 - X \sec^2 \theta_0 \quad (42)$$

Where  $X$  is the nondimensional range from initial point to impact point, thus

$$X = \frac{g(x_1 - x_0)}{v_0^2} \quad (43)$$

Solving for  $\tan^2 \theta_1$  in Equation (40) yields

$$\tan^2 \theta_1 = \tan^2 \theta_0 - 2Y \sec^2 \theta_0 \quad (44)$$

Where  $Y$  is the nondimensional elevation from initial point to impact point, thus

$$Y = \frac{g(y_1 - y_0)}{v_0^2} \quad (45)$$

By squaring Equation (42) and equating to Equation (44) we have

$$[\tan \theta_0 - X \sec^2 \theta_0]^2 = \tan^2 \theta_0 - 2Y \sec^2 \theta_0 \quad (46)$$

which results

$$[-2 \tan \theta_0 + X \sec^2 \theta_0] X = -2Y \quad (47)$$

We can define a quantity  $m$  to be the target slope of the impact point from the initial point.



SHEN

$$m = \frac{y_1 - y_0}{x_1 - x_0} = \frac{Y}{X} \quad (48)$$

Solving for the nondimensional range from Equation (47) and noting the definition of the target slope from Equation (48) one obtains

$$X = \frac{2(\tan\theta_0 - m)}{1 + \tan^2\theta_0} \quad (49)$$

Equation (49) is the key result to determine the range for any target slope  $m$  and initial elevation angle  $\theta_0$ .

(a) It is noted that the nondimensional range  $X$  becomes zero when the numerator of Equation (40) is zero

$$X = 0 \text{ at } \tan\theta_0 = m \quad (50)$$

(b) If the initial elevation angle  $\theta_0$  becomes zero the nondimensional range becomes

$$X = -2m \quad (51)$$

(c) In a flat terrain the target slope  $m$  is zero, one obtains

$$X = 2\tan\theta_0 \cos^2\theta_0 = \sin 2\theta_0 \quad (52)$$

(d) For a maximum nondimensional range we set

$$\frac{dx}{d(\tan\theta_0)} = 0 = (1 + \tan^2\theta_0) - (\tan\theta_0 - m)2\tan\theta_0 \quad (53)$$

or

$$\tan^2\theta_0^* - 2m\tan\theta_0^* - 1 = 0 \quad (54)$$

Solving for  $\tan\theta_0^*$  we have

$$\tan\theta_0^* = m + \sqrt{m^2 + 1} \quad (55)$$

where  $\theta_0^*$  is the elevation angle for maximum range.

Equation (54) can be solved for  $m$  which results

$$m = -\frac{1 - \tan^2\theta_0^*}{2\tan\theta_0^*} = -\cot 2\theta_0^* \quad (56)$$

From the above equation one obtains

SHEN

$$\theta_o^* = \frac{1}{2} \tan^{-1} \left( \frac{-1}{m} \right) \quad (57)$$

Substituting Equation (56) into (49) gives the maximum range in terms of  $\theta_o^*$  as

$$X_{\max} = \frac{2 \left( \tan \theta_o^* + \frac{1 - \tan^2 \theta_o^*}{2 \tan \theta_o^*} \right)}{1 + \tan^2 \theta_o^*}$$

which simplifies to

$$X_{\max} = \cot \theta_o^* \quad (58)$$

Equations (57) and (58) are the key equations for determining the initial elevation angle  $\theta_o^*$  and the value  $X_{\max}$  for the maximum range.

#### THE RANGE RATIO

The maximum nondimensional range given in Equation (58) is not unity when  $\theta_o \neq 45^\circ$ . This needs a further normalizing factor to make the maximum nondimensional range unity. Let us define the range ratio  $R$  as

$$R = X/X_{\max} \quad (59)$$

where  $X_{\max}$  is the maximum range at the same target slope  $m$  belonging to range  $X$ .

$$\text{Thus as } X \rightarrow X_{\max}, R \rightarrow 1 \quad (60)$$

By the above definition any range ratio  $R$  can be compared to unity to determine whether the amount of energy supply is fully put into useful work. One can aim the target points first and find the target slope  $m$ . From Equations (55) and (58) we have the elevation angle  $\theta_o^*$  and value  $X_{\max}$  for maximum range. Then we take a fraction of this maximum range which is called range ratio  $R$  in Equation (59), from which the nondimensional range  $X$  is determined. Two new elevation angles  $\theta_o$  can be obtained by solving Equation (49) as  $m$  and  $X$  are known, for the high and low trajectories as follows

$$\tan \theta_o = \frac{1}{X} \pm \left[ \left( \frac{1}{X} \right)^2 - \left( 1 + \frac{2m}{X} \right) \right]^{1/2} \quad (61)$$

SHEN

# THE ERROR INCREMENTS IN HITTING A TARGET

For the case with no head wind or drag, the coefficient  $c$  in Equation (24) becomes zero. Equations (38) and (40) then reduce to

$$x_i - x_0 = \frac{v_0^2 \cos^2 \theta_0}{g} (\tan \theta_0 - \tan \theta_i) \quad (62)$$

$$y_i - y_0 = \frac{v_0^2 \cos^2 \theta_0}{g} (\tan \theta_0 - \tan \theta_i) \frac{1}{2} (\tan \theta_0 + \tan \theta_i) \quad (63)$$

The ratio of the vertical projection to the horizontal projection is then,

$$\frac{y_i - y_0}{x_i - x_0} = \frac{1}{2} (\tan \theta_0 + \tan \theta_i) \quad (64)$$

One may take natural logarithm of Equations (62) and (63) as

$$\ln(x_i - x_0) = -\ln g + 2\ln v_0 + 2\ln \cos \theta_0 + \ln(\tan \theta_0 - \tan \theta_i) \quad (65)$$

$$\begin{aligned} \ln(y_i - y_0) = & -\ln 2g + 2\ln v_0 + 2\ln \cos \theta_0 + \ln(\tan \theta_0 - \tan \theta_i) \\ & + \ln(\tan \theta_0 + \tan \theta_i) \end{aligned} \quad (66)$$

If the above expressions are differentiated, we have the error increments in hitting a target.

$$\frac{\Delta(x_i - x_0)}{x_i - x_0} = 2 \frac{\Delta v_0}{v_0} - \frac{2 \sin \theta_0}{\cos \theta_0} \Delta \theta_0 + \frac{\sec^2 \theta_0 \Delta \theta_0 - \sec^2 \theta_i \Delta \theta_i}{\tan \theta_0 - \tan \theta_i} \quad (67)$$

$$\begin{aligned} \frac{\Delta(y_i - y_0)}{y_i - y_0} = & 2 \frac{\Delta v_0}{v_0} - \frac{2 \sin \theta_0}{\cos \theta_0} \Delta \theta_0 + \frac{\sec^2 \theta_0 \Delta \theta_0 - \sec^2 \theta_i \Delta \theta_i}{\tan \theta_0 - \tan \theta_i} \\ & + \frac{\sec^2 \theta_0 \Delta \theta_0 + \sec^2 \theta_i \Delta \theta_i}{\tan \theta_0 + \tan \theta_i} \end{aligned} \quad (68)$$

These error increments are in terms of the incremental changes  $\Delta v_0$  of the initial velocity,  $\Delta \theta_0$  of the initial elevation angle and  $\Delta \theta_i$  of the impact angle.

SHEN

### SENSITIVITY COEFFICIENT

In order to hit a target, the increments  $\Delta(x_1-x_0)$  and  $\Delta(y_1-y_0)$  become zeroes for a bull's eye landing. Comparing Equations (67) and (68) one obtains

$$2 \frac{\Delta v_0}{v_0} - 2 \tan \theta_0 \Delta \theta_0 + \frac{\sec^2 \theta_0 \Delta \theta_0 - \sec^2 \theta_i \Delta \theta_i}{\tan \theta_0 - \tan \theta_i} = 0 \quad (69)$$

and

$$\sec^2 \theta_0 \Delta \theta_0 + \sec^2 \theta_i \Delta \theta_i = 0 \quad (70)$$

Solving for  $\Delta \theta_i$  in Equation (70) and substituting into Equation (69) we have

$$2 \frac{\Delta v_0}{v_0} - 2 \tan \theta_0 \Delta \theta_0 + \frac{2 \sec^2 \theta_0 \Delta \theta_0}{\tan \theta_0 - \tan \theta_i} = 0 \quad (71)$$

or

$$2 \frac{\Delta v_0}{v_0} + \frac{2(1 + \tan \theta_0 \tan \theta_i)}{\tan \theta_0 - \tan \theta_i} \Delta \theta_0 = 0 \quad (72)$$

Solving for  $\Delta \theta_0$  one obtains

$$\Delta \theta_0 = S \frac{\Delta v_0}{v_0} \quad (73)$$

where

$$S = \frac{-(\tan \theta_0 - \tan \theta_i)}{1 + \tan \theta_0 \tan \theta_i} \quad (74)$$

The above equation is the sensitivity of exterior ballistics. It is seen that if an error  $\Delta v_0$  of the initial velocity is made at firing, it can be compensated by the initial elevation angle  $\Delta \theta_0$  to yield a zero error increment at the target.

Solving Equation (64) for  $\tan \theta_i$  we have

$$\tan \theta_i = -\tan \theta_0 + 2 \frac{y_1 - y_0}{x_1 - x_0} \quad (75)$$

For flat horizontal terrain the impact elevation  $y_1$  is the same as the initial elevation  $y_0$ . Then from Equation (74) one can show that the impact elevation angle  $\theta_i$  becomes the negative of the initial elevation angle  $\theta_0$ .

$$y_1 - y_0 = 0 \quad (76)$$

SHEN

$$\tan\theta_1 = -\tan\theta_0 \quad (77)$$

$$\theta_1 = -\theta_0 \quad (78)$$

Substituting Equation (75) into Equation (74) we have

$$S = \frac{\Delta\theta_0}{\Delta v_0/v_0} = - \frac{2(\tan\theta_0 - m)}{1 - \tan^2\theta_0 + 2m\tan\theta_0} \quad (79)$$

Where  $m$  is the target slope of the impact point from the initial point as already given in Equation (48), Equation (79) is the key result to determine sensitivity for any target slope  $m$  and initial elevation angle  $\theta_0$ .

(a) It is noted that the sensitivity  $S$  becomes zero when the numerator of Equation (79) is zero.

$$S = 0 \text{ at } \tan\theta_0 = m \quad (80)$$

However, the nondimensional range is also zero as given in Equation (50). Thus it will not give any practical advantage to use this sensitivity.

(b) If the initial elevation angle  $\theta_0$  becomes zero the sensitivity becomes

$$S = +2m \quad (81)$$

(c) For a flat terrain the target slope  $m$  is zero, one obtains

$$S = \frac{-2\tan\theta_0}{1 - \tan^2\theta_0} = -\tan 2\theta_0 \quad (82)$$

For the angle  $\theta_0 = 45^\circ$ ,

$$S \rightarrow \pm \infty \quad (83)$$

This is the elevation angle for maximum range when  $m = 0$ .

(d) It is noted that if the denominator of Equation (79) is zero the sensitivity becomes  $\pm \infty$ . That is,

$$1 - \tan^2\theta_0^* + 2m\tan\theta_0^* = 0 \quad (84)$$

or

$$m = -\cot 2\theta_0^* \quad (85)$$

SHEN

However, this is the same as Equations (54) and (56) for location of maximum nondimensional range. Because the sensitivity becomes unbound at maximum range, it is thus very undesirable to design any sensitivity in the neighborhood of maximum range.

#### NUMERICAL RESULTS FOR NONDIMENSIONAL RANGE AND RANGE RATIO

The numerical values of ranges are listed in Tables 1 and 2. The following ranges are evaluated.

##### (a) Maximum Ranges

For each terrain slope  $m$  there is a corresponding maximum nondimensional range  $X_{\max}$  equal to  $\cot\theta_0^*$  by Equation (58). This range is at a location where the initial elevation angle  $\theta_0$  is given by Equation (57). These are marked with a bracket in Table 1 for terrain angle  $\tan^{-1} m$  from  $-60^\circ$  to  $+60^\circ$ , in  $15^\circ$  intervals. The quantity  $X_{\max}$  ranges from 3.7333 at  $\tan^{-1} m = -60^\circ$ , to unity at  $0^\circ$  and 0.2680 at  $60^\circ$ . This is due to the shape of the trajectories as shown in Figure 2. The trajectory for a flat horizontal terrain is indicated by Figure 2b, where the nondimensional range is unity. The downhill trajectory in Figure 2a has the value of  $X_{\max} = 1.7322$ . From Equation (43) the nondimensional range is the actual range  $(x_i - x_0)$  divided by the kinetic energy term  $(v_0^2/g)$ , which is a constant for any given gun. This kinetic energy remains the same initially whether the target point stays below or above the firing point. Thus the downhill trajectory is longer due to the aid of the gravitational force. Similarly, the uphill trajectory shown in Figure 2c is shorter because of the lack of gravitational help. A normalizing factor is introduced so that all the maximum nondimensional ranges are kept as unity as given by Equation (59). This range ratio  $R$  is also marked with a bracket in Table 2 for every terrain slope  $m$ .

##### (b) Minimum Range

A minimum range of zero can be obtained at  $\theta_0 = 90^\circ$ . It indicates the trivial case when a gun shoots overhead. A second minimum range of zero can be obtained at  $\tan\theta_0 = m$ . This time the initial elevation angle is aligned straight to the target with no allowance of gravity.

##### (c) Ranges For Horizontal Initial Elevation Angle $\theta_0 = 0$

For this case the nondimensional range is twice the absolute value of the terrain slope as given by Equation (51) when the target point is below the firing point.

TABLE 1. VALUES OF NONDIMENSIONAL RANGE X

$\theta_0$	$\tan^{-1} \frac{m}{\tan \theta_0}$	-60°	-45°	-30°	-15°	0°	15°	30°	45°	60°
-60°	-1.7321	0								
-45°	-1.0000	0.7318	0							
-30°	-0.5774	1.7320	0.6339	0						
-22.5°	-0.4142	2.2497*	1.0000	0.2786						
-15°	-0.2679	2.7321	1.3662	0.5775	0					
-11.25°	-0.1989		1.5412*	0.1327						
0°	0	3.4642	2.0000	1.1547*	0.5358					
11.25°	0.1989		2.3066		0.8980*	0.4226				
15°	0.2679	(3.7322)	2.3660	1.5774	1.0000	0.5000	0			
22.5°	0.4142		(2.4138)	1.6928	1.1644	0.7071*	0.2498			
30°	0.5774	3.4642	2.3660	(1.7322)	1.2679	0.8660	0.4642	0		
33.75°	0.6682		2.3066			0.9239	0.5535*			
37.5°	0.7673			1.6928	(1.3033)	0.9658	0.6287			
45°	1.0000	2.7321	2.0000	1.5774	1.2679	(1.0000)	0.7321	0.2591		
52.5°	1.3032	2.2497			1.1644	0.9659	(0.7673)	0.4226*	0	
56.25°	1.4966		1.5412			0.9329		0.5580	0.2447	
60°	1.7321	1.7320	1.3660	1.1547	1.0000	0.8660	0.7321	(0.5774)	0.3066*	0
67.5°	2.4142		1.0000			0.7071	0.6287	0.5380	(0.4142)	0.1998*
75°	3.7321	0.7318	0.6339	0.5775	0.5358	0.5000	0.4642	0.4226	0.3660	(0.2680)

TABLE 2. VALUES OF RANGE RATIO R

$\theta_0$	$\tan^{-1} \frac{m}{\tan \theta_0}$	-60°	-45°	-30°	-15°	0°	15°	30°	45°	60°
-60°	-1.7321	0		-0.5774	-0.2679	0	0.2679	0.5774	1.0000	1.7321
-45°	-1.0000	0.1961	0							
-30°	-0.5774	0.4641	0.2626	0						
-22.5°	-0.4142	0.6028*	0.4143	0.1608						
-15°	-0.2679	0.7320	0.5660	0.3334	0					
-11.25°	-0.1989		0.6465*		0.1018					
0°	0	0.9282	0.8286	0.6667*	0.4111	0				
11.25°	0.1989									
15°	0.2679	(1.0000)	0.9556	0.9106	0.6891*	0.4226				
22.5°	0.4142		0.9801	0.9773	0.7673	0.5000	0			
30°	0.5774	0.9282	(1.0000)	0.9773	0.8934	0.7071*	0.3256			
33.75°	0.6682		0.9801	(1.0000)	0.9728	0.8660	0.6050	0		
37.5°	0.7673		0.9556	0.9773	(1.0000)	0.9239	0.7213*			
45°	1.0000	0.7320	0.8286	0.9106	(1.0000)	0.9659	0.8194	0.4140		
52.5°	1.3032	0.6028		0.9106	0.9728	(1.0000)	0.9541	0.7319*	0	
56.25°	1.4996		0.6465		0.8934	0.9659	(1.0000)	0.9318	0.5425	
60°	1.7321	0.4641	0.5660	0.6667	0.7673	0.9239	0.9541	(1.0000)	0.7401*	0
67.5°	2.4142		0.4143			0.8660	0.8194	0.9318	(1.0000)	0.7455*
75°	3.7321	0.1961	0.2626	0.3334	0.4111	0.5000	0.6050	0.7319	0.8837	(1.0000)



SHEN

(d) Range For Flat Terrain Where  $m = 0$

In this case the usual formulae given by Equation (52) applies. The maximum nondimensional range is unity at  $\theta_0 = 45^\circ$ . The range ratio is the same as maximum nondimensional range.

(e) Ranges at Different Terrain Slopes  $m$

The nondimensional range given by Equation (49) are listed in Table 1 for different initial elevation angle  $\theta_0$ , in  $15^\circ$  intervals and different terrain angles, also in  $15^\circ$  intervals. Similarly, values in range ratio given by Equations (58) and (59) are listed in Table 2. It is observed from these tables that for each  $m$  there exists a symmetry about the optimal initial elevation angle  $\theta_0^*$  where the maximum range locates. Since at  $\theta_0 = 90^\circ$  and at  $\theta_0 = \tan^{-1}m$  the ranges are zeroes. The symmetry is located at

$$\theta_h - \theta_0^* = \theta_0^* - \theta_l \quad (86)$$

where  $\theta_h$  = initial elevation angles for high trajectory and  $\theta_l$  = initial elevation angles for low trajectory. As an example for a terrain angle of  $\tan^{-1}m = -30^\circ$ . The value of optimal initial elevation angle is at  $\theta_0 = 30^\circ$ , with a maximum nondimensional range of  $X_{\max} = 1.7322$  and range ratio of  $R = 1$ . The gun is fired at initial elevation angle of  $\theta_h = 45^\circ$  (for a high trajectory) and  $\theta_l = 15^\circ$  (for a low trajectory). Both cases give the same nondimensional range of  $X = 1.5774$  and range ratio of  $R = 0.9106 < 1$ .

(f) Interpolation

It is noted that for maximum range the optimal initial elevation angle  $\theta_0^*$  derived from Equation (56) is

$$\theta_0^* = \frac{1}{2} (90^\circ + \tan^{-1}m) \quad (87)$$

While at zero range Equation (50) becomes

$$\theta_0 = \tan^{-1}m \quad (88)$$

A linear interpolation from the above gives

$$\theta_0 = \frac{1}{2} [(1-\alpha)(90^\circ) + \alpha \tan^{-1}m + \tan^{-1}m] \quad (89)$$

$$\text{for } 0 < \alpha < 1$$

The ranges evaluated by the above equation for  $\alpha = 1/2$  are listed in Table 1 and 2 and marked with the symbol \*. It shows a relatively small changes of range ratio  $R$  for the interval  $-60^\circ \leq \tan^{-1}m \leq +60^\circ$ , giving the values of  $R$  from 0.6028 to 0.7455.

(g) Plot of Range Ratio  $R$  vs  $\theta_0$  For Various Values of  $\tan^{-1}m$ 

Figure 3 plots the range ratio  $R$  in Table 2 as a function of initial elevation angle  $\theta_0$  for different values of terrain angle  $\tan^{-1}m$ . The middle curve where  $\tan^{-1}m = 0$  is sinusoidal. This is evaluated from Equation (59) with a maximum of unity at  $\theta_0 = 45^\circ$ . It is noted that the initial elevation angle  $\theta_0$  spreads out over wider intervals for downhill target points and compressed into short intervals for uphill target points.

## NUMERICAL RESULTS FOR SENSITIVITY COEFFICIENTS

The numerical values for Sensitivity coefficients are listed in Table 3. They are as follows.

## (a) Sensitivity Coefficient at Maximum Ranges

It has been noted from Equation (85) that the sensitivity coefficient become infinite at maximum ranges. Therefore, design for maximum ranges are not suitable if sensitivity coefficients are of importance.

## (b) Sensitivity Coefficient at Minimum Ranges

Sensitivity coefficients also become zero at minimum ranges located at  $\theta_0 = 90^\circ$  and  $\theta_0 = \tan^{-1}m$ . Zero sensitivity should be avoided since zero ranges give no practical applications.

(c) Sensitivity for Horizontal Initial Elevation Angle  $\theta_0 = 0$ 

For this case the sensitivity coefficient is twice the terrain slope as given by Equation (81). This is for target points below the firing point.

(d) Sensitivity for Flat Terrain Where  $m = 0$ 

The sensitivity for this case is negative when  $\theta_0 < 45^\circ$  and positive when  $\theta_0 > 45^\circ$  as given by Equation (82). The sensitivity becomes  $-\infty$  as  $\theta_0$  approaches  $45^\circ$  from below and goes to  $+\infty$  as  $\theta_0$  approaches  $45^\circ$  from above.

(e) Sensitivity at Different Terrain Slopes  $m$ 

The sensitivity given by Equation (79) are listed in Table 3 for different initial angle  $\theta_0$ . It is also observed that an anti-symmetry exists for sensitivity just as symmetry exists for the range. For each  $m$  the anti-symmetry is about the optimal initial elevation angle  $\theta_0^*$  where the maximum range locates. Equation (86) for the ranges applies also here for sensitivities. As an example for a terrain angle of  $\tan^{-1}m = -30^\circ$  the value of optimal initial elevation

TABLE 3. VALUES OF SENSITIVITY COEFFICIENT S

$\theta_0$	$\tan^{-1} \frac{m}{m_0}$	$\tan \theta_0$	-60°	-45°	-30°	-15°	0°	15°	30°	45°	60°
-60°	-1.7321	0	-1.7321	-1.0000	-0.5774	-0.2679	0	0.2679	0.5774	1.0000	1.7321
-45°	-1.0000	-0.4227	0	0	0	0	0	0	0	0	0
-30°	-0.5774	-0.8660	-0.4640	-0.4640	0	0	0	0	0	0	0
-22.5°	-0.4142	-1.1646*	-0.7071	-0.7071	-0.2498	0	0	0	0	0	0
-15°	-0.2679	-1.5776	-1.0000	-1.0000	-0.5000	0	0	0	0	0	0
-11.25°	-0.1989	-1.1796*	-1.1796*	-1.1796*	-0.5000	-0.1293	0	0	0	0	0
0°	0	-3.4642	-2.0000	-2.0000	-1.1548*	-0.5358	0	0	0	0	0
11.25°	0.1989	± ∞	-4.2617	-4.2617	-2.7316	-1.0934*	-0.4663	-0.4663	0	0	0
15°	0.2679	± ∞	-6.4620	-6.4620	-5.6643	-1.3656	-0.5774	-0.5774	0	0	0
22.5°	0.4142	3.4635	± ∞	± ∞	± ∞	-2.2493	-1.0000*	-0.2786	0	0	0
30°	0.5774	1.5773	-6.4620	-6.4620	± ∞	-4.7324	-1.7321	-0.6342	0	0	0
33.75°	0.6882	1.1646	4.2617	4.2617	5.6640	± ∞	-2.4142	-0.8783*	0	0	0
37.5°	0.7673	1.1646	1.5773	2.0000	2.7319	4.7327	-3.7321	-1.2145	-0.2928	-0.3178	-0.5664*
45°	1.0000	1.1646	1.5773	2.0000	2.7319	2.2499	± ∞	-2.7327	-0.7319*	-0.5664*	-1.0000
52.5°	1.3032	0.8660	1.1796	1.0000	1.1546	1.3660	3.7321	± ∞	-1.7996	0	0
56.25°	1.4966	0.7010	1.1796	1.0000	1.1546	1.3660	2.4142	± ∞	± ∞	-0.3178	-0.5664*
60°	1.7321	0.4227	0.8660	1.0000	1.1546	1.3660	1.7321	2.7314	± ∞	-1.0000	0
67.5°	2.4142	0.4227	0.7010	0.7010	0.5000	0.5358	1.0000	1.2144	1.8233	± ∞	-0.3859*
75°	3.7321	0.4227	0.4640	0.4640	0.5000	0.5358	0.5774	0.6340	0.7320	1.0000	± ∞

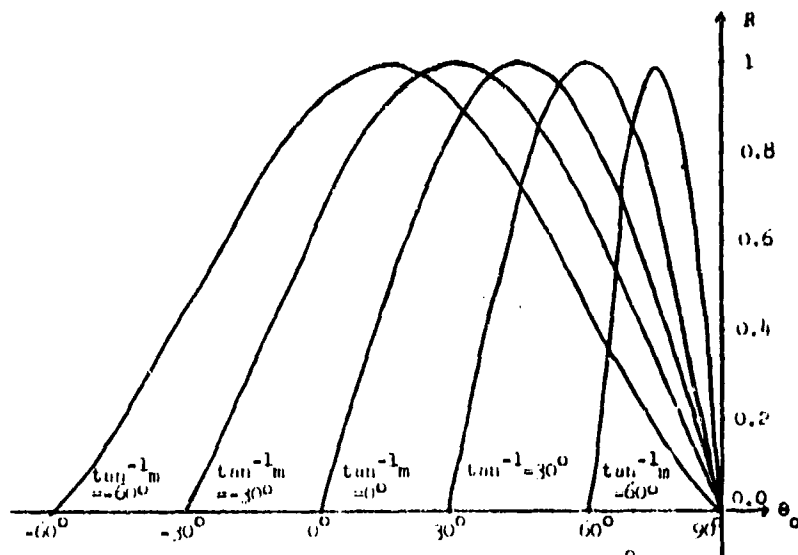


Figure 3: Range Ratio vs. Initial Elevation Angle  $\theta_0$   
for Various Terrain Angles  $\tan^{-1}m$

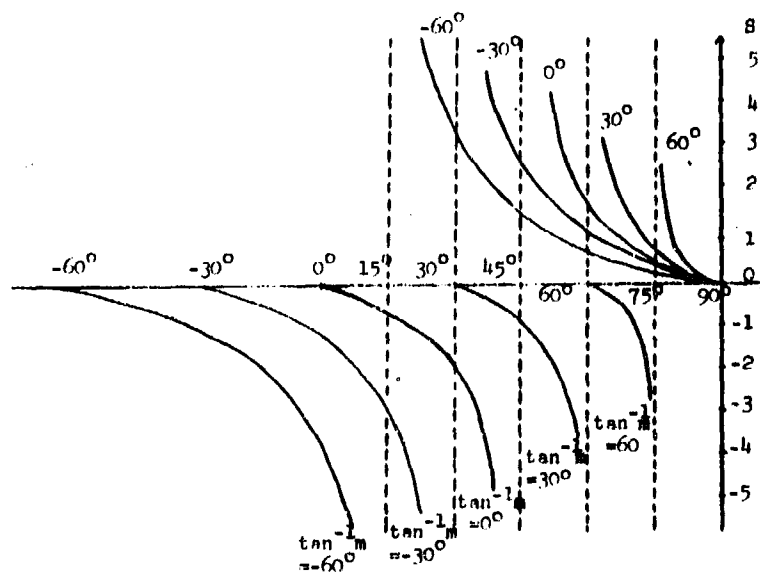


Figure 4: Sensitivity Coefficient  $S$  vs. Initial Elevation Angle  $\theta_0$  for Various Terrain Angles  $\tan^{-1}m$

SHEN

angle is at  $\theta_0^* = 30^\circ$ . If the gun is fired at initial elevation angle of  $\theta_h = 45^\circ$  for a high trajectory the sensitivity is listed as 2.7319 in Table 3. On the other hand if the gun is fired at  $\theta_0 = 15^\circ$  for a low trajectory the sensitivity is listed as -2.7319, which is the same in magnitude but different in polarity as that for a high trajectory. The above facts are important in that there exists a sign change for designing sensitivity for high and low trajectories.

(f) Interpolation

The interpolation formulae given by Equation (89) also applies to sensitivity study. For  $\alpha = 1/2$  the sensitivity coefficients are listed in Table 3 and marked with the symbol \*. It shows that for the interval  $-60^\circ < \tan^{-1}m < 60^\circ$ , the sensitivity coefficient S has the interval from -1.1646 to -0.3859. If a logarithm is taken on the absolute value of S, which varies from zero to infinity, the change of  $\ln|S|$  becomes small in the interval mentioned above.

(g) Plot of Sensitivity Coefficient S vs  $\theta_0$  For Various Values of  $\tan^{-1}m$

Figure 4 plots the sensitivity coefficient S as a function of initial elevation angle  $\theta_0$  for different values of terrain angle  $\tan^{-1}m$ . The values of S become unbounded at maximum range where the initial elevation angle is  $\theta_0^*$ . It is also noted that the initial elevation angle  $\theta_0$  spreads out over wider intervals for downhill target points and compressed into short intervals for uphill target points. These are evaluated by Equation (79) and listed in Table 3.

CONSTANT SENSITIVITY

A gun can be designed to produce a constant interior sensitivity as shown in Equation (9) by selecting a muzzle elevation angle deviation proportional to the muzzle velocity deviation ratio. To match the exterior sensitivity to the interior sensitivity, the former should also be kept constant. Thus from Equation (79) we have

$$S = - \frac{2(\tan\theta_0 - m)}{1 - \tan^2\theta_0 + 2m\tan\theta_0} = \ell \quad (90)$$

where  $\ell$  is a constant.

Solving for m from Equation (90) one obtains

$$m = \frac{2\tan\theta_0 + \ell - \ell\tan^2\theta_0}{2 - 2\ell\tan\theta_0} \quad (91)$$

SHEN

The difference between two slopes gives

$$\tan\theta_0 - m = \frac{-\ell(1 + \tan^2\theta_0)}{2 - 2\ell\tan\theta_0} \quad (92)$$

The range ratio  $X$  for constant exterior sensitivity  $\ell$  from Equation (49) becomes

$$X = \frac{-\ell}{1 - \ell\tan\theta_0} \quad (93)$$

The range ratio  $R$  from Equations (58) and (59) for the above is

$$R = \frac{-\ell\tan\theta_0^*}{1 - \ell\tan\theta_0} \quad (94)$$

where  $\tan\theta_0^*$  is given in Equation (55) for any terrain slope  $m$ .

Usually the terrain slope  $m$  is given first and the value of  $\ell$  is then assigned according to the matching of sensitivities. Instead of using the relationship in Equations (94) and (55) we proceed to solve for  $\tan\theta_0$  from Equation (79) in terms of the terrain slope  $m$  and constant sensitivity coefficient  $\ell$ .

$$\tan^2\theta_0 - 2(m + \ell^{-1})\tan\theta_0 + (2m\ell^{-1} - 1) = 0 \quad (95)$$

Solving for the above quadratics one obtains

$$\tan\theta_0 = (m + \ell^{-1}) + [(m + \ell^{-1})^2 + (1 - 2m\ell^{-1})]^{1/2} \quad (96)$$

Table 4 gives  $\tan\theta_0$ ,  $\theta_0$ ,  $\tan\theta_0^*$ ,  $X$ ,  $X_{\max}$  and range ratio  $R$  for constant sensitivity.

$$S = \ell = -1 \quad (97)$$

It is noted that by keeping the interval of terrain slope  $\tan^{-1}m$  within  $15^\circ$  the change of  $R$  in Table 4 is less than 0.060. For example to fire a target downhill at  $-15^\circ$  and horizontally at  $0^\circ$  the range ratios  $R$  are 0.6550 and 0.7071 respectively if the sensitivity coefficient is kept constant at  $S = \ell = -1$ .

TABLE 4. RANGE RATIO R FOR CONSTANT SENSITIVITY OF  $\lambda = -1$

	-60°	-45°	-30°	-15°	0°	15°	30°	45°	60°
$\tan^{-1}l_m$									
$\tan\theta_0$	-0.4960	-0.2679	-0.0499	0.1715	0.4142	0.7073	1.1049	1.7321	2.9682
$\theta_0$	-26.5°	-15°	-2.85°	9.8°	22.5°	35.3°	47.9°	60°	71.3°
$\tan\theta_0^*$	0.2680	0.4142	0.5774	0.7673	1.0000	1.3033	1.7321	2.4138	3.7322
X	1.9841	1.3122	1.0525	0.8536	0.7071	0.5857	0.4751	0.3660	0.2520
$X_m$	3.7322	2.4138	1.7321	1.3033	1.0000	0.7673	0.5714	0.4142	0.2680
R	0.5316	0.5436	0.6077	0.6550	0.7071	0.7634	0.8228	0.8837	0.9403

SHEN

## CONCLUSIONS

The principal equation of exterior ballistics is derived with the elevation angle as independent variable. Solutions for tangential velocity are determined in terms of this elevation angle and initial parameters for the case of drag proportional to square of velocity. The trajectory equations are expressed as function of velocity. The closed form solutions for range and elevation of the impact point are found for the case of zero drag.

The nondimensional range and elevation are obtained from the actual range and elevation divided by an energy terms involving the square of initial velocity. A terrain slope is defined as the elevation divided by the range. The nondimensional range is then a function of this terrain slope as well as the tangent of the initial elevation angle. The maximum range is located at an optimal initial elevation angle, which is a function of the terrain slope. The range ratio is the nondimensional range divided by the corresponding maximum range. This range ratio has a maximum of unity and is used to determine whether the amount of energy supply is fully put into useful work.

The error increments in hitting a target are derived and set to zero for a bull's eye landing. The sensitivity coefficient is defined as the ratio of increments of the initial elevation angle to the increments of the natural logarithm of the velocity. It is expressed as a function of the initial elevation angle and the terrain slope.

Maximum range is found to be located at an optimal initial elevation angle, which is half the sum of  $90^\circ$  and the terrain angle. Minimum ranges of zero have two locations: one has the initial elevation angle equal to the terrain angle and the other has the initial elevation angle equal to  $90^\circ$ . The ranges have a symmetry about the maximum range for high and low trajectories. Both the nondimensional range and the range ratio for different initial elevation angles under different terrain slopes are listed and plotted. An interpolation factor is introduced to take advantage of the fact that it is the location where small variation in range ratio occurs.

Sensitivity coefficients become infinite at maximum ranges and zero at minimum ranges of zero. The sensitivity coefficients are anti-symmetrical about an optimal initial elevation angle at the same location for maximum range. The sensitivity coefficient is positive for high trajectories and negative for low trajectories. An interpolation factor is also employed for selecting sensitivity coefficient within a reasonable bound. This together with the small variation in range ratio gives the opportunity for the gun to hit a target reasonably well.



SHEN

Due to the uncertain of muzzle velocity deviation a gun may be designed by its interior ballistics to give automatically a proportional deviation of its initial elevation angle when the gun fires. This is equivalent to keep the sensitivity coefficient constant for any nominal initial elevation angle and terrain slope. The range ratio can thus be determined in terms of this constant and other parameters. It is found that if the terrain slopes are held with a certain domain, the range ratios can also be kept within a small bound.

#### DISCUSSION AND FUTURE WORK

The present work gives some general characteristics of the sensitivity coefficient vs. range. Future work will consider drag as function of velocity and solve analytically or numerically, for solutions of range and elevation as function of the initial velocity, initial and impact elevation angles. After that the sensitivity coefficients will be derived accordingly, not only in the direction of the plane of the trajectory, but also in the perpendicular direction thereof. A stochastic analysis giving the analytical expression of the covariances may also be desirable.

The interior ballistic coefficient will be investigated further in the future. First the dynamics in partial differential equation must have a term involving velocity. This velocity can be that of the shell mass or some kinetic energy terms effecting the muzzle velocity of the projectile. Taking the partial differentiation of this P.D.E. with respect to this velocity, a modified P.D.E. is obtained. Sensitivity coefficients for interior ballistics can be found by solving this new P.D.E. for certain partial differentials at muzzle location, provided that all the boundary conditions are known.

#### REFERENCES

1. Simkins, T. E., "Radial and Transverse Response of Gun Tubes by Finite Element Methods," Proceedings First Conference on Dynamics of Precision Gun Weapons, held at Rock Island, Illinois, under the auspices of U.S. Army Armament Research and Development Command Dover, New Jersey, January 26-27, 1977.
2. Miele, Angelo, "Flight Mechanics, Volume 1 - Theory of Flight Paths," Addison Wesley, 1962.
3. Rheinmetall Staff, "Rheinmetall Weapons Engineering Handbook," September 1975. Translation from German. Original Second Edition by Rheinmetall GmbH, Dusseldorf, FRG.

KASTEN, MADIWALE & WU

TITLE: Closed Loop Control of  
Recoil Mechanisms

ROBERT E. KASTEN  
Ware Simulation Division, SARRI-ENW-3900  
Rock Island Arsenal, Rock Island, Illinois 61299

APPA N. MADIWALE  
Department of Mechanical Engineering  
University of Wisconsin  
Madison, Wisconsin 53706

S. M. WU  
Department of Mechanical Engineering  
University of Wisconsin  
Madison, Wisconsin 53706

ABSTRACT:

This paper describes a pressure feedback controller for a modified hydropneumatic recoil mechanism which incorporates a servo-valve in a flow path in parallel with the conventional control orifice. The feedback control system achieves greatly improved rod pull characteristics for both high and low zone charges. The pressure feedback controller is described, the mathematical model used for design and evaluation is described and results of computer simulations of the system response to several zone charges are compared with conventional and optimally controlled recoil mechanisms.

## CLOSED LOOP CONTROL OF RECOIL MECHANISMS

ROBERT E. KASTEN  
WARE SIMULATION DIVISION  
SARRI-ENW-3900  
ROCK ISLAND ARSENAL  
ROCK ISLAND, ILLINOIS 61299

APPA N. MADIWALE  
DEPARTMENT OF MECHANICAL ENGINEERING  
UNIVERSITY OF WISCONSIN  
MADISON, WISCONSIN 53706

S. M. WU  
DEPARTMENT OF MECHANICAL ENGINEERING  
UNIVERSITY OF WISCONSIN  
MADISON, WISCONSIN 53706

### I. INTRODUCTION

The reaction forces resulting from the firing of an artillery round are transmitted to the gun carriage through the recoil mechanism. The gun carriage in turn transmits these forces to the ground or weapon emplacement. The objective of the recoil mechanism is to control the force transmitted to the gun carriage so as to minimize the stress on the carriage and the emplacement. Large recoil forces are undesirable because they shorten the fatigue life of the carriage and require more frequent re-emplacment of the weapon. The recoil mechanism reduces the recoil force by spreading out its time duration, and hence, the recoil distance. The available recoil distance is limited and is a major design constraint. The peak force transmitted to the carriage is a minimum when the recoil force is constant over the available recoil distance, and this is the usual goal for the recoil mechanism designer. Army howitzers, however, fire a variety of projectiles with several different propellant charges (zone charges). The recoil mechanism, therefore, must function satisfactorily for a wide range of firing impulses as well as a full range of elevation angles.

Modern army howitzers utilize hydropneumatic recoil mechanisms of the modified Puteaux type, shown schematically in Figure 1. In these recoil mechanisms, the kinetic energy imparted to the recoiling parts by weapon

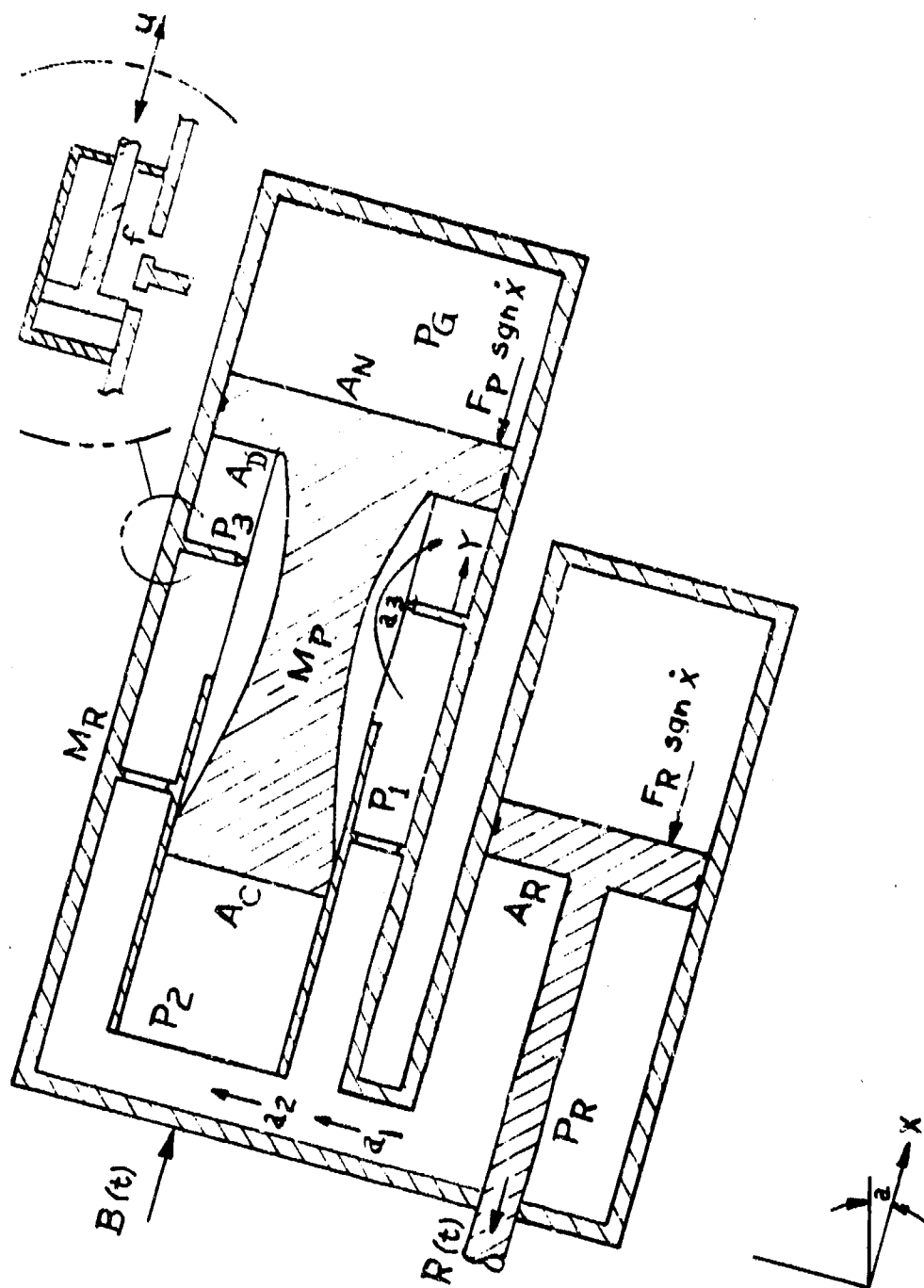


FIG 1. BLOCK DIAGRAM OF CONVENTIONAL RECOIL MECHANISM

## KASTEN, MADIWALE & WU

firing is dissipated mainly by throttling hydraulic fluid through a variable area control orifice. Some energy is stored in the gas spring of the recuperator cylinder to return the weapon to battery (firing position) in the counter recoil cycle. The variable area of the control orifice is usually implemented by machining a groove of varying depth into the control rod. As the control rod moves relative to the recuperator cylinder, the area of the orifice formed by the groove changes.

Coberly (1), and Frantz and Nerdahl (2) have developed mathematical models of the dynamics of hydro-pneumatic recoil mechanisms, and design procedures for the control orifice. These procedures allow the design of a control orifice which achieves a nearly optimal (flat) rod pull characteristic for a specific breech force or zone charge. It is not practical, however, to have a separate control orifice for each zone charge, therefore, the designer optimizes the control orifice for the highest impulse expected. The rod pull characteristics obtained for lower zone charges exhibit peak forces that are significantly higher than the optimal characteristic for that round but still smaller than the peak force for the highest zone charge. While the resulting recoil mechanism performance is satisfactory, the large peak forces for the low zone rounds reduce the fatigue life of the carriage and require more frequent re-emplacement of the weapon.

A more serious problem often arises when a higher impulse round is introduced for a fielded weapon system. The rod pull characteristic for such rounds often exhibit peak forces greater than required by an optimized recoil system and much greater than the force for which the system was designed. Because the control orifice is machined into the control rod, it is expensive and often impractical to modify it. The potential user of the new round must then trade off weapon life and carriage stability in return for the increased performance of the high impulse round.

A modification to a conventional recoil mechanism, shown in the inset in Figure 1, suggested by engineers at the General Thomas J. Rodman Laboratory, would permit the control orifice to be adapted for the particular round fired. This system and the derivation and evaluation of an optimal controller designed for it have been reported in reference 3. For convenience a brief description is included here. The modification to the conventional recoil mechanism consists of an added flow path through an externally controlled servo-valve, associated sensors, and the controller. The added flow path is in parallel with the

KASTEN, MADIWALE & WU

conventional control orifice. The choice of sensors, which monitor the state of the system, is not unique and depends on the control law chosen for the servo-valve. Possible states to be monitored include the recoil position, velocity, and acceleration, oil pressure and rod pull. The controller is a device which processes signals from the sensors and uses them to generate a command to the servo-valve. Presently an analog or digital electronic device is contemplated for the controller, however, a fluidic control system is an attractive concept for a fielded system.

The main features of this concept are that it can be added to an existing system, it requires no external hydraulic power, and, since the servo-valve carries only a small fraction of the total flow, it can be implemented with state-of-the-art components. The flow rate through the servo-valve seems to offer another advantage in that computer predictions of the feedback controller response have thus far exhibited no tendency toward instability as would a higher gain system.

Two basically different design procedures for the feedback controller have been examined by applying them to the M37 recoil mechanism for the M102, 105mm howitzer: a classical design technique for a pressure regulator system; and an optimal design technique where the goal of the design procedure is to find gains for position and velocity feedback which minimize a cost function.

Computer simulations of the resulting controllers have been very encouraging for both design procedures. Reference 3 reported the results for the optimal system while Section IV of this paper reports the results for the conventional pressure feedback system and compares them with the standard M37/M102 rod pull characteristics and with the results for an optimal controller derived using an improved objective function.

## II. SYSTEM DESCRIPTION

A conventional hydropneumatic recoil mechanism is shown schematically in Figure 1. The assembly of recoiling parts consisting of the gun barrel, the recuperator cylinder, the control rod (floating piston) and the recoil cylinder slide on the piston which is attached to the carriage by the recoil rod. When the weapon is fired, the breech force,  $B(t)$ , is applied to the recoiling parts, and the recoil force (rod pull) is transferred to the carriage through the recoil rod. The hydraulic fluid in the recoil cylinder and chambers 1, 2 and 3 acts as a mechanical linkage between

# KASTEN, MADIWALE & WU

the recoil cylinder and the control rod. The hydraulic fluid also dissipates energy due to its flow through various orifices, principally through the control orifice,  $a_3$ . As the system recoils, the control rod moves relative to the recuperator cylinder and the effective area of the variable depth groove which forms the control orifice changes. Simultaneously, the control rod compresses the nitrogen in the gas chamber of the recuperator cylinder, storing energy to return the recoiling parts to battery (firing position) in the counter recoil cycle.

The equations of motion for this type of recoil mechanism have been developed and reported elsewhere (1, 2, 3). It can be shown that the system dynamics can be described by a single, highly non-linear, second order differential equation:

$$m\ddot{x} + \frac{\rho}{2} (C + C_0(x)) \dot{x}^2 + F \operatorname{sgn}(\dot{x}) + k_0 (1 - k_1 x)^k = B(t) + w \sin a \quad (1)$$

The first term on the left hand side of this equation is the force required to accelerate the effective mass,  $m$ , of the recoiling parts. The second term is the force generated by the potential flow across two orifices, a fixed orifice with effective area  $C$  and a variable orifice of effective area  $C_0(x)$ .  $\rho$  is the density of the hydraulic fluid. The third term on the left hand side is an effective coulomb friction term and the fourth term represents the force required to compress the gas spring. The applied forces on the right hand side are the effective weight of the recoiling parts acting through the elevation angle,  $a$ , and the breech force,  $B(t)$ . The relationships between the coefficients of equation (1) and the parameters of the recoil mechanism are given in Appendix A.

The addition of the servo-valve in the modified recoil mechanism has little effect on the form of equation (1); it is only necessary to replace the effective area of the variable orifice area  $C_0(x)$  by a term  $C_0(x, u)$  where  $u$  is the effective area of the servo-valve. It can be shown that  $C_0(x, u)$  can be obtained from  $C_0(x)$  by replacing the orifice area,  $a_3(x)$ , everywhere by  $(a_3(x) + u)$ , the area of the new control orifice. The servo-valve dynamics may be approximated in the model by a first order differential equation:

$$\dot{u} = (u_c - u) / T \quad (2)$$

KASTEN, MADIWALE & WU

where  $u_c$  is the commanded valve area (the output of the feedback controller) and  $T$  is the time constant of the servo-valve.

The parameters of the servo-valve were chosen to be consistent with the parameters of a standard electro-hydraulic servo-valve capable of handling 20% of the maximum design flow of the recoil mechanism. It is recognized that the servo-valve used for this application might differ from the typical electrohydraulic servo-valve used in control applications, however, in the authors judgement these modifications will not affect the dynamics significantly.

### III. DERIVATION OF THE SERVO-VALVE CONTROLLER

Two types of controller have been investigated for this application: An optimal controller and a classical pressure feedback controller.

#### Optimal Controller:

The goal of the optimal control design was to find the gains for a linear state variable feedback law of the form

$$u_c = g_1 x + g_2 \dot{x} \quad (3)$$

such that some cost function  $J(g_1, g_2)$  is minimized without violating the physical constraints of the system. The constrained optimization problem was transformed into an unconstrained optimization problem by adding quadratic penalty functions for violation of constraints to the objective function. The physical constraints of the problem are; the recoil distance,  $x$ , is limited by  $x_m$ , the maximum recoil length, the servo-valve area,  $u$ , is always less than  $u_m$ ; and, there is no cavitation in chamber 3 or  $P_3(t) > P_{min}$  for all  $t$ .

The objective function must be selected by engineering judgement to achieve the desired effect. The cost function used for the previous work (3) was

$$J(g_1, g_2) = \int_0^T \left\{ w_1 (R(t) - R(0))^2 + w_2 \left( \frac{dR}{dt} \right)^2 + w_3 (x(t) - x_m)^2 + w_4 (P_3(t) - P_{min})^2 + w_5 (u - u_m)^2 \right\} dt \quad (4)$$



## KASTEN, MADIWALE & WU

where the first two terms form the objective function while the last three terms are penalty functions for constraint violations. The first term of the objective function is a cost for large values of rod pull,  $R(t)$ , while the second term assesses a cost for deviations from a flat rod pull characteristic. It was found that an iterative process of changing the relative weighting factors  $w_1$  and  $w_2$  was required to obtain a satisfactory solution. The procedure was effective but time consuming. A new cost function has since been devised:

$$J(g_1, g_2) = \underset{0, T}{\text{Max}} (R(t)) + \int_0^T \{ w_3 (x(t) - x_m)^2 + w_4 (P_3(t) - P_{min})^2 + w_5 (u - u_m)^2 \} dt \quad (5)$$

where the operator  $\underset{0, T}{\text{Max}} (R(t))$  selects the maximum value that  $R(t)$  takes on over the interval 0 to T. The remaining terms of the cost function are the penalty functions which are unchanged. The control law obtained from the use of this objective function is essentially the same as with the previous cost function, however, the result is obtained directly without iteration.

An unconstrained non-linear optimization algorithm known as the Davidon-Fletcher-Powell method was used to solve for the optimal gains for both cost functions. The results are presented in Section IV. It should be noted that the optimal gains obtained are different for each zone charge so that the correct zone must be entered into the controller either by the gun crew or an automatic zone sensor.

### Classical Pressure Feedback Controller:

The relationship between the rod pull,  $R(t)$ , and the oil pressure in the recoil cylinder,  $P_r(t)$ , is

$$R(t) = P_r(t) A_r - F_r \text{sgn}(\dot{x}). \quad (6)$$

From this expression it is evident that holding the oil pressure constant over the recoil cycle will result in a constant rod pull. The control problem is a typical regulator problem where an electrical signal proportional to the pressure difference between the actual and the desired or set pressure is applied to the servo-

KASTEN, MADIWALE & WU

valve in such a way that the magnitude of this pressure difference is reduced. However, due to the highly non-linear nature of the system equations, the highly developed tools for linear control system design and analysis such as Bode plots, Nyquist Criterion and Root Locus can not be applied.

The required set pressures for the pressure regulator for each zone charge were obtained from the simulation results for the optimal controller. They could also have been calculated by the moment area method of Frantz and Nerdahl (2).

Modifications to the pressure regulator were required for the highest zone round simulated. The breech force for this round was obtained by increasing the breech force for the maximum standard round (zone 7) by 10% at each point in time. For convenience this mythical round is referred to in this paper as a zone "8". When these large forces were applied to the recoil mechanism computer simulation, the recoil pressure would rise too rapidly and cavitation ( $P_3 < 0$ ) would occur in chamber 3. To prevent this rapid pressure buildup, an additional feedback loop was added that increased the servo-valve area whenever  $P_3$ , the pressure in chamber 3, dropped below 100 psi. In addition, due to the time delay in the initial servo-valve response, it was necessary to require that the servo-valve be held partially open at  $t = 0$ .

The feedback gains were found by an iterative trial and error procedure using the digital computer simulation. If the simulated performance was not acceptable or if system constraints were violated, the pressure feedback gain or the set pressure was modified to improve performance. The system showed no tendency to oscillate for any of the gains used. This is attributed to the low servo-valve flow rates required by the modified recoil mechanism.

The system was found to be quite sensitive to variations in set pressure but fairly insensitive to gain variations. It was found that a single fixed feedback gain gave improved performance for zones 5 through "8", although a higher gain improved performance for zones 5 and 6. Zones lower than zone 5 were not examined. It was apparent from the results for the higher zones that very high servo-valve flow rates would be required to achieve good results for low zone rounds. These high flow rates coupled with the relatively low peak forces for the low zones make it unattractive to attempt to achieve optimal, flat response for all zones.

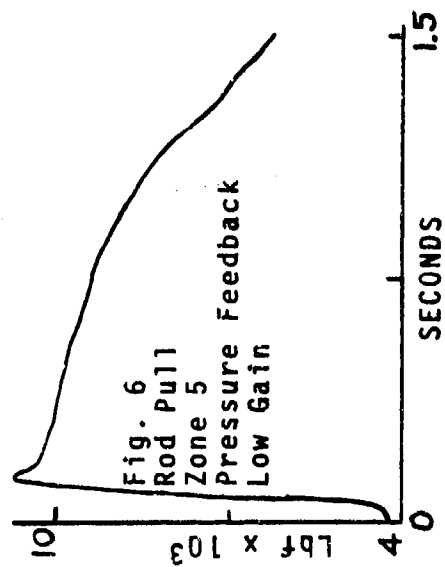
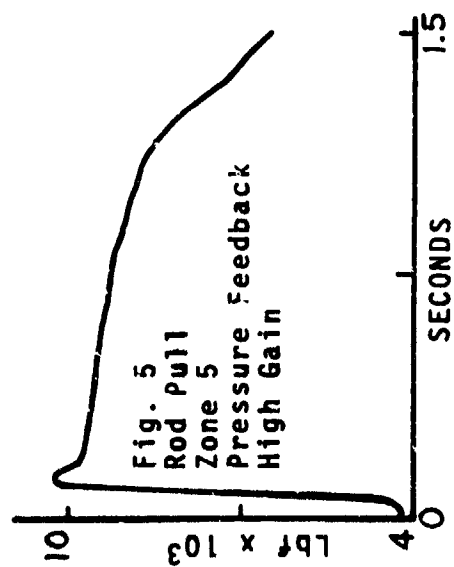
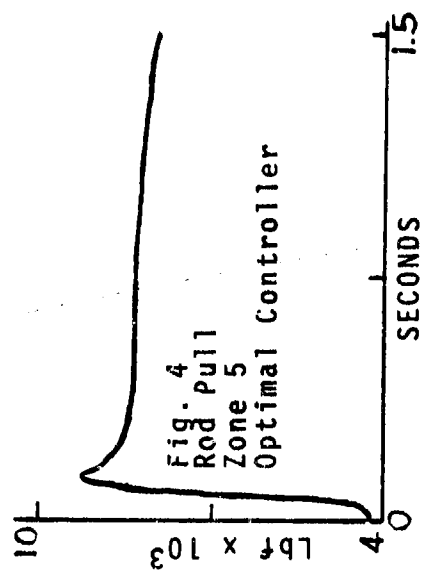
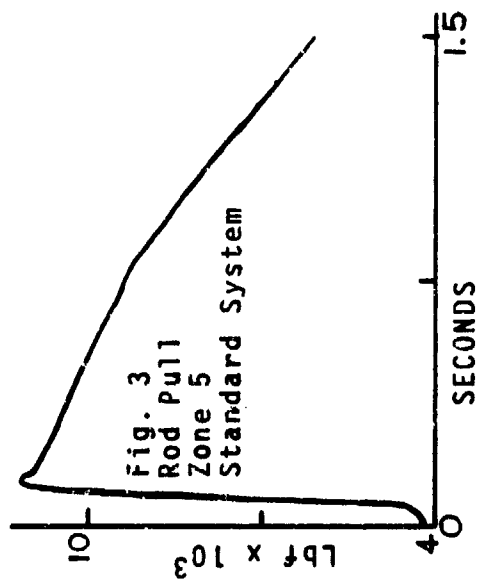
## IV. RESULTS AND DISCUSSION

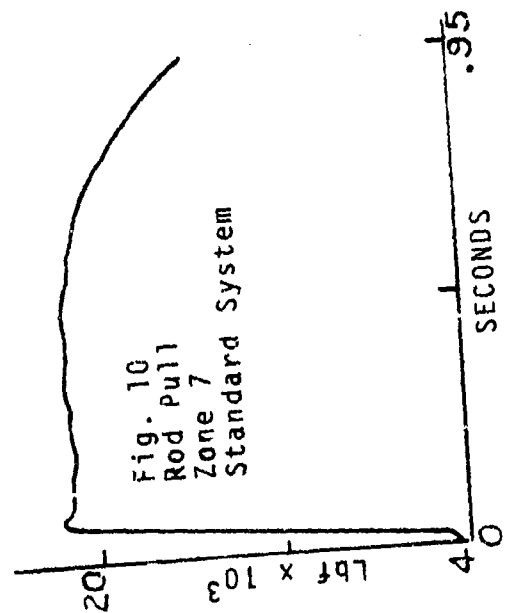
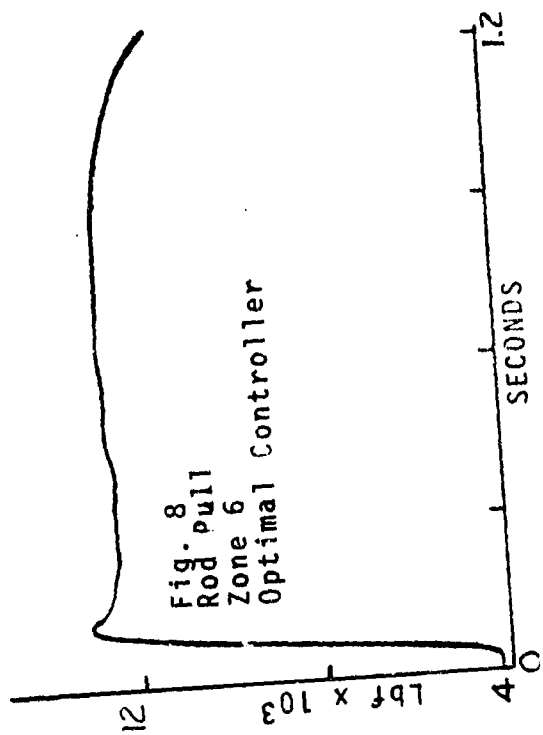
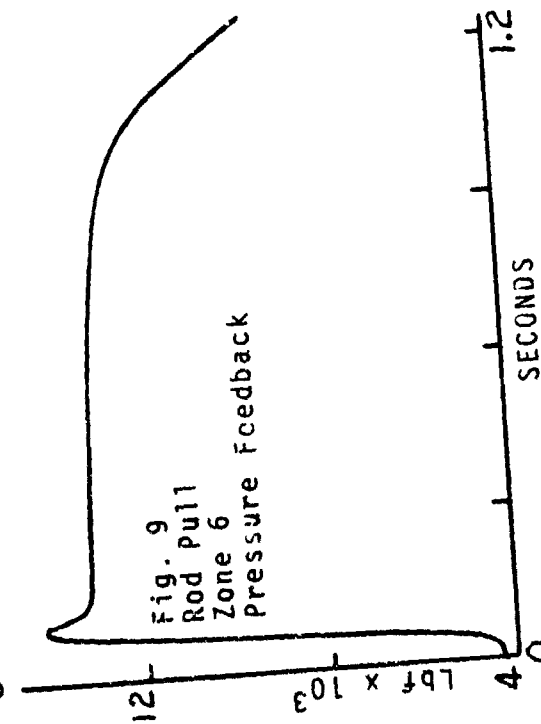
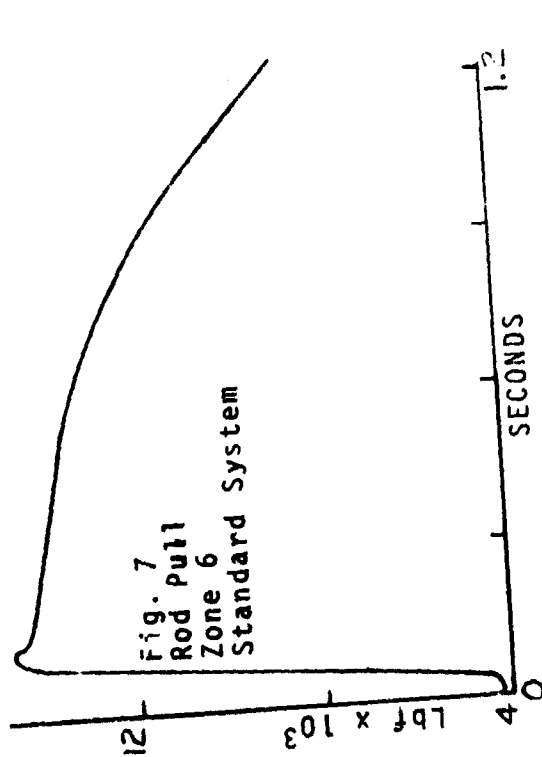
The dynamic equations for the M102 howitzer's conventional M37 recoil mechanism; for a modified recoil mechanism with an optimal feedback controller; and for a modified recoil mechanism with a pressure feedback controller were modeled on a digital computer utilizing the Continuous System Modeling Program (CSMP). The computer simulation included the modified equations of motion for the hydraulic system, the dynamics of the servo-valve (modeled as a first order lag network), and an initial time delay (6 ms.) before servo-valve actuation. The initial time delay was included to simulate the time required for an automatic zone detector to identify the zone fired and select the proper feedback gains for that zone. Some time delay would be encountered in the servo-valve itself since the spool valve cannot respond to commands until hydraulic pressure builds up and flow begins.

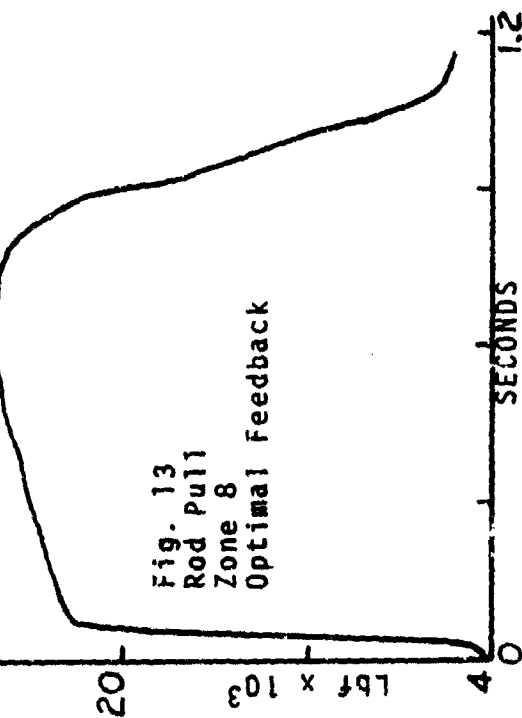
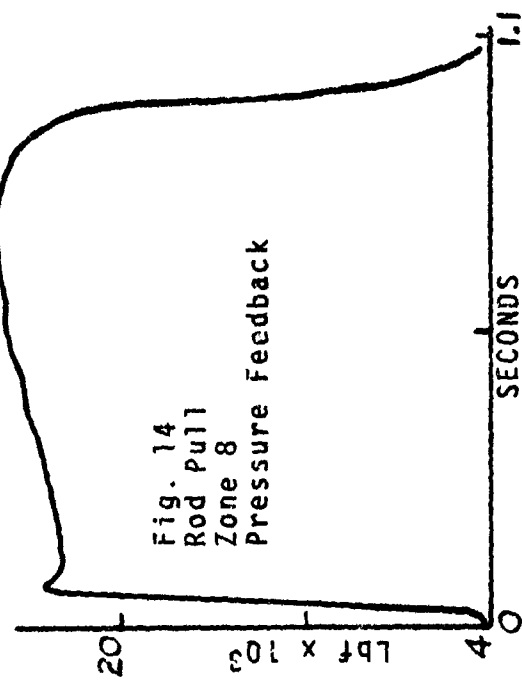
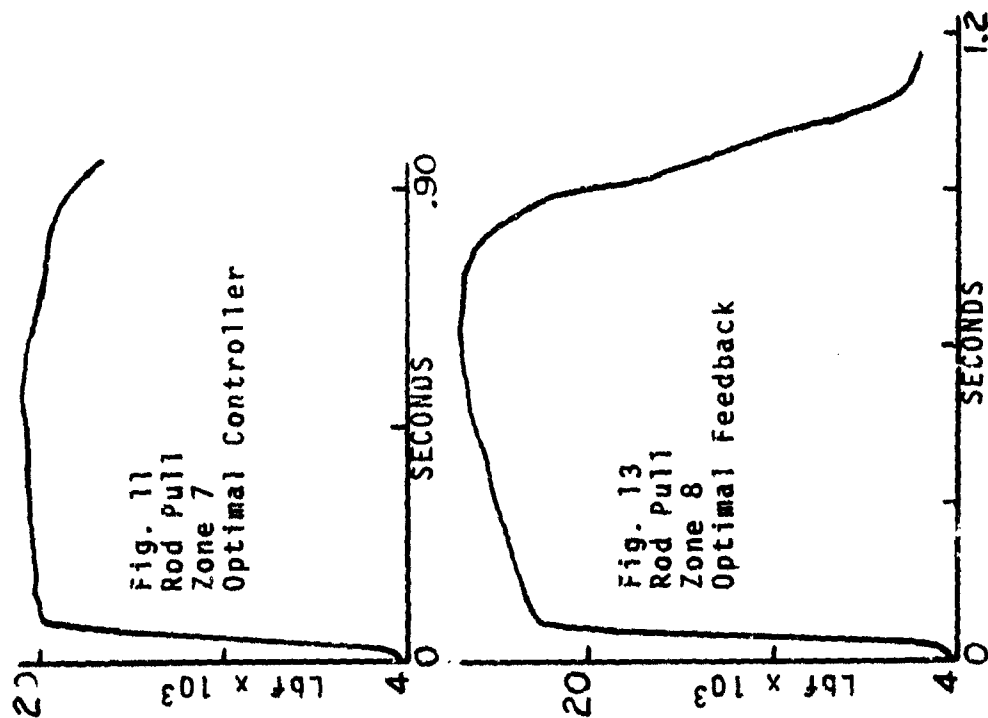
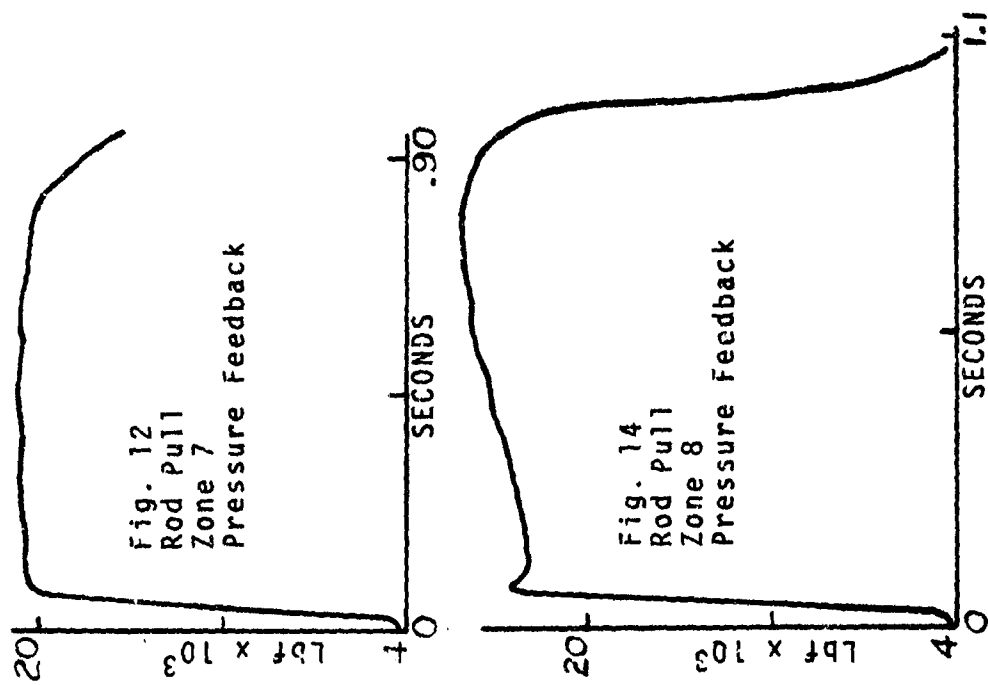
The computer simulations of all three systems were exercised for zone charges 5 through "8" (zone 7 is the highest zone charge for the M102 howitzer). Breech force data for the standard rounds was obtained from M. Nerdahl of Rock Island Arsenal. In addition, the breech force for a high impulse round was approximated by increasing the zone 7 breech force at every time instant by 10%. This hypothetical round is referred to in this paper as a zone "8".

It was found from the computer simulation of the standard recoil mechanism that the zone "8" round would produce cavitation in chamber 3. Similarly, with the initial time delay in the servo-valve model, the zone "8" round caused cavitation even with the feedback controllers. However, by firing with the servo-valve initially partially open, cavitation would be avoided and satisfactory performance was obtained. (See Figures 13 and 14). Since an automatic zone detector was assumed, the same initial servo-valve opening was used in the simulations for all rounds with the feedback controllers. The resulting rod pull characteristics for zone 5 are given in Figures 3 through 5, zone 6 in Figures 7 through 9, zone 7 in Figures 10 through 12, and zone "8" in Figures 13 and 14. Figure 6 shows the rod pull characteristic for a zone 5 round with reduced gain for the pressure feedback system. Table 1 compares the most important parameters of the recoil cycle for the different rounds and recoil mechanisms.

These results indicate that both feedback control systems perform about equally well for zone "8". Although the need to avoid cavitation in chamber 3 prevented







KASTEN, MADIWALE & WU

TABLE 1  
RESULTS OF FEEDBACK CONTROL OF THE  
RECOIL MECHANISM FOR ZONES 5, 6, 7 and "8"

<u>ZONE</u>	<u>CONTROLLER</u>	<u>MAX RECOIL LENGTH</u>	<u>RECOIL TIME (SEC)</u>	<u>MAX ROD PULL (Lbf)</u>	<u>MAX SERVO-VALVE AREA (Sq. In.)</u>
"8"	Pressure	27.4	.11	25500	.008*
"8"	Optimal	27.3	.11	25650	.008*
7	Standard	27.0	.13	21500	0.0
7	Pressure	27.0	.13	21000	.008*
7	Optimal	27.4	.13	20725	.008*
6	Standard	25.8	.17	14700	0.0
6	Pressure	26.3	.17	14200	.008*
6	Optimal	27.5	.16	13060	.135
5	Standard	24.0	.19	11360	0.0
5	Pressure	25.0	.19	10300	.0107
5	Optimal	28.2	.20	9280	.032

\* Initial Servo-valve Area

KASTEN, MADIWALE & WU

both systems from achieving an optimal, flat rod pull characteristic, the performance is a substantial improvement over the conventional recoil mechanism, which, as mentioned above, suffered cavitation.

For zone 7, performance of both feedback control systems was about equal to the standard recoil mechanism. This is to be expected, since the standard recoil mechanism was optimized for this round.

Substantial decreases in peak rod pull are achieved at zones 5 and 6 by the optimal feedback controller. The pressure feedback system shows a more modest improvement for these zones, however, the peak servo-valve areas and flow rates are significantly lower than those of the optimal controller. Increasing the feedback gains for the pressure controller would cause both the performance of the pressure feedback system and the required servo-valve area to approach that of the optimal system. The effect of gain on the performance of the pressure feedback system is evident from a comparison of Figures 5 and 6.

It is apparent from an examination of Table 1 that achieving the desired, flat rod pull characteristic at lower zone rounds would require increasingly large servo-valve areas and larger, more expensive servo-valves. Since the peak recoil forces drop off rapidly at lower zone charges, it is probably not cost effective to attempt to achieve the flat rod pull characteristic over the full range of firing impulses.

It should be noted that the computer simulations of the optimal feedback controller reported in this paper contained several effects not included in the design model. The design model assumed an idealized servo-valve. The performance of the controller, however, was substantially unaffected, indicating a basically robust design.

Because of the difficulty experienced to date in obtaining reliable position and velocity data in the hostile, high g environment of the recoil mechanism, the use of pressure feedback in the modified recoil mechanism may be a less risky approach, even if some loss of performance is suffered at the lower zones.

#### V. FUTURE WORK

Computer simulations have been utilized to demonstrate the potential for feedback control of recoil mechanisms. A limited amount of testing in support of this



program has indicated that automatic zone sensing based on the initial acceleration of the recoiling parts is feasible. It remains to demonstrate that a servo-valve can be made to perform as modeled in the high pressure, high flow region and survive the high shock environment of the recoil mechanism.

Both of the controllers discussed above for the modified recoil mechanism could be implemented with either analog or digital electronic systems. Because of the logic required to adjust gains and/or set points for the various zone rounds, a microprocessor based digital controller is preferred. This digital controller would have several advantages: gains and set points could be easily adjusted as required by experimental data; different control laws could be implemented with minimal hardware changes, and the same controller, with suitable programming changes, could be utilized by a variety of artillery systems. A microprocessor based controller would consist of a microprocessor with a real time clock and power supply, a programmable interface, transducers for measuring system states and, possible, for automatic zone sensing, and the servo-valve and servo-valve driver. The analog signals from the transducers are transferred to the microprocessor through a multiplexer, a sample and hold circuit and an analog to digital converter. The microprocessor will process the digital signals based on software in a read-only-memory and the control output would be applied to the servo-valve through a digital to analog converter and to a suitable booster amplifier.

Acknowledgement: The authors greatly appreciate the patient assistance of Henry J. Plude, III in providing the graphics for this paper and Susi Hamilton, the typist.

References:

- (1) Coberly, R., "Mathematical Simulation of Carriage Motion Under Dynamic Conditions of Recoil", Tech Report #RIA-67-381, Rock Island Arsenal, 1967.
- (2) Nerdahl, M. C. and Frantz, J. W., "Mathematical Models For Engineering Analysis and Design of Howitzer, Medium, Towed:155mm, XM198 (Airborne)", Tech Report #RE-TR-70-186, USAWECOM, October 1970.
- (3) Wu, S. M. and Madiwale, A. N., "Optimal Control of Active Recoil Mechanisms", Tech Report #R-TR-77-024, USARRCOM, February 1977.

APPENDIX A

The parameters of the M37 recoil mechanism pertinent to the dynamic equations are shown in Figure 1 and listed below:

- $M_r$  = Mass of recoiling parts
- $M_p$  = Mass of floating piston
- $P$  = Density of hydraulic fluid
- $P_0$  = Initial gas pressure in gas spring
- $V_0$  = Initial volume of gas
- $K$  = Gas constant
- $A_r$  = Area of recoil piston
- $A_c$  = Area of control rod
- $A_d$  = Area of floating piston
- $C_1=C_2=C_3$  = Discharge coefficients
- $A_1$  = Area of orifice 1
- $A_2$  = Area of orifice 2

The relationship between the M37 physical parameters and the coefficients of equation (1) are given below:

$$m = M_r + M_p (1 + A_r/A_n)^2$$

$$m_1 = M_r + M_p (1 + A_r/A_n)$$

$$w = m_1 g$$

$$F = F_r + F_p (1 + A_r/A_n)$$

$$C = (A_r/A_n) [ (A_r/A_1 C_1)^2 A_n + (A_r A_c / A_n A_2 C_2)^2 A_c ]$$

$$C_o(x) = (A_r/A_n) (A_r A_o / A_n A_3(x) C_3)^2$$

$$C_1(x,u) = (A_r/A_n) [A_r A_o / A_n C_3 (A_3(x) + u)]^2$$

$$K_o = A_r/P_o$$

$$K_v = A_r/V_o$$

ABSTRACT

DONNALLY, WILLIAM

TITLE: A NEW IN-BORE DATA ACQUISITION TECHNIQUE FOR GUN  
TUBE/PROJECTILE DYNAMICS

\*William Donnelly, USA-ARRADCOM  
Telemetry Br, ID, TSD, Dover, NJ 07801

ABSTRACT:

An advance in the state of the art has been achieved in providing a method of obtaining gun tube and projectile interface dynamics. The basis of this innovation is a telemeter which utilizes analog delay circuitry to delay the transmission of in-bore information until the projectile clears the gun tube. This removes many of the problems associated with measuring the in-bore environment. Since the in-bore information is transmitted by means of an RF link outside the gun tube environment, requirements on the transmitter are greatly reduced and the data link reliability is improved.

A prototype in-bore telemeter has been successfully tested in a 5" air gun at 19,000 G's. Further soft-recovery tests using a 155mm Howitzer are planned.

This telemeter is also being packaged for other specific applications.

BIOGRAPHY:

PRESENT ASSIGNMENT: Electronic Engineer, USA ARRADCOM, Dover, NJ

PAST EXPERIENCE: Electronic Engineer, US Naval Electronics  
Systems Command, Washington DC 1967-1969; US Navy Electronics  
Laboratory, San Diego, CA 1964-1969

DEGREES HELD: BSEE, San Diego State College, CA; MSEE, New Jersey  
Institute of Technology

DONNALLY

A NEW IN-BORE DATA ACQUISITION  
TECHNIQUE FOR GUN TUBE/PROJECTILE DYNAMICS

WILLIAM DONNALLY  
USA-ARRADCOM  
TELEMETRY BR, ID, TSD  
DOVER, NJ 07801

In-bore data has been taken by means of a direct wire technique and by a telemetry system which uses the gun barrel as a waveguide for direct RF radiation. These techniques have been limited in their application and loss of data has been a significant problem.

A new type of telemeter (TM) has been designed and tested which avoids the problems frequently encountered with conventional approaches for taking in-bore data. The simplicity of the system is due to the use of a charge-coupled analog delay device (CCD). By means of this device, in-bore information is telemetered after the projectile is clear of the gun barrel and the ionized cloud. In-bore data is received outside the gun over a straightforward RF transmission link, as shown, Fig. 1. Consequently, the RF transmitter is not required to operate under high-G loading as is the case when the direct radiating technique is used.

The problems of transmitter pulling, extreme changes in RF loading and voltage-standing wave ratio (VSWR), battery supply voltage fluctuations and other difficulties are all avoided. Overall data link reliability is improved. Concurrently, the ground station (for receiving and recording data) is simplified. A further advantage is that the reception of data is independent of gun tube wear and the rotating or obturator band gas seal (ionized propellant gases escaping past the projectiles are known to cause RF dropouts when a direct-radiating telemetry system is used).

C

DONNALLY

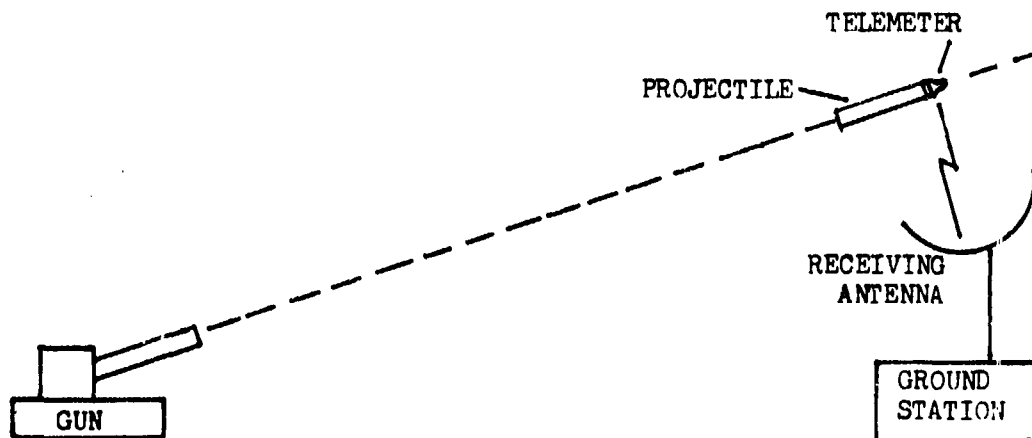


Figure 1. In-bore Telemeter application

The cost of an in-bore telemeter package utilizing CCD-delay circuitry is estimated to be a nominal \$350 per channel over the cost of a direct-radiating telemeter. The additional delay circuitry required is quite cost effective when the savings in equipment setup time and the many other advantages are considered.

The operation of the CCD delay circuitry is described in terms of data sampling. However, this sampling technique is not strictly digital (i.e., a system using A/D converters and digital shift registers), but rather a hybrid digital/analog concept. The CCD circuit has a series of connected cells. This circuit takes successive samples of the filtered input signal whereby the signal is represented as a series of charge packets.

## DONNALLY

In bucket-brigade fashion, these packets are transferred from one CCD cell to the next. A clock sets the rate of charge transference from cell to cell. At the output of the CCD, a filter is used to reconstruct and smooth the successive charge packets.

There are many tradeoffs that must be considered in the design of a multichannel in-bore telemeter. Since the delay is achieved through data sampling, there is a theoretical limit to the information frequency called the Nyquist Criterion. This criterion states that, for an ideal system, the highest information frequency that can be conveyed is limited to one-half the sampling rate. Therefore, the input signal bandwidth must be limited by filtering.

Since an ideal sampling system is not physically realizable, practical CCD delay circuit design considerations indicate that the sampling rate should be approximately five times the highest data frequency. These design considerations include the following:

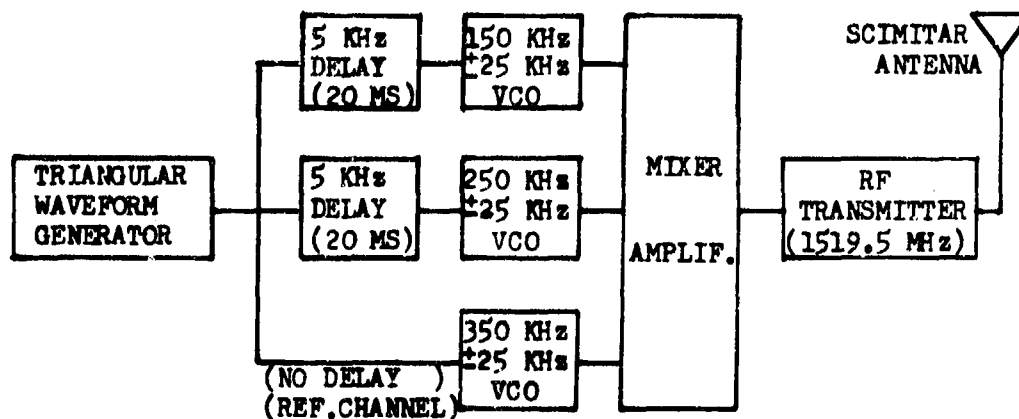
1. Delay circuit input and output filter designs involve compromises of several interacting parameters, such as abruptness of cutoff, phase and amplitude linearity and the number of filter elements.
2. The signal delay is equal to the number of CCD cells divided by twice the clock frequency. For the CCD circuit, the clock frequency is equal to the data sample rate. Consequently, time delay can be traded off for signal bandwidth.
3. The CCD sampling system exhibits aperture distortion because it actually takes finite duration or "flat-topped" samples of the input signal. An ideal system would take instantaneous samples.
4. Data accuracy increases with sample rate. The more samples taken of a given waveform, the better the waveform can be reproduced.

Two complete prototype three-channel high-G telemeters with an FM/FM modulation format have been designed and constructed for engineering evaluation. Each telemeter has two subcarrier channels having a twenty millisecond time delay with 5KHz data bandwidth and a dynamic range of 1000 to 1 (60 dB).

# DONNALLY

A third channel having no time delay circuitry is included. The remainder of each telemeter consists of a mixer amplifier and a L-band crystal-controlled transmitter (1519MHz) radiating through a scimitar nose-mounted antenna. The size of the overall package has been reduced through the use of thick-film hybrid circuitry. A complete data channel is placed on a single ceramic substrate. For convenience, the telemeter hardware has been packaged in a modified fuze housing readily accommodated by a standard 105, 155mm or 8 in projectile.

A circuit block diagram for the first of two prototype telemeters is shown in Fig. 2. It has a triangular waveform reference generator circuit with a period of 40 milliseconds connected to the inputs of the two delay channels.



BLOCK DIAGRAM

Figure 2. Prototype In-bore TM

DONNALLY

In this first telemeter, the third channel (no delay) serves as a reference for the delay circuitry. This package, shown in Figures 3 & 4, has been successfully test fired at a peak acceleration of over 19,000 G's in the five-inch air gun located at the ARRADCOM Dover site.

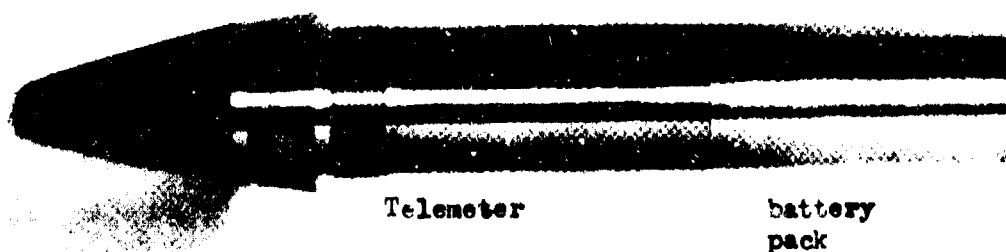


Figure 3. Prototype In-bore Telemeter with battery pack

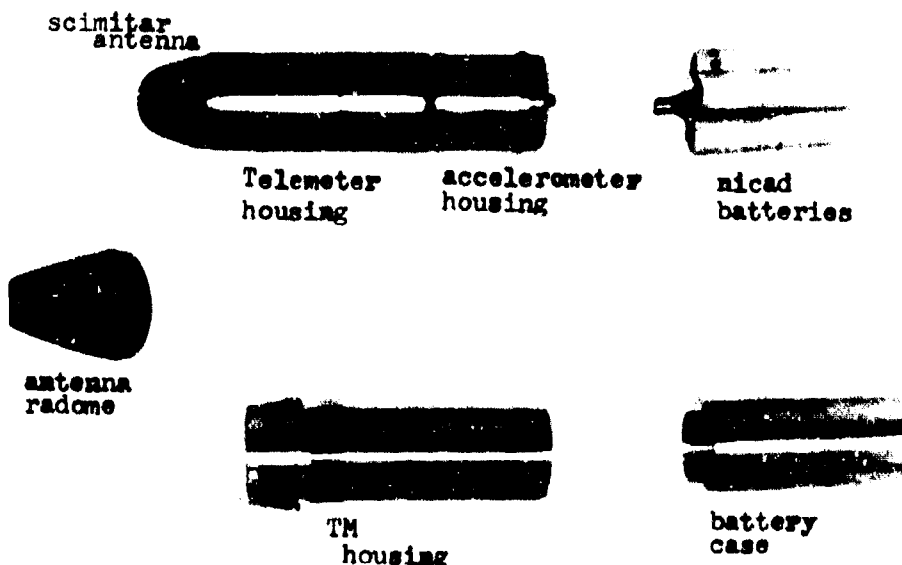
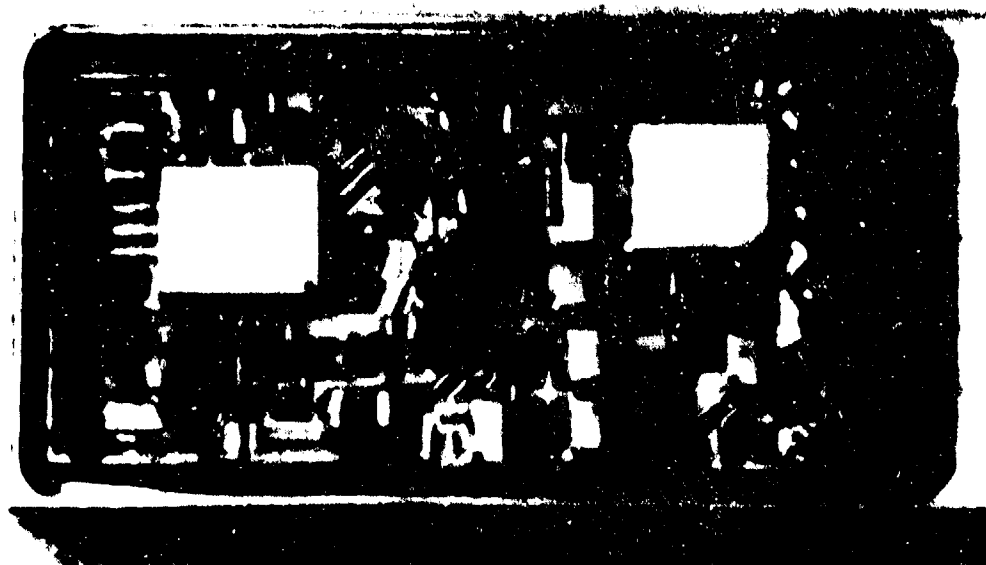


Figure 4. Components used in prototype telemeter package

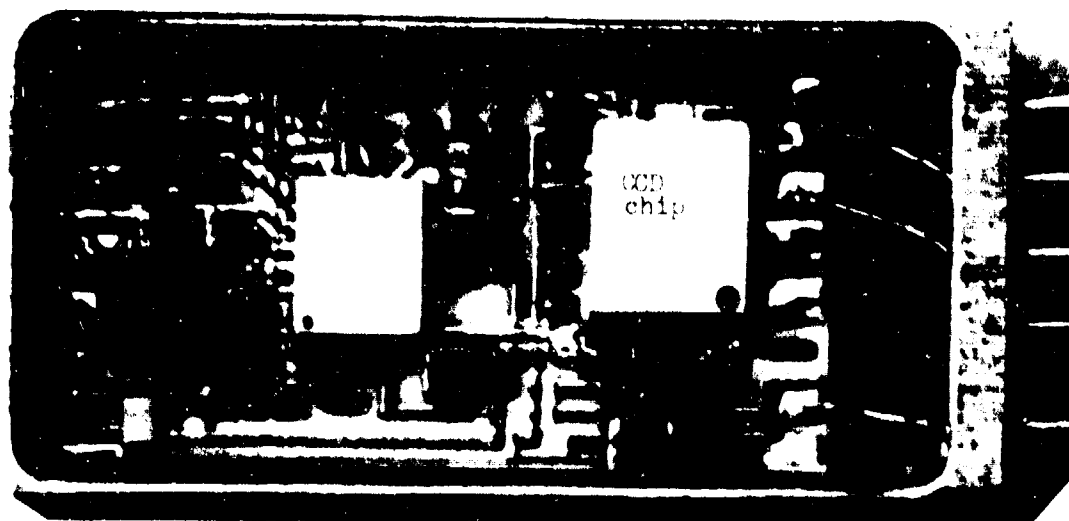


DONNALLY

The OCP analog CMOS hybrid circuit is shown in Fig. 1.



Reverse side of hybrid tube circuit



Front side of hybrid OCP circuit  
(overall package size is .75x.68x.2 inches)

Figure 1. Analog CMOS hybrid package

DONNALLY

The process of loading the test projectile into the air gun and the telemetry ground station used to receive and record the data are shown in Figures 6 & 7

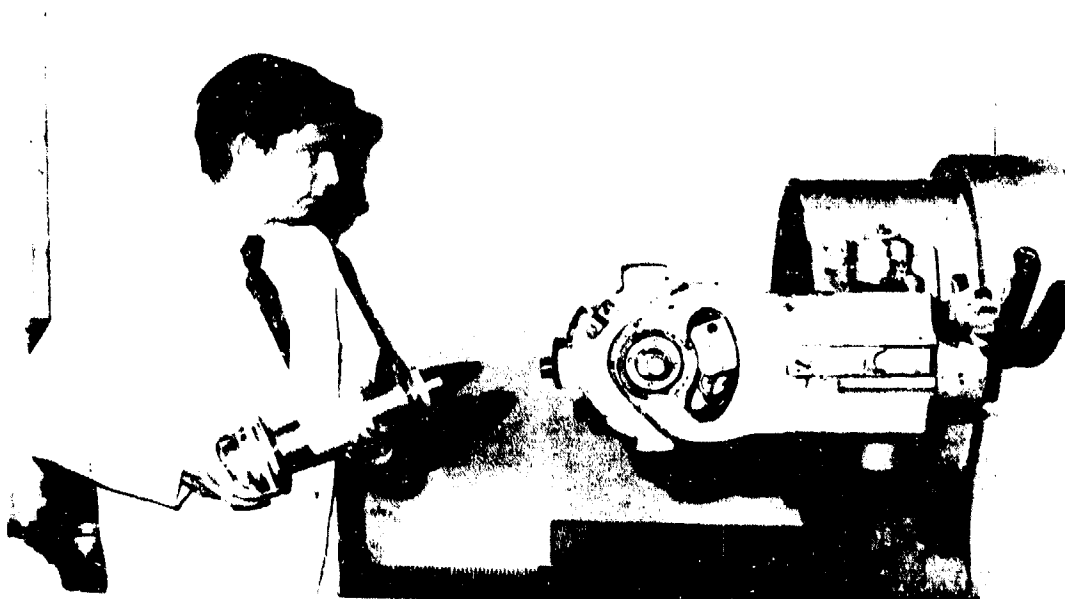


Figure 6. Loading prototype in-bore TM into 5" air gun  
(TM is shown mounted in front end of air gun piston)

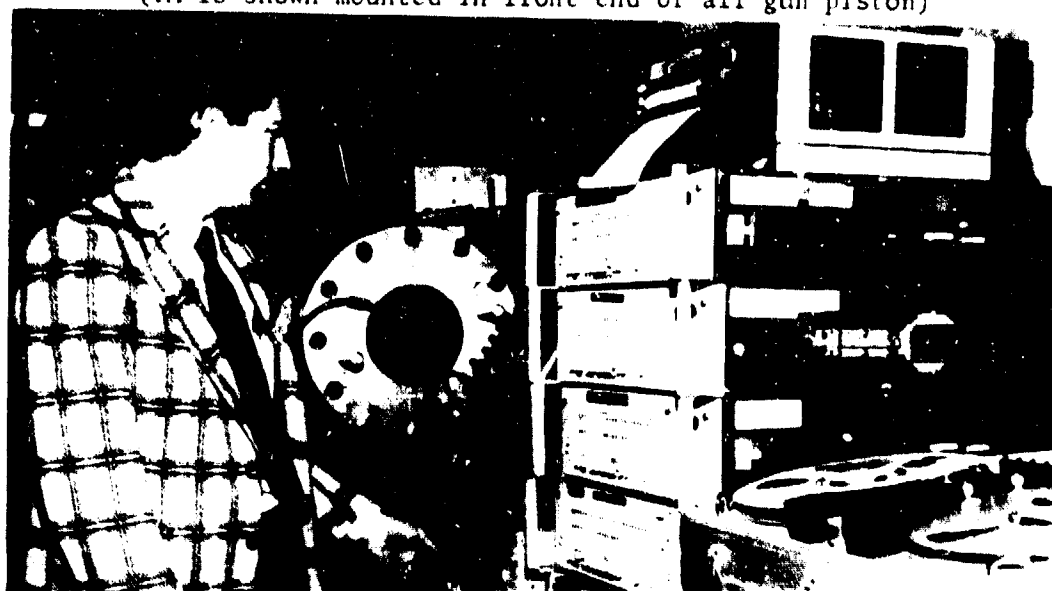


Figure 7. Ground station for receiving, demodulating and  
recording test data at rear of 5" air gun

DONNALLY

Figure 8 shows the received triangular waveform as recorded on an Oscilloscope during the application of 19,000 G's. This data indicated that the CCD-delay circuitry functioned properly under high-G loading (19,000 G's).

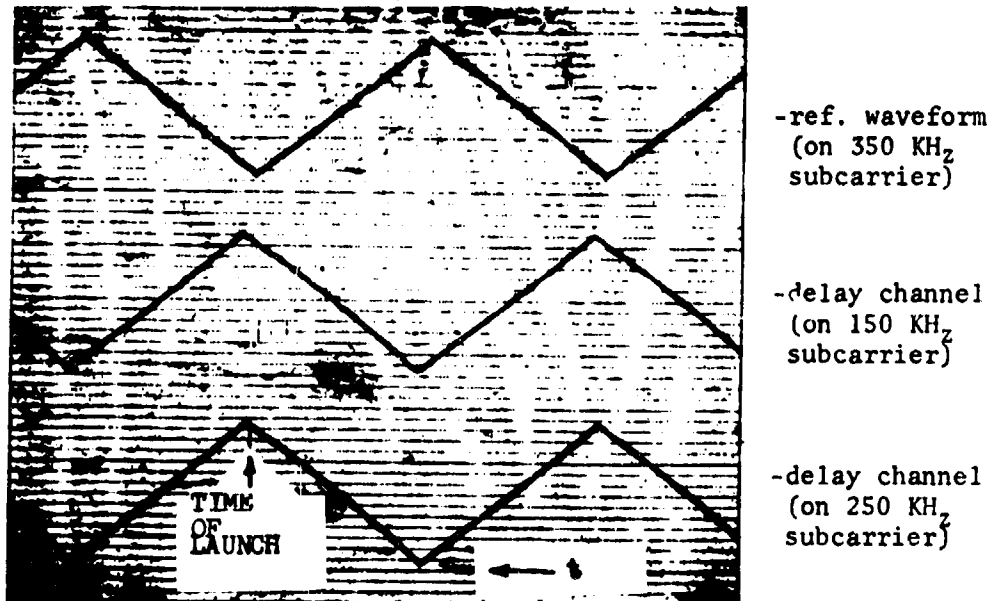


Fig 8. 5" AIR-GUN TEST TELEMETRY DATA

The second prototype telemeter has a Columbia Research triaxial piezo-electric accelerometer installed in lieu of the triangular waveform simulator.

Additional gun tests are planned using one or both of two soft-recovery 155mm howitzer facilities as follows:

a. The ARRADCOM Dover site 155mm Rail Gun: The rear section of a M483A1 carrier projectile would be modified to accept the second prototype TM, which is equipped with an accelerometer. This TM will be able to characterize both in-bore and water-trough acceleration environments at all zones.

DONNALLY

b. The "Vertical Recovery System" located at Aberdeen, MD: In this soft-recovery system, a 155mm projectile does not turn over during flight and impacts on it's base. Consequently, the nose-mounted TM should not be damaged.

A wideband (20KH<sub>z</sub> frequency response) analog delay circuit has been designed and bench tested. This circuit is known to be needed for many important shell test programs. In order to obtain this wideband response together with a 20 millisecond delay, a new 2000 stage large-scale integrated (LSI) CCD circuit is employed. This LSI-CCD has the advantage of excellent signal-to-noise performance with low distortion. A prototype wideband delay circuit is being packaged in hybrid form.

In addition to the CCD delay concept, some additional innovations to the state of the art are being considered. These techniques simplify or lower the cost of experimental investigations of projectile tube interface dynamics. They are as follows:

1. An inductive transmission link for simplifying the ground station and eliminating the costly RF transmitter. Preliminary laboratory tests of a breadboard system have indicated that this approach is feasible.

2. An alternative technique for delaying analog signals by means of digital encoding and binary shift registers. For telemetry applications requiring moderate bandwidths, this technique can be implemented at a lower cost.

3. A low cost RF transmitter which offers frequency stability comparable to crystal-controlled transmitters. Modular, compartmentalized, thick film hybrid circuitry allows the transmitter to be mass produced without the usual hand adjustments. The high isolation achieved between the oscillator and antenna output results in exceptional stability and very low pulling. Since the RF shift is minimal, a simple broad-band ground station receiver may be used.

4. A prototype analog compandor circuit for improving TM channel immunity to noise. This compandor circuit logarithmically compresses the amplitude range of a transducer signal. The inverse operation of expansion is performed at the receiving ground station to restore the signal waveform amplitude to that which occurred at the transducer.

#### DONNALLY

The result of this sequence of signal processing operations is improved TM channel signal-to-noise and dynamic range.

The in-bore telemeter uses a modular package concept. At present, the TM can be configured in three different forms; namely:

1. A front-mounted fuze housing with a scimitar antenna.
2. A pit-mounted configuration which has a center or ogive-mounted antenna.
3. A rear-mounted package with a stub antenna. A polyurethane radome protects the antenna from the severe pressures generated by the propellant gases.

A new telemeter package has been designed for the ARRADCOM Dover site 155mm Rail-Gun. The rail-gun is a soft-recovery system which fires projectiles fitted with a nose-mounted water scoop (for stopping the projectile in a water trough). Accordingly, the TM package mounts in the boat-tail section of the projectile. A rear-mounted stub antenna is used of the same design as with the flight qualified telemeter for the M454 155mm Nuclear Shell. The analog delay method is the only practical approach for obtaining rail gun in-bore data, since direct radiation of RF signals is prevented by the carrier projectile scoop. A further benefit is that the rail-gun TM will also provide deceleration and balloting data as the projectile travels along the water trough.

In conclusion, a new technique is available for making useful in-bore measurements. Other approaches for taking in-bore data have been limited in their application and often lacking in reliability. For this reason, only a small amount of experimental data about the actual in-bore environment is available. Even less information is available about the rate-of-change of axial acceleration (called "JERK") during launch. A significant advantage of the in-bore TM is that axial acceleration and jerk magnitudes can be realistically simulated using the 155mm rail-gun by varying the payload weight of the M483A1 carrier projectile (the propellant charge can also be varied).

The CCD analog delay technique is the only practical means of making in-bore measurements for the rail-gun, since direct RF radiation in-bore is prevented by the carrier projectile's front-mounted scoop.

FANSLER and SCHMIDT

TITLE: Muzzle-Blast Induced Trajectory Perturbation of  
Nonconical and Conical Boattail Projectiles.  
KEVIN S. FANSLER and EDWARD M. SCHMIDT  
Launch and Flight Division  
Ballistic Research Laboratory  
Aberdeen Proving Ground, Maryland 21005

ABSTRACT:

The muzzle blast loadings on spin stabilized projectiles are analyzed and used to compute resultant trajectory deflections. Both conical and nonconical boattail rounds are treated. The approximations made in the analysis permit the loadings on the projectile to be integrated; the result is used to develop a "universal" momentum transfer function that can be directly related to projectile jump. Although nonconical boattail configurations are more sensitive to muzzle blast than conical designs, the computed trajectory deviation in either case is small compared to the total measured dispersion of typical systems.

BIOGRAPHY:

PRESENT ASSIGNMENT: Research Physicist, Launch and Flight Division, Ballistic Research Laboratory, Aberdeen Proving Ground, Maryland

PAST EXPERIENCE: Physicist, Aerosol Physics Branch, Edgewood Arsenal, Maryland, 1965-1967; Physicist, Naval Ordnance Laboratory, White Oak, Maryland, 1960-1962.

DEGREES HELD: Bachelor of Science, Oklahoma State University, 1960; Master of Science, University of Hawaii, Honolulu, 1964; Ph.D. University of Delaware, Newark, 1974.

\*FANSLER and SCHMIDT

MUZZLE-BLAST INDUCED TRAJECTORY PERTURBATION OF  
NONCONICAL AND CONICAL BOATTAIL PROJECTILES

\*KEVIN S. FANSLER, Ph.D.  
EDWARD M. SCHMIDT, Ph.D.  
LAUNCH AND FLIGHT DIVISION  
BALLISTIC RESEARCH LABORATORY  
ABERDEEN PROVING GROUND, MD 21005

I. INTRODUCTION

On the modern battlefield, weapon systems must deliver ordnance with a high degree of precision if they are to survive; ideally the weapon designer should be capable of quantifying the sources of delivery inaccuracy in order to meet these precision standards. One source of perturbation to the desired trajectory is projectile deviation due to gasdynamic loadings experienced in the weapon muzzle blast. For fin-stabilized projectiles, dispersion caused by the blast environment has been investigated (1-2); however, treatment of spin-stabilized projectiles has been largely neglected. With the introduction of novel boattail designs (3), there is also interest in comparing the sensitivity to muzzle blast of the nonconical boattail configurations with the conical boattail configurations.

The present paper examines the influence of muzzle blast loadings upon the trajectory of both of these spin-stabilized rounds. The analytical approach is similar to that used previously for fin-stabilized projectiles; namely, the most significant gasdynamic loadings are assumed to occur within the quasi-steady, supersonic core of the propellant gas jet. Pressure distributions on the projectiles are estimated by application of both theoretical and empirical estimations obtained for steady state flows. This procedure is not locally exact; however, it produces a reasonable estimate of the overall muzzle blast induced impulse. Transverse angular and linear momentum imparted by the blast are calculated for triangular, square, and conical boattails and used to determine the contribution to the dispersion of 155mm, M549 type projectiles.

II. ANALYSIS OF GASDYNAMIC LOADS

Two distinct regions are considered. First, a model is developed

for the flow following separation of the rotating/obturator band. When this gas seal is released, the boattail is still within the tube, but the forward portion of the projectile is immersed in the expanding propellant gases. The existence of asymmetry in this flow field due to projectile angle of attack results in transverse loads. For conical boattail rounds, these loads alter the transverse momentum; however, due to the cylindrical 'wheelbase' characteristic of non-conical boattail designs (3), momentum exchange occurs only when the non-planar surfaces are not contacting the bore. The second region of interest commences as the projectile base clears the muzzle and terminates as the base passes through the Mach disc of the propellant gas jet.

In both regions, the analysis seeks an upper-bound estimate of the propellant gas loadings. This approach is supported by previous work (1,2) showing that (upper-bound estimates of) muzzle blast induced dispersion of fin-stabilized projectiles is a negligible component of the total measured dispersion levels. Thus, it was not worthwhile to seek more accurate, but lower magnitude, estimates.

#### Region 1: Projectile base still within the bore

A schematic of the flow field is shown in Figure 1. For convenience, the flow behind the projectile is assumed to be sonic (occurs for  $V \cong 700$  m/s). At separation of the obturator band, the propellant gases are released to expand into the atmosphere generating the characteristic muzzle blast wave. Due to the presence of the projectile, this free expansion is constrained and if the projectile is at an angle of attack,  $\alpha_1$ , relative to the bore-line, the propellant gases will be deflected. Assuming that the projectile acts somewhat like a plug nozzle and that all of the flow is deflected through the angle  $\alpha_1$  at the sonic line, the resultant transverse lift force on the projectile can be simply estimated from momentum considerations:

$$L_1 = (p^* + \rho^* V^{*2}) A_u \alpha_1 \quad (1)$$

where  $A_u$  is the area of the muzzle that is unplugged (a function of boattail geometry),  $p^*$  is the pressure at the muzzle,  $\rho^*$  is the gas density at the muzzle and  $V^*$  is the gas velocity at the muzzle.

Equation (1) is an estimate for a stationary projectile. It may be corrected to account for projectile velocity. Consider a coordinate system moving with the projectile. The velocity of the fluid in this system is given as  $V_r$ . If the fluid near the projectile is deflected to flow parallel to the projectile surface, the transformation between the stationary and moving coordinates is

$$V_r \exp(i\alpha_1) = V \exp(i\alpha) - V_p \quad (2)$$



\*FANSLER and SCHMIDT

where  $\alpha$  is the turning angle for the fluid in the gun-tube coordinate system.  $V_r$  may be eliminated and with the help of a trigonometric identity, such that for small angles

$$\alpha = (1 - V_p/V) \alpha_1 \quad (3)$$

The largest angle for  $\alpha$  corresponds to the Mach number of the fluid approaching infinity; thus, for  $V_p = V^*$ ,

$$\alpha = 2\alpha_1/3 \quad (4)$$

Substituting this value of  $\alpha$  for  $\alpha_1$  in Eq. (1) and using the isentropic flow relations results in

$$L_1 = \frac{2}{3} (\gamma+1) p^* A_u \alpha_1 \quad (5)$$

The transverse momentum transferred to the projectile during the time between obturator separation and base emergence from the muzzle is the integral of the lift force over the time of passage. Transforming the variable of integration from time to space,  $t = (X/D) (D/V_p)$ , allows the momentum integral to be written:

$$P_1 = \frac{2}{3} (\gamma+1) (D/V_p) p^* \alpha_1 \int A_u d(X/D) \quad (6)$$

where  $X$  is the distance traveled since unplugging started and  $D$  is the bore diameter of the gun tube.

Nonconical Boattails: The value of  $P_1$  depends upon the boattail geometry because of the appearance of the vent area term,  $A_u$ , under the integral sign. This expression is addressed in detail in Appendix A where it is found for nonconical boattails that

$$P_1 = (16n/45) (\gamma+1) (p^* D^3/V_p) \theta^{3/2} \alpha_1 (X/D)^{5/2} \quad (7)$$

where  $n$  is number of plane boattail surfaces and  $\theta$  is the boattail angle. The total amount of momentum transferred to the projectile by the venting flow is obtained by evaluating this expression at the maximum travel of the round, i.e., when the projectile base is at the muzzle exit plane. For nonconical boattails which terminate in a polygon shape:

$$P_{1t} = [\pi^5/(90n^4)] (\gamma+1) [p^* D^3/(\theta V_p)] \alpha_1 \quad (8)$$

It is useful to define a nondimensional momentum transfer function,  $\bar{P}$ , similar to that developed in Ref. 4,

\*FANSLER and SCHMIDT

$$\bar{P} \equiv P / [(D/V_p)(\gamma+1)p^*A_{eq}\alpha_1] \quad (9)$$

For nonconical boattail projectiles, the surfaces are treated as miniature airfoils. In Ref. 4, it was shown that the equivalent lifting surface in the plane of angle of attack for a multiple finned missile is  $A_{eq} = nA/2$ .

Since the nonconical designs have only one surface to the "airfoil", the following definition is used:

$$A_{eq} = nA/4. \quad (10)$$

where A is the area of each plane surface.

This definition permits the momentum transfer functions to be written (See Appendix A):

$$\bar{P}_1 = (128/15)(n/\pi)^3 (\theta \underline{X}/D)^{5/2} \quad (11)$$

and

$$\bar{P}_{1t} = [(4\pi^2)/(15n^2)] \quad (12)$$

Conical Boattails: Using similar logic, the momentum transfer function for a conical boattail design is

$$P_1 = (\pi/3)(\gamma+1)(p^*D^3/V_p)\alpha_1(\underline{X}/D)^2 \quad (13)$$

and in non-dimensional form, with  $A_{eq} = \pi D^2/4$ :

$$\bar{P}_1 = (4\theta/3)(\underline{X}/D)^2 \quad (14)$$

Region 2: Projectile base out of the gun tube

Nonconical Boattails: There is no data available describing the aerodynamics of nonconical boattails in reverse flow. Since the three dimensional nature of the muzzle flow makes direct computation difficult, the lift force on the boattail will be estimated using two-dimensional airfoil theory. This approximation neglects any effects of base bluntness due to truncation of the boattail; however, the side force on a bluff body is generally smaller than that on a slender body at an equal angle of attack. Therefore, the current approximation should produce an upper bound on the transverse force exerted on these nonconical surfaces by muzzle gas loadings. The value of  $\bar{P}_2(\underline{X}/D)$  can be obtained directly from earlier results (1) using the definition of  $A_{eq}$  in Eq. (10). The center of force is taken as the area centroid for the plane surfaces. This center of force value would be correct for two-dimensional airfoil theory but may be quite different than the experimental results. Nevertheless, for this analysis, the approximation should be sufficient since the percent error between differing possible moment-arm values would be small.

Conical Boattails: The transverse force on conical boattail projectiles is estimated using experimental data (5) acquired on blunt, flared cone

cylinders at a variety of Mach numbers. This data was obtained using a sphere-cone where the ratio of the diameter of the cone at the sphere-cone junction to the base diameter was 0.8. The smallest cone half angle of this set of data was  $10^\circ$ . For the purposes of the present analysis, it is desired to compare the muzzle blast sensitivity of a  $7^\circ$  nonconical boattail with the sensitivity of a similar half angle cone. Thus, the data (5) is extrapolated to this angle, Figure 2. The center of force is taken to be halfway along the boattail length.

### III. RESULTS AND DISCUSSION

The M549 projectile is used as a basis for the computations since flight data is available on this round with both the standard  $7^\circ$  boat-tail and a triangular boattail. The properties of the projectiles are given in the tables below.

Table I: Projectile Parameters

$$\begin{aligned} M_p &= 43.0 \text{ kg} \\ D &= 0.155 \text{ m} \\ V_p &= 670 \text{ m/s} \\ p^* &= 1.52 \times 10^7 \text{ Pa} \\ \gamma &= 1.25 \\ C_{M_\alpha} &= 3.30 \\ C_{L_\alpha} &= 2.95 \\ I_x &= 0.13 \text{ kg-m}^2 \\ \rho &= 1.23 \text{ kg/m}^3 \end{aligned}$$

Table II. Differing M549 Projectile Properties

	Standard Conical	Triangular NCBT	Square NCBT
$A_{eq} (\text{m}^2)$	0.0189	0.028	0.016
$\theta$	$7^\circ$	$7^\circ$	$7^\circ$
$\Delta (\text{m})$	0.295	0.293	0.340
$l (\text{m})$	0.097	0.347	0.195
$I_y (\text{kg-m}^2)$	1.93	1.71	1.71

Here  $\Delta$  is the distance between the force acting on the planar surface and the center of gravity. The value  $\ell$  is the length of the boattail.

The values of  $\bar{P}$  through both the in-bore and exterior regions of interest are shown in Figures 3-5 for the three boattails considered. The coordinate,  $X$ , is the location of the projectile center of pressure along the bore axis, with  $X = 0$  corresponding to the muzzle. Since the momentum transfer function is cumulative, the asymptotic value of each curve is equal to the total momentum transferred in the blast,  $\bar{P}_t$ . From Eq. (14), it is apparent that the  $\bar{P}_{1t}$  for the conical boattail has an explicit dependence on  $\ell/D$  and  $\theta$ ; however, for the nonconical boattails considered (those taken back to the intersection of planar surfaces), this is not the case.  $\bar{P}_{1t}$  and  $\bar{P}_t$  are independent of all boattail and projectile parameters, i.e., the curves are 'universally' applicable to any projectile with an n-sided nonconical boattail launched at  $M_p = 1.0$ .

The momentum functions are used to compute the transverse angular and linear velocities imparted to the projectiles in the blast region using the approach of Reference 4. These velocities are input into the aerodynamic jump relations (6) resulting in

$$\theta/\alpha_1 = [1 + (C_{L_\alpha} \Delta)/(C_{M_\alpha} D)] (\gamma+1) p^* A_{eq} [D/(M_p V_p^2)] \bar{P}_t \quad (15)$$

For nonconical boattails, the working equation, using Eqs. (10) and Eq. (A12), is

$$\theta/\alpha_1 = [\pi^3 (\gamma+1)/24] [p^* D^3/(M_p V_p^2)] \times [1 + (C_{L_\alpha} \Delta)/(C_{M_\alpha} D)] [\bar{P}_t/(n^2 \theta)] \quad (16)$$

An expression for the first maximum yaw may also be derived (6)

$$|\xi_{\max}|/\alpha_1 = [2(\gamma+1) A_{eq} \Delta D^2 p^* \bar{P}_t/(I_y V_p^2)] / [(I_x \phi'_0/I_y)^2 - \pi p D^5 C_{M_\alpha}/(2I_y)]^{1/2} \quad (17)$$

For nonconical boattails, the working equation is, using Eqs. (A12) and (10),

$$|\xi_{\max}|/\alpha_1 = [\pi^3 (\gamma+1)/12] [\Delta D^4 p^* \bar{P}_t/(I_y V_p^2 n^2 \theta)] [(I_x \phi'_0/I_y)^2 - \pi p D^5 C_{M_\alpha}/(2I_y)]^{1/2} \quad (18)$$

Here  $\phi'_0$  is the initial spin.

\*FANSLER and SCHMIDT

The projectile parameters from Tables 1 and 2 with the above relations are used to determine the values in the following table:

Table III. Launch Dynamic Characteristics

	Standard Conical	Square NCBT	Triangular NCBT
$\bar{P}_t$	0.21	0.52	0.48
$ \xi_{\max} /\alpha_1$ (deg/deg)	.167	0.37	.57
$\Theta/\alpha_1$ (mil/deg)	0.051	0.11	0.18
$ \xi_{\max} $ (degs for $1\sigma$ with $\alpha_1 = 0.1^\circ$ )	0.02	0.04	0.06

Comparing these results for  $\Theta/\alpha_1$  with those obtained for fin-stabilized projectiles (1), we find that values for both cases are near each other.

Table 3 shows that the jump sensitivity of the nonconical boattail rounds is more than twice that of the standard conical boattail. However, the last row gives the contribution to the first maximum yaw of this muzzle blast induced jump. For a reasonable distribution in the in-bore yaw level ( $1\sigma, \alpha_1 \cong 0.1^\circ$ ), the resultant contribution to the first maximum yaw is  $0.06^\circ$  in the worst case. This value is judged negligible compared with the frequently observed values for the M549 of approximately  $5^\circ$ . Since the first-maximum-yaw value is proportional to the aerodynamic jump, we may infer that muzzle blast contributes only a small amount to the total observed dispersion.

#### IV. SUMMARY AND CONCLUSIONS

A model is developed to determine the effect of muzzle gasdynamic loadings upon the trajectory of spin-stabilized projectiles for both conical and nonconical boattail configurations. The analysis consists of two parts. First, the passage of the boattail out of the gun following separation of the obturator is addressed. Second, the region exterior to the muzzle but prior to the projectile's passage through the Mach disc is modelled. The conical boattail aerodynamics are determined from experimental data acquired on sphere cones; two-dimensional airfoil theory is applied to approximate the loadings on nonconical boattails.

The loadings are integrated to determine the momentum transferred to each of the M549 projectile configurations launched at a muzzle velocity of 670 m/s from a 155mm gun. The nonconical boattail configurations are found to be more than twice as sensitive to blast as the conical design; however, in neither case is the contribution to dispersion due to muzzle gasdynamic loadings significant when compared to the total dispersion of the gun system.

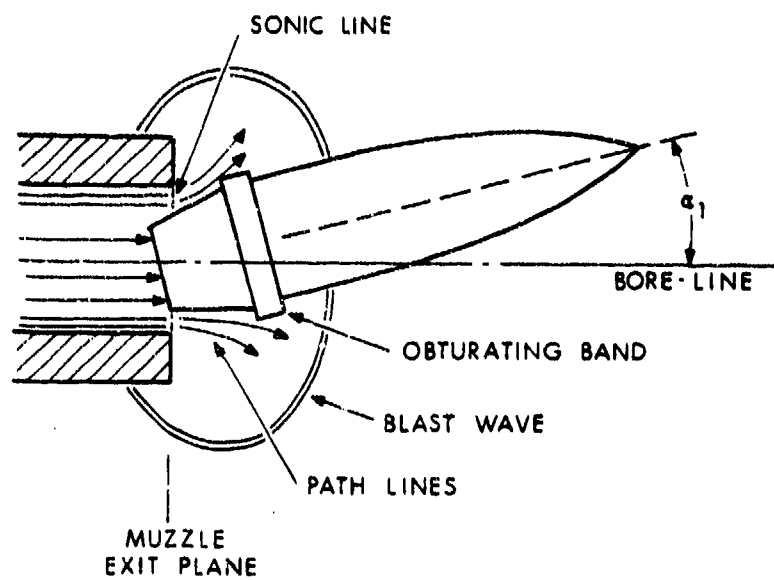


Figure 1. Flowfield schematic

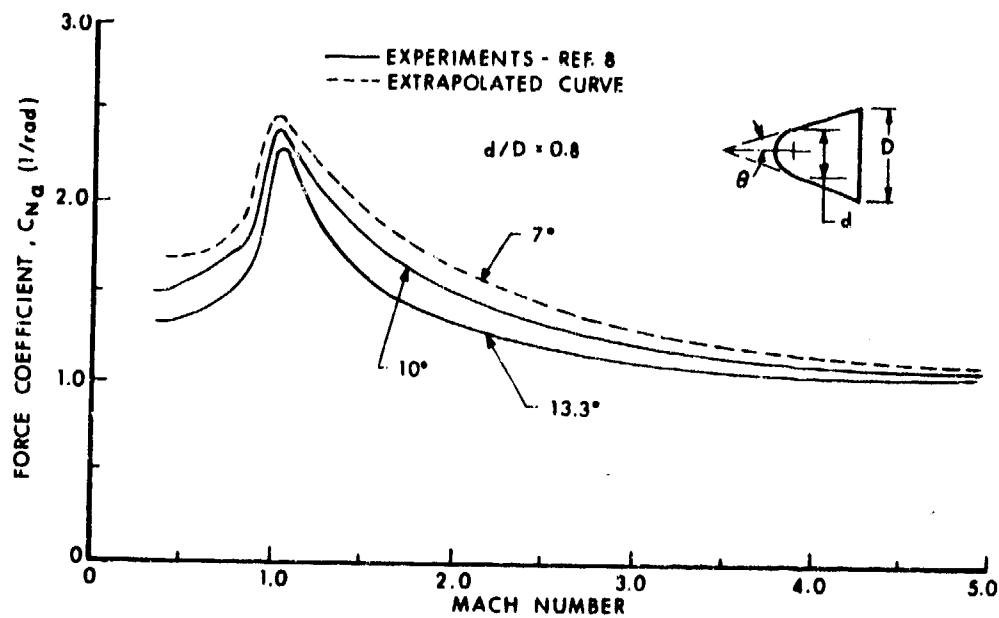


Figure 2. Experimental and extrapolated lift data for sphere-cones

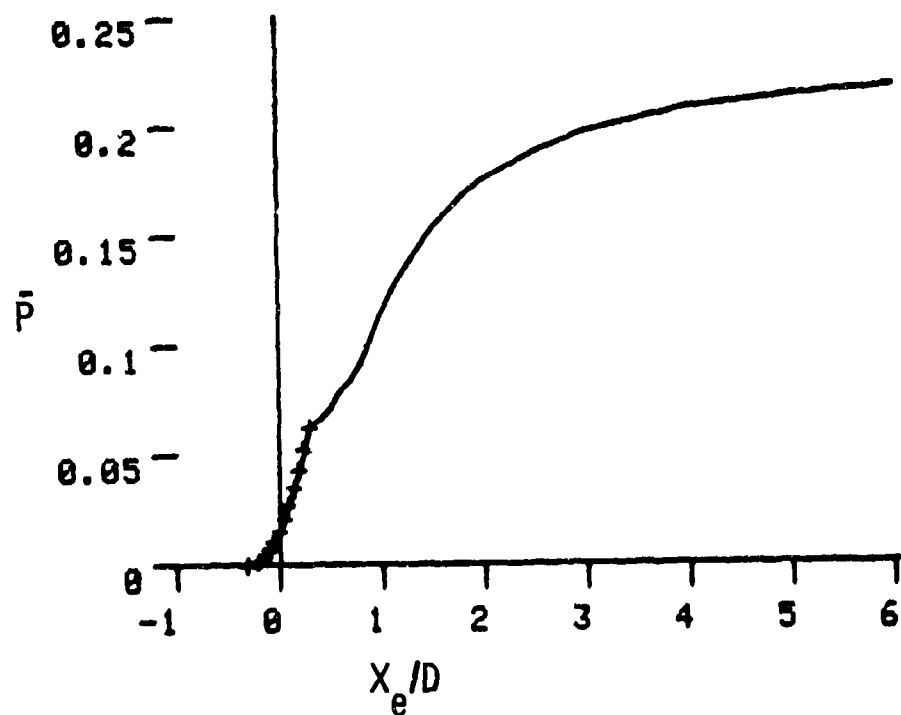


Figure 3. Momentum function for the conical 549 boattail

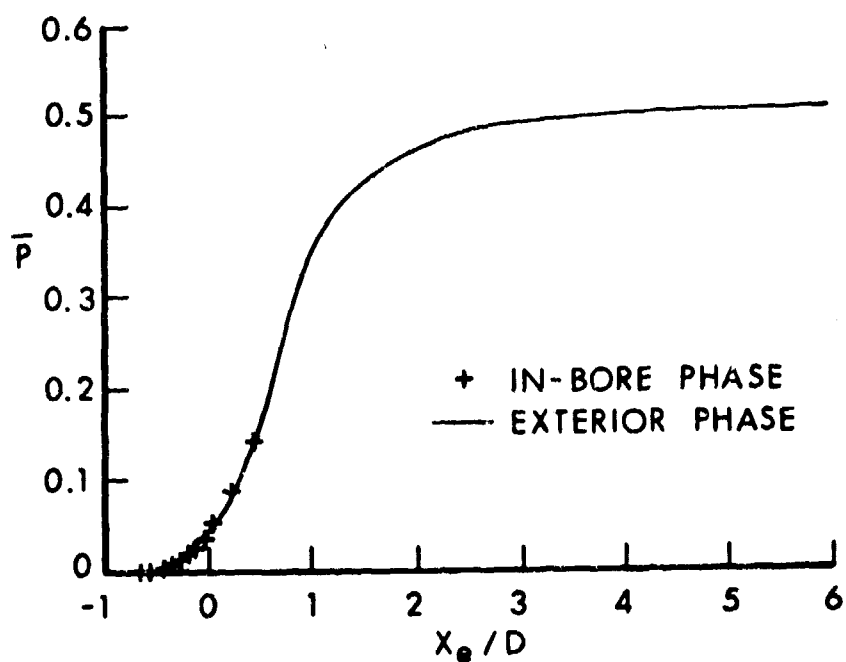


Figure 4. Momentum function for the square boattail

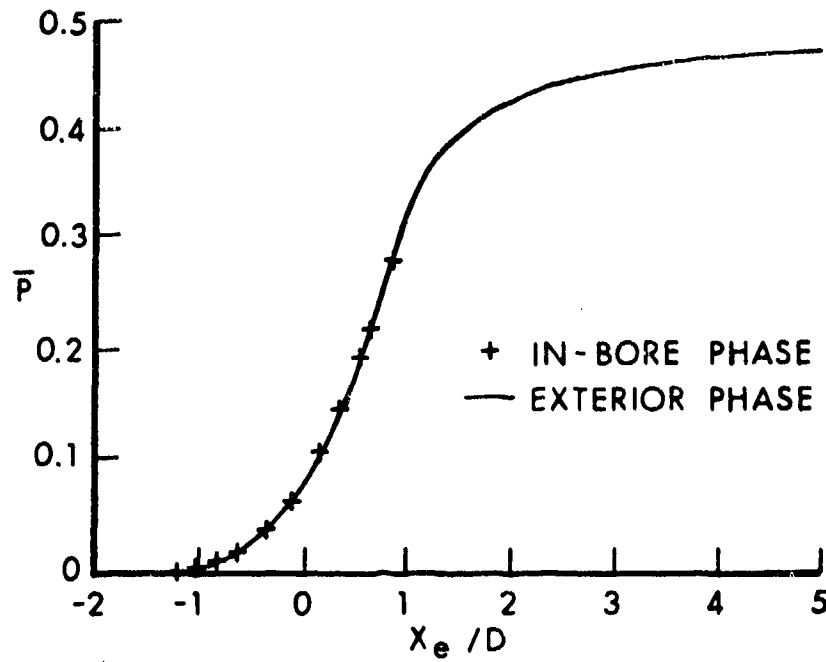


Figure 5. Momentum function for the triangular boattail

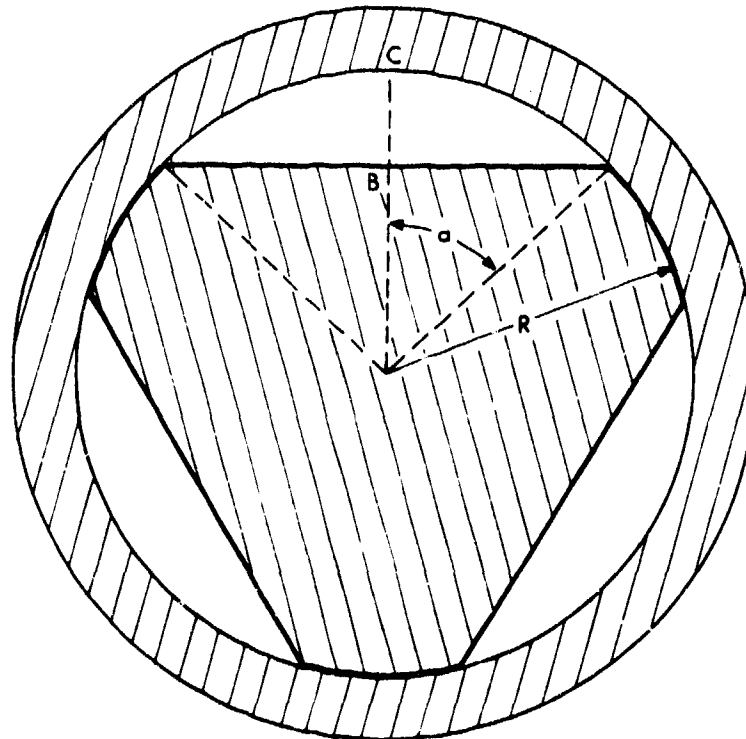


Figure 6. Cross-section of nonconical boattail in muzzle plane



\*FANSLER and SCHMIDT

REFERENCES

1. Schmidt, E. M., Fansler, K. S., and Shear, D. D., "Trajectory Perturbations of Fin-Stabilized Projectiles Due to Muzzle Blast," Journal of Spacecraft and Rockets, Vol. 14, No. 6, June 1977, pp. 339-344.
2. Fansler, K. S., and Schmidt, E. M., "Trajectory Perturbations of Asymmetric Fin-Stabilized Projectiles Caused by Muzzle Blast," Journal of Spacecraft and Rockets, Vol. 15, No. 1, January-February 1978, pp 62-64.
3. Platou, A. S., "An Improved Projectile Boattail," BRL MR 2395, US Army Ballistic Research Laboratories, APG, MD, July 1974. (AD 785520).
4. Fansler, K. S. and Schmidt, E. M., "The Influence of Muzzle Gasdynamics Upon the Trajectory of Fin-Stabilized Projectiles," BRL R 1793, U. S. Army Ballistic Research Laboratory, Aberdeen Proving Ground, MD, June 1975, AD B005379L.
5. Foster, A. D., "A Compilation of Longitudinal Aerodynamic Characteristics Including Pressure Information for Sharp and Blunt-nose Cones Having Flat and Modified Bases," Sandia Corporation Report No. SC-R-64-1311, January 1965.
6. Murphy, C. H., "Free Flight Motion of Symmetric Missiles," U.S. Army Ballistic Research Laboratories Report Number 1216, Aberdeen Proving Ground, Maryland, July 1963. AD 442757.

# APPENDIX A. EXPRESSION FOR TRANSVERSE MOMENTUM

In order to evaluate the integral in Eq. (6), it is desirable to obtain closed form expressions for  $A_u$ .

Nonconical Boattail: Figure 7 shows the cross section of a boattail in the muzzle plane. The bore radius is R and the area of the circular segment can be readily determined to be

$$A_{u_1} = R^2 (a - \sin 2a/2) \quad (A1)$$

The expression in brackets may be expanded in series yielding:

$$A_{u_1} = \frac{D^2}{6} (a^3 - \frac{a^5}{5} + \frac{2}{105} a^7 \dots) \quad (A2)$$

In keeping with the upper bound approach the series is truncated after the first term to give

$$A_{u_1} = D^2 a^3/6 \quad (A3)$$

The distance BC, Figure 6, is

$$\begin{aligned} BC &= R(1 - \cos a) \\ &= \frac{R}{2} (a^2 - a^4/12 + \dots) \end{aligned} \quad (A4)$$

However, BC is also related to the boattail angle and the distance traveled by the origin of the boattail (taken to correspond with the obturator termination) by

$$BC = \underline{X} \tan \theta \quad (A5)$$

Assuming small  $\theta$  ( $\theta \cong 7^\circ$ ) and taking the first term in the series of Eq. (A4) gives

$$a^2 = 4\theta \underline{X}/D \quad (A6)$$

which can be substituted into Eq. (A3):

$$A_{u_1} = (4D^2/3) (\underline{X}/D)^{3/2} \theta^{3/2} \quad (A7)$$

For an n-sided boattail,

$$A_u = nA_{u_1} = (4nD^2/3) (\underline{X}/D)^{3/2} \theta^{3/2} \quad (A8)$$

\*FANSLER and SCHMIDT

This formulation for  $A_u$  may be substituted into Eq. (6) and integrated to provide

$$P_1 = (\gamma+1) [16 n D^3 p^* \alpha_1 / 45 V_p] \theta^{3/2} (\underline{X}/D)^{5/2} \quad (A9)$$

If the boattail terminates where the planar surfaces intersect,

$$a_m = \pi/n. \quad (10)$$

This permits the evaluation of the total momentum transferred in-bore

$$P_{1t} = (\pi^5/90 n^4) (\gamma+1) (p^* D^3 / \theta V_p) \quad (A11)$$

This type of boattail has a surface area which is readily computed. Since the surface is an ellipse formed by intersecting the cylindrical body with a plane at angle  $\theta$  to the axis,

$$\begin{aligned} A &= A_{u_1} / \theta \quad (\text{evaluated at the muzzle station}) \\ &= D^2 (\pi/n)^3 / (6\theta) \end{aligned} \quad (A12)$$

Conical Boattail: The unplugged area is

$$A_u = \pi(R^2 - r^2) \quad (A13)$$

where  $r$  is the diameter of the section of the boattail passing the muzzle plane. Since  $R - r = \underline{X} \tan \theta \cong \underline{X} \theta$ ,

$$A_u = \pi(2R - \underline{X}\theta) \underline{X}\theta, \quad (A14)$$

which may be substituted into Eq. (6) to give

$$P_1 = (\pi/3) (\gamma+1) (p^* D^3 / V_p) \theta \alpha (\underline{X}/D)^2 \quad (A15)$$

LIST OF SYMBOLS

$a$	= angle defined in Figure 7
$A$	= area of a plane surface of the nonconical boattail
$A_b$	= base area of the projectile
$A_{eq}$	= the equivalent area of an airfoil in two-dimensional flow
$A_u$	= the area at the muzzle that is unplugged
$C_{DR}$	= projectile drag coefficient in muzzle blast

\*FANSLER and SCHMIDT

$C_{L_\alpha}$	= lift coefficient in forward flight
$C_{M_\alpha}$	= moment coefficient in forward flight
D	= the diameter of the bore and projectile
$I_x$	= axial moment of inertia
$I_y$	= transverse moment of inertia
L	= the lift force on the projectile
$L_1$	= lift force on projectile in the first part of its transit
$\ell$	= length of boattail
$M_p$	= projectile mass
n	= the number of plane surfaces possessed by the boattail
p	= pressure
P	= the momentum given the projectile
$P_1$	= momentum given the projectile during the first part of the projectile's transit
$\bar{P}$	= the value of P nondimensionalized according to Equation (10)
$\bar{P}_t$	= the total amount of $\bar{P}$ imparted by the muzzle blast
t	= time variable
V	= local velocity of gases
$V_p$	= velocity of projectile
$V_r$	= velocity of gases relative to a coordinate system located
x	= position along the axis of the center of force for the projectile relative to the muzzle
$\underline{x}$	= distance traveled since unplugging started
y	= axis coordinate in the angle of attack plane that is perpendicular to the x-axis

\*FANSLER and SCHMIDT

$\alpha$	= maximum angle between projectile and gun-tube axis-- angle of attack
$\alpha$	= angle determined by $\alpha$ and fluid flow velocity relative to the projectile
$\alpha_1$	= angle of attack upon emergence from muzzle
$\alpha_0$	= angle of attack upon emergence from muzzle blast
$\alpha'$	= derivative of $\alpha$ with respect to distance in calibers
$\alpha'_0$	= value of $\alpha'$ upon emergence from muzzle blast
$\gamma$	= ratio of specific heats
$\Delta$	= distance from center of force to center of gravity for flight through muzzle-blast region
$\xi$	= complex angle of attack
$\phi$	= roll angle of projectile
$\theta$	= boattail angle
$\rho$	= local density of gases.

TITLE: MEASUREMENT of BALLOTTING and FREE RUN EFFECTS for a  
PROJECTILE DURING GUN LAUNCH.  
G. A. BENEDETTI, Ph.D.  
Analytical Mechanics Division  
Sandia Laboratories  
Livermore, California 94550

ABSTRACT:

An experimental program is underway with two major objectives 1) detect the presence of projectile balloting by comparing measured and predicted strain gage time histories for a cantilever beam mounted within an eight-inch diameter projectile subjected to gun launch accelerations; and 2) determine the initial angular acceleration resulting from projectile "free run." It is also necessary to measure projectile base pressure and projectile axial acceleration with respect to time as the projectile travels along the gun tube. An onboard telemetry system is used to obtain measured quantities.

To detect balloting three analytical problems are solved. The first predicts the quasi-static response of a beam mounted within a projectile and subjected to the known rigid body motions associated with launching a projectile from a rifled tube. The second predicts the natural frequencies of vibration for the beam. The third problem is an approximation for the dynamic response of the beam when subjected to transverse balloting accelerations and consists of a mass particle elastically mounted in the plane of a rigid disk. Combining these results enables in the detection of balloting.

Finally, experimental results associated with special cases for the first two problems are discussed. Namely, a spinning beam experiment and the natural frequencies for transverse beam vibration. Comparison between measured and calculated results is excellent for these special cases.

BIOGRAPHY:

PRESENT ASSIGNMENT: Member of Technical Staff, Sandia Laboratories.

PAST EXPERIENCE: Member of Technical Staff, Sandia Laboratories, Livermore, California, 1962 - present. Structural Lead Engineer on various strategic and tactical nuclear weapon systems.

DEGREES HELD: Bachelor of Mechanical Engineering, Univ. of Santa Clara, Santa Clara, Ca., 1960; Master of Science in Mechanical Engineering, Oregon State University, Corvallis, Oregon, 1962; Ph.D. Arizona State Univ., Tempe, Ariz., 1973.

BENEDETTI

## Table of Contents

Abstract

Nomenclature

Introduction

Equations of Motion

    Quasi-Static Response of Beam

    Beam Natural Frequencies

        Natural Frequencies for Bending Vibration

        Natural Frequencies for Axial and Torsional Vibration

    Equations of Motion for a Mass Particle (Beam) Elastically Mounted on a Rigid Disk (Projectile)

Response Calculations

    Quasi-Static Response of Beam

    Dynamic Response of Mass Particle (Beam) Elastically Mounted on a Rigid Disk (Projectile)

Experimental Measurements

    Special Cases

        Comparison of Measured and Calculated Bending Strains for Spinning Beam Experiments

        Comparison of Measured and Calculated Beam Bending Natural Frequencies

Acknowledgements

References

## BENEDETTI

## Nomenclature

a	offset distance; also, $2\epsilon/l$
A	cross sectional area of beam
$b^2$	$J_D/M_D l^2$
D	beam diameter
$D_D$	diameter of rigid cylinder
E	modulus of elasticity
$f_i$	$i$ th natural frequency
G	shear modulus of elasticity
$h_D$	length of rigid cylinder
I	area moment of inertia for beam about y or z axis
$I_p$	area moment of inertia for beam about x axis
$I_{pD}$	mass moment of inertia of rigid mass about x axis
$J_D$	mass moment of inertia of rigid mass about y or z axis located at its mass center
$k_y, k_z, k_x$	elastic rotational restraints beam length
m	beam mass per unit length
$m_D$	disk mass
$m_p$	particle mass
$M_D$	mass of rigid body
S	rotational restraint stiffness
t	time
u, v, w	displacements of beam longitudinal centerline in directions of xyz axes; also, displacements of mass particle
$\ddot{U}, \ddot{V}, \ddot{W}$	specified translational accelerations along xyz axes of beam; also, along XYZ axes of rigid disk
xyz	body fixed coordinate system
XYZ	fixed coordinate system
$\rho$	mass density
$\zeta$	position along x axis
$\xi$	damping factor
$\alpha$	angular location; also, $M_D/ml$
$\alpha_T$	$I_{pD}/\rho I_p l^2$



BENEDETTI

- $\omega_i$   $i$ th natural circular frequency  
 $\omega_p$  natural circular frequency of mass particle  
 $\omega_x, \omega_y, \omega_z$  specified rotational speeds about xyz axes  
 $\dot{\omega}_x, \dot{\omega}_y, \dot{\omega}_z$  specified rotational accelerations about xyz axes  
 $\theta$  angular position of disk  
 $\phi_x$  angle of twist of beam cross section  
 $\epsilon$  strains in direction of x axis; also, distance from end of beam to mass center of rigid mass along x axis  
 $(\dot{\phantom{x}})$  indicates differentiation with respect to time  
 $(\phantom{x})'$  indicates differentiation with respect to x

TITLE: MEASUREMENT OF BALLOTTING AND FREE RUN EFFECTS FOR A  
PROJECTILE DURING GUN LAUNCH

G. A. BENEDETTI, Ph.D.  
ANALYTICAL MECHANICS DIVISION  
SANDIA LABORATORIES  
LIVERMORE, CALIF. 94550

INTRODUCTION:

Since projectile balloting during gun launch can cause components mounted within eight-inch diameter projectiles<sup>†</sup> to respond dynamically, balloting may represent a serious potential structural problem.<sup>††</sup> However, measured balloting environments for eight-inch diameter projectiles are not explicitly defined. In fact, it is not known if significant balloting accelerations exist. Consequently, it appears appropriate to experimentally determine if significant balloting exists for eight-inch diameter projectiles during gun launch.

One way to accomplish this is by mounting a beam within a projectile (refer to Figure 1) and measure the beam's bending strain response as the projectile accelerates along the gun tube. The frequencies associated with the transverse vibration of the beam are selected so that the beam will not vibrate due to the known rigid body accelerations associated with launching the projectile from the gun tube. However, the beam will undergo transverse vibration due to calculated projectile balloting accelerations (refer to Figures 9 and 10 [5]).

If the measured and predicted quasi-static beam response are in good agreement, then significant projectile balloting is not present. However, if the measured transverse beam response differs from the predicted quasi-static response, then projectile balloting may be present.

An additional objective associated with the experimental program is to measure the initial angular acceleration resulting from

<sup>†</sup> Specifically, components associated with the XM753 projectile.

<sup>††</sup> This report does not address the affect of projectile balloting and/or projectile-gun tube interactions on the initial ballistic flight of the projectile.

BENEDETTI

"free run" of the projectile.<sup>†††</sup> Data will be presented at the Symposium concerning this problem.

An onboard telemetry system is essential for obtaining quantitative measurements while the projectile is traveling along the gun tube. The test projectile, associated instrumentation, telemetry system and recovery system are shown in Figure 1.

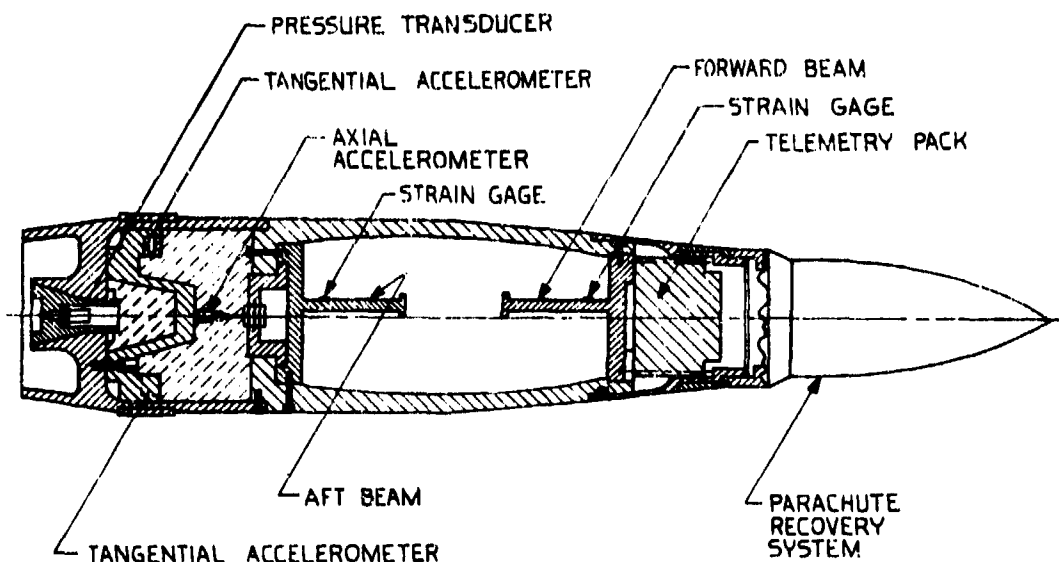


Figure 1. Test projectile

The following quantities are continuously measured with respect to time and transmitted to down-range receivers.

1. Projectile base pressure.
2. Projectile axial acceleration.
3. Projectile tangential acceleration. (This measurement provides a means for determining the initial and subsequent rigid body angular acceleration of the projectile.)
4. Beam bending and axial strains.

In addition, the chamber pressure and projectile tube exit velocity are measured using ground based instrumentation.

<sup>†††</sup> Projectile "free run" and its associated consequences were first defined at SLL in December 1976, subsequent to a test projectile failure. The failure occurred at a threaded joint which connected the rocket motor case to the aft bulkhead.

## BENEDETTI

### EQUATIONS OF MOTION:

The beam under consideration, shown in Figure 2, is a Bernoulli-Euler beam of constant circular cross section. The boundary condition equations for the beam are those associated with the following end conditions.

1. The free end of the beam has a symmetrical rigid mass attached to it. (The primary purpose of the mass is to adjust the first bending natural frequency of the beam to a prescribed value which is the same as the first natural frequency for an important structural component within the XM753 projectile.)
2. The other end of the beam is simply supported but has elastic rotational restraints in the x-y and x-z planes. (The beam base plate thickness can be specified such that the beam is essentially cantilevered.)

The beam is subjected to three specified translational accelerations (along the body fixed xyz axes) and three specified rotational accelerations (about the xyz axes). The partial differential equations of motion describing the coupled (axial, torsional, and transverse (or lateral)) dynamic response of the beam and the associated boundary and initial conditions are derived in [1,2]. For the general problem, these equations are quite lengthy, nonlinear, and difficult to solve. Consequently, a simpler problem, more amenable to solution, is considered.

### Quasi-Static Response of Beam

The partial differential equations of motion in [2] are greatly simplified by incorporating the following assumptions.

1. Quasi-static response is assumed so that no vibration occurs. That is,

$$\dot{u} = \ddot{u} = \dot{v} = \ddot{v} = \dot{w} = \ddot{w} = \dot{\phi}_x = \ddot{\phi}_x = 0$$

2. Balloting is assumed not to occur so that the beam is only subjected to specified accelerations and velocities along and about its longitudinal or x axis. These accelerations and velocities ( $\ddot{U}$ ,  $\omega_x$ , and  $\dot{\omega}_x$ ) correspond to the known rigid body motions associated with launching the projectile from the gun tube. That is,

$$\ddot{v} = \ddot{w} = \omega_y = \dot{\omega}_y = \omega_z = \dot{\omega}_z = 0$$

BENEDETTI

and

$\ddot{U}$ ,  $\dot{\omega}_x$ , and  $\omega_x$  are known from measurement.

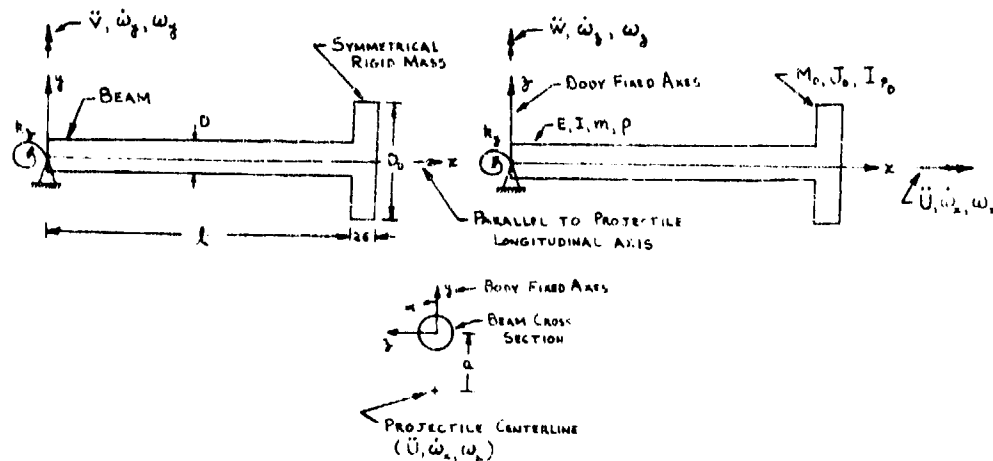


Figure 2. Bernoulli-Euler beam, end conditions, and specified accelerations along and about body fixed axes.

Experimental beam parameters:  $l = 4.0$  in.,  $p = 0.40$  in.,  $D_0 = 0.2$  in.,  $D_p = 1.20$  in.,  
 $a = 0.375$  in.,  $E = 30 \times 10^6$  lb/in<sup>2</sup>,  $G = 11.4 \times 10^6$  lb/in<sup>2</sup>,  
 $\rho = 0.283 \times 10^{-4}$  lb/in<sup>3</sup>,  $\dot{\omega}_x = 8\pi \times 10^4$  rad/sec<sup>2</sup>, uniaxial strain gauges  
 located at  $x = 1.0$  in. and  $\alpha = 0^\circ, 90^\circ, 180^\circ, 270^\circ$ .  
 Material: 4140 steel, yield stress is 180,000 lb/in<sup>2</sup>.

Using these assumptions, the partial differential equations in [2] reduce to the following set of coupled, ordinary differential equations for the quasi-static response of the beam [2]\* (refer to Figure 2).

$$EIv'''' - [-m\ddot{U}(l-x) - M_D\ddot{U} + \rho I\dot{\omega}_x^2]v'' - m\ddot{U}v' - m\dot{\omega}_x^2v - m\dot{\omega}_xw + 3\rho I\dot{\omega}_xw'' + [-2\rho I\dot{\omega}_x(l-x) - I_{pD}\dot{\omega}_x]w''' = ma\dot{\omega}_x^2 \quad (1)$$

$$EIw'''' - [-m\ddot{U}(l-x) - M_D\ddot{U} + \rho I\dot{\omega}_x^2]w'' - m\ddot{U}w' - m\dot{\omega}_x^2w + m\dot{\omega}_xv - 3\rho I\dot{\omega}_xv'' - [-2\rho I\dot{\omega}_x(l-x) - I_{pD}\dot{\omega}_x]v''' = -ma\dot{\omega}_x \quad (2)$$

\*These equations have been derived for the case where the circular cross sectional area of the beam,  $A$ , is an arbitrary function of  $x$ . However, in this report, the cross sectional area of the beam is independent of  $x$  and the equations are considerably simplified.

# BENEDETTI

The boundary conditions associated with equations (1) and (2) are expressed by Equations (3) through (10).

$$\text{at } x = 0: \quad (3)$$

$$v = 0 \quad (4)$$

$$w = 0 \quad (5)$$

$$\frac{EI}{k_z} v'' - v' = 0 \quad (6)$$

$$\frac{EI}{k_y} w'' - w' = 0 \quad (7)$$

$$\text{at } x = \ell:$$

$$\left\{ EI v'' + \frac{1}{(1+\phi_x^2)} \left[ [-\epsilon M_D \ddot{U} + J_D \omega_x^2 + \dot{\omega}_x \phi_x (I_{pD} - J_D) + \epsilon^2 M_D (-\omega_x^2 + \dot{\omega}_x \phi_x)] v' + \epsilon M_D (-\omega_x^2 + \dot{\omega}_x \phi_x) v + [\epsilon M_D \ddot{U} \phi_x + J_D \omega_x^2 \phi_x - \dot{\omega}_x (I_{pD} - J_D) - \epsilon^2 M_D (\dot{\omega}_x + \omega_x^2 \phi_x)] w' - \epsilon M_D (\dot{\omega}_x + \omega_x^2 \phi_x) w \right] \right\}_{x=\ell} = - \frac{1}{(1+\phi_x^2)} \left[ \epsilon M_D (-a \omega_x^2 + a \dot{\omega}_x \phi_x) \right]_{x=\ell} \quad (8)$$

$$\left\{ -EI w'' + \frac{1}{(1+\phi_x^2)} \left[ [+ \epsilon M_D \ddot{U} - J_D \omega_x^2 - \dot{\omega}_x \phi_x (I_{pD} - J_D) + \epsilon^2 M_D (+\omega_x^2 - \dot{\omega}_x \phi_x)] w' + \epsilon M_D (+\omega_x^2 - \dot{\omega}_x \phi_x) w + [-\epsilon M_D \ddot{U} \phi_x + J_D \omega_x^2 \phi_x - \dot{\omega}_x (I_{pD} - J_D) - \epsilon^2 M_D (\dot{\omega}_x + \omega_x^2 \phi_x)] v' - \epsilon M_D (\dot{\omega}_x + \omega_x^2 \phi_x) v \right] \right\}_{x=\ell} = + \frac{1}{(1+\phi_x^2)} \left[ \epsilon M_D (+a \dot{\omega}_x + a \omega_x^2 \phi_x) \right]_{x=\ell} \quad (9)$$

BENEDETTI

$$\left[ -EIv''' - [M_D \ddot{U} + \epsilon M_D \dot{\omega}_x^2] v' - M_D \dot{\omega}_x^2 v - M_D \dot{\omega}_x w - \epsilon M_D \dot{\omega}_x w' + I_{pD} \dot{\omega}_x w'' \right]_{x=\ell} = + M_D a \dot{\omega}_x^2 \quad (9)$$

$$\left[ -EIw''' - [M_D \ddot{U} + \epsilon M_D \dot{\omega}_x^2] w' - M_D \dot{\omega}_x^2 w + M_D \dot{\omega}_x v + \epsilon M_D \dot{\omega}_x v' - I_{pD} \dot{\omega}_x v'' \right]_{x=\ell} = - M_D a \dot{\omega}_x \quad (10)$$

The angle of twist for the beam cross section,  $\phi_x$ , is given by Equation (11). Note  $I_p = 2I$  for a circular cross section.

$$\phi_x = - \frac{1}{2GI} [2\rho I \dot{\omega}_x x(\ell - \frac{x}{2}) + I_{pD} \dot{\omega}_x x] \quad (11)$$

Equations (1) and (2), for the quasi-static response of the beam shown in Figure 2, and their associated boundary conditions (Equations (3) through (10)) represent a two point, linear boundary value problem and the system of equations is solved numerically using a superposition method since  $\ddot{U}$ ,  $\dot{\omega}_x$ , and  $\dot{\omega}_x$  are known quantities. The equations are valid in the gun tube (provided the assumptions associated with Equations (1) and (2) are valid) as well as during free flight provided the nutation and precession of the projectile during free flight has a negligible effect on the quasi-static response of the beam. However, the equations are not valid during gun tube exit since the beam will experience a coupled transient dynamic response due to the rapid decay ( $\sim 0.1 \times 10^{-3}$  sec to  $\sim 0.5 \times 10^{-3}$  sec) of the projectile base pressure and almost instantaneous reduction ( $\sim 67 \times 10^{-6}$  sec) in the projectile's rigid body angular acceleration,  $\dot{\omega}_x$ . This, of course, implies a similar reduction in rotating band pressure.

Using the above mentioned calculations, the bending and axial strains in the beam can be predicted. If the calculated quasi-static axial strains agree with the measured strains, then significant projectile balloting is not present. However, if the measured strains indicate a significant vibratory bending response during projectile travel in the tube, then projectile balloting is present. In this manner, projectile balloting is detected.

## BENEDETTI Beam Natural Frequencies

The natural frequencies associated with the vibrations of the beam (refer to Figure 2) are such that the beam will not vibrate due to the known rigid body accelerations (i.e.,  $\ddot{U}$ ,  $\omega_x$ , and  $\omega_y$ ). This is illustrated by noting that the "load" application times (refer to Figures 4 through 6) are long relative to the calculated fundamental periods of oscillation for the beam. The derivation of the frequency equations are given in [3].

### Natural Frequencies for Bending Vibration

The bending natural frequencies depend not only upon the mechanical, geometrical, and physical properties of the beam and symmetrical rigid mass, but also on the boundary conditions (e.g., the elastic rotational restraints,  $k_y$  and  $k_z$ ). If  $k_y$  and  $k_z$  are sufficiently large, the boundary condition Equations (5) and (6) are simplified and reduce to those for a cantilever beam. The bending frequency equation, expressed by Equation (12) in non-dimensional form, neglects the affect of rotary inertia and shear deformation and, in addition, neglects the affects of  $\ddot{U}$ ,  $\omega_x$ , and  $\omega_y$  on the natural frequencies for the beam.

$$\begin{aligned} & 2 + 2b^2\alpha^2\beta^4 + \{-2\alpha\beta^3(a^2 + b^2) - 2\alpha\beta + \frac{\beta}{S} [2\alpha^2\beta^4(a^2 + b^2) \\ & - 2(1 + \alpha\alpha\beta^2)^2]\} \sin \beta \cosh \beta + [-4\alpha\alpha\beta^2 - \frac{4\alpha\beta^2}{S}] \sin \beta \sinh \beta \\ & + [2 + 2a^2\alpha^2\beta^4 - 2\alpha^2\beta^4(a^2 + b^2) - \frac{4\alpha\beta^4}{S} (a^2 + b^2)] \cos \beta \cosh \beta \\ & + \{2\alpha\beta - 2\alpha\beta^3(a^2 + b^2) + \frac{\beta}{S} [2(1 - \alpha\alpha\beta^2)^2 \\ & - 2\alpha^2\beta^4(a^2 + b^2)]\} \cos \beta \sinh \beta = 0, \end{aligned} \quad (12)**$$

$$\text{where } a = \frac{\epsilon}{\ell}, \quad b^2 = \frac{J_D}{M_D \ell^2}, \quad \alpha = \frac{M_D}{m \ell}, \quad S = \frac{k \ell}{EI}, \quad \text{and } \omega_i = \frac{\beta_i^2}{\ell^2} \sqrt{\frac{EI}{m}}.$$

Note  $k = k_y$  or  $k = k_z$ .

\*\*Laboratory experiments on test beams indicate that Equation (12) accurately predicts the natural frequencies of lateral vibration for the beam. Shear deformation and rotary inertia become more important for the higher modes of vibration.



# BENEDETTI

Solution of Equation (12) for  $\beta_1$  and  $\beta_2$  for various values of  $S$  (or  $k$ ) results in Table 1.

Table 1

Bending Natural Frequencies for Beam (Figure 2)  
for Various Values of  $k$   
(Beam parameters:  $a = 0.025$ ,  $b^2 = 0.005833$ ,  $\alpha = 0.45$ )

$\beta_1$	$\beta_2$	$S$	$k$ $\frac{\text{inch-lb}}{\text{radian}}$	$f_1$ Hz	$f_2$ Hz
0.999812	3.36199	1.061	$1 \times 10^4$	201.2	2275.5
1.33228	3.69983	$1.061 \times 10^1$	$1 \times 10^5$	357.3	2755.8
1.41438	3.88670	$1.061 \times 10^2$	$1 \times 10^6$	402.7	3041.2
1.42405	3.91391	$1.061 \times 10^3$	$1 \times 10^7$	408.3	3083.9
1.42503	3.91675	$1.061 \times 10^4$	$1 \times 10^8$	408.8	3088.4
1.42513	3.91704	$1.061 \times 10^5$	$1 \times 10^9$	408.9	3088.9
1.42514	3.91707	$1.061 \times 10^{12}$	$1 \times 10^{16}$	408.9	3088.9

The calculated value of  $k$  ( $k_y$  or  $k_z$ ) is  $\sim 2.15 \times 10^7 \frac{\text{in-lb}}{\text{rad}}$  ( $S = 2.273 \times 10^3$ ) and for practical purposes the beam (refer to Figure 2) is considered a cantilever beam with first and second natural bending frequencies of 408.6 Hz and 3086.6 Hz, respectively. Consequently, boundary condition Equations (5) and (6) reduce to those for a cantilever beam. The fundamental bending frequency for the beam is significantly higher than the maximum roll frequency of the projectile so that parametric instability is eliminated as a potential problem for the beam during projectile free flight.

## Natural Frequencies for Axial and Torsional Vibration

The axial and torsional frequency equations for the beam (refer to Figure 2) are given by Equations (13) and (14), respectively.

$$\tan \lambda - \frac{1}{\alpha \lambda} = 0 \quad (13)$$

$$\text{where } \alpha = \frac{M_D}{m \ell} \text{ and } \omega_i = \frac{\lambda_i}{\ell} \sqrt{\frac{E}{\rho}} ;$$

$$\tan \lambda - \frac{1}{\alpha_T \lambda} = 0 \quad (14)$$

$$\text{where } \alpha_T = \frac{I_{pD}}{\rho I_p \ell} \text{ and } \omega_i = \frac{\lambda_i}{\ell} \sqrt{\frac{G}{\rho}} .$$

BENEDETTI

Solution of Equations (13) and (14) for  $\lambda_1$  and  $\lambda_2$ , respectively, results in Table 2.

Table 2  
Axial and Torsional Natural Frequencies for Beam  
(Refer to Figure 2)  
(Beam parameters:  $\alpha = 0.45$ , and  $\alpha_t = 4.05$ )

$\lambda_1$	$\lambda_2$	$f_1$ Hz	$f_2$ Hz	
1.10820	3.68433	8924.1	29,669.	=> Axial Vibration
0.477355	3.21817	2384.0	16,071.9	=> Torsional Vibration

Equations of Motion for a Mass Particle (Beam) Elastically Mounted on a Rigid Disk (Projectile)

To obtain an approximation for the lateral dynamic response of the beam when subjected to transverse (balloting) and rotational accelerations, the beam is modeled as a mass particle elastically mounted and constrained to move in the plane of a rigid disk. The projectile is modeled as the disk, which is massive compared to the mass particle (or beam), and undergoes specified rigid body translational and rotational accelerations in its plane. The translational accelerations (V and W) simulate projectile balloting accelerations and the rotational acceleration simulates projectile "spin up" as it accelerates along the length of a rifled gun tube. The idealized model is shown in Figure 3 and the equations of motion for the mass particle are expressed by Equations (15) and (16) [4].

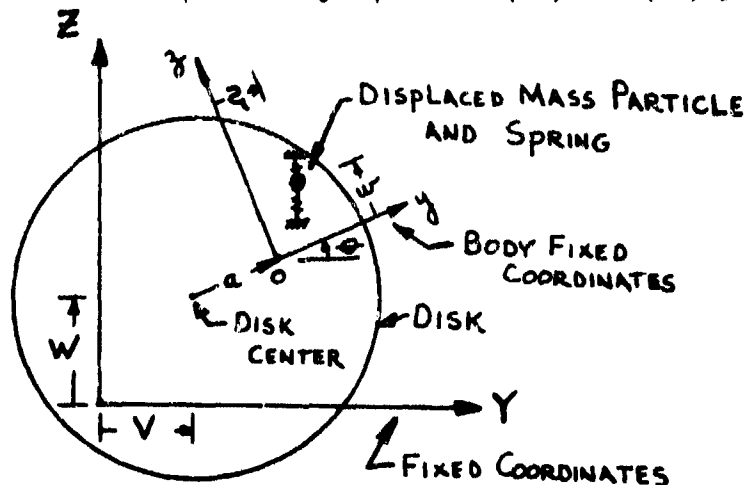


Figure 3. Idealized model of beam (mass particle) and projectile (disk). Note:  $\dot{\theta} = \omega_x$  and  $\ddot{\theta} = \dot{\omega}_x$ .

BENEDETTI

$$\ddot{V} + 2\xi\omega_p \dot{V} + (\omega_p^2 - \dot{\theta}^2) V - \ddot{\theta} W - 2\dot{\theta}\dot{W} = -V \cos \theta - W \sin \theta + a\dot{\theta}^2 \quad (15)$$

$$\ddot{W} + 2\xi\omega_p \dot{W} + (\omega_p^2 - \dot{\theta}^2) W + \ddot{\theta} V + 2\dot{\theta}\dot{V} = +V \sin \theta - W \cos \theta - a\ddot{\theta} \quad (16)$$

Solution of Equations (15) and (16) results in the dynamic response ( $V$  and  $W$ ) for the mass particle. When  $V$  and  $W$  are zero, the response of the mass particle to the projectile "spin up" ( $\theta$  and  $\ddot{\theta}$ ) is obtained.

#### RESPONSE CALCULATIONS:

##### Quasi-Static Response of Beam

Figures 4, 5, and 6 are typical for the known rigid body motions associated with launch. (The shape of the angular acceleration versus time is identical to the shape of the axial acceleration versus time, provided the rotating band on the projectile initially engages the tube rifling.) Using Figures 4, 5, and 6 as inputs for Equations (1) through (10) (refer to Figure 2), the quasi-static axial strains at a specified location along the beam are calculated and are shown in Figure 7. The parameters associated with Figure 7 are:  $\ell = 4.0$  in.,  $D = 0.40$  in.,  $2e = 0.20$  in.,  $D_D = 1.20$  in.,  $a = 0.375$  in.,  $E = 30 \times 10^6$  lb/in<sup>2</sup>,  $G = 11.54 \times 10^6$  lb/in<sup>2</sup>,  $\rho = \rho_D = 7.324 \times 10^{-4}$  lb-sec<sup>2</sup>/in<sup>4</sup>. The axial strain location is at  $\zeta = x/\ell = 0.25$  and  $\sigma = 0^\circ, 180^\circ$ .

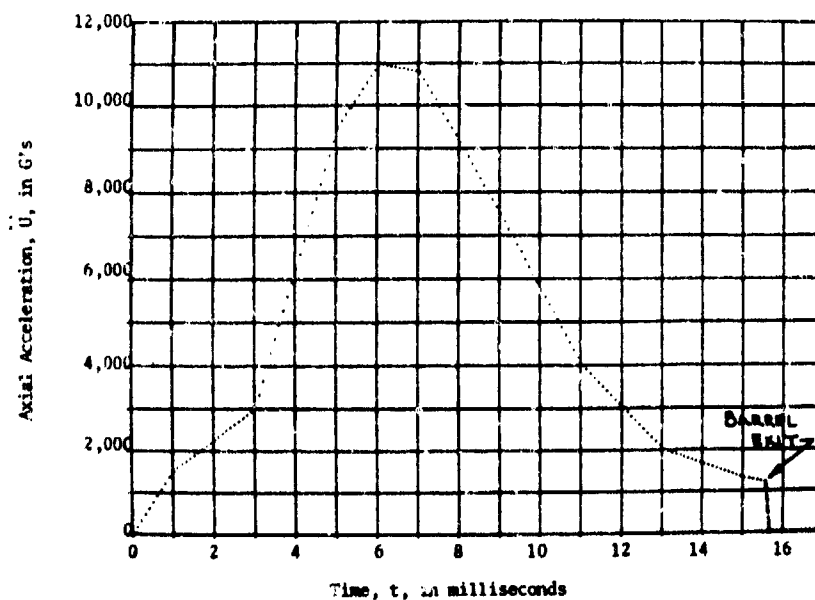


Figure 4. Axial acceleration of projectile versus time.  
Test number GB054.

# BENEDETTI

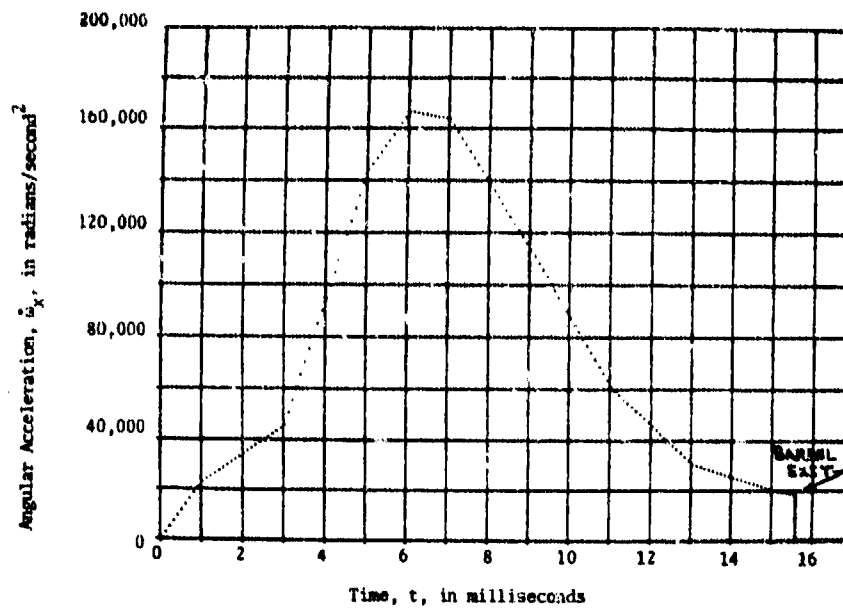


Figure 5. Angular acceleration of projectile versus time.  
Test number GB054.

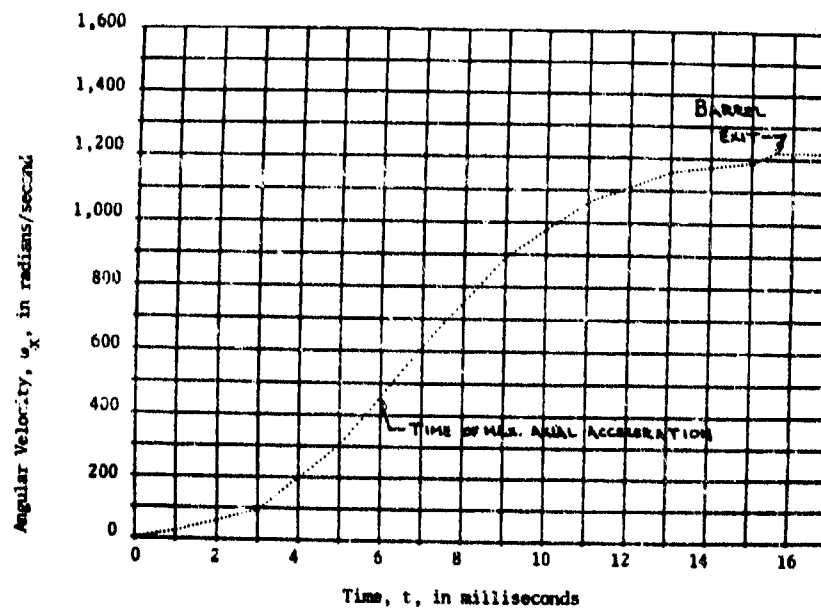


Figure 6. Angular velocity of projectile versus time.  
Test number GB054.

# BENEDETTI

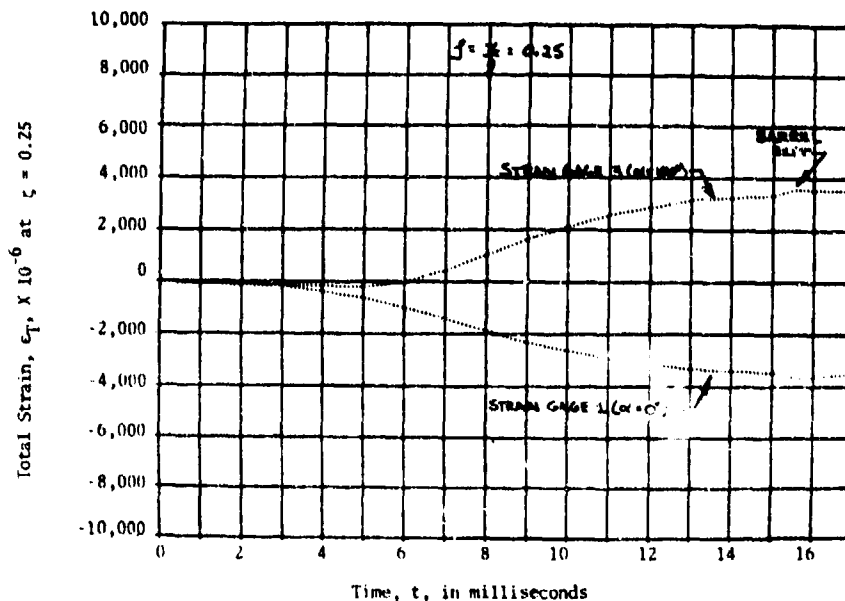


Figure 7. Calculated total strain in beam at  $\zeta = \frac{x}{l} = 0.25$  for strain gages 1 and 3 versus time.

## Dynamic Response of Mass Particle (Beam) Elastically Mounted on a Rigid Disk (Projectile)

Figures 8, 9, and 10 are used as inputs for Equations (15) and (16); i.e., the mass particle-disk problem shown in Figure 3. Figures 11 and 12 are calculated particle displacements when the balloting accelerations [5] (Figures 9 and 10) are not present. Note the particle displacements ( $v$  and  $w$ ) are quasi-static, except during gun tube exit. Figures 13 and 14 are calculated particle displacements when the angular acceleration (Figure 8) as well as the balloting accelerations (Figures 8 and 9) are present. Note the particle displacements ( $v$  and  $w$ ) are not quasi-static but dynamic. The parameters associated with the numerical solutions for the mass particle-disk problem are:  $\omega_D = 400 (2\pi)$  rads/sec,  $\xi = 0.03$ ,  $a = 0.375$  in.,  $m_p = 5.3313 \times 10^{-3} \frac{\text{lb-sec}^2}{\text{in}}$ , and  $m_D = 0.521 \frac{\text{lb-sec}^2}{\text{in}}$ . Note the natural circular frequency for the mass particle is essentially equal to the first natural circular frequency for transverse vibration of the beam (refer to Table 1).

The response plots illustrate a quasi-static response (Figures 11 and 12) when balloting is not present and a dynamic response (Figures 13 and 14) when balloting is present. Consequently, the axial strain gages on the beam, which is mounted within the test projectile (Figure 1), are expected to respond dynamically (i.e.,

# BENEDETTI

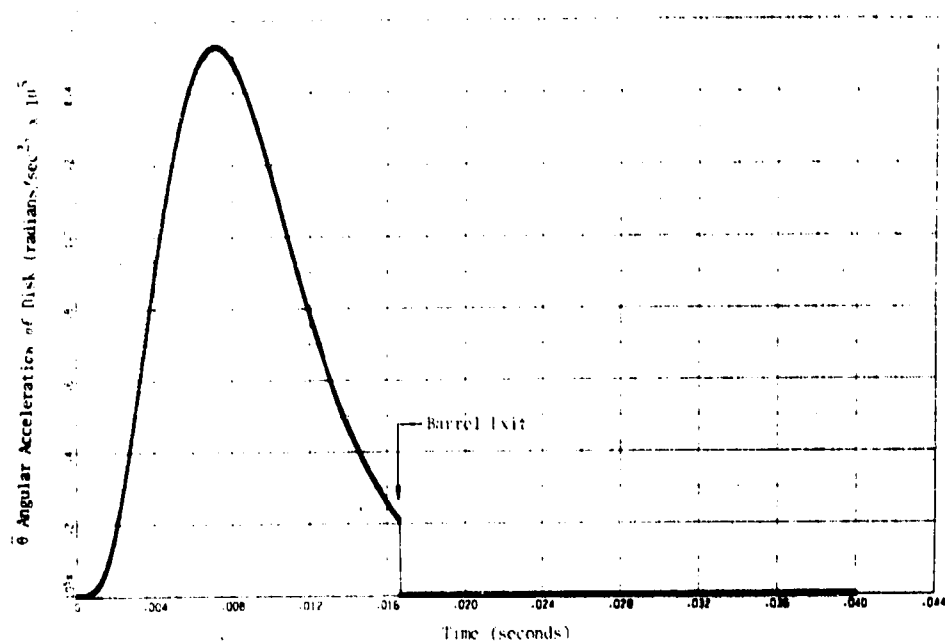


Figure 8. Angular acceleration,  $\ddot{\theta}$ , versus time,  $t$ .

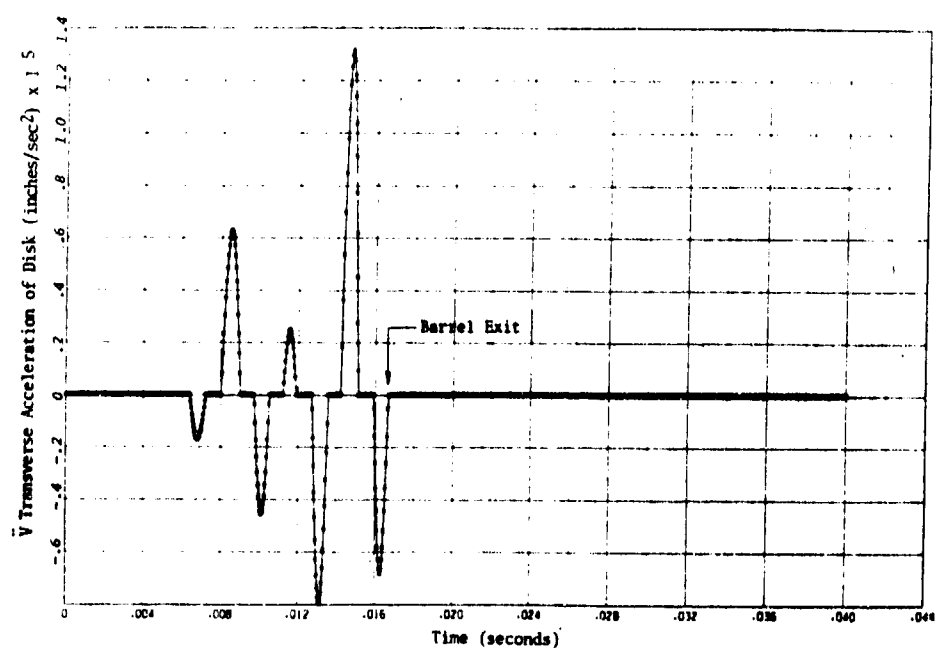


Figure 9. Transverse balloting acceleration,  $\ddot{V}$ , of disk versus time,  $t$ .

# BENEDETTI

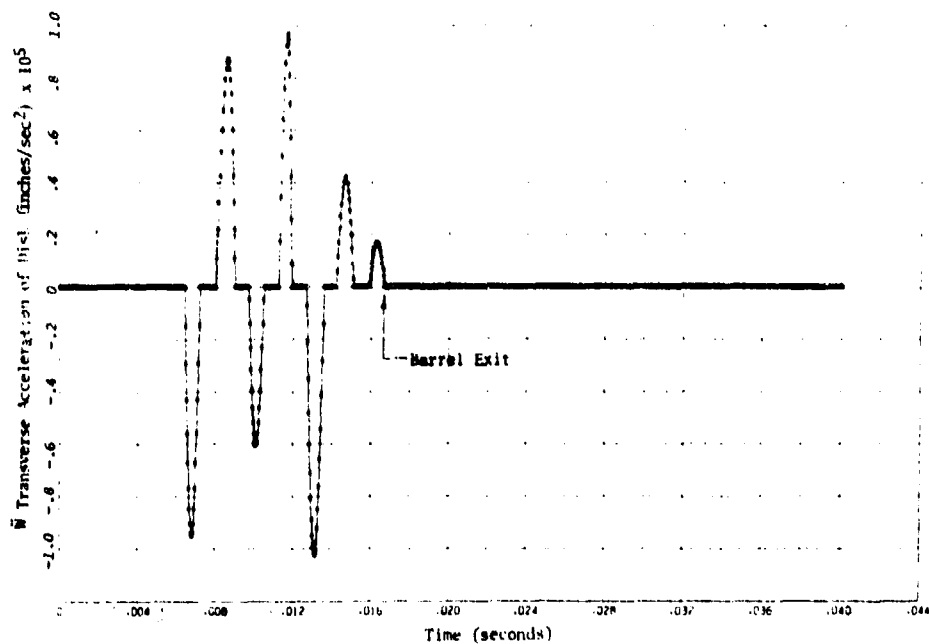


Figure 10. Transverse balloting acceleration,  $W$ , of disk versus time,  $t$ .

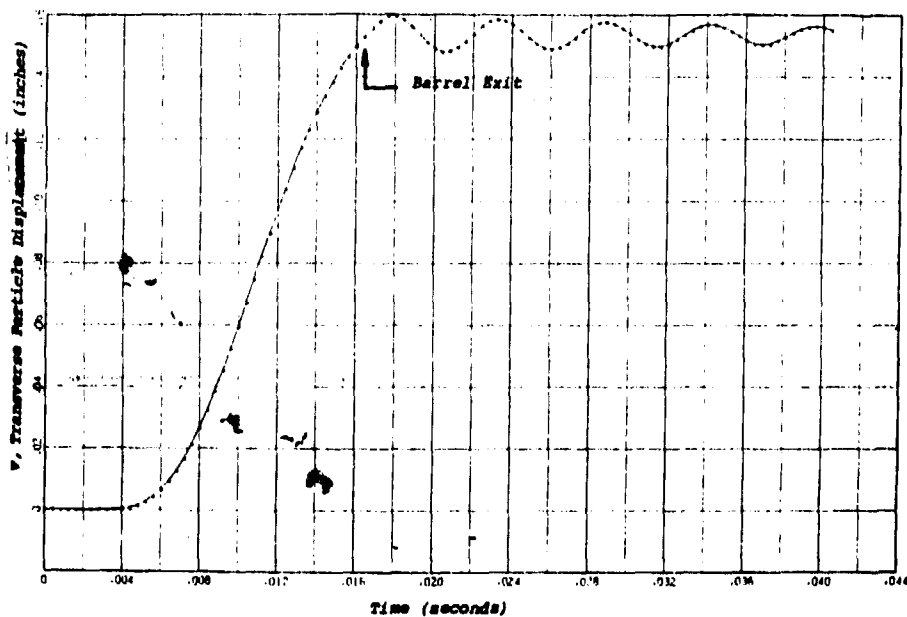


Figure 11. Transverse particle displacement,  $V$ , versus time,  $t$ .  
Balloting not present.

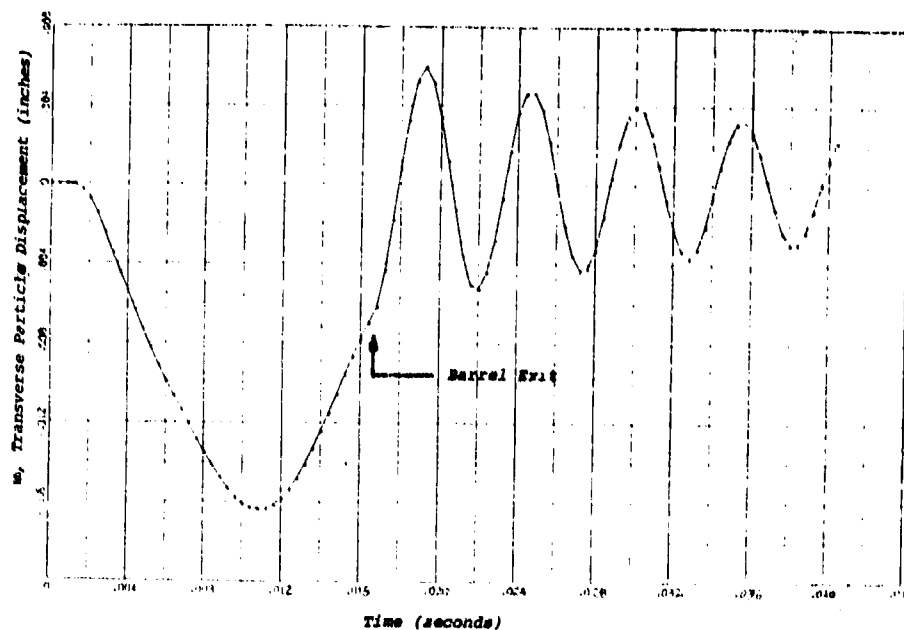


Figure 12. Transverse particle displacement,  $w$ , versus time,  $t$ . Balloting not present.

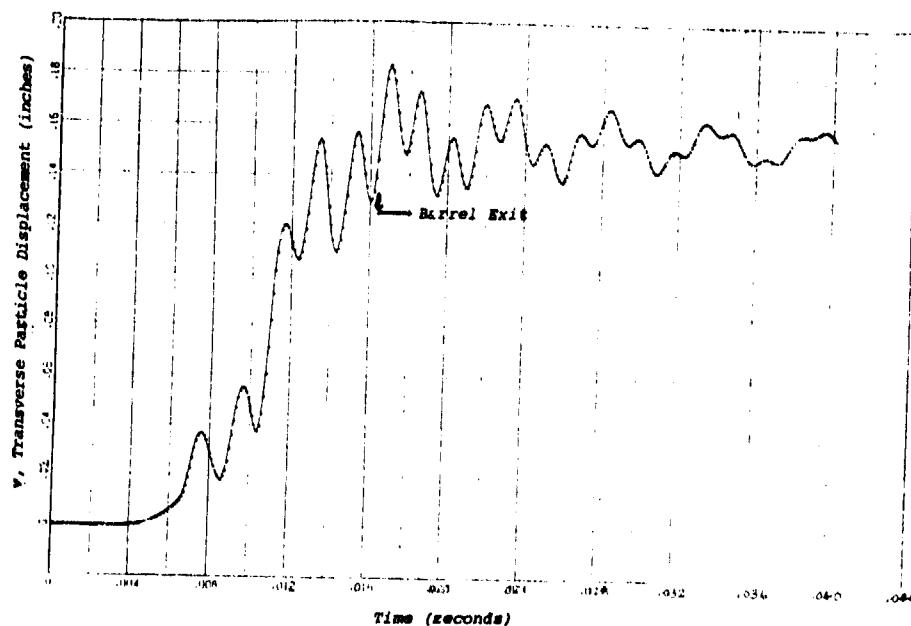


Figure 13. Transverse particle displacement,  $v$ , versus time,  $t$ . Balloting present.



## BENEDETTI

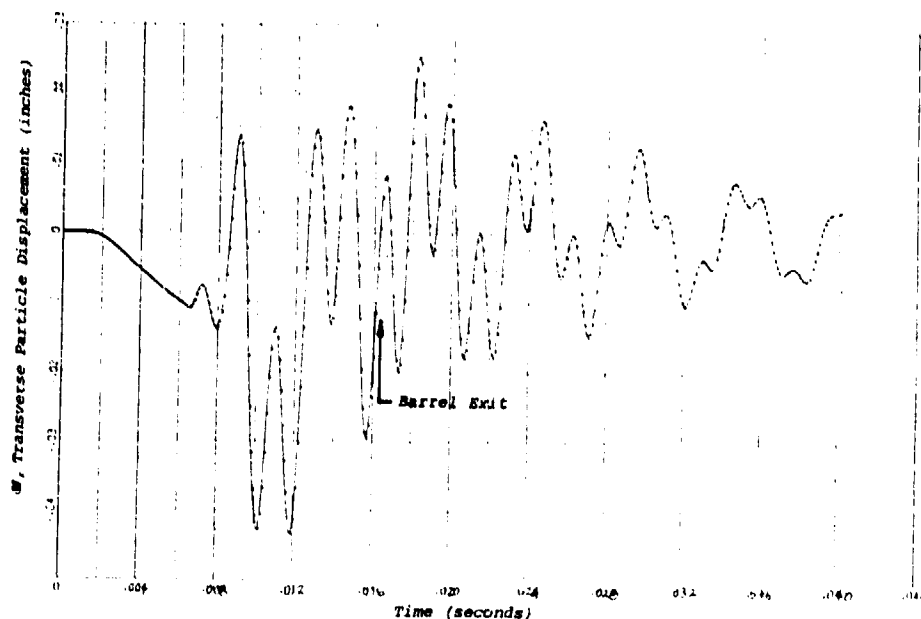


Figure 14. Transverse particle displacement,  $w$ , versus time,  $t$ . Balloting present.

vibratory motion) when balloting of the projectile occurs thus indicating the presence of balloting. In addition, the strain gage response will consist of a dynamic response superimposed on a quasi-static response. This assumes the balloting accelerations are similar to those in [5]. Conversely, if the projectile does not ballot, the strain gage response is quasi-static and calculable by using Equations (1) through (10).

### EXPERIMENTAL MEASUREMENTS:

Figure 1 illustrates the instrumentation and its location within the test projectile. Table 3 lists some specifics associated with the instrumentation. The onboard telemetry system continuously monitors the measurements listed in Table 3 during projectile travel along the gun tube as well as during free flight. When the projectile is launched in a nearly vertical position, the parachute recovery system provides a "soft recovery" for the projectile and telemetry system. Consequently, the telemetry system and test projectile, when fitted with a new rocket motor case and recovery system, are used on subsequent tests.

Table 3

## Projectile Instrumentation (refer to Figure 1)

Description	Instrumentation Response Freq. Hz	Recorded Data	
Chamber press. ( $p_c$ )	2,000	$p_c$ vs. $t$	
Base press. ( $p_b$ )	8,000	$p_b$ vs. $t$	} Monitored by onboard telemetry system.
Axial accel. ( $a_x$ )	8,000	$a_x$ vs. $t$	
Tangential accels. ( $a_T$ )	8,000	$a_T$ vs. $t$	
Uniaxial strain gages ( $\epsilon$ )	1,000 to 2,000	$\epsilon$ vs. $t$	

Since the experimental program is not scheduled to begin until July 1978, the measured data and associated conclusions will be presented at the Symposium.

Special Cases

## Comparison of Measured and Calculated Bending Strains for Spinning Beam Experiments

To provide measured data to verify the computer solution for a special case of the two point, linear boundary value problem (i.e., Equations (1) through (10)), several spinning beam experiments were performed [1]. At a given location along the length of each beam, four uniaxial strain gages were mounted.

For these experiments, it was not possible to subject the beams to the gun induced accelerations,  $\ddot{U}$  and  $\dot{\omega}_x$ . However, the free flight or spin speed,  $\omega_x$ , was simulated. For this particular case, the axial and angular accelerations ( $\ddot{U}$  and  $\dot{\omega}_x$ ) are zero.

A typical comparison between measured beam bending strains (dots) and calculated beam bending strains (solid line) versus angular speed is shown in Figure 15. Since the agreement is excellent, it was concluded the mathematical model and the equations for the quasi-static response for the spinning beams are accurate.

# BENEDETTI

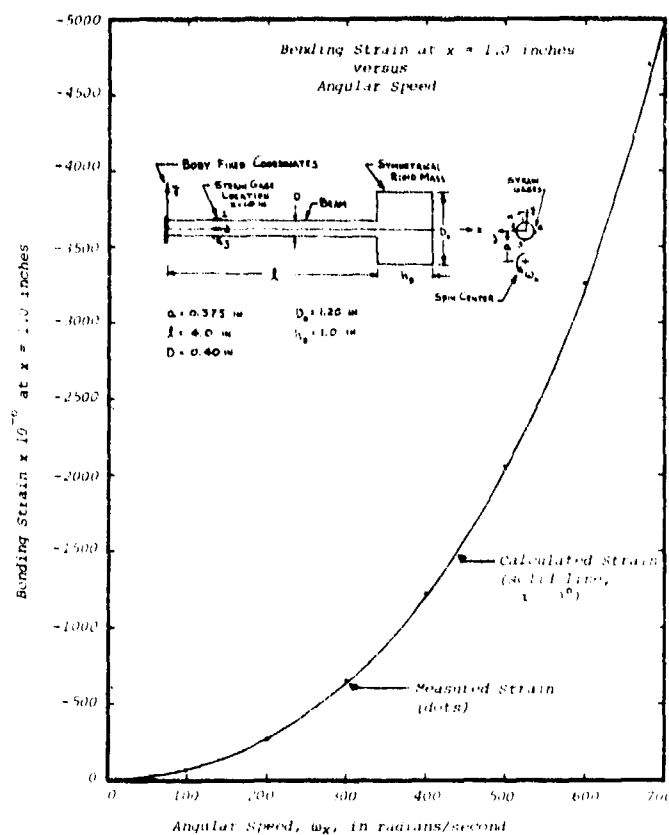


Figure 15. Bending strain at  $x = 1.0$  in. versus angular speed,  $\omega_k$ , for offset distance,  $a$ , equal to 0.375 in. Material: 4340 steel,  $G_{43} = 140,000$  lb/in<sup>2</sup>.

## Comparison of Measured and Calculated Beam Bending Natural Frequencies

Laboratory experiments on test beams indicate Equation (12) accurately predicts the natural frequencies for lateral vibration. Tables 4 and 5 list the measured and calculated natural frequencies (the first two) for the beams illustrated in Figure 15 and Figure 2, respectively.

Table 4

Beam parameters:  $a = \frac{e}{l} = 0.125$ ,  $b^2 = \frac{J_D}{M_D l^2} = 0.010833$ ,  $\alpha = \frac{M_D}{m l} = 2.25$ ,

$E = 30 \times 10^6$  lb/in<sup>2</sup>,  $S = \frac{k l}{E I} = 2.273 \times 10^3$  (refer to Figure 15)

Mode No.	Measured Natural Frequency (Hz)	Calculated Natural Frequency (Hz)	Percent Difference
1	183.3	186.6	1.8
2	1914.	2004.8	4.74

# BENEDETTI

Table 5

Beam parameters:  $a = \frac{\epsilon}{l} = 0.025$ ,  $b^2 = \frac{J_D}{M_D l^2} = 0.005833$ ,  $\alpha = \frac{M_D}{m l} = 0.45$ ,

$E = 30 \times 10^6 \text{ lb/in}^2$ ,  $S = \frac{k l}{E I} = 2.273 \times 10^3$  (refer to Figure 2)

Mode No.	Measured Natural Frequency (Hz)	Calculated Natural Frequency (Hz)	Percent Difference
1	393	408.6	3.97
2	2925	3086.6	5.52

Note that if the modulus of elasticity,  $E$ , is  $28 \times 10^6 \text{ lb/in}^2$  rather than  $30 \times 10^6 \text{ lb/in}^2$ , the calculated natural frequencies are reduced by 3.39%. Consequently, the differences listed in the fourth columns could be due to material property variations.

## Acknowledgments

The author is grateful to many co-workers for their assistance and is especially grateful to Gene L. Angvick for many hours of tedious programming and for most of the numerical solutions presented herein.

## References

1. Benedetti, G. A., "Equations of Motion for a Beam Mounted within a Rigid Body Subjected to Three Translational and Three Rotational Accelerations," SAND77-8207, August 1977.
2. Benedetti, G. A., "Derivation of the Coupled Equations of Motion for a Beam Subjected to Three Translational Accelerations and Three Rotational Accelerations," October 1977. In process of publication.
3. Benedetti, G. A., "Natural Frequencies of Tapered Beams with a Symmetrical Rigid Mass Attached to Free End," March 1978. In process of publication.
4. Benedetti, G. A., "Equations of Motion for a Mass Particle Elastically Mounted on a Disk Subjected to Transverse and Rotational Accelerations," SAND76-8262. March 1977.
5. Chu, S. H., "Transverse Motion of Eight-Inch Projectile XM753 in Gun Tube XM201," Picatinny Arsenal, Dover, New Jersey, December 1975. Technical Report 4918.

SOO HOO

TITLE: Experimental Correlation of a Theoretical Model for  
Predicting Projectile Balloting  
GEORGE SOO HOO  
Naval Surface Weapons Center  
Dahlgren, Virginia 22443

ABSTRACT:

A theoretical model for simulating the dynamics of projectile launch has been developed at the Naval Surface Weapons Center. Knowledge of the inbore environment is essential to ensuring the survival of the projectile and any fuzes, electronics, or mechanical components that may be mounted inside the shell. The inbore projectile dynamics in combination with barrel motion and vibration will determine at the instant of muzzle ejection, the initial conditions governing the shell's free flight. These in turn affect shot accuracy and dispersion.

The major emphasis of this paper concerns the experimental verification of the results of the balloting code only. Correlation of the theoretical and experimental transverse projectile motions would greatly enhance user confidence in the computer model. The experimental results provide the means of validating certain model assumptions and suggesting various modifications.

BIOGRAPHY:

PRESENT ASSIGNMENT: Mechanical Engineer, Naval Surface Weapons  
Weapons Center

DEGREES HELD: Bachelor of Mechanical Engineering, City College of  
New York, New York, New York, 1971; Master of Science in Engineering  
Science and Mechanics, Virginia Polytechnic Institute and State Univer-  
sity, Blacksburg, Virginia, 1978.

## EXPERIMENTAL CORRELATION OF A THEORETICAL MODEL FOR PREDICTING PROJECTILE BALLOTING

GEORGE SOO HOO  
NAVAL SURFACE WEAPONS CENTER  
DAHLGREN, VIRGINIA 22448

### INTRODUCTION

The dynamics of the in-bore launch have a significant influence upon the projectile's performance outside the gun tube. Knowledge of the in-bore environment is essential for ensuring the survival of the projectile itself and the functioning of fuzes as well as other electronics and mechanical packages that may be mounted inside the round. Magnitudes of the forces and accelerations need to be specified for the establishment of adequate design criteria. While the severity of the forces and accelerations witnessed by the projectile in the transverse directions may be small in comparison to the axial direction, the frequency of the loading resulting from balloting in the gun tube may excite resonant frequencies of the projectile and its components. This may result in malfunctions detrimental to the mission of the projectile.

The in-bore projectile dynamics in conjunction with barrel motion and vibration define, at the instant of shot ejection from the gun barrel, the initial conditions governing the shell's free flight. These in turn determine accuracy and dispersion of the round downrange. The ability to correlate various projectile parameters (such as the location of the center of gravity, location of the bourrelet, moments of inertia, unbalances, tolerances, etc.) and barrel parameters (such as wear, droop, stiffness, etc.) to the initial conditions at muzzle exit provides important inputs for minimizing yaw and yaw rate and improving shot accuracy and dispersion.

The need to more fully define the dynamics of projectile launch has led to the development at the Naval Surface Weapons Center of a computer model for simulating the projectile balloting and barrel motion concurrently. This theoretical model couples two distinct computer codes developed previously. The first is a Lagrangian dynamics treatment of a six degree of freedom model for predicting the projectile balloting

S00 H00

motion. The second simulates barrel motion and vibration as a finite difference model of a Bernoulli-Euler beam. Forces resulting from projectile and gun bore contact, as determined in the balloting program, provide the forcing function inputs into the barrel motion model. New barrel displacements, velocities, and accelerations are then used in the balloting program. The coupling of the two codes permits the simultaneous solution of the two problems. Thus, the influence of barrel motion upon the projectile dynamics and vice versa can be calculated.

The emphasis of this paper concerns itself with the projectile in-bore motion only. Experimental verification of the theoretical balloting model is essential for increasing user confidence in the results. Brief descriptions of the model and experimental setup are provided in the next sections. Theoretical and test results are presented and a comparison between the two is made.

#### DESCRIPTION OF BALLOTING MODEL

The equations of motion for the balloting model are derived using Lagrange's equation,

$$\frac{d}{dt} \left[ \frac{\partial T}{\partial \dot{q}} \right] - \frac{\partial T}{\partial q} = F_q$$

where

$T$  = kinetic energy,

$q$  = generalized coordinates specifying the location and orientation of the projectile, and

$F_q$  = applied forces and moments in the directions of the generalized coordinates.

Substitution of the expression for the kinetic energy of a free rigid body yields six coupled partial differential equations of motion from which accelerations can be obtained. The accelerations are integrated to yield new velocities and displacements.

The various forces and moments considered to act upon the projectile include gravity, the force due to the pressure acting on the base of the projectile, forces due to bourrelet contact, forces acting at the rotating band, and moments due to the rifling twist. The bourrelet contact is simulated as a spring deflection model with the restoring force proportional to the theoretical displacement of the projectile into the gun tube. The rotating band stiffness is modeled by both transverse and torsional springs. The values of these spring constants must be determined analytically or experimentally.

The significant input quantities include projectile mass, location of the center of gravity, moments and products of inertia, various projectile radii and lengths, the initial projectile orientation, bore diameter, travel distance, the interior ballistics for the propellant charge (specifically, projectile base pressure versus time), and the various spring constants.

Further details of the model are given in Reference 1.

#### EXPERIMENTAL SETUP FOR MEASURING BALLOTING MOTION

In order to meet the requirement of measuring the balloting motion free from the influence of any barrel effects, it is necessary to restrain the gun tube as much as possible. A 40mm gun was utilized in the tests. This setup was actually a 40mm MK 1 barrel modified and assembled in the jacket of a 6 pounder gun MK A MOD 1. This test configuration provided a relatively rigid structure with a recoil distance of about 6 inches. Any recoil during the in-bore period was considered to be minimal. In addition, a cradle like fixture support was constructed at the muzzle end to restrict transverse barrel motion far from the gun trunnion. A photograph of the experimental setup is shown as Figure 1.

An optical lever technique is used for measuring the angular displacements of the projectile. The system is similar to one employed at the Ballistic Research Laboratories (Reference 2). A schematic of the setup is depicted in Figure 2. The light source is a 15 mw HeNe (6328Å) continuous wave laser. A lens focuses the beam at the focal length of an off-axis parabolic mirror. This mirror is an essential element in the optical system and collimates the laser beam such that axial motion of the projectile along the gun centerline has no effect upon the measured yaw angles. The laser beam is directed down the gun tube by two aiming mirrors to a mirror mounted on the nose of a 40mm MK 2 projectile. The return beam retraces its path through the optics, where finally a portion of the signal is reflected from a beam splitter to a photodiode detector and recorded on magnetic tape. The optical setup provides a magnification factor at the detector of about 25 times the bourrelet displacements.

#### OBTURATION

From tests conducted at NSWC during FY 75 on a 76mm projectile, the leakage of propellant gases around the rotating band was known to present a problem in obtaining a continuous signal over the duration of the in-bore period. Two alternatives were attempted for circumventing this obstacle for the 40mm tests. The first choice was to fire reduced charge weights. However, test results showed that this did not improve the total duration of data acquisition. The second alternative was to



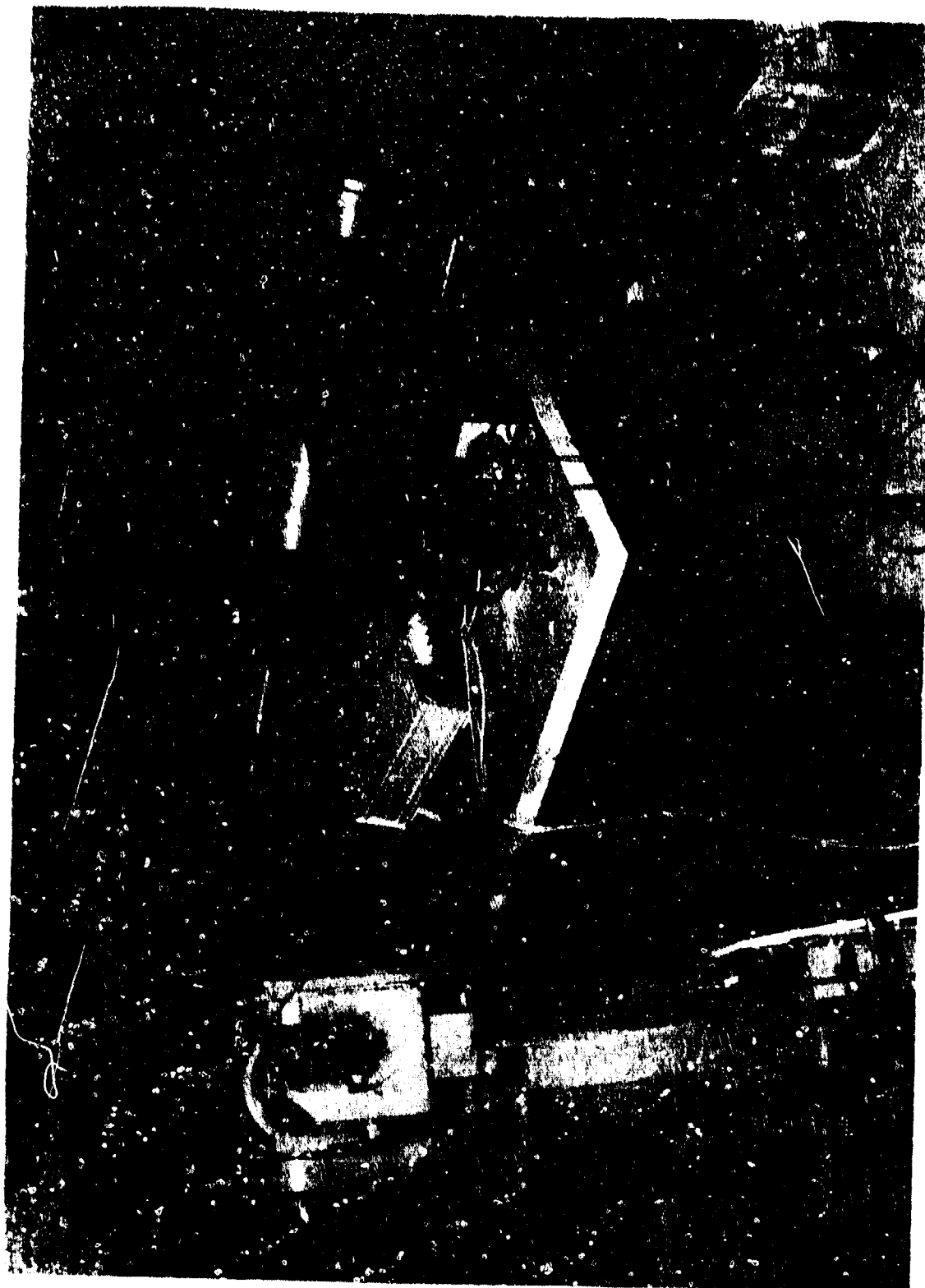


Figure 1. Experimental Setup for 40mm Balloting Measurement

S00 H00

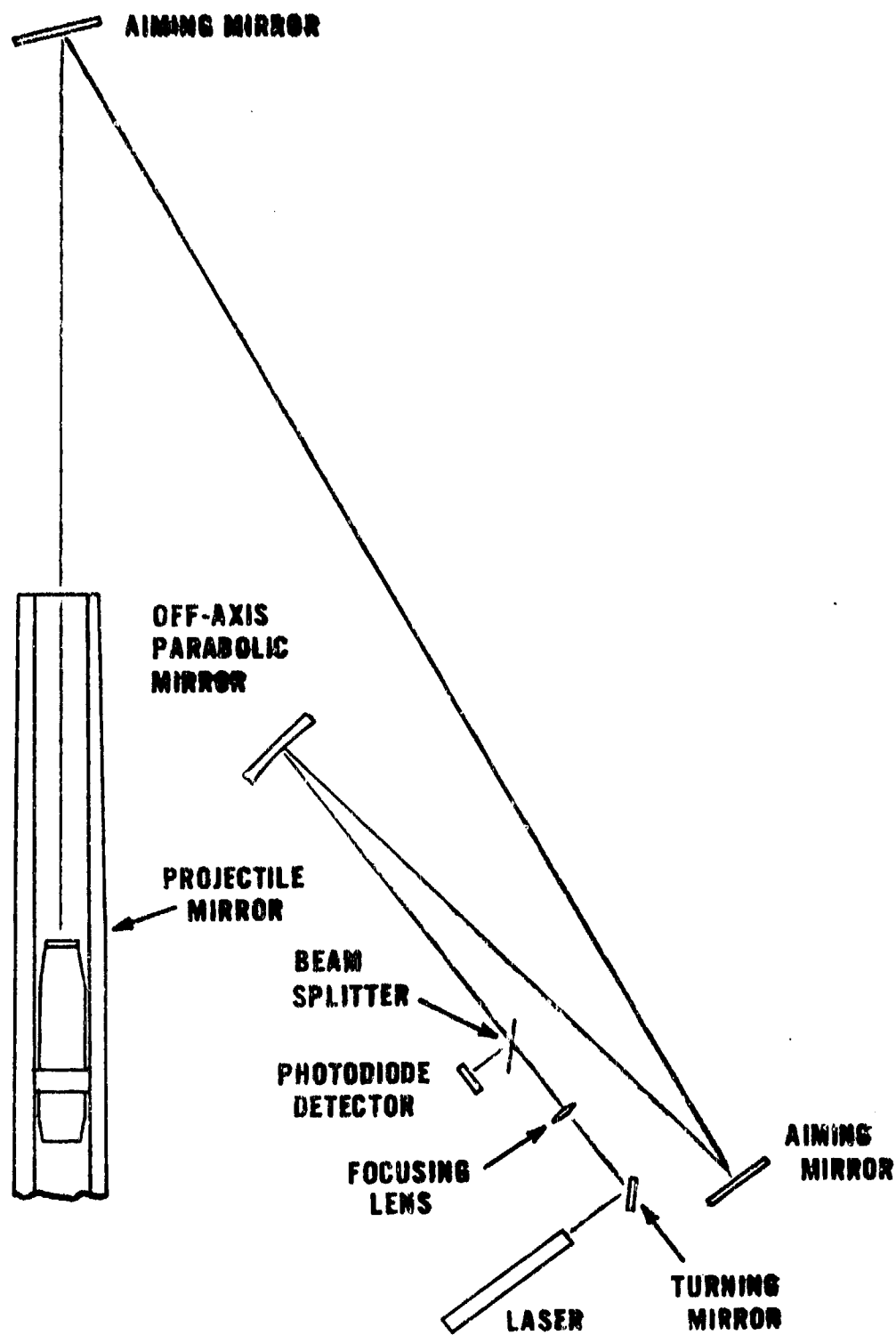


Figure 2. Schematic of Optical Lever Setup

S00 H00

develop a plastic rotating band. Rather than design a new rotating band completely which would both spin up the projectile and provide greater obturation, an additional teflon band was emplaced behind the conventional copper band. This lengthened data acquisition out to approximately 75% of the total in-bore period of 4.50 msec or slightly more than 50% of the in-bore travel of 78 inches.

#### COMPARISON OF THEORETICAL AND EXPERIMENTAL RESULTS

Theoretical balloting results were obtained for a 40mm projectile in a stationary, rigid gun tube. In these computations, the wear characteristics of the barrel, shown in Figure 3, and the gain twist of the rifling, which increases from 1 turn in 45 calibers at the origin of rifling to 1 turn in 30 calibers near the muzzle, were incorporated into the program. Projectile base pressures were assumed to be approximately 90% of the experimentally measured chamber pressure values. The magnitudes of the rotating band stiffnesses were scaled from experimentally determined values for a 76mm projectile.

Figure 4 illustrates the theoretical transverse projectile motion at the bourrelet as viewed from the breech end of the barrel. The center of the plot corresponds to the bore centerline. The circle indicates the clearance between the bourrelet and an average gun bore diameter representative of the entire projectile travel distance. The initial projectile orientation is such that the shell contacts the gun tube in the lower right quadrant as shown by the small dot. The projectile possesses a minor counterclockwise motion initially but basically moves in a clockwise direction in accordance with the rifling twist, with several contacts between the shell and gun tube in evidence. The plot represents 3.50 msec of the total in-bore period. The numbers next to the tick marks on the trace indicate the in-bore time in milliseconds from shot start.

Experimentally measured transverse motions of the bourrelet are shown in Figure 5 and 6. The initial projectile position is again indicated by the small dot. The view is seen from the base of the projectile. The center of these plots corresponds to the center of the surface of the photodiode detector but closely approximates the bore centerline. Figure 5 illustrates 3.30 msec of the in-bore period and Figure 6, 3.50 msec of data. The times shown on these traces have been adjusted such that projectile ejection from the muzzle occurs at 4.50 msec. The failure to obtain a continuous signal for the duration of the in-bore period was probably due to obscuration of the laser beam. Theoretical interior ballistics calculations indicate that at 3.50 msec, the shell is about 35 inches from muzzle exit which corresponds to the portion of the barrel with the greatest wear as shown in Figure 3. The projectile velocity at this instant in time is approximately 2500 feet per second.

500 H00

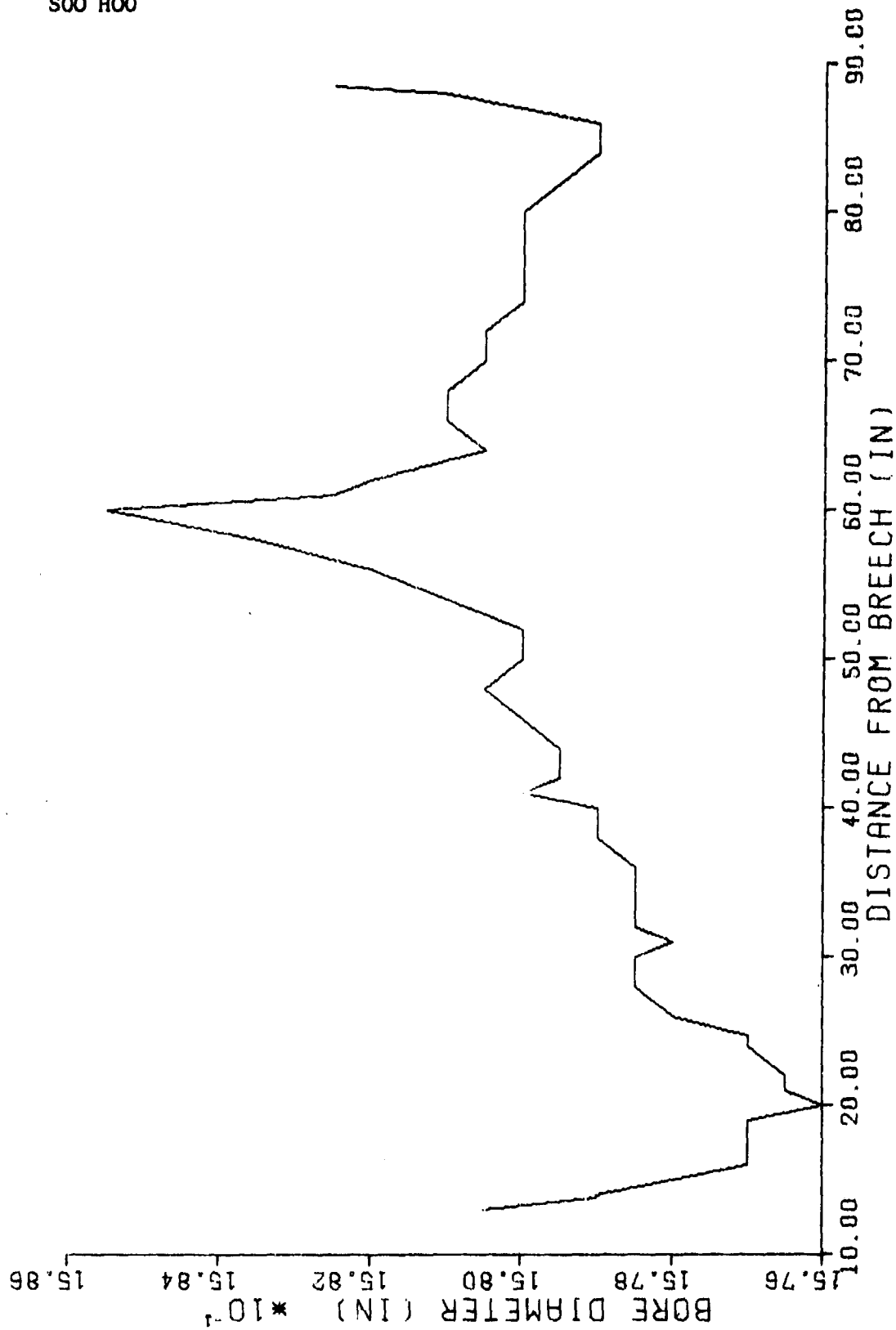


Figure 3. Star Gauge Data for 40mm MK A MOD 1 (SN32930)

S00 H00

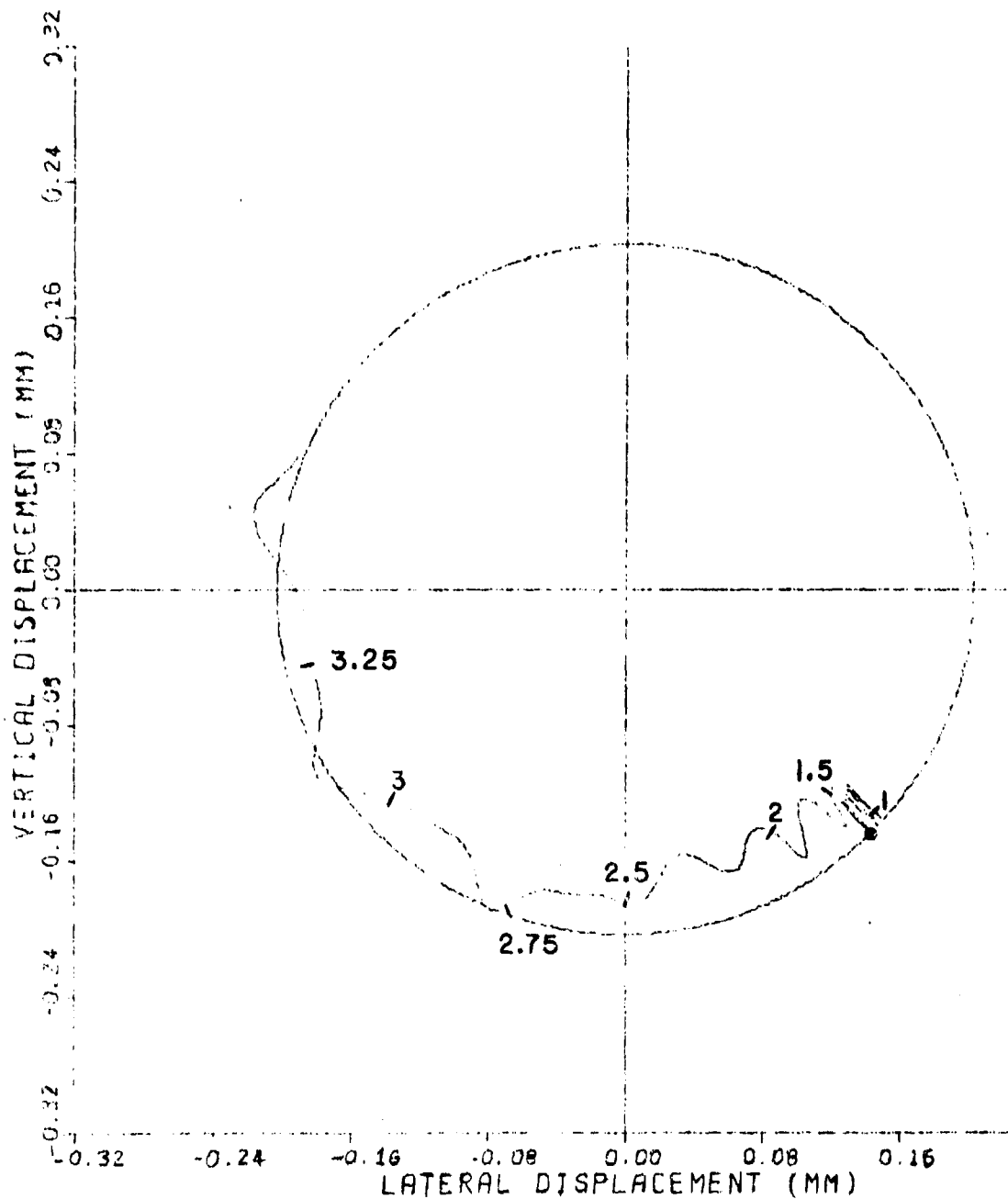


Figure 4. Transverse Motion of Bourrelet  
Case A40.00.31

S00 H00

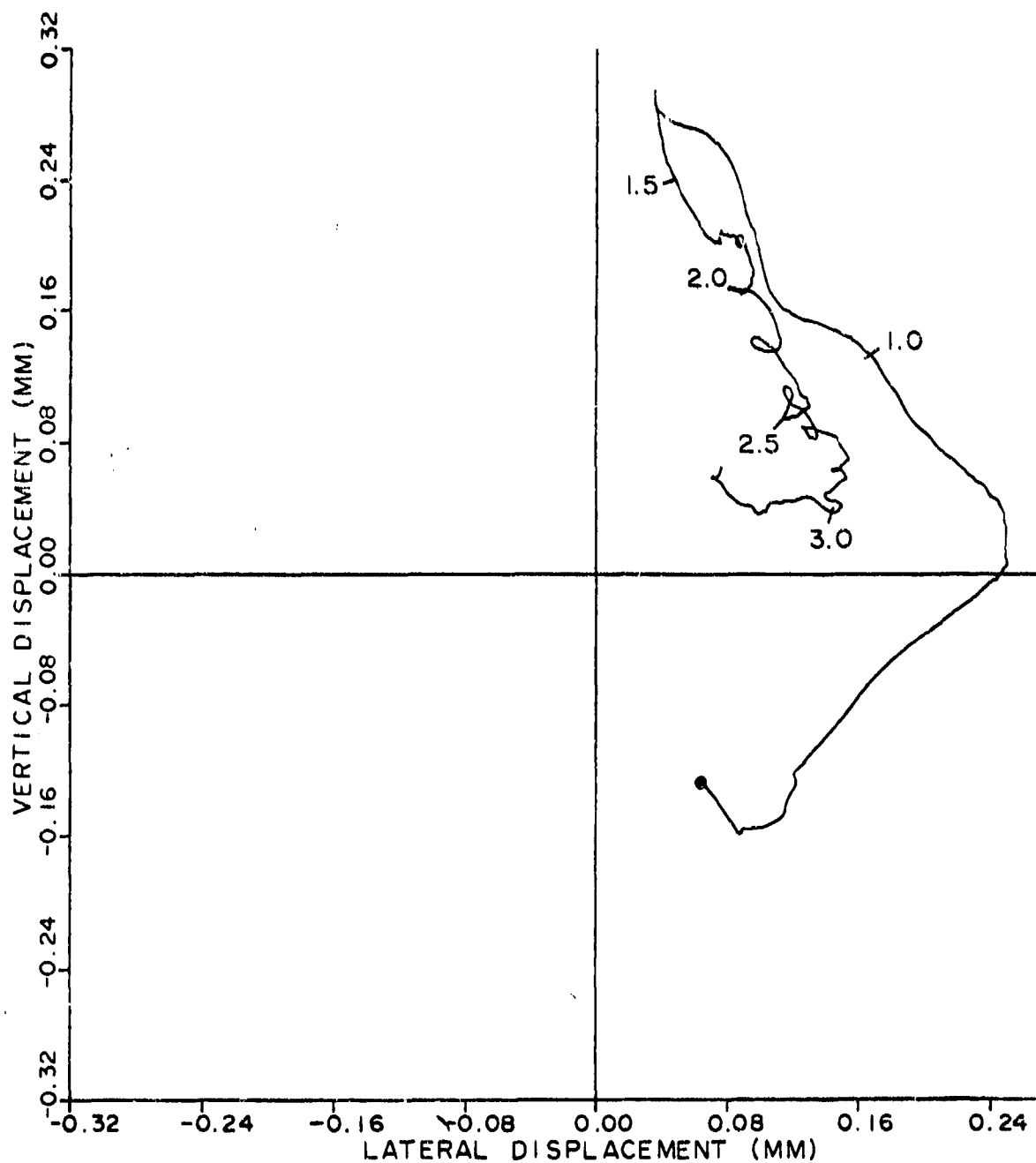


Figure 5. Transverse Motion of Bourrelet  
40mm Test C Round 3

S00 H00

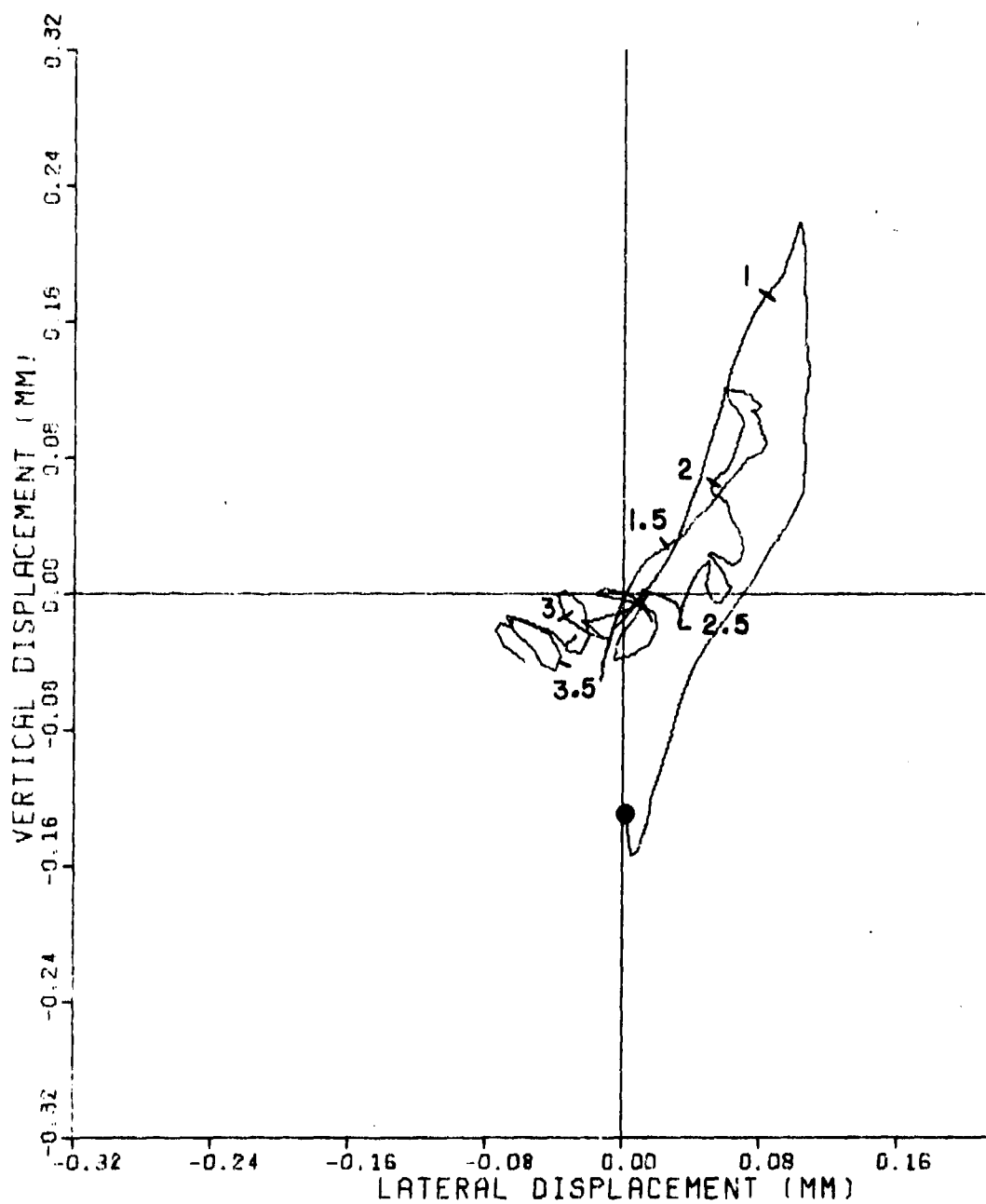


Figure 6. Transverse Motion of Bourrelet  
40mm Test C Round 6

The traces of Figures 5 and 6 show the projectile to initially proceed in a counterclockwise direction and eventually to move in a clockwise direction. This initial counterclockwise motion corresponds to about one to one and one half milliseconds of the inbore period. During this time, theoretical interior ballistics calculations predict the projectile to have traveled only one inch along the bore. The magnitudes of the projectile deflections are much larger than would be expected from the theoretical predictions. The balloting model therefore imposes too much constraint on the projectile motion during shot start to be able to simulate the test results. In the actual tests, the 40mm projectile and cartridge case were hand loaded with the rotating band barely reaching the origin of rifling. No effort was made to seat the projectile in the gun tube. The initial bourrelet motion seen in these experimental traces probably occurs before the rotating band becomes fully engraved, and in effect shows the projectile righting itself in the gun bore. The clockwise motion predicted by the theoretical model occurs after the rotating band is fully engraved.

#### MODIFICATION OF BALLOTING MODEL

The spring stiffnesses used in the balloting model assume the rotating band to be fully engraved at shot start. In order to account for the initial projectile motion witnessed experimentally, the model's constraints on the band have to be removed. The balloting code was modified to account for this situation by permitting the spring constants to increase linearly from zero to their full values over the first inch of projectile travel in the gun tube.

However, the removal of the rotating band constraint alone does not yield the large deflections seen in the first millisecond of the experimental traces. Mechanisms other than the pressure acting on the projectile base are probably responsible for these displacements. Several methods exist in the balloting code for producing such motions. The first is to regard the projectile to lie initially on the bore surface. Thus, any motion of the shell into the gun will yield the forces required to initiate the transverse motions. A second method is to introduce an unbalance into the round. Physically, this consideration provides a better correspondence to the actual situation since a dynamically balanced projectile represents an idealized case. For simplicity in the treatment of projectile unbalances, no products of inertia are introduced. The mass and moments of inertia obtained for a symmetrical shell are utilized in the balloting code. Only the location of the center of gravity is offset from the projectile axis. A third means of introducing motion is to view the rotating band as being engraved eccentrically in the bore. Basically, the treatment of this case is similar to that of an unbalanced round. In this situation, the entire projectile axis is displaced a given amount. Similar results are provided by the balloting code for both a projectile unbalance and an eccentrically engraved round.



S00 H00

Figure 7 shows the theoretical projectile motion for a linearly increasing rotating band model with the shell initially in contact with the gun tube. Large deflections are obtained early during launch, but due to the nature of the spring deflection model for bourrelet contact, the projectile rebound is directed towards the axis of the barrel. The forces resulting from this initial projectile contact also have a pronounced influence upon the subsequent motion producing much larger amplitudes than those predicted by the unmodified model.

The theoretical projectile motion illustrated in Figure 8 considers an additional program change that eliminates the torsional spring of the rotating band model over the first inch of projectile travel. A center of gravity offset of 0.020 inch is also included. The plot shows a more defined counterclockwise motion that is illustrative of the experimentally determined motions. Again the magnitudes of the motion following the engagement of the rotating band are affected.

#### CONCLUSIONS

The major obstacle towards the simulation of the experimental projectile motion is the modeling of the rotating band engraving process. While the modification of the computer code is capable of yielding the magnitudes of the displacements witnessed experimentally during shot start, large forces are also introduced which have a significant bearing upon the subsequent projectile motion. Since no control was exercised, during the tests, over factors such as the initial projectile orientation within the gun tube, the degree of the projectile unbalance, or the eccentricity of the rotating band engraving, the effects of these parameters are also imposed upon the experimental results shown in Figures 5 and 6. Although the barrel muzzle was constrained to help reduce as much transverse motion as possible, the barrel effects upon the recorded projectile motion are not entirely known since no attempt was made to measure the barrel deflection or vibration during launch. The experimental traces do indicate that there may be some gun jump superimposed upon the projectile motion. For instance, the displacements appear to have shifted upwards such that they do not return to the lower extremes established initially by the projectile.

The limited amount of experimental data hinders any attempts at an extensive correlation with the theoretical predictions. The obturation problem needs to be overcome if data out until muzzle ejection are to be obtained. If the problem is due to barrel wear, a new barrel may be part of the solution.

An exact determination of the spring stiffnesses utilized by the balloting code is also required. The values used in the 40mm theoretical calculations were scaled from those obtained experimentally for a 76mm projectile. The computed results, however, showed similar appearing results when the stiffnesses were varied from one half to twice the scaled values.

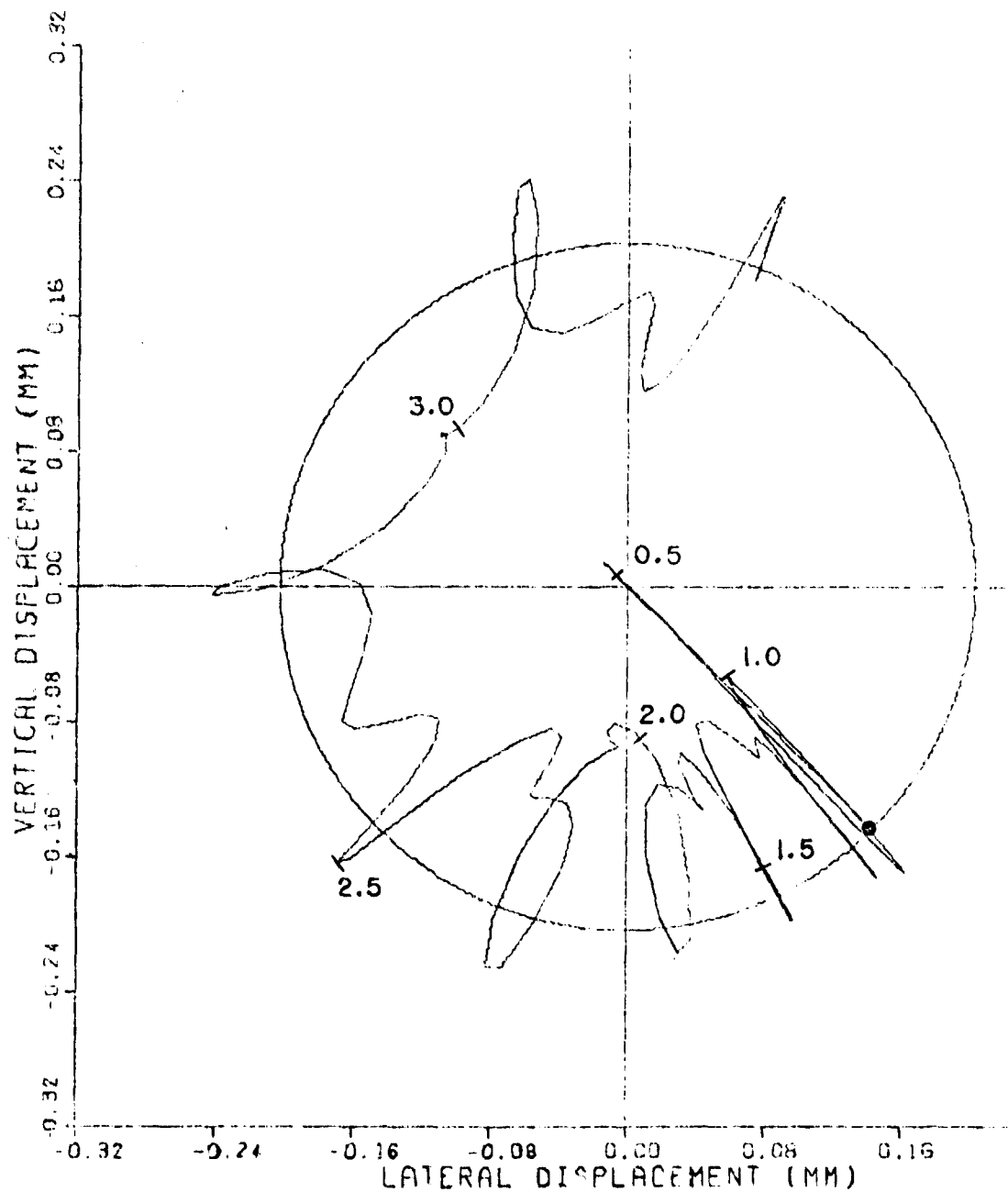


Figure 7. Transverse Motion of Bourrelet  
Case A40.00.62

S00 H00

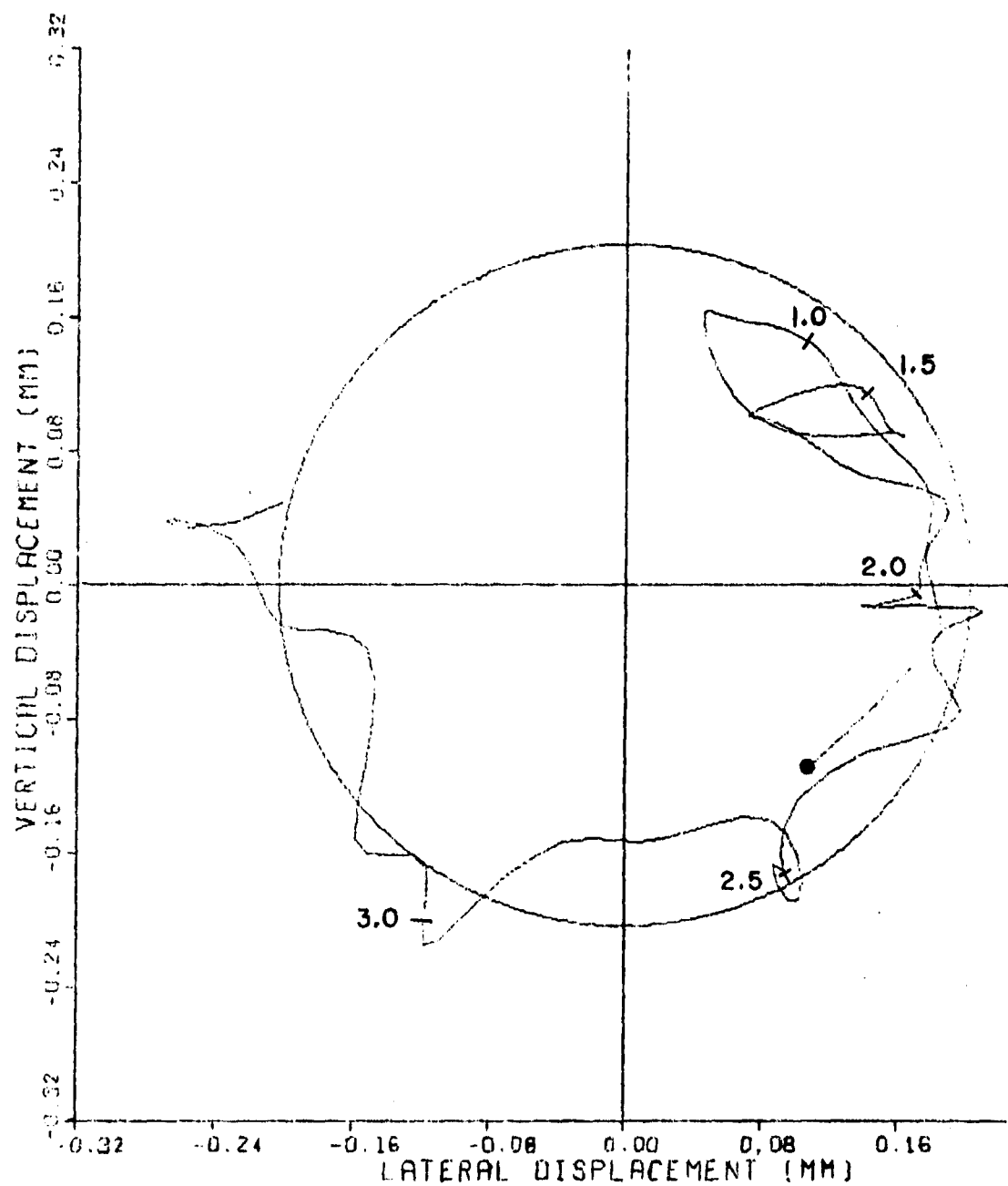


Figure 8. Transverse Motion of Bourrelet  
Case A40.00.58

SOO HOO

While the balloting code fails to account for all the aspects of the actual test situation, the model is useful for analyzing and interpreting the projectile's behavior. If the projectile is considered to run free in the gun tube over the first inch of travel, the removal of the rotating band constraints shows that the large displacements and general counterclockwise motion witnessed experimentally may be attributed to a combination of influences from factors such as the initial projectile orientation, the degree and position of a projectile unbalance, and the eccentric engraving of the rotating band. Once the band is considered fully engraved, the experimental motions start to conform with the predicted results of the original unmodified balloting model, i.e., the projectile does move in a clockwise direction following closely to the bore surface. This is best illustrated in the experimental record of Figure 6. While it is impossible to distinguish a definite balloting motion in the trace (due to the amplitudes of the noise and vibration being on the order of the predicted balloting motions), the trends in the data prove favorable. In addition, the magnitudes of the measured deflections lie within the limits established by the bourrelet and gun bore clearances.

#### REFERENCES

1. Soo Hoo, G., "A Theoretical Model for In-bore Projectile Balloting/Barrel Motion" published in the *Proceedings, First Conference on Dynamics of Precision Gun Weapons*, R-TR-77-008, U.S. Army Armament Research and Development Command, Dover, New Jersey, January 1977.
2. Haug, B. T., "Optical Device for Determining Small Angular Motion" published in the *Proceedings, First Conference on Dynamics of Precision Gun Weapons*, R-TR-77-008, U.S. Army Armament Research and Development Command, Dover, New Jersey, January 1977.

LEVIN

TITLE: Accuracy Improvement of Flexible Gun Tubes--  
A Kalman Filter Approach  
VICTOR LEVIN  
Innovative Technology, Inc.  
Columbus, Ohio 43221

ABSTRACT:

The purpose of this study was to investigate the means for improving the accuracy of a flexible gun tube by controlling its time-to-fire. The emphasis was placed on estimation and prediction techniques that would be incorporated into a time-to-fire algorithm.

The analysis was based on the use of optimal linear filtering theory. In particular, the extension of the Kalman-Bucy filter developed by Bryson and Johansen was utilized. This theory allows the inclusion of corrupting colored measurement noise and colored forcing noise. A black box approach employing a second-order system was taken toward the analytical description of the plant.

Computer-derived solutions of the steady-state estimation errors were obtained. The results give a strong indication that (1) an estimation filter based on a highly simplified black box model may be completely satisfactory and (2) direct measurements of only muzzle displacement and/or slope is sufficient and that the improvement attained by the addition of muzzle acceleration measurements is not significant.

A straightforward time-to-fire algorithm and its analog component implementation was shown. It is expected that the cost of this special purpose analog computer would be less than several hundred dollars.

BIOGRAPHY:

PRESENT ASSIGNMENT: Vice President, Innovative Technology, Inc.

PAST EXPERIENCE: Aerodynamics Engineer, Arnold Research Organization, Tullahoma, Tennessee, 1952-1953; Aerodynamics Engineer, North American Aviation, Columbus, Ohio, 1954-1956; Consultant, Bell Aircraft, Buffalo, 1957; Senior Technical Specialist, Rockwell International, Columbus, Ohio, 1958-1969; Principal Engineer, Battelle Columbus Laboratories, Columbus, Ohio, 1969-1976; Vice President, Innovative Technology, Inc., Columbus, Ohio, 1976 to present.

DEGREES HELD: Bachelor of Science, The Ohio State University, Columbus, Ohio, 1950; Master of Science, The Ohio State University, Columbus, Ohio, 1952.

ACCURACY IMPROVEMENT OF FLEXIBLE GUN TUBES--  
A KALMAN FILTER APPROACH

VICTOR LEVIN, VICE PRESIDENT  
INNOVATIVE TECHNOLOGY, INC.  
COLUMBUS, OHIO 43221

INTRODUCTION AND BACKGROUND

The ability to fire-on-the-move while retaining a high single-shot hit probability is becoming an increasingly desirable attribute for all classes of armored fighting vehicles (AFVs). In addition, AFVs employing relatively high rate-of-fire automatic cannons are certain to make their appearance in the 1980s. To obtain good effectiveness it is important that, after the first shot in a burst, each succeeding round is not influenced by the previous one. Vehicle movement will certainly increase the possibility of unwanted coupling from round to round. Thus both characteristics, fire-on-the-move and burst fire, will force the system designer to address and solve the problem of gun tube vibration and its adverse effect on accuracy.

There are three general methods that could be applied for reducing the inaccuracies resulting from gun tube vibration:\* stiffen the barrel, establish projectile exit conditions by applying external lateral forces at the muzzle during the appropriate time span, and selection of the instant for primer ignition such that the vibrating muzzle will pass through an optimum condition as the projectile exits. The first method implies additional weight, whereas, the second method implies both additional weight and mechanical complexity. Certain aspects of the third method, which will be denoted hereafter as time-to-fire control, are the subject of this report. A more detailed discussion is given in Reference 1.

\* It is tacitly assumed that although the structure may already be optimized by advanced analysis techniques such as those found in Reference 2, the flexural response in many situations will exceed the bounds imposed by the requirement for a high single-shot hit probability.

LEVIN

Time-to-fire control can be characterized as a type of open loop control of a discrete event, thus closed loop analyses do not apply. In other words the phenomenon of interest, the state of the muzzle during projectile exit, is not being measured for the purpose of feeding information back to a controller and closing a loop. Instead the process is one of predicting the future and then choosing an instant in time for initiating an uncontrolled (but, hopefully quite predictable) series of events that will yield the desirable results. An accurate prediction of the muzzle's state at a particular instant in the future, which is the ultimate goal, must be based on an estimate of the present and/or past that, in turn, is derived from processing transducer measurement data. Thus, the overall time-to-fire problem can be divided into four categories: measurement, estimation, prediction, and computation. In the present study the major effort has been placed on understanding and developing particular estimation and prediction procedures that will allow tradeoffs to be made with the requirements for measurement and computation.

In view of the rapid advancing state of computer and transducer technology, it would seem particularly suitable to investigate the merits of time-to-fire control. This is especially true of computational power which has been advancing at an exponential rate for more than 20 years. Considerations of the effect on total system design should also be made. The possibility of achieving high aim-point accuracy without adding, and conceivably significantly reducing gun tube weight is certainly important to net AFV performance and cost. In fact, if a true systems engineering approach were applied, the gun and time-to-fire control apparatus should be seen as subsystems whose design parameters are subservient to the goal of high total system performance of the AFV. Thus for example, the flexural transverse response of the gun tube to disturbances may be large compared to the presently accepted standards. Accuracy is improved, however, since the flexural properties are well matched to the prediction capabilities of the time-to-fire controller.

For the sake of convenience the term "time-to-fire algorithm" will denote any consistent set of estimation and prediction procedures. There are two critical decisions that must be made before a suitable algorithm is developed: the type of mathematical model to be used in describing the physical system (some times referred to as the "plant") and the technique to be employed for fitting noisy transducer data. Let the mathematical model be considered first. Two apparently quite diverse approaches can be taken. A more or less detailed model of the plant is employed in one approach. The components of the model could include such factors as the flexible properties of the gun tube and the dynamic properties of the fire control system's servomechanisms and the hull's suspension system. A number of transducers on the gun and the hull might be required in order to satisfy the inputs demanded by the model. At the other extreme is the second approach. It takes a "black box" viewpoint of the muzzle's behavior, i.e., the model is

## LEVIN

simplistic and contains parameters that must be obtained from tests. The number of real-time measurements and the degree of real-time computation is kept to a minimum. In the limit the difference between the two approaches is not significant. Thus, an algorithm based on either a simplified physical model or a complex black box are similar with regard to their measurement and computational requirements.

The black box approach to the time-to-fire algorithm was the one that was chosen for the present effort. This choice was made for two reasons. First the possibility exists that satisfactory estimation and prediction techniques will be relatively simple and, therefore, low cost to implement. More complexity can be added if necessary. Second, since the black box parameters are based directly on test results, each individual gun and vehicle combination could conceivably utilize a separate set of test-derived parameter values. These test values could be updated periodically, even by measurements in the field, to account for changes due to aging or purposeful modifications.

As mentioned above, the second critical decision concerning the time-to-fire algorithm is the choice of a technique for fitting noisy transducer data. The measurement data must be fit to an implied or explicit model of the system that is indicative, for at least a short period of time, of the behavior of particular state variables. The time period must be of sufficient length to (a) allow some of the state variables to be estimated by performing a "best" fit to noisy historical data and (b) yield an adequate prediction of the future. In practice some type of quadratic cost function such as one associated with a least squares technique is the criterion typically utilized for fitting noisy data to the model.

In general terms, fitting of noisy historical data to a system model by application of a cost function can be thought of as a regression method. The particular methodology that will be described and then used in the remainder of this report is based on an outgrowth of Kalman and Bucy's (references 3 and 4) original development of optimal linear filtering and prediction. The reasons for choosing the Kalman filter alternative as opposed to more conventional regression methods will be discussed briefly.

Conventional regression can be divided into the two broad categories of linear and nonlinear regression. Nonlinear regression requires the use of an iterative estimation technique such as steepest descent or dynamic programming in order to realize a solution. This usually implies considerable computational time and computer memory. Linear regression methods, in general will impose a significantly reduced computational burden. In most instances, however, some historical data must be retained and the inversion of a sizeable matrix is necessary. Real-time computational speed, therefore, may be incompatible with the capabilities of a low-cost computer.



The Kalman filter exhibits certain disadvantages as well as advantages with respect to the standard linear and nonlinear regression formulations. The plant must be modeled with a set of linear differential equations. The derivation of the filter (i.e., the estimate) equations can be tedious and time consuming. The time-dependent filter requires the solution of an associated set of nonlinear differential equations in order to obtain the filter gains. In many instances, however, the steady-state filter is completely adequate; but even then a closed form solution for the constant filter gains is rarely feasible. Thus computer derivation of the filter gains is usually necessary. In addition, some knowledge of the noise statistics associated with the physical plant and the measurement transducers are needed. It is also possible that the filter will diverge rather than converge on a valid estimation of the plant's state vector. This can occur when the data is very noisy, but in a comparable situation the regression type of data fit will typically yield completely erroneous results. The advantages associated with the utilization of a Kalman filter are given in Table 1.

TABLE 1. ADVANTAGES OF THE KALMAN FILTER

- Historical data are automatically factored into the most recent state vector estimate.
- The operating filter (in contrast with the derivation process) does not require matrix inversion.
- For a linear plant the Kalman filter is the best estimate possible when a quadratic cost function is used.
- Analog as well as digital filters are feasible.
- Physical significance can be attached to the individual filter gains.
- From a computational viewpoint the filter will often be quite straightforward (even though its derivation may be rather laborious).
- For many situations the steady-state filter yields highly satisfactory results. Employing the steady-state filter simplifies the real-time computations considerably.
- The estimate will usually degrade gracefully with increasing system noise.
- Prediction is obtained by multiplying the latest estimate by a constant if the system plant is represented as a lumped parameter set of linear differential equations.

TECHNICAL DISCUSSIONLinear Filter Containing Colored Noise

Optimal linear filtering theory assumes that the plant can be described by a set of linear differential equations in which time is the independent variable, i.e.,  $\dot{x} = Fx$ . In the equation  $x$  denotes an  $n$  vector of the plant's state variables and  $F$  is an  $n \times n$  matrix of known functions that describe the plant.  $F$  can be a function of time. Basic to the analysis is the additional assumption that the plant is forced by noise and that measurements are corrupted by noise. Figure 1 shows a generalized schematic of the total system model. The original

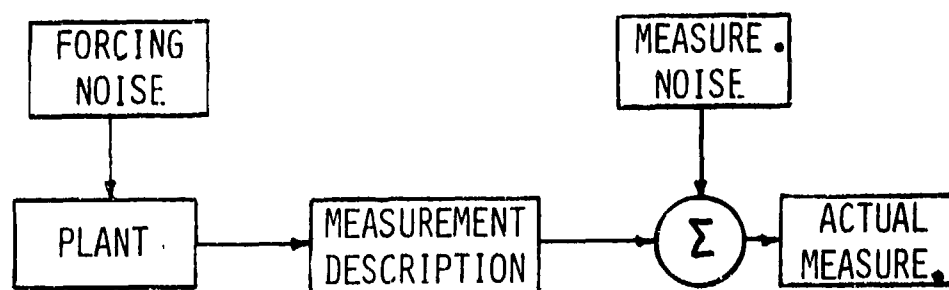


FIGURE 1. SCHEMATIC OF SYSTEM MODEL ASSUMED BY KALMAN FILTER

developments by Kalman and Bucy would only allow white noise in the measurements and the forcing function. Although the results are extremely useful conceptual difficulties arise when only white noise is allowed since such noise sources cannot exist in real life (infinite noise power would be required). Most of the implementations of the Kalman filter have involved digital computers that utilize the discrete form of the equations. By sampling a white noise source many of the continuous system conceptual problems are obviated. It was felt, however, that at this stage of the analysis of the vibrating gun tube problem it is well to remain in the continuous realm where physical intuition can help lead the way. Because of these considerations it was decided to utilize the extension to the Kalman filter that was developed by Bryson and Johansen (Ref. 5) and which is applicable to a continuous system with measurements corrupted by colored noise. Although the Bryson-Johansen theory still assumes that the plant, i.e., the matrix  $F$  mentioned above, is forced with white noise, the plant can be extended into a pseudo plant which contains an analog filter. The analog filter is then forced by white noise and its output, in turn, then forces the "true" plant.

The general format of the matrix differential and algebraic equations are given below. The assumption is made that the colored

LEVIN

noise corrupting the measurements is the result of passing white noise through a first-order analog filter. The symbols are explained in Appendix A.

Format of Matrix Equations Describing Plant, Measurements,  
Estimation Error, Estimate, and Prediction

Plant (i.e., the physical process being modeled):

$$\dot{\mathbf{x}} = \mathbf{F}\mathbf{x} + \mathbf{u} \quad (1)$$

where

$$\mathbf{E} [\mathbf{u}(t)\mathbf{u}^T(\tau)] = \mathbf{Q}_p(t)\delta(t-\tau) \quad (2)$$

Measurements:

$$\mathbf{y} = \mathbf{C}\mathbf{x} - \mathbf{m} \quad (3)$$

where

$$\dot{\mathbf{m}} = -\mathbf{B}\mathbf{m} + \mathbf{B}\mathbf{v} \quad (4)$$

$$\mathbf{E} [\mathbf{v}(t)\mathbf{v}^T(\tau)] = \mathbf{Q}_m(t)\delta(t-\tau) \quad (5)$$

Covariance of the estimation error for  $\mathbf{x}$ :

$$\dot{\mathbf{P}} = \mathbf{F}\mathbf{P} + \mathbf{P}\mathbf{F}^T - \mathbf{Q}_p - (\mathbf{P}\mathbf{H}^T + \mathbf{Q}_p\mathbf{C}^T)\mathbf{R}^{-1}(\mathbf{C}\mathbf{Q}_p + \mathbf{H}\mathbf{P}) \quad (6)$$

where

$$\mathbf{R} = \mathbf{C}\mathbf{Q}_p\mathbf{C}^T + \mathbf{B}\mathbf{Q}_m\mathbf{B}^T \quad (7)$$

$$\mathbf{H} = \dot{\mathbf{C}} + \mathbf{C}\mathbf{F} - \mathbf{B}\mathbf{C} \quad (8)$$

Filter for obtaining the estimate of  $\mathbf{x}$ :

$$\dot{\mathbf{x}}^* = \mathbf{F}\mathbf{x} - \mathbf{K}(\mathbf{B}\mathbf{y} + \mathbf{H}\mathbf{x}) - \dot{\mathbf{K}}\mathbf{y} \quad (9)$$

$$\hat{\mathbf{x}} = \mathbf{x}^* + \mathbf{K}\mathbf{y} \quad (10)$$

where

$$\mathbf{K} = (\mathbf{P}\mathbf{H}^T - \mathbf{Q}_p\mathbf{C}^T)\mathbf{R}^{-1} \quad (11)$$

Prediction of  $\mathbf{x}$  at time  $t + \Delta t$  when the last estimate is made at  $t$ :

$$\hat{\mathbf{x}}(t + \Delta t) = \mathbf{S}(t, t + \Delta t)\hat{\mathbf{x}}(t) \quad (12)$$

## LEVIN

All of the noise process are assumed to be uncorrelated with each other. In particular, this infers the following relations:

$$E [u(t)v^T(\tau)] = 0$$

$$E [m(t)x^T(\tau)] = 0$$

$$E [m_i(t)m_j^T(\tau)] = 0 \text{ for } i \neq j \text{ where } v_i \text{ and } v_j \text{ are two separate components of the measurement noise vector}$$

The above equations are fairly general since all of the terms except B can be arbitrary (but well behaved) functions of time. The major restrictions are the linearity of the plant equations, the coloring of white measurement noise by a first-order analog filter, and the requirement that the various noise processes be uncorrelated.

### Plant Model

A black box approach has been suggested as the means for establishing the analytical form of the plant model. In practice this means that special tests would be performed on a given vehicle gun combination type in order to determine the specific format of the black box dynamic equations for that combination. In addition the stochastic properties of the transducers involved in the real-time estimation procedure should be determined from tests or manufacturer's specifications. This complete set of information would then allow derivation of one or more Kalman filters of varying complexity. The simplest filter that could be utilized satisfactorily in conjunction with a time-to-fire algorithm would then be used. The general properties of the Kalman filter as applied to a vibrating gun tube, however, can be investigated without special test information as long as a rational plant model can be deduced that bears some relationship with reality. Fortunately, a limited amount of test data were found\* that can be used to establish a plant model and which will allow the analysis to be continued. The data pertains to the Rarden gun that was fired both on a hard mount and a Sheridan tank chassis. Measurements were made of the vertical and horizontal muzzle motion during single round and burst firings and with various settings of the vertical and horizontal damping pads. A small portion of the results is shown in Figures 2 through 5.

From an overview perspective the Rarden gun data is encouraging for several reasons. The hard-mount data indicates the presence of a strong single frequency component at any given instant even though the frequency may change somewhat during the first few cycles after a round is fired. Vertical muzzle motion when the gun is mounted on a tank

---

\* These data were obtained informally from A. Baran of the Ballistics Research Lab in Aberdeen, Maryland.

LEVIN

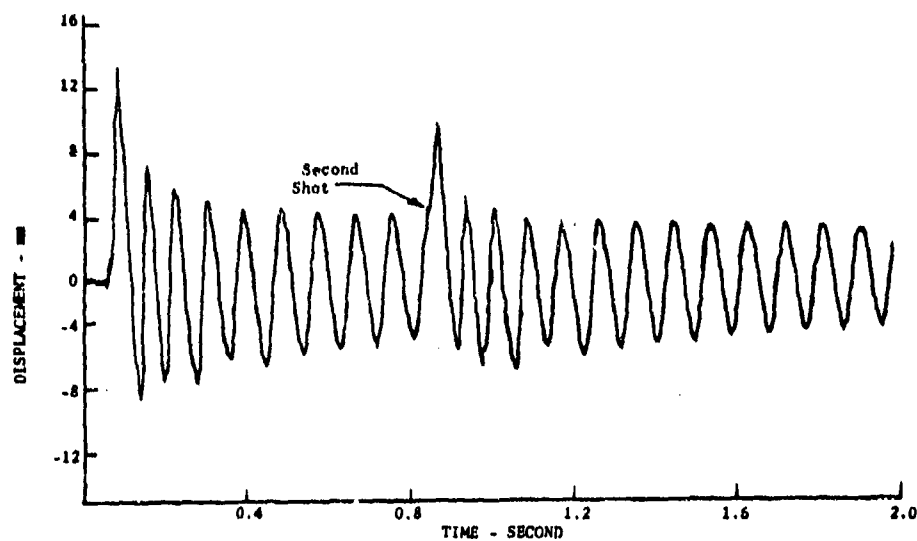


FIGURE 2. RARDEN GUN TEST DATA -- HARD MOUNT, VERTICAL MUZZLE MOTION, TWO-SHOT BURST

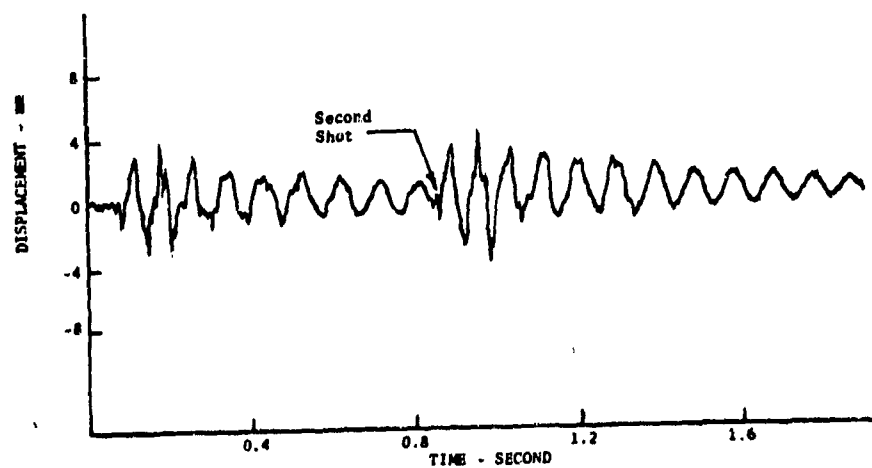


FIGURE 3. RARDEN GUN TEST DATA -- HARD MOUNT, HORIZONTAL MUZZLE MOTION, TWO-SHOT BURST

LEVIN

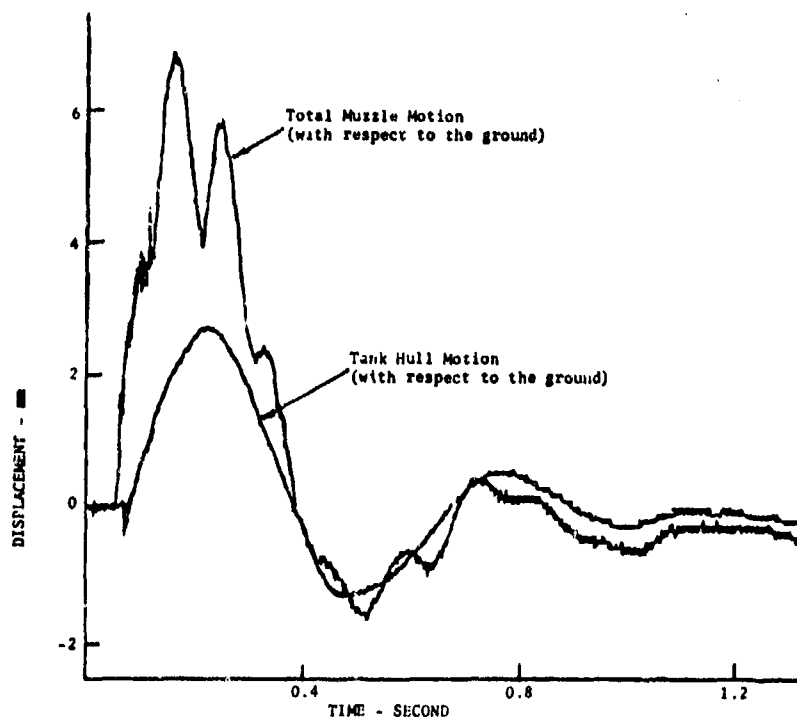


FIGURE 4. RARDEN GUN TEST DATA -- SHERIDAN TANK MOUNT, VERTICAL PLANE MOTION OF MUZZLE AND HULL, SINGLE SHOT

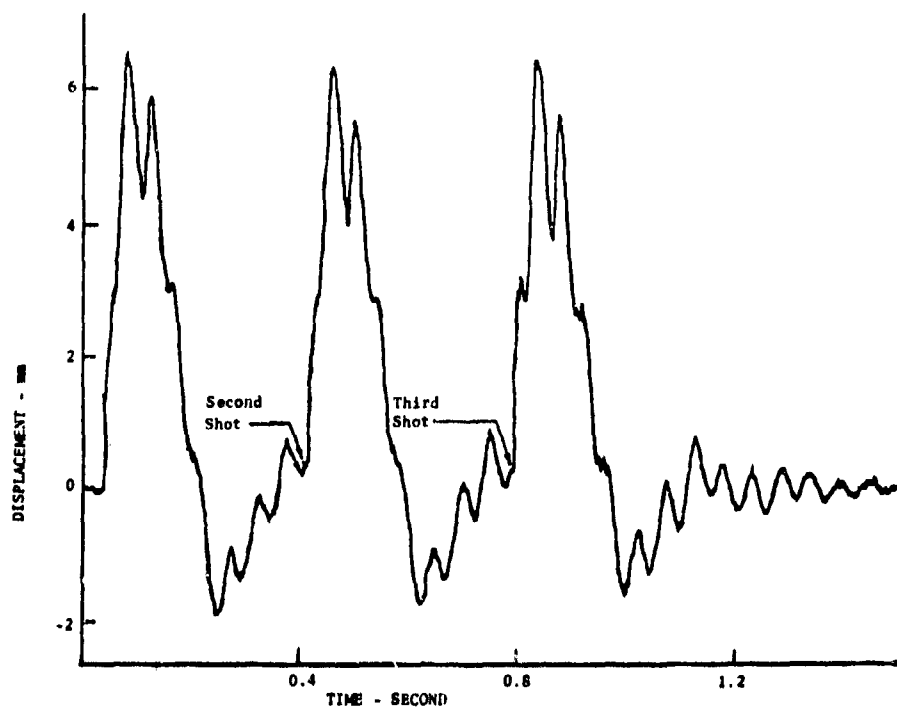


FIGURE 5. RARDEN GUN TEST DATA -- SHERIDAN TANK MOUNT, VERTICAL MUZZLE MOTION, THREE-SHOT BURST

## LEVIN

chassis is highly repeatable throughout a burst and definitely not complex. Horizontal motion is not quite as repeatable but is still well behaved. Part of the reason for the more erratic behavior in the horizontal plane is that the motion of the ammunition feed mechanism is primarily in this plane.

A broad generalization of the test data is probably invalid for several reasons. First the Rarden gun has unusual design characteristics such as the utilization of damping pads whose purpose is to reduce round-to-round dispersion. Interesting, however, is the fact that even though the damping pads introduce a strong non-linearity into the system's dynamics the response to an impulse-type input appears to be linear. In other words, from a black box point of view this highly complex nonlinear system can be treated as a simple linear system. Another criticism is that for the tank-mounted firings a direct measurement was not made of the quantity of interest to the present analysis. This quantity is the displacement of the muzzle with respect to the "rigid part" of the gun near the trunions. It is the motion of the muzzle relative to this rigid part that is of direct concern. The tacit assumption is made throughout the study that the vehicle's fire control system can either adequately control or at least predict the orientation of the rigid part.

The black box model that is suggested by the Rarden gun test data and which will be employed in the remainder of the analysis is as follows: the motion of the muzzle (in both the horizontal and vertical planes) relative to the rigid part at the trunions can be described as a second-order lumped parameter system, i.e., mass-spring dashpot.\* The parameters of interest in this model are the natural frequency,  $\omega_p$ , and the damping coefficient,  $\zeta$ .

Basing the time-to-fire algorithm on parameters derived from a second-order system black box model is not as restrictive or idealistic as it first appears. This is because the parameters in the algorithm need only be constant for a short period of time--200 to 300 milliseconds is probably adequate. That is, if necessary, the values of the algorithm parameters could be established by a computer via a table look-up procedure. Entry to the table would be a function of the output of various transducers, whose output implies the most appropriate set of  $\omega_p$  and  $\zeta$ . These transducers are not necessarily special purpose but are likely to be already incorporated into the standard fire control system. Thus, the linearity of the gun tube vibrations implied by the black box need only be thought of as a local linearity that is approximately correct for conditions over a short period of time.

---

\* The differential equation describing the second order system is:

$$\ddot{\zeta} + 2 \zeta \omega_p \dot{\zeta} + \omega_p^2 \zeta = \text{acceleration forcing input}$$

where  $\zeta$  = muzzle displacement or slope with respect to its undisturbed value.

### Effect of Noise on Estimation and Prediction

Now that a particular black box model has been chosen it must become integrated into a total system model which is commensurate with the scheme shown in Figure 1. Three system models of varying complexity were given consideration, but only the one of medium complexity (see Figure 6) was studied in depth. It is noted that the model represents the motion in a single plane. Thus, in order to produce the desired firing signal the time-to-fire algorithm must combine the output of two simultaneous but separate filters associated with motion in two orthogonal planes.

Computer analyses were made of the rms estimation errors resulting from varying system parameters and the level of input forcing noise. As seen in Figure 6, three individual first-order analog filters are used to produce colored noise from separate white noise sources. The colored noise then corrupts the displacement and acceleration measurements and also serves as a forcing acceleration input. Forcing the black box's second order system with colored noise as opposed to white noise serves two purposes. First it is easier to relate the forcing input to real-world phenomena that either directly or indirectly result in muzzle oscillations. Second it allows acceleration measurements to be incorporated into the model since the measurement is now being made on a source whose power and bandwidth are both limited.

The detailed differential and algebraic equations for evaluating rms estimation errors (Ref. 1) are quite nonlinear and complicated and will not be shown. It is interesting and instructive, nevertheless, to see the specific matrix equations that describe the plant and measurements and the corresponding format of the steady-state filter. These equations are found in Appendix C.

The rms errors in estimating the muzzle's state that result when the steady-state filter is used were obtained by integrating the covariance matrix error equations until steady-state conditions were reached. These differential equations, which are often referred to as the Riccati equations, are quite nonlinear and lengthy and will not be shown here but can be found in Reference 1. Typical results pertaining to the rms state estimation errors are shown in Figures 7 - 12. The values of the relevant parameters, both for the system model of Figure 6 and the gun tube, are presented in Table 2. The figures are based on the assumption that the gun tube is a hollow, constant thickness, cantilevered tube whose response to sinusoidal forcing at the trunion has characteristics somewhere between those of a free-free and a clamped-free uniform beam. A highly simplified analysis was used to relate the rms colored forcing acceleration noise,  $\text{rms}(n)$ , to an equivalent muzzle displacement. In some of the figures a nondimensional forcing noise acceleration,  $N$ , is employed.



2

LEVIN

TABLE 2. PARAMETER VALUES FOR FIGURES 7 THROUGH 13

(In Figures 7 through 13, except where explicitly noted, the following system model (see Figure 2) and gun tube parameters have been assumed.)

---

White Noise Zero Frequency Spectral Densities

Forcing Acceleration =  $20,000 \text{ mm/sec}^3$   
Acceleration Measurement =  $1000 \text{ mm}^2/\text{sec}^3$   
Displacement Measurement =  $2 \text{ mm/sec}$

Bandwidth of Analog Coloring Filters

$\beta = B_1 = B_2 = 10 \text{ rad/sec}$

Derived RMS Values of Colored Noise

Forcing Acceleration =  $316 \text{ mm/sec}^2$   
Acceleration Measurement =  $70.7 \text{ mm/sec}^2$   
Displacement Measurement =  $3.16 \text{ mm}$

Properties of "Black Box" Second Order System

Natural Frequency =  $1.0 \text{ Hz}$   
Damping Coefficient =  $0.1$

Gun Tube Parameters

Modulus of Elasticity =  $2.07 \times 10^{11} \text{ Newton/m}^2$   
Material Density =  $7.78 \times 10^3 \text{ kg/m}^3$   
Outside Diameter =  $150 \text{ mm}$   
Inside Diameter =  $75 \text{ mm}$   
Length =  $78 \text{ Calibers}$   
RMS of Trunion Input Acceleration =  $0.35 \text{ g}$   
RMS of Muzzle Displacement =  $12 \text{ mm}$   
RMS of Muzzle Slope =  $2.8 \text{ mil}$

---

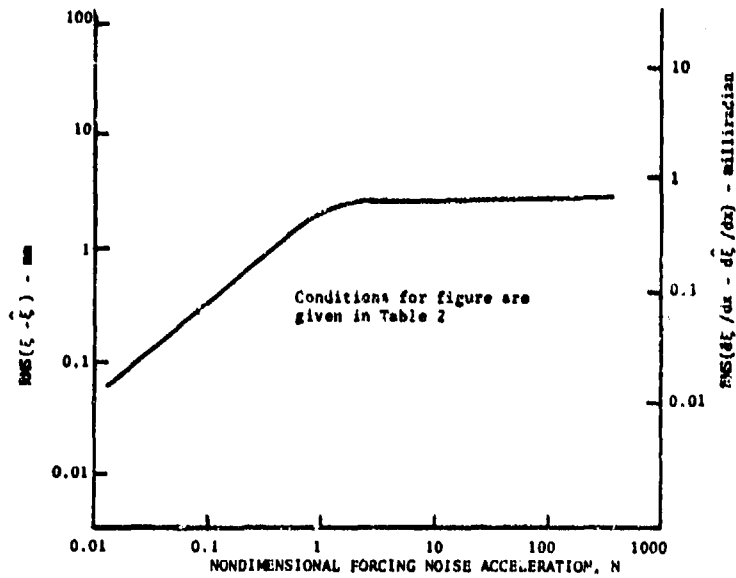


FIGURE 7. MUZZLE DISPLACEMENT AND SLOPE ESTIMATION ERRORS FOR FIRST MODE FREQUENCY OF 1 HZ AND VARYING FORCING NOISE ACCELERATION

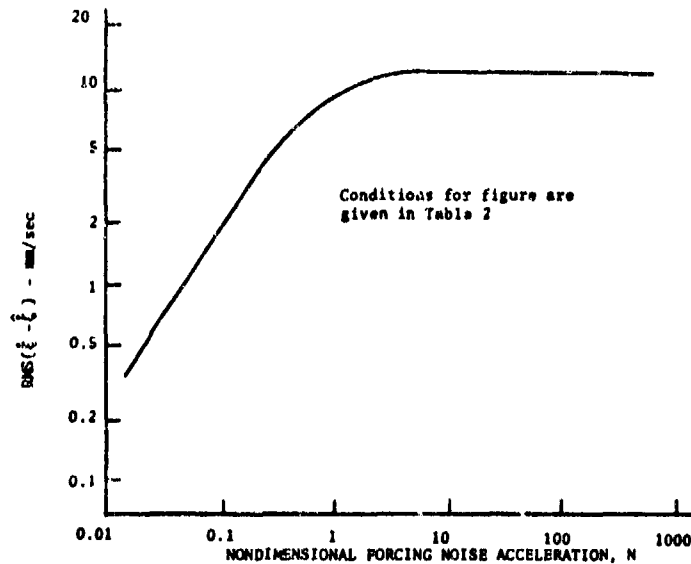


FIGURE 8. MUZZLE TRANSVERSE VELOCITY ESTIMATION ERROR FOR FIRST MODE FREQUENCY OF 1 HZ AND VARYING FORCING NOISE ACCELERATION

LEVIN

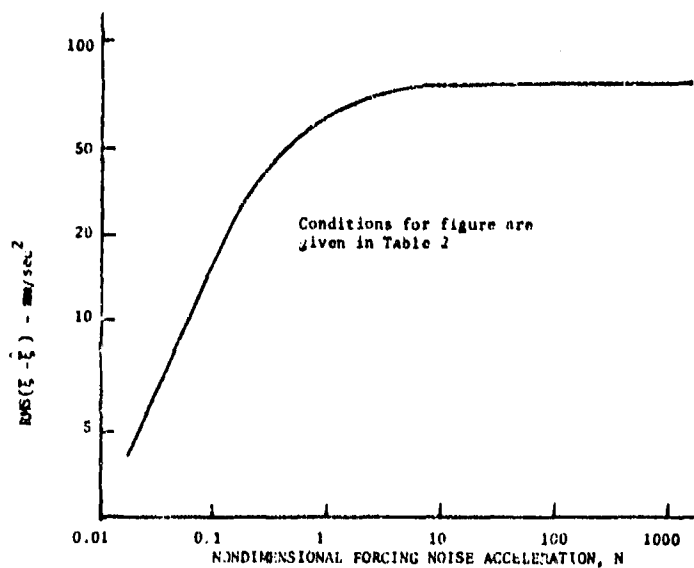


FIGURE 9. MISSILE TRANSVERSE ACCELERATION ESTIMATION ERROR FOR FIRST MODE FREQUENCY OF 1 HZ AND VARYING FORCING NOISE ACCELERATION

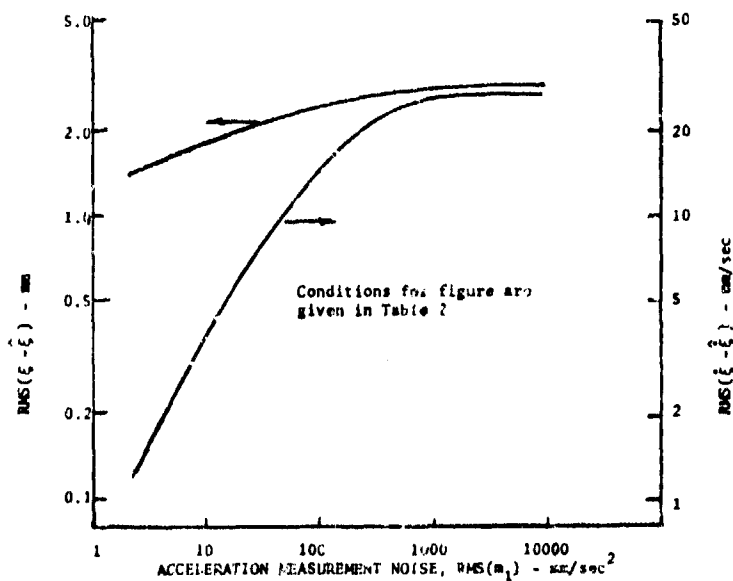


FIGURE 10. EFFECT OF VARYING ACCELERATION MEASUREMENT NOISE MAGNITUDE

LEVIN

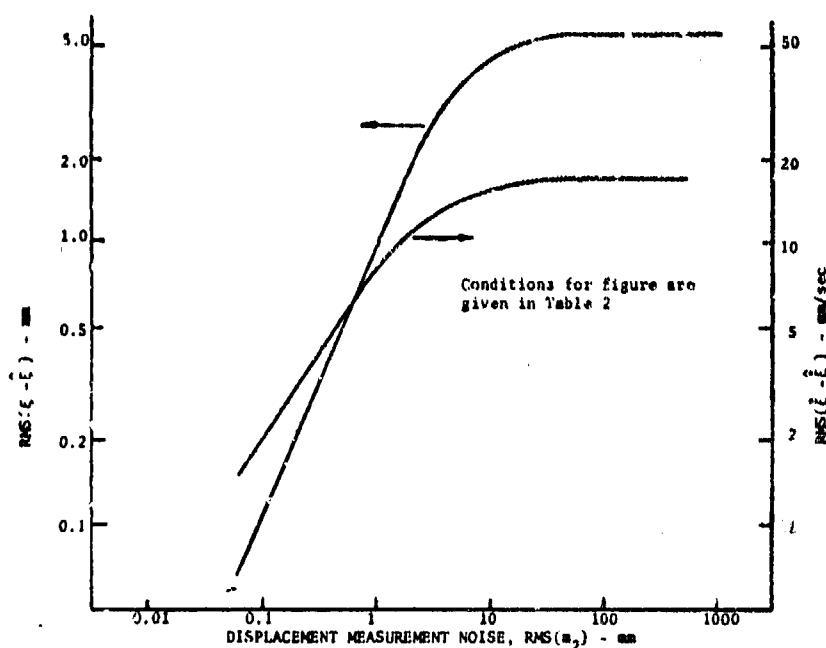


FIGURE 11. EFFECT OF VARYING DISPLACEMENT MEASUREMENT NOISE MAGNITUDE

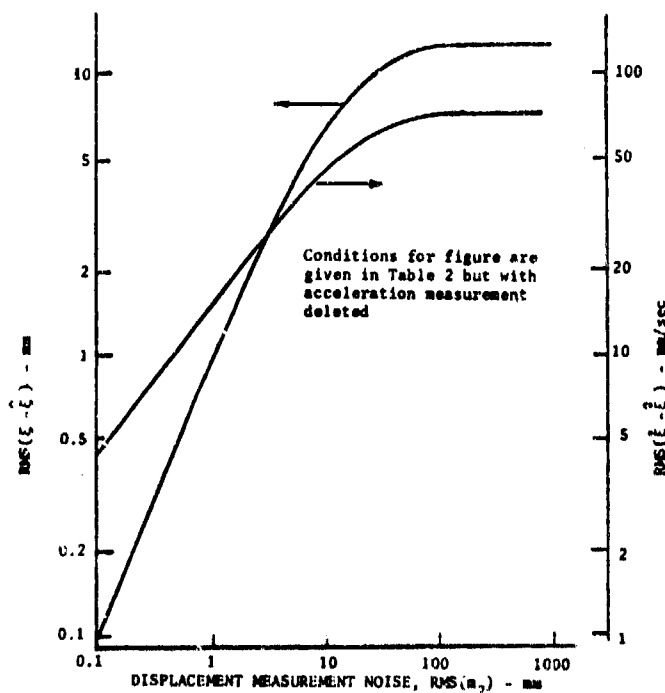


FIGURE 12. EFFECT OF VARYING DISPLACEMENT MEASUREMENT NOISE MAGNITUDE WITH ACCELERATION MEASUREMENT DELETED

## LEVIN

N is defined as the ratio of  $\text{rms}(n)$  to that value of  $\text{rms}(n)$  for which the rms value of the muzzle slope will be one milliradian, i.e., when  $N = 1$  then  $\text{rms}(d\xi/dx) = 0.001$  radian.

Most of the trends shown by the figures are not surprising. In Figures 7 - 9 it is seen that if N becomes quite small and the measurement errors remain constant then the error in the estimates of the muzzle's states also becomes small. In the limit as N goes to zero then the estimation error must also go to zero even though the measurements are noisy. As N becomes large it becomes possible for the filter to differentiate between the effects of a noisy forcing input and noisy measurements. After N reaches a particular magnitude the steady-state filter is indifferent to any further increase in forcing input noise power and the estimation errors remain essentially constant. It is to be emphasized, however, that these comments apply only to steady-state conditions. The price that is paid for accepting a large forcing input is the time required for the filter to reach steady state. It is appropriate to insert an important comment at this point. It is legitimate to consider the forcing input acceleration noise as the sum of two separate inputs. One is the true forcing noise at the trunion. The other is the modeling error, i.e., the deviation of the black box model from the "true" model. Thus a large value of N could, in certain situations, be attributed primarily to large modeling error.

Figures 10 through 12 show the effect of varying measurement noise while holding all other system parameters constant, including N. It is seen that the curves in these figures are similar in shape to those found in the previous figures. In other words, the errors in the estimates of the state variables decreases monotonically with decreasing measurement noise when the measurement noise is below a certain value. Above this value the estimation errors soon reach a plateau. This effect can be readily explained qualitatively. For small values of measurement noise the estimation filter cannot differentiate between the relatively large forcing noise and its own measurement noise so that the full value of the rms measurement noise remains in the filter's state estimates. As the measurement noise, as seen by the filter, approaches a certain magnitude relative to the effect produced by the forcing acceleration noise, the filter can separate the effects so that the steady-state error is essentially independent of further increases in measurement noise power. Again, it must be emphasized that only state-state errors are being considered.

LEVIN

Several additional comments concerning Figures 10 through 12 are warranted. First, as one would expect, acceleration measurement noise magnitude,  $\text{rms}(m_1)$ , has a much stronger effect on muzzle velocity error than it does on muzzle displacement error. In fact even for quite small values of acceleration noise, say  $\text{rms}(m_1) = 1 \text{ mm/sec}^2$ , the rms displacement error is still in the vicinity of 1 mm (see Figure 10). As seen in Figure 11 the situation is definitely improved when displacement measurement noise magnitude,  $\text{rms}(m_2)$ , is varied. For low values of  $\text{rms}(m_2)$  accurate estimates of both displacement and velocity are attained. In Figure 12 the conditions of Figure 11 are repeated except that the acceleration measurement has been deleted completely. Little difference is seen for small values of  $\text{rms}(m_2)$  in the state estimation errors. For large values of  $\text{rms}(m_2)$ , however, the lack of an acceleration measurement produces a noticeable degradation in the estimation errors.

Several other interesting results were found that are not illustrated in the figures. For example, it can be shown that varying the damping coefficient from 0.01 to 1.0 has almost no influence on the estimation errors. The bandwidth of the first-order white noise coloring filters has only a minor effect on the errors as long as the bandwidth is higher than the natural frequency ( $\omega_p$ ) of the second order system that represents the plant. Of considerable significance are the results obtained with a large forcing acceleration,  $N = 200$ . When the variable is  $\text{rms}(m_2)$  little difference is found in the estimation errors for low values of  $\text{rms}(m_2)$  with respect to the curves shown in Figures 11 and 12.

The major tentative conclusions to be drawn from the analysis of the state estimation errors are: (1) acceleration measurements are considerably less significant than displacement measurements and probably are unnecessary in a practical system, and (2) large modeling errors can be tolerated since the estimation errors for  $\text{rms}(m_2)$  less than about 1 mm are practically insensitive to large variations in  $N$ .

So far the discussion has dealt strictly with the error in estimating the state variables, whereas, the more direct concern is with the error in prediction. As indicated previously the prediction is obtained by multiplying the most recent estimate of the state vector by the state transition matrix. For the type of plant model being used the prediction is obtained by a set of linear algebraic equations in terms of the state variable estimates. Even though the prediction is quite straightforward, determination of the error associated with the prediction is a fairly cumbersome task. The difficulty was obviated by utilizing a simplified extrapolation equation for the prediction which, in turn, infers an easy to calculate formulation for the displacement prediction error. The extrapolation equation and the attendant prediction errors are shown in Figure 13 for prediction time intervals from zero to 40 milliseconds. It is seen in the figure that even for the largest time

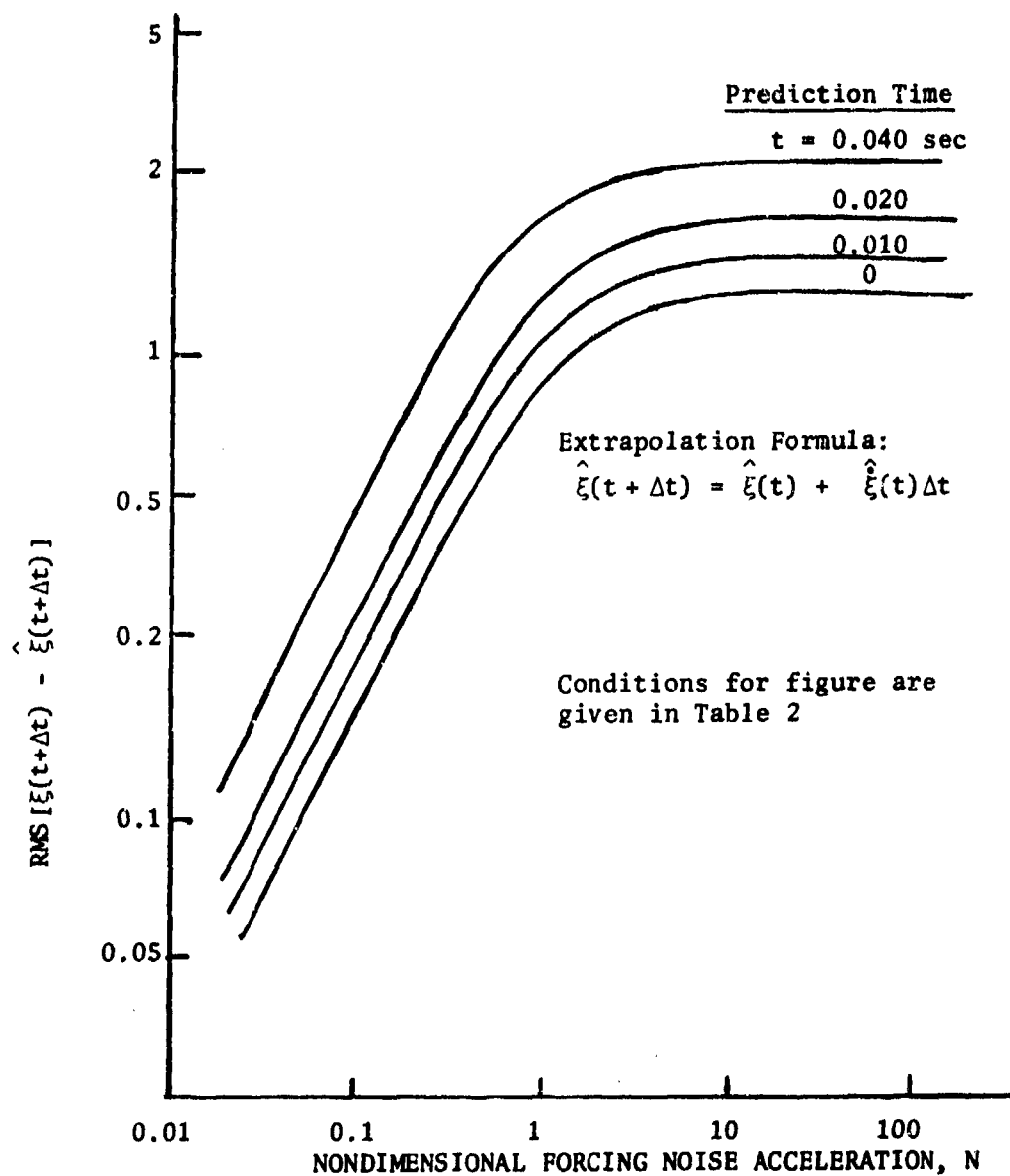


FIGURE 13. PREDICTION ERROR ASSOCIATED WITH LINEAR EXTRAPOLATION



LEVIN

interval shown the degradation of the displacement prediction with respect to the estimate is not very significant.

In practice the prediction formulation given by the theory would be used, so that the results given in the figure are actually pessimistic. On the other hand no attempt was made to take into account the motion of the muzzle due to the physical events that arise during the firing and projectile travel through the gun tube. From the limited amount of data seen it would appear that this motion is small enough that it can be neglected. Even if this is not the case, as long as the motion can be predicted accurately then the results shown in the figure are still a valid indication of error due to prediction.

#### Time-to-Fire Algorithm

Figure 14 shows the simplest estimation and prediction scheme that is in the spirit of the Kalman filter and that also employs a second-order system plant. The computation indicated in the figure is based on a system that is less complex than the one discussed so far. This particular estimation filter and predictor was derived from a system model with only a single measurement transducer (for each plane), with white noise directly corrupting the measurement and directly forcing the plant. In practice the Kalman filter gains,  $k_1$  and  $k_2$ , would be obtained by utilizing recordings of real world data. The gains would then be optimized for minimization of estimation and prediction errors. The constants  $g_1$  and  $g_2$  are used to obtain the prediction based on the estimation of  $\xi$  and  $\dot{\xi}$ .

To obtain a prediction of muzzle position the separately measured motion in the vertical and horizontal planes must be combined in some rational manner. Let the plane at the muzzle which is perpendicular to the gun tube's undisturbed centerline be denoted as the V-H plane. Now define displacement in the vertical and horizontal planes as  $\xi_V$  and  $\xi_H$  and let  $2\phi$  denote the square of the deviation of the muzzle from its nominal position, i.e.,

$$2\phi(t) = \hat{\xi}_V(t)^2 + \hat{\xi}_H(t)^2$$

Further, if it is assumed that  $\dot{\xi}_V$  and  $\dot{\xi}_H$  contribute little to the projectile's inaccuracy, then the time-to-fire criterion should be

$$\dot{\phi}(t + \Delta t) = 0 \quad \text{given that } \ddot{\phi} > 0$$

The derivative of  $\phi$  is equal to the sum of the products of the displacement and velocity.

$$\dot{\phi}(t + \Delta t) = \hat{\xi}_V(t + \Delta t) \dot{\hat{\xi}}_V(t + \Delta t) + \hat{\xi}_H(t + \Delta t) \dot{\hat{\xi}}_H(t + \Delta t)$$

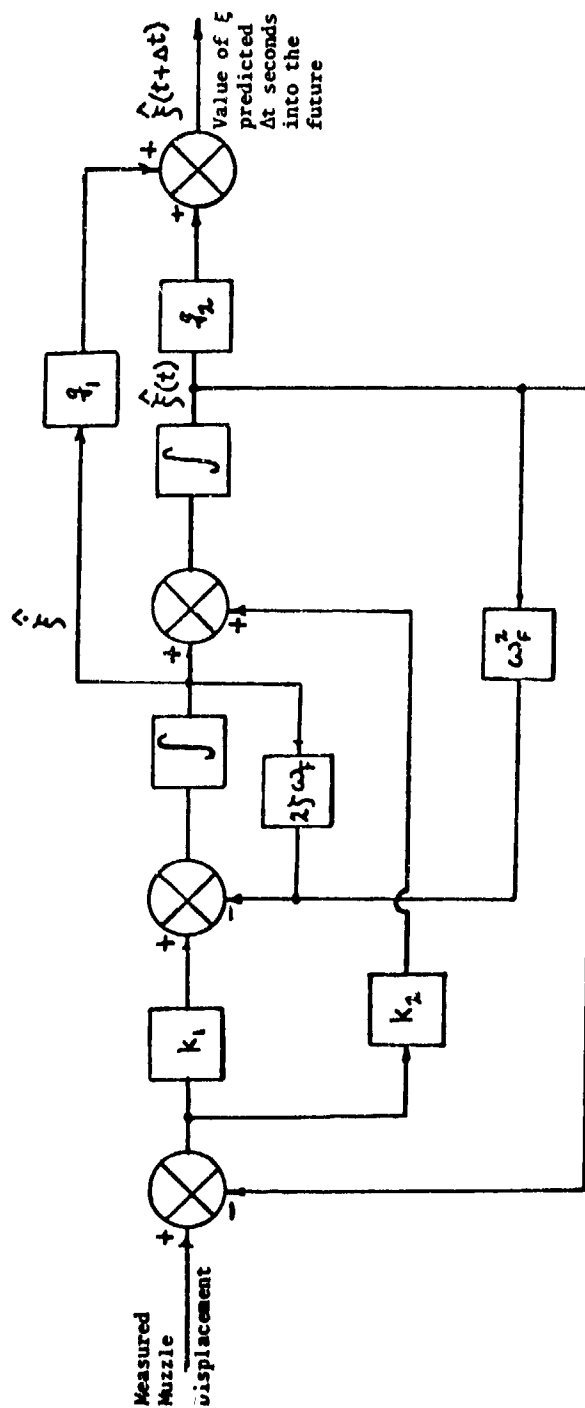


FIGURE 14. ANALOG COMPUTATION OF PREDICTION SCHEME

LEVIN

An indication of the sign of  $\ddot{\phi}$  can be determined by passing the signal through a first-order analog filter and then comparing it with the original signal. A block diagram of a computational scheme for producing the firing signal is shown in Figure 15. The total analog computation for the proposed simplified time-to-fire algorithm is found in Figures 14 and 15. It is seen from the figures that the computation requires only the following major components:

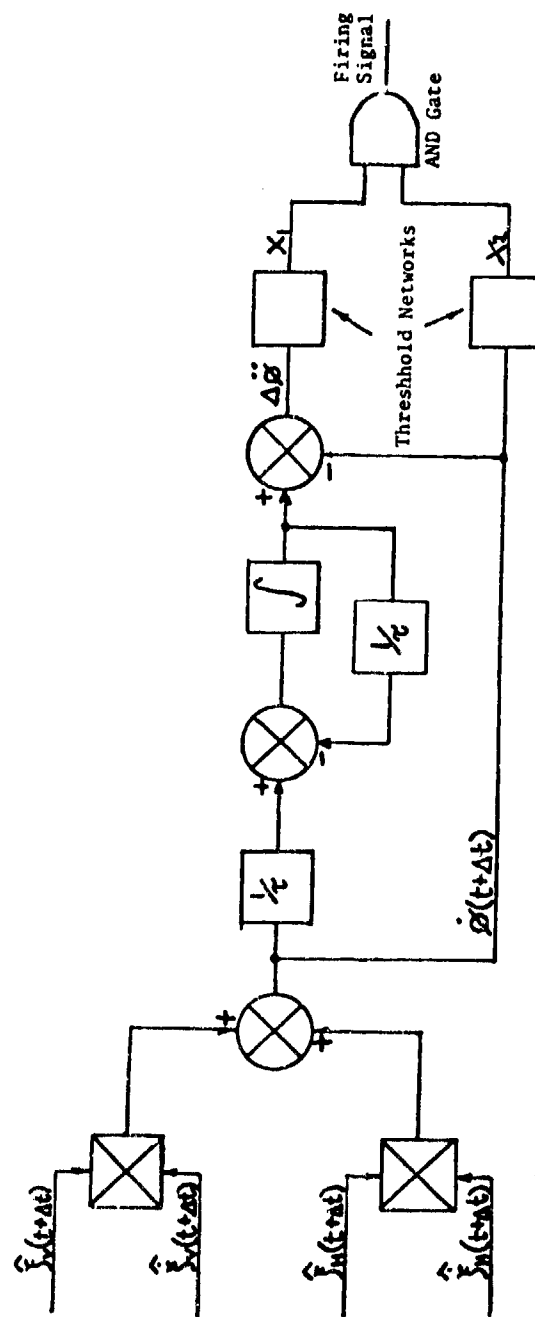
- 5 integrators
- 2 analog multipliers
- 2 threshold networks
- 1 AND gate

It is expected that hardware implementation would cost only a few hundred dollars since only low-cost "electronic store" type components are needed.

### CONCLUSIONS

A list of conclusions that can be drawn from this study effort are given below.

- (1) A Kalman filter is the best choice for conducting muzzle state estimation and prediction within the context of a time-to-fire algorithm.
- (2) The analytical model of the physical plant should be based on a black box approach.
- (3) Rarden gun experimental data suggest that the following black box representation can be utilized: motion in the horizontal and vertical planes can be treated separately and, in each plane, the motion can be given by a linear second-order differential equation with constant coefficients. The black box can be thought of as a local linearity such that the black box's parameters can be varied in accordance with the generalized conditions prevailing at the time that the time-to-fire calculation is to be exercised.
- (4) A total system model that utilizes colored forcing noise and measurements corrupted with colored noise can be used to lend insight into the effects of measurement noise, modeling errors, and magnitude of forcing input acceleration.



Firing Logic:  $x_1 = 1$  for  $\Delta\phi < 0$   
 $x_2 = 1$  for  $|\phi| < \text{Threshold}$   
 Fire when  $x_1$  AND  $x_2 = 1$

FIGURE 15. SCHEMATIC OF ANALOG COMPUTATION TO PRODUCE TIME-TO-FIRE SIGNAL

LEVIN

- (5) If it required that  $\text{rms}(\text{muzzle displacement})$  be less than several tenths of a millimeter then acceleration measurements will contribute little unless the accuracy is considerably better than 0.001 g. Thus, muzzle displacement or slope measurement alone is probably sufficient.
- (6) Reasonably good estimates of muzzle linear transverse velocity and acceleration can be derived from the displacement measurements.
- (7) The comments in (5) and (6) are applicable even when the input noise forcing the second-order physical system is extremely large. Since part of this noise input can be attributed to modeling error, the rather crude second-order model may be adequate even for fairly complex muzzle behavior. All of these comments are predicated, however, on computer-derived values of the steady-state estimation errors. The time to reach steady-state conditions may be excessive when the forcing noise input is very large, which would then indicate that very large modeling errors are not suitable.
- (8) It is suggested that a particular highly simplified time-to-fire algorithm may be adequate. The computations inferred by the algorithm can be performed with low-cost analog components. The analog computations would be extremely fast, thus, keeping the prediction time interval to a minimum.

APPENDIX A

NOMENCLATURE

B	Matrix whose elements represent the bandwidth, in rad/sec, of the first-order analog filters that are used to color white noise.
C	Measurement gain matrix
E()	Expected value of a random variable
$f_F$	First mode frequency of vibrating uniform thickness gun tube and/or natural frequency of second-order system plant representing muzzle oscillations in a single plane, Hz
F	Matrix of known functions that describe the system plant. In this report the plant is augmented to include the analog filter that colors the forcing input acceleration noise
m	Matrix of colored noise elements that corrupt the measurements
N	Nondimensional forcing input
n	Colored forcing acceleration noise
P	Covariance matrix of estimation errors of the state variables, if $x$ is defined as the state vector then $P$ is given as $E[(x - \hat{x})(x - \hat{x})^T]$
$Q_p, Q_m$	Zero white noise spectral densities
$RMS()$ , $rms()$	Root-mean-square value of the quantity within the parentheses, for a random variable $rms(x) = \sqrt{E(x^2)}$
S	State transition matrix
u	Matrix of white noise forcing acceleration
v	Matrix of white noise sources that are fed into the first-order analog coloring filters
x	Distance along the gun tube centerline
y	Measurement matrix whose elements contain colored noise
$\beta$	Bandwidth of first-order analog filters that color white noise
$\zeta$	Damping ratio of second-order system
$\xi$	Transverse displacement of muzzle due to gun tube vibration
$\xi_V, \xi_H$	Transverse displacements of the muzzle in the vertical and horizontal planes, respectively.

## LEVIN

- $d\xi/dx$  Slope of gun tube at the muzzle which can be attributed to gun tube vibration
- $\omega_F$  First mode frequency of gun tube and/or natural frequency of second-order system, rad/sec

## APPENDIX B

### REFERENCES

- (1) Levin, V., "Accuracy Improvement of Flexible Gun Tubes", Contract No. DAAK10-77-C-0174, Innovative Technology, Inc., Columbus, Ohio, June 1978.
- (2) Arora, J. S. and Haug, E. J., "A Finite Element Method of Optimizing Precision of a Vibrating Weapons", Proc., First Conference on Dynamics of Precision Gun Weapons, Rock Island, Illinois, January 1977.
- (3) Kalman, R. E., "A New Approach to Linear Filtering and Prediction Problems", Journal of Basic Engineering (ASME), Vol. 82D, March 1960.
- (4) Kalman, R. E., AND Bucy, R., "New Results in Linear Filtering and Prediction, Journal of Basic Engineering (ASME), Vol. 83D, 1961.
- (5) Bryson, A. E., Jr., and Johansen, D. R., "Linear Filtering for Time-Varying Systems Using Measurements Containing Colored Noise", IEEE Transactions on Automatic Control, January 1965.

APPENDIX C

FORMAT OF MATRIX EQUATIONS CORRESPONDING  
TO SYSTEM SHOWN IN FIGURE 6

Plant Matrix Equations  
(See Equations (1) and (2))

$$\begin{bmatrix} \ddot{n} \\ \ddot{\xi} \\ \ddot{\eta} \end{bmatrix} = \begin{bmatrix} -\beta & 0 & 0 \\ 0 & 0 & 1 \\ 1 & -\omega & -2\zeta\omega \end{bmatrix} \begin{bmatrix} n \\ \xi \\ \eta \end{bmatrix} + \begin{bmatrix} \beta u \\ 0 \\ 0 \end{bmatrix}$$

where

$$Q_p = \begin{bmatrix} Q_{p1} & 0 & 0 \\ 0 & 0 & 0 \\ 0 & 0 & 0 \end{bmatrix}$$

and

$$E[u(t)u(\tau)] = \frac{1}{\beta^2} Q_{p1} \delta(t-\tau)$$

Measurement Equations  
(See Equations (3) through (5))

$$\begin{bmatrix} y_1 \\ y_2 \end{bmatrix} = \begin{bmatrix} c_1 & -c_1\omega^2 & -2c_1\zeta\omega \\ 0 & c_2 & 0 \end{bmatrix} \begin{bmatrix} n \\ \xi \\ \eta \end{bmatrix} + \begin{bmatrix} m_1 \\ m_2 \end{bmatrix}$$

where

$$\begin{bmatrix} \dot{m}_1 \\ \dot{m}_2 \end{bmatrix} = \begin{bmatrix} -B_1 & 0 \\ 0 & -B_2 \end{bmatrix} \begin{bmatrix} n_1 \\ m_2 \end{bmatrix} - \begin{bmatrix} v_1 \\ v_2 \end{bmatrix}$$

and

$$Q_m = \begin{bmatrix} V_{11} & 0 \\ 0 & V_{22} \end{bmatrix}$$

$$V_{11} \delta(t-\tau) = E[v_1(t)v_1(\tau)]$$

$$V_{22} \delta(t-\tau) = E[v_2(t)v_2(\tau)]$$



Format of the Steady-State Kalman Filter Equations  
(See Equations (9) and (10))

$$\begin{bmatrix} \dot{\hat{n}} \\ \dot{\hat{s}} \\ \dot{\hat{s}} \end{bmatrix} = \begin{bmatrix} a_{11} & a_{12} & \cdot & \cdot & \cdot \\ \cdot & \cdot & \cdot & \cdot & \cdot \\ \cdot & \cdot & \cdot & \cdot & a_{35} \end{bmatrix} \begin{bmatrix} \hat{n} \\ \hat{s} \\ \hat{s} \\ y_1 \\ y_2 \end{bmatrix}$$

$$\begin{bmatrix} \hat{n} \\ \hat{s} \\ \hat{s} \end{bmatrix} = \begin{bmatrix} 1 & b_{12} & b_{13} \\ 1 & b_{22} & b_{23} \\ 1 & b_{32} & b_{33} \end{bmatrix} \begin{bmatrix} \hat{n} \\ \hat{s} \\ \hat{s} \end{bmatrix}$$

where the  $a_{ij}$  and the  $b_{ij}$  are constants for the steady-state filter but can be functions of time for the transient filter.

Prediction Equation  
(See Equation (12))

$$\begin{bmatrix} \hat{s}(t+\Delta t) \\ \hat{s}(t+\Delta t) \end{bmatrix} = \frac{1}{a_2 \cdot a_1} \begin{bmatrix} a_1 e^{-a_1 \Delta t} & -a_1 e^{-a_1 \Delta t} & e^{-a_1 \Delta t} \cdot e^{-a_1 \Delta t} \\ a_1 a_2 (e^{-a_1 \Delta t} - e^{-a_2 \Delta t}) & a_2 e^{-a_2 \Delta t} - a_1 e^{-a_1 \Delta t} \end{bmatrix} \begin{bmatrix} \hat{s}(t) \\ \hat{s}(t) \end{bmatrix}$$

where

$$a_1 = \omega(\zeta - j\sqrt{1-\zeta^2})$$

$$a_2 = \omega(\zeta + j\sqrt{1-\zeta^2})$$

$$j = \sqrt{-1}$$

$\Delta t =$  prediction time interval